

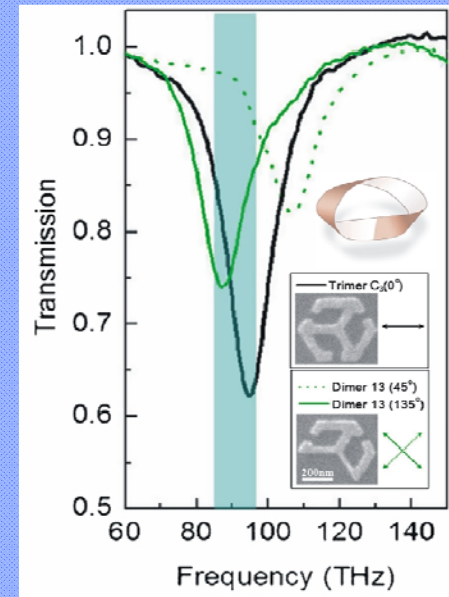
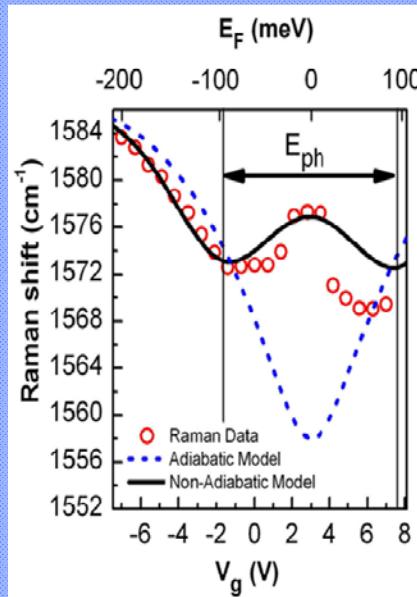
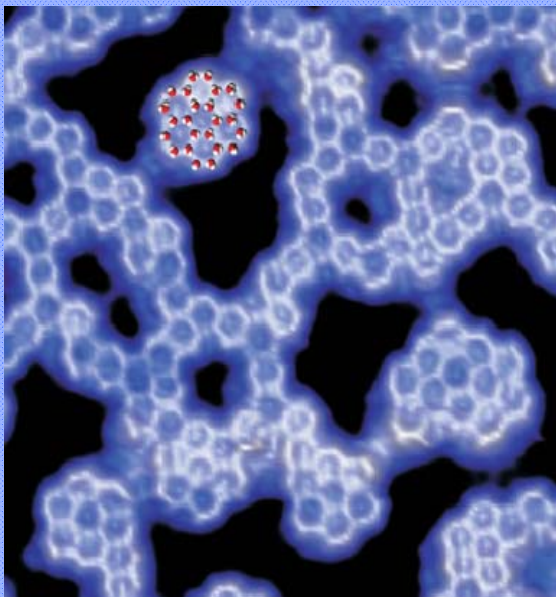
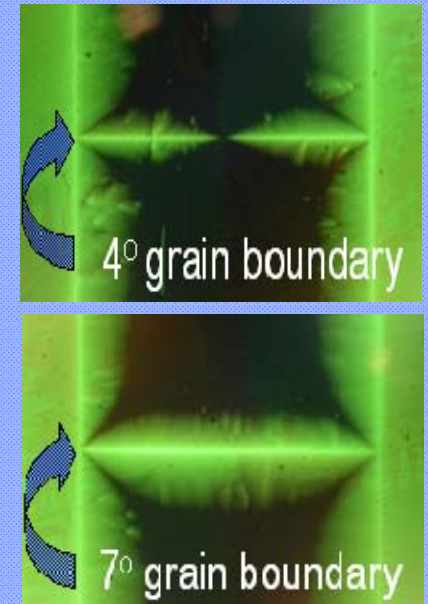
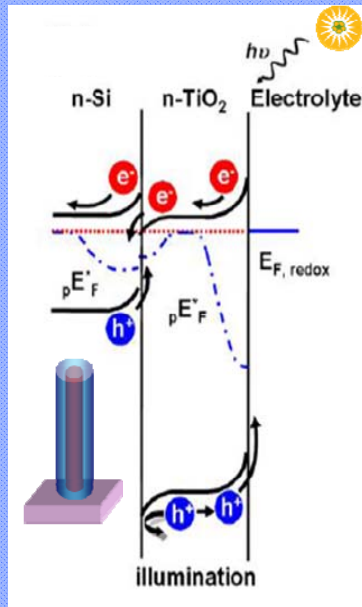
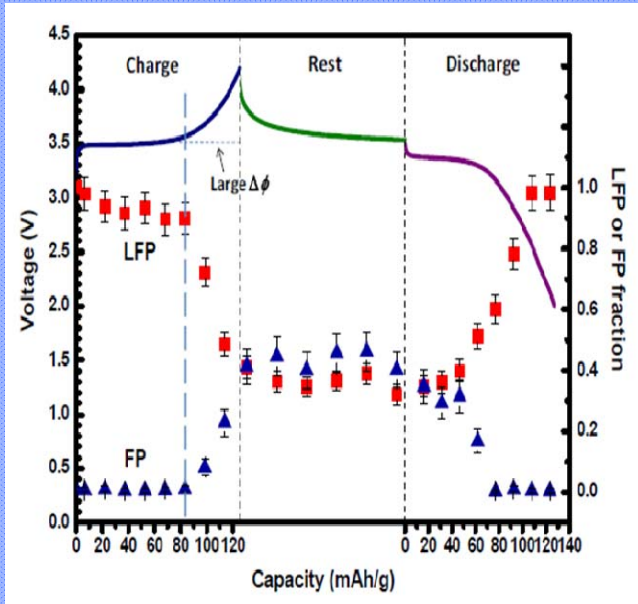
DOE - BES Contractors Meeting

Physical Behavior of Materials

Airlie Center, Warrenton, VA, March 6-9, 2011

Program and Abstracts

Chairs: Peidong Yang (LBNL), Gary L. Kellogg (SNL)



U.S. Department of Energy
Office of Science - Basic Energy Sciences
Division of Materials Sciences and Engineering



COVER

Top Left – In-situ synchrotron X-ray diffraction of lithium half-cell containing 34 nm $\text{Li}_{1-x}\text{FePO}_4$ as the positive electrode material undergoing galvanostatic charge and discharge at 1C rate with open-circuit hold in between. First charge/discharge cycle is shown. Results obtained at beamline X14A at BNL. (Yet-Ming Chiang et al., MIT)

Top Center – High-density Si/TiO₂ core-sheath nanowire arrays have been synthesized, using scalable processes (electroless etching and atomic layer deposition). Si/TiO₂ core/shell nanowire arrays show enhanced photoactivity compared to TiO₂ thin film on Si planar substrate. HELIOS SERC (Peidong Yang, Paul Alivisatos et al., LBNL)

Top Right – Magneto-optical images show that high angle grain boundaries are the key critical current limiting factor in YBa₂Cu₃O₇ film. These findings may enable superconducting magnet energy storage ARPA-e (SMES) for GRIDS. (Qiang Li et al., BNL)

Bottom Left – Scanning tunneling microscope image (courtesy of Miquel Salmeron) of water on palladium reveals hexagonal rings of water molecules self-assembled into narrow chains and clusters, as depicted in the superimposed illustration. This arrangement belies the long-held idea of the first water layer as a two-dimensionally continuous molecular mesh, similar to a single "puckered hexagonal" layer of a naturally occurring ice crystal. (Peter Feibelman, Sandia Nat. Labs.)

Bottom Middle – Pristine, nearly defect-free, suspended carbon nanotubes possess extremely long electron lifetimes, which result in a breakdown of the Born-Oppenheimer (adiabatic) approximation. This results in very different vibrational energies than occur in the adiabatic regime. (Steve Cronin et al., Univ. South. California)

Bottom Right – A new topological symmetry in electromagnetic metamaterial systems that is equivalent to the structural symmetry of a Möbius strip is observed. Figure shows the transmission spectra of trimer C3 and its constituent dimer (dimer 13). The number in the parenthesis and the arrows denote the incident polarization (chosen only to reveal the resonance frequencies clearly) angle. Trimer C3 spectrum shows a dip at 94 THz. Dimer 13 shows an antisymmetric mode at 87 THz and a symmetric mode at 107 THz; thus, coupling constant 13 is negative. The shaded area highlights the region where trimer C3 and dimer 13 exhibit overlapping resonances, indicating that the degenerate resonance of trimer C3 occurs at 94 THz. (Xiang Zhang et al., LBNL)

This document was produced under contract number DE-AC05-06OR23100 between the U.S. Department of Energy and Oak Ridge Associated Universities.

The research grants and contracts described in this document are supported by the U.S. DOE Office of Science, Office of Basic Energy Sciences, Materials Sciences and Engineering Division.

Foreword

This volume summarizes the scientific content of the 2011 research program meeting “Physical Behavior of Materials,” sponsored by the Division of Materials Sciences and Engineering (DMS&E) of the Office of the Department of Energy, Basic Energy Sciences (BES). The primary purpose of these BES program meetings is to provide an environment for the exchange of new information and ideas among grantees and contractors, and to foster synergistic activities among researchers. For the grantees, it facilitates an overview of the program useful to define a future scope for the program and identify promising new research directions. These meetings are designed to stimulate crosscutting and inspiring of new ideas, as it brings together leading experts in diverse fields of interest.

This meeting was held March 6–9, 2011, at the Airlie Conference Center in Warrenton, Virginia. The meeting was chaired by Peidong Yang (UC Berkeley) and Gary Kellogg (Sandia National Labs) and was attended by over 100 scientists, with 28 oral and 60 poster presentations in two different poster sessions. This year we were very pleased to have two very distinguished invited speakers, Prof. Ellen Williams, Chief Scientist of BP and Distinguished Professor of the University of Maryland, and Prof. Charles M. Lieber of Harvard University. They inspired us with their talks: *“Making energy sustainable – scientific challenges in determining the pathways to the future,”* and *“Semiconductor nanowires: a platform for nanoscience and nanotechnology,”* respectively.

The Physical Behavior of Materials program covers a very broad range of research activities, as suggested by its name. We organized this year’s presentations into seven different sessions using their subject similarities. These sessions were (1) Nano-Enabled Behavior, (2) Novel Electronic Materials, (3) Interfaces/Surfaces, (4) Hydrogen/Fuel Cells, (5) Magnetism/Spintronics, (6) Thermoelectrics/Structural Properties, and (7) Photovoltaics/Photon.

We gratefully acknowledge the contributions of all the participants for their investment of time and for their willingness to share their ideas with the meeting participants. We also want to gratefully acknowledge the excellent support of Lee-Ann Talley and Joreé O’Neal from the Oak Ridge Institute for Science and Education, and Teresa Crockett of our Division, and the staff of the Airlie Conference Center.

Refik Kortan
Program Manager,
Division of Materials Sciences and Engineering
Office of Basic Energy Sciences
Department of Energy
March 2011

Table of Contents

Foreword	i
Table of Contents	iii
Agenda	xi

Invited Talks

Making Energy Sustainable – Scientific Challenges in Determining the Pathways to the Future <i>Ellen Williams</i>	1
Semiconductor Nanowires: A Platform for Nanoscience and Nanotechnology <i>Charles M. Lieber</i>	2

Session I: Nano-Materials

Electrochemically-Driven Phase Transitions in Battery Storage Compounds <i>Yet-Ming Chiang and Craig Carter</i>	3
Imaging Carrier Generation, Transport, and Collection in Nanostructured Materials <i>Lincoln J. Lauhon</i>	7

Session II: Novel Electronic Materials

Superconducting Materials <i>Qiang Li</i>	11
Investigation of Sb-Doped p-Type ZnO Thin Films for Solid State Lighting <i>Jianlin Liu</i>	15
Red, Green, Blue Luminescent Media Incorporating Colloidal Semiconductor Quantum Dots within a Nanoporous Gallium Nitride LED Matrix <i>Arto V. Nurmikko and Jung Han</i>	19
The Electronic Materials Program at LBNL <i>E. E. Haller, J. W. Ager III, D. C. Chrzan, O. D. Dubón, Z. Liliental-Weber, W. Walukiewicz, and K. M. Yu</i>	20

Session III: Interfaces/Surfaces

Proximity Effects in Charged Oxide Heterostructures <i>J. A. Eastman, D. D. Fong, P. H. Fuoss, and P. Zapol</i>	25
Nanometer-Scale Surface and Interface Phenomena <i>Peter Feibelman, Norman Bartelt, Gary Kellogg, Kevin McCarty, Nancy Missert, Brian Swartzentruber, Konrad Thürmer, and Kevin Zavadil</i>	29
Classical and Quantum Stress Effects in Nano Thin Films and in Doping of Semiconductors <i>Feng Liu</i>	33
Interfaces in Electronic and Structural Materials <i>Yuri Mishin</i>	37

Session IV: Hydrogen-Energy, Fuel Cells, Membranes

Thermodynamic, Kinetic and Electrochemical Studies in Mixed Proton, Oxygen Ion, and Electron (Hole) Conductors <i>Anil V. Virkar</i>	41
Complex Hydrides – A New Frontier for Future Energy Applications <i>V. K. Pecharsky, M. Pruski, L. S. Chumbley, and P. Jena</i>	45
NMR of Hydrogen Storage Solids: Ionic Hydrides and Mobile Species <i>Mark S. Conradi</i>	49

Session V: Magnetism/Multiferroics/Spintronics

Field-Structured Composites <i>James E. Martin</i>	53
Intensive Variables and Nanostructuring in Magnetostructural Materials <i>Laura H. Lewis</i>	57
Coherent Control of Spin States in Organic Electronics <i>Christoph Boehme and John M. Lupton</i>	59
Magnetic Frustration and Cooperative Phenomena in Correlated Electron Oxide Materials <i>Hariharan Srikanth, M. H. Phan, Nicholas Bingham, Nicholas Laurita</i>	63

Session VI: Thermoelectrics, Ferroelectrics, and Structural Properties

Measurement of Near-Field Thermal Radiation between Flat Surfaces with a Nanogap
Zhuomin Zhang67

Electric Field Effects in Liquid Crystals with Dielectric Dispersion
Oleg D. Lavrentovich and Sergij V. Shiyankovskii71

Characterization of High Density/High Stability Glasses
Mark Ediger, Kevin Dawson, Zahra Fakhraai, and Shakeel Dalal75

Bridging Atomistic and Continuum Scales in Phase-Field Modeling of Stressed Polycrystalline Materials
Alain Karma.....79

Session VII: Photovoltaics–Solar Energy, Photonic Crystals, Nanophosphors

Optical Metamaterial Physics and Applications
Xiang Zhang, Eli Yablonovitch, Yuen-Ron Shen, and Feng Wang.....83

Light Trapping with Photonic Crystals
Sajeev John and Guillaume Demesy.....84

Nanophotonics-Enhanced Solar Cells
Shanhui Fan and Mark Brongersma86

Nanocrystal-Based Dyads for Solar to Electric Energy Conversion
David Waldeck, D. N. Beratan, and Ron Naaman90

Structure-Optical-Thermal Relationships of Carbon Nanotubes Energy Transport in Graphene
Stephen Cronin and Li Shi.....94

Poster Sessions

Poster Session I99

Poster Session II.....102

Poster Abstracts

Electron and Hole Transport in Indium Nitride
J. W. Ager III, K. M. Yu, J. Wu, E. E. Haller, Z. Liliental-Weber, W. Walukiewicz, Y. Nanishi, J. Speck, W. J. Schaff, and I. Gherasoiu105

Understanding Compound Phase Transitions in New Heusler Alloy Giant Magnetocaloric Materials: Extension to Multifunctional Materials <i>Naushad Ali and Shane Stadler</i>	108
Plasmonic Photovoltaics <i>Harry A. Atwater</i>	112
High Performance Nano-Crystalline Oxide Fuel Cell Materials: Defects, Structures, Interfaces, Transport, and Electrochemistry <i>S. A. Barnett, D. Ellis, L. D. Marks, T. O. Mason, K. Poepelmeier, and P. W. Voorhees</i>	116
The Factors that Influence Graphene Growth on Metal Surfaces <i>N. C. Bartelt, E. Starodub, P. J. Feibelman, S. Nie, and K. F. McCarty</i>	120
Theory and Modeling of Materials for Hydrogen Storage <i>Gerbrand Ceder</i>	124
Near-Field Thermal Radiation at Extreme Separations <i>Gang Chen</i>	126
Experimental and Theoretical Studies of Embedded Nanostructures <i>Daryl C. Chrzan, Joel W. Ager III, Ali Javey, and Eugene E. Haller</i>	130
Characterization of Functional Nanomachines <i>M. F. Crommie, C. Bustamante, M. L. Cohen, J. M. J. Frechet, S. G. Louie, and A. Zettl</i>	134
Nanocomposite Proton Conductors <i>Lutgard C. De Jonghe, Mark Asta, Jeffrey A. Reimer, and Philip N. Ross</i>	138
Ultra-fast, Laser-Thermal Processing of Semiconductors <i>O. D. Dubón, E. E. Haller, J. W. Ager III, D. C. Chrzan, Z. Liliental-Weber, W. Walukiewicz, K. M. Yu, and J. Wu</i>	142
Structural and Electrostatic Effects in Self-Assembled Nanostructures <i>Helen H. Farrell</i>	146
Crystallization and Thermoelectric Transport in Silicon Microstructures and Nanostructures under Extreme Electrical Stress <i>Ali Gokirmak and Helena Silva</i>	150
Extraordinary Responsive Magnetic Rare Earth Materials <i>K. A. Gschneidner Jr. and Vitalij K. Pecharsky</i>	154

Supported, Coated, and Ligated Metal Clusters <i>Puru Jena</i>	158
Understanding and Design of Polymer Device Interfaces <i>Antoine Kahn, Jean-Luc Brédas, Anil Duggal, George Malliaras, and Bernard Kippelen</i>	163
Ultrathin Iron Oxide Growth on YSZ Single-Crystal Surfaces <i>G. L. Kellogg and Ivan Ermanoski</i>	166
Enhancement of the Field-Induced Strain in Multiferroics <i>Wei-Feng Rao and A. G. Khachatryan</i>	170
Hydrogen Absorption in Pd-Based Nanostructures <i>David Lederman</i>	174
Manipulation of Phonons with Phononic Crystals <i>Zayd Chad Leseman and Ihab El-Kady</i>	178
MuSR Investigations of Magnetic Semiconductors for Spintronics Applications <i>Roger L. Lichti</i>	182
Architectural Photonics for Maximizing Solar Energy Conversion <i>Shawn-Yu Lin</i>	186
Exceeding the Planck Free-Space Energy Transfer Limit through Photonic Density of States Control and Near Field Coupling <i>Ting S. (Willie) Luk</i>	190
Dipolar Ferromagnets for Magnetocaloric Effect Nanocomposites <i>Sara A. Majetich</i>	194
Surface Engineering by Simultaneous Action of Multiple External Fields <i>Dimitrios Maroudas and M. Rauf Gungor</i>	198
Electronic Processes in Solid State Organic Electronic Materials <i>Richard L. Martin, Enrique Batista, Ian Campbell, and Darryl Smith</i>	202
Electronic and Optical Processes in Novel Semiconductors for Energy Applications <i>A. Mascarenhas, Brian Fluegel, Kirstin Alberi, and Yong Zhang</i>	206
Optical Properties of Doped ZnO Nanocrystals and Ceramics <i>Matthew D. McCluskey and Leah Bergman</i>	210

Evolution of Oxide Stability during Localized Corrosion of Model Al-Cu Alloys <i>Nancy Missert, R. Guild Copeland, Paul Kotula, Jonathan Rivera, and Robert Garcia</i>	214
Nanophosphors: Fundamental Science of Insulators in the Nanoscale Regime <i>Ross E. Muenchausen, Markus P. Hehlen, John C. Gordon, Cindy F. Welch, Michael W. Blair, Nickolaus A. Smith, Bryan L. Bennett, Stephanie A. Tornga, and Kalyan V. Vasudevan</i>	218
Carbon Surface Diffusion and Strain Development during the Growth of Epitaxial Graphene on SiC <i>Taisuke Ohta, Norman C. Bartelt, Shu Nie, Konrad Thürmer, Gary L. Kellogg, Laura B. Biedermann, Thomas E. Beechem, Stephen W. Howell, and Diedrich A. Schmidt</i>	222
Enhancement in Thermoelectric and Photovoltaic Properties by Nanostructure Approach <i>Z. F. Ren</i>	226
Fundamental Studies of Unconventional Sulfide Semiconductors for Cost-Effective and Environmentally Benign Thin Film Photovoltaics <i>Mike Scarpulla and Loren Rieth</i>	229
Nanostructured Thermoelectric Materials <i>Rachel A. Segalman, Peidong Yang, Ramesh Rammamorthy, Joel More, Jeffrey J. Urban, Renkun Chen, Shannon K. Yee, Nelson Coates, Jayakanth Ravichandran, Hung-Ta Wang, Pouyan Ghaemi, and Kedar Hippalgaonkar</i>	233
Study of Materials and Interface Properties for High-Efficiency Spin Injection <i>Jing Shi</i>	237
Energy Transport in Graphene <i>Li Shi, S. B. Cronin</i>	241
Phase Transformations in Confined Nanosystems <i>Jeffrey E. Shield, Kirill Belashchenko, Matthew J. Kramer, and G. Malcolm Stocks</i>	245
Spin Polarized Functionality through Complex Oxide Heteroepitaxy <i>Yuri Suzuki</i>	249
Structure and Magnetism in Novel Group IV Element-Based Magnetic Materials <i>Frank Tsui</i>	252
Understanding the Spin-Lattice Coupling in Multiferroic Oxides <i>Trevor A. Tyson</i>	255

Complex Amorphous Transition-Metal Dielectrics <i>R. Bruce van Dover, Taro Naoi, and Hanjong Paik</i>	261
Mesoscale Interfacial Dynamics in Magnetoelectric Nanocomposites <i>Dwight Viehland, Shashank Priya, and Armen Khachaturyan</i>	265
Domain Microstructures and Mechanisms for Large, Reversible and An hysteretic Strain Behaviors in Phase Transforming Ferroelectric Materials <i>Yu U. Wang</i>	269
Piezoelectric Nanogenerators for Self-Powered Nanosystems and Nanosensors <i>Zhong Lin Wang</i>	273
Dynamical Materials Nanostructures for Energy Technology <i>Junjiao Wu, Daryl C. Chrzan, Kin M. Yu, Jeffrey C. Grossman, L. Q. Chen, Renkun Chen, and Markus Raschke</i>	276
Fabricating Efficient p-Type Dye-Sensitized Solar Cells <i>Yiying Wu</i>	280
Nanolamellar Magnetoelectric BaTiO₃-CoFe₂O₄ Bicrystal <i>Shenqiang Ren and Manfred Wuttig</i>	284
Nanoscale Oxide Thin Films and Heterostructures by Laser Molecular Beam Epitaxy <i>Xiaoxing Xi</i>	285
Suspensions of Monodisperse Nanoparticles as Model Systems for Probing Heat Transfer Mechanisms in Nanofluids <i>Bao Yang and Michael R. Zachariah</i>	287
Machine Learning Approaches to Crystal Structure Prediction <i>Lusann Yang, Geoffroy Hautier, and Gerbrand Ceder</i>	291
Fundamentals of Semiconductor Nanowires <i>Peidong Yang</i>	292
Interband Cascade Photovoltaic Cells <i>Rui Q. Yang, Michael B. Santos, and Matthew B. Johnson</i>	296
Hetero-junctions of Boron Nitride and Carbon Nanotubes: Synthesis and Characterization <i>Yoke Khin Yap</i>	300

Advanced Concepts and Materials for Solar Power Conversion: From Basic Science to Applications <i>K. M. Yu, Z. Liliental-Weber, O. D. Dubón, J. Wu, and W. Walukiewicz</i>	304
Elucidation of Hydrogen Interaction Mechanisms with Metal Doped Carbon Nanostructures <i>Ragay Zidan, Joseph A. Teprovich Jr., Douglas A. Knight, and Lucile Teague</i>	308
Author Index	313
Participant List	315

Physical Behavior of Materials Contractors Meeting

AGENDA

Sunday, March 6, 2011

3:00 – 6:00 pm	Registration
5:00 – 6:00 pm	Reception (No Host)
6:00 – 7:00 pm	***** Dinner *****
7:30 – 8:00 pm	Welcome Division and Program Updates Linda Horton, <i>Director, Division of Materials Science and Engineering</i> Refik Kortan, <i>Program Manager, Physical Behavior of Materials</i>
8:00 – 8:45 pm	Ellen Williams, <i>Chief Scientist, BP</i> <i>Distinguished University Professor, Univ. of Maryland</i> <i>Invited Talk: “Making Energy Sustainable – Scientific Challenges in Determining the Pathways to the Future”</i>

Monday, March 7, 2011

7:00 – 8:00 am	Breakfast
Session I	Nano-Materials <i>Chair: Peidong Yang (UC Berkeley)</i>
8:05 – 8:45 am	Charles M. Lieber (<i>Harvard University</i>) <i>Invited Talk : “Semiconductor Nanowires: A Platform for Nanoscience and Nanotechnology”</i>
8:45 – 9:15 am	Yet-Ming Chiang (<i>MIT</i>)
9:15 – 9:45 am	Lincoln Lauhon (<i>Northwestern Univ.</i>)
9:45 – 10:00 am	***** Break *****
Session II	Novel Electronic Materials <i>Chair: Antoine Kahn (Princeton)</i>
10:00 – 10:30 am	Qiang Li (<i>BNL</i>)
10:30 – 11:00 am	Jianlin Liu (<i>UC Riverside</i>)

11:00 – 11:30 am	Arto Nurmikko (<i>Brown Univ.</i>)
11:30 – 12:00 pm	Wladek Walukiewicz (<i>LBNL</i>)
12:00 – 1:00 pm	***** Lunch *****
1:00 – 3:00 pm	Time for Interactions & Discussions
3:00 – 5:30 pm	Poster Session I
5:30 – 6:30 pm	***** Dinner *****
Session III	Interfaces/Surfaces <i>Chair: Gary L. Kellogg (SNL)</i>
6:30 – 7:00 pm	Jeffrey Eastman (<i>ANL</i>)
7:00 – 7:30 pm	Peter J. Feibelman (<i>SNL</i>)
7:30 – 8:00 pm	Feng Liu (<i>Univ. of Utah</i>)
8:00 – 8:30 pm	Yuri Mishin (<i>George Mason Univ.</i>)
8:30 – 10:00 pm	Continuation of Poster Session I

Tuesday, March 8, 2011

7:00 – 8:00 am	Breakfast
Session IV	Hydrogen-Energy, Fuel Cells, Membranes <i>Chair: Puru Jena (Virginia Commonwealth Univ.)</i>
8:15 – 8:45 am	Anil Virkar (<i>Univ. of Utah</i>)
8:45 – 9:15 am	Vitalij Pecharsky (<i>Ames Laboratories</i>)
9:15 – 9:45 am	Mark Conradi (<i>Washington Univ.</i>)
9:45 – 10:00 am	***** Break *****
Session V	Magnetism/Multiferroics/Spintronics <i>Chair: Karl A. Gschneidner (Ames Laboratories)</i>
10:00 – 10:30 am	Jim Martin (<i>SNL</i>)
10:30 – 11:00 am	Laura Lewis (<i>Northeastern Univ.</i>)
11:00 – 11:30 am	Christopher Boehme (<i>Univ. of Utah</i>)
11:30 – 12:00 pm	Hariharan Srikanth (<i>Univ. of South Florida</i>)
12:00 – 1:30 pm	***** Lunch *****
1:30 – 3:00 pm	Time for Interactions & Discussions
3:00 – 5:30 pm	Poster Session II
5:30 – 6:30 pm	***** Dinner *****
Session VI	Thermoelectrics, Ferroelectrics and Structural Properties <i>Chair: Gang Chen (MIT)</i>

6:30 – 7:00 pm	Zhuomin Zhang (<i>Georgia Institute of Technology</i>)
7:00 – 7:30 pm	Oleg Lavrentovich (<i>Kent Univ.</i>)
7:30 – 8:00 pm	Mark Ediger (<i>Univ. of Wisconsin</i>)
8:00 – 8:30 pm	Alain Karma (<i>Northeastern Univ.</i>)
8:30 – 8:50 pm	Special Presentation: "How Rare are Rare-Earths; a Global Crisis ?" Karl A. Gschneidner (<i>Ames Laboratories</i>)
8:50 – 10:00 pm	Continuation of Poster Session II

Wednesday, March 9, 2011

7:00 – 8:00 am	Breakfast
Session VII	Photovoltaics—Solar Energy, Photonic Crystals, Nanophosphors <i>Chair: Harry Atwater (Caltech)</i>
8:15 – 9:00 am	Xiang Zhang (<i>UC Berkeley</i>)
9:00 – 9:30 am	Sajeev John (<i>Univ. of Toronto</i>)
9:30 – 10:00 am	Shanhui Fan (<i>Stanford Univ.</i>)
10:00 – 10:15 am	***** Break *****
10:15 – 10:45 am	David Waldeck (<i>Univ. of Pittsburgh</i>)
10:45 – 11:15 am	Steve Cronin (<i>Univ. South. California</i>)
11:15 – 11:45 am	Closing Remarks by Meeting Chairs and PM Peidong Yang and Gary Kellogg, Refik Kortan
11:45 am – 1:00 pm	Lunch, Open Discussions, and Adjourn

Invited Talks

Prof. Ellen Williams

Chief Scientist, BP

Distinguished University Professor, Univ. Maryland

**Making energy sustainable – Scientific challenges in determining the pathways
to the future**

The scale and cost of the energy challenge are immense. Everyone wants secure, reliable, and affordable energy, but climate change, demand growth and, increasingly, resource scarcity, are transforming the energy landscape and it will continue to evolve.

There are many possible technical pathways to a low-carbon energy future, and each presents unresolved technical challenges that will influence the time, money and global-scale asset and infrastructure deployment that will take place over the next decades. BP's energy portfolio demonstrates many of the research challenges in this arena, and some examples from Carbon Capture and Storage and Biofuels will be discussed here specifically. Ultimately, research, technology, policies and partnerships will determine the pace of change – get the balance right, and we can accelerate the transition to a more sustainable energy future.

Prof. Charles M. Lieber

Harvard University

Semiconductor Nanowires:

A Platform for Nanoscience and Nanotechnology

Advances in nanoscience and nanotechnology depend critically on development of nanostructures whose properties are controlled during synthesis. Here we focus on this critical concept using semiconductors nanowires, which provide the capability for synthetic design to realize unprecedented structural and functional complexity in building blocks, as a platform material. First, a brief review of the synthesis of complex modulated nanowires in which rational design can be used to precisely control composition, structure and most recently structural topology will be discussed. Second, the unique functional characteristics emerging from our exquisite control of nanowire materials will be illustrated with several selected examples from nanoelectronics, quantum electronics and nano-enabled energy. Third, the remarkable power of nanowire building blocks will be further highlighted through their capability to create unprecedented active electronic interfaces with biological systems. Recent work pushing the limits of both multiplexed extracellular recording at the single cell level and the first examples of intracellular recording will be described, as well as the prospects for truly blurring the distinction between nonliving and living information processing systems.

Session I

Nano-Materials

Electrochemically-Driven Phase Transitions in Battery Storage Compounds (DOE-BES grant no. DE-SC0002626)

PI: Yet-Ming Chiang Co-PI: W. Craig Carter
Room 13-4086, Massachusetts Institute of Technology
Cambridge, MA 02139
E-mail: ychiang@mit.edu

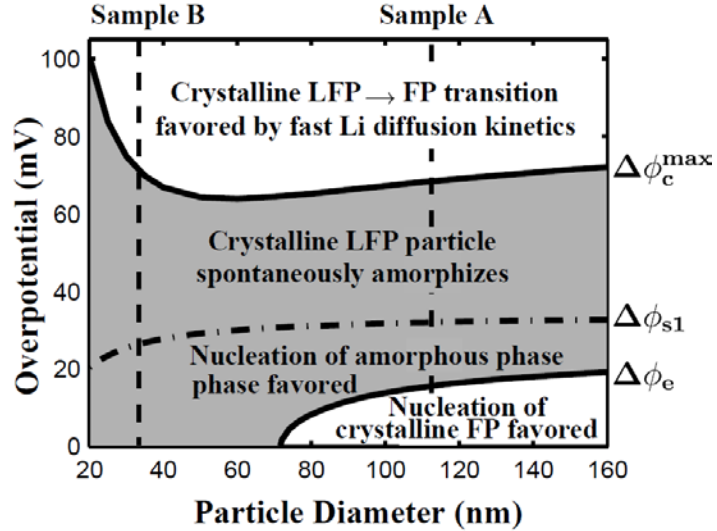
Objectives: This program is a combined experimental and theoretical investigation of the effect of electrochemical driving force (applied electrical potential and current) on phase stability and phase transformation pathway in lithium intercalation compounds. The initial focus has been on lithium transition metal olivines, exemplified by LiFePO_4 . In particular, the effects of particle size and electrical over- and underpotential, which are the electrical analogs to undercooling and superheating, have been explored.

Recent results from a phase-field model [1-3] are summarized in Figure 1. Starting with fully lithiated LiFePO_4 , the preferred phase transition as the compound is delithiated (charged, in a lithium-ion battery) is shown as a function of particle size and overpotential. The overpotential-dependence of the phase transformation pathway can be understood as an influence of driving force on nucleation and growth kinetics of competing phase transitions. We previously developed a diffuse-interface (phase-field) model from which the nucleation energy barriers associated with the crystalline-to-crystalline and crystalline-to-amorphous transitions can be calculated as a function of the overpotential, particle size and misfit strain. In this model, the delithiated amorphous phase has lower surface energy than its crystalline counterpart. The amorphous-phase nucleation activation-energy decreases with particle size; and, during charging, this nucleation barrier decreases with increasing overpotential, $\Delta\phi$. The results, calculated using materials parameters appropriate to $\text{Li}_{1-x}\text{FePO}_4$, map the preferred phase transformation pathway in a $\Delta\phi$ - particle size coordinate system as seen in Figure 1. The crystalline-to-amorphous phase transition is preferred (i.e., having a smaller activation energy) above a critical value of overpotential, $\Delta\phi_{\text{crit}}$, which at large particle sizes is calculated to be ~ 20 mV (equivalent to an undercooling of $\sim 230\text{K}$ for a thermal phase transition). The model predicts that $\Delta\phi_{\text{crit}}$ decreases with particle size, and vanishes below a critical size of about 70 nm.

In the current work, a new prediction of the model is the existence of a secondary crystalline-to-crystalline phase transition pathway above a critical overpotential, $\Delta\phi_c^{\text{max}}$ (Fig. 1). $\Delta\phi_c^{\text{max}}$ is a predicted upper bound to the overpotential at which amorphization is preferred. In contrast to supercooled thermal phase transitions, here the kinetics does not have a similar decrease with increasing driving force. At larger overpotentials ($> \Delta\phi_{s1}$), nucleation of the amorphous phase is expected to become very facile, and its *growth* may become rate-limiting. The phase-field model includes competing kinetic processes involved in the two transformation pathways. In addition, a higher overpotential should generate a larger Li^+ out-flux from the particles while having no direct effect on the structural disordering kinetics. In contrast to the crystalline-crystalline transformation

where the relative atomic positions are fixed, the crystalline LFP to delithiated amorphous transition requires coupled lithium diffusion and structural disordering at the growth front. At sufficiently large overpotentials, the structural disordering process becomes slow compared to lithium diffusion. As a result, the direct crystalline phase transformation, which can be accommodated by lithium diffusion alone, reemerges as the preferred transition. Note that the range of overpotentials over which amorphization is preferred broadens with decreasing particle size.

Figure 1. Phase transition map calculated from a phase-field model, showing the preferred phase transition pathways upon delithiation of a crystalline LFP particle as a function of the overpotential, $\Delta\phi$, and particle size. Results are calculated for 2% linear misfit strain, appropriate to crystalline LiFePO_4 (LFP) and FePO_4 (FP). Samples A and B correspond to experimental samples.



A dramatic experimental confirmation of the results in Figure 1 is the observation that it is possible to completely amorphize LiFePO_4 by electrochemical cycling over an appropriate range of overpotentials. This is shown by the galvanostatic test results in Figure 2, obtained using *in-situ* synchrotron X-ray diffraction experiments conducted at Brookhaven National Laboratory. In Fig. 2A, Sample A, having 113nm crystallite size, was first cycled for 4 cycles at a 1C rate (1 hr for complete charge or discharge), then at 5C rate (1/5 hr for complete charge or discharge) for an additional 4 cycles. At the 1C rate, the fraction of the lithiated phase, LFP, oscillates within each cycle, but diminishes with sequential cycles. The amount of delithiated phase, FP, in the first cycle was negligible because the sample was only charged to 50% state-of-charge (SOC) before discharging. Thereafter, the fraction of FP increases during charge but never exceeds 40%. At a cycling rate of 5C, however, the both crystalline phase fractions diminish sharply and remain below 20% throughout cycling. The capacity obtained during each cycle is also shown in the figure; the coulombic efficiency was $> 98\%$ for all cycles. Results for Sample B (Figure 2B) show similar oscillations in the amount of LFP and FP during 1C cycling, but upon 5C cycling, virtually no FP phase is detectable, and the LFP fraction is only a few percent. Note that in both samples, the measured capacity at 5C rate cannot be explained by the amount of crystalline phase present. This shows unequivocally that the amorphous phase is electrochemically active; in fact it contributes most of the observed reversible capacity.

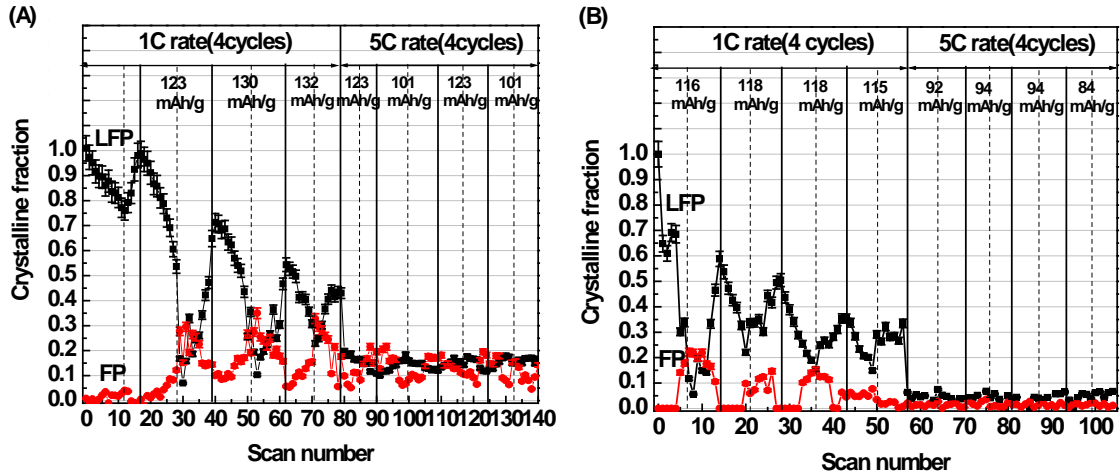
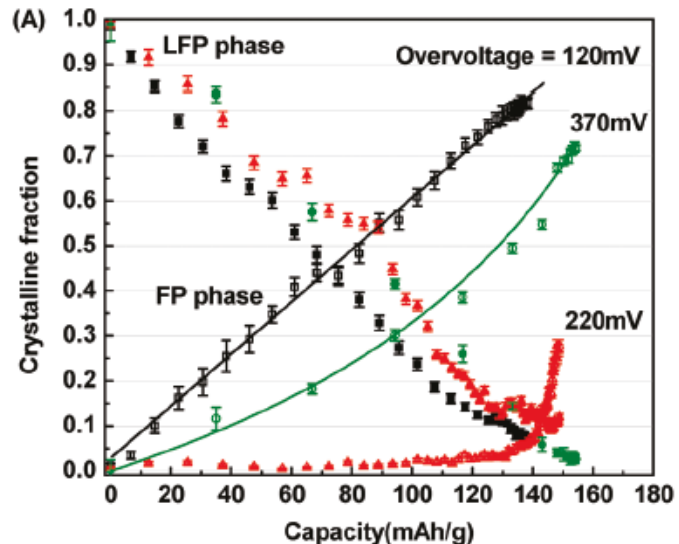


Figure 2. *In-situ* synchrotron XRD measurement of phase fractions for two LiFePO_4 materials during galvanostatic cycling at 1C rate for four cycles followed by 5C rate for four cycles. (A) Sample A of 113nm mean particle size; and (B) Sample B of 34nm mean particle size.

In addition, we have precisely resolved the overpotential dependence using a series of *in-situ* potentiostatic tests, and have shown that the overpotentials at which amorphization is preferred agree quite well with predictions (Figure 1). Figure 3 shows an example of such *in-situ* results for Sample A (113nm). The variation in crystalline phase fractions as the sample is potentiostatically charged (delithiated) is shown. (For simplicity, this figure plots the overvoltage dependence (not overpotential); the results are converted to overpotential in [3] for more detailed comparison with the model, as will be discussed in the presentation.)

Figure 3. *In-situ* synchrotron XRD measurement of phase fractions during potentiostatic charging of Sample A, of 113nm mean particle size. The variation of LFP and FP crystalline fractions is shown. While all three cells show a linear decrease in the LFP fraction with charge capacity, whether the FP fraction increases correspondingly is strongly dependent on the potentiostatic voltage.



Three values of overvoltage (OV), 120 mV, 220 mV and 370 mV, are tested. The LFP fraction, f_{LFP} , decreases approximately linearly with increasing charge capacity at each voltage. The corresponding FP fraction, however, shows different evolution behavior at each potentiostatic voltage. At OV=120 mV, the FP-fraction, f_{FP} , has a corresponding

linear increase—consistent with $f_{\text{LFP}} + f_{\text{FP}} = 1$. This is “conventional” behavior in which only the two crystalline phases are present, and their respective fractions obey the binary lever rule. At $\text{OV} = 220$ mV, a markedly different behavior is observed: no FP phase is detected until $\sim 67\%$ state of charge occurs (100% SOC corresponds to the complete removal of lithium). When the potentiostatic charge was terminated the SOC was $\sim 82\%$ —*however*, f_{FP} corresponded to only 30% and $f_{\text{LFP}} + f_{\text{FP}} = 0.4$. We conclude that the remaining 60% of the $\text{Li}_{1-x}\text{FePO}_4$ *must be noncrystalline*. At the largest overvoltage, 370 mV, the phase-fraction vs. SOC behavior is *intermediate* between that at 120 and 220 mV. At all SOC, the sum $f_{\text{LFP}} + f_{\text{FP}} < 1$, indicating presence of amorphous phase, and when potentiostatic charging is complete $f_{\text{LFP}} + f_{\text{FP}} \approx 0.7$, indicating $\sim 30\%$ residual amorphous phase. The striking conclusion is that the crystalline-to-crystalline phase transition appears to be preferred at both low (120 mV) and high (370 mV) overvoltage, while amorphization dominates at intermediate overvoltage (220 mV).

There are significant practical consequences to the demonstrated overpotential-dependent phase transition behavior. For example, in applications such as hybrid or all-electric vehicle batteries, charge/discharge protocols produce frequent voltage transients, and thus overpotentials; these may produce unexpected and history-dependent phase states. As such, phase-state hysteresis in storage electrodes would depend on instantaneous operating conditions and usage history. This has direct consequences on *in-situ* monitoring of state-of-charge (SOC), impedance, storage kinetics, and battery durability due to electrochemical-mechanical coupling. In-depth knowledge of overpotential- and time-dependent phenomena would also permit phase states and transition pathways to be electrochemically controlled during the pre-conditioning and operation of batteries.

Planned activities: We next plan to: 1) Systematically investigate particle size dependence and behavior during discharging (lithiation), in collaboration with Dr. Jianming Bai (Oak Ridge National Laboratory) and using *in-situ* synchrotron X-ray diffraction at Brookhaven National Laboratory. 2) Develop a more detailed kinetic model for the amorphization transition, in collaboration with Dr. Ming Tang at Lawrence Livermore National Laboratory. 3) Begin to investigate other systems in which crystalline-to-crystalline and crystalline-to-amorphous phase transitions are likely to occur, including for example $\text{Li}_2\text{FeSiO}_4$, a cathode of much recent interest for low cost lithium ion batteries for transportation and other applications.

Publications:

1. M. Tang, W. C. Carter, Y.-M. Chiang, “Electrochemically-Driven Phase Transitions in Insertion Electrodes for Lithium-Ion Batteries: Examples in Lithium Metal Phosphate Olivines,” *Annu. Rev. Mater. Res.*, Vol. 40: 501–529 (2010) (doi: 10.1146/annurev-matsci-070909-104435).
2. M. Tang, W.C. Carter, J.F. Belak, Y.-M. Chiang, “Modeling the Competing Phase Transition Pathways in Nanoscale Olivine Electrodes,” *Electrochimica Acta*, 56, 769 (2010) (doi:10.1016/j.electacta.2010.09.027).
3. Y.-H. Kao, M. Tang, N. Meethong, J. Bai, W.C. Carter, Y.-M. Chiang, “Overpotential-Dependent Phase Transformation Pathways in Lithium Iron Phosphate Battery Electrodes,” *Chem. Mater.*, 22[21], 5845-5855 (2010). (DOI: 10.1021/cm101698b)

Program Title: Imaging carrier generation, transport, and collection in nanostructured materials

Principle Investigator: Lincoln J. Lauhon, Associate Professor

Department of Materials Science and Engineering, Northwestern University

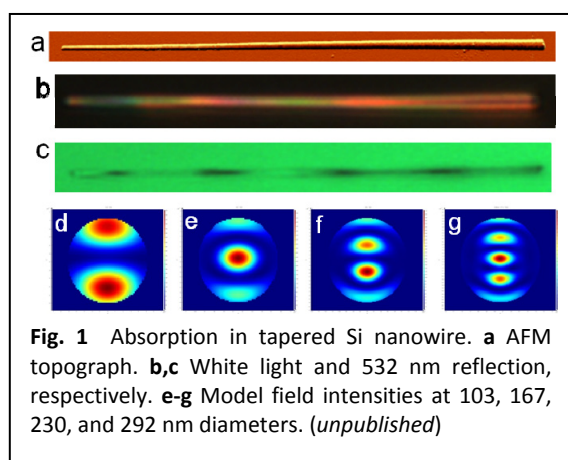
2220 Campus Drive, Evanston, IL 60208 e-mail: lauhon@northwestern.edu

Program Scope

The objective of our program is to develop a fundamental, quantitative understanding of charge carrier generation and transport between and within components of nanostructured materials to support the design and optimization of new materials for energy conversion. Our experimental approach is based on combining electrical transport measurements with local probes, particularly scanning photocurrent microscopy (SPCM) and micro-Raman spectroscopy, to spatially map carrier generation and collection efficiency in semiconductor nanowire heterostructures and hybrid nanowire-organic devices. Combinations of spatially-resolved, time-resolved, and spectrally-resolved sources and detectors are integrated to isolate various steps in the energy conversion process, including carrier generation, exciton diffusion, majority/minority carrier transport, and collection by metal contacts.

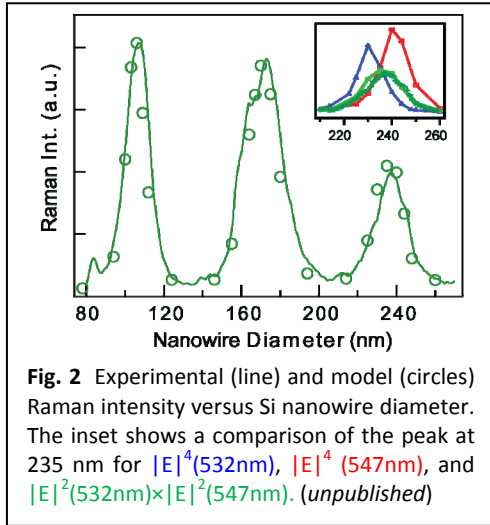
Recent Progress

This abstract summarizes progress reported over the last two years in two areas. First, we made advances in correlated electron microscopy, Raman spectroscopy, and modeling that have enabled the identification of new polytypes of Si that occur as inclusions within nanowires. This correlated analysis has also been applied to analysis of carrier separation in core-shell heterostructures. Second, we have implemented spectrally resolved SPCM to understand doping and potential profiles in Si nanowires, and to analyze plasmonically enhanced carrier generation in nanoparticle-nanowire heterostructure devices.



We will first describe recent advances in the analysis of nanowires and nanowire heterostructures by Raman spectroscopy, and the modeling of the Raman spectra using finite difference time domain (FDTD) techniques. Figure 1 reveals the diameter dependent reflectivity in a Si nanowire probed by white light, 532 nm excitation (for Raman studies), and FDTD modeling. The single crystal nanowire is tapered (Fig. 1a), producing periodic absorption maxima (Fig. 1c) associated with maxima in simulated integrated field intensities (from patterns in Fig.

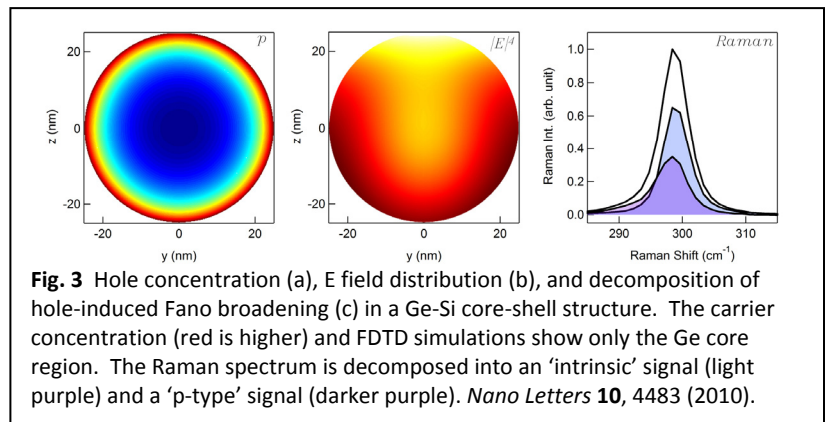
1d-g). For very small nanowires, the absorption minima and maxima are well described by Mie theory, and the images from FDTD confirm intuitive expectations that the diameter dependent optical properties are related to modal structure. For nanowire diameters of relevance to solar energy collection, however, a more quantitative description is needed; the Raman scattered measurements described below provide a stringent test of the quality of our model.



In modeling the local field enhancement of Raman scattering from molecules, it is commonly assumed that the incoming and outgoing wavelength are approximately equal, leading to field enhancement proportional to $|E|^4$. The inset to Figure 2 shows that such an assumption leads to significant errors in the expected position of geometrical resonances. Our more complete model quantitatively reproduces the Raman scattering intensity versus diameter (Figure 2) by integrating the point by point product of the field intensities at both the incoming and scattered wavelengths. We find that the Raman scattering intensity is enhanced by several orders of magnitude by the field confinement qualitatively seen in Figure 1. The

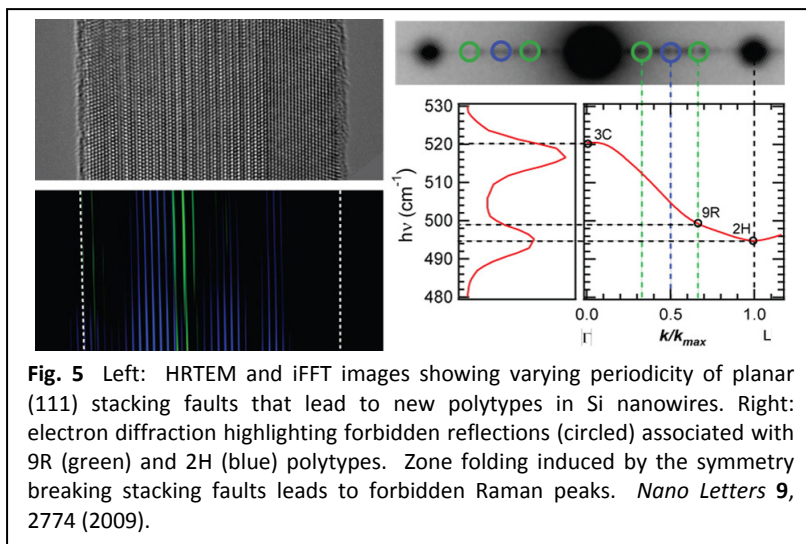
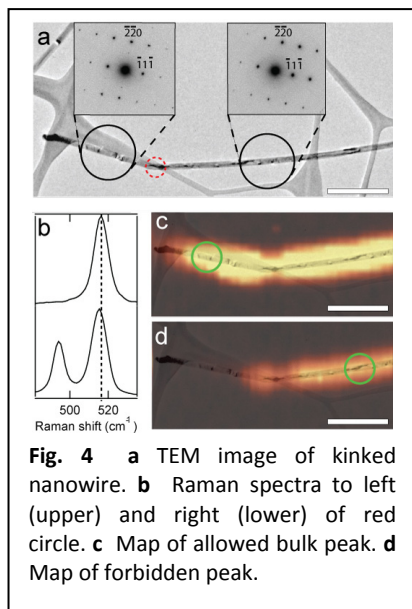
quantitative agreement is significant in that it demonstrates our ability to model absorption in (homogeneous) nanostructured materials. The extension to heterogeneous materials, and photocarrier collection, is described in the last section of this abstract.

Our FDTD model has been applied to the analysis of more complex Ge-Si core-shell nanowire heterostructures to analyze hole accumulation at the Ge-Si heterojunction (Figure 3). [1] High hole concentrations induce a Fano resonance in Si and Ge Raman spectra, enabling non-contact analysis of carrier concentration in



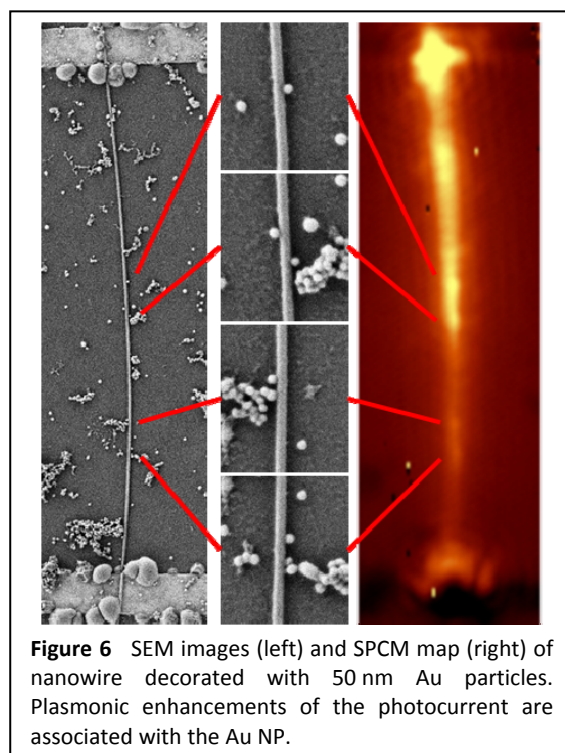
these novel materials of interest for solar energy utilization. The measurement is enabled by a Raman enhancement of up to 10^4 , which is captured quantitatively by our model.[1] Both the carrier concentration (Fig. 3, left) and the electromagnetic field (Fig. 3, middle) vary strongly with position, however, indicating that Raman spectrum (Fig. 3, right) is inhomogeneously broadened. At the same time, the modeling enables the Raman spectrum to be deconvolved into contributions from the intrinsic middle of the wire the region of high hole concentration near the Ge-Si interface (Fig. 3, right).

We have utilized the enhanced Raman scattering in Si nanowires to identified new polytypes of silicon that occur as inclusions within nanowires. [3] Novel polytypes are of interest because they support homojunction bandgap engineering, which in turn may enable useful charge-carrier separation even in the absence of dopant homojunctions or heterojunctions. The nanowire shown in Figure 4a kinks at the location marked with the red circle. Raman spectra to the right (Fig. 4c) of the red circle show a forbidden peak. Spatial maps of the intensities of allowed (Fig. 4c) and forbidden (Fig. 4d) peaks indicate a change in nanowire structure. Figure 5



reveals the origin of the forbidden peak through correlated high resolution transmission electron microscopy and Raman spectroscopy. The extra Raman peak arises from planar faults (Fig. 5, upper left) along the [111] direction. An inverse fast Fourier transform (Fig. 5, lower left) highlights regions of distinct periodicity that lead to forbidden reflections in electron diffraction (Fig. 5 upper right) and forbidden Raman peaks (Fig. 5, lower right) through zone-folding. Additional studies are underway to correlate nanowire growth conditions with the prevalence of 2H and 9R polytypes, and to confirm their distinct electronic structure through resonant Raman scattering and spectrally resolved SPCM measurements.

The second major thrust of our research program concerns the imaging of charge collection in nanostructured materials by SPCM, with a focus on nanowire and hybrid nanowire devices. Our strategy is to exploit the nanowire geometry to establish the efficiency of key energy conversion processes. At right (Figure 6) is recent unpublished data showing the local photocurrent associated with local surface plasmon enhanced excitation. An n-type Si nanowire device was decorated with Au nanoparticles (electrodes are visible at top and bottom of SEM image). The photocurrent generated by confocal excitation is shown at right in Figure 6. SPCM maps were recorded for both parallel (TM) and transverse (TE) polarizations at multiple wavelengths across the Au plasmon resonance. The photocurrent response was modeled in an FDTD simulation; Figure 7 compares the experiment with the model.



The field intensity maps (Fig. 7, upper) show significant enhancements in absorption in the nanowire when the illumination wavelength is resonant with the Au nanoparticle (to the right of the nanowire, not shown) for TE excitation. TM absorption is not significantly perturbed by the presence of the Au particle, and the absorption generally decreases monotonically with wavelength. The peak in photocurrent at 550 nm is therefore clearly due to plasmonic excitation of the nanoparticle. Ongoing analysis will enable us to quantify the rate of energy exchange and identify competing absorption mechanisms associated with the imperfections present in real materials.

We have also used SPCM to (1) quantitatively extract electrostatic potential profiles in nanowire devices from SPCM images; (2) determine effective carrier concentrations in nanowires and their dependence on position; and (3) quantify dopant distributions and establish that surface doping can occur even in the absence of measurable deposition on nanowire surfaces.[3] These measurements provide important insights into the structure-property relationships in nanowires of high relevance for photovoltaic, photodetector, and transistor applications. We also recently showed that these doping inhomogeneities can be mitigated by altering nanowire growth conditions, thereby enabling quantitative control over doping gradients. [4]

Summary of Plans

Our current efforts are directed towards three main tasks. (1) We will extend SPCM measurements to energy-resolved SPCM with both above-gap and sub-gap illumination to analyze the electronic structure of polytype homojunctions in semiconductor nanowires. (2) We will continue and expand investigation of hybrid nanowire/plasmonic structures, beginning with the study of silicon nanowires functionalized with metal nanoparticles and integrated into fabricated plasmonic structures. (3) In collaboration with others at Northwestern, we are applying spectrally resolved SPCM imaging to organic/hybrid solar cells to correlate spatial variations in carrier collection efficiency with underlying variations in electrode and active layer morphology.

References to DOE Sponsored Research

- [1] S. Zhang, **F. J. Lopez**, **J. K. Hyun** & L. J. Lauhon, "Direct Detection of Hole Gas in Ge-Si Core-Shell Nanowires by Enhanced Raman Scattering" *Nano Lett.* **10**, 4483 (2010).
- [2] **F. J. Lopez**, E. R. Hemesath, and L. J. Lauhon, "Correlated Raman microscopy and transmission electron microscopy of twinning superlattices in silicon nanowires," *Nano Lett.* **9**, 2774 (2009).
- [3] **J. E. Allen**, E. R. Hemesath, D. E. Perea, and L. J. Lauhon, "Non-Uniform Nanowire Doping Profiles Revealed by Scanning Photocurrent Microscopy," *Adv. Mater.* **21**, 3067 (2009)
- [4] E. Koren, **J. K. Hyun**, U. Givan, E. R. Hemesath, L. J. Lauhon & Y. Rosenwaks, "Obtaining Uniform Dopant Distributions in VLS-Grown Si Nanowires" *Nano Lett.* **11**, 183 (2011).

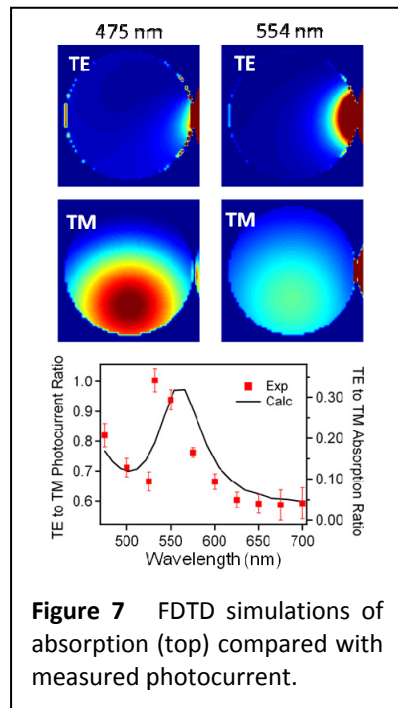


Figure 7 FDTD simulations of absorption (top) compared with measured photocurrent.

Session II

Novel Electronic Materials

Superconducting Materials

Qiang Li (Principle Investigator)

Condensed Matter Physics & Materials Science Department, Bldg. 480
Brookhaven National Laboratory
Upton, NY 11973-5000

Phone: 631-344-4490, Fax: 631-344-4071, Email: qiangli@bnl.gov

Program Scope:

This program studies basic relationships between nanostructures and the macroscopic properties of superconductors. Both basic understanding and understanding of materials aspects for practical use are sought. Emphasis is on improving the critical temperature T_c , the upper critical field H_{c2} , and the critical current density J_c , because they determine limits to energy applications. Due of recent developments and new opportunities, research activities focus on: (1) the response of superconductivity to chemical and structural tuning. This could provide new strategies for enhancing T_c and H_{c2} , and designing entirely new superconducting materials; (2) response and control of superconducting transport properties by structural tuning, where the simultaneous increase of $J_c(H)$ and reduction of the J_c anisotropy ratio can be achieved by tuning the defect structures. This could lead to effective and practical superconductors, for electricity transmission, and grid-scale energy storage. Coordinated studies involve synthesis, structural characterization, transport, and magnetic property characterization. By exploiting the range of advanced experimental techniques available at Brookhaven National Laboratory, we seek to understand and control the transport properties of superconducting materials by tackling the key science issues, from the macroscopic to the atomic levels. These activities are aligned with the Grand Challenge for the BES Directorate to understand strongly correlated electron behavior in materials

Introduction:

A vital mission of the Department of Energy (DOE) is to advance the energy security of the United States. As the electricity demand increases, driven by continuing urbanization and economic activities, the challenge to the national electricity grid to provide reliable power reaches new heights. The superconductor's lossless current flow enables the design of highly power-dense and compact equipment, such as high capacity cables and fault-current limiters, and hence offers powerful opportunities for restoring the reliability of the power grid and increasing its capacity and efficiency.

In recent years, as renewable energy utilization grows, the increasing mismatch between variation of renewable energy resources and electricity demand makes it necessary to capture electricity generated by wind, solar and other renewable energy generation for later use. Storage can help smooth fluctuations in generation inherent in wind or solar energy. In 2010, the DOE Office of ARPA-E awarded several transformative projects to develop grid-scale energy storage technologies capable of addressing emerging intermittency and ramping challenges for the transmission of renewable electric energy. Among them, is a project, titled "Superconducting Magnet Energy Storage (SMES) System with Direct Power Electronics Interface" developed by the Brookhaven National Laboratory (BNL-P. I. Qiang Li, also the P. I. of this FWP) with its industrial partners: ABB, Inc. and SuperPower, Inc. The nature of this proposed ultra-high field SMES system is such that massive energy storage, fast response, and a nearly infinite cycling capability will be attained, representing a significant advantage over alternative energy storage devices, which are severely limited in terms of lifetime and environmental constraints when disposed. In practice, the performance of superconductors – the major and critical component of SMES - will have to be propelled far beyond the present state-of-the-art. Although present high temperature superconductor (HTS) technology is positioned to play a key role in addressing our national and global energy challenges and can be deployed for some of the grid functions, significant barriers to achieving the full potential of superconductivity for transforming the power grid and grid-scale energy storage have remained. The latter are pri-

marily related to material properties. Bridging the gaps in performance improvement of superconductors and identifying the limiting factors requires a fundamental understanding of the microscopic origin of superconducting behavior.

This program continues the long-standing *Superconducting Materials program* at BNL to study basic relationships between nanostructures and macroscopic properties of superconductors. Both basic understanding and understanding of materials needs for practical use are sought. Several themes that extend from past work on HTS are retained, while research activities on emergent materials like iron-chalcogenides, are proposed. These include understanding of the origin and limits of critical temperature, upper critical field, vortex-pinning and critical current densities, and their response to structural and electronic tuning.

Recent Progress (selected):

The high quality superconducting iron-chalcogenide ($\text{FeSe}_{0.5}\text{Te}_{0.5}$) epitaxial thin films were successfully grown on a variety of single crystal substrates *for the first time* in our group by using pulsed laser deposition. We demonstrated that these films have significantly higher T_c (onset $T_c \sim 19$ K, zero resistance $T_c > 16$ K), as compared to single crystal or bulk polycrystalline samples (onset $T_c \sim 15$ K) for the entire doping regime of $\text{FeSe}_{1-x}\text{Te}_x$. (Fig. 1). Structural analysis by x-ray diffraction and high resolution transmission electron microscopy (TEM) reveal that these films generally have significantly shorter c-axis lattice constant than the bulk value, suggesting that the out-of-plane changes have a dominating impact on the superconducting transition in iron-based superconductors. The extrapolated $H_{c2}(0)$ of those films reaches as high as 50 T. [1]

Superconducting thin films of $\text{Fe}_{1.08}\text{Te}:\text{O}_x$ have been epitaxially grown on SrTiO_3 substrates by pulsed-laser deposition in controlled oxygen atmosphere *for the first time* in our group. Although the bulk parent compound Fe_{1+x}Te is not superconducting, thin films with oxygen are superconducting with an onset and a zero resistance transition temperature around 12 and 8 K, respectively. Oxygen was found to be crucial to the superconducting properties of these films, suggesting that the oxygen

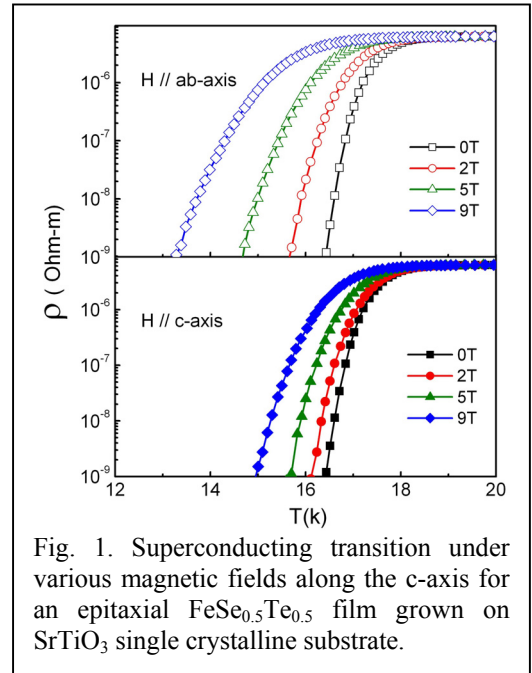


Fig. 1. Superconducting transition under various magnetic fields along the c-axis for an epitaxial $\text{FeSe}_{0.5}\text{Te}_{0.5}$ film grown on SrTiO_3 single crystalline substrate.

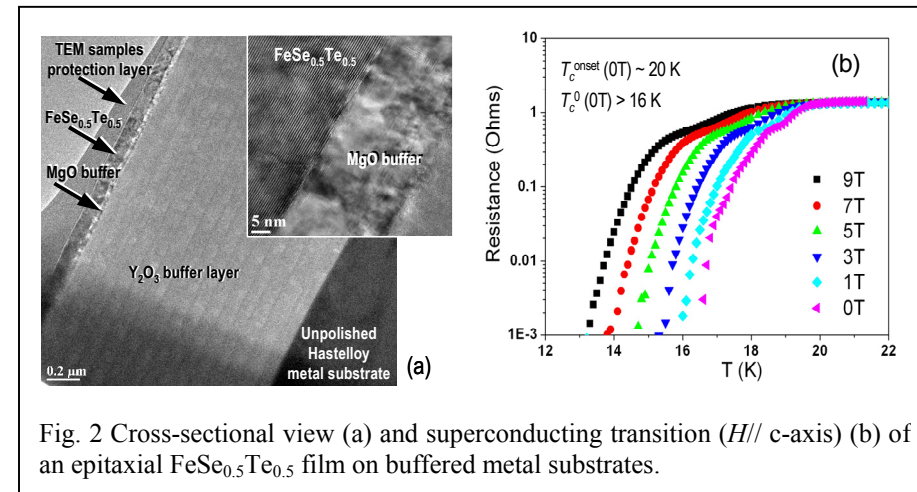


Fig. 2 Cross-sectional view (a) and superconducting transition ($H//$ c-axis) (b) of an epitaxial $\text{FeSe}_{0.5}\text{Te}_{0.5}$ film on buffered metal substrates.

incorporation can induce superconductivity in FeTe thin films. What is surprising is its extraordinarily high H_{c2} , with $-dH_{c2}/dT$ reaching 23 T/K. [2]

Robust superconducting thin films of ($\text{FeSe}_{0.5}\text{Te}_{0.5}$) were successfully grown *for the first time* in our group on technical metal substrates used for second generation 2G HTS wires, such

as IBAD (ion-beam assisted deposition) MgO buffered polycrystalline Ni alloys, (e.g. Hastelloy C-276 tapes), or rolling-assisted, biaxially textured substrates (RABiTS). Long length superconducting tapes or wires are necessary for large-scale applications for electricity transmission cables and magnets. This discovery opens the door for the application of the iron-based superconductors. We found that these $\text{FeSe}_{0.5}\text{Te}_{0.5}$ films on MgO buffered metal substrates have excellent crystallinity (Fig. 2a), higher T_c (Fig. 2b) and J_c in magnetic field, as well as excellent reproducibility.

Inelastic neutron scattering, magneto-resistivity, and susceptibility measurements have been performed on the optimally doped superconductor $\text{FeTe}_{0.5}\text{Se}_{0.5}$, in collaborating with the Neutron Scattering group of BNL. The magnetic scattering at the stripe antiferromagnetic wave vector $Q = (0.5, 0.5)$ exhibits a “resonance” behavior. These results provide clear evidence for the intimate relationship between superconductivity and magnetic excitations in the iron based superconductors. Also, short-range incommensurate magnetic order was observed in the $\text{Fe}_{1.07}\text{Te}_{1-x}\text{Se}_x$ samples with $x = 0.25$ and 0.3 . Furthermore, we observed short-range static magnetic order with an in-plane wave vector near the $(0.5, 0)$ (using the two-Fe unit cell), and strong low-energy magnetic excitations in all non-superconducting samples for Se doping up to 45%. [3][4][5]

The magneto-resistive and in-plane complex optical properties of the iron-chalcogenide superconductor $\text{FeTe}_{0.55}\text{Se}_{0.45}$ have been determined above and below T_c , in collaborating with the Electron Spectroscopy group of BNL. At room temperature the conductivity is described by a weakly interacting Fermi liquid; however, below 100 K the scattering rate develops a frequency dependence in the terahertz region, signaling the increasingly correlated nature of this material. The estimated dc conductivity σ_{dc} ($T \geq T_c$) $\approx 3500 \pm 400 \text{ } \Omega^{-1}\text{cm}^{-1}$, and the superfluid density $\rho_{s0} \approx 9 \pm 1 \times 10^6 \text{ cm}^{-2}$, both place this material close to the scaling line $\rho_{s0}/8 \approx 8.1\sigma_{dc}T_c$ for a BCS dirty-limit superconductor. Below T_c , the optical conductivity reveals two gap features at $\Delta_{1,2} \approx 2.5$ and 5.1 meV . [6][7]

We used nano-grain (001) ceria buffers acting like a strong catalyst to modify the structure of epitaxial $\text{YBa}_2\text{Cu}_3\text{O}_7$ and found previously unknown metastable phases, that could be utilized to achieve strong vortex pinning without an accompanying reduction in T_c . It is demonstrated that the low-temperature (400°C) treatment of these samples induces partial transformation of the $\text{YBa}_2\text{Cu}_3\text{O}_7$ matrix into a new, long-period perovskite phase with $c \sim 3.5 \text{ nm}$, intercalated into the $\text{YBa}_2\text{Cu}_3\text{O}_7$ matrix. [8]

Future plans:

1) To investigate the response of superconductivity in iron-chalcogenides to dimensionality, and provide the baseline data on the thickness dependence of T_c , J_c and H_{c2} , the planned experiments will use nano-scale single crystals. One or a few unit-cell thick iron-chalcogenide devices will be fabricated using the combined mechanical exfoliation and electron-beam lithography techniques, we established [9][10]. Fig. 3 shows an exfoliated 9 nm (~ 15 unit-cell) thick $\text{FeSe}_{0.5}\text{Te}_{0.5}$ single crystal with 6-terminal gold metallic (tested) contacts designed for measurements of temperature and field dependence of resistivity and charge carrier density (Hall effect).

2) To investigate the response of superconductivity in iron-chalcogenides to chemical and structural tuning, and determine the most potent means of enhancing H_{c2} and T_c , the planned experiments are based primarily on the high quality epitaxial films grown by PLD method (Fig. 4). These experiments will be augmented by similar experiments on single crystals aiming to explore the effect of disorder on superconductivity. The advantages of using high quality PLD films here include 1) much broader

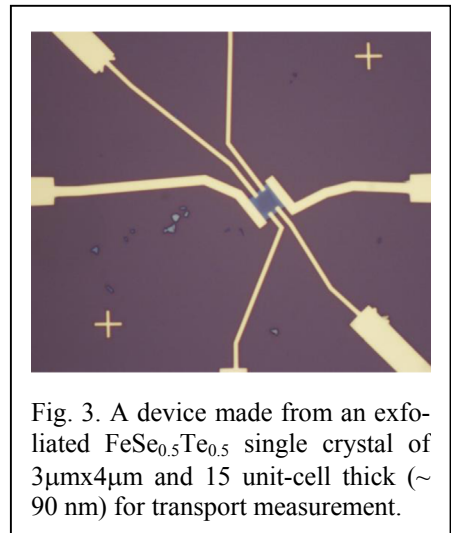


Fig. 3. A device made from an exfoliated $\text{FeSe}_{0.5}\text{Te}_{0.5}$ single crystal of $3\mu\text{m} \times 4\mu\text{m}$ and 15 unit-cell thick ($\sim 90 \text{ nm}$) for transport measurement.

compositional phase space (higher doping/substitution level) accessible only by the non-equilibrium method, such as PLD, 2) easier application of tensile strain to samples, and 3) the success here can be readily applied in practice for the iron-based superconducting tapes and wires.

3) To gain a quantitative understanding of the candidate pinning defects, their interaction with magnetic vortices, impact to the T_c of the $\text{YBa}_2\text{Cu}_3\text{O}_7$ (YBCO) matrix, and grain boundary transport properties. We will investigate the YBCO derivative phases we identified to be responsible for significant J_c enhancement. The planned experimental activities must coordinate all efforts from the synthesis to transport and structural properties characterization of these YBCO films. The goal is the development of model systems in which a specific defect type is introduced in a controlled way and thus can be studied unambiguously, and applied in a practical way.

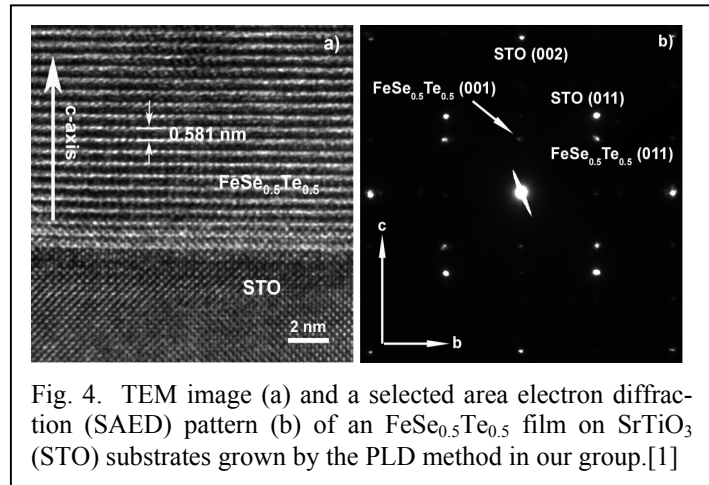


Fig. 4. TEM image (a) and a selected area electron diffraction (SAED) pattern (b) of an $\text{FeSe}_{0.5}\text{Te}_{0.5}$ film on SrTiO_3 (STO) substrates grown by the PLD method in our group.[1]

Publications of This program, 2008-2010

- [1] W. Si, et al, Appl. Phys. Lett. **95**, 052504 (2009)
- [2] W. Si, et. al, Phys. Rev. B **81**, 092506 (2010)
- [3] J. Wen, et al, Phys. Rev. B **81**, 100513(R) (2010)
- [4] J. Wen, et al, Phys. Rev. B **80**, 104506 (2009)
- [5] Z. Xu, et al, Phys. Rev. B **82**, 104525 (2010)
- [6] C. C. Homes, et al, Phys. Rev. B **81**, 180508(R) (2010)
- [7] C. C. Homes, et al, J. of Phys. And Chem. of Solid. *published on line* Oct. 7 2010
- [8] V. F. Solovyov, et al, J. Appl. Phys. **108**, 113912 (2010)
- [9] L. Zhang, et al, Phys. Rev. Lett. **105** 046804 (2010)
- [10] L. Zhang, et al, Phys. Rev. B **80** 241412(R) (2009)
- [11] I. K. Dimitrov, et al, Phys. Rev. B **81**, 17431 (2010)
- [12] V. Solovyov, et al, Supercond. Sci. Technol. **23** 014008 (2010)
- [13] N. Katayama, et al, J. Phys. Soc. Jpn. **79** 113702 (2010)
- [14] A. Ofan, et al, Phys. Rev. B **82**, 104113 (2010)
- [15] W. Liu, et al, Physica B **406** 52 (2011)
- [16] C. C. Homes, et al, Phys. Rev. B **81**, 220502(R) (2010)
- [17] S. H. Lee, et al, Phys. Rev. B **81**, 220502(R) (2010)
- [18] Q. Li, et al, J. of Electronic Materials, **38** 1268 (2009)
- [19] X. Ke, et al, Phys. Rev. Lett. **103**, 145502 (2009)
- [20] V. F. Solovyov, et al, J. Appl. Phys. **105** 113927 (2009)
- [21] T. A. Tyson, et al, Phys. Rev. B **79**, 024109 (2009)
- [22] W. Wang, et al, J. Renewable and Sustainable Energy, **1**, 023104 (2009)
- [23] J. Tang, et al, J. Phys. Condens. Matter **21** 205703 (2009)
- [24] L. Wu, et al, J. Appl. Phys. **105**, 094317 (2009)
- [25] W. Wong-Ng, et al, J. Appl. Phys. **105** 063706 (2009)
- [26] N. D. Lowhorn, et al, Appl. Phys A **94** 231–234 (2009) (Rapid Communication)
- [27] J. M. Tranquada, et al, Phys. Rev. B **78**, 174529 (2008)
- [28] V. F. Solovyov, et al, Supercond. Sci. Technol. **21** 125013 (2008)
- [29] C. K. Xie, et al, Phys. Rev. B **77**, 201403(R) (2008)
- [30] P. Woodward, et al, J. of Amer. Ceramic Society, **91** 1796-1806 (2008)
- [31] H. J. Noh, et al, Europhysics Letters, **81** 57006 (2008).

Program Title: Investigation of Sb-doped p-type ZnO thin films for solid state lighting

Principle Investigator: Jianlin Liu, Department of Electrical Engineering, University of California, Riverside, CA 92521. Email: jianlin@ee.ucr.edu.

Program Scope:

The objective of this program is to achieve insightful knowledge in ZnO material properties, p-doping strategies for efficient light emitting diodes (LEDs). ZnO has a large exciton binding energy of 60 meV and a bandgap of 3.37 eV at room temperature, which attracts profound interest in R&D for future solid states lighting. However, the major problem that hinders the development of ZnO based devices is the difficulty to obtain reliable p-type conductivity. Due to high-concentration background defects, undoped ZnO exhibits n-type conductivity with high electron concentrations. The background electrons and low solubility of many acceptor elements make the p-type ZnO very difficult to be realized and the p-type is often unreliable or unrepeatable. To solve this problem, we utilized plasma-assisted molecular beam epitaxy (MBE), in the aim of providing precise control of ZnO thin film growth and device development. We experimentally demonstrated Sb to be an efficient dopant in producing p-type ZnO films. Prototype homojunction diodes and photodetectors were demonstrated previously. Under the support of this project, we have made progress on the development of LEDs based on ZnO p-n junctions to further prove the robustness of Sb-doped p-type thin films. Pure ultraviolet emissions have been achieved in such LEDs. In order to improve the crystallinity and output power of ZnO p-n junctions, p-type ZnO films and LEDs were grown on c-plane sapphire substrates. Drastically enhanced output power of 457 nW has been realized recently by inserting a MgZnO/ZnO double heterojunction in the ZnO p-n junction on c-sapphire. Furthermore, to explore the possibility of bandgap engineering and heterojunctions in ZnO, Cd was alloyed in ZnO to tune the bandgap of ZnO from 3.3 eV to 2.4 eV or lower. Functional light emitting devices were fabricated.

Recent Progress:

1. Realization of dominant UV emissions in ZnO homojunction: In this research, Sb-doped p-type ZnO/Ga-doped n-type ZnO homojunction on Si (100) substrate was grown by MBE. High-quality, closely packed ZnO nanocolumnar structures were achieved, as shown in Fig. 1 (a). Mesa structures were defined and Ohmic contacts were placed. The p-n junction yielded almost pure ultraviolet emissions (Fig. 1(b)), which originate from near band edge emissions in ZnO.

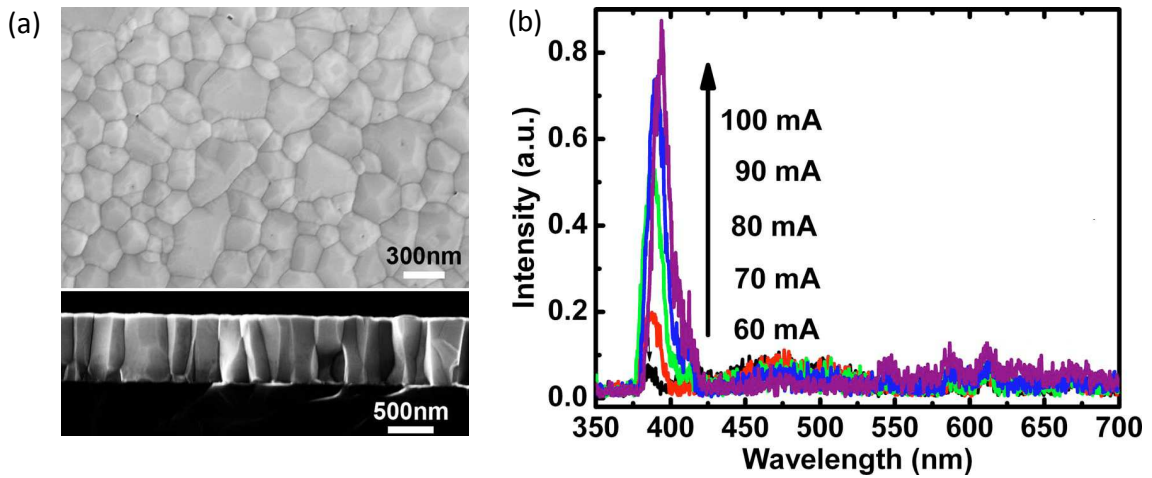


Figure 1 (a) Scanning electron microscope image of surface-view (top) and side-view (bottom) of the ZnO homojunction sample. (b) Electroluminescence (EL) spectra of the device with injection current from 60 mA to 100 mA.

- Enhancement of LED output power: Although the LEDs on large lattice-mismatched Si substrate showed UV emissions, the output power was low due to poor crystallinity. Dislocations and grain boundaries from mismatched growth on Si substrate may act as non-radiative recombination centers and thus decrease the efficiency of the device. To improve the output power, we have performed the investigations of p-type ZnO films and LEDs on c-sapphire substrate (smaller lattice mismatch of 18%). By Sb doping, p-type ZnO film with hole concentration of $1 \times 10^{17}/\text{cm}^3$ was achieved. To utilize such p-type ZnO films, homojunction LED was grown and fabricated. In terms of crystallinity, XRD rocking curve measurements were used to compare the ZnO LEDs on Si (100) and c-sapphire. The full width at half maximum of the rocking curve on c-sapphire is about 1/20 of the one on Si (100). The improved crystallinity yielded increased output power of 32 nW at 60 mA injection current, which is more than one order of magnitude larger than the output power of the LED on Si substrate at the same injection current. In order to further enhance the LEDs' output power, a MgZnO/ZnO/MgZnO double heterojunction was inserted between p-type and n-type ZnO while the composition of Mg was designed to be 10% (Mg: Zn=1:10). This LED showed strong ultraviolet emissions (Fig. 2). The upper inset of Fig. 2 presents a photo of the operating device and strong blue/purple light can be observed. The overall output power was calibrated to be 457 nW at the injection current of 140 mA and 287 nW at 60 mA, which is one order of magnitude larger than the one without double heterojunction (32 nW, 60 mA).

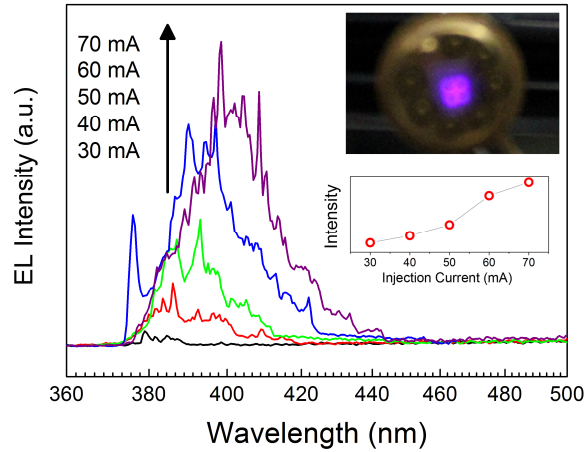


Figure 2 EL spectra of the double heterojunction device from 30 mA to 70 mA. Top inset is a photo image of operating device. Bottom inset is the relationship between the integrated spectra intensity and injection current.

3. **Bandgap engineering of CdZnO:** By alloying with Cd, the bandgap of ZnO can be tuned from 3.3 eV to 2.4 eV. The ability to grow CdZnO is very important to achieve quantum structures in future ZnO devices and also to fabricate future green LEDs. Structural and optical emission properties of CdZnO thin films were systematically studied. The bandgap shrinkage effect was investigated by temperature dependent photoluminescence spectra and hopping process was observed to be associated with band tail states due to alloying effect and non-uniform Cd distributions. Heterojunction light emitting devices were fabricated using CdZnO as active layers. A Sb-doped p-type ZnO/CdZnO/Ga-doped n-type ZnO LED showed blue emission around 430 nm. Another device included n-type ZnO/CdZnO/p-type Si yielded cyan emission around 470 nm. All these results indicate that CdZnO was successfully grown and is promising for optoelectronics applications.
4. **Growth of high-quality ZnO films:** Two-dimensional ZnO films were successfully grown on r-plane and c-plane sapphire substrates. The background electron concentration was optimized to $\sim 10^{16}/\text{cm}^3$ for next-step reliable p-type doping. High-quality ZnO films are critical for further enhancement of LED performance.

Future Plans:

The future research plan will be to further enhance p-type quality toward improvement of the output power of the ZnO-based LEDs. To improve the device quality, we have developed single crystalline, two-dimensional ZnO thin films on c-sapphire substrates by optimizing MgO buffer layer growth. These films show superior structural qualities as well as low electron concentration ($\sim 10^{16}/\text{cm}^3$) and high mobility. The next-step involves doping of Sb into the two-dimensional

films to make it reliable p-type while maintain the structural properties. If this is successful, the LEDs based on single crystalline, two-dimensional films will show much enhanced output power on the order of μW to mW . In the meantime, improved bandgap engineering based on MgZnO and CdZnO can be used to grow double heterojunctions and quantum well structures.

Publications:

1. J. Kong, S. Chu, M. Olmedo, L. Li, Z. Yang, and J. L. Liu, *Applied Physics Letters* 93, 132113 (2008).
2. Z. Yang, S. Chu, W. V. Chen, L. Li, J. Y. Kong, J. J. Ren, P. K. L. Yu, and J. L. Liu, *Appl. Phys. Express* 3, 032101(2010).
3. S. Chu, J. Zhao, Z. Zuo, J. Kong, L. Li, and J. L. Liu, *J. Applied Physics*, (submitted).
4. L. Li, Z. Yang, Z. Zuo, J. Y. Kong, and J. L. Liu, *J. Vac. Sci. Tech. B* 28(3), C3D13, 1071 (2010).
5. L. Li, Z. Yang, Z. Zuo, J. H. Lim, and J. L. Liu, *Appl. Surf. Sci.* 256, 4734 (2010)
6. Z. Yang, L. Li, Z. Zuo, J. L. Liu, *J. of Crystal Growth* 312, 68 (2009).
7. L. Li, Z. Yang, J. Y. Kong, and J. L. Liu, *Appl. Phys. Lett.* 95, 232117 (2009).
8. L. Li, Z. Yang and J. L. Liu, *MRS Fall 2009, Boston, USA, Mater. Res. Soc. Symp. Proc.* Vol. 1201, 1201-H01-09, (2010).
9. Z. Yang, H. M. Zhou, W. V. Chen, L. Li, J. Z. Zhao, P. K. L. Yu, and J. L. Liu, *J. Appl. Phys.* 108, 066101 (2010).
10. J. Y. Kong, L. Li, Z. Yang, and J. L. Liu, *J. Vac. Sci. Tech. B* 28(3), C3D10, 1071(2010).
11. J. Z. Zhao, H. W. Liang, J. C. Sun, Q. J. Feng, J. M. Bian, L. Z. Hu, G. T. Du, J. J. Ren, and J. L. Liu, *Physica Status Solidi (a)* 2011 (in press).

Red, Green, Blue Luminescent Media Incorporating Colloidal Semiconductor Quantum Dots within a Nanoporous Gallium Nitride LED Matrix

Arto V. Nurmikko
School of Engineering, Brown University
Providence RI 02912

Jung Han
Department of Electrical Engineering, Yale University
New Haven, CT

This DOE/BES grant is aimed at the development of a luminescent red, green, blue (RGB) nanocomposite materials where high brightness colloidal II-VI nanocrystals (quantum dots, QDs) are embedded within an electrochemically prepared nanoporous gallium nitride semiconductor thin film host. The GaN nanoporous medium, in turn, is part of an active LED which provides the optical source of excitation. The transfer of the QDs from their native solution environment to the nanoporous host is one research focus for strategies to preserve their key light emitting features of high quantum yield (~ 90%), photostability, and narrow spectral linewidths, respectively. Varying the GaN or InGaN nanopore size in the range from 20-60nm in conjunction with the QD diameter suggests that the luminescent medium may be a candidate for wavelength-engineered, multicolor nanotextured materials, materially and physically integrated to inorganic nitride LEDs, so as to be applicable to solid state lighting.

The Electronic Materials Program at LBNL

E. E. Haller, PI, J. W. Ager III, Co-PI, D. C. Chrzan, Co-PI, O. D. Dubón, Co-PI, Z. Liliental-Weber, Co-PI, W. Walukiewicz, Co-PI, K. M. Yu, Co-PI
Lawrence Berkeley National Laboratory, Materials Sciences Division, MS 2R0200,
1 Cyclotron Road, Berkeley, CA 94720

Advances in the understanding of semiconductor materials systems are essential for the identification of the factors affecting the performance, reliability, and lifetime of devices and the development of new advanced materials with improved performance and greater stability in thermal, radiation, and corrosive environments. These factors become increasingly important as the scale of devices continues to decrease and as semiconductors find ever broader applications (e.g. solar cells and broad-based solid state lighting). The Electronic Materials Program is a collaborative effort encompassing growth and synthesis of high quality semiconductors in bulk, thin film and nanocrystalline form and studies of their basic electronic, optical, magnetic, and structural properties combined with theoretical modeling.

Engineering the electronic band structure

Group III-nitrides The band gap tuning range of the $\text{In}_x\text{Ga}_{1-x}\text{N}$ alloys, 0.65 to 3.4 eV, provides a near-perfect match to the solar spectrum. Fundamental study of this materials system has been a focus of the program since we discovered, along with researchers in Russia and Japan, the correct InN bandgap, 0.7 eV. The large electron affinity of InN, close to 6 eV and the largest of any III-V semiconductor, creates a strong driving force for native donor formation, both in the bulk and at surfaces. Until recently, it was very much an open question whether native defects would make p-type indium nitride an impossibility. The program developed and applied novel electrical and electrothermal measurement approaches which not only have established that Mg-doping leads to mobile holes in InN, but also that the surface accumulation layer of electrons, which had interfered with all standard electrical measurements on InN thin films, can be mitigated.^{1,2} These techniques have also produced a quantitative understanding of the crucial role of charged line defects in limiting electron transport. Most recently, preliminary data supporting p-n junction rectification has been observed.

Highly mismatched semiconductor alloys

The program has pioneered the development and application of “highly mismatched” alloys (HMAs). We have shown that the electronic structure of these alloys is determined by the band anticrossing interaction between the localized states of the substituted element and the extended states of the matrix. In the last three years, we greatly expanded the range of mismatched alloys and added flexibility to the engineering of the electronic band structures for energy related

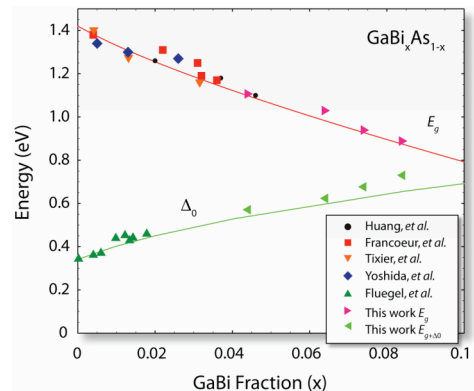


Fig. 1. Composition dependence of the energy gap and the spin-orbit splitting in $\text{GaBi}_x\text{As}_{1-x}$ alloys. The solid lines are result of VBAC calculations

applications.^{3,4} We made major progress in understanding the properties of a specific class of mismatched semiconductor alloys in which smaller electronegative host anion atoms are substituted with larger, more metallic atoms. Changes in the electronic structure of such alloys are mainly determined by an anticrossing interaction between localized states of the minority atoms and the extended valence band states of the matrix. Our valence band anticrossing model (VBAC) encompasses all the complexity of the valence band structure and accurately describes the optical and transport properties of the alloys.

The measured band gap and the spin orbit splitting of one of such alloys, Arsenic-rich $\text{GaBi}_x\text{As}_{1-x}$ are shown in Fig. 1 together with data reported in the literature. In addition to a rapid decrease of the energy gap the data show a very large increase in the spin orbit splitting, Δ_o , at small Bi content; both these observations are consistent with the VBAC model. In order to find out if the BAC concept also applies to elemental semiconductors, we have investigated Ge-rich SnGe alloys. In MBE grown $\text{Ge}_{1-x}\text{Sn}_x$ with $0 < x < 0.06$ the energy gap decrease with increasing x is much faster than predicted from virtual crystal approximation but can be well explained by the VBAC model.

$\text{GaN}_{1-x}\text{As}_x$ alloys have been well studied at the As-rich end and to a lesser extent at the N-rich end. However, due to the large miscibility gap of the GaNAs system, alloys with intermediate compositions have not been achieved. Recently, our collaborators at the University of Nottingham have grown $\text{GaN}_{1-x}\text{As}_x$ alloys over the whole composition range using molecular beam epitaxy at low temperature (LT-MBE).⁵

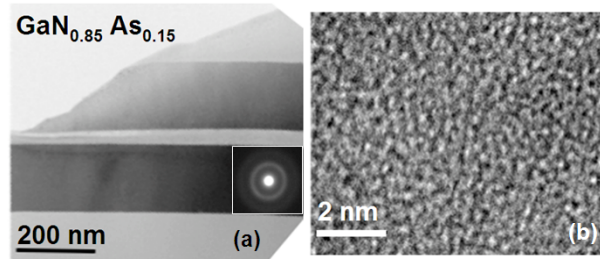


Fig. 2. (a) Cross-sectional TEM micrographs and the SAD patterns for a $\text{GaN}_{0.85}\text{As}_{0.15}$ samples on Pyrex glass substrate, (b) high resolution image indicating amorphous structure

Alloys in the composition range of $0.10 < x < 0.8$ are amorphous (Fig. 2). The band gap of these alloys is tunable from 0.8eV to 3.4eV, which is in good agreement with the predictions of the BAC model.

Isotopically pure semiconductors

Research with stable enriched semiconductor isotopes has been a continuing strength of the EMAT program. Using a unique poly-Si reactor, our program produced bulk single crystals of Si enriched in all three of its stable isotopes: 99.92% ^{28}Si , >90% ^{29}Si , and >90% ^{30}Si . These isotopically enriched Si single crystals are among the purest ever made, with electrically active impurities (P and B) as low as $\text{mid-}10^{13} \text{ cm}^{-3}$, other impurities at low or undetectable concentrations ($\text{C} < 10^{16} \text{ cm}^{-3}$, $\text{O} < 10^{15} \text{ cm}^{-3}$), and no dislocations. The prospect of realizing *quantum information processing* with semiconductors has led to increasing recent interest in the properties of spins in the solid state. In this context, the decoherence time (T_2) of an isolated spin is a key figure of merit. It has been known since the invention of electron spin resonance in the 1950's that the T_2 of the electron bound to ^{31}P is increased in ^{28}Si enriched material, due to derichment of ^{29}Si with its odd spin nucleus. Current "world record" with a T_2 at 10 K of

5 ms has been measured on a ^{28}Si LBNL single crystal. LBNL isotopically enriched ^{28}Si was used for the first demonstration of solid-state quantum memory.⁶

Synthesis and spin and charge doping of novel semiconductors

Diluted magnetic semiconductors Because of their potential as both injectors and filters of spin-polarized carriers, ferromagnetic semiconductors formed by the substitution of a relatively small fraction of host atoms with a magnetic species may play an important role in future spin-based electronics.

There is controversy concerning the underlying mechanism of hole-mediated exchange in Mn-doped group III-V semiconductors. Using the VBAC model, we were able to determine the value of the coupling parameter and describe quantitatively the transport properties of the holes in the impurity band. We find an almost order of magnitude lower hole mobility in Mn-doped GaAs compared with the hole mobility found in GaAs doped with nonmagnetic shallow acceptors. These results have far reaching consequences for the field of spintronic materials as they provide guidance in a search for higher Curie temperature materials.⁷

It has been proposed that alloying GaAs with GaP may yield a host in which the itinerancy of the mediating holes is maintained while p - d exchange is enhanced due to the shorter average Mn-anion bond length. We have developed a novel process to synthesize quaternary ferromagnetic semiconductors. Using a combination of ion implantation and pulsed-laser melting, we have produced epitaxial, single crystalline $(\text{Ga,Mn})(\text{As,P})$ films for our studies of anion substitution on ferromagnetism. Substitution of merely 2.4% of As by P induces a metal-insulator transition (MIT) at a constant Mn doping of $x=4.6\%$ (Fig. 3). This remarkable behavior is consistent with a scenario in which holes located within an impurity band—predicted to exist from the VBAC model—are scattered by alloy disorder in the anion sublattice and thus become localized.⁸

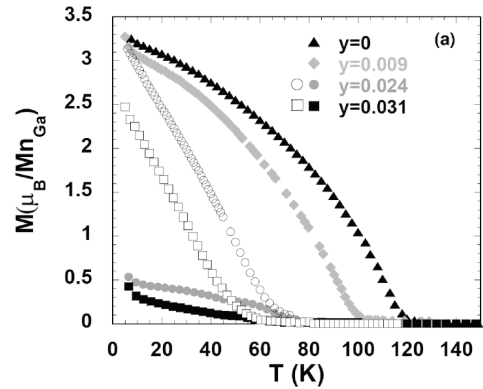


Fig. 3. A dramatic change in the temperature dependent magnetization observed at the metal-insulator transition of $(\text{Ga,Mn})(\text{As,P})$ alloys with 4.6% Mn and different concentration of P (y).

Ion beam synthesis of nanostructures Nanocrystals embedded in an amorphous matrix can display unusual properties. There have been extensive efforts to model the ion beam synthesis (IBS) process. However, a generally applicable theory for IBS was not available. Our new and detailed model for IBS identifies two characteristic lengths governing the resulting shape: the capillary length, and the (newly identified) length, $L \equiv (Dn_\infty/F)^{1/2}$, with D the effective diffusion coefficient, n_∞ the effective solubility, and F the volumetric implantation rate of the implanted species. L determines the shape of the size distribution, and the capillary length then controls the average size. The model provides a quantitative description of the experimentally available data and has predicted processing routes which form nearly monodisperse embedded nanocrystals.⁹

We expect that alloy nanocrystals embedded within matrices will have equilibrium morphologies determined by the relevant interface energies. We also expect that the control over transformation kinetics available at the nanoscale can be used to synthesize nonequilibrium morphologies. As an initial effort to explore this possibility, we have fabricated GeSn nanocrystals embedded in silica.¹⁰ We find that a segregated bi-lobe structure is the

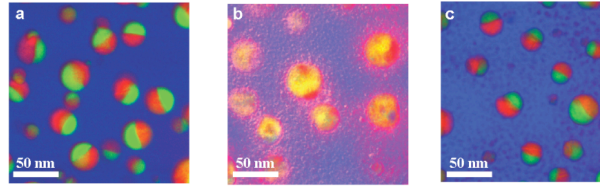


Fig. 4. False color energy-filtered transmission electron microscopy images of GeSn nanocrystals (Ge:Sn=4:2) (a) as-formed (900C, 1hr anneal), (b) after pulsed laser melting, and (c) after reannealing (rapid thermal annealing 500C 10s). Blue regions are silica, red regions are rich in Ge, green regions are rich in Sn, and orange regions represent a mixture of Ge and Sn.

equilibrium state (Fig. 4). Pulsed laser melting (PLM) melts the segregated nanocrystals, and the subsequent rapid cooling freezes a nearly homogeneously mixed amorphous state. Reannealing followed by slow cooling regenerates the equilibrium lobe/lobe structure. The opto-electronic properties of the different nanocrystals with different morphologies are likely to be very different, and may form the basis for new devices.

Selected BES-supported publications (from a total of 121) 2008-2010

1. G. F. Brown, J. W. Ager III, W. Walukiewicz, W. J. Schaff and J. Wu, "Probing and Modulating Surface Electron Accumulation in InN by the Electrolyte Gated Hall Effect," *Appl. Phys. Lett.* **93**, 262105 (2008).
2. N. Miller, J. W. Ager III, H. M. Smith III, M. A. Mayer, K. M. Yu, E. E. Haller, W. Walukiewicz, W. J. Schaff, C. Gallinat, G. Koblmüller, and J. S. Speck, "Hole transport and photoluminescence in Mg-doped InN," *J. Appl. Phys.* **107**, 113712 (2010).
3. Marie A. Mayer, Derrick T. M Speaks, Kin Man Yu, Samuel S. Mao, Eugene E. Haller, and Wladek Walukiewicz, "Band structure engineering of ZnO_{1-x}Se_x alloys," *Appl. Phys. Lett.* **97**, 022104 (2010).
4. Nair López, Lothar, A. Reichertz, K. M. Yu, Kenneth Campman, and Wladek. Walukiewicz, "Engineering the Electronic Band Structure for Multiband Solar Cells," *Phys. Rev. Lett.* **106**, 028701 (2011).
5. K. M. Yu, S. V. Novikov, R. Broesler, I. N. Demchenko, J. D. Denlinger, Z. Liliental-Weber, F. Luckert, R. W. Martin, W. Walukiewicz, and C. T. Foxon, "Highly Mismatched GaN_{1-x}As_x Alloys in the Whole Composition Range," *J. Appl. Phys.* **106**, 103709 (2009).
6. J. J. L. Morton, A. M. Tyryshkin, R. M. Brown, S. Shankar, B. W. Lovett, A. Ardavan, T. Schenkel, E. E. Haller, J. W. Ager, and S. A. Lyon, "Solid state quantum memory using the ³¹P nuclear spin," *Nature* **455**, 1085 (2008).
7. M. A. Mayer, P. R. Stone, N. Miller, H. M. Smith III, O.D. Dubon, E. E. Haller, K. M. Yu, W. Walukiewicz, X. Liu and J.K. Furdyna, "Electronic structure of Ga_{1-x}Mn_xAs analyzed according to hole-concentration-dependent measurements," *Phys. Rev. B* **81**, 045205 (2010).
8. P.R. Stone, K. Alberi, S.K.Z. Tardif, J.W. Beeman, K. M. Yu, W. Walukiewicz and O.D. Dubon, "Metal-insulator transition by isovalent anion substitution in Ga_{1-x}Mn_xAs: Implications to ferromagnetism," *Phys. Rev. Lett.* **101**, 087203 (2008).
9. C. W. Yuan, D. O. Yi, I. D. Sharp, S. J. Shin, C. Y. Liao, J. Guzman, J. W. Ager, III, E. E. Haller and D. C. Chrzan.. "Theory of Nanocluster Size Distributions from Ion Beam Synthesis," *Phys. Rev. Lett.* **102**, 146101 (2009).
10. S. J. Shin, J. Guzman, C.W. Yuan, C. Y. Liao, C. N. Boswell-Koller, P. R. Stone, O. D. Dubon, A. M. Minor, M. Watanabe, J. W. Beeman, K. M. Yu, J. W. Ager, III, D. C. Chrzan and E. E. Haller, "Embedded Binary Eutectic Alloy Nanostructures: A New Class of Phase Change Materials," *Nano Letters* **10**, 2794 (2010).

Session III

Interfaces / Surfaces

Proximity Effects in Charged Oxide Heterostructures

PIs: J.A. Eastman, D.D. Fong, P.H. Fuoss, P. Zapol
Materials Science Division
Argonne National Laboratory
9700 S. Cass Ave., Bldg 212
Argonne, IL 60439
630-252-5141, jeastman@anl.gov

Research Scope: This program focuses on controlling heterointerfacial charge and space charge in thin film oxide heterostructures to provide insight into factors that beneficially enhance ionic conductivity and influence ferroelectric behavior. We exploit proximity effects associated with charged interfaces, which are amplified when heterostructure layer spacings are reduced below distances where the charges at neighboring interfaces strongly interact. The resulting knowledge is furthering basic understanding of charge interactions near interfaces, and has great potential to impact energy-related technologies.

The program is organized into three interrelated thrusts involving synthesis, structure, and interfacial charge-induced behavior. One thrust emphasizes achieving breakthroughs in ionic conduction through control of interfacial charge, including the manipulation of charged interfaces to suppress oxygen vacancy ordering. A second thrust examines the interplay between ionic conductivity and ferroelectricity in layered structures. Here, we use polarization in a ferroelectric layer to control interfacial charge and oxygen transport in an adjacent ionic conductor layer. Conversely, we also explore how the electrical boundary conditions imposed by charged interfaces impact polarization behavior in a ferroelectric film. The third thrust focuses on advancing synthesis science to create the epitaxial layered and nanocomposite thin film heterostructures that have the greatest potential for enhancing ionic conduction and ferroelectric properties.

Our approach employs forefront in-situ synchrotron x-ray scattering and spectroscopy techniques to determine depth-resolved atomic-level structure and film composition in real-time, in the elevated temperature, controlled oxygen partial pressure environments that are integral to both the growth and behavior of ionic conductors and ferroelectrics. The synthetically engineered heterostructures of interest are based on fluorite- or perovskite-structured materials, including naturally- or artificially-layered variants of the perovskite structure. Growth techniques that enable precise control of each atomic plane in a growing heterostructure of these materials are employed. X-ray characterization of interfacial structure/chemistry, strain/composition gradients, and defect behavior is combined with in-situ electrical characterization to provide unique insight into structure-property relationships. The program integrates a unique combination of experimental measurements with a theoretical effort that uses first-principles calculations to elucidate the factors that control strain, composition, and structure during growth, identify charge transport mechanisms and the structures of charged interfaces, and facilitate the development of predictive models for the design of oxide heterostructures with emergent properties.

Recent Progress: Our program has made significant progress in using in-situ synchrotron x-ray techniques during growth and characterization of ionically conducting and ferroelectric thin film oxide heterostructures. In the following, we describe two brief highlights of our recent progress that demonstrate capabilities and phenomena that will be exploited in our future plans.

δ -Bi₂O₃ Epitaxial Stabilization and Oxygen Ordering (in collaboration with D. Proffitt, a Ph.D. student co-advised by J.A. Eastman, and Prof. T.O. Mason from Northwestern University): Oxide ion conductors are critical components in many important energy conversion devices, including solid oxide fuel cells (SOFCs), oxygen separation membranes, and oxidation catalysts. The fluorite-structured δ -phase of bismuth oxide (δ -Bi₂O₃) has attracted significant attention because it exhibits much larger ionic conductivity than all other oxides discovered to date [1]. In bulk materials, however, this high conductivity phase is stable only from 729-825°C, and transformation to other Bi₂O₃ polymorphs when cooling to room temperature results in a significant reduction in ionic conductivity and may cause deleterious cracking because of the large changes in volume [1].

We recently demonstrated that δ -Bi₂O₃ nanostructures [2] and continuous films can be stabilized to room temperature by epitaxial growth onto oxide substrates having good lattice match to the δ -phase. Synchrotron x-ray scattering results characterizing the orientation relationships and strain states of Bi₂O₃ nanostructures are shown in Fig. 1(a, b). Our findings, which were published in Applied Physics Letters [2], represent the first observation of δ -

Bi_2O_3 epitaxial stabilization on oxide substrates and the first demonstration of a tunable $\delta\text{-Bi}_2\text{O}_3$ strain state by substrate misfit.

The high ionic conductivity of $\delta\text{-Bi}_2\text{O}_3$ derives from the fact that 25% of the oxygen sites in the fluorite structure are vacant. Ordering of these vacant sites, and an accompanying reduction in conductivity, occurs when the δ -phase is stabilized to low temperature by cation doping [3]. Previous studies of undoped $\delta\text{-Bi}_2\text{O}_3$ samples did not report oxygen vacancy ordering [4], but were performed only at high temperatures ($>729^\circ\text{C}$), where bulk $\delta\text{-Bi}_2\text{O}_3$ is stable. As seen in Fig. 1(c), we recently observed that epitaxial nanoislands of pure $\delta\text{-Bi}_2\text{O}_3$ grown onto SrTiO_3 or DyScO_3 substrates exhibit 1/3-order superstructure peaks at room temperature, in addition to the normal Bragg peaks from the film and the substrate. These superstructure peaks are likely indicative of vacant oxygen site ordering, which has been theoretically predicted to occur in pure $\delta\text{-Bi}_2\text{O}_3$ [5]. We are currently determining the detailed ordered structure of stabilized $\delta\text{-Bi}_2\text{O}_3$ from our diffraction data. These results motivate future work, in which we will focus on understanding the factors that lead to oxygen vacancy ordering and explore strategies for suppressing ordering using proximity effects in oxide heterostructures.

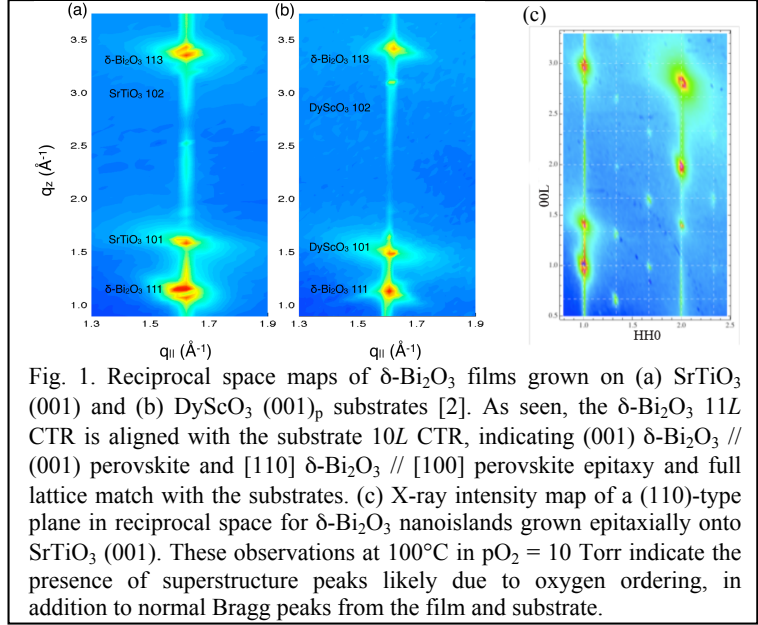


Fig. 1. Reciprocal space maps of $\delta\text{-Bi}_2\text{O}_3$ films grown on (a) SrTiO_3 (001) and (b) DyScO_3 (001)_p substrates [2]. As seen, the $\delta\text{-Bi}_2\text{O}_3$ 11L CTR is aligned with the substrate 10L CTR, indicating (001) $\delta\text{-Bi}_2\text{O}_3$ // (001) perovskite and [110] $\delta\text{-Bi}_2\text{O}_3$ // [100] perovskite epitaxy and full lattice match with the substrates. (c) X-ray intensity map of a (110)-type plane in reciprocal space for $\delta\text{-Bi}_2\text{O}_3$ nanoislands grown epitaxially onto SrTiO_3 (001). These observations at 100°C in $p\text{O}_2 = 10$ Torr indicate the presence of superstructure peaks likely due to oxygen ordering, in addition to normal Bragg peaks from the film and substrate.

Reversible Chemical Switching of Ferroelectric Oxide Thin Films (in collaboration with G.B. Stephenson and S.K. Streiffer of ANL, and C. Thompson of Northern Illinois University): Ferroelectric materials display a spontaneous electrical polarization that can be switched to different orientations, typically through application of an electric field. In this study, we demonstrated for the first time that ferroelectric polarization can also be fully and reversibly switched by changing the chemical environment in contact with the surface of the material. This work was published in *Physical Review Letters* [6] and was the subject of a Viewpoint commentary in *Physics* [7].

In-situ synchrotron x-ray scattering measurements (Fig. 2) show that high or low $p\text{O}_2$ induces outward or inward polarization, respectively, in ultrathin PbTiO_3 films. While x-ray scattering is not sensitive to interfacial charge from polarization, it is very sensitive to the atomic positions in the crystal structure of a ferroelectric film that determine its polarization. By characterizing film structure in-situ, under conditions of controlled $p\text{O}_2$ and temperature, one sees that the oxygen chemical potential determines the electric potential at the film surface, and that the relationship between electrical and chemical potential is complex. These experiments show that the chemical environment can play a dominant role in determining the behavior of nanoscale ferroelectrics.

We extended these studies recently to samples that include a Y_2O_3 -stabilized ZrO_2 (YSZ) layer grown on top of a similar $\text{PbTiO}_3/\text{SrRuO}_3/\text{SrTiO}_3$ thin film heterostructure. We find that the YSZ layers are continuous and are epitaxially oriented with respect to the PbTiO_3 . Furthermore, the now-buried PbTiO_3 layer remains ferroelectric below T_C , indicating that the YSZ provides sufficient electrical compensation at the YSZ/ PbTiO_3 heterointerface to avoid depolarization. The PbTiO_3 polarization direction again can be switched by changing the $p\text{O}_2$ of the gas environment, indicating that oxygen can rapidly diffuse through the YSZ and provide the required compensating charge at the YSZ/ PbTiO_3 heterointerface for both orientations of the ferroelectric polarization. These discoveries position us to explore, for the first time, the detailed interplay between ferroelectricity and ionic conductivity in oxide heterostructures.

Future Plans: Our planned research explores promising opportunities for creating new oxide heterostructures possessing enhanced material properties through control of heterointerfacial charge.

Enhanced Ionic Conductivity in Oxide Thin Film Heterostructures: It is known that grain boundaries in oxide perovskites are often positively charged relative to the bulk [8]. This leads to an oxygen vacancy depletion layer adjacent to the boundary and a consequent reduction in the in-plane conductivity. To achieve enhanced ionic transport in oxide systems where oxygen vacancies are the dominant carriers, we will construct an interface with a

net negative charge and produce an oxygen vacancy *enrichment* layer. With the many recent advances in oxide heterostructure synthesis, it is possible to fabricate such polar oxide interfaces and create new fast ion conductors by polar interface doping. For our initial studies, the heterostructures will be comprised of the perovskite LaGaO_3 layered with the spinel MgAl_2O_4 , both of which exhibit polar (001) planes. In bulk form, these oxides have poor ionic conductivity, but LaGaO_3 can demonstrate extremely high ionic conductivity when substitutionally doped [9]. Negatively charged interfaces requiring compensating defects will be synthesized, providing a strong driving force for enhancing the oxygen vacancy concentration and thus the in-plane ionic conductivity in the space charge region adjacent to the interface.

Interplay between Ionic Conductivity and Ferroelectric Behavior:

Studies of the interplay between different properties of complex oxides have drawn increasing attention in recent years. For example, multiferroics, exhibiting both magnetism and ferroelectricity, are of great interest because of the possibility of influencing one ferroic property by tuning another (e.g., magnetic control of ferroelectricity). We will investigate a different type of coupled behavior in heterostructures containing a ferroelectric material in close proximity to an ionic conductor. The polarization in a ferroelectric layer is expected to induce a strong effect on the distribution and possibly concentration of oxygen vacancies in an adjacent oxide ionic conductor. If successful, such heterostructures would exhibit ionic conduction localized to the space charge region of the heterointerface, i.e., would show the ionic conduction analogue of the quasi-two-dimensional electron gas (q2DEG) behavior reported in oxide heterostructures such as $\text{LaAlO}_3 / \text{SrTiO}_3$ [10]. As the magnitude and direction of the ferroelectric polarization are changed (by either changing $p\text{O}_2$ or an applied electric field), we expect this vacancy distribution to also change. Both experimental and theoretical studies of heterostructures consisting of undoped LaGaO_3 layered with PbTiO_3 will characterize the polarization-induced changes in oxygen vacancy concentration and distribution, and determine the possible effects of ferroelectric polarization on ionic transport behavior. A key question that will be addressed is whether the oxygen vacancies induced in proximity to ferroelectric/ionic conductor interfaces are sufficiently mobile to contribute to altering the oxygen diffusion rate in the ionic conductor.

Studies of interface charge in heterostructures containing both ionically conducting and ferroelectric materials not only provide an opportunity to enhance ionic conductivity, but also are of interest because of the possible effects of interfacial charge on the behavior of the ferroelectric. We thus will also continue to investigate the behavior of $\text{PbTiO}_3/\text{YSZ}$ heterostructures to determine the effects of ionic compensation on the switching behavior of PbTiO_3 films.

Synthesis Science of Charged Oxide Heterostructures: The strength of proximity effects in thin film oxide heterostructures can be tuned through manipulation of the interfacial spacing and morphology during synthesis. We will utilize state-of-the-art in-situ x-ray monitoring techniques to enable the creation of specially designed interfaces during the synthesis of layered or nanocomposite epitaxial oxide thin films. We have already developed unique facilities at the APS for in-situ studies of oxide MOCVD [11] and ALD [12], and are working to develop new capabilities for growing heterostructures by magnetron sputter deposition and by plasma-assisted ALD. We will focus on growing high quality epitaxial heterostructures of interest for the studies described above.

References

1. AM Azad, S Larose, and SA Akbar, *J. Mater. Sci.* **29** (16), 4135 (1994).
2. D.L. Proffit, G.-R. Bai, D.D. Fong et al., *Appl. Phys. Lett.* **96** (2), 021905 (2010).
3. T Takahashi and H Iwahara, *J Appl. Electrochem.* **3** (1), 65 (1973).
4. G. Gattow and H. Schröder, *Zeitschrift für anorganische und allgemeine Chemie* **318**, 176 (1962); H.A. Harwig, *ibid* **444**, 151 (1978).

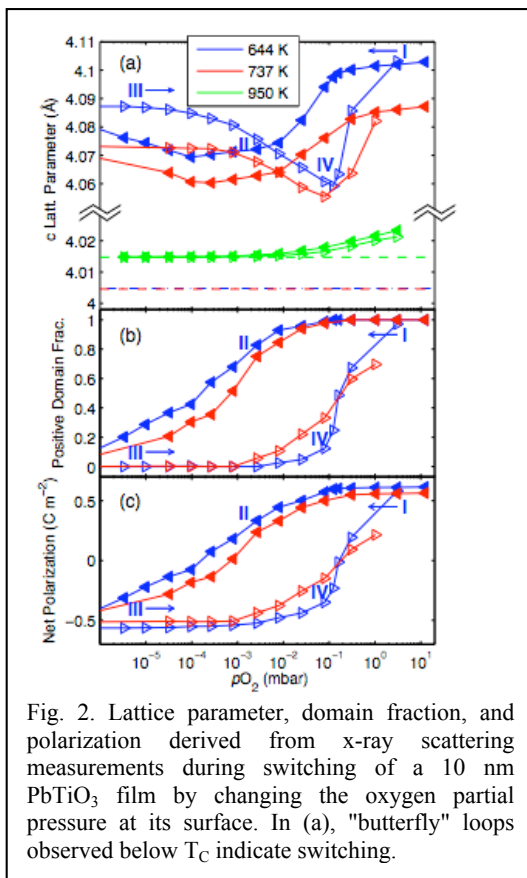


Fig. 2. Lattice parameter, domain fraction, and polarization derived from x-ray scattering measurements during switching of a 10 nm PbTiO_3 film by changing the oxygen partial pressure at its surface. In (a), "butterfly" loops observed below T_C indicate switching.

5. D. Aidhy, S. Sinnott, E. Wachsman et al., *J. Sol. St. Chem.*, **182**, 1222 (2009)
6. R. V Wang, D. D Fong, F Jiang et al., *Phys. Rev. Lett.* **102**, 047601 (2009).
7. Jirka Hlinka, *Physics* **2** (2009).
8. R.A. De Souza, *Phys. Chem. Chem. Phys.* **11**, 9939 (2009); R.A. De Souza and R. Meyer, *Phys. Rev. B* **72**, 056101 (2005).
9. S. Hull, *Rep. Prog. Phys.* **67**, 1233 (2004).
10. A Ohtomo and H. Y Hwang, *Nature* **427** (6973) (2004).
11. M.V.R. Murty, S.K. Streiffer, G.B. Stephenson, J.A. Eastman, G.-R. Bai, A. Munkholm, O. Auciello, C. Thompson, *Appl. Phys. Lett.*, **80**, 1809 (2002).
12. D.D. Fong, J.A. Eastman, P.H. Fuoss, P.M. Baldo, T.T. Fister, M.J. Highland, *Appl. Phys. Lett.*, **97**, 191904 (2010).

DOE Sponsored Publications (2008-2011)

“In situ characterization of strontium surface segregation in epitaxial $\text{La}_{0.7}\text{Sr}_{0.3}\text{MnO}_3$ thin films as a function of oxygen partial pressure,” T.T. Fister, D.D. Fong, J.A. Eastman, P.M. Baldo, M.J. Highland, P.H. Fuoss, K.R. Balasubramaniam, P.A. Salvador, *Applied Physics Letters*, **93**, 151904 (2008).

“Critical thickness of high structural quality SrTiO_3 films grown on orthorhombic (101) DyScO_3 ,” M.D. Biegalski, D.D. Fong, J.A. Eastman, P.H. Fuoss, et al., *Journal of Applied Physics*, **104**, 114109 (2008).

"Imaging and alignment of nanoscale 180° stripe domains in ferroelectric thin films," C. Thompson, D.D. Fong, R.-V. Wang, F. Jiang, S. K. Streiffer, K. Latifi, J.A. Eastman, P.H. Fuoss, and G.B. Stephenson, *Applied Physics Letters* **93**, 182901 (2008).

"Reversible Chemical Switching of a Ferroelectric Film," R.-V. Wang, D.D. Fong, F. Jiang, M.J. Highland, P.H. Fuoss, C. Thompson, A.M. Kolpak, J.A. Eastman, S.K. Streiffer, A.M. Rappe, and G.B. Stephenson, *Physical Review Letters* **102**, 047601 (2009).

"Ferroelectricity in Ultrathin Strained BaTiO_3 Films: Probing the Size Effect by Ultraviolet Raman Spectroscopy," D.A. Tenne, P. Turner, J.D. Schmidt, M. Biegalski, Y.L. Li, L.Q. Chen, A. Soukiassian, S. Trolier-McKinstry, D.G. Schlom, X.X. Xi, D.D. Fong, P. Fuoss, J. Eastman, G.B. Stephenson, C. Thompson, and S.K. Streiffer, *Physical Review Letters* **103**, 177601 (2009).

“Phase Transitions in Nanoscale Ferroelectric Structures,” S.K. Streiffer and D.D. Fong, *MRS Bulletin*, **34**, 832 (2009).

“In-Situ Synchrotron X-Ray Characterization of ZnO Atomic Layer Deposition,” D.D. Fong, J.A. Eastman, S.K. Kim, T.T. Fister, M.J. Highland, P.M. Baldo, P.H. Fuoss, *Appl. Phys. Lett.*, **97**, 191904 (2010).

"Polarization Switching without Domain Formation at the Intrinsic Coercive Field in Ultrathin PbTiO_3 ," M.J. Highland, T.T. Fister, M.-I. Richard, D.D. Fong, P.H. Fuoss, Carol Thompson, J.A. Eastman, S.K. Streiffer, and G.B. Stephenson, *Physical Review Letters*, **105**, 167601 (2010).

“Phase Stabilization of $\delta\text{-Bi}_2\text{O}_3$ Nanoislands by Epitaxial Growth onto Single Crystal SrTiO_3 or DyScO_3 Substrates,” D.L. Proffit, G.-R. Bai, D.D. Fong, T.T. Fister, S.O. Hruszkewycz, P.M. Baldo, P.H. Fuoss, T.O. Mason, J.A. Eastman, *Applied Physics Letters*, **96**, 021905 (2010).

“X-ray Probes for *In Situ* Studies of Interfaces,” D.D. Fong, C.A. Lucas, M.-I. Richard, and M.F. Toney, *MRS Bulletin* **35**, 504 (2010).

“In Situ Synchrotron Characterization of Complex Oxide Heterostructure,” T.T. Fister and D.D. Fong, in *Thin Film Metal-Oxides: Fundamentals and Applications in Electronics and Energy*, ed. S. Ramanathan (New York, NY: Springer Science + Business Media, LLC, 2010).

“Total-Reflection Inelastic X-Ray Scattering from a 10-nm Thick $\text{La}_{0.6}\text{Sr}_{0.4}\text{CoO}_3$ Thin Film,” T.T. Fister, D.D. Fong, J.A. Eastman, H. Iddir, P. Zapol, P.H. Fuoss, et al., *Phys. Rev. Lett.*, **106**, 037401 (2011).

“Strongly-correlated Two-Dimensional Electron Gas at Oxide Interfaces,” H. W. Jang, D. A. Felker, C. W. Bark, Y. Wang, M. K. Niranjana, C. T. Nelson, Y. Zhang, D. Su, C. M. Folkman, S. H. Baek, S. Lee, K. Janicka, Y. Zhu, X. Q. Pan, D. D. Fong, E. Y. Tsybal, M. S. Rzechowski, C. B. Eom, accepted for publication in *Science*.

“Tailoring a Two-Dimensional Electron Gas at the $\text{LaAlO}_3/\text{SrTiO}_3$ (001) Interface by Epitaxial Strain,” C. W. Bark, D. A. Felker, Y. Wang, Y. Zhang, H. W. Jang, C. M. Folkman, J. W. Park, S. H. Baek, X. Q. Pan, H. Zhou, D. D. Fong, E. Y. Tsybal, M. S. Rzechowski, C. B. Eom, accepted for publication in *Proc. Nat'l. Acad. Sci.*

Nanometer-Scale Surface and Interface Phenomena

Peter Feibelman,¹ Norman Bartelt, Gary Kellogg, Kevin McCarty,
Nancy Missert, Brian Swartzentruber, Konrad Thürmer, and Kevin Zavadil
Sandia National Laboratories, Livermore, CA and Albuquerque, NM

Program Scope

This program is aimed at atomic/molecular-scale understanding of processes occurring at solid-vacuum, solid-solid and solid-liquid interfaces. Its goal is to provide the scientific underpinnings needed to control surface/interface properties for materials applications, particularly those relevant to energy-related technologies. With the goal of determining how atomic-scale processes relate to the longer-range interactions that control interfacial behavior, our approach combines state-of-the-art experimental capabilities with theory and simulation. The project has four synergistic tasks:

1) *Atomistic dynamics of surfaces* focuses on the mechanisms and energetics of atom transport across surfaces and into the interiors of solids. Experimental tools include scanning tunneling microscopy (STM), *atom-tracking* STM and low-energy electron microscopy (LEEM). Theoretical interpretations emerge from density functional theory (DFT) studies, molecular dynamics/Monte Carlo simulations and thermodynamic modeling. We have identified diffusion processes underlying the growth and stability of surface alloys, thin-film growth and surface nanostructure formation.

2) *Collective phenomena in surface dynamics* quantifies collective processes that govern the surface structures and morphologies of functional materials. We use STM and LEEM to measure the time-evolution of surface structure on nanometer length scales. We develop equations of motion, which account for the observed time dependences precisely and relate their parameters to the atomic processes studied in Task 1. Our new insights into materials behavior include determining the forces that stabilize self-assembling patterns, identifying the kinetic pathways that promote film instability and revealing that unexpected processes of cluster diffusion and bulk/surface mass exchange can guide materials growth.

3) *Materials at interfaces: structural and mechanical properties* measures adhesion, wetting, and mechanical properties at the nanometer to micron scale, using highly sensitive interfacial probes, and interprets them with ideas stemming from atomic-level studies. We have recently been using STM to probe the structure of the first few layers of atoms or molecules such as water near an interface, and DFT both to interpret images and guide experiments.

4) *Nanoscale electrochemistry* uses advanced electrochemical, morphological, chemical and structural analytical tools to clarify corrosion and nanostructure-formation mechanisms. Primary goals are a quantitative understanding of the mechanisms of localized corrosion initiation in passive metals and measurements of the critical parameters governing nanostructure formation in model systems. We apply novel and unique nanofabrication techniques to produce tailored surfaces, and to simulate specific defect types on controlled substrates in well-defined locations.

Recent Progress

Atomistic dynamics of surfaces Our recent progress includes: 1) understanding defect-mediated diffusion of embedded Ge atoms in Ge/Si(001), 2) analyzing atom transport during surface alloy formation in the Pd-Cu(001) system, 3) determining the mechanism of Si adatom diffusion on the Au-Si(111) 5x2 surface alloy, 4) understanding labyrinth island growth in Pd/Ru(0001) heteroepitaxy, 5) revealing the competition between bulk and surface diffusion in the chemically

¹ Email: pjfeibe@sandia.gov

reactive system of Al alloying with NiAl, 6) quantifying the mobility of water molecules on ice and 7) determining the atomic structure of graphene on metals.

Collective phenomena in surface dynamics Our recent progress includes: 1) understanding how B induces self-assembly of one-dimensional nanostructures on Si(001), 2) determining why patterns form after metal deposition on graphene, 3) identifying the mechanism and energetic driving force for 3D pattern formation, 4) explaining nanoscale periodicity in the high-temperature limit, 5) elucidating how stress relaxes at the nanoscale beyond continuum theories, 6) showing that graphene grows on metals by adding clusters of C atoms, 7) revealing the mechanisms of graphene growth by SiC decomposition and 8) characterizing the growth of ice films on Pt(111).

Materials at interfaces: Structural and mechanical properties Our recent progress includes: 1) explaining epitaxial water nucleation on the surface of salt, 2) first-principles calculations of water-solid interfaces, including water on β -AgI, Pd(111), Ru(0001) and muscovite, 3) understanding NaCl hydration by ice, 4) measuring friction on a self-lubricating surface, 5) evaluating nanoscale adhesion beyond classical descriptions, 6) developing a molecular basis for interfacial deformation, friction, and wear and 7) determining the structure of the water wetting layer on Pt(111) (Fig. 1).

Nanoscale electrochemistry: Our recent progress includes: 1) characterizing passive oxide breakdown events on Al microelectrodes, 2) defining the role of oxygen vacancy generation in oxide passivity, 3) creating artificial pit nuclei on aluminum at pre-determined locations to measure local pitting susceptibility, 4) using first-principles calculations of Al and O bonding in the presence of a H-impurity atom to conclude that oxide-metal bonding is weaker at interfacial steps, 5) discovering that activation of the oxide surface towards the oxygen reduction reaction occurs in alkaline solutions due to a dramatic increase in electron transfer rates, 6) showing that localized attack in model alloy systems is metastable because of the high pH environment, and 7) showing that self-assembly of surface nanostructures can be controlled electrochemically through manipulation of surface stress from specifically adsorbed anion layers.

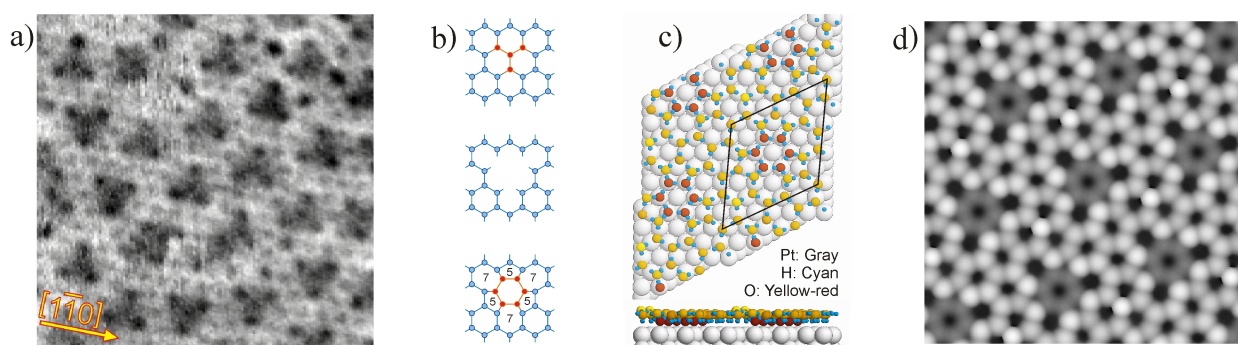


Fig. 1. The ice/Pt(111) wetting layer. (a) 8nm \times 8nm STM image of submonolayer water deposited on Pt(111) at 140 K. (b) Formation of the structural motif: a “575757” di-interstitial defect. (c) DFT model of the wetting layer incorporating this defect. (d) Simulated STM image based on DFT charge densities.

Future Plans

Atomistic dynamics of surfaces: We intend to begin atomic-level studies of transport on oxide and ice surfaces as well as between the surface and bulk of oxide materials relevant to energy-storage applications.

Collective phenomena in surface dynamics: We plan new studies of: 1) nanoscale-pattern formation, including metal clusters on graphene, stripes on boron-doped Si, and water films on metals, 2) cooperative mechanisms of material growth, including those that cause graphene to

grow by cluster addition and 3) the stability of thin films, including the amorphous-to-crystalline ice conversion, and the dewetting of metal films on solid-state electrolytes.

Materials at interfaces: Structural and mechanical properties: Future work includes simulations of water transport in narrow channels - to resolve a long-standing question of viscosity enhancement - also studies aimed at predictive understanding of wetting layer structure vs. close-packed Group VIII metal surface, and STM investigations of proton order in near-substrate layers of ice films.

Nanoscale electrochemistry: We plan to continue exploring the correlation between nanostructure evolution and pit initiation in pure Al and model Al-Cu alloys. We will expand our in-situ studies of nanostructure formation to energy storage and conversion materials.

DOE Sponsored Publications 2009-2010

- E. Bussmann, J. Sun, K. Pohl and G. L. Kellogg, "Palladium Diffusion into Bulk Copper via the Cu(100) Surface," *J. Physics: Condensed Matter* **21**, 314016 (2009).
- G. A. Crawford, N. Chawla, and J.E. Houston, "Nanomechanics of biocompatible TiO₂ nanotubes by Interfacial Force Microscopy (IFM)." *J. Mech. Behav. Biomed. Mat.* **2**, 580-587 (2009).
- F. El Gabaly, N. C. Bartelt and A. K. Schmid, "Preparing arrays of large atomically flat regions on single crystal substrates," *J. Phys.-Condens. Matter* **21**, 314019 (2009).
- K.V. Emtsev, A. Bostwick, K. Horn, J. Jobst, G. L. Kellogg, L. Ley, J. L. McChesney, T. Ohta, S. A. Reshanov, J. Rohrl, E. Rotenberg, A. K. Schmid, D. Waldmann, H. N. Weber and T. Seyller, "Towards wafer-size graphene layers by atmospheric pressure graphitization of silicon carbide," *Nat. Mater.* **8**, 203-207 (2009).
- P. J. Feibelman, "Concluding Remarks, Water - From Interfaces to the Bulk," *Faraday Disc.* **141**, 467(2009).
- P. J. Feibelman, "Onset of three-dimensional Ir islands on a graphene/Ir(111) template," *Phys. Rev. B* **80**, 085412 (2009).
- P. J. Feibelman, "Pentagonal ice in chains," *Nature Materials (News and Views)* **8**, 372(2009).
- M. P. Goertz, B. L. Stottrup, J. E. Houston, and X. Y. Zhu, "Nanomechanical Contrasts of Gel and Fluid Phase Supported Lipid Bilayers," *J. Phys. Chem. B* **113**, 9335 (2009).
- M. P. Goertz, X.-Y. Zhu, and J.E. Houston, "Temperature Dependent Relaxation of a 'Solid-Liquid'," *J. Poly. Sci. B-Poly. Phys.* **47**, 1285 (2009).
- J. C. Hamilton and W. G. Wolfer, "Theories of surface elasticity for nanoscale objects," *Surf. Sci.* **603**, 1284-1291 (2009).
- E. Loginova, S. Nie, K. Thürmer, N. C. Bartelt and K. F. McCarty, "Defects of graphene on Ir(111): Rotational domains and ridges," *Phys. Rev. B* **80**, 085240 (2009).
- E. Loginova, N. C. Bartelt, P. J. Feibelman and K. F. McCarty, "Factors influencing graphene growth on metal surfaces," *New J. Phys.* **11**, 063046 (2009).
- A. Mascaraque, L. Aballe, J. F. Marco, T. O. Mendes, F. El Gabaly, C. Klein, A. K. Schmid, K. F. McCarty, A. Locatelli, and J. de la Figuera, "Measuring the magnetization of three monolayer thick Co islands and films by x-ray dichroism," *Phys. Rev. B* **80**, 172401 (2009).
- K. F. McCarty, P. J. Feibelman, E. Loginova and N. C. Bartelt, "Kinetics and thermodynamics of carbon segregation and graphene growth on Ru(0001)," *Carbon* **47**, 1806-1813 (2009).
- K. F. McCarty, J. C. Hamilton, Y. Sato, A. Saa, R. Stumpf, J. de la Figuera, K. Thürmer, F. Jones, A. K. Schmid, A. A. Talin and N. C. Bartelt, "How metal films de-wet substrates-identifying the kinetic pathways and energetic driving forces," *New J. Phys.* **11**, 043001 (2009).
- K. F. McCarty, J. C. Hamilton, Y. Sato, A. Saa, R. Stumpf, J. de la Figuera, K. Thürmer, F. Jones, A. K. Schmid, A. A. Talin and N. C. Bartelt, "How metal films de-wet substrates -identifying the kinetic pathways and energetic driving forces," *New J. Phys.* **11**, 043001 (2009).
- N. W. Moore, J. H. Luo, J. Y. Huang, S. X. Mao, and J. E. Houston, "Superplastic Nanowires Pulled from the Surface of Common Salt," *Nano Letters* **9**, 2295-2299 (2009).
- N. Murer, N. A. Missert, R. G. Buchheit, "Using finite element modeling to determinate the origin of trenching in aluminum alloys", Proceedings, EUROCORR 2009, Nice, France.
- N. Murer, N. A. Missert, R. Oltra, R.G. Buchheit, "Towards the modeling of microgalvanic coupling in aluminum alloys : the choice of boundary conditions", *Proceedings, COMSOL Boston 2009*.
- S. Nie, N. C. Bartelt and K. Thürmer, "Observation of Surface Self-Diffusion on Ice," *Phys. Rev. Lett.* **102**, 136101 (2009).

- B. Santos, E. Loginova, A. Mascaraque, A. K. Schmid, K. F. McCarty, and J. de la Figuera, "Structure and magnetism in ultrathin iron oxides characterized by low energy electron microscopy," *J. Phys.-Condens. Matter* **21**, 314001 (2009).
- A. Seyeux, N. Missert, G.S. Frankel, L.H. Klein, A. Galtayries, P. Marcus, "Combination of ToF-SIMS imaging and AFM to study the early stages of corrosion in Al-Cu thin films", Proceedings, EUROCORR 2009, Nice, France.
- D. A. Siegel, S. Y. Zhou, F. El Gabaly, A. K. Schmid, K. F. McCarty and A. Lanzara, "Three-fold diffraction symmetry in epitaxial graphene and the SiC substrate," *Phys. Rev. B* **80**, 241407(R) (2009).
- E. Starodub, S. Maier, I. Stass, N. C. Bartelt, P. J. Feibelman, M. Salmeron, and K. F. McCarty, "Graphene growth by metal etching on Ru(0001)," *Phys. Rev. B* **80**, 235422 (2009).
- B. Unal, Y. Sato, K. F. McCarty, N. C. Bartelt, T. Duden, C. J. Jenks, A. K. Schmid and P. A. Thiel, "Work function of a quasicrystal surface: Icosahedral Al-Pd-Mn." *J. Vac. Sci. Tech. A* **27**, 1249-1250 (2009).
- K.R. Zavadil, J.A. Ohlhausen and P.G. Kotula, "Proton Induced Point Defect Generation and Subsequent Interfacial Void Formation in Model Passive Oxides on Aluminum," *J. Electrochem. Soc.*, submitted, 2009.
- E. Bussmann and B. S. Swartzentruber, "Ge Diffusion at the Si(100) Surface," *Phys. Rev. Lett.* **104** (2010).
- P. J. Feibelman, "DFT Versus the "Real World" (or, Waiting for Godft)," *Top. Catal.* **53**, 417-422 (2010).
- P. J. Feibelman, "The first wetting layer on a solid," *Phys. Today* **63**, 34-39 (2010).
- T. Herranz, K. F. McCarty, B. Santos, M. Monti and J. de la Figuera, "Real Space Observations of Magnesium Hydride Formation and Decomposition," *Chem. Mat.* **22**, 1291-1293 (2010).
- S. Nie, P. J. Feibelman, N. C. Bartelt and K. Thurmer, "Pentagons and Heptagons in the First Water Layer on Pt(111)," *Phys. Rev. Lett.* **105** (2010).
- T. Ohta, N. C. Bartelt, S. Nie, K. Thurmer and G. L. Kellogg, "Role of carbon surface diffusion on the growth of epitaxial graphene on SiC," *Phys. Rev. B* **81** (2010).
- B. Santos, J. M. Puerta, J. I. Cerda, T. Herranz, K. F. McCarty and J. de la Figuera, "Structure of ultrathin Pd films determined by low-energy electron microscopy and diffraction," *New Journal of Physics* **12** (2010).
- Y. Sato, B. Unal, T. A. Lograsso, P. A. Thiel, A. K. Schmid, T. Duden, N. C. Bartelt and K. F. McCarty, "Periodic step arrays on the aperiodic i-Al-Pd-Mn quasicrystal surface at high temperature," *Phys. Rev. B* **81** (2010).
- J. Soltis, D. P. Krouse, N. J. Laycock and K. R. Zavadil, "Automated processing of electrochemical current noise in the time domain: I. Simulated signal," *Corrosion Sci.* **52**, 838-847 (2010).
- E. Starodub, N. C. Bartelt and K. F. McCarty, "Oxidation of Graphene on Metals," *J. Phys. Chem. C* **114**, 5134-5140 (2010).
- P. J. Feibelman, N.C. Bartelt, S. Nie, and K. Thürmer, "Interpretation of high-resolution images of the best-bound wetting layers on Pt(111)," *J. Chem. Phys.* **133**, 154703(2010).
- Y. Murata, E. Starodub, B. B. Kappes, C. V. Ciobanu, N. C. Bartelt, K. F. McCarty, and S. Kodambaka "Orientation-dependent work function of graphene on Pd(111)," *Appl. Phys. Lett.* **97**, 143114(2010).
- J. M. Wofford, S. Nie, K. F. McCarty, N. C. Bartelt, O. D. Dubon, "Graphene Islands on Cu Foils: The Interplay between Shape, Orientation, and Defects," *Nano Lett.* **10**, 4890(2010).
- J. L. McChesney, A. Bostwick, T. Ohta, T. Seyller, K. Horn, J. Gonzalez, E. Rotenberg, "Extended van Hove Singularity and Superconducting Instability in Doped Graphene", *Phys. Rev. Lett.* **104**, 136803(2010).
- T. Herranz, B. Santos, K. F. McCarty and J. de la Figuera, "Real-space study of the growth of magnesium on ruthenium," *Surface Science*, submitted (2010).
- E. Starodub, A. Bostwick, L. Moreschini, S. Nie, F. E. Gabaly, K. F. McCarty and E. Rotenberg, "In-plane orientation effects on the electronic structure, stability and Raman scattering of monolayer graphene on Ir(111)," *Physical Review B*, submitted (2010).
- S. Nie, A. L. Walter, N. C. Bartelt, E. Starodub, A. Bostwick, E. Rotenberg and K. F. McCarty, "Growth from below: graphene multilayers on Ir(111)," *ACS Nano*, submitted (2010).
- I. Ermanoski, N. C. Bartelt, and G. L. Kellogg, "Self-assembly of defect-free nano stripe arrays on B-doped Si(001)," *Phys Rev. B*, submitted
- D. A. Schmidt, Taisuke Ohta, L. B. Biedermann, T. E. Beechem, S. W. Howell, and G. L. Kellogg, "Inhomogeneous strain fields in epitaxial graphene," *Phys. Rev. B*, submitted
- E. Bussmann, I. Ermanoski, P. J. Feibelman, N. C. Bartelt, and G. L. Kellogg, "Subsurface palladium slows surface diffusion on the Cu(001)-c(2 × 2)-Pd buried alloy," *Phys. Rev. B*, submitted
- A. Seyeux, G. S. Frankel, N. Missert, K. A. Unocic, L. H. Klein, A. Galtayries, P. Marcus, "ToF-SIMS imaging study of the early stages of corrosion in Al-Cu thin films", *J. Electrochem. Soc.*, submitted (2010).

Classical and Quantum Stress Effects in Nano Thin Films and in Doping of Semiconductors

Feng Liu (fliu@eng.utah.edu)
Department of Materials Science & Engineering
University of Utah, Salt Lake City, UT 84112

Program Scope

Stress effect is ubiquitous in thin film and bulk materials. In this program, on the one hand, we continue and expand our previous investigations in the area of stress/strain induced self-assembly and self-organization of nanostructures in heteroepitaxial growth of thin films, and on the other hand, initiate a new research direction of exploring the “quantum stress” effect, a new conceptual extension over the classical stress effect we developed recently. Our main objective is to achieve a better fundamental understanding of stress (strain) effect on physical behavior of materials. Specifically, we will focus on two topics: (1) heterogeneous nucleation of strained islands on patterned substrate, such as quantum dot molecules, and (2) quantum manifestations of bulk stress effect in doping of semiconductors and surface stress effect in nanofilms. Our studies will significantly improve our fundamental understanding of effects of stress/strain on physical behavior of materials, especially in the area of strain induced nanoscale assembly and doping of semiconductors. They will provide useful guidelines for future experimental efforts in strain engineering of formation of nanostructures and doping of semiconductors. They will also have direct technological impact on advancing electronic and optoelectronic materials for energy applications, to fulfill the mission of the Department of Energy.

Recent Progress

Topic 1. Strain Induced Growth Instability and Island Nucleation on Patterned Substrate.

Strain induced self-assembly provides an attractive route to nanofabrication of semiconductor quantum dots on surfaces. Recent experiments have demonstrated that combining the strain induced self-assembly with surface patterning provides an effective method to further improve the size uniformity and spatial ordering of quantum dots [1]. However, the underlying mechanisms responsible for such improvement remain poorly understood. We have performed vigorous theoretical analyses of strain induced growth instability [2] and island nucleation [3] on patterned substrates. We show that [2] the growth of a strained film is inherently less stable on a wavy substrate than on a flat substrate. For small surface undulation, the critical wavelength characterizing the initial instability on a wavy substrate is effectively half of that on a flat substrate. Furthermore, on patterned substrates (see Fig. 1), island

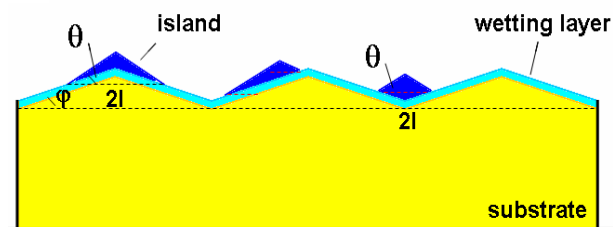


Fig. 1. Schematic illustration of island nucleation on a patterned substrate with a sawtooth pattern having a slope of constant angle ϕ , indicating different possible island nucleation positions.

nucleation is directed to the preferred sites by a much lower energy barrier and smaller critical size [3]. Strain relaxation directs island nucleation to the bottom of a pit rather than the top of a ridge as commonly perceived, while large surface energy anisotropy leads to nucleation at both places. Our theory explains some puzzling experimental results and provides useful guidelines for future exploration of directing the self-assembly of quantum dots on patterned substrates.

Topic 2. Dual-surfactant effect on enhancing p-type doping in III-V semiconductor thin films. Surfactants have been widely used in epitaxial growth [4], as an effective “additional” parameter, to control the thin film microstructure, composition and morphology. The role of surfactant is usually considered to be achieved by one single foreign surface element (or chemical species) that is different from the film. Recently, we introduced a new “dual-surfactant” effect [5], for which the role of surfactant can only be achieved by the combined effects of two foreign surface elements while neither of the two can act alone as an effective surfactant. We demonstrated the dual-surfactant effect for the case of enhancing p-type doping in III-V semiconductors [5]. We carried out first-principles calculations of Zn incorporation in the (001) GaP films under the influence of surface Sb and H (see Fig. 2). We found that Sb alone has little effect on the doping energy of Zn in GaP, and it is only when H is also present that the Zn doping energy is substantially lowered by Sb. Also, surface H does not function as effectively alone without Sb. Thus, it is the combined effect of Sb and H that makes the Zn doping process thermodynamically favorable, manifesting a unique dual-surfactant effect. The dual-surfactant with two surface elements will greatly broaden the scope and application of the conventional surfactant effect with one surface element. Specifically, in order to accommodate the *p*-type (Zn) doping, the role of first surfactant Sb (a “metallic” element) is to provide an electron reservoir to redistribute electrons, while the role of second surfactant H (a “single electron”) is to add one electron by each H to help satisfy the electron counting rule. We believe the dual-surfactant effect can be used as a general strategy for enhancing *p*-type doping of III-V semiconductors by using a metallic-element with H as dual-surfactants.

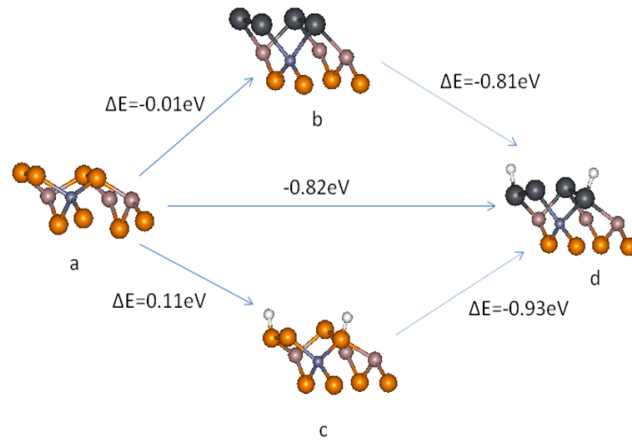


Fig. 2. Schematic illustration of dual surfactant effect showing change of doping energy (E) in various doping configurations: with dopant Zn atom (small blue sphere) replacing a Ga atom (medium wine) in GaP (P: large orange). Sb is one surfactant (largest black) and H is the second surfactant (smallest white).

Topic 3. Strain-Enhanced Doping in Semiconductors: Effects of Dopant Size and Charge State. In addition to the effect of stress/strain on the morphology of surface and thin films, we explored the effect of strain on alloy composition and doping of semiconductors. Using extensive first-principles calculations, we demonstrated that [6] the dopant induced volume change arises as a result of two factors: the intrinsic atomic size difference V_a and the electronic environment-induced volume change V_e ; the latter is a manifestation of quantum stress effect induced by adding an electron or a hole (i.e., removing an electron) to the lattice. n-type dopants induce a positive V_e (or a compressive quantum lattice stress) due to the extra valence electron that expands the lattice, whereas p-type dopants induce a negative V_e (tensile quantum stress) due to the hole in valence band that shrinks the lattice. Contrary to “common perception”, we show that the doping energy does not exhibit a minimum at a particular volume (or strain) but changes monotonically in a linear fashion with the applied external strain. We propose that the intriguing unbounded strain-induced change in impurity formation energy can be used effectively to enhance dopant solubility in a wide range of semiconductors.

Future Plans

We will continue to expand our studies to explore the effect of stress/strain on physical behavior of materials, in particular on two topics: (1) strain induced self-assembly of epitaxial thin films, and (2) quantum stress effect. On the first topic, one interesting problem we are studying is the heterogeneous nucleation and growth of quantum dot molecules (QDMs), i.e., growth of multiple islands mediated by a pit in the surface (see Fig. 3). We will develop a theoretical model to reveal the physical origin of the reduced critical size and energy barrier for QDM nucleation, and try to explain some interesting experimental results associated with QDMs. On the second topic, we plan to expand our study of quantum stress effect to structural phase transitions induced by photo excitation, such as the graphite-to-diamond transition under pulse laser irradiation. We believe this class of transitions can be understood in terms of “quantum stress” induced by charge carriers (electrons, holes and excitons) generated by photo excitation, in analogy to phase transitions induced by hydrostatic pressure. We will develop theoretical methods to calculate quantum stress induced by charge carriers from first principles.

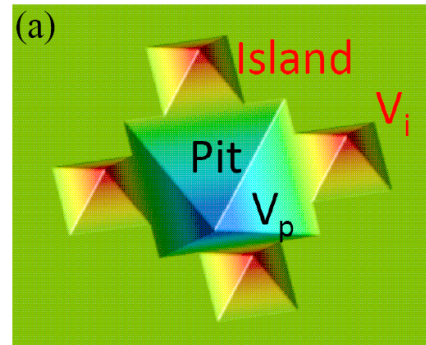


Fig. 3. Schematics of a QDM with four strained island surrounding a pit.

References

1. See, e.g., “Lateral Alignment of Epitaxial Quantum Dots”, Ed. O. Schmidt, Springer (2007).
2. H. Wang, Y. Zhang, and Feng Liu, *J. Appl. Phys.* 104, 054301 (2008).
3. H. Hu, H.J. Gao and Feng Liu, *Phys. Rev. Lett.* 101, 216102 (2008).
4. M. Copel, M. C. Reuter, E. Kaxiras, and R. M. Tromp. *Phys. Rev. Lett.* **63**, 632 (1989).
5. J. Zhu, Feng Liu, G.B. Stringfellow, *Phys. Rev. Lett.* 101, 196103 (2008).
6. J. Zhu, Feng Liu, G. B. Stringfellow, and S.-H. Wei, *Phys. Rev. Lett.* 105, 195503 (2010).

The DOE Program Sponsored Publications in 2008-2010

Invited Papers:

1. “Coulomb sink effect on coarsening of metal nanostructures on surfaces”, Y. Han and Feng Liu, *Front. Phys. China*, **3**, 41 (2008). (**Invited review**)
2. “Nanomechanical Architecture --- A Mechanics-Driven Nanofabrication Approach”, Feng Liu, M. G. Lagally and J. Zang, *MRS Bulletin* **34**, 190 (2009). (**Invited review**).

Refereed journals:

3. “Controlled surface functionalization via self-selective metal adsorption and pattern transformation on the vicinal Si(111) surface”, A. L. Chin, F. K. Men and Feng Liu, *Phys. Rev. B* **82**, 201406(R) (2010).
4. “Strain-Enhanced Doping in Semiconductors: Effects of Dopant Size and Charge State”, J. Zhu, Feng Liu, G. B. Stringfellow, and S.-H. Wei, *Phys. Rev. Lett.* **105**, 195503 (2010).
5. “Tunable interfacial properties of epitaxial graphene on metal substrates”, M. Gao, Y. Pan, C. Zhang, H. Hu, R. Yang, H. Lu, J. Cai, S. Du, Feng Liu, and H.-J. Gao, *Appl. Phys. Lett.* **96**, 053109 (2010).
6. “Enhanced cation-substituted p-type doping in GaP from dual surfactant effects”, J. Zhu, Feng Liu, and G. B. Stringfellow, *J. Cryst. Growth* **312**, 174 (2010).
7. “Nanopumping Molecules by Mechanical Carbon Nanotube Actuation”, M. Chen, J. Zang, D. Xiao, C. Zhang and Feng Liu, *Nano Res* **2**, 938 (2009).
8. “Bistability of Nanoscale Ag Islands on Si(111)-(4x1)-In Surface Induced by Anisotropic Stress”, Y. Li, M. Liu, D. Ma, D. Yu, X. Chen, X. Ma, Q. Xue, K. Xu, J. Jia, and Feng Liu, *Phys. Rev. Lett.* **103**, 076102 (2009).
9. “Band Gap Scaling of Graphene Nanohole Superlattices”, W. Liu, Z. F. Wang, Q. W. Shi, J. Yang, and Feng Liu, *Phys. Rev. B* **80**, 233405 (2009).
10. “Directed self-assembly of monodispersed platinum nanoclusters on graphene Moiré template”, Y. Pan, M. Gao, L. Huang, Feng Liu, and H.-J. Gao, *Appl. Phys. Lett.* **95**, 093106 (2009).
11. “Vacancy trapping mechanism for hydrogen bubble formation in metal”, Y.-L. Liu, Y. Zhang, H.-B. Zhou, G.-H. Lu, Feng Liu, and G.-N. Luo, *Phys. Rev. B* **79**, 172103 (2009).
12. “Mechanical Wave Propagation in Carbon Nanotubes Driven by an Oscillating Tip Actuator”, M. Chen, J. Zang, D. Xiao and Feng Liu, *J. Appl. Phys.* **105**, 026102 (2009).
13. “Highly Ordered, Millimeter-Scale, Continuous, Single-Crystalline Graphene Monolayer Formed on Ru (0001)”, Y. Pan, H. Zhang, D. Shi, J. Sun, S. Du, Feng Liu, H.-J. Gao, *Adv. Mat.* **21**, 2777 (2009).
14. “Theory of Directed Nucleation of Strained Islands on Patterned Substrates” H. Hu, H.J. Gao and Feng Liu, *Phys. Rev. Lett.* **101**, 216102 (2008).
15. “Dual-surfactant effect on enhancing p-type doping in III-V semiconductor thin films” J. Zhu, Feng Liu, G.B. Stringfellow, *Phys. Rev. Lett.* **101**, 196103 (2008).
16. “Magnetism in Nanopatterned Graphite Film”, L. Chen, D. Yu, Feng Liu, *Appl. Phys. Lett.* **93**, 223106 (2008).
17. “Unified Design Rule for Nanomagnetism in Graphene”, D. Yu, E. M. Lupton, H.J. Gao, C. Zhang and Feng Liu, *Nano Res.* **1**, 497 (2008).
18. “Enhanced growth instability of a strained film on a wavy substrate”, H. Wang, Y. Zhang, and Feng Liu, *J. Appl. Phys.* **104**, 054301 (2008).
19. “The role of vacancy on trapping interstitial O in heavily As-doped Si”, G.H. Lu, Q. Wang and Feng Liu, *Appl. Phys. Lett.* **92**, 211906 (2008).
20. “Collective Magnetic Behavior of Graphene Nanohole Superlattices”, D. Yu, E. M. Lupton, M. Liu, W. Liu and Feng Liu, *Nano Res.* **1**, 56 (2008).
21. “Suppression of spin-polarization in graphene nanoribbon by edge defect and impurity”, B. Huang, Feng Liu, J. Wu, B.-L. Gu, and W. Duan, *Phys. Rev. B* **77**, 153411 (2008).

Interfaces in Electronic and Structural Materials

Yuri Mishin, PI

Department of Physics and Astronomy
George Mason University, MSN 3F3
4400 University Drive, Fairfax, VA

Phone: 703-993-3984
Fax: 703-993-1269
Email: ymishin@gmu.edu

Program Scope

Interfaces play a critical role in many processes in materials, including plastic deformation, fracture, thin film deposition and microstructure evolution. Many important interface properties are not yet understood on the fundamental level. The goal of this project is to develop a deeper fundamental understanding of atomic structure, phase transformations, mechanical response and the dynamics of motion of interfaces in materials relevant to energy applications. The particular interface properties studied in this project include: (1) thermodynamic properties such as interface free energy and interface stress, (2) GB melting and premelting, (3) atomic and chemical disorder at solid-solid interfaces in intermetallic compounds, (4) wetting and dewetting of liquids on solid surfaces, and (5) the ability of grain boundaries (GBs) to move under applied shear stresses. The interface processes and properties are studied by atomistic computer simulation methods, primarily by the molecular dynamics (MD) and Monte Carlo techniques. These atomistic simulations are integral part of a larger multi-scale approach involving first-principles electronic structure calculations for calibration of atomistic potentials and phase-field and phase-field crystal (PFC) methods for accessing larger systems size and diffusion time scales.

Recent Progress

1. We proposed a thermodynamic theory of solid-fluid and solid-solid interfaces in multi-component systems subject to non-hydrostatic mechanical stress. A generalized form of the adsorption equation was derived, which includes the work terms representing the interface stress tensor. The theory rigorously defines the interface free energy and interface stress in non-hydrostatic systems and introduces new interfacial quantities, e.g. excess shears, that are not present in Gibbsian thermodynamics. Based on this theory we proposed thermodynamic integration methods permitting interface free energy calculations using interface excess quantities easily accessible by atomistic methods. The proposed methodology was applied to MD and Monte Carlo simulations of solid surfaces and solid-liquid interfaces in binary alloys in the presence of large tensile stresses. The calculations demonstrate an excellent computational efficiency and good agreement with experimental data. This methodology is currently used by several other groups for calculations of interface thermodynamic properties.

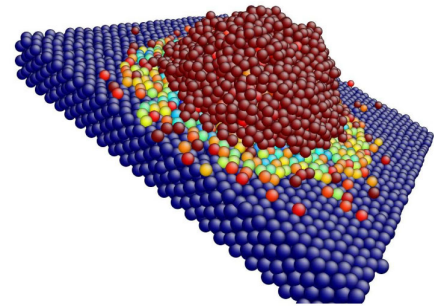
When applying the above methodology to binary systems, we found a fundamentally interesting case of *negative* and strongly curvature-dependent interface free energy. This leads to the formation of a thermodynamically stable colloidal structure with nanometer-size Ta particles suspended in liquid Cu. The feasibility of stable nano-disperse structures can have an impact on nanotechnology and is now being tested experimentally in collaboration with the Army Research Laboratory.

2. We have studied the premelting behavior of solid surfaces and GBs in pure metals and binary systems by two approaches: (i) atomistic simulations and (ii) phase field modeling with input parameters from experiment and atomistic calculations. The results of both methods are in

qualitative agreement with each other and demonstrate a rich variety of possible premelting scenarios, ranging from continuous premelting when approaching the bulk melting point or the solidus line from below to a discontinuous transition accompanied by a hysteresis. It has been shown that most of the melting behaviors can be rationalized in terms of different types of disjoining potentials.

3. Chemical composition and atomic ordering at the (111) anti-phase boundary (APB) in the Ni₃Al-based γ' phase have been studied by semi-grand canonical Monte Carlo simulations over a wide range of temperatures. The atomic interactions were modeled with an embedded-atom potential reproducing the relevant part of the Ni–Al phase diagram. In a certain range of bulk compositions and temperatures within the γ' phase stability domain, the APB undergoes a pre-wetting phase transformation by becoming a layer of disordered γ phase. The pre-wetting transformation line has been mapped onto the bulk phase diagram, allowing predictions of the APB state under various thermochemical conditions. The APB disordering transition can have a significant impact on mechanical behavior of commercial γ/γ' superalloys by modifying the dissociation of dislocations into partials and their interaction with disperse coherent γ' particles.

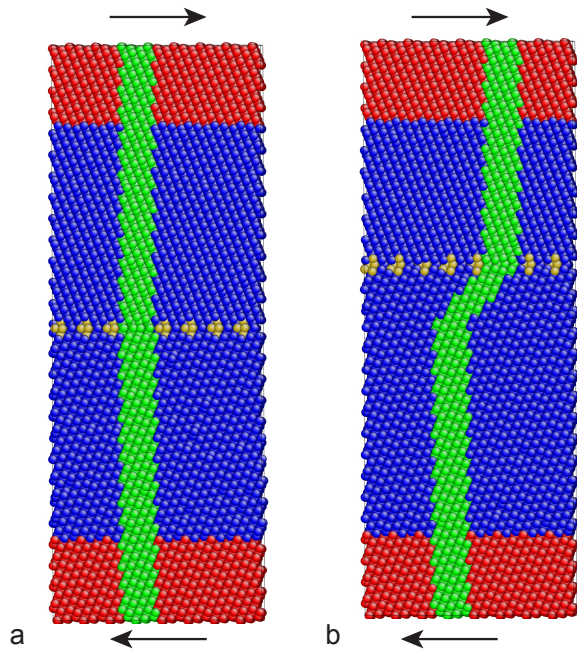
4. Wetting of Ta surfaces by liquid Cu has been studied by a combination of first-principles calculations and MD simulations. It was found that a Cu film placed on Ta surface dewets from it, forming a Cu droplet on top of a stable Cu monolayer. A droplet of liquid Cu placed on a clean Ta surface quickly spreads over it as a stable monolayer. The remaining Cu atoms remain in the droplet, which forms a non-wetting angle with the Cu-covered Ta surface. This stability of a Cu monolayer and instability of thicker Cu films are consistent with recent experiments and first-principles calculations. Our findings provide a theoretical understanding of the dynamics of Cu deposition on Ta layers (diffusion barriers), which is a step in the fabrication of interconnection lines in integrated circuits.



Snapshot of molecular dynamics simulations of liquid copper spreading on the (110) surface of tantalum at the temperature of 1400 K. Note the formation of the precursor monolayer of copper and the nonwetting angle of the remaining droplet relative to the monolayer.

5. Significant efforts were dedicated to studying the so-called *coupling effect*, in which GBs are moved by applied stresses producing shear deformation of the lattice they traverse. This process does not require atomic diffusion and can be implemented at low temperatures by deformation and rotation of structural units. GB motion coupled to stress is relevant to plastic deformation of nanocrystalline materials and can explain the stress-induced grain growth observed experimentally at room temperature and even at cryogenic temperatures. Dynamic regimes of coupled GB motion have been studied by MD simulations and using a proposed analytical model. The highly nonlinear dynamics observed at low temperatures and/or large velocities are associated with the stick-slip motion of GBs. At high temperatures and/or slow velocities, the character of the motion changes from stick-slip to driven random walk and the stress-velocity relation becomes approximately linear. The MD simulations also reveal a transition from coupling to sliding at high temperatures.

Previous simulation and experimental studies of the coupling effect were performed for symmetrical tilt GBs. It was unknown if the effect exists for asymmetrical boundaries and if it follows the geometric model of coupling proposed in previous work. The importance of this



Stress-induced motion of a $\Sigma 17$ symmetrical tilt grain boundary in copper at room temperature. The red and blue regions contain fixed and dynamic atoms, respectively. The yellow atoms have an excess energy and decorate the grain boundary. The green stripe indicates marker atoms selected for tracing the deformation of the system. In experiments it could be a scratch in the surface of a sample. a: initial state, b: the grain boundary moved upwards, producing shear deformation of the lower grain and rigid translation of the upper grain. The continuity of the marker line is the signature of coupled grain boundary motion.

question is emphasized by the fact that most GBs in real polycrystalline materials are asymmetric. To answer this question we have launched a combined MD-PFC study in collaboration with Prof. A. Karma (Northeastern

University) who is also sponsored by the Physical Behavior of Materials Program. Preliminary results for [001]-type asymmetrical tilt GBs obtained by both methods indicate that (1) such boundaries are indeed moved by applied shear stresses exhibiting the coupling effect; (2) the GB motion occurs by glide of different types of dislocations on their slip planes and involves a chain for dislocation reactions; (3) the coupling factor and the steady-state stress of the process depend on the inclination angle; (4) for some inclination angles, the GB motion is a mixture of coupling and sliding and in some cases switches to pure sliding. The agreement between the MD and PFC results points to the generic character of these results. It also demonstrates the ability of the PFC methodology to capture the most essential features of atomic processes and the fruitfulness of the multi-scale MD-PFC approach.

Future Plans

1. A generalized geometric model of coupling will be developed to explain the inclination-angle dependence of the coupling factor of asymmetrical tilt GBs found by MD and PFC simulations.
2. We are planning to continue the study of stress-driven GB motion, focusing on the effect of bicrystallography of more complex boundaries. This will include pure twist boundaries and boundaries with a mixed tilt-twist character. This is a completely uncharted territory since even the existence of coupled motion of such boundaries has not been established.
3. Coupled motion of curved GBs can produce a grain rotation. We will study the process of curvature-driven shrinkage and rotation of a cylindrical grain as a simple model of grain rotation in nanocrystalline materials. Geometrical rules of grain rotation will be derived, including high-angle misorientations and multiple coupling modes. For a comprehensive understanding of the grain rotation, it will be important to study the effect of the grain size, temperature and applied stress on the rotation dynamics.
4. As the next level of complexity, the studies 1, 2 and 3 will be extended to situations when the grains contain high concentrations of dislocations and/or vacancies. These cases are relevant to the processes of recovery, recrystallization and radiation damage of energy related materials.

5. The methodology of this project will continue to be a combination of first-principles calculations, classical MD and PFC simulations. The new understanding of atomic-level mechanisms of interface-controlled processes and the physical parameters computed by atomistic methods will be used as input to phase-field and other continuum methods, further extending the length and time scales of covered by this work. This hierarchical multi-scale approach to interface phenomena has proven to be very efficient in advancing the fundamental knowledge of interfaces while simultaneously generating valuable quantitative information needed for computer design of future materials.

Publications of DOE sponsored research (2008-2010)

1. Y. Mishin, M. Asta and J. Li: Atomistic modeling of interfaces and their impact on microstructure and properties, *Acta Mater.* **58**, 1117 - 1151 (2010).
2. T. Frolov and Y. Mishin: Stable nanocolloidal structures in metallic systems, *Phys. Rev. Letters* **104**, 055701 (2010).
3. T. Frolov and Y. Mishin: Effect of non-hydrostatic stresses on solid-fluid equilibrium. I. Bulk thermodynamics, *Phys. Rev. B* **82**, 174113 (2010).
4. T. Frolov and Y. Mishin: Effect of non-hydrostatic stresses on solid-fluid equilibrium. I. Bulk thermodynamics, *Phys. Rev. B* **82**, 174114 (2010).
5. T. Frolov and Y. Mishin: Orientation dependence of the solid-liquid interface stress: atomistic calculations for copper, *Model. Simul. Mater. Sci. Eng.* **18**, 074003 (2010).
6. C. A. Becker and Y. Mishin: Temperature dependence of the pre-wetting transition at the (111) anti-phase boundary in Ni₃Al: an atomistic study, *Model. Simul. Mater. Sci. Eng.* **18**, 074004 (2010).
7. Y. Mishin and W. J. Boettinger: Thermodynamic model of hydride formation and dissolution in spherical particles, *Acta Mater.* **58**, 4968-4977 (2010).
8. T. Frolov, W. J. Boettinger and Y. Mishin: Atomistic simulation of hillock growth, *Acta Mater.* **58**, 5471-5480 (2010).
9. T. Frolov and Y. Mishin: Solid-liquid interface free energy in binary systems: Theory and atomistic calculation for the (110) Cu-Ag interface, *J. Chem. Phys.* **131**, 054702 (2009).
10. T. Frolov and Y. Mishin: Temperature dependence of surface free energy and surface stress: An atomistic calculation for Cu (110), *Phys. Rev. B* **79**, 045430 (2009).
11. Y. Mishin, W. J. Boettinger, J. A. Warren and G. B. McFadden: Thermodynamics of grain boundary premelting in alloys: I. Phase-field modeling, *Acta Mater.* **57**, 3771-3785 (2009).
12. P. L. Williams and Y. Mishin: Thermodynamics of grain boundary premelting in alloys: II. Atomistic simulation, *Acta Mater.* **57**, 3786-3794 (2009).
13. T. Frolov and Y. Mishin: Molecular dynamics modeling of self-diffusion along a triple junction, *Phys. Rev. B* **79**, 174110 (2009).
14. J. W. Cahn and Y. Mishin: Recrystallization initiated by low-temperature grain boundary motion coupled to stress, *Int. J. Mater. Res.* **100**, 510-515 (2009).
15. V. A. Ivanov and Y. Mishin: Dynamics of grain boundary motion coupled to shear deformation: an analytical model and its verification by molecular dynamics, *Phys. Rev. B* **78**, 064106 (2008).
16. A. Hashibon, A. Y. Lozovoi, Y. Mishin, C. Elsässer and P. Gumbsch: Interatomic potential for the Cu-Ta system and its application to surface wetting and dewetting, *Phys. Rev. B* **77**, 094131 (2008).
17. C. A. Becker, Y. Mishin and W. J. Boettinger: The pre-wetting transition at antiphase boundaries: an atomistic modeling study of Ni₃Al, *J. Mater. Sci.* **43**, 3873-3880 (2008).

Session IV

Hydrogen-Energy, Fuel Cells, Membranes

Program Title: Thermodynamic, Kinetic and Electrochemical Studies in Mixed Proton, Oxygen Ion, and Electron (Hole) Conductors

DOE Grant Number: DE-FG02-06ER46086

Principal Investigator: Anil V. Virkar
Department of Materials Science & Engineering
122 S. Central Campus Drive
University of Utah
Salt Lake City, UT 84112
Email: anil.virkar@utah.edu
Phone: (801) 581-5396

Program Scope or Definition: This work is on thermodynamic, kinetic, and electrochemical studies on mixed proton, oxygen ion, and electron (hole) conducting materials, although broad principles are applicable to virtually all electrochemical systems. The materials of interest exhibit predominantly ionic conduction with electronic conductivity being a smaller component. Fundamental transport theory for liquids and solids is based on the assumption of local thermodynamic equilibrium, which is the cornerstone of virtually all reported work. The basic assumption is that thermodynamic relations are locally satisfied even when the system as a whole is not in global equilibrium. This assumption allows one to write fluxes as functions of gradients in chemical potentials (electrically neutral species) or gradients in electrochemical potentials (electrically charged species). Many studies have been reported on defect chemistry and transport. Studies have also been reported on electrochemical devices such as batteries, fuel cells and electrolyzers. However, little information exists in the literature on local thermodynamics in materials used in such systems; for example very little information exists on the chemical potential of oxygen, μ_{O_2} , within a solid. Complete characterization of a material system requires the knowledge of local thermodynamics. The present work has led to an important, fundamental result which shows that local chemical potential of a neutral species, such as μ_{O_2} , in a solid electrolyte may go outside the thermodynamic stability range under certain electrolytic conditions, even when exposed to stable conditions at the electrodes. Our work seeks to investigate not only transport and electrochemical studies in these materials, but also to measure local thermodynamic behavior and determine stability criteria.

Our recent work has shown that local thermodynamics in solid electrolytes can be probed using embedded reference electrodes or probes which are isolated from the atmosphere. Such probes only exchange electrons with the solid electrolyte thus allowing for a direct measurement of the electrochemical potential of electrons. Typical electrochemical characterization of fuel cells and batteries involves the use of externally placed reference electrodes and electrochemical impedance spectroscopy (EIS). Often impedance spectra are difficult to de-convolute making interpretation difficult. Our preliminary work has shown that noble metal 'screen' electrodes can be embedded within a solid electrolyte membrane. EIS spectra can be obtained between working and counter electrodes, and embedded 'screens'. These measurements allow for a clear separation and unequivocal determination of electrode polarizations. These measurements combined with DC probe and electrochemical studies facilitate the determination of the chemical potentials of neutral species inside a solid electrolyte. In this work, our focus is on the explicit determination of the chemical potentials of hydrogen (μ_{H_2}), oxygen (μ_{O_2}) and water vapor (μ_{H_2O}) *inside* a solid electrolyte.

Work is underway in the following areas: **(1)** Fabrication of anode-supported cells with ceria, zirconia, and proton-conducting thin electrolyte films with probes and screen electrodes embedded in the electrolyte. **(2)** Investigation of time and position dependent electric potential, $\varphi(\vec{r}, t)$, using embedded probes. **(3)** Investigation of electrode polarizations and resistive contributions by EIS across 'screen' electrodes and cathode/anode. **(4)** Determination of chemical potentials (μ_{H_2} , μ_{O_2} , and μ_{H_2O}) inside dense membranes using: (i) EIS, (ii) Measurement of $\varphi(\vec{r}, t)$, and (iii) Measurement of fluxes. **(5)** Theoretical analysis of transport through mixed proton, oxygen ion, electron (hole) conductors. An important objective of the work is to investigate thermodynamic stability of materials under electrolytic conditions. This work forms the basis for electrochemical/thermodynamic stability of materials with implications concerning active electrochemical devices such as fuel cells, batteries, and electrolyzers.

Recent Progress: Recent work has been in the following areas: **(1)** Analysis of transport in mixed proton, oxygen ion, and electron (hole) conductors under fuel cell, driven fuel cell, and electrolyzer modes. Transport equations are written using an equivalent circuit which describes transport in steady state. The equivalent circuit uses internal emfs instead of charged capacitors, and thus provides a direct connection with thermodynamics. Using this approach, Onsager transport coefficients are obtained in terms of the various transport properties of the membrane and interfaces, and operating conditions. It is shown that in the fuel cell mode, the chemical potentials of neutral species, namely oxygen (μ_{O_2}) and hydrogen (μ_{H_2}), are mathematically bounded by the values at the electrodes. However, in the driven fuel cell and electrolyzer conditions, the μ_{O_2} and μ_{H_2} need not be mathematically bounded by the values at the electrodes. Conditions could occur under which the thermodynamic stability of the membrane is compromised despite being exposed to stable conditions at the electrodes. These effects are related to the Onsager reciprocity relations and form the basis of degradation mechanisms of electrochemical devices. The general conclusions are: (a) Electronic current through an ionically conducting medium cannot be assumed to be identically zero (except under short circuit and/or identical conditions at electrodes). (b) Whenever ionic and electronic currents through an electrolyte membrane are in opposite directions, chemical potentials of neutral species in the membrane are mathematically bounded by the values at the electrodes. (c) Whenever ionic and electronic currents through an electrolyte membrane are in the same direction, the chemical potentials of neutral species need not be mathematically bounded by the values at the electrodes. These results are general and applicable to all electrochemical systems. **(2)** Measurement of electric potentials using embedded probes: Several of our published papers are on embedding platinum probes into ceria-based and Nafion-based electrolytes. The probes afford measurements of the electrochemical potential of electrons. This, combined with measurement of voltage-current and EIS, allows one to estimate the chemical potentials of neutral species (e.g. μ_{O_2}) inside an electrolyte. Figure 1 shows an SEM micrograph of a Nafion membrane fuel cell and a schematic of embedded 'screen' electrodes in Nafion membranes.

Using the embedded 'screen' electrodes, both DC and EIS measurements were conducted. Figure 2(a) shows the measured electric potentials at the 'screen' probes under various operating conditions. The large drop in electric potential across the cathode-electrolyte interface is a measure of the interfacial electronic resistance (contact resistance in the semiconductor terminology), and is not related to electrode polarization. Impedance spectroscopy in principle gives the 'ionic' resistances (in a predominantly ionic conductor). The DC probe measurements give the electric potentials, which are related to 'electronic' resistances and 'electronic current', however small, passing through the electrolyte. Figure 2(b) gives the measured EIS spectra. These measurements, combined with the measurement of current density allow one to estimate the chemical potential of neutral species within

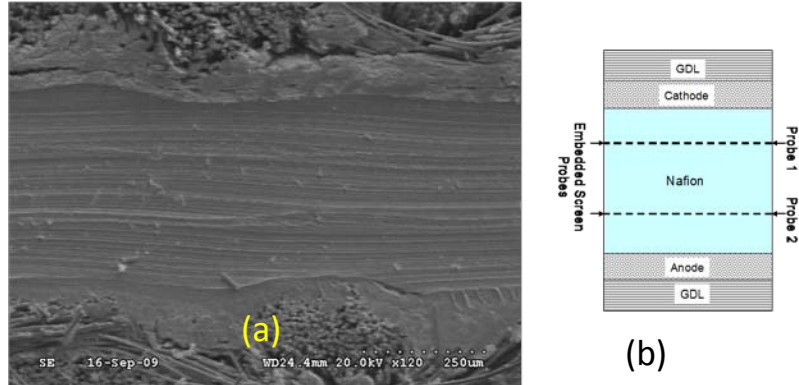


Figure 1: (a) An SEM of a Nafion membrane with embedded 'screen' electrodes. (b) A schematic showing the positions of the embedded 'screen' electrodes.

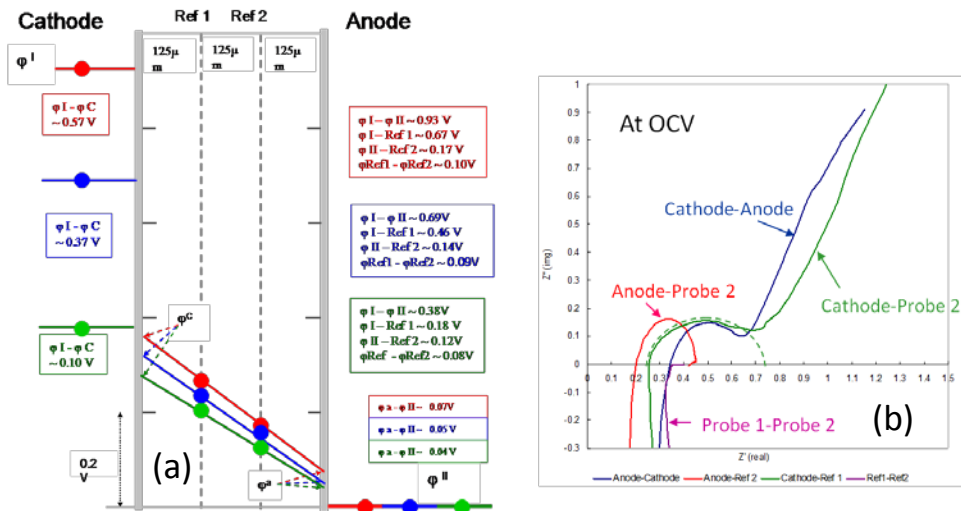


Figure 2: (a) Measured electric potentials across the Nafion MEA. Large drop in potential across the cathode-electrolyte interface indicates a large electronic resistance – not polarization. (b) Electrochemical impedance spectra across cathode – screen 2, screen 1 – screen 2, anode – screen 2, and cathode – anode. Note, unequivocal de-convolution of the cathode-anode spectra is not possible.

the electrolyte. The relevant equation, for example (given below), describes a relationship between measurable entities and oxygen chemical potential, $\mu_{O_2}(x)$. A similar equation applies to $\mu_{H_2}(x)$. Also, similar equations are applicable to other electrochemical systems, using either anion conducting or cation conducting electrolytes. The aim is to obtain chemical potentials within the membrane by an equation of the type

$$\mu_{O_2}(x) = \mu_{O_2}(x_o) + 4e^+ r_{O_2^-}(x, x_o) I_{O_2^-} + \{ \varphi(x) - \varphi(x_o) \}$$

By EIS Measurements With Embedded Screens (points to the $r_{O_2^-}$ term)

By DC Measurements With Embedded Screens (points to the $\{ \varphi(x) - \varphi(x_o) \}$ term)

By Voltage Current Performance Measurements (points to the $I_{O_2^-}$ term)

What the above equation shows is that by a combination of: (a) Current-voltage measurements, (b) EIS spectra using embedded 'screen' electrodes, and (c) Electric potential measurements at the embedded

electrodes, in principle, one can have a complete local thermodynamic description of the electrolyte. This approach should be applicable to systems describable by linear non-equilibrium thermodynamics, and possibly extendable to nonlinear non-equilibrium thermodynamics. **(3)** Electrochemical Ostwald ripening: Many electrochemical processes are coupled. Degradation of carbon-supported catalysts or those in direct contact with each other in liquid media occurs by a coupled transport of ions and electrons. We have recently investigated electrochemical Ostwald ripening of copper powders.

Future Plans: These include: **(1)** Linear non-equilibrium thermodynamic analysis and its application to other electrochemical systems, including lithium-ion batteries and electrolyzers. The analysis leads to a model for the degradation of lithium-ion and lithium-metal batteries. Specifically, the analysis identifies what should be the transport properties of the various cell components to minimize the propensity to degradation. **(2)** Experimental measurements in thin film fuel cells, batteries, and electrolyzers. These measurements will be made using embedded probes. The analysis and measurements should lead to a general theory for the design of membranes/cells resistant to degradation. **(3)** Extension of the analysis to transient linear systems. In many instances, an electrochemical cell may not exhibit a steady state behavior. The present analysis, which is for steady states, will be extended to transient states. More importantly, the study will identify 'apparent' steady states. An apparent steady state is a state which appears to be a steady state in terms of externally measurable parameters (such as fixed voltage and fixed current), yet exhibits transient behavior for other, not so easily measurable, parameters. An example is that of the chemical potential of a neutral species, which can be probed using embedded electrodes, and can vary with time even when voltage and current are fixed. **(4)** Analysis of nonlinear, non-equilibrium systems in steady state. Virtually all transport theory is based on linear non-equilibrium thermodynamics (linear flux-force relations). However, many systems often are far from thermodynamic equilibrium. In such cases, linear flux-force relations may not be applicable. The long range objective of our work is to both theoretically and experimentally examine such phenomena in electrochemical systems. The presentation will cover our recent results and planned activities.

Refereed Papers Published:

- 1) R. Abbaraju, N. Dasgupta and A. V. Virkar, 'Composite Nafion membranes containing nanosize $\text{TiO}_2/\text{SnO}_2$ for proton exchange membrane fuel cells" *J. Electrochem. Soc.*, **155** (12) B1307-B1313 (2008).
- 2) H-T. Lim and A. V. Virkar, 'Measurement of oxygen chemical potential in thin film, anode-supported solid oxide fuel cells', *J. Power Sources*, **180** 92-102 (2008).
- 3) H-T. Lim and A. V. Virkar, 'A study of solid oxide fuel cell stack failure by inducing abnormal behavior in a single cell test', *J. Power Sources*, **185** 790-800 (2008).
- 4) H. C. Park and A. V. Virkar, 'Bimetallic (Ni-Fe) anode-supported solid oxide fuel cells with gadolinia-doped ceria electrolyte', *J. Power Sources*, **186** 133-137 (2009).
- 5) A. V. Virkar, 'Transport through mixed proton, oxygen ion and electron (hole) conductors: Goldman-Hodgkin-Katz-type equation', *J. Power Sources*, **194** 753-762 (2009).
- 6) H-T. Lim and A. V. Virkar, 'Measurement of oxygen chemical potential in Gd_2O_3 -doped ceria- Y_2O_3 -stabilized zirconia bi-layer electrolyte, anode-supported solid oxide fuel cells', *J. Power Sources*, **192** 267-278 (2009).
- 7) A. V. Virkar, F. F. Lange, and M. A. Homel, 'A simple analysis of current collection in tubular solid oxide fuel cells', *J. Power Sources*, **195** 4816-4825 (2010).
- 8) P. Parthasarathy and A. V. Virkar, 'Electrochemical coarsening of copper powder in aqueous media', *J. Electrochem. Soc.*, **157** (5) B768-B775 (2010).

Complex hydrides – A new frontier for future energy applications

V.K. Pecharsky (presenting, vitkp@ameslab.gov), M. Pruski, and L.S. Chumbley
Ames Laboratory, Iowa State University, Ames, IA 50011-3020

and

P. Jena, Virginia Commonwealth University, Richmond, VA 23284-2000

Program scope

Hydrogen storage is one of the critical enabling materials technologies required to ensure a successful future transition from fossil-based to hydrogen-based energy. We seek materials that mimic the structure of methane or ammonia, where four or three hydrogen atoms encapsulate a single carbon or nitrogen atom, forming neutral CH_4 or NH_3 molecules. Solids under consideration include tetrahydroaluminates (or alanates), hexahydroaluminates, and borohydrides, in which the Al or B atom is surrounded by four to six hydrogen atoms forming complex hydrogen-rich $[\text{MeH}_n]^{p-}$ anions, and the ammonia derivatives – amides and imides. We address issues related to their physical and chemical properties, and establish basic knowledge of the nature of mixed complex hydrides, hydrogenation-dehydrogenation mechanisms, equilibrium and nonequilibrium thermodynamics, and the kinetics of direct synthesis from the elements or intermediary compounds. Our focus is discovery of novel material systems and suitable processing approaches in order to create advanced ultra-high capacity hydrogen storage solids.

All things considered, large scale commercial applications of hydrogen are at least 10 to 15 years, and possibly, as far as 25 to 40 years away. Consequently, real progress in solving hydrogen storage problems is required now. We achieve this through basic knowledge of transformation mechanisms in complex hydrides-hydrogen systems, thus precipitating discoveries needed for future transition to hydrogen—a renewable, clean, and safe energy carrier. Specific objectives of this multidisciplinary team effort are to address issues that have the potential to advance basic science of complex hydrides and open up possibilities for their future use by drawing on the experience and expertise of principal investigators in materials science, physics, and chemistry of complex hydrides, x-ray diffraction, high resolution solid-state nuclear magnetic resonance, electron microscopy, and first principles theory and modeling. Following are our goals:

- Examine both thermal energy-driven and mechanical energy-driven phase transformations in selected model hydride systems, which, respectively, occur at and away from thermodynamic equilibrium.
- Establish the nature and structure of the products and intermediaries using state-of-the-art characterization techniques.
- Identify events critical to achieving reversibility of hydrogen in model systems.
- Create a knowledge base, relating composition, structure, and properties of model hydrides by investigating the effects of varying stoichiometry and processing history on their crystal and microscopic structures, chemical, thermodynamic, and physical properties.
- Refine and extend the current understanding of the mechanisms of solid-state transformations from a few known hydrides to complex hydride-hydrogen

systems by examining how chemical and structural modifications affect dehydrogenation/hydrogenation behaviors of selected model systems.

- Explore the potential of nanoscale for improving behaviors of chosen complex hydride-hydrogen systems by considering length scales ranging from a few tenths of a nanometer (a single interatomic distance) to microns (a single grain) and centimeters (assemblies of particles).
- Integrate experiment with modeling and first principles theory to provide a fundamental understanding of the nature of hydrogen bonding, the structure and stability of the model systems, the effects of mechanical energy, temperature, and pressure in altering the nature of hydrogen-metal bond, and the role of nanostructuring on the absorption and desorption properties of hydrogen.
- Develop predictive tools guiding the discovery of materials at the atomic scale and tuning processing to control the nano-, meso- and microscopic structures.

Recent progress

Mechanically induced reactions: liquid eutectics or solid-state processes?

Despite recent advancements of mechanochemistry, understanding of physical and chemical events that take place in both organic and some low-melting inorganic solids (the latter include alanates under study) during mechanical processing remains limited. Often, it is even not apparent in which phase (liquid or solid) mechanochemical reactions really occur. Our experiments have confirmed the formation of an orange liquid immediately after o-valinilin (oV) and p-tuluidine (pT) are ground together at room temperature. The liquid also forms if both compounds are ground separately using a mortar and a pestle, and then thoroughly mixed together at room temperature. On the other hand, no phase or color changes occur if the materials are ground at 0 °C for 5 min. The prepared powder, however, turns orange and melts once it is quickly warmed up to room temperature. The melt that forms remains liquid for several minutes, i.e. long enough to be studied by ^1H and ^{13}C NMR techniques. Our results have revealed a distinct possibility that mechanochemical reactions, which appear to be true solid-state processes, may in fact occur in a liquid phase. The major condition for such reactions is the formation of low-melting eutectics from starting materials upon mechanical processing. The mechanical processing is an essential element of mechanochemical reactions since it enhances surface interactions between reacting materials, supports their intimate mixing, provides mass transfer and initial energy required for the formation of low-melting eutectics.

Mechanochemically driven non-equilibrium processes in complex hydride systems

Mechanochemical transformations of lithium and sodium amides with calcium hydride taken in different molar ratios lead to the formation of calcium imide, alkali metal monohydrides and gaseous hydrogen. In all cases, the overall mechanochemical transformations are equimolar and proceed as one step reactions: $\text{MNH}_2 + \text{CaH}_2 \rightarrow \text{CaNH} + \text{MH} + \text{H}_2$, where $\text{M} = \text{Li}$ or Na . If the concentrations of starting materials are different from equimolar, then the component whose concentration in the starting mixture was greater remains in excess and does not transform up to 24 hours of high energy ball milling. The reactions in lithium systems are faster compared to systems with sodium. Difference in hydrogen release kinetics can be related to differences in mobilities of

lithium and sodium atoms, to differences in strength of ionic bonding of the imides, and different thermodynamics. Total energies and enthalpies of formation for different reaction products during the dehydrogenation of CaH_2 - MNH_2 mixtures indicate that there may exist two dehydrogenation pathways for CaH_2 - MNH_2 systems: a mechanochemical transformation driven by mechanical ball milling and two-step thermochemical transformations driven by heating. Compared to thermochemical transformations, which proceed in accordance with thermodynamic equilibrium, reactions induced by mechanical energy drive the MNH_2 - CaH_2 systems to nonequilibrium configurations with different final products.

Partial rehydrogenation of the sodium amide-magnesium hydride system

Phase transformation mechanism during the thermal decomposition of the 2MNH_2 - 3MgH_2 (where $\text{M} = \text{Li}$ or Na) systems has been established. Thermally induced reactions in both systems are stoichiometric and proceed as a following overall solid state reaction: $2\text{MNH}_2 + 3\text{MgH}_2 = \text{Mg}_3\text{N}_2 + 2\text{MH} + 4\text{H}_2$. A total of 6.45 wt.% of hydrogen is released by the 2LiNH_2 - 3MgH_2 (hydrogen release starts at 186 °C) and 5.1 wt.% H_2 is released by the 2NaNH_2 - 3MgH_2 system starting from 130 °C. Combined structure/property investigations revealed that the transformations in the lithium containing system proceed in two steps. In the first step, lithium amide reacts with MgH_2 to form $\text{Li}_2\text{Mg}(\text{NH})_2$ and hydrogen. In the second step, reaction between $\text{Li}_2\text{Mg}(\text{NH})_2$ and MgH_2 leads to formation of the Mg_3N_2 nitride, lithium hydride and additional gaseous hydrogen. The transformation mechanism in the sodium containing system proceeds through a series of competing solid state processes in which $\text{Mg}(\text{NH}_2)_2$ and NaMgH_3 form as intermediates. The 2NaNH_2 - 3MgH_2 system can be partially rehydrogenated in 190 bar hydrogen at 395 °C with formation of the MgNH imide.

Future plans

Although details of future breakthroughs and new science are difficult to predict, the overall success of this project will continue to rely upon integrating innovative processing approaches with state-of-the-art characterization and theoretical modeling:

- The studies of mechanochemical and temperature-induced transformations of mixed systems containing magnesium will be completed by establishing relevant details of their mechanisms.
- The effort toward direct synthesis of AlH_3 with high yields will continue, as well.
- Mechano- and thermo-chemical studies will be extended to include several new systems, specifically those that contain borohydrides and aminoborane.
- The effectiveness of using mechanical energy to create nonequilibrium rehydrogenation pathways under low hydrogen pressures and temperatures will be thoroughly studied.
- New hybrid materials consisting of complex hydrides and intermetallic hydrogen absorbers will be developed and tested.
- We will continue to employ and improve characterization methods, such as gas-volumetric analyses, solid-state NMR spectroscopy, x-ray diffraction, and electron microscopy to determine to the best extent possible the structure and properties of all materials developed in this project.

- The theoretical modeling will emphasize multi-scale techniques based on density functional theory.

Specifically, we will:

- Complete examination of the mechanism of thermochemical transformations in the $MNH_2 - MAIH_4$ ($M = Li, Na$) systems, using PCT and temperature-programmed decomposition, and x-ray diffraction, solid state NMR, and TEM.
- Initiate mechanochemical investigations of systems containing amides of Li and Na and conventional AB_5 and AB_2 metallic hydrogen absorbers.
- Initiate low temperature experiments on mechanochemical synthesis of AlH_3 , using high pressure ball milling in hydrogen.
- Examine suitability of selected aluminum-rich intermetallic compounds for direct mechanochemical synthesis of AlH_3 .
- Initiate destabilization of aminoborane with different complex hydrides to establish reaction mechanisms and solid state transformation pathways.
- Using first principles modeling examine thermodynamics of most probable intermediaries, and, therefore, support experimental studies of the mechanisms of mechanochemical transformations (already studied experimentally) and thermochemical transformations (ongoing studies) in $MNH_2 - MAIH_4$ systems.
- Initiate first principles calculations of clusters to model effects of nanostructuring on the properties of mixed complex hydrides.

Publications of DOE sponsored research (2008-2010)

1. P. Larsson, C.M. Araujo, J.A. Larsson, P. Jena, and R. Ahuja, "Role of Catalysts in Dehydrogenation of MgH_2 Nanoclusters," *Proc. Nat. Acad. Sci.* **105**, 8227 (2008).
2. A. Grubistic, X. Li, S.T. Stokes, K. Vetter, G.F. Gantefor, K.H. Bowen, P. Jena, B. Kiran, R. Burgert, and H. Schnockel, " $Al_{13}H$: Hydrogen Atom Site Selectivity and the Shell Model," *J. Chem. Phys.*, **131**, 121103 (2009).
3. Q. Wang, Q. Sun, P. Jena, and Y. Kawazoe, "Potential of AlN nanostructures as Hydrogen Storage Materials," *ACS Nano*, **3**, 621 (2009).
4. O. Dolotko, J.W. Wiench, K.W. Dennis, V.K. Pecharsky, and V.P. Balema, "Mechanically Induced Reactions in Organic Solids: Liquid Eutectics or Solid-state Processes?" *New. J. Chem.* **34**, 25 (2010).
5. O. Dolotko, N. Paulson, and V.K. Pecharsky, "Thermochemical Transformations in $2MNH_2-3MgH_2$ Systems ($M = Li$ or Na)," *Int. J. Hydrogen Energy* **35**, 4562 (2010).
6. O. Dolotko, H. Zhang, S. Li, P. Jena, and V.K. Pecharsky, "Mechanochemically Driven Nonequilibrium Processes in MNH_2-CaH_2 Systems ($M = Li$ or Na)," *J. Alloys Compds.* **506**, 224 (2010).
7. S. Li, R. Ahuja, C.M. Araujo, B. Johansson, and P. Jena, "Dehydrogenation Associated with Ti Catalyst in Sodium Alanate," *J. Phys. Chem. Solids*, **71**, 1073 (2010).
8. S. Li, M. Willis, and P. Jena, "Reaction Intermediates During the Dehydrogenation of Metal Borohydrides: A Cluster Perspective," *J. Phys. Chem. C*, **114**, 16849 (2010).

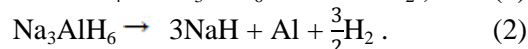
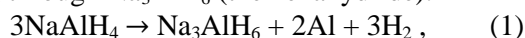
NMR of Hydrogen Storage Solids: Ionic Hydrides and Mobile Species

Mark S. Conradi, PI. Washington University, Dept. of Physics, St. Louis MO 63130

Email msc@wuphys.wustl.edu

Program scope: Nuclear magnetic resonance is used to understand the diffusivity of hydrogen and metal atoms in hydrogen storage solids and to discover mobile intermediate species in the hydrogen reactions.

Recent progress- Discovery of a new species in the chemistry of NaAlH₄: Sodium alanate is the archetype of complex hydrides (covalent bonding within AlH₄⁻ anions, ionic bonding to Na⁺). It dehydrides in two steps, going through Na₃AlH₆ (the hexahydride):



It was reported in 1997 that addition of Ti or other metal catalysts to NaAlH₄ at the percent level makes these reactions reversible under H₂ gas pressure. This discovery opened an exciting chapter in hydride research that continues today with the interstitial metallic systems (e.g., TiH₂, TiFeH_x) being abandoned because of their insufficient mass percentages of H, in favor of ionic and ionic-covalent hydrides using inexpensive and lightweight metal atoms from the upper left region of the periodic table (e.g., Li, Na, Al, B, Mg). *Despite many years of intense study, the solid-state reaction mechanisms of (1) and (2) and the role(s) of the catalyst are not known.* In particular, many workers have called attention to the need for a metal-atom-bearing mobile species to bring Al and Na into intimate contact for the rehydriding reaction, starting from NaH and Al metal, the reverse of reactions (1) and (2).

We recently reported the discovery of a new species in the “hydrogen chemistry” (the chemistry of dehydriding and rehydriding) of NaAlH₄, using *in situ* NMR (i.e., NMR measurements at the high temperature, high-T, and high pressure, high-P, conditions of the reactions, as distinct from NMR at ambient conditions of material recovered from a reaction). The evidence indicates that the new species is a form of NaAlH₄ with a high concentration of AlH₃ (neutral) vacancies. The work proposed herein springs directly from the previous study, so that the important aspects of the earlier study are summarized below.

In Figure 1 is a series of three static ²⁷Al NMR spectra recorded at 180°C on Sc-catalyzed NaAlH₄ from the University of Hawaii (UH, **Craig Jensen**), dehydriding into a vacuum. Initially, only NaAlH₄ is present; at t=12 min (time measured from sample reaching temperature), some Na₃AlH₆ appears as expected from reaction (1); this signal is narrower because of rapid AlH₆ reorientations. We note the spectra use neither hydrogen-decoupling nor magic-angle spinning (MAS) conditions to achieve line-narrowing. But at t=6 min, a new narrow resonance appears; we call this species **S105** because of its approximate +105 ppm shift relative to the standard reference, aqueous Al(NO₃)₃ (10 kHz here is 108 ppm). The S105 resonance is narrow, indicating rapid reorientation and translational diffusion; thus, *S105 is likely the hypothesized species responsible for metal-atom transport.* Hence S105 appears to play a crucial role in the dehydriding and

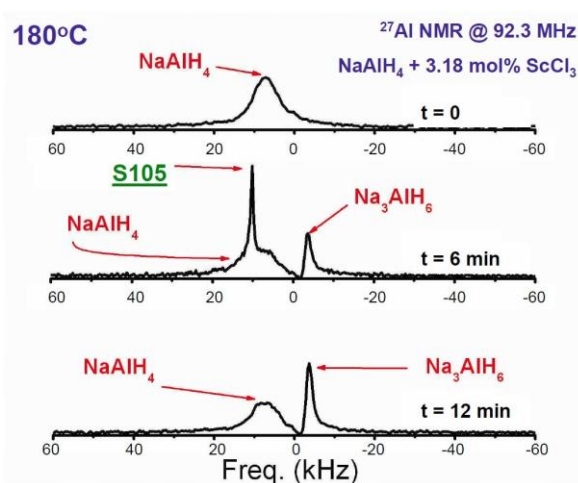


Fig. 1. The new sharp signal S105 at +105 ppm appears here only transiently during dehydriding of NaAlH₄; static ²⁷Al NMR.

rehydriding chemistry of NaAlH₄. Unfortunately, the S105 signal is only evident for a few minutes, making identification difficult.

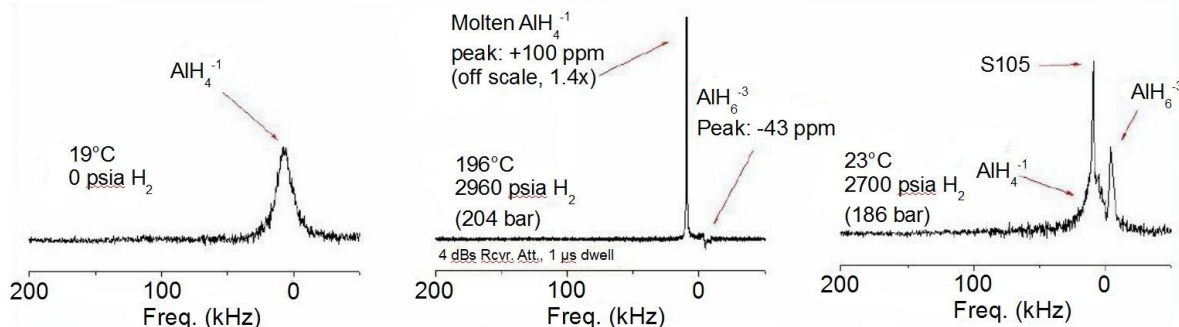


Fig. 2. P,T cycle yields S105 for unlimited time at room temperature and (eventually) room pressure; static ²⁷Al spectra. Middle spectrum shows molten NaAlH₄.

We subsequently discovered a P,T cycle (protocol) capable of generation of S105 from bare NaAlH₄ (without any catalyst) and allowing S105 to be returned to ambient conditions where it is stable indefinitely. As in Figure 2, the NaAlH₄ is held at 200 bar of H₂ pressure, thermodynamically blocking the dehydriding reactions (1) and (2) (see Figure 3). The material is heated into the molten state and then cooled under pressure; at room-T, the pressure is eventually removed. The H₂ overpressure is indeed successful at blocking the dehydriding – no H₂ is evolved and no Al metal appears (its 1640 ppm Knight shift (150 kHz here) makes metallic Al easy to detect). But S105 still appears and persists, along with Na₃AlH₆; evidently a reaction other than (1) or (2) is at work which had been hidden by reaction (1) in previous studies. Crucially, this P,T cycle, suitable for generation of S105 in catalyzed or bare sodium alanate, allows material with S105 to be returned to ambient conditions for analysis by other techniques.

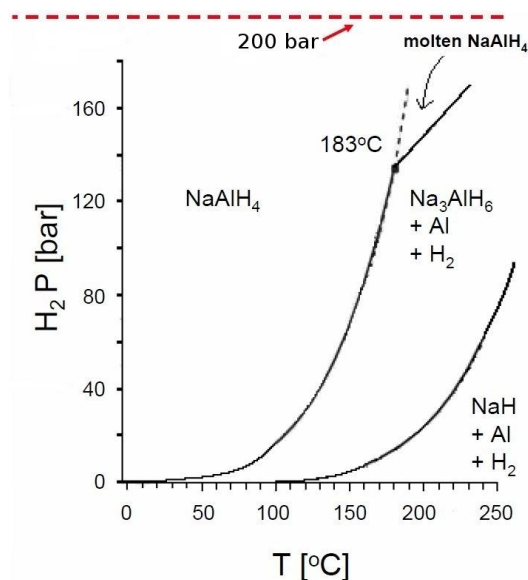


Fig. 3. Under 200 bar of H₂ pressure, both forward reactions (1) and (2) are thermodynamically blocked for T < 240°C.

So what do we know about S105? NMR studies of S105 find that it has a very fast ²⁷Al T₁ (longitudinal relaxation time, 1-2 ms from 20 to 180°C; compared to 0.1-1 s for the other species), indicating a strong rapidly modulated electric field gradient (EFG). Variable-temperature studies find the sharp ²⁷Al signal disappears into the broad signals of AlH₄ and AlH₆ at -40 to -70°C (presumably by broadening of S105). A sharp “companion” hydrogen NMR signal appears along with the 105 ppm aluminum signal; this hydrogen signal becomes undetectable (due to broadening) in the same temperature range. Thus, the new species is very mobile and contains Al and H (but no Na, according to our ²³Na NMR). This picture is confirmed by aluminum MAS and ²⁷Al-¹H CPMAS (cross-polarization MAS) NMR as in Figure 4 (both H-decoupled). The S105 aluminum signal does not cross-polarize from hydrogen near room-T because of motional averaging of the Al-H dipole interaction, but S105 does appear in cross-polarization below -40°C. This finding confirms the proximity of Al and H in the new species. The chemical shift of S105 is quite close (see Figures 1 and 2) to that of NaAlH₄, suggesting they are chemically similar. Powder x-ray

diffraction comparison of the initial (bare) NaAlH_4 and material after P,T treatment (a sample verified to have a strong S105 ^{27}Al NMR signal) shows that disorder is present after P,T treatment, with a weaker primary diffraction peak and with much weaker or absent higher-order peaks, as in Figure 5.

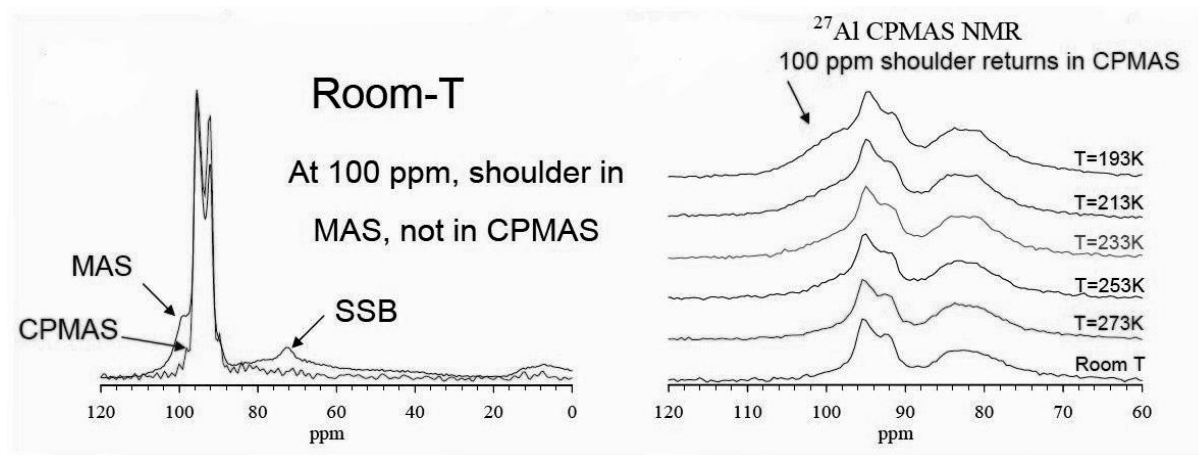


Fig. 4. In ^{27}Al MAS NMR, the S105 signal is the shoulder near 100 ppm. S105 is not evident in room-T CPMAS because of motional averaging, but is present at low-T where the motions are frozen out (spectra at right). All spectra are H-decoupled; SSB = spinning sideband.

The above observations point to our identification of **S105 as a defect-ridden version of NaAlH_4** . To result in mobile Al and H, the defects must be Al_xH_y . Along those lines, Ozolins et al predicted neutral AlH_3 vacancies (that is, H⁻ sitting on AlH_4^- sites) would be likely and would be very mobile in NaAlH_4 . AlH_3 vacancies provide natural explanations of the several observations about S105 in the paragraph above.

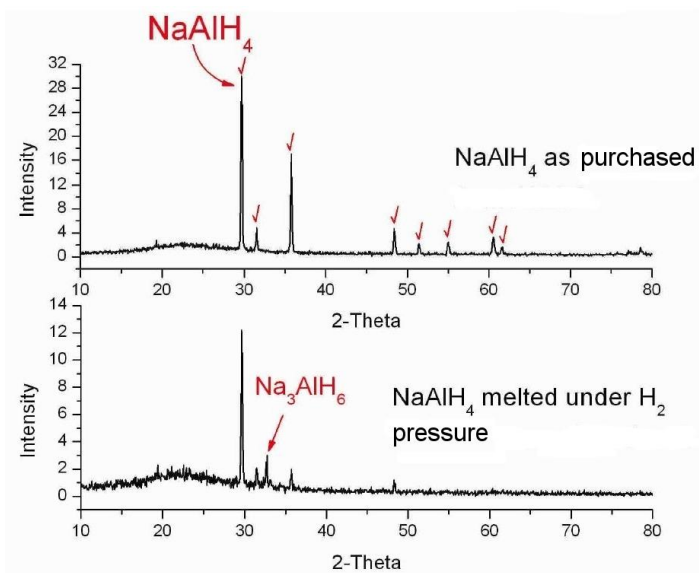


Fig. 5. Powder x-ray diffraction of NaAlH_4 before and after creation of S105 by P,T cycle. Checks mark known NaAlH_4 reflections.

Future plans:

Many questions remain, which are especially important since S105 may be the dynamic species crucial for the reversibility of these reactions. We plan further study in NaAlH_4 itself and in related complex hydrides, including other alanates, alumino-hexahydrides, and borohydrides.

Recently, the group at Pacific Northwest Nat'l Labs (PNNL) has reported the use of *in situ* NMR to study ammonia borane (**AB**, NH_3BH_3 solid). Their work uses magic-angle spinning, primarily on ^{11}B and at elevated temperatures (but 1 bar pressure). They report **AB** transforms over time at elevated temperature to a new form, **AB***. **AB*** shares several properties with S105 (in NaAlH_4) – a much narrower NMR line, short relaxation times, a *small* shift from the

parent material, recoverability at ambient conditions, and an x-ray diffraction pattern displaying disorder (diminution of the higher-order peaks). The similarities suggest AB* may be a defect-ridden form of AB. The PNNL group notes that H₂ evolution does not occur until AB* forms, strongly suggesting AB* plays a crucial role in the hydrogen chemistry.

These results from *in situ* MAS NMR strongly encourage us to expect further insights into the H reactions of complex hydrides using this technique. Moreover, the PNNL results demonstrate that *in situ* MAS NMR, with its superior spectral resolution, can be a useful tool, either in its own right or by augmenting the static (non-MAS) *in situ* technique. Of course, high pressures are not available in any MAS apparatus.

Publications from DOE Support:

1. "Hydrogen NMR of Palladium Hydride to Measure the Hydride-Gas Exchange Rate," L.H. Rayhel, R.L. Corey, D.T. Shane, D.F. Cowgill, and M.S. Conradi, *J. Phys. Chem. C* (in review).
2. "A Comprehensive NMR Study of Magnesium Borohydride," D.T. Shane, L.H. Rayhel, Z. Huang, J.-C. Zhao, X. Tang, V. Stavila, and M.S. Conradi, *J. Phys. Chem. C* (in review).
3. "NMR Study of LiBH₄ with C₆₀," D.T. Shane, R.L. Corey, L.H. Rayhel, M. Wellons, J.A. Teprovich, Jr., R. Zidan, S.-J. Hwang, R.C. Bowman, Jr., and M.S. Conradi, *J. Phys. Chem. C* (in press, available on-line).
4. "Discovery of a New Al Species in Hydrogen Reactions of NaAlH₄," T.M. Ivancic, S.-J. Hwang, R.C. Bowman, Jr., D.S. Birkmire, C.M. Jensen, T.J. Udovic, and M.S. Conradi, *J. Phys. Chem. Lett.* **1**, 2412-2416 (2010).
5. "LiBH₄ in Carbon Aerogel Nanoscaffolds: An NMR Study of Atomic Motions," D.T. Shane, R.L. Corey, C. McIntosh, L.H. Rayhel, R.C. Bowman, Jr., J.J. Vajo, A.F. Gross, and M.S. Conradi, *J. Phys. Chem. C* **114**, 4008-4014 (2010).
6. "NMR Studies of the Hydrogen Storage Compound NaMgH₃," D.T. Shane, R.L. Corey, R.C. Bowman Jr., R. Zidan, A.C. Stowe, S.-J. Hwang, C. Kim, and M.S. Conradi, *J. Phys. Chem. C* **113**, 18414-18419 (2009).
7. "Exchange of Hydrogen Atoms Between BH₄ in LiBH₄," D.T. Shane, R.C. Bowman, Jr., and M.S. Conradi, *J. Phys. Chem. C* **113**, 5039-5042 (2009).
8. "High Pressure NMR," Mark S. Conradi, in *Encyclopedia of Magnetic Resonance*, edited by R.K. Harris and R. Wasylishen, Wiley, Chichester UK, 2008. DOI: 10.1002/9780470034590.emrstm1075, published 15 December 2008; on-line only.
9. "Hydrogen Motion in Magnesium Hydride by NMR," R.L. Corey, T.M. Ivancic, D.T. Shane, E.A. Carl, R.C. Bowman, Jr., J.M. Bellosta von Colbe, M. Dornheim, R. Bormann, J. Huot, R. Zidan, A.C. Stowe, and M.S. Conradi, *J. Phys. Chem. C* **112**, 19784 -19790 (2008).
10. "Atomic Motions in LiBH₄ by NMR," R.L. Corey, D.T. Shane, R.C. Bowman, Jr. and M.S. Conradi, *J. Phys. Chem. C* **112**, 18706-18710 (2008).
11. "Hydrogen NMR of H₂-TDF-D₂O Clathrate," L. Senadheera and M.S. Conradi, *J. Phys Chem. B* **112**, 13695-13700 (2008).
12. "Hydrogen Nuclear Spin Relaxation in Hydrogen-Ice Clathrate," L. Senadheera and M.S. Conradi, *J. Phys Chem. A* **112**, 8303-8309 (2008).
13. "Molecular H₂ Trapped in AlH₃ Solid," L. Senadheera, E. A. Carl, T. M. Ivancic, M. S. Conradi, R. C. Bowman, Jr., S.-J. Hwang, and T. J. Udovic, *J. Alloys Compounds* **463**, 1-5 (2008).

Session V

*Magnetism /
Multiferroics /
Spintronics*

Field-Structured Composites

James E. Martin

Sandia National Laboratories

Albuquerque, New Mexico 87185-1415

e-mail: jmartin@sandia.gov

Program Scope: The goal of this program is to discover useful methods of manipulating particle suspensions with time-dependent, multi-axial magnetic or electric fields, and to develop a scientific understanding of these phenomena and the impact they can have on technology, including sensing, actuation, microfluidic mixing, and heat and mass transfer. This program on manipulation of materials with multi-axial fields has two thrusts: 1) the development of field-structured composite materials and; 2) the stimulation of functional fluid flows.

The composites thrust focuses on using multi-axial fields to create unique particle assemblies that give composites both optimized physical properties and tailorable anisotropy. Physical properties of interest include the magnetic permeability, electric permittivity, and electrical and thermal conductivity. Technological impact is focused on the magnetostrictive actuation of these composites, and their use as chemical and strain sensors. A significant component of this work involves relating the composite properties to structure with a combination of theory and simulations of structural evolution.

The functional fluid flow thrust focuses on developing methods of using multi-axial magnetic fields to initiate vigorous fluid mixing on the microscale, and to stimulate the formation of both advection lattices and chaotic advection in fluid suspensions. The advection lattices are a new and surprising discovery, and much of our current work is concentrated on exploring the formation of the unique flow patterns and free standing fluid structures we have discovered, and quantifying the attendant heat and mass transfer. These flow patterns have symmetries that are distinct from those produced by natural convection, and offer the possibility of cooling in microgravity environments and transferring reactants and nutrients to a chemical or biological process without extracting heat.

Recent Progress: This program has impacted a variety of areas of science and technology. We have developed robust, *tunable* sensors for volatile organic chemicals that are licensed and being commercialized for environmental monitoring of leaking gasoline tanks [1-5]. We have developed a new generation of moldable thermal interface materials [6] with exceptional conductivities by using magnetic fields to optimally organize magnetic platelets for heat transfer. These materials have thermal conductivities significantly better than diamond-filled polymers. We have published both theoretical and experimental papers on our discovery of the ability to mix fluids containing magnetic particles by subjecting them to particular multi-axial magnetic fields [7-8]. We have shown that anisometric particles, such as platelets and nanorods are especially effective [9], and this technology will enable efficient mixing in microfluidic devices. Our work on functional fluid flows has resulted in discoveries that impact both science and technology, and rival Benard's discovery of convection cells by demonstrating field-controllable functional flows having unique symmetries [10]. We have discovered spontaneous flow symmetry breaking, spontaneous chiral symmetry breaking, helical flow, free-standing fluid structures, and chaotic advection. *Isothermal Magnetic Advection* enables hand's-off, directed transport of heat and mass without gravity or a thermal gradient and can be used in situations where convection fails, such as in microgravity environments or in stable thermal gradients. This work has generated a patent application. Finally, we have demonstrated spontaneous magnetization in field-structured assemblies of superparamagnetic nanoparticles [11], and developed a novel model of the luminescence dynamics in acceptor-donor phosphors [12].

Most of our work this year has focused on thermal interface materials. These materials are based on moldable, thermosetting polymers. These polymers are modified by the addition of multilayered magnetic platelets. During thermoset cure these platelets are oriented by uniaxial or biaxial magnetic fields in such a manner as to direct heat transfer. These platelets are comprised of a magnetic, Ni core that is 80 nm thick, which is symmetrically coated with 120-200 nm thick layers of a thermally conducting material such as Al or Cu, which in turn are coated with 200 nm layers of MgF₂ for stability to oxidation. The platelets are generally about 20 microns across and can be irregularly shaped, square, or rectangular. The platelets can be flat or corrugated.

Platelets offer a substantial advantage over the use of spherical particles, which have been extensively investigated for conductivity enhancement. When a spherical particle of relatively high thermal conductivity is added to a continuous phase to which a thermal gradient is applied, the isotherms are nearly completely excluded from the particle. Because the temperature gradient in the particle is small, thermal conduction within the particle is small. The exact solution to the thermal conductivity K_{eff} of a random composite of particles is

$K_{eff} = K_{poly}(1 + \alpha\phi + \dots)$, where α is the first virial coefficient and K_{poly} is the thermal conductivity of the polymer phase. For spherical particles of high thermal conductivity the first virial coefficient approaches 3, so the thermal conductivity enhancement is really very modest. For example, adding 10% spherical diamond particles ($K=2000$ W/m²K) to an epoxy ($K=0.23$ W/m²K) gives a composite thermal conductivity of $K=0.30$ W/m²K. Most notably, the virial coefficient is independent of the thermal conductivity of the material of which the particles are comprised, provided this significantly exceeds that of the polymer phase. However, the virial coefficient is a strong function of particle shape, so improvements in thermal transport can be achieved by exploiting this shape dependence.

The virial coefficient is the subject of shape functional theory, and has been worked out exactly for generalized ellipsoids and a few other shapes. For anisometric particles the efficiency of thermal transport is dependent on the orientation of the particles relative to the applied thermal gradient. For a platelet there are two principal directions where thermal conduction is high, and one direction (normal to the plane of the platelet) where thermal conduction is low (principal moments of the so-called ‘‘polarizability’’ tensor). For a random composite the virial for thermal conduction would be the average of these three values, which could still be significantly better than the sphere result, in practice something on the order of 20 or so. However, by choosing magnetic platelets we can do much better than this, fundamentally because of the isomorphism between the thermal conductivity and magnetic permeability of a particle composite. In short, the application of a magnetic field to a suspension of platelets causes the platelets to orient and agglomerate in such a way as to maximize the effective permeability of the composite, since this minimizes its magnetostatic energy. The resulting composite structure is just that which maximizes thermal transport along the applied field direction. In the following we describe the connection between magnetism and thermal conductivity, which ultimately derives from the fact that the magnetic static potential and the temperature field during steady-state heat conduction both obey LaPlace’s equation.

When a magnetic particle is inserted into an initially uniform magnetic field the particle magnetizes, producing capping magnetic ‘‘monopole’’ layers that create a field within the particle that opposes the applied field \mathbf{H}_0 . This effect can be quantified by the so-called demagnetization factor n , defined by

$$\mathbf{H}_{int} = \mathbf{H}_0 - n\mathbf{M} \quad (1)$$

where \mathbf{H}_{int} is the internal macroscopic field and \mathbf{M} is the particle magnetization. This equation implies that the internal field is uniform, which is at least the case for ellipsoidal particles. For ellipsoidal particles the demagnetization factor along the principal axes x, y, z is subject to the sum rule $n_x + n_y + n_z = 1$, and the magnitude of each component is independent of the susceptibility of the material of which the particle is comprised. For a sphere the demagnetization factor is isotropic and is simply 1/3. In any case, here we treat the case where the particle is aligned along one of its principal axes.

In the linear response regime the magnetization of a particle is related to the internal macroscopic field by its susceptibility, $\mathbf{M} = \chi\mathbf{H}_{int}$. Here χ is $\mu_r - 1$, where μ_r is the permeability of the material of which the particle is comprised relative to that of the continuous phase. Substituting this relation into Eq. 1 gives $\mathbf{H}_{int} = \mathbf{H}_0 / (1 + n\chi)$ for the internal field. The *apparent* particle susceptibility is defined by $\mathbf{M} = \chi_{app}\mathbf{H}_0$ and thus is $\chi_{app} = \chi / (1 + n\chi)$. The effective permeability of a composite can be computed by considering the magnetization in a unit field, with the result $\mu_{eff} = \mu_{poly}(1 + \chi_{app}\phi + \dots)$, which is analogous to the virial expansion for the thermal conductivity. The first virial coefficient is thus simply the apparent particle susceptibility. This calculation shows that at least for ellipsoidal objects, the dependence of the virial coefficient on the permeability contrast factor μ_r is simple, since n is independent of this contrast factor. Numerical work on the virial coefficient can thus be restricted to n as a function of particle shape. As a matter of interest, for large positive contrast ($\mu_r = \infty$) the virial coefficient is $1/n$, and for large negative contrast ($\mu_r = 0$) this virial is $-1/(1-n)$. For a sphere these limits are 3 and $-3/2$. Finally, the magnetic induction inside the particle can be computed from $\mathbf{B}_{int} = \mu_0(\mathbf{H}_{int} + \mathbf{M})$, which gives $\mathbf{B}_{int} = \frac{1 + \chi}{1 + n\chi} \mathbf{B}_0$.

The heat conduction problem can be mapped onto the permeability problem. The thermal flux density within the particle is $\mathbf{G}_{int} = K_p \nabla T_{int}$. The thermal gradient is isomorphic to the magnetic field, so the thermal gradient *within* the particle is related to the applied thermal gradient by $\nabla T_{int} = \nabla T_0 / (1 + n\chi)$, where the thermal susceptibility is defined by $\chi = K_r - 1$ in terms of the relative thermal conductivity $K_r = K_p / K_{poly}$ of the two phases. Combining these expressions gives $\mathbf{G}_{int} = \frac{1 + \chi}{1 + n\chi} \mathbf{G}_0$, showing that the thermal flux density is analogous to

the magnetic flux density. From this relation the demagnetization factor can be written as $n = \frac{K_r - G_r}{(K_r - 1)G_r}$ in terms of the relative thermal flux density $G_r = G_{\text{int}}/G_0$. The incremental thermal flux density within the particle is $\Delta \mathbf{G}_{\text{int}} = (K_p - K_{\text{poly}})\nabla T_{\text{int}} = \chi_{\text{app}} \mathbf{G}_0$, where we recall $\chi_{\text{app}} = \chi/(1 + n\chi)$ is the virial coefficient. The incremental flux density is thus analogous to the magnetization. For the sake of completeness we mention that in numerical studies described below we obtain the virial coefficient from $\chi_{\text{app}} = \frac{K_r - 1}{K_r} G_r$.

Our work on heat transfer in these platelet composites includes both laser flash diffusivity measurements on a wide variety of composites we have fabricated, as well as simulations of heat transfer in these materials. In the experimental work we have demonstrated virial coefficients as high as 87 for magnetically aligned and structured composites of single phase Ni platelets, which compares quite well to the virial coefficient of 3 for random composites of spherical particles. This high value is due both to the magnetic alignment of the platelets, as well as to the interactions between particles. In the magnetic sense particles agglomerate so as to maximize the local field at a platelet site. In the thermal problem these agglomerations boost the local thermal gradient at a platelet, which increases their thermal transport. For magnetically structured spherical particles this local field effect increases the virial coefficient by $\sim 8/3$. For platelets the magnitude of this local field enhancement is difficult to assess.

For the more stable multilayered platelets the virial coefficients are not quite as high, due to the relatively low thermal conductivity of the 200 nm thick MgF_2 coatings ($K=10.0$ W/mK) relative to the 80-200 nm Al ($K=390$ W/mK) and 80 nm Ni ($K=91$ W/mK) layers. For irregularly shaped platelets the virial coefficients are in the range of ~ 25 -45, increasing somewhat with the thickness of the Al coatings. The Al thickness effect is a balance of two factors: thicker Al coatings increase the platelet thickness and thus reduce the aspect ratio, which reduces the internal thermal gradient, but the increased thickness reduces the effect of the rather thick, low thermal conductivity MgF_2 outside coatings. We are now doing detailed numerical calculations to understand this balance of factors. For square platelets having the same layer thicknesses the virial coefficient is $\sim 20\%$ larger, an effect that is most likely due to more favorable agglomeration of these platelets. Finally, we were surprised to discover that irregular corrugated platelets give virial coefficients of ~ 65 . We do not yet have square corrugated platelets, but we would expect these to exhibit virial coefficients approaching 80. At a loading of 25 vol%, which we have already achieved with irregular multi-layered platelets, this would give a thermal conductivity enhancement of 21.

Numerical work has focused on the computation of the virial coefficient for platelets as a function of their aspect ratio and thermal contrast. There are two basic approaches to the computation of the virial coefficient: discrete element and Brownian walk algorithms. We have taken the discrete element approach. The virial coefficient can be computed in a straightforward manner by simply meshing the desired object in a simulation volume, then relaxing Laplace's equation to find the effective thermal conductivity. The virial coefficient can then be estimated by inverting the virial expansion to first order to obtain

$$\alpha_\kappa(\Delta, \phi) = \frac{K_{\text{eff}} - K_{\text{poly}}}{\phi K_{\text{poly}}}. \quad (2)$$

This *computed* virial coefficient is a function of the relative thermal conductivity $K_r = K_p / K_{\text{poly}}$, where K_p is the thermal conductivity of the material of which the particle is comprised, as well as both the discrete mesh size Δ and the volume fraction of the particle in the simulation volume, ϕ . To compute the true first virial coefficient requires that both the mesh size dependence and particle volume fraction dependence be removed by extrapolations to zero. The volume fraction extrapolation is analytic in form, being related to the image fields created by the boundary conditions of the simulation volume, which are dipolar in form to first order.

In fact, we do not actually compute our virial coefficients from the increase in thermal conduction, but from the “demagnetizing fields” within the particle (these could be called “dethermalizing fields” in this context), which is numerically more accurate. Our simulations are 2-d, so we consider heat conduction along the principal axes normal to the long axis of infinite rods with a generally rectangular cross section. The field inside a particle is nonuniform, so the demagnetization factor is defined for average properties and becomes a weak function of the relative thermal conductivity. By symmetry the flux density averaged over the particle volume is still parallel to the applied thermal gradient, so $\overline{\mathbf{G}}_{\text{int}}$ and \mathbf{G}_0 are parallel. The average internal flux density can be computed from the average thermal gradient, which is just the average of the temperature difference on the two surfaces normal to the applied gradient divided by the gap between these surfaces. Computing the demagnetization factor from this average flux density gives exactly the same result as Eq.2, but we find extrapolating to zero mesh size is more

accurate, due to the weaker dependence of this approach on mesh size. A second advantage is the weak dependence of the demagnetization factor on the relative conductivity, compared to the strong dependence of the virial coefficient on this factor. We find we can fit the demagnetization factor from our simulations to

$$n_K = n_\infty + \frac{A}{1 + K_r}$$

where $A/(1 + K_r)$ is generally quite small compared to n_∞ and we recall that $\alpha = (K_r - 1)/[1 + n_K(K_r - 1)]$.

To test the accuracy of our approach, we first considered the case of the 2-d square, since for the limiting case of infinite thermal contrast (where $\alpha = 1/n_\infty$) this problem has been solved exactly by conformal mapping. Our result is $n_\infty = 0.45,828$ and $A = 0.86,659 \times 10^{-1}$. For infinite conductivity contrast this gives $\alpha = 2.1854$. The exact result is $\alpha = \frac{1}{4} \Gamma^2(1/4)/\pi^{3/2} \approx 2.1884$. So our accuracy is about 0.14%, which is certainly adequate for comparison to experimental results. Our numerical results for platelets of aspect ratios A from 1 to 64 are well described by

$$n_K = \frac{1}{1.343 + 0.8829\sqrt{A}} \left[1 + \frac{0.1814 + 8.448 \times 10^{-2} A^{3/4}}{1 + K_r} \right].$$

This result is valid for thermal contrast ratios from 1 to ∞ . The resulting virial coefficients show the strong dependence of the virial coefficient on aspect ratio and relative conductivity. This will be discussed in my talk. Current work is focused on thermal modeling of the multilayered platelets.

Future directions: Our research will continue to emphasize thermal transport, and in addition to developing composites with high thermal conductivities, we will focus on measuring heat transfer with isothermal magnetic advection. IMA has as its principal parameters the relative field frequencies, absolute field frequencies, and their phase relation. This new phenomenon should make possible the transport of mass and/or heat in any arbitrary direction, regardless of the thermal gradient or of gravity.

Acknowledgements: Sandia National Laboratories is a multi-program laboratory operated by Sandia Corporation, a wholly owned subsidiary of Lockheed Martin Company, for the U.S. Department of Energy's National Nuclear Security Administration under contract DE-AC04-94AL85000. This work was supported by the Division of Materials Science, Office of Basic Energy Sciences, U.S. Department of Energy (DOE).

References

1. *Field-Structured Chemiresistors*. Read D H and Martin J E, 2010 Adv. Func. Mats., **20** (10), 1577–1584.
2. *Strain-Tunable Chemiresistor*. Read D H and Martin J E, 2010 Anal. Chem., **82** (5), 2150–2154.
3. *Master Transduction Curve for Field-Structured Chemiresistor Calibration*. Read&Martin, 2010 Anal. Chem. **82**, 5373-9.
4. *Analyte Discrimination from Chemiresistor Response Kinetics*. Read&Martin, 2010 Anal. Chem. **82**, 6969-75.
5. *Role of Stress on Field-Structured Chemiresistor Response*. Read&Martin, 2011 Anal. Chem. XX, XXXX.
6. *Field-Structured Composites for Efficient, Directed Heat Transfer*. Martin J E and Gulley G, 2009 J. Appl. Phys. **106**, 084301-084307. (see also 2009 Virt. J. of Nanoscale Sci. & Tech. **20** [19].
7. *Strong Intrinsic Magnetic Mixing in Vortex Magnetic Fields*. Martin J E, Shea-Rohwer L, Solis, K J, 2009 Phys. Rev. E. **80** 016312-016317.
8. *Theory of Strong Intrinsic Mixing of Particle Suspensions in Vortex Magnetic Fields*. Martin, J E, 2009 Phys. Rev. E. **79** 011503-011514.
9. *Vortex Magnetic Field Mixing with Anisometric Particles*. Solis K J, Bell R C, and Martin J E, 2010 J. Appl. Phys. **107** 114911-1 to 114911-4.
10. *Isothermal Magnetic Advection: Creating Functional Fluid Flows for Heat and Mass Transfer*. Solis K J and Martin J E, 2010 Appl. Phys. Lett. 97, 034101.
11. *Giant Magnetic Susceptibility Enhancement in Field-Structured Nanocomposites*. Martin J E, Venturini E L, and Huber D L, 2008 J. Mag. and Mag. Mats. **320**, 2221-2227.
12. *A 1-D Model of the Luminescent Decay of ZnS Phosphors as a Function of Excitation Conditions*. Martin J E, Shea-Rohwer L E, 2008 J. Lumin. **128** 1407-1420.

Program Title: Intensive Variables and Nanostructuring in Magnetostructural Materials
Principle Investigator Laura H. Lewis
Mailing Address Department of Chemical Engineering, 342 Snell Engineering Center,
Northeastern University, Boston, MA 02115
E-mail Address lhlewis@neu.edu

Program Scope

Magnetostructural transitions comprise simultaneous magnetic and structural phase changes that have their origins in very strong orbital-lattice coupling. Research is underway to delineate the effects of intensive variables, including the structural scale, on magnetostructural phase transitions in model systems, with the objectives to understand, predict and tailor these unique phase transitions to defined outcomes. The model systems are MnBi (hexagonal NiAs structure) and FeRh (cubic CsCl structure) with lines of inquiry as:

- i) understand materials aspects of the transition, including the roles of stoichiometry, chemical and crystallographic ordering;
- ii) probe characteristics of the transitions as driven by simultaneous temperature and magnetic and/or stress fields variations;
- iii) investigate the effects of nanostructure evolution (*i.e.*, bulk to nanoscaled) on the transition.

Both conventional (metallurgical) and advanced (rapid solidification, molecular-beam epitaxy (MBE), nanopatterning) techniques will be employed for materials synthesis and processing. In-depth characterization and understanding of the phase constitution, crystalline and magnetic attributes will be accomplished by experiments carried out at the National Synchrotron Light Source (NSLS) at Brookhaven National Laboratory (BNL), employing probes that interrogate the structure via scattering techniques and/or the energy states via advanced spectroscopy. In this manner a much deeper understanding of magnetostructural transitions and influencing factors in these materials may be obtained than previously achieved; these investigations will support aspirations of directed design of materials for optimal functionality.

Recent Progress:

So-called “kinetically-structured” materials may be produced by non-equilibrium synthesis (*i.e.*, rapid solidification processing) that exploit a balance between thermodynamics and kinetics to trap metastable phases and nanostructures into a 3-D materials architecture. To this end, creation of a hypothesized nanostructured magnetostuctural system was carried out via rapid solidification of an alloy of composition (FeRh)₅Cu₉₅ to precipitate nanoscaled isolated FeRh precipitates in a Cu matrix upon annealing. Bulk FeRh has a quasi-discontinuous antiferromagnetic - ferromagnetic transition with increasing temperature around $T \sim 370$ K and a Curie temperature of 690 K, a difference of 320 degrees (Figure 1). Laboratory X-ray diffraction performed on the (FeRh)₅Cu₉₅ alloy in its as-quenched state indicates only the presence of Cu with a slightly expanded lattice parameter $a=3.62$ Å, with ferromagnetism confirmed at room temperature by SQUID magnetometry. Field-cooled and zero-field-cooled magnetization measurements performed at relatively low fields (100 – 250 Oe) on the ribbons in various annealing conditions point to the existence of a complex multiphase state that likely encompasses spin glass, ferromagnetic and paramagnetic phases. Upon isochronal vacuum annealing at 200 °C a secondary phase starts to appear in the magnetic signal. This secondary phase continues to develop with increased annealing temperature and exhibits a clear magnetic phase transition at $T_t = 130$ K, Figure 2. However, this phase is never apparent in the x-ray diffraction data, suggesting the formation of nanoparticles that are too small and too dilute to be detected by laboratory x-ray diffraction. By fitting the magnetic susceptibility response for $T <$

100 K to a Curie-Weiss law, it is possible to decompose the overall magnetic response into two contributions: one attributed to a metamagnetic phase and one attributed to a paramagnetic phase. The noted transition is highly reminiscent of the bulk FeRh magnetostructural transition shown in Figure 1; while it remains to be confirmed, it appears that the hypothesized nanoscaled phase in Figure 2 possesses a Curie temperature T_C of 350 K, resulting in a temperature span between transitions of 230 degrees. If indeed the unusual magnetic response arises from the presence of nanoscaled FeRh particles, this represents an unprecedented reduction in magnetic transition temperatures by virtue of nanoscaling.

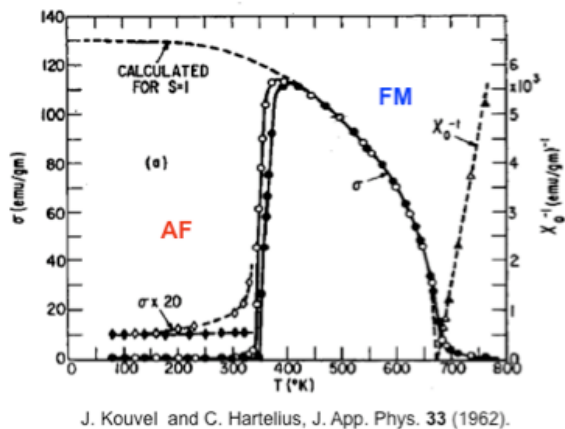


Figure 1: Magnetostructural transition in bulk FeRh

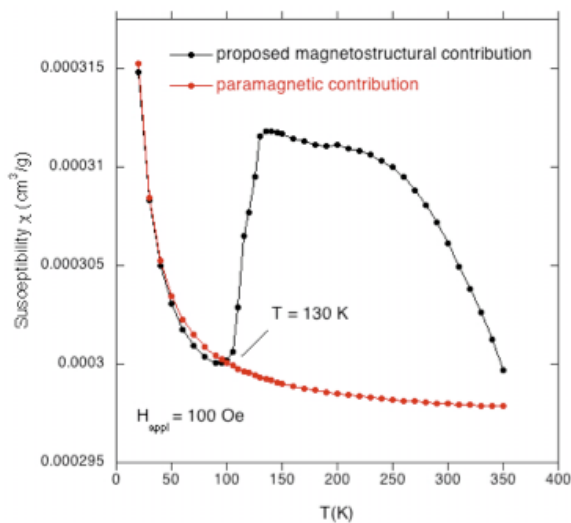


Figure 2: Hypothesized magnetostructural transition in nanoscaled FeRh

Future Plans

Future plans include efforts to further investigate the phase constitution and magnetic behavior and magnetic transitions inherent in the melt-spun $(\text{FeRh})_5\text{Cu}_{95}$ ribbons by employing laboratory-based structural and magnetic probes as well as synchrotron-based probes. The creation of nanopatterned films of FeRh is underway; such materials will display 2-D magnetostructural character and provide interesting analogs to the 3-D character of the hypothesized FeRh nanoparticles.

Acknowledgements: Contributions from R. Barua, D. Heiman and F. Jiménez-Villacorta, Northeastern University, are gratefully acknowledged.

Coherent control of spin states in organic electronics

PI: Christoph Boehme, co-PI: John M. Lupton
 University of Utah, Department of Physics and Astronomy,
 115S 1400E, Salt Lake City, Utah, 84112, boehme@physics.utah.edu

Program Scope or Definition

In semiconductors with weak spin-orbit coupling, spin-selection rules allow electron spins and nuclear spins to influence electrical and optical materials properties. Such spin-dependent processes enable a number of applications ranging from readout devices for spin quantum computers and spintronics [1] to semiconductor spin spectroscopy [2]. The latter is particularly important for the exploration of organic semiconductors, since the spin-degree of freedom therein crucially determines many performance-limiting processes. Examples include charge carrier recombination which critically determines efficiencies of organic solar cells or exciton-formation processes which crucially determine the efficiency of organic light emitting diodes (OLEDs). Figure 1 sketches spin-dependent exciton formation and recombination in OLEDs. It illustrates how spin-lattice relaxation of weakly spin-coupled excitonic precursor pairs (so called polaron pairs) is crucially responsible for the efficiency of the OLED device.

The focus of this project is on the application of a spin-selection rule based *coherent* spin spectroscopy to organic semiconductor materials and devices. The experimental approach is the combination of coherent, “pulsed” electron paramagnetic resonance spectroscopy, with optical, and with electrical detection techniques. Optically and electrically detected magnetic resonance spectroscopies (ODMR and EDMR, respectively) have been used for decades to explore spin-dependent processes in materials, including organic semiconductors. However, while conventionally detected magnetic resonance spectroscopy is today performed almost exclusively as a pulsed experiment, ODMR and EDMR are still used mostly as adiabatic field sweep experiments whose experimental insights are limited and therefore, due to the restricted range of accessible parameters, the interpretation of experimental results is oftentimes ambiguous. Because of this, this project aims to systematically study spin-dependent processes in organic materials with pulsed EDMR and ODMR for the first time. For the example given in Fig. 1, a pulsed EDMR experiment can be carried out by coherent transfer of singlet precursor pairs into triplet states and vice versa. Such a coherent back-and-forth transfer can be detected electrically [4] or optically [5] as the changed charge carrier spin states change conductivity and radiative exciton decay rates. The observation of this so-called Rabi-oscillation can then serve as a direct measure of the polaron pair spin-relaxation rate. Since coherent transfer and spontaneous relaxation occur at the same time, the oscillation is attenuated by the relaxation. Figure 2 shows an example for such an electrically detected Rabi oscillation [4] and the decay of this observed oscillation provides a lower limit for the spin relaxation rate.

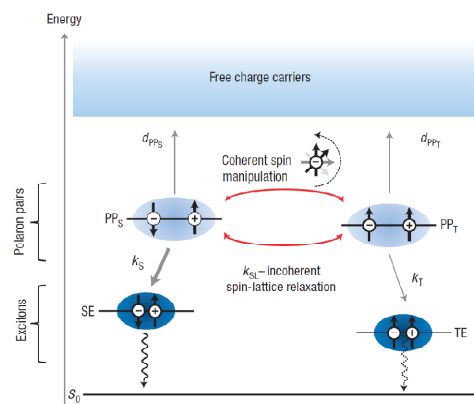


Fig. 1: Exciton formation in (hydrocarbon) OLEDs takes place in a two step process. First, weakly spin coupled charge carrier pairs (so called polaron pairs, PP) form, which then undergo a transition into strongly spin exchange coupled excitons. Only singlet excitons contribute to light emission, the formation of triplet excitons constitutes an energy loss. Since the formation of the singlet excitons crucially depends on the spin-lattice relaxation rate k_{S1} of the PPs, any efficiency optimization process requires experimental access to the PP relaxation [3].

Recent Progress

The program is currently in its second project year which started on 07/15/2010. The major scientific accomplishment of the first project period (07/15/2009-07/14/2010) was the demonstration of hyperfine field-mediated spin beating in OLEDs [4]. Using the Rabi oscillation experiment described above at

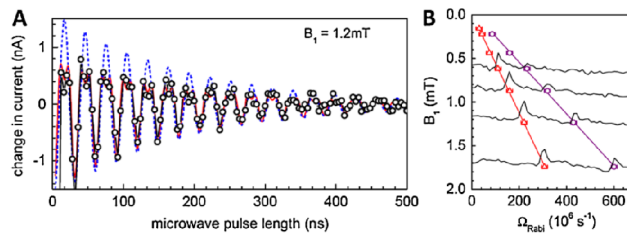


Fig. 2: (a) Coherent oscillations of the ensemble of spin pairs, observed by measuring the change in OLED current after application of resonant microwave pulses of increasing length. The fit with an exponentially damped sinusoidal function with two harmonic components is shown (solid red line), as is a fit with only a single harmonic frequency component (dashed blue line). (b) Sample Fourier transform spectra of Rabi nutation traces obtained at different B_1 field strengths. The frequency of the two peaks was determined, and plotted as a function of B_1 .

experiment was described in the proposal, we could not have predicted such an outcome.

A technical accomplishment achieved during the first project period lies in the fact that we have dramatically improved our signal-to-noise ratio in the experiment by almost three orders of magnitude. This enhancement now allows us to map variations in resonance field (g -factor) and the actual resonance line shape with unprecedented accuracy [6]. This enabled us to search for systematic influences on the spin resonance line shape (such as current, temperature, electric field, microwave intensity, device geometry, and the specifics of the material).

We have succeeded in demonstrating spin coherence (Rabi flopping) in the device current at room temperature as shown in Fig. 3. We can pose a lower limit on the spin coherence time of several hundred nanoseconds at room temperature. This result is remarkable in that there is plentiful speculation in the literature that this process should be ~ 5 orders of magnitude faster [5]. The results are also encouraging for potential applications of OLEDs in quantum information processing: OLEDs may ultimately pose a viable alternative to the diamond NV system, with the crucial benefit of being electrically addressable.

The focus of the second project period has been on a crucial test of the understanding developed during the first project period. The schematic of Fig. 1, illustrates that, if it is correct, all the coherent spin effects which are seen through current measurements must be detectable in an identical manner by measurement of the radiative emission of OLEDs and OLED materials. Thus, a series of pulsed ODMR experiments on MEH-PPV were conducted at B_1 fields below

significantly higher driving field (B_1) of the oscillation, we were able to resolve signatures of two spin-1/2 species. At low driving fields (low incident microwave intensity), the two spin species precess independently of each other: periodic Rabi flopping is observed in the current. At high fields (B_1 larger than the hyperfine fields), the precessing spins beat, leading to a beating modulation of the device current. The experiment provides one of the first quantitative handles on the influence of hyperfine fields (from the hydrogen nuclei) in organic semiconductors. What is quite remarkable is that the hyperfine fields are of order millitesla, yet our experiments are carried out at static fields two orders of magnitude greater. We were certainly not anticipating this result – while the

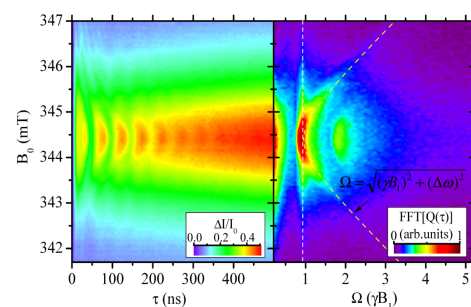


Fig. 3: Spin-Rabi-flopping observed through current measurement of an OLED under operating conditions at room temperature. Left: The time domain plot as a function of the applied magnetic field B_0 . Right: The Fourier transform of the data shown on the left. The frequency scale is in units of the gyromagnetic ratio times the applied B_1 field. It shows a spin-1/2 component at γB_1 and the beating feature at $2\gamma B_1$. The peaks in the FFT's hyperbolic feature show an excellent agreement with Rabi's formula.

carriers. Figure 6 displays a sketch of the device with a hole injection layer (PEDOT:PSS) as used for the devices discussed above, and of a device in which electrons constitute the majority carrier due to the absence of a hole injection layer. Pulsed EDMR spectra show that at room temperature, only weakly coupled spin systems (such as the excitonic precursor pairs) can be detected. At low temperatures, the balanced devices show a very weak (about two orders of magnitude weaker) signal due to strongly coupled spin systems (such as excitons) as detected via the half-field resonance at $g \approx 4$. In contrast, the electron-dominated devices exhibit at low temperatures a very pronounced half-field signal which was confirmed to be correlated with the full field (i.e. the polaron signal). This additional signal never exhibited any Rabi beat behavior and thus resulted from a single carrier not coupled to any other charge carrier. This observation is clear evidence for a spin-dependent process involving a triplet exciton and a polaron, which can control the electrical device current. The triplet/polaron mechanism has been investigated theoretically for many years. The experimental study of this process using continuous wave EDMR and ODMR experiments has led to considerable controversy regarding its existence. The direct observation of a correlated polaron-triplet exciton system here has unambiguously resolved this discussion.

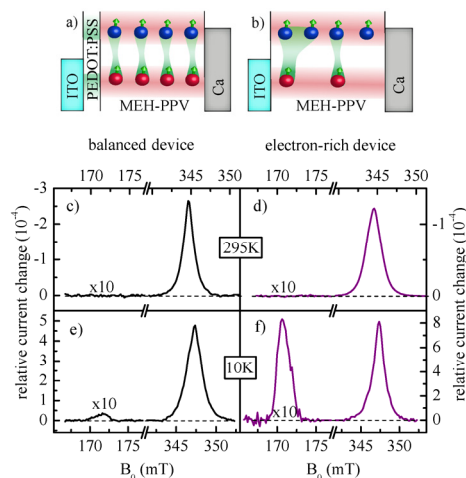


Fig. 6: Pulsed EDMR of OLEDs with carrier balance (a) and electron surplus (b). c, d): At 295K, only full-field resonances are seen. e, f): At 10K, half-field resonances are seen weakly in balanced devices, but strongly in electron-dominated devices.

Future Plans

We have started applying the technique of pulsed optically-detected (photoluminescence) magnetic resonance to hybrid organic-inorganic semiconductor materials, such as CdSe nanocrystal tetrapod light-harvesting structures. Surprisingly, we have identified signatures of spin coherence in these strongly spin-orbit coupled materials. One of our long-term goals is to unravel the effect of spin-orbit coupling in pure organic and hybrid organic-inorganic devices such as plastic photovoltaic cells.

Published and accepted Publications of DOE sponsored research in 2008-2010

- [1] C. Boehme* and D. R. McCamey, **Investigating spin-dependent processes in organic semiconductors** in *Organic Spintronics*. Z. V. Vardeny ed. (CRC Press, 2010). ISBN: 978-1-4398-0656-2.
- [2] J. M. Lupton, D. R. McCamey, C. Boehme, **Coherent Spin Manipulation in Molecular Semiconductors: Getting a Handle on Organic Spintronics**, *Chem. Phys. Chem.* 11 (14), 3040 (2010). <http://dx.doi.org/10.1002/cphc.201000186>
- [3] D. R. McCamey, S.-Y. Lee, S.-Y. Paik, J. M. Lupton, and C. Boehme, **Spin-dependent dynamics of polaron pairs in organic semiconductors**, *Phys. Rev. B* **82**, 125206 (2010). <http://dx.doi.org/10.1103/PhysRevB.82.125206>
- [4] D. R. McCamey, K. J. van Schooten, W. J. Baker, S.-Y. Lee, S.-Y. Paik, J. M. Lupton, and C. Boehme, **Hyperfine-field mediated spin beating in electrostatically-bound charge carrier pairs**. *Phys. Rev. Lett.* **104**, 017601 (2010). <http://dx.doi.org/10.1103/PhysRevLett.104.017601>
- [5] S.-Y. Lee, S.-Y. Paik, D. R. McCamey, J. Yu, P. L. Burn, J. M. Lupton, and C. Boehme, **Tuning hyperfine fields in conjugated polymers for coherent organic spintronics**, to be published in *JACS*, (2011).
- [6] C. Boehme, D. R. McCamey, K. J. van Schooten, W. J. Baker, S.-Y. Lee, S.-Y. Paik, J. M. Lupton, **Pulsed electrically detected magnetic resonance in organic semiconductors** *Phys. Stat. Sol. B.* **246**, 11-12, 2750 (2009). <http://dx.doi.org/10.1002/pssb.200982357>

Project Title: Magnetic frustration and cooperative phenomena in correlated electron oxide materials

Principal Investigator: Prof. Hariharan Srikanth

University of South Florida, Department of Physics, PHY 114

4202 East Fowler Ave, Tampa, FL 33620

E-mail: sharihar@usf.edu

Project Participants: Dr. M. H. Phan (Research Assistant Professor), Mr. Nicholas Bingham (Ph.D student), Mr. Nicholas Laurita (Undergraduate student)

Program Scope:

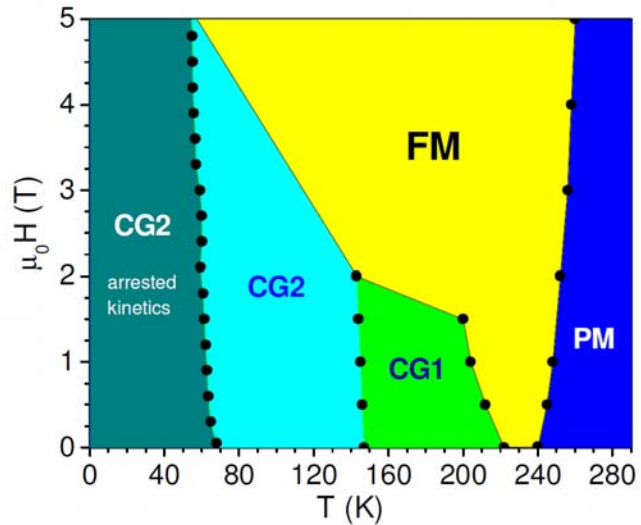
Transition-metal oxides exhibit rich complexity in their fundamental physical properties determined by the intricate interplay between structural, electronic and magnetic degrees of freedom. Our DoE funded effort during the past 3 years (2007-2010) yielded new insights into the role of interplay between intrinsic strain, structural transitions, electronic phase separation, magnetic anisotropy and magnetic entropy in a broad range of correlated electron oxide materials such as single crystalline (LuFe_2O_4), nanostructured garnets ($\text{GdFe}_3\text{O}_{12}$), manganites ($\text{Pr}_{0.5}\text{Sr}_{0.5}\text{MnO}_3$) and $\text{La}_{0.7}\text{Ca}_{1-x}\text{Sr}_x\text{MnO}_3$ ($x=0, 0.05, 0.1, 0.2, 0.25$), and cobaltites $\text{Pr}_{1-x}\text{Sr}_x\text{CoO}_3$ ($x=0.3-0.5$). We have demonstrated the importance of combining conventional DC and AC magnetometry with relatively unconventional RF transverse susceptibility (TS) and magnetocaloric effect (MCE) methods to probe the ground state magnetic properties and glassy behavior in several classes of frustrated magnetic systems.

In addition to continuing our studies further on the geometrically frustrated oxides identified in the past grant period, the current project period addresses some of the outstanding issues in mixed phase manganites $\text{La}_{5/8}\text{Pr}_{3/8-x}\text{Ca}_x\text{MnO}_3$ (LPCMO) with competing charge ordered and ferromagnetic phases strongly influenced by strain and low dimensionality; AB_2O_4 type spinel ferrites with multiple spin re-orientation configurations and $\text{Ca}_3\text{Co}_2\text{O}_6$ having Ising spin chains arranged on a triangular lattice geometry. All these systems are of current interest and have important unresolved issues that we intend to explore through our combination of DC and AC magnetization, TS and MCE studies coupled with neutron scattering and other local structural probes. We present here selected representative results on LuFe_2O_4 single crystals and LPCMO in single crystalline and nanocrystalline forms.

1. Complex magnetic phase diagram in LuFe_2O_4

LuFe_2O_4 is a complex oxide of great current interest as it presents a rare example of a ferroelectric in which the ferroelectricity is not due to conventional covalent bonding but rather due to Fe^{2+} - Fe^{3+} valence ordering and strong electron correlation [1]. The dielectric constant increases sharply below 330 K and interestingly, LuFe_2O_4 also exhibits multiferroic behavior as it displays large magnetocapacitance at room temperature [2]. All these signatures point to a strong coupling between the electronic, structural and magnetic degrees of freedom somewhat similar to colossal magnetoresistive (CMR) manganites. Limited studies of the fundamental magnetism in LuFe_2O_4 in the past indicated that it undergoes an antiferromagnetic transition with a Neel temperature of 240 K [3].

However, our comprehensive DC and AC magnetization studies on high quality single crystals LuFe_2O_4 (grown in Dr. David Mandrus' laboratory at ORNL) resolve the correct origin of the transition at 240 K as being a 3D ferromagnetic order (along the c-axis) immediately followed by a re-entrant spin glass transition at 225 K [4,5]. In addition, we observed a new magnetic transition at 170 K, which is also in agreement with the neutron diffraction results recently reported by the Oak Ridge group [6]. We demonstrate for the first time that the origin of giant magnetic coercivity is attributed to collective freezing of ferrimagnetic clusters and enhanced domain wall pinning associated with a structural transition at 170 K.



A complete magnetic phase of LuFe_2O_4 is established from DC, AC susceptibility and MCE data. It shows the system undergoing a paramagnetic (PM) to ferromagnetic (FM) transition followed by the two cluster-glass transitions (CG1 and CG2) at 225 K and 170 K respectively and finally a kinetically arrested state below 55 K.

Magnetocaloric effect measurements provide additional vital information about the multiple magnetic transitions, the glassy states and the kinetically arrested phenomena at low temperature below 55 K. Our results lead to the emergence of a complex magnetic phase diagram (see Fig. 1) in LuFe_2O_4 that consistently accounts for many observations from other groups that were not fully understood. From the magnetic cooling perspective, our MCE study on LuFe_2O_4 reveals that the intrinsic spin frustration in this material and the presence of multiple magnetic transitions result in a broad MCE response over a large temperature range. This holds promise for enhanced refrigerant capacity when compared with other classes of MCE systems such as intermetallic alloys. We presented our results in an oral presentation at INTERMAG (Madrid, 2008) conference and in an invited talk at APS meeting (Portland, 2010), with the main results summarized in two publications (*Journal of Applied Physics 2010 and Solid State Communications 2010*).

2. Phase coexistence and magnetocaloric effect in $\text{La}_{5/8}\text{Pr}_{3/8-x}\text{Ca}_x\text{MnO}_3$

$\text{La}_{5/8-y}\text{Pr}_y\text{Ca}_{3/8}\text{MnO}_3$ (LPCMO) manganites exhibit a complex phase diagram due to coexisting and competing magnetic and electronic phases [7]. LPCMO is a mixture of $\text{La}_{5/8}\text{Ca}_{3/8}\text{MnO}_3$ ($y = 0$) and $\text{Pr}_{5/8}\text{Ca}_{3/8}\text{MnO}_3$ ($y = 5/8$) exhibiting low-temperature FMM and COI ground states, respectively. In this system, the substitution of smaller Pr ions for larger La ions reduces W thus leading to micrometer scale multiple phase coexistence or phase separation. It has been suggested that the different crystal structures of the FMM and COI phases generate long-range strain interactions leading to an intrinsic variation in elastic energy landscape, which in turn leads to phase separation (PS) into the strain-liquid and strain-glass regimes [8]. The phase separated regions strongly interact with each other via martensitic accommodation strain leading to a cooperative freezing of the combined charge/spin/strain degrees of freedom. As a result, LPCMO undergoes a transition from the strain-liquid state to the strain-glass state. Despite these studies, the effect of magnetic field on the strain-liquid and strain-glass states has not been studied in detail. Another emerging issue that is still under debate is regarding the underlying origin of the sharp increase of the magnetization below the Curie temperature (T_C) in the strain-liquid region. Two different

mechanisms have been proposed for interpreting this phenomenon [7,8]. In the first scenario, it is proposed that with lowering temperature, the COI state is spontaneously destabilized to the FMM phase giving rise to a coexistence of these two phases, and the sharp increase of the magnetization below T_C is due to the melting of the COI state. This is similar to the case of charge-ordered $R_{0.5}Sr_{0.5}MnO_3$ ($R = La, Pr$ and Nd) manganites. In the second scenario, it has been suggested that the sharp increase of the magnetization occurs via the growth of FMM domain regions that are already present in the material even in zero magnetic field.

To provide physical insights into these important unresolved issues, it is essential to employ experimental methods that allow detailed investigations of the temperature and magnetic field response of the different phases. In this study, we demonstrate MCE experiments as being ideally suited for this purpose [9]. The MCE has been measured to probe the nature of phase coexistence of structurally different FMM and COI phases in $La_{5/8-y}Pr_yCa_{3/8}MnO_3$ ($y = 0.275$ and 0.375) single crystals. The LPCMO single crystals were synthesized in an optical floating-zone furnace and provided by Prof. Sang Wook Cheong's group at Rutgers University. Our magnetic and MCE studies show that the MCE peaks with both positive and negative values are observed in the vicinity of the multiple phase transitions in the system. The large MCE is observed in the "dynamic" strain liquid state, while it is relatively small in the "frozen" strain-glass state. The MCE data reveal that the sharp increase of the magnetization below the Curie temperature in the strain-liquid region is attributed to the enhancement of the FM domain regions that are already present in the material. These point to the fact that the sharp increase of the magnetization occurs via the growth of FMM domain regions that are already present in the material even in zero magnetic field. Figure 2 shows MCE as a useful method to probe the subtle balance of coexisting phases in LPCMO. These results were presented in an invited talk at the APS meeting (Portland, 2010) and have been published in *Physical Review B* 2010.

In first attempts to investigate the influence of nanostructuring on the FMM and COI phases in LPCMO, our comparative studies of the magnetic and magnetocaloric properties of LPCMO in single crystalline and nanocrystalline forms have revealed the collapse of charge ordering and enhancement of MCE in the nanocrystalline LPCMO sample [10]. We show that while the conventional trend is reduction of magnetization and MCE with nanostructuring, we show that the opposite is true in the case of mixed phase manganites. The charge-ordered state is largely suppressed and ferromagnetic order is established in the nanocrystalline sample with an average particle size of 50 nm. Consequently, a strong enhancement of MCE and refrigerant capacity (RC) and a strong reduction of thermal and

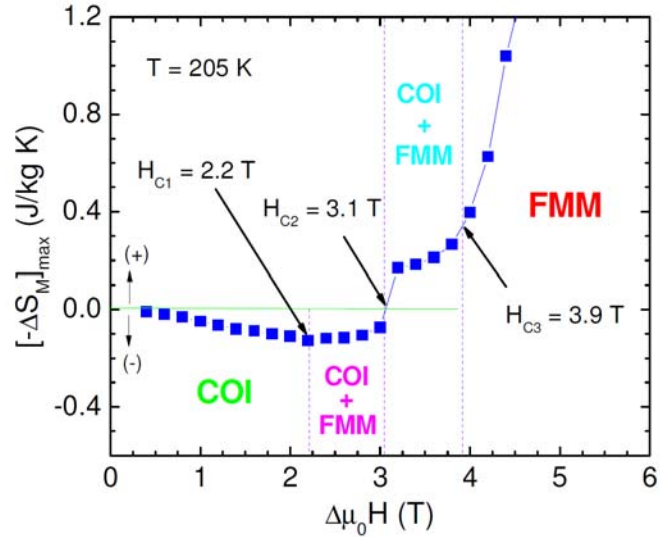


Fig. 2 Magnetic field dependence of maximum magnetic entropy change ($-\Delta S_M^{\max}$) for LPCMO at 205 K; (b) The magnetic hysteresis loop $M(H)$ measured at 205 K. $H_{C1} = 2.2$ T - the critical magnetic field at which the COI state starts to convert into the FM state; $H_{C2} = 3.1$ T - the critical magnetic field at which the half of the COI phase converts to the FMM phase; $H_{C3} = 3.9$ T - the critical magnetic field at which the COI state converts fully into the FMM state. COI = charge-order insulator; FMM = ferromagnetic metal; the mixed phase range (both the COI and FMM phases coexist) is between H_{C1} and H_{C3} .

field hysteresis losses are achieved in the nanocrystalline sample. This finding opens up a way of exploring magnetic refrigerant materials at the nanometer scale for active magnetic refrigerators. The results were presented at 11th Joint MMM-Intermag (Washington, 2010) and APS (Portland, 2010) meetings and have been published in *Applied Physics Letters* 2010.

Overall, we present DC and AC magnetization, RF transverse susceptibility and magnetocaloric effect studies in different classes of correlated electron oxide systems. Our results reveal new phenomena and glass characteristics that can be correlated to the geometric frustration in these materials. Our studies also point to the presence of competing COO and FMM phases in bulk LPCMO and the importance of the low dimensionality and strain effects on these states in nanostructured LPCMO. Future work will continue to explore the ground magnetic states and collective phenomena in these oxides and others as proposed in the renewal grant project.

Work at USF supported by DOE through grant number DE-FG02-07ER46438.

REFERENCES

- [1] N. Ikeda et al., *Nature* 436, 1136 (2005).
- [2] M. A. Subramanian et al., *Adv. Mater.* 18, 1737 (2006).
- [3] J. Iida et al., *J. Phys. Soc. Jpn.* 55, 1434 (1986); Y. Yamada et al., *Phys. Rev. B* 62, 12167 (2000); K. Yoshii et al., *Phys. Rev. B* 76 (2007) 024423; W. Wu et al., *Phys. Rev. Lett.* 101 (2008) 137203.
- [4] M.H. Phan et al., *J. Appl. Phys.* 105, 07E308 (2009)
- [5] M.H. Phan et al., *Sol. Stat. Commun.* 150, 341 (2010)
- [6] A. D. Christianson et al., *Phys. Rev. Lett.* 100, 107601 (2008); M. Angst et al., *Phys. Rev. Lett.* 101, 227601 (2008)
- [7] M. Uehara et al., *Nature* 399, 560 (1999)
- [8] T. Dhakal et al., *Phys. Rev. B* 75, 092404 (2007)
- [9] M.H. Phan et al., *Phys. Rev. B* 81, 094413 (2010)
- [10] M.H. Phan et al., *Appl. Phys. Lett.* 97, 242506 (2010)

Session VI

*Thermoelectrics,
Ferroelectrics and
Structural Properties*

Measurement of Near-Field Thermal Radiation between Flat Surfaces with a Nanogap

Zhuomin Zhang zhuomin.zhang@me.gatech.edu
George W. Woodruff School of Mechanical Engineering
Georgia Institute of Technology, Atlanta, GA 30332

Program Scope

Evanescent waves and photon tunneling are responsible for the predicted near-field energy transfer being several orders of magnitude greater than that between two blackbodies, i.e., breaking Planck's law. The enhanced energy transfer may be used for improving the performance of energy conversion devices, augmenting laser cooling, developing novel nanothermal manufacturing techniques, and imaging structures with high spatial resolutions. Recent works by other groups have demonstrated significant enhancement of nanoscale radiation using sphere-plate geometry. We propose to fabricate ultrasmall gaps for measuring nanoscale radiation between flat surfaces with relatively large areas. The ultimate goal is to quantitatively demonstrate near-field radiation between relatively large flat surfaces at a distance of tens of nanometers for the application of near-field thermophotovoltaic devices.

The activities progress summarized below include some theoretical calculations that enable the materials selection and geometric optimization. The results also help the fundamental understanding of nanoscale thermal radiation. A spectral emissometer is developed to study the effect of optical resonance on the far-field thermal emission from layered structures.

Recent Progress (references are according to the list of publications)

Nanoscale thermal radiation can be utilized to improve the performance of near-field thermophotovoltaic (TPV) devices and near-field scanning-tunneling thermal imaging systems. The enhancement can be well explained by the excitation of surface plasmon polaritons [3-8]. An optimization was performed to investigate the parameters in the Drude model or Lorentz model in order to give guidelines to the selection of materials [6]. The results show that it is possible to optimize the given models. In general, the high-frequency constant should be as close to unity as possible and the resonance frequency (transverse optical phonon frequency) should be as small as possible. However, trade-offs exist in regards the scattering rate (damping coefficient) and the plasma frequency. The calculated net fluxes for a few sets with optimized parameters (under certain constraints) and for some real materials are compared to facilitate the selection and design of materials for enhanced nanoscale radiative transfer [6].

The PI's group has elucidated the fundamental characteristics of nanoscale thermal radiation by considering the energy pathways in the near field. It is shown that the energy streamlines can be obtained by computing the Poynting vectors for individual values of the parallel wavevector component. For near-field thermal radiation, the electric and magnetic fields with different parallel wavevector components are decoupled. This is a unique characteristic of thermally emitted electromagnetic waves, which arise from random fluctuating currents. Due to the coupling of forward and backward evanescent waves, photon tunneling may occur and can greatly enhance radiative heat transfer at the nanoscale. Our recent studies provide a method to compute the lateral shift of the streamlines not only inside the vacuum gap but also in the emitters and receivers [4,9].

The spectral and total Poynting-vector distributions are plotted in Fig. 1 for SiC-vacuum-SiC arrangement, where the emitter and receiver are set to 300 K and 0 K, respectively. The ordinate is normalized to the Poynting vector inside the gap. The energy flux increases in the emitter toward the surface and decreases in the receiver away from the surface. Surprisingly, the distributions are “symmetric” in the emitter and the receiver. It can be shown that the distribution function inside the receiver can be characterized by an exponential decay function. The penetration depth of approximately $0.19d$ at $\lambda = 10.54 \mu\text{m}$, where SPP is excited, and the penetration depth based on the total energy flux is $0.25d$. The results suggest that for $d = 10 \text{ nm}$, a SiC coating of 10 nm can be essentially opaque to nanoscale radiation [4].

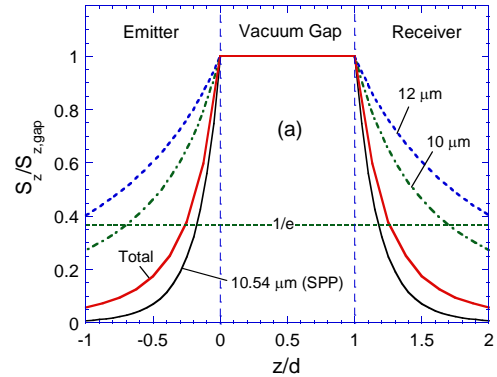


Figure 1: The (z -component) Poynting-vector distributions inside the vacuum gap and in the emitter and receiver near the interfaces [4].

We have fabricated Fabry-Perot resonance cavities and observed spatial and temporal coherence of thermal radiation using a Fourier-transform infrared (FTIR) spectrometer and a laser scatterometer [1]. The structures are composed of a SiO_2 optical cavity with a thin Au film ($< 30 \text{ nm}$) and a thick (200 nm) Au film deposited on a Si substrate, as shown in Fig. 2. Sharp dips were observed in the infrared reflectance spectra, while narrow angular lobes were observed in the angle-resolved measurement [1]. The results suggest strong spectral and directional selectivity in thermal emission. This structure has potential applications in solar cells, thermophotovoltaic devices, and radiation emitters.

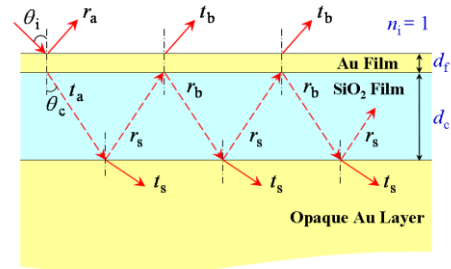


Figure 2: Schematic of a coherent thermal emission source made from asymmetric Fabry-Perot structures [1].

The determination of emissivity of layered structures is critical in many applications, such as radiation thermometry, microelectronics, radiative cooling, and energy harvesting. Two different approaches, i.e., the “indirect” and “direct” methods, are commonly used for computing the emissivity of an object. For an opaque surface at a uniform temperature, the indirect method involves calculating the spectral directional-hemispherical reflectance to deduce the spectral directional emissivity based on Kirchhoff’s law. On the other hand, a few studies have used a combination of Maxwell’s equations with the fluctuation-dissipation theorem to directly calculate the emissivity. We have attempted to unify the direct and indirect methods for calculating the far-field thermal emission from layered structures with a nonuniform temperature distribution. Formulations for both methods were given to illustrate the equivalence between the indirect and the direct methods [10]. The equivalence between the spectral directional emissivity and absorptivity of each layer can be viewed as the generalized Kirchhoff’s law. This allows the thermal emission from and the brightness temperature of a multilayered structure with a nonuniform temperature distribution to be evaluated using the indirect method. The local density of states, however, can only be calculated using the direct method. Thermal emission from an asymmetric Fabry-Perot resonance cavity with a nonuniform temperature distribution was taken as an example to show how to predict the intensity, emissivity, and brightness temperature.

We have designed and built a high-temperature emissivity measurement facility (emissometer), as shown in Fig. 3 (left). The sample was mounted in a heater stage that can be rotated to measure the thermal emission at different angles. An infrared polarizer can be inserted in the optical path to measure the emission for given polarization. A blackbody was used as the reference and a FTIR spectrometer collects the emission spectra. A DTGS detector can be used for higher temperatures (800 K) at longer wavelengths (up to $15 \mu\text{m}$). A liquid-nitrogen-cooled InSb detector can be used for intermediate temperatures in the spectral range from 2 to $5.5 \mu\text{m}$. The measured results for a Fabry-Perot structure are shown in Fig. 3 (right). In this figure, the emissivity at 300 K was obtained indirectly from the measured reflectance with the FTIR spectrometer using the Kirchhoff's law. Modeling and analysis of the emission spectra with the asymmetric Fabry-Perot structure is underway.

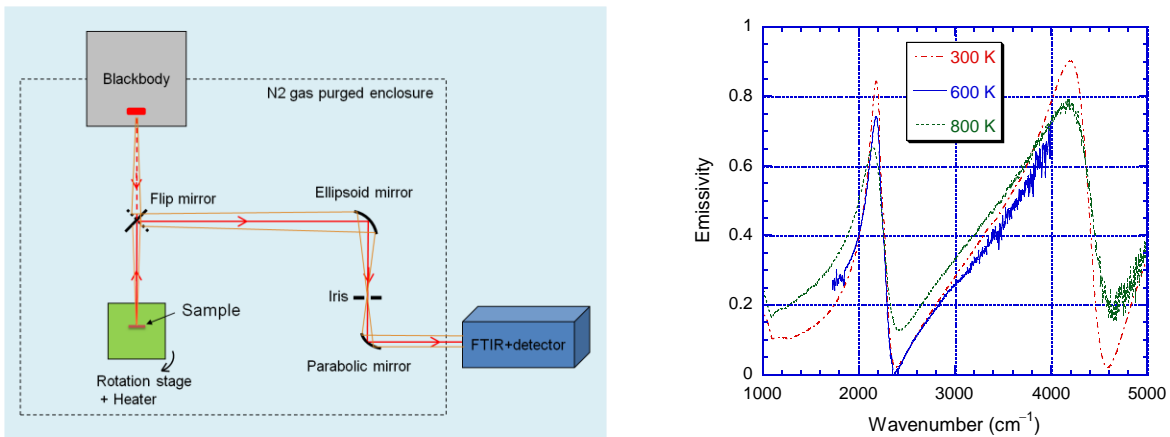


Figure 3: Schematic of the emissometer (left) and the measured spectra of a Fabry-Perot structure (right).

Future Plans

We will perform a fundamental investigation on nanoscale thermal radiation with a planar vacuum gap of large lateral extension using nanospacers. The proposed study aims at fabricating nanogaps as small as 20 nm over a 1 cm^2 area, using electron-beam lithography (EBL) and atomic layer deposition (ALD) techniques. Furthermore, the method will allow the creation of a thin heavily doped Si layer near the interface or a SiO_2 layer to study nanoscale radiative transfer between heavily doped Si surfaces as well as between SiO_2 surfaces. The nanogap structure will be placed in vacuum and the heat flux at temperatures near room temperature will be measured. The nanogaps will allow unambiguous experimental determination of radiative transfer above room temperature at distances as small as 20 nm.

Furthermore, a theoretical analysis will be performed by introducing the entropy concept into near-field thermal radiation in order to justify its consistency with the second law of thermodynamics.

This study will facilitate promising applications of nanoscale thermal radiation to energy conversion devices, such as TPV and effective laser cooling.

Selected Publications Supported by the DoE Contract

1. L.P. Wang, B.J. Lee, X.J. Wang, and Z.M. Zhang, "Spatial and Temporal Coherence of Thermal Radiation in Asymmetric Fabry-Perot Resonance Cavities," *Int. J. Heat Mass Transfer* **52**, 3024 (2009).
2. L.P. Wang and Z.M. Zhang, "Resonance Transmission or Absorption in Deep Gratings Explained by Magnetic Polaritons," *Appl. Phys. Lett.* **95**, 111904 (2009).
3. S. Basu and Z.M. Zhang, "Maximum Energy Transfer in Near-Field Thermal Radiation at Nanometer Distances," *J. Appl. Phys.* **105**, 093535 (2009).
4. S. Basu and Z.M. Zhang, "Ultrasmall Penetration Depth in Nanoscale Thermal Radiation," *Appl. Phys. Lett.* **95**, 133104 (2009).
5. S. Basu, Z.M. Zhang, and C.J. Fu, "Review of Near-Field Thermal Radiation and Its Application to Energy Conversion," *Int. J. Energy Research* **33**, 1203 (2009).
6. X.J. Wang, S. Basu, and Z.M. Zhang, "Parametric Optimization of Dielectric Functions for Maximizing Nanoscale Radiative Transfer," *J. Phys. D: Appl. Phys.* **42**, 245403 (2009).
7. S. Basu, B.J. Lee, and Z.M. Zhang, "Infrared Radiative Properties of Heavily Doped Silicon at Room Temperature," *J. Heat Transfer* **132**, 023301 (2010).
8. S. Basu, B.J. Lee, and Z.M. Zhang, "Near-Field Radiation Calculated with an Improved Dielectric Function Model for Doped Silicon," *J. Heat Transfer* **132**, 023302 (2010).
9. S. Basu, L.P. Wang, and Z.M. Zhang, "Direct Calculation of Energy Streamlines in Near-Field Thermal Radiation," *J. Quant. Spectrosc. & Radiative Transfer* (2011, in press).
10. L.P. Wang, S. Basu, and Z.M. Zhang, "Direct and Indirect Methods for Calculating Thermal Emission from Layered Structures with Nonuniform Temperatures," *J. Heat Transfer* (2011, accepted).

**Electric Field Effects in Liquid Crystals with Dielectric Dispersion
DE-FG02-06ER46331**

PI: Dr. Oleg D. Lavrentovich (olavrent@kent.edu)
Co-PI: Dr. Sergij V. Shiyanovskii (sshiano@kent.edu)
Chemical Physics Interdisciplinary Program, Liquid Crystal Institute
Kent State University, Kent, OH 44242-0001

Program scope

Liquid crystals (LCs) are anisotropic fluid dielectrics. When an external field is applied, the LC director, depicting average orientation of LC molecules, reorients and thus causes optical effects that are at the heart of numerous applications of LCs. In the widely accepted standard approach, the director dynamics is described assuming that the dielectric response is instantaneous, i.e., the electric displacement is determined by the electric field at the very same moment time. Such an approximation is limited, as it does not account for the effects of dielectric dispersion, i.e., the finite rate of the dielectric response. The long-term goal of this project is to develop physical understanding of the time-dependent dielectric response of LCs.

At the initial stage of the project, we developed a physical description of the time-dependent dielectric response of a simple uniaxial nematic LCs (NLC) such as those used in modern displays, in which the dielectric permittivity is a function of frequency [1]. We demonstrated that the correct physical description of the dielectric response of NLCs to the applied electric field should include the dependence of electric displacement not only on the present value of the field, but also on its past values and, importantly, on the past and present director orientations. The main accomplishment was the development of a theoretical model of uniaxial director dynamics in the applied electric field that takes into account the dielectric dispersion effect and detailed experimental verification of different aspects of the theory [1,2,3]. The current stage of research expanded to more complex issues, such as the discovered polarity-dependent dielectric torque in NLC [4,5], role of dielectric dispersion in field-induced phase transition [6], dielectric response of the LCs with the potentially biaxial nematic LC order [7,8] and, finally, exploration of AC electrokinetic phenomena associated with the dielectric anisotropy of LCs, using either “normal” thermotropic LCs formed by organic molecules [9,10], or assemblies of gold nanorods in dielectric fluids in which the dielectrophoretic forces create an orientationally ordered state with spatially varying properties such as dielectric permittivity and optical anisotropy [11,12].

Recent progress

(1) Polarity-dependent dielectric torque. We discovered a new type of dielectric response of a NLC, with a dielectric torque that is linear in the applied electric field $\mathbf{E}(t)$ and thus depends on the polarity of this field [4,5]. In the classic description of NLC, the dielectric torque scales as E^2 and is thus polarity-insensitive. The torque in our model exists due to the “memory” polarization: the dielectric torque $\mathbf{M}(t) = \mathbf{D}(t) \times \mathbf{E}(t)$ is proportional to one power of $\mathbf{E}(t)$ that is instantaneous and to another power of (past) electric field $\mathbf{E}(t')$ that depends on the prehistory. This unusual effect presents an important opportunity to actively accelerate the switching-off of LC cells [4,5]. When the applied voltage is switched off, the director reorients to its original state driven by surface anchoring at the bounding plates. The director reorientation is “passive” and relatively slow effect. However, if the electric polarization does not disappear instantaneously after the field is switched off, then one can apply a very short electric pulse, with

the duration of the order of the characteristic time of dielectric relaxation and accelerate the director reorientation [4,5].

(2) Effect of dielectric relaxation on the field induced isotropic-to-nematic transition. We study the dynamics of the isotropic-to-nematic phase transition caused by the applied electric field at the time scales of dielectric relaxation [6]. In the classic Landau-Khalatnikov theory of the phase transition dynamics, the nematic (non-polar) order parameter is an instantaneous function of the applied field. We demonstrate that when the field is changing faster than the time of dielectric relaxation, the induced polar order dynamics influences the dynamics of the non-polar order parameter. We develop a model based on the Langevin equations to describe the simultaneous dynamics of both polar $\bar{P}_1(t)$ and non-polar $\bar{P}_2(t)$ order parameters. The model is supported by the experiment [6].

(3) Dielectrically induced dynamics of NLC visualized by colloidal particles and their assembly. Dielectric response of the LC causes reorientation of molecular orientation. In its turn, the reorientation of the director causes a material flow. This effect, called a “backflow”, is of great importance in practical applications of LCs but is poorly understood because of the difficulty of experimental study of flows. We used colloidal particles added to the LC and studied their trajectories through an independently developed (with the NSF support) technique of 3D microscopy

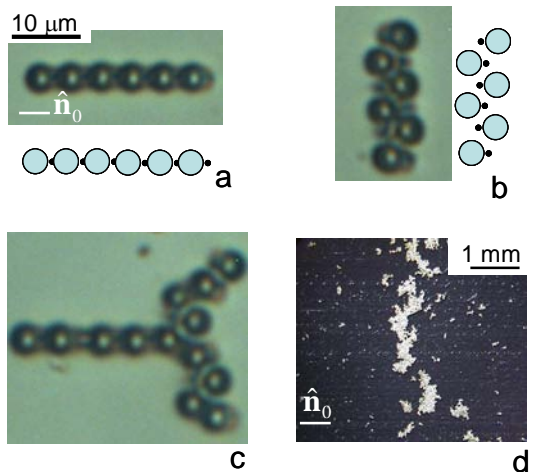


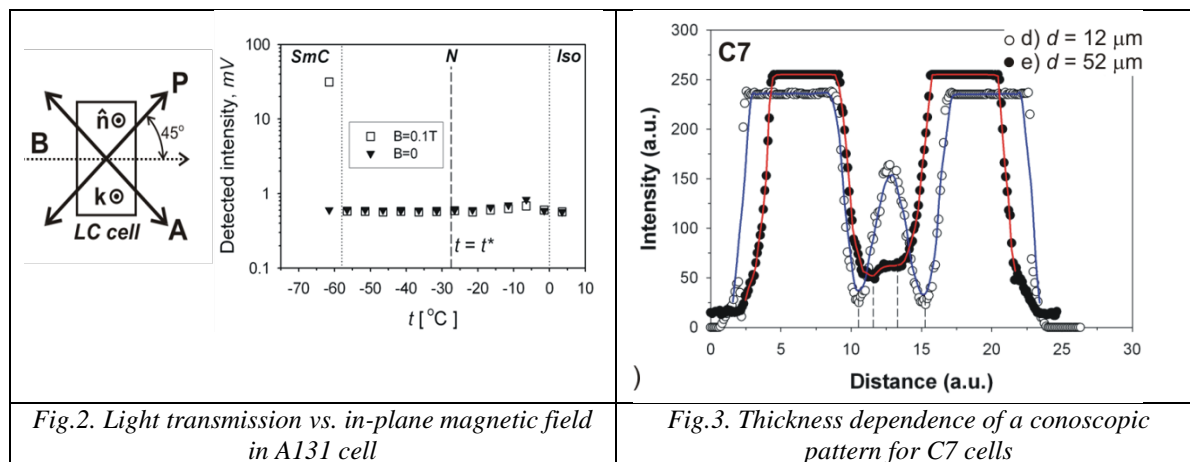
Fig. 1. Dielectric reorientation couples to the flow of the LC, as visualized by the dynamics of colloidal particles and their anisotropic aggregation [9,10].

of LCs. At the micron scales, the inertial effects are negligible and the particles are carried by the backflow, thus tracing the direction and velocity of the flow [10]. Furthermore, the dielectric-hydrodynamic coupling allowed us to develop a

“nematic collider” for controlled out-of-equilibrium anisotropic aggregation of spherical colloidal particles [10]. The nematic surrounding imparts dipolar interactions among the spheres. A bidirectional backflow of the LC in a periodic electric field forces the spheres to collide with each other [10]. The inelastic collisions are of two types, head-to-tail, Fig.1a, and head-to-head, Fig.1b. Head-to-tail collisions of dipoles result in longitudinal aggregation while head-to-head collisions promote aggregation in the transversal direction. The frequency of head-to-head collisions is set by the impact parameter that allows one to control the resulting shape of aggregates, their anisotropy and fractal dimension, Fig.1c,d.

(4) Experimental verifications of N_b order for bent-core molecules. We study dielectric and other properties of thermotropic nematic bent-core materials, namely, A131 with positive dielectric anisotropy [7], and C7 and C12 with negative dielectric anisotropy [8]. The focus is on the features associated with orientational order as the materials have been reported to exhibit not only the usual uniaxial nematic but also the biaxial nematic phase. All three materials show electrooptic response and structural feature typical for the uniaxial rather than biaxial nematic LCs. For example, in A131, the applied electric field causes director realignment along the field

with an establishment of the optically isotropic pattern for polarized light that propagates along the direction of the applied field. In C7 and C12, small splitting of isogyres in conoscopic patterns that is typically associated with the structural biaxiality, is shown to depend on the cell thickness; the feature suggests that the material is a uniaxial LC with the surface orientation different from the bulk orientation. We found no evidence of the “polycrystalline” biaxial behavior in the cells placed in crossed electric and magnetic fields, Fig.2. The studied materials exhibit stable topological point defects (boojums and hedgehogs) and nonsingular “escaped” disclinations in the entire nematic temperature range pertinent only to the uniaxial order, Fig. 3.



Our conclusion is that A131, C7 and C12 feature only a uniaxial nematic phase and that the apparent biaxiality is caused by surface effects rather than by the bulk biaxial phase.

(5) Dielectrophoretic response of dispersions of metal nanorods. Dielectric dispersion is a widely spread phenomenon that is actively used in AC electrokinetics, i.e., in the electrically-controlled motion of colloids and nanoparticles. The motion of particles is typically caused by the electrophoretic force that emerges in a non-uniform electric field. The gradient electric field is typically created by non-planar electrodes. We explore whether the effect can lead to the formation of orientationally ordered structure with spatially varying physical properties such as refractive index. We used dispersions of gold nanorods in toluene. The initial volume fraction of nanorods was only about 0.1%, too low for a formation of any ordered structure. By placing the dispersion in a strongly divergent electric field created by coaxial wire and cylindrical electrode, we demonstrated a strong condensing effect that manifested itself in a formation of orientationally ordered nematic formed by nanorods with the field-induced anisotropy of the refractive index on the order of 0.1. The finding paves the way for new approaches in manufacturing switchable metamaterials for transformation optics applications. Our research on dielectric-hydrodynamic coupling in a LC lead to a natural extension [9,10] of the concept to the case when the electric field becomes inhomogeneous not because of the curved geometry of electrodes, but because of the realignment of the director field. Director reorientation means a variable dielectric permittivity and a corresponding dielectrophoretic force that acts on the particles to move them into the regions with the lowest permittivity, to reduce the dielectric energy. According to the theoretical estimates, the particles can be transported within a LC even if the electric field is applied with flat parallel electrodes [9, 10].

Future plans.

Our studies will be focused on the electric field effects in LCs with dielectric dispersion, including materials with lower symmetry of orientational order. Whether they exhibit the biaxial nematic phase or not, their coupling to the electric field should be very different as compared to rod-like molecules such as the classic rod-like nematic material 5CB. The work will consist in both theoretical and experimental studies of the spontaneously and field-induced broken symmetries. We will further explore the dielectrophoretic effect caused by non-uniform properties of a distorted LC, in particular, a case when the dielectric anisotropy changes its sign as a function of the field frequency. The longer-term goal of the investigations is to come as closely as possible to the complete understanding of anisotropic soft media and their interaction with the electric field.

List of publications:

1. S. V. Shiyankovskii and O. D. Lavrentovich, "Dielectric relaxation and memory effects in nematic liquid crystals", *Liquid Crystals* **37**, 737-745 (2010).
2. O. D. Lavrentovich, H. A. Wonderly, M. Gu, and S. V. Shiyankovskii, "Electro-optical effects in liquid crystals with dielectric dispersion", *Proc. SPIE* **7050**, 70500S (2008).
3. O. D. Lavrentovich, H. A. Wonderly, M. Gu, and S. V. Shiyankovskii, "Effects of dielectric relaxation in electrooptics of nematic cells", *Proc. SPIE* **7232**, 723206 (2009).
4. M. Gu, S. V. Shiyankovskii, and O. D. Lavrentovich, "Polarity-dependent dielectric torque in nematic liquid crystals", *Phys. Rev. Lett.* **100**, 237801 (2008).
5. S. V. Shiyankovskii, M. Gu, and O. D. Lavrentovich, "Polarity-dependent dielectric torque in dispersive nematic liquid crystals", Patent Application 61/035,938, filed on March 12, 2008.
6. M. Gu, S. V. Shiyankovskii, and O. D. Lavrentovich, "Polar and nonpolar orderings in the electrically induced isotropic-nematic phase transition", *Phys. Rev. E* **78**, 040702(R) (2008).
7. B. Senyuk, H. Wonderly, M. Mathews, Q. Li., S. V. Shiyankovskii, O. D. Lavrentovich "Surface alignment, anchoring transitions, optical properties, and topological defects in the nematic phase of thermotropic bent-core liquid crystal A131" *Phys. Rev. E* **82**, 041711 (2010).
8. B. Senyuk, Y.-K. Kim, L. Tortora, S.-T. Shin, S. V. Shiyankovskii, O. D. Lavrentovich "Surface alignment, anchoring transitions, optical properties, and topological defects in nematic bent-core materials C7 and C12" *Mol. Cryst. Liq. Cryst.*, accepted (2011).
9. O. P. Pishnyak, S. Tang, J. R. Kelly, S. V. Shiyankovskii, O. D. Lavrentovich, "Electrically induced dynamics of colloidal particles in nematic liquid crystal", *Ukr. J. Phys.* **54**, 101-108 (2009).
10. O. P. Pishnyak, S. V. Shiyankovskii, O. D. Lavrentovich, "Inelastic collisions and anisotropic aggregation of particles in a nematic collider driven by backflow", *Phys. Rev. Lett.* **106** accepted (2011).
11. A.B. Golovin, O.D. Lavrentovich, Electrically reconfigurable optical metamaterial based on colloidal dispersion of metal nano-rods in dielectric fluids, *Appl. Phys. Lett.* **95**, 254104, 3 pages (2009).
12. A.B. Golovin, J. Xiang, Y.A. Nastishin, O.D. Lavrentovich, Electrically reconfigurable optical metamaterials based on orientationally ordered dispersions of metal nano-rods in dielectric fluids, *Proc. SPIE* **7775**, 777502, 14 pages (2010).

Program Title: Characterization of High Density/High Stability Glasses

Principal Investigator: Mark Ediger (PI), Kevin Dawson, Zahra Fakhraai, Shakeel Dalal

Mail address: Department of Chemistry, University of Wisconsin-Madison,

1101 University Avenue, Madison, WI 63706

E-mail: ediger@chem.wisc.edu

Program Scope: We have recently discovered that organic glasses with high density, low enthalpy, and extraordinarily high kinetic stability can be prepared by physical vapor deposition.¹ Prior to our recent work, these high density/high stability glasses would have been considered to be “impossible materials” in that one would have to age an ordinary glass for thousands of years or more to achieve similar properties. In order to reveal the full potential of these stable vapor-deposited glasses for a variety of applications, and to answer fundamental questions about the amorphous state, we are working to achieve the following objectives: 1) Prepare stable glasses via vapor deposition from a wide range of materials. 2) Characterize the local packing in stable organic glasses using wide-angle x-ray scattering (WAXS). 3) Measure density changes of stable glasses during thermal cycling with spectroscopic ellipsometry. 4) Compare vapor uptake of stable and ordinary glasses. 5) Prepare the most stable glasses ever prepared in a laboratory by utilizing considerably lower deposition rates.

Recent Progress: *Stable glasses have been prepared from a wide variety of materials.* We have successfully prepared stable glasses from all four isomers in the trisnaphthylbenzene (TNB) family: α,α,α -TNB, α,α,β -TNB, α,β,β -TNB, and β,β,β -TNB.² In addition to our work, other groups reported evidence for stable glass formation in new systems bringing the total number of known stable glassformers to 12.³⁻⁵ Given that stable glass formation occurs for systems with drastically different glass transitions and glassforming ability, we conclude that stable glass formation is a reasonably general phenomenon produced by the vapor deposition process when the correct deposition conditions are utilized.

Figure 1 shows differential scanning calorimetry (DSC) results for the four TNB isomers deposited at $0.85 T_g$ and at a rate of 2 \AA/s , along with the results for the ordinary glasses prepared by cooling the supercooled liquid. With these conditions, surface mobility allows efficient configurational sampling during the deposition process. All four molecules show the very large enthalpy overshoot characteristic of stable glass formation; in comparison, the C_p step of the ordinary glass at T_g is barely visible. The mobility onset temperature exceeds the T_g of the ordinary glass by about 30 K for each isomer. Surprisingly, even β,β,β -TNB, which is not a good glassformer, forms a minimally crystalline stable glass under these conditions. The stable glass of α,β,β -TNB shows no signs of crystallization after transformation to the supercooled liquid ($T_m = 421$). This is the first stable glass system that we have investigated that contains no crystal nuclei in the as-deposited sample. This makes α,β,β -TNB ideal for experiments involving long annealing times where crystallization becomes an experimental concern. We are also investigating the TNB

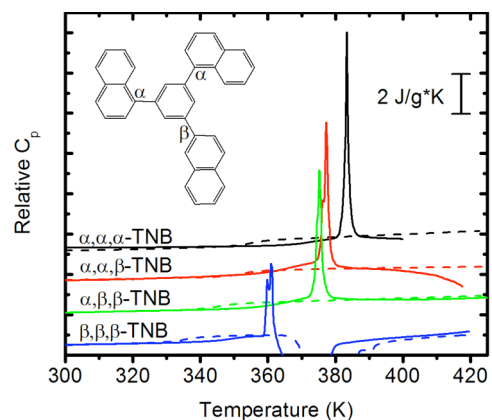


Figure 1. DSC curves for stable (solid) and ordinary (dashed) TNB glasses.

isomers using wide-angle x-ray scattering, x-ray reflectivity, ellipsometry, and quasi-elastic neutron scattering. All these experiments show evidence of stable glass formation.

WAXS finds anisotropy in vapor-deposited glasses. Since first reporting the unusual one-dimensional wide-angle x-ray scattering (1D WAXS) patterns of stable glasses,⁶ we have implemented more sophisticated two-dimensional WAXS experiments.⁷ While the 1D WAXS gave evidence of a new peak for stable glasses, the new experiments shows that this peak results from periodic modulation in the electron density normal to the film surface; the period of this modulation is roughly the 1 nm center-of-mass spacing between vapor-deposited molecules.

Figure 2 shows a 2D WAXS pattern taken in reflection geometry for an indomethacin (IMC) sample vapor-deposited at $0.85 T_g$ and 2 \AA/s . Two areas of high x-ray scattering (yellow regions) are observed and the q position of these areas are indicated by the white circles. While the scattering at high q is isotropic (the sample partially blocks the detector resulting in only a semi-circle), the scattering at low q is clearly a spot and represents anisotropy in the sample. The position of the spot indicates that the orientation is directed perpendicular to the substrate surface and may represent a tendency toward layering at the molecular level.

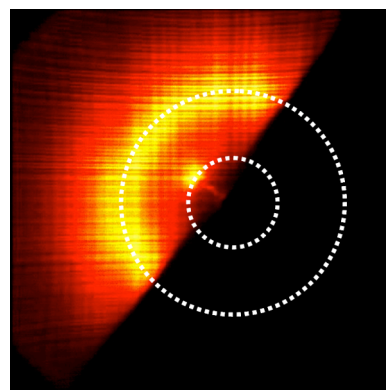


Figure 2. 2D WAXS for a stable glass sample of IMC.

Spectral ellipsometry reveals high density and birefringence of vapor-deposited glasses. Spectroscopic ellipsometry has been performed on vapor-deposited organic glasses prepared at a range of substrate temperatures. Figure 3 shows the thickness of α,α,β -trisnaphthyl benzene glass during temperature ramping in the manner of a dilatometry measurement. This method allows determination of the density of the as-deposited glass relative to the ordinary glass, the onset temperature, the fictive temperature, T_g , and the thermal expansion coefficients. Relative to the ordinary glass, this sample deposited at $0.85 T_g$ is 1% more dense, shows a decrease in the fictive temperature of 27 K, and has an increase in the onset temperature of 22 K; for comparison, these latter two quantities change only 5 K after aging an ordinary glass for 4 months.

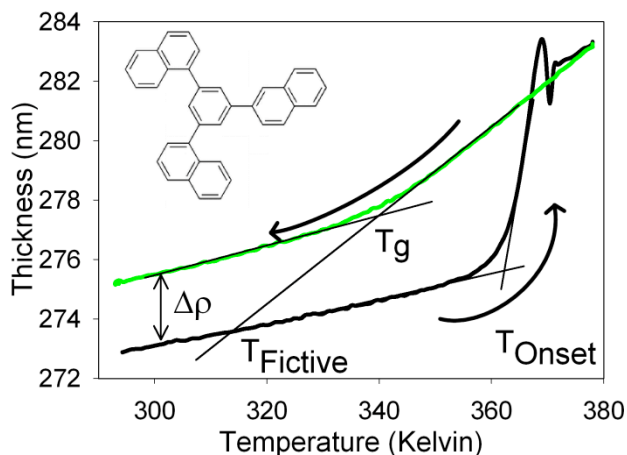


Figure 3. Spectral ellipsometry measurement of a vapor-deposited glass of α,α,β -trisnaphthyl benzene during a temperature cycle.

While the experiments above are insightful, many individual depositions must be performed to understand how the substrate temperature influences the properties of the vapor-deposited glass. We have developed a linear temperature gradient stage (80 K range) as an efficient means to quickly investigate the properties of many different glasses.⁸ Figure 4 illustrates the use of the

temperature gradient stage with spectral ellipsometry to measure the density of many vapor-deposited glasses of indomethacin. For IMC, the most dense glasses are prepared at substrate temperatures near $0.9 T_g$ while depositions at $0.6 T_g$ produce glasses that are less dense than the ordinary glass. For these measurements, ellipsometry was used to measure the sample thickness before and after annealing; several 80 K temperature ranges were overlapped to acquire the data shown in Figure 4.

We have utilized the temperature gradient stage to investigate the optical properties of an organic semiconductor often vapor-deposited in OLED fabrication: N,N'-bis(3-methylphenyl)-N,N'-diphenylbenzidine (TPD). Figure 5 shows the optical birefringence measured by spectral ellipsometry for samples deposited over a broad range of substrate temperatures. The inset shows the orientation of the coordinate axes relative to the substrate. Birefringence measurements establish that vapor-deposited glasses can be spatially anisotropic and thus may have improved stacking of π -systems for molecules such as TPD. Control of such local structure may provide an opportunity to increase the conductivity of organic semiconductors by as much as two orders of magnitude.⁹

Mechanical moduli depend significantly upon substrate temperature during deposition. Although we did not originally propose to measure the moduli of vapor-deposited glasses, we have added this component to our program because of the importance of this quantity for many applications. Brillouin light scattering (BLS) has been used in conjunction with the temperature gradient stage to obtain the moduli of vapor-deposited glasses of indomethacin over a wide range of substrate temperature. Figure 6 shows that the modulus can be controlled over a 30% range in this manner. The highest moduli glasses are obtained from depositions near $0.7 T_g$. Low substrate temperatures gave rise to a range of different results as illustrated in the

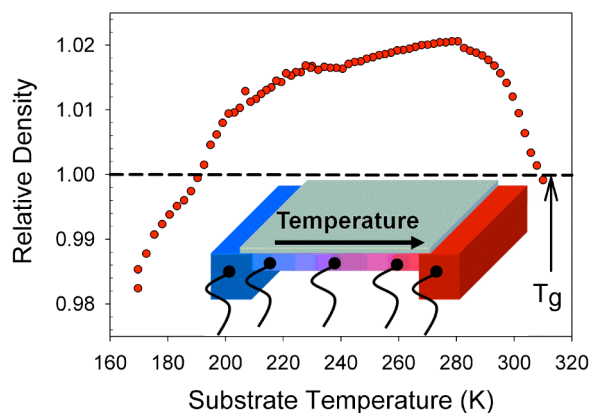


Figure 4. Density of vapor-deposited IMC glasses as a function of substrate temperature during deposition.

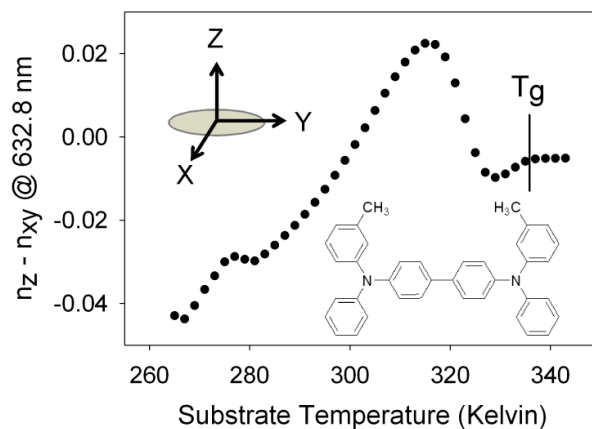


Figure 5. Birefringence of TPD as a function of substrate temperature during deposition.

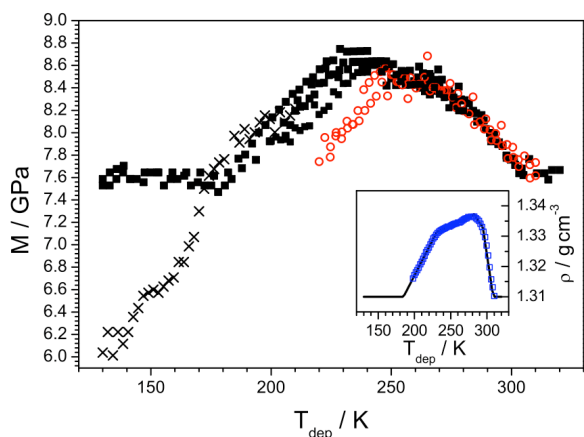


Figure 6. Room-temperature longitudinal modulus of vapor-deposited IMC glasses as a function of substrate temperature, as measured by BLS.

figure. Black symbols illustrate results from depositions at 2 Å/s while red symbols represent depositions at ~ 20 Å/s. As expected, lower deposition rates result in better packing and higher moduli, except near T_g .

Future Plans: In the remaining 19 months of our project, we have these priorities: 1) Complete a coordinated sets of measurements on the 4 TNB isomers. 2) Additional refinement of ellipsometric measurements with direct checks against x-ray reflectivity. 3) Understand the influence of the substrate on the properties of submicron stable glasses. 4) Integrate anisotropy information from WAXS and birefringence to obtain molecular view of packing. 5) Use lower deposition rates to try to produce even more stable glasses. 6) Monitor vapor uptake of stable glasses using ellipsometry.

References:

- (1) Swallen, S. F.; Kearns, K. L.; Mapes, M. K.; Kim, Y. S.; McMahon, R. J.; Ediger, M. D.; Wu, T.; Yu, L.; Satija, S. *Science* **2007**, *315*, 353.
- (2) Whitaker, C. M.; McMahon, R. J. *J. Phys. Chem.* **1996**, *100*, 1081.
- (3) Zhu, L.; Yu, L. *Chem. Phys. Lett.* **2010**, *499*, 62.
- (4) Ishii, K.; Nakayama, H.; Moriyama, R.; Yokoyama, Y. *Bull. Chem. Soc. Jpn.* **2009**, *82*, 1240.
- (5) Leon-Gutierrez, E.; Sepulveda, A.; Garcia, G.; Clavaguera-Mora, M. T.; Rodriguez-Viejo, J. *Phys. Chem. Chem. Phys.* **2010**, *12*, 14693.
- (6) Dawson, K. J.; Kearns, K. L.; Yu, L.; Steffen, W.; Ediger, M. D. *Proc. Natl. Acad. Sci. U. S. A.* **2009**, *106*, 15165.
- (7) Dawson, K. J.; Zhu, L.; Yu, L.; Ediger, M. D. *J. Phys. Chem. B*, *accepted*.
- (8) Fakhraai, Z.; Still, T.; Fytas, G.; Ediger, M. D. *Journal of Physical Chemistry Letters*, *submitted*.
- (9) Lee, S. S.; Loo, Y. L. Structural Complexities in the Active Layers of Organic Electronics. In *Annual Review of Chemical and Biomolecular Engineering, Vol 1*, 2010; Vol. 1; pp 59.

DOE-sponsored Research Publications:

- (1) Dawson, K. J.; Zhu, L.; Yu, L.; Ediger, M. D. *J. Phys. Chem. B*, *accepted*.
- (2) Fakhraai, Z.; Still, T.; Fytas, G.; Ediger, M. D. *Journal of Physical Chemistry Letters*, *submitted*.

Program Title: Bridging Atomistic and Continuum Scales in Phase-Field Modeling of Stressed Polycrystalline Materials

Principal Investigator: Alain Karma

Address: Department of Physics and Center for Interdisciplinary Research on Complex Systems, Northeastern University, 360 Huntington Avenue, Boston, Massachusetts 02115

Email: a.karma@neu.edu

Program Scope

This research seeks to develop state-of-the-art and scale-bridging phase-field methodologies to understand the physical behavior of stressed polycrystalline materials at high homologous temperature. It focuses on elucidating both equilibrium structures of hot grain boundaries (GBs) and fundamental mechanisms of stress-driven GB motion in the high-dimensional parameter space of GB bicrystallography and in the presence of interfacial defects, including: (i) nanometer thin intergranular liquid films that reduce shear resistance and can lead to hot tearing during the late stages of solidification—a casting defect widely impacting the automotive and aerospace industries—and (ii) liquid inclusions that are common defects in several metals (e.g., Pb in Cu and Ni) and sintering of ceramics and lead to stress concentration and failure. This research takes advantage of the unprecedented opportunity to tackle those complex phenomena based on a wealth of new observations from in situ imaging studies of internal material interfaces together with recent advances in atomistic and continuum simulations. Through a collaborative effort, conventional phase-field (PF) and phase-field-crystal (PFC) simulations are carried out jointly with molecular dynamics (MD) simulations in order to bridge quantitatively atomistic and continuum length and time scales. Multiscale modeling is expected to contribute new scientific understanding of interfacial processes relevant for the improved performance, design, and safety of advanced structural and electronic materials for diverse energy-related applications.

Recent progress

Quantitative computation of structural disjoining forces. The atomic structure of a GB can exhibit pronounced disorder at high homologous temperatures. This structural disorder commonly involves the formation of nanometer-scale intergranular films with liquid-like properties below the bulk melting point, a phenomenon commonly referred to as GB premelting. In collaboration with Mark Asta and co-workers, we have developed a novel methodology applicable to both MD and PFC simulations to characterize for the first time quantitatively disjoining forces that hinder crystal cohesion at high homologous temperature and drive GB premelting. The application of this method shows that repulsive structural disjoining forces for high angle GBs are at least an order of magnitude larger than dispersion forces, thereby demonstrating unambiguously the existence of GB premelting in pure metallic systems. Computations focused on extracting the disjoining potential $V(w)$ defined through the expression for the total GB excess free-energy where $-dV(w)/dw$ is a direct quantitative measure of the “thermodynamic driving force” that produces a net attraction or repulsion between crystal-melt interfaces depending on whether the slope of the disjoining potential is positive or negative, respectively. The accurate computation of the disjoining potential $V(w)$ is a non-trivial challenge for both PFC and MD simulations owing to the

small magnitude of disjoining forces and the presence of strong thermal fluctuations of liquid layer width at high homologous temperature. In both PFC and MD simulations, we exploited the fact that the layer width exhibits large fluctuations governed by a Boltzmann distribution

$$P(w, T) \sim \exp\left[-\frac{A\Delta G(w, T)}{k_B T}\right]$$

where A and $\Delta G(w, T)$ are the GB area and excess free-energy, respectively. By monitoring the width fluctuations, it is therefore possible to extract $\Delta G(w, T)$ and hence the disjoining potential from width histograms in the spirit of umbrella sampling (Hoyt et al. 2009, Fensin et al. 2010). The results of this method are illustrated in **Fig. 1** for a high angle symmetric tilt GB in bcc Fe that exhibits premelting, characterized by a repulsive disjoining potential and a log divergence of the liquid layer width at the melting point. Importantly, the magnitude of the disjoining potential, which is characterized for the first time using this approach, is of the order of tens of mJ/m^2 and hence at least an order of magnitude larger than estimates of attractive dispersion forces based on theoretical computations of the Hamaker constant.

GB premelting condition. The ability to predict when GB premelting occurs within the high-dimensional parameter space of grain boundary bicrystallography is important for modeling the mechanical response of polycrystals at high homologous temperature. GBs that premelt can slide and concentrate stresses at grain junctions, in turn causing cracking. Premelting should in principle occur when $\gamma_{gb} > 2\gamma_{sl}$, implying that an intergranular liquid-like layer becomes energetically favored when the GB energy γ_{gb} exceeds twice the solid-liquid interfacial energy, γ_{sl} . Application of this condition is made difficult by the fact that γ_{gb} is generally not known at the melting point. To circumvent this limitation, we have recently proposed a criterion to predict premelting that takes into account the elastic softening of the material at high homologous temperature (Mellenthin et al. 2008 and Olmsted et al. 2011). MD simulations show that this

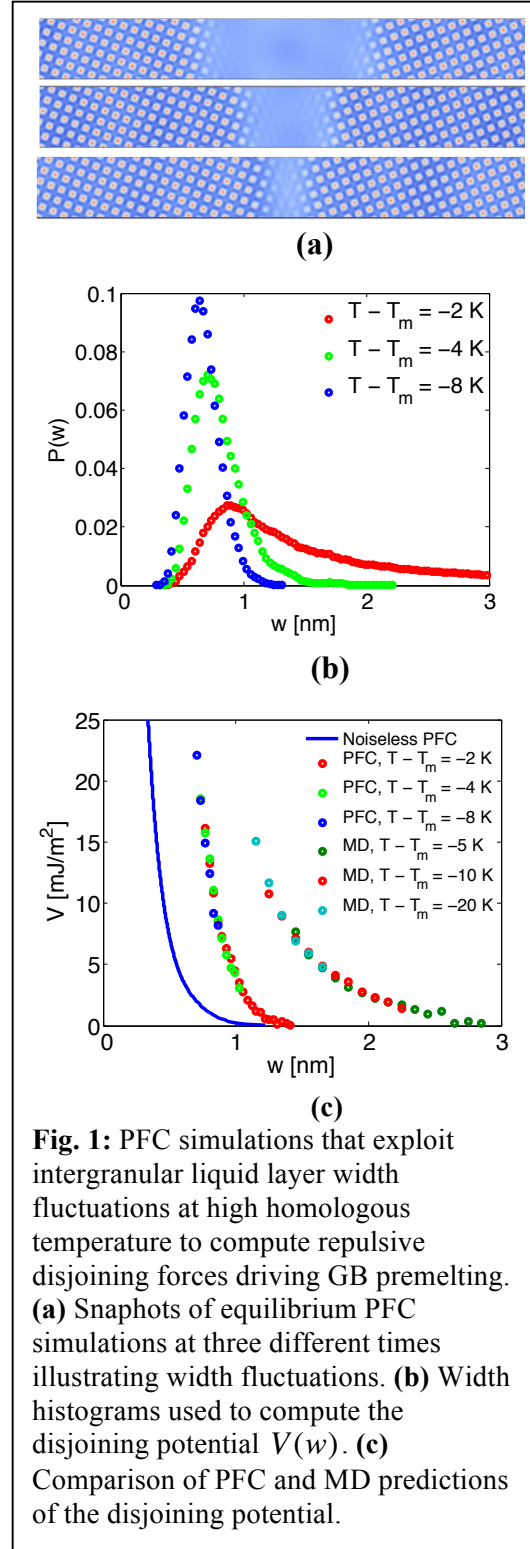


Fig. 1: PFC simulations that exploit intergranular liquid layer width fluctuations at high homologous temperature to compute repulsive disjoining forces driving GB premelting. **(a)** Snapshots of equilibrium PFC simulations at three different times illustrating width fluctuations. **(b)** Width histograms used to compute the disjoining potential $V(w)$. **(c)** Comparison of PFC and MD predictions of the disjoining potential.

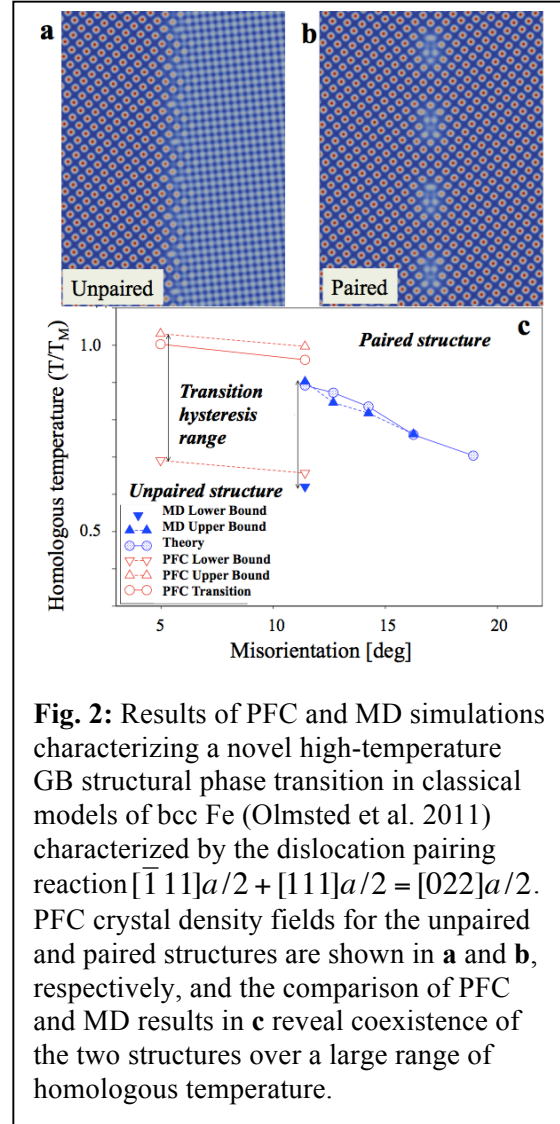
criterion is a reasonably good predictor of premelting for symmetric tilt boundaries in bcc Fe (Olmsted et al. 2011) as well as for several GBs in fcc Ni.

Novel high-temperature GB structural phase transitions. Our PFC simulations and MD simulations carried out by Asta and co-workers have revealed the existence of novel GB structural transition at high homologous temperatures characterized by the “pairing” of dislocations with mixed screw and edge character (Olmsted et al. 2011) as illustrated in **Fig. 2**. An important aspect of this transition is that it delays premelting to higher misorientation angles and is thus potentially significant. For example, the solid-bridges that are present in the paired state should lead to enhanced strength to higher homologous temperatures. We have also developed a simple theory of pairing in the framework of the Read-Shockley law for the GB energy and concluded that it can be driven by a reduction in elastic energy and/or increased atomic disordering within dislocation cores.

Stress-effects on intergranular voids and liquid inclusions. We have developed and used a volume-conserving multi-phase-field approach to investigate stress-effects on the equilibrium shapes of intergranular voids and liquid metal inclusions in a metal matrix. Results in **Fig. 3** show that the void flattens to release the applied stress. This is seen plotting the aspect ratio $c=b/a$ of the elliptical cross-section of the void as a function of the dimensionless parameter $\Lambda = \sigma_{ext}^2 V^{1/d} / (\gamma_{sl} E)$, which is a dimensionless measure of the ratio of strain and interfacial energies, where σ_{ext} is the externally applied stress, V is the volume of the inclusion (with d the dimension), and E is Young’s modulus. Our results reproduce the existence of a *bifurcation* associated with the disappearance of equilibrium shapes above a critical value of $\Lambda \equiv \Lambda_c$, corresponding to a threshold stress for fracture beyond which the void flattens indefinitely. In contrast, the liquid inclusion shape is insensitive to applied stress in agreement with theoretical expectation.

Future Plan

Our future studies will concentrate in three areas. Firstly, we will extend our studies of GB structures at high homologous temperature to binary alloys using a recently developed model that describes quantitatively the interaction between composition and stress (Spatschek and



Karma, 2010). A main focus will be to understand how and predict when solute addition extends premelting to substantially lower temperature below the liquidus temperature. Second, we will carry out a combined MD and PFC simulation investigation of stress-driven GB motion in collaboration with Yuri Mishin's group funded in the same Physical Behavior's program to elucidate fundamental mechanisms of GB coupled motion and sliding as a function of temperature and GB bicrystallography. Thirdly, we plan to extend our multi-phase-field investigation of stress-effect on intergranular liquid inclusions to test the hypothesis that small voids created by vacancy accumulation at triple junctions under tensile stress can dramatically alter the shape of liquid inclusions as experimentally observed, with a similar shape bifurcation as for voids.

References to DOE sponsored publications (2008-2010)

1. Phase-field crystal study of grain-boundary premelting, J. Mellenthin, A. Karma, and M. Plapp, *Phys. Rev. B* **78**, 184110 (2008).
2. Method for computing short-range forces between solid-liquid interfaces driving grain boundary premelting, J. J. Hoyt, D. Olmsted, S. Jindal, M. Asta, and A. Karma, *Phys. Rev. E* **79**, 020601 (2009).
3. Solidification microstructures and solid-state parallels: Recent developments, future directions, M. Asta, C. Beckermann, A. Karma, W. Kurz, R. Napolitano, M. Plapp, G. Purdy, M. Rappaz, and R. Trivedi, *Acta Materialia* **57**, 941–971 (2009).
4. Laws of crack motion and phase-field models of fracture, V. Hakim and A. Karma, *J. Mech. Phys. Solids* **57**, 342-368 (2009).
5. Phase-field crystal model for fcc ordering, K.-A. Wu, A. Adland, and A. Karma, *Phys. Rev. E* **81**, 061601 (2010).
6. Multi-phase-field analysis of short-range forces between diffuse interfaces, N. Wang, R. Spatschek, and A. Karma, *Phys. Rev. E* **81**, 051601 (2010).
7. Amplitude equations for polycrystalline materials with interaction between composition and stress, R. Spatschek and A. Karma, *Phys. Rev. B* **81**, 214201 (2010).
8. Structural disjoining potential for grain-boundary premelting and grain coalescence from molecular-dynamics simulations, S. J. Fensin, D. Olmsted, D. Buta, M. Asta, A. Karma, and J. J. Hoyt, *Phys. Rev. E* **81**, 031601 (2010).
9. Helical crack-front instability in mixed mode fracture, A. J. Pons and A. Karma, *Nature* **464**, 85-89 (2010).
10. Dislocation-Pairing Transitions in Hot Grain Boundaries, D. L. Olmsted, D. Buta, A. Adland, S. M. Foiles, M. Asta, and A. Karma, *Phys. Rev. Lett.* (in press 2011).

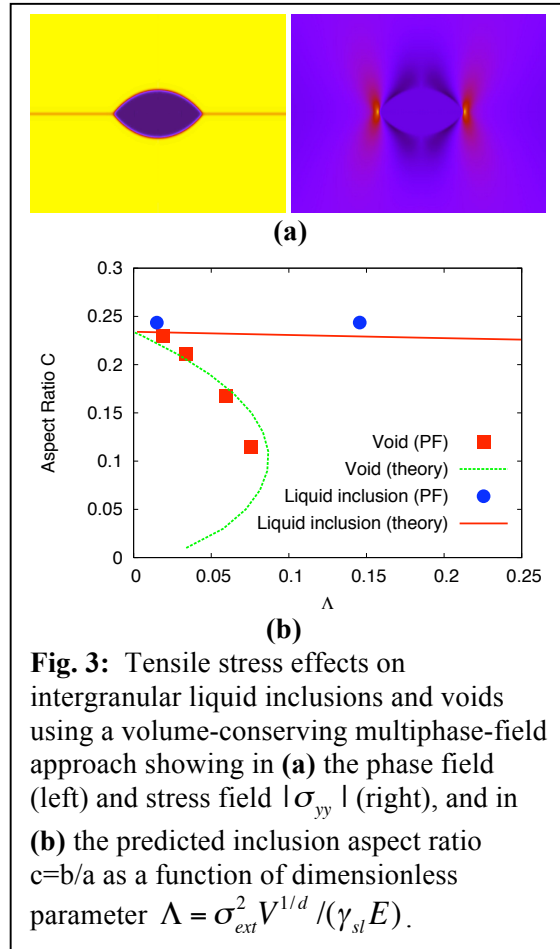


Fig. 3: Tensile stress effects on intergranular liquid inclusions and voids using a volume-conserving multiphase-field approach showing in (a) the phase field (left) and stress field $|\sigma_{yy}|$ (right), and in (b) the predicted inclusion aspect ratio $c=b/a$ as a function of dimensionless parameter $\Lambda = \sigma_{ext}^2 V^{1/d} / (\gamma_{sl} E)$.

Session VII

*Photovoltaics–
Solar Energy,
Photonic Crystals,
Nanophosphors*

Optical Metamaterial Physics and Applications

PI: Xiang Zhang; Co-PI: Eli Yablonovitch, Yuen-Ron Shen, Feng Wang

Materials Science Division
Lawrence Berkeley National Laboratory and
University of California, Berkeley

Abstract

Metamaterials enable the realization of novel physical properties that are unattainable from natural materials. The metamaterials have shown unprecedented characteristics such as negative index, super-lensing and optical magnetism, which promise to create entirely new prospects for manipulating the photon. This project sets to explore some new physical phenomena originating from the optical metamaterials. We believe that the fundamental discoveries from this project will have profound impacts on a wide range of applications in accord with DOE's strategic plans, such as fundamental understanding of light-matter interaction, imaging and solar energy conversion with high efficiency. The following outlines the research scope of the newly started DOE Metamaterials project.

We will investigate the physics of indefinite metamaterials and the dynamic characters of reconfigurable chiral metamaterials. The indefinite metamaterial consists of aligned metallic nanowires with deep subwavelength spacing, embedded in porous dielectric matrix in a self-organized hexagonal lattice. This new metamaterial can be characterized as an effective uniaxial medium with negative effective permittivity in the direction parallel to the nanowires, and positive permittivity perpendicular to the wires. This property results in a unique hyperbolic equifrequency contour (EFC), which gives rise not only to negative refraction, but also to anomalous diffraction. We aim at demonstrating the unique diffraction (propagation) features of EM waves in indefinite media, by directly mapping the phase front. For the fundamental studies of light-matter interaction, we will also explore reconfigurable chiral metamaterials whose chirality can be controlled dynamically by optical pumping. The characterization of the optically tunable metamaterials will be carried out with a time domain spectroscopy setup. The accomplishment of these tunable metamaterials would enable unprecedented control of the photons in a dynamic way.

We will also investigate the dispersion physics of metamaterials for far-field imaging of 2D objects with a broad-band performance. We will conduct theoretical and experimental studies of the metamaterial hyperlens and its frequency responses. By tuning the working wavelength from UV to visible, a new dispersion design will work for a broad-band performance. The material loss and fabrication constraints will be explored to improve the resolution of the hyperlens well below diffraction limit.

Light Trapping with Photonic Crystals

Sajeev John and Guillaume Demesy
Dept of Physics
University of Toronto
Toronto, Ontario, Canada

ABSTRACT

The earth receives solar radiation at levels of up to $\sim 1.7 \times 10^{17}$ W in the upper atmosphere whereas the rate of current worldwide energy consumption is about 10,000 times smaller, at $\sim 1.6 \times 10^{13}$ W. However, first generation solar cells currently used have poor solar-to-electricity conversion (or External Quantum Efficiency, EQE), around 10% of the incident solar power. These solar cells use relatively thick bulk silicon wafer. A second generation exists in which the semiconductor medium is textured into thin films with substantially reduced costs, but a much lower EQE due to lack of light trapping over a broad spectrum. For a third generation of photovoltaic cells, the requirement is to be both efficient in light absorption and use the least semi-conductor material as possible.

Silicon is advantageous for its (1) natural abundance, (2) absence of negative environmental, health or safety issue, (3) process knowledge driven by a highly competitive semiconductor industry and (4) compatible band gap centered near the peak emission of the solar emission spectrum. However, its band gap does not cover the entire solar spectrum between 350 and 2.5 μm . This represents a major issue for the use of silicon in photovoltaics. Existing silicon-based devices have poor quantum efficiency in the near infrared spectral region.

Earlier theoretical work [A. Chutinan and S. John., *Physical Review A* **78**, 023825 (2008)] showed that thin slab 3D photonic crystals were a promising way to harvest light even in weakly absorbing semiconductors (as silicon is in the near IR spectral region) due to their ability to trap and localize light. Many simple cubic 3D photonic crystal geometries exhibit the so-called “Parallel to Interface Refraction” effect enabling long dwell times for incoming light from a broad range of incident angles and a broad frequency range. Various architectures, using this principle, are under current investigation for use as broadband absorbers.

A parallel vector Finite Element code has been implemented on a dedicated high performance cluster to numerically model photonic crystal-based, ultra-thin, and efficient solar cells. This involves the rigorous calculation, in the frequency domain, of the diffraction of a plane wave of arbitrary angle of incidence and polarization on a 3D photonic crystal slab of arbitrary shape and constitutive material. From these accurate field maps, we obtain the quantities relevant to photovoltaics, such as Reflection, Transmission, and Optical Absorption taking place in different regions of device. Our method allows us to study materials with an arbitrary complex frequency-dependent dielectric function and to capture the role of metallic nano-inclusions (arising from electrodes or other deliberate embedding) and plasmonic resonances. As a diagnostic of our method, many results from previously published work on solar-cell light-trapping architectures have been accurately (and more efficiently) recaptured.

Other important numerical tools for the study of ultra-thin photonic crystal solar cells have been implemented such as the Plane Wave Expansion method and a modal Finite Element Method adapted to calculate of photonic bandstructures of infinitely periodic counterparts. The Cutting-Surface Method [O.Toader *et al.*, Physical Review E **70**, 046605 (2004)] has also been applied to evaluate the importance of the dispersion of the materials on the design. The FEM diffraction code was also adapted to the determination of an appropriate interference pattern for the experimental and large scale synthesis of the optimized cubic photonic crystals using phase mask lithography [T. Chan *et al.*, Physical Review E **73**, 046610 (2006)].

An extensive study has been carried out over various architectures of 3D cubic photonic crystal slabs (woodpiles, modulated cylindrical rods, modulated cylindrical holes...) and compared to previously published designs such as nanohole and nanowire arrays. A first simple cubic woodpile design has been provided to Prof. Shawn Lin for fabrication and characterization of the structures. This first experimental realization will test the ability of our models to capture reality and provide us feedback for improved modeling.

Our numerical results reveal significant improvement of the response in the near infrared region. In particular, modulated rods, comprising a 3D photonic crystal, reveal a significant improvement compared to the classical nanowires. Their topology remains compatible with a radial coaxial junctions [B. Tian *et al.*, Nature **449**, 885 (2007)].

Several antireflective mechanisms have been studied to couple as much of incident light into the main absorber. Two of them are very promising. The deposition of a quintic graded-index layer [J.Q. Xi *et al.*, Nature Photonics **176** (2007)] enhances the response of the solar cell. Another anti-reflective coating consists in the deposition or shaping, on top of a cubic photonic crystal slab, of a crossed grating made of nano-cones or pyramids. Both approaches lead to a broadband enhancement of the air-to-absorber coupling.

Back reflectors have also been considered to improve the confinement of light inside the absorber. Our numerical studies reveal that a bulk metallic (such as silver) layer is not a suitable back reflector given the existing light-trapping capability of our photonic crystal design. Even though the metal reflects some frequencies back into the engineered semiconductor absorber, it also leads to high Joule losses. Preliminary 2D studies show that a better solution consists in the use of another photonic crystal with large stop gap centered in a targeted spectral region.

Finally, a carrier transport model is being implemented in order to accurately take into account the charge collection process in these complex 3D micro-structured materials. Of particular interest is the embedding of electrodes throughout the interior of a 3D photonic crystal for hot-carrier collection.

Nanophotonics-enhanced solar cells

PI: Shanhui Fan, Department of Electrical Engineering, Stanford University, Stanford, CA 94305. Phone: 1-650-724-4759. Email: Shanhui@stanford.edu

Co-PI: Mark Brongersma, Department of Material Science and Engineering, Stanford University, Stanford, CA 94305. Email: brongersma@stanford.edu

Supported by: Department of Energy, Office of Basic Energy Sciences. Grant No. DE-FG-07ER46426

Program Manager: Dr. Refik Kortan.

1. Program Scope

The objectives of our research program are twofold. On the theory side, we aim to determine the fundamental upper limit in broadband (over the entire solar spectrum) absorption enhancements in thin semiconductor films. We will also propose nanophotonic structures that can reach this limit. On the experimental side, we will verify the theoretical predictions and identify practical high-performance light-trapping structures that can be fabricated using scalable synthesis techniques.

2. Recent Progress

We have made substantial progresses towards achieving our objective. On the theory front, we have established a rigorous electromagnetic theory of light trapping. This theory reproduces the conventional theory of light trapping, and moreover predicts structures in which one can significantly overcome the limitation of conventional light trapping through the use of nanophotonic structures. On the experimental front, we have established a rapid prototyping platform to study the fundamental physics of light trapping, based on well-established silicon-on-insulator (SOI) technology. Below, we discuss in some details the progress that we have made on both directions.

2.1. The theory for nanophotonic light trapping in solar cells

In solar cells, light trapping enables effective absorption of sunlight using an active material layer that is much thinner than the material's intrinsic absorption length. This then reduces the amount of materials used in PV cells, which cuts cell cost in general, and moreover facilitates mass production of PV cells that are based on less abundant materials. In addition, light trapping can improve cell efficiency, since thinner cells facilitate better collection of photo-generated charge carriers and an increased open-circuit voltage.

The theory of light trapping was initially developed for conventional cells where the light trapping film is typically many wavelengths thick. This theory, based on geometric optics, showed that for a cell with an isotropic response, the absorption enhancement factor has an upper limit of $4n^2$, where n is the refractive index of the semiconductor material. This theory has had strong influences for light management in solar cell designs. For silicon bulk cells, it is now possible to approach this limit with the use of pyramidally textured surfaces.

For nanophotonic structures with features comparable or even smaller than the wavelength of light, however, the assumptions in the conventional theory is no longer valid. Whether the conventional $4n^2$ limit still holds in nanophotonic structures therefore becomes a very important open question.

As a major progress supported by this DOE program, we have developed a rigorous theory of light trapping based on electromagnetics. Using this theory, we have re-derived the conventional limit. Our new theory shows that the conventional limit in fact applies even when the thickness of the film is minimized to single-wavelength scale, since the integrated density of state in such a system is comparable to the bulk. We have further shown that by reducing the thickness of the film to deep sub-wavelength scale, and by employing techniques that ensure deep subwavelength confinement in the film, one in fact can overcome the conventional limit of light trapping of solar cells by at least an order of magnitude, over a broad range of wavelengths and all angles (Figure 1). We believe such a theory will prove to be very important in fundamentally understand the design trade-off of nanophotonic light trapping in general.

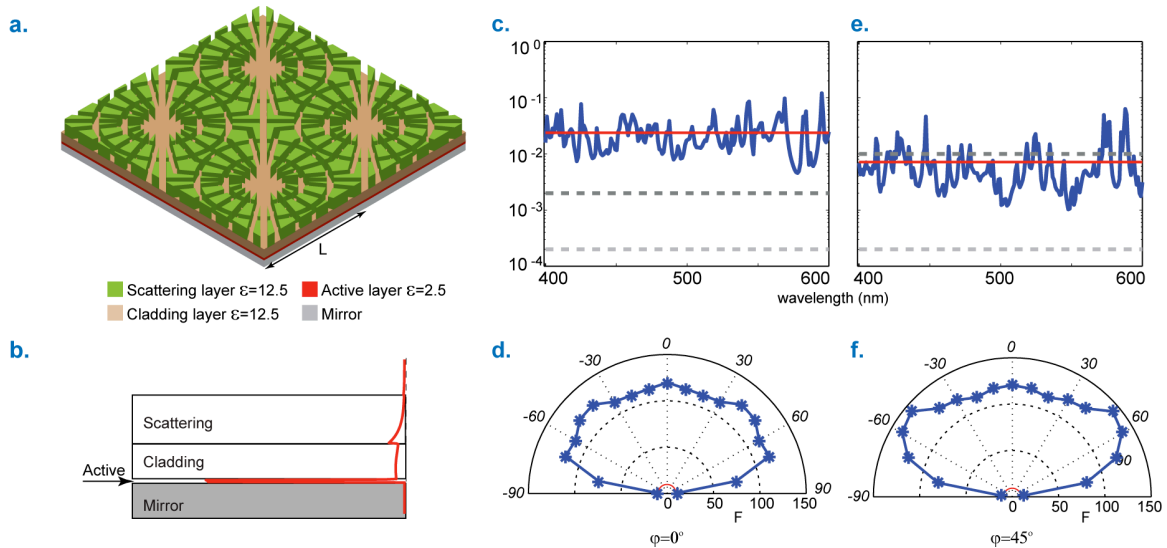


Figure 1. (a) A nanophotonic light-trapping structure. The scattering layer consists of a square lattice of air groove patterns with periodicity $L = 1200\text{nm}$. The thicknesses of the scattering, cladding, and active layers are 80nm , 60nm , and 5nm respectively. The mirror layer is a perfect electric conductor. (b) The profile of electric-field intensity for the fundamental waveguide mode. Fields are strongly confined in the active layer. (c) Absorption spectrum for normally incident light for the structure shown in (a). The spectrally-averaged absorption (red solid line) is much higher than both the single pass absorption (light gray dashed line) and the absorption as predicted by the conventional $4n^2$ limit (dark gray dashed line). (e) Absorption spectrum without light confinement. The structure is the same as that of a) except that the dielectric constant of the active layer is now the same as the cladding layer. The dark gray dashed line represents the absorption as predicted by the conventional $4n^2$ limit. (d, f) Angular dependence of the spectrally-averaged absorption enhancement factor for the structure in (a). Incident angles are labeled on top of the semi-circles. Incident planes are oriented at 0 (c) and 45 (d) degrees (azimuthal angles) with respect to the $[10]$ direction of the lattice. The red circles represent the conventional $4n^2$ limit.

2.2. A rapid prototyping platform to study the physics of light trapping

On the experimental side, in order to study the physics of light trapping, we have constructed a rapid prototyping platform based on well-established silicon-on-insulator (SOI) technology. The use of the SOI technology for our proposed fundamental light trapping studies has a number of advantages. First, our goal is to explore light trapping in (optically) thin semiconductor layers. SOI wafers can be obtained in a wide range of thicknesses ranging from a few tens of nanometer to a micron. Second, these wafers exhibit well-defined electrical and optical properties that are uniform over large areas (e.g. an entire 6" Si wafer). Third, the SOI structure constitutes a very simple model system as compared to a state-of-the-art solar cell, in which many geometrical and materials parameters determine the final performance. Fourth, the cost of readily available SOI wafers are low compared to the cost associated with realizing a completed state-of-the-art PV cell. Finally, the results from this study are very general and can be translated to a wide variety of solar cell designs and materials.

As a demonstration of our rapid prototype system, Figure 2 shows an example of a photolithography mask and scanning electron microscopy (SEM) images of test structures. Each mask consists of 100 dies per wafer and there will be ~ 150 devices per die. On each die we can generate different light trapping structures by e.g. focused ion beam milling, electron-beam lithography, or by chemical means. The left image in Figure 2 shows a mask of an individual device with the electrical contacts and a central metal pad ($100\ \mu\text{m} \times 100\ \mu\text{m}$) where the light trapping structure is located. The center image shows a realized device with a couple test structures with which we verified the successful operation of the devices. The right image shows an aperiodic metal grating that will be used to trap light into the thin Si layer of the SOI structures. Photocurrent measurements will be performed as a function of wavelength using an available white light source coupled to a monochromator. These measurements will enable us to assess the spectral dependence of the photocurrent enhancement.

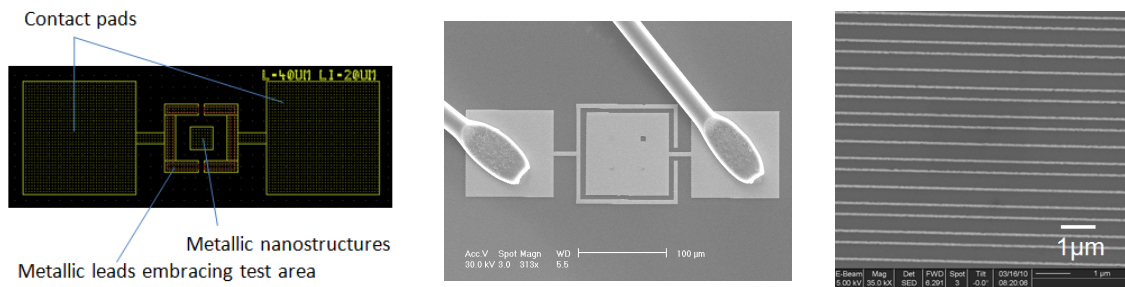


Figure 2. Left Image: Overview of the photolithography mask of a test structure with two metallic contact pads for current extraction that embrace a test area in which metallic metal nanostructure for light trapping can be defined. Middle Image: SEM image of an individual device showing two wire-bonded metallic leads that are connected to the large contact pads for easy current extraction. Right Image: SEM image of an aperiodic grating that was designed according to a Fibonacci sequence. It contains multiple periodicities that can effectively trap sunlight at multiple wavelengths and a wide range of angles.

3. Future Plans

Based upon the theoretical and experimental progress up to date, we have planned the future activities along the following directions: On the experimental side, the efforts are

on-going in demonstrating aperiodic plasmonic grating structures for light trapping purposes. An aperiodic grating should result in a broader range of operating wavelengths in light trapping compared with the periodic structures. On the theoretical side, we will continue to develop the theory for understanding light trapping in solar cells. In particular, we aim to apply our theoretical framework to calculate the fundamental limit of light trapping in plasmonic solar cells. In addition, while most of the theory of light trapping is developed for weak absorption, the ultimate goal of the theory will be to understand the possibility for enhancement over the entire spectral range, for both the weak and strongly absorbing regions. The theory and experiments will be closely coupled together, in order to understand some of the experimental data in our rapid prototyping platform, and in designing structures with better performance.

4. Publications 2008-2010

1. P. B. Catrysse and S. Fan, "Understanding the dispersion of coaxial plasmonic structures through a connection with the planar metal-insulator-metal geometry", *Applied Physics Letters* 94, 231111 (2009).
2. R. A. Pala, J. White, E. Barnard, J. Liu, and M. L. Brongersma, "Design of Plasmonic Thin-Film Solar Cells with Broadband Absorption Enhancements," *Advanced Materials* 21, 3504 (2009).
3. A. Raman and S. Fan, "Photonic band structure of dispersive meta-materials formulated as a Hermitian eigenvalue problem", *Physical Review Letters* 104, 087401 (2010).
4. J. Zhu, C. -M. Hsu, Z. Yu, S. Fan, and Y. Cui, "Nanodome solar cells with efficient light management and self-cleaning", *Nano Letters* 10, 1979 (2010).
5. S. B. Mallick, M. Agrawal and P. Peumans, "Optimal light trapping in ultra-thin photonic crystal crystalline silicon solar cells", *Optics Express* 18, 5691 (2010).
6. Z. Ruan and S. Fan, "Temporal coupled-mode theory for Fano resonance in light scattering by a single obstacle", *Journal of Physical Chemistry C*, 114, 7324 (2010).
7. Z. Ruan and S. Fan, "Super-scattering of light from sub-wavelength nano-structures", *Physical Review Letters* 105, 013901 (2010).
8. P. Catrysse and S. Fan, "Nano-patterned metallic films for use as transparent conductive electrodes in optoelectronic devices", *Nano Letters* 10, 2944 (2010).
9. Z. Yu, A. Raman, and S. Fan, "Fundamental limit of light trapping in grating structures", *Optics Express* 10, A366 (2010).
10. Z. Yu, A. Raman, and S. Fan, "Fundamental limit of nanophotonic light trapping in solar cells", *Proceedings of the National Academy of Sciences* 107, 17491 (2010).
11. Z. Yu and S. Fan, "Angular constraint on light-trapping absorption enhancement in solar cells", *Applied Physics Letters* 98, 011106 (2011).
12. Z. Ruan and S. Fan, "Design of subwavelength superscattering nanospheres", *Applied Physics Letters* (accepted).

Program Title: Nanocrystal-Based Dyads for Solar to Electric Energy Conversion

Principal Investigator: David Waldeck

Institution: University of Pittsburgh

Address: 219 Parkman Avenue, Pittsburgh PA 15260 USA

Email: dave@pitt.edu

Collaboration: D. N. Beratan, Duke University, and Ron Naaman, Weizmann Institute of Science.

Program Scope

We are exploring nanoparticle-based materials that promise to provide a systematic and modular approach to creating a new generation of solar energy conversion devices. The proposed device architecture is illustrated in Figure 1. The project team (comprised of researchers at U. Pittsburgh, Duke Univ., and the Weizmann Institute of Science) is working to develop a systematic and quantitative approach to creating supramolecular assemblies of linked nanoparticles that function as charge transfer elements. Because their synthesis and individual properties have been well studied, we have selected CdSe/CdTe as the bandgap-staggered (Type II) nanoparticle composites that we would explore first. Although synthetic control over their size (and somewhat their shape) is well developed, the manipulation of their ligand coatings and their self-assembly into functional structures remain open questions and are a particular focus of our current studies.

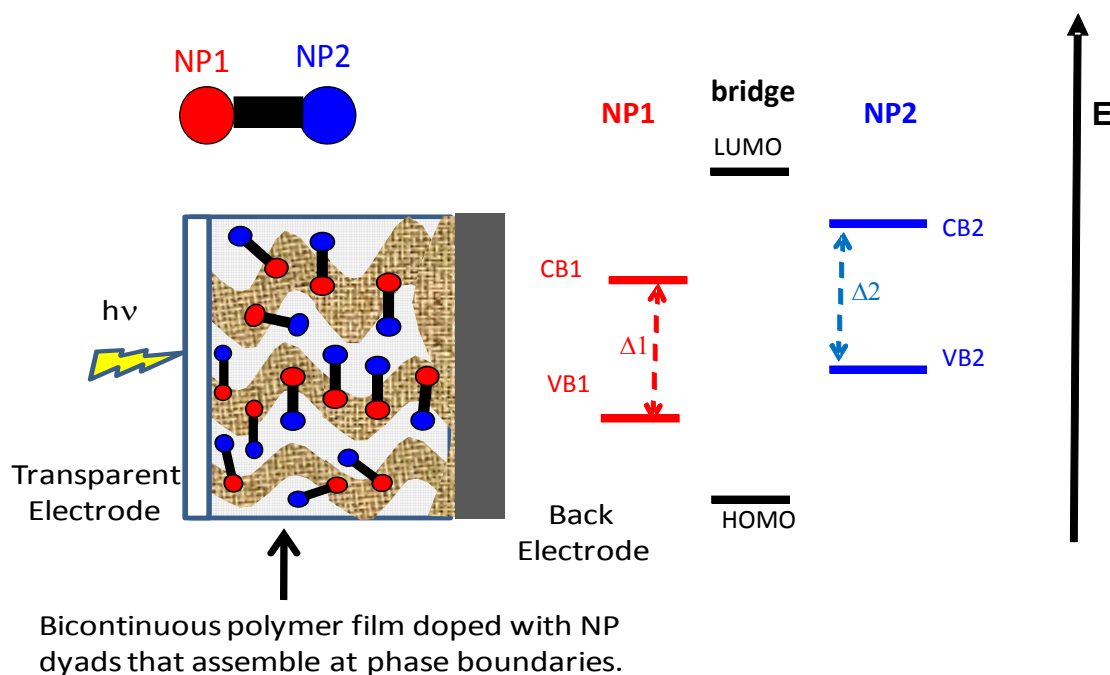


Figure 1 The left panel illustrates a device architecture for a bulk heterojunction solar cell in which sets of nanoparticles, shown here as linked pairs or dyads, act as a p-n junction with a tunable bandgap. The panel on the right shows the intended band alignment for the nanoparticles.

Predicting and Controlling NP Energetics

We describe our efforts toward quantifying the band energies of the nanoparticles and their assemblies. Assemblies of CdSe NPs and CdTe NPs on a dithiol coated Au electrode were created, and their electronic energetics was characterized (see Figure 2) by using cyclic voltammetry in an electrochemical cell and by photoemission spectroscopy in vacuo.¹ Comparison of these two different measures shows good agreement if the IUPAC accepted value of the absolute electrode potential is used

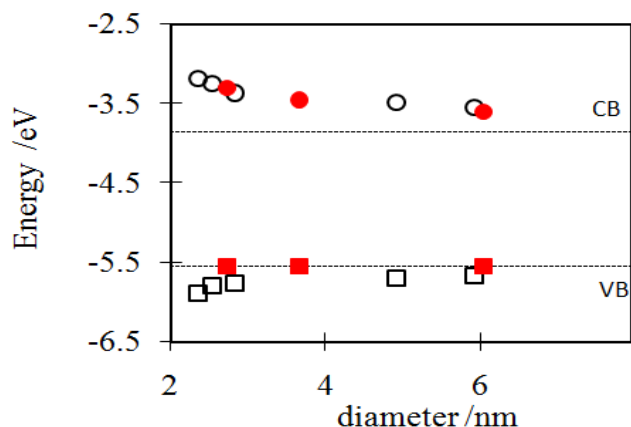


Figure 2: The graph plots the HOMO energies (open squares from electrochemistry and filled squares from photoemission measurements) and LUMO energies (open circles from electrochemistry and filled circles from photoemission measurements) of the different CdSe NPs as a function of their diameter. The dashed lines mark the bulk CdSe band positions, assuming that its valence band is pinned at 1.25 eV below the Fermi level of Au.

to rescale the electrochemically determined band edges (Figure 1 shows data for CdSe NPs immobilized on Au electrodes). The most interesting and surprising finding of these studies is that the HOMO energy of the NPs, when attached to the surface via thiol linkers, is pinned; its energy does not vary with the NP size (for sizes greater than 2.3 nm). The LUMO apparently couples more weakly to the substrate than does the HOMO, and it is more localized on the NPs.

Capping ligand composition and particle size effects on the electronic properties of both individual and coupled CdSe and CdTe NPs were investigated by quantum chemical methods in the size range of 0.5-6.0 nm. The NPs were built from a crystal fragment, wurtzite for CdSe and zinc blende for CdTe, and their surfaces were passivated with either -NH_3 , -OPH_3 , or -SCH_3 ligands. Fig. 3 shows the HOMO localization and energetics as a function of ligand and particle size variation. The HOMO energy plateaus with size indicating development of the valence band, as expected. The ligands have a significant effect on the electronic energy and electronic localization characteristics of the NP. Passivation with OPH_3 shifts the HOMO to higher energies while SCH_3 lowers the HOMO energy, both compared to NH_3 passivated NPs. The HOMO is strongly localized on the NP atoms when the structure is passivated by NH_3 or OPH_3 , while the HOMO is localized dominantly on the surface ligands when passivated with SCH_3 . This orbital structure may explain the observed energy pinning in the CdSe nanoparticles with capping thiols bound to gold. Our quantum chemical studies point to a simple hypothesis for Fermi level pinning; *i.e.*, surface termination with species that project frontier ligand-localized orbitals in the valence band – conduction band energy gap of the NPs can pin the Fermi energy.

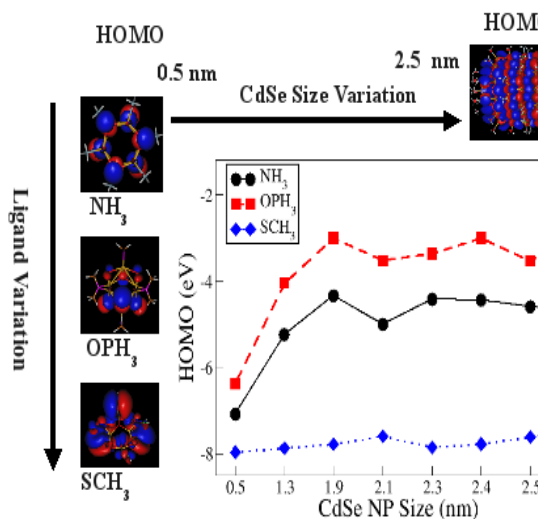


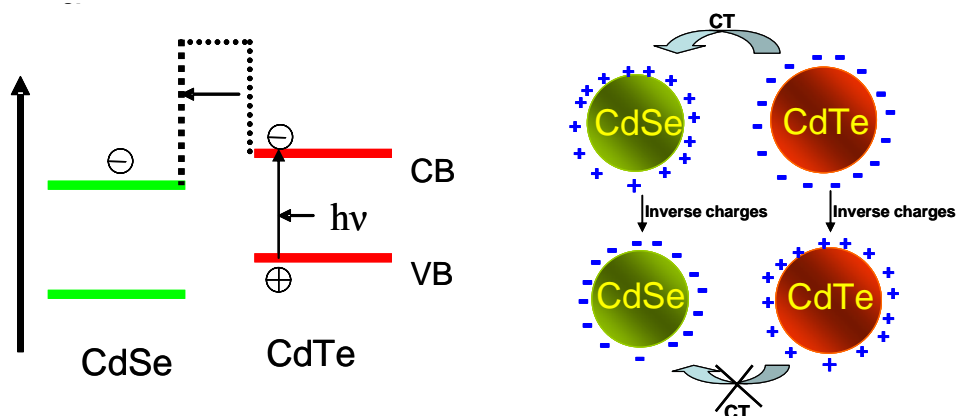
Figure 3: Ligand and particle size effects on the HOMO of CdSe nanoparticles. Note pinning of the HOMO in SCH_3 capped nanoparticles.

Predicting and Controlling NP-NP Charge Transfer

A major element of our effort is aimed at understanding how the solvation properties of the ligands, e.g., hydrophobicity and charge, can be manipulated to control the self-assembly of NPs into supramolecular structures and to arrange the NP-NP energetics in a way that facilitates charge transfer.

The nature of the ligand (e.g., saturated versus unsaturated, its length) can play a critical role in facilitating, or inhibiting, charge transfer. The use of ligand interactions can be exploited to arrange different NPs in space and to manipulate the NP electronic states. We are exploring various aspects of how the ligand properties affect NP to NP charge transfer and NP to electrode charge transfer.

We have used electrostatic charge on ligand coated CdSe and CdTe nanoparticles (NPs) to aggregate them in solution and study their charge transfer.² Electron transfer was found to depend on three factors: the interparticle distance, the energy alignment of the NPs (hence the NP size), and the direction of the electric field between the NPs, established by their surface charges (see Scheme 1). The inhibition of electron transfer by the interparticle electric field is particularly significant, because it may provide an avenue for inhibiting back electron transfer in NP assemblies. We are also using theoretical methods to probe the donor-acceptor interactions in coupled CdSe-CdTe NPs.³



Scheme 1. The left panel shows a schematic drawing of type II staggered band gap alignment for the CdTe and CdSe NPs. The right panel shows a schematic drawing of assemblies formed between MPA-CdSe/DEA- CdTe for two different choices of surface charge.

Photoluminescence (PL) measurements were used to probe how the nature of the organic linker changes the electronic coupling between two different sizes of nanoparticles (NPs) in hybrid bilayer assemblies that are adsorbed on GaAs and on quartz.^{4,5} The photoluminescence response of the bilayer assemblies depends on their hierarchy, namely on the ordering of differently sized nanoparticles with respect to the surface; however, the surface photovoltage does not. Based on these studies, it was possible to determine the relative importance of charge transfer and energy transfer mechanisms for quenching of the electron-hole pair excitation. At room temperature, it was found that a conjugated linker, 1,4-benzenedimethanethiol (BDT), couples between the NPs better than a saturated alkyl linker of the same order of length; at 80 K, the coupling via the BDT linker is lower and equal to that found for the saturated hydrocarbon. The PL quenching mechanism that explains all of the observations is exciton energy transfer between the NPs by the Dexter mechanism. The GaAs was found to interact strongly with the NP assemblies and to quench their PL very efficiently as compared to the same assemblies adsorbed on quartz; however, the substrate does not affect the mechanism of energy transfer between the NPs.

Core shell (c/s) nanoparticles (NPs) are of great interest for their use in controlling NP surface properties and their promise for facilitating charge transfer. For such applications it is important to quantify how well isolated the electronic states of the core are from the surface. We created self-assembled films of c/s NPs on Au substrates via a dithiol (DT) organic linker and used photoemission spectroscopy to compare the electronic states of CdSe core only and CdSe/ZnS c/s NPs.⁶ The results indicate that in the c/s NPs the HOMO interacts strongly with electronic states in the Au substrate and is pinned at the same energies, relative to the Fermi level, as the core only NPs. The LUMO states of the CdSe NPs were found to be strongly coupled to the NP surface traps, independent of their size, but this coupling was found to be size dependent in the case of the CdSe/ZnS c/s NPs. For a large core, the

LUMO is decoupled from the surface trap states, whereas the LUMO is delocalized for the small core NPs and interacts with these states.

Future Directions

The fundamental quantitative understanding of NP assemblies and their charge-transfer dynamics will be extended to develop strategies for manipulating the NP energy level alignment by surface ligand variation and using it to facilitate charge transfer between NPs and between NPs and conjugated polymer materials. We will measure the band energies of nanoparticles that have different surface capping ligands, in an effort to systematically tune the electronic energy levels of the nanoparticles. In concert with these efforts, we will investigate how the charge transfer efficiency changes with the NP energy-band alignment and how it depends on the magnitude of the energy gradient through a cascade of NPs. Because the effective incorporation of NPs into organic (or even inorganic) bulk-heterojunction solar cells will require charge transfer from NPs to organic polymers, we are creating nanoparticle/polymer composites that will allow us to explore the charge injection from inorganic NPs into conjugated polymers.

Publications

1. T. Z. Markus, M. Wu, L. Wang, D. H. Waldeck, D. Oron, and R. Naaman *Electronic Structure of CdSe Nanoparticles Adsorbed on Au Electrodes by an Organic Linker: Fermi Level Pinning of the HOMO* J. Phys. Chem. C **113** (2009) 14200-14206.
2. M. Wu, P. Mukherjee, D. N. Lamont and D. H. Waldeck *Electron Transfer and Fluorescence Quenching of Nanoparticle Assemblies* J. Phys. Chem. C **114** (2010) 5751–5759.
3. D. Balamurugan, S.S. Skourtis and D.N. Beratan, *A theory for charge separation from multi-exciton states*, in preparation (2010).
4. G. Gotesman, D. H. Waldeck, and R. Naaman *Self-Assembly of Nanoparticle Arrays on Semiconductor Substrate for Charge Transfer Cascade* J. Phys. Chem. A **113** (2009) 7213-7217.
5. Gilad Gotesman and Ron Naaman *Temperature-Dependent Coupling in Hybrid Structures of Nanoparticle Layers Linked by Organic Molecules* J. Phys. Chem. Letters 2010, 1, 594–598.
6. Zuoti Xie, Tal Z. Markus, Gilad Gotesman, Zvicka Deutsch, Dan Oron, and Ron Naaman, *How Isolated Are the Electronic States of the Core in Core/Shell Nanoparticles?* ACS Nano (2011) accepted.

Additional Publications

A. Bardea and R. Naaman *Magnetolithography: From Bottom-Up Route to High Throughput* Small **5** (2009) 316.

D. Balamurugan, S.S. Skourtis and D.N. Beratan, *A theory for charge separation from multi-exciton states*, in preparation (2010).

Program Title: Structure-Optical-Thermal Relationships of Carbon Nanotubes Energy Transport in Graphene
Principal Investigator: Stephen Cronin
Institution: University of Southern California
Address: 3737 Watt Way, Los Angeles, CA 90089
Email: scronin@usc.edu
DOE Grant Number: DE-FG02-07ER46376
Collaboration: Prof. Li Shi, University of Texas, Austin

Program Scope or Definition

The objective of this proposed research is to develop a better understanding of phonon transport and coupled electron-phonon transport in graphene. As a monatomic layer of sp^2 carbon atoms, graphene is a promising material for future-generation energy-efficient electronic devices and thermal management solutions because of its superior charge mobility, mechanical strength, and thermal conductivity. Building on the results from our current study of carbon nanotubes and preliminary results on graphene, this project aims to

- (i) Clarify whether the flexural vibration modes make an important or negligible contribution to thermal conductivity of graphene;
- (ii) Investigate the effects of inter-layer coupling, substrate interaction, stress and morphology on phonon transport in suspended and supported single- and few-layer graphene;
- (iii) Characterize the interfacial thermal transport between supported graphene and underlying dielectric, metallic, and polymeric substrates;
- (iv) Evaluate interfacial thermal transport between graphene and its surrounding gas environment;
- (v) Determine whether or not coupled electron-phonon transport in graphene is highly non-equilibrium as in carbon nanotubes; and
- (vi) Reveal the effects of inter-layer coupling, substrate interaction, stress, morphology, and gas environment on electron-phonon coupling in graphene.

Recent Progress

1.) *Acoustic Phonon Temperature Distribution in Electrically Biased Graphene:* We have performed scanning thermal microscopy (SThM) and Raman spectroscopy measurements of thermal transport in electrically biased, 6.7-9.7 μm long graphene channels. By comparing the temperature profiles obtained with these two techniques, we find the low-frequency acoustic phonon temperature to be in equilibrium with the anharmonic scattering temperature determined from the Raman 2D peak position. With ~ 100 nm

scale spatial resolution, the SThM reveals a shifting of local hot spots corresponding to low-carrier concentration regions with the bias and gate voltages.

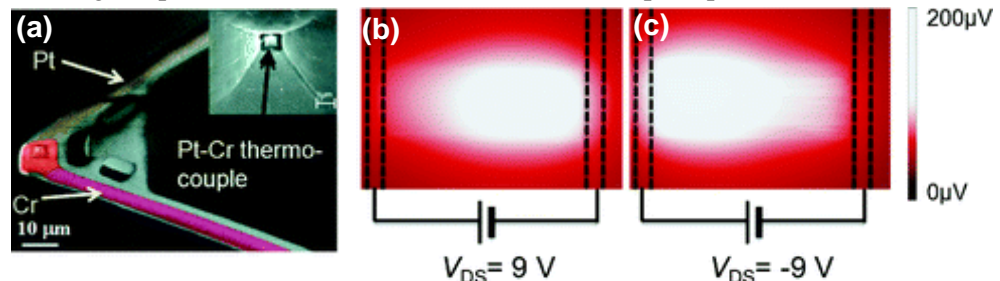


Figure 1. (a) Scanning electron micrograph (SEM) of the SThM probe with a submicrometer thermocouple fabricated at the apex of the tip. The inset shows the Pt-Cr thermocouple. (b,c) Thermal mapping of device under different bias and gate voltages.

2.) *Ripple Formation in Suspended Graphene:* Well-ordered ripples can be formed in a controllable fashion by thermally cycling suspended graphene. Figure 2 shows an AFM image of these periodic ripples. In this work, graphene membranes, ranging from single layers (0.35nm) to multiple layers (2nm) in thickness, and 0.5 to 20 μm in width, are deposited suspended across pre-defined trenches on Si/SiO₂ substrates using mechanical exfoliation. The samples are then cycled thermally to several hundred degrees Celsius under standard atmospheric conditions. Our Raman spectroscopy measurements of this periodic ripple formation process reveal that these ripples arise from the compression induced in graphene due to the difference in thermal expansion coefficients between graphene and the underlying Si

substrate. This compression (a) is quantified by measuring the change in the G band Raman frequency, while the amplitude and wavelength of the ripples are measured by AFM. Spatial mappings of the G band Raman shift taken before and after thermal cycling to 700K are shown in Figure 2b. Before thermal cycling, a slight upshift in the Raman frequency can be seen in the trench region. This indicates either a small compression in the suspended region or, more likely, a small strain in the substrate region. After thermal cycling, however, a large upshift of $\Delta\omega_G=25\text{cm}^{-1}$ is observed in the substrate region, while the trench region remains unchanged, indicating the presence of significant compression in the single layer graphene on the substrate. Such compression arises from the differential thermal expansion between graphene and the substrate, in particular, from the negative thermal expansion of graphene.

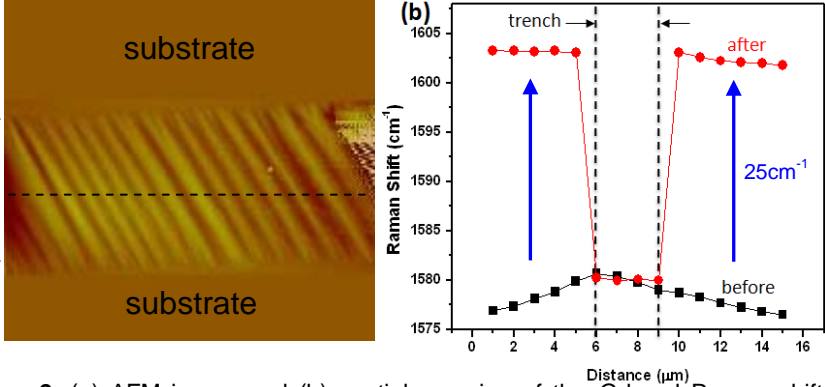


Figure 2. (a) AFM image and (b) spatial mapping of the G band Raman shift taken before and after thermal cycling to 700K.

3.) *The effect of gas environment on electrical heating in suspended carbon nanotubes:* We report micro-Raman spectroscopy measurements of the temperature distribution of current-carrying, 5 μm long, suspended carbon nanotubes in different gas environments near atmospheric pressure. At the same heating power, the measured G band phonon temperature of the nanotube is found to be significantly lower in gaseous environments than in vacuum.

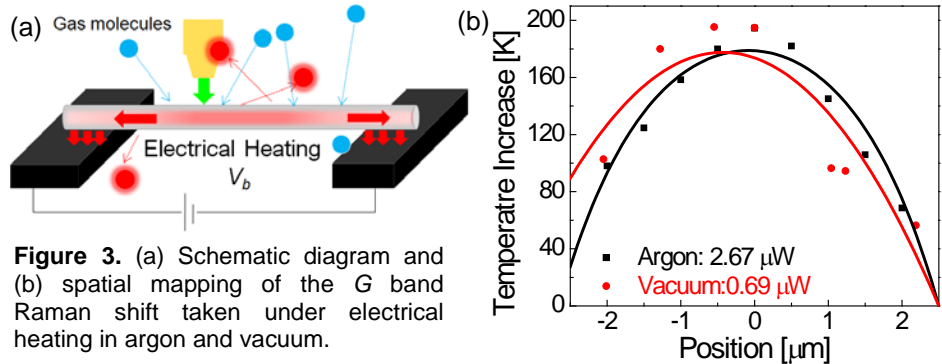


Figure 3. (a) Schematic diagram and (b) spatial mapping of the G band Raman shift taken under electrical heating in argon and vacuum.

Theoretical analysis of these results suggests that about 50%–60% of the heat dissipated in the suspended nanotube is removed by its surrounding gas molecules, and that the thermal boundary conductance is higher in carbon dioxide than in nitrogen, argon, and helium, despite the lower thermal conductivity of carbon dioxide.

4.) *Gate Voltage-Controllable Acoustic Phonon Scattering:* One of the unique aspects of carbon nanotubes is that we can modulate the electron scattering dramatically by modulating the gate voltage. Figure 4 shows the $I-V_{bias}$ curves taken from the same individual suspended nanotube under different gating conditions. For the undoped case (Figure 4a), $V_g=0$, we observe Ohmic (linear) $I-V_{bias}$ behavior. For the doped case (Figure 4b), $V_g=-2\text{V}$, we observe NDR. The ability to shift the $I-V_{bias}$ characteristics so dramatically arises from the gate dependence of the group velocity of the electrons. In the doped case, the electron dispersion is linear with a group velocity of 840km/s. Since metallic nanotubes are known to have a small bandgap on the order of tens of meV, the group velocity drops to zero as the Fermi energy approaches the band edge. In the constant relaxation time approximation, the acoustic phonon scattering mean-free path (MFP) is directly proportional to

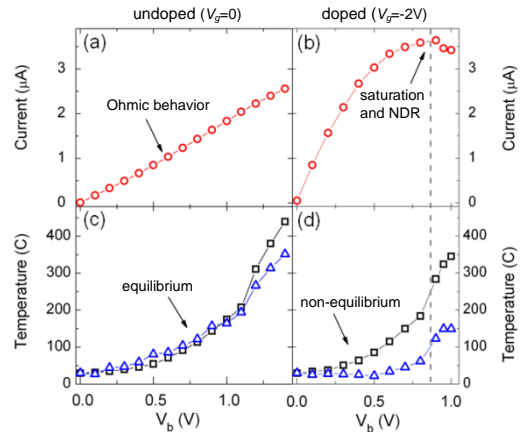


Figure 4. (a, b) Electrical current and (c, d) G band phonon temperatures for a suspended CNT at two different values of V_g .

this group velocity ($\lambda_{ac} = v_g \tau$) and drops to zero at the band edges. In most one-dimensional systems, acoustic phonon scattering is greatly suppressed due to the restricted possible scattering states in k -space. However, in nanotubes, this situation is more complicated because of the gate dependence of the group velocity. By applying a gate voltage, we can vary the acoustic phonon scattering mean-free path from $\sim 2.4 \mu\text{m}$ in the doped case to almost zero in the undoped case. In the undoped cases, the acoustic phonon scattering is dominant because of the slow velocity of the electrons. In the doped case at low bias, the acoustic phonon scattering is suppressed, but the electrons do not have enough kinetic energy to emit optical phonons, resulting in ballistic transport. In the doped case at high bias, the acoustic phonon scattering is suppressed, but the electrons have enough kinetic energy to emit optical phonons, and optical phonon scattering becomes the dominant scattering mechanism. The gate- and bias-voltage dependences of these two scattering mechanisms allow us to switch between Ohmic behavior, where the nanotube is in thermal equilibrium (Figure 4c), and negative differential resistance, where the nanotube is out of thermal equilibrium (Figure 4d).

5.) *Breakdown of the Born-Oppenheimer Approximation:* In the adiabatic Born-Oppenheimer approximation (BOA), electrons relax to the instantaneous ground state of the system faster than the atoms vibrate. In carbon nanotubes and graphene, this approximation breaks down because of the fast vibrational motion of the tightly bound, light carbon atoms ($\tau_{op} = 0.02\text{ps}$) and the long lifetimes of the electrons ($\tau_{el} = 2\text{ps}$). Time-dependent density functional theory (DFT) calculations performed in the non-adiabatic regime (when the BOA is relaxed) predict a W-shape profile in the phonon frequency versus Fermi energy (or gate voltage) dependence. The separation between the two minima in this profile is equal to the phonon energy (E_{ph}). Figure 5 shows the Raman data taken on a nearly defect-free, suspended, pristine carbon nanotube, exemplifying this theoretically predicted W-shaped profile. While many other research groups have measured the gate voltage dependence of the Raman modes of CNTs, this theoretically predicted W-shape profile has been observed clearly only in our pristine, nearly defect free, suspended CNTs. The data in Figure 5 represents the first experimental confirmation of the

breakdown of the Born-Oppenheimer approximation in CNTs. It is not surprising that the BOA is not valid in carbon nanotubes; however, it is remarkable that no one has observed this before. This is a true testament to the great influence that defects, surface contaminants, and substrate interactions can have on their behavior. The dashed curve in Figure 5 shows a fit to an adiabatic model in which the BOA is valid. The large discrepancy between this model and the observed data illustrates the great importance of these non-adiabatic effects in suspended, defect-free nanotubes, which must be included in order to represent the electron-phonon interactions accurately. This non-adiabatic model also predicts a change in the linewidth of this phonon mode (not shown), which fits our data nicely without any additional fitting parameters. A similar breakdown of the BOA has been observed in substrate supported graphene at temperatures below 77K. The data shown in Figure 5 was taken at room temperature.

Future Plans

In the remaining funding period of this project, we have planned the following experiments:

- 1.) Characterize the interfacial thermal transport between supported graphene and underlying dielectric, metallic, and polymeric substrates;
- 2.) Determine whether or not coupled electron-phonon transport in graphene is highly non-equilibrium as in carbon nanotubes;
- 3.) Reveal the effects of inter-layer coupling, substrate interaction, stress, morphology, and gas environment on electron-phonon coupling in graphene; and
- 4.) Demonstrate a novel two-laser technique for measuring thermal transport in carbon nanotubes and graphene using a non-contact configuration.

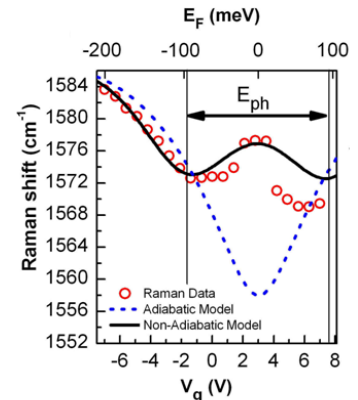


Figure 5. G band Raman shift plotted versus gate voltage (V_g). The lines show the adiabatic (dashed) and non-adiabatic (solid) phonon renormalization models.

References to publications of DOE sponsored research that have appeared in 2008-2010 or that have been accepted for publication.

1. **"Low-Frequency Acoustic Phonon Temperature Distribution in Electrically Biased Graphene"** Insun Jo, I-Kai Hsu, Yong J. Lee, Mir Mohammad Sadeghi, Seyoung Kim, Stephen Cronin, Emanuel Tutuc, Sanjay K. Banerjee, Zhen Yao, and Li Shi, *Nano Letters* 11, 85 (2011)
2. **"Memristive Behavior Observed in a Defected Single-Walled Carbon Nanotube"** Adam W. Bushmaker, Chia-Chi Chang, Vikram V. Deshpande, Moh. R. Amer, Marc W. Bockrath, Stephen B. Cronin, *IEEE Transactions on Nanotechnology*, PP, 99 (2010)
3. **"The effect of gas environment on electrical heating in suspended carbon nanotubes"** I-Kai Hsu, Michael T. Pettes, Mehmet Aykol, Li Shi, and Stephen B. Cronin, *Journal of Applied Physics*, 108, 084307 (2010)
4. **"A New Lower Limit for the Ultimate Breaking Strain of Carbon Nanotubes"** Chia-Chi Chang, I-Kai Hsu, Mehmet Aykol, Wei-Hsuan Hung, Chun-Chung Chen, and Stephen B. Cronin, *ACS Nano*, 4, 5095-5100 (2010)
5. **"Raman Spectroscopy of Ripple Formation in Suspended Graphene"** Chun-Chung Chen, Wenzhong Bao, Jesse Theiss, Chris Dames, Chun Ning Lau, and Stephen B. Cronin, *Nano Lett.*, 9, 4172 (2009)
6. **"Large Modulations in the Intensity of Raman-Scattered Light from Pristine Carbon Nanotubes"** Adam W. Bushmaker, Vikram V. Deshpande, Scott Hsieh, Marc W. Bockrath, and Stephen B. Cronin, *Physical Review Letters*, 103, 067401 (2009)
7. **"Gate Voltage Controllable Non-Equilibrium and Non-Ohmic Behavior in Suspended Carbon Nanotubes"** Adam W. Bushmaker, Vikram V. Deshpande, Scott Hsieh, Marc W. Bockrath and Stephen B. Cronin, *Nano Lett.*, 9, 2862 (2009)
8. **"Top-down lithographic method for inducing strain in carbon nanotubes"** Rajay Kumar, Mehmet Aykol, Kounghmin Ryu, Chongwu Zhou, and Stephen B. Cronin, *Journal of Applied Physics*, 106, 014306 (2009)
9. **"Selective destruction of individual single walled carbon nanotubes by laser irradiation"** Bardia Zandian, Rajay Kumar, Jesse Theiss, Adam Bushmaker and Stephen B. Cronin, *Carbon*, 47, 1292 (2009)
10. **"Spatially Resolved Temperature Measurements of Electrically Heated Carbon Nanotubes"** V. V. Deshpande, S. Hsieh, A. W. Bushmaker, M. Bockrath, S. B. Cronin, *Physical Review Letters*, 102, 105501 (2009)
11. **"Direct Observation of Born-Oppenheimer Approximation Breakdown in Carbon Nanotubes"** Adam W. Bushmaker, Vikram V. Deshpande, Scott Hsieh, Marc W. Bockrath, and Stephen B. Cronin, *Nano Lett.*, 9, 607 (2009)
12. **"Optical Absorption and Thermal Transport of Individual Suspended Carbon Nanotube Bundles"** I-Kai Hsu, Michael T. Pettes, Adam Bushmaker, Mehmet Aykol, Li Shi, and Stephen B. Cronin, *Nano Lett.*, 9, 590 (2009)
13. **"Effect of nanotube-nanotube coupling on the radial breathing mode of carbon nanotubes"** Rajay Kumar, Mehmet Aykol, and Stephen B. Cronin, *Phys. Rev. B*, 78, 165428 (2008)
14. **"Optical measurement of thermal transport in suspended carbon nanotubes"** I-Kai Hsu, Rajay Kumar, Adam Bushmaker, Stephen B. Cronin, Michael T. Pettes, Li Shi, Todd Brintlinger, Michael S. Fuhrer, and John Cumings, *Appl. Phys. Lett.*, 92, 063119 (2008)

Poster Sessions

Physical Behavior of Materials Contractors Meeting
U. S. Department of Energy
Office of Basic Energy Sciences

POSTER SESSION I

- 1) Fundamentals of Semiconductor Nanowires
Peidong Yang, Lawrence Berkeley National Laboratory
- 2) Characterization of Functional Nanomachines
Ivan Pechenezhskiy, University of California, Berkeley/LBNL
- 3) Enhancement in Thermoelectric and Photovoltaic Properties by Nanostructure Approach
Zhifeng Ren, Boston College
- 4) Piezoelectric Nanogenerators for Self-Powered Nanosystems and Nanosensors
Zhong Lin Wang, Georgia Institute of Technology
- 5) Nanolamellar Magnetolectric BaTiO₃-CoFe₂O₄ Bicrystal
Manfred Wuttig, University of Maryland
- 6) Fabricating Efficient p-Type Dye-Sensitized Solar Cells
Yiyang Wu, Ohio State University
- 7) Energy Transport in Graphene
Li Shi, University of Texas at Austin
- 8) Electron and Hole Transport in Indium Nitride
Joel Ager, Lawrence Berkeley National Laboratory
- 9) Electronic Materials Program
Ali Javey, Lawrence Berkeley National Laboratory
- 10) Experimental and Theoretical Studies of Embedded Nanostructures
Daryl Chrzan, Lawrence Berkeley National Laboratory

- 11) Advanced Concepts and Materials for Solar Power Conversion: From Basic Science to Applications
Kim Man Yu, Lawrence Berkeley National Laboratory
- 12) Ultra-fast, Laser-Thermal Processing of Semiconductors
Oscar D. Dubón, Lawrence Berkeley National Laboratory
- 13) Dynamical Materials Nanostructures for Energy Technology
Junqiao Wu, Lawrence Berkeley National Laboratory
- 14) Electronic and Optical Processes in Novel Semiconductors for Energy Applications
Angelo Mascarenhas, National Renewable Energy Laboratory
- 15) Machine Learning Approaches to Crystal Structure Prediction
Lusann Yang, Massachusetts Institute of Technology
- 16) Theory and Modeling of Materials for Hydrogen Storage
Tim Mueller, Massachusetts Institute of Technology
- 17) Hetero-junctions of Boron Nitride and Carbon Nanotubes: Synthesis and Characterization
Yoke Khin Yap, Michigan Technological University
- 18) Interband Cascade Photovoltaic Cells
Rui Yang, University of Oklahoma
- 19) Understanding and Design of Polymer Device Interfaces
Antoine Kahn, Princeton University
- 20) Optical Properties of Doped ZnO Nanocrystals and Ceramics
Matthew McCluskey, Washington State University
- 21) Properties and Defect Luminescence of ZnO Flexible Films
Leah Bergman, University of Idaho
- 22) Structural and Electrostatic Effects in Self-Assembled Nanostructures
Helen Farrell, Idaho National Laboratory

- 23) Electronic Processes in Solid State Organic Electronic Materials
Richard Martin, Los Alamos National Laboratory
- 24) Ultrathin Iron Oxide Growth on YSZ Single-Crystal Surfaces
Gary Kellogg, Sandia National Laboratories
- 25) The Factors that Influence Graphene Growth on Metal Surfaces
Norman Bartelt, Sandia National Laboratories
- 26) Evolution of Oxide Stability during Localized Corrosion of Model Al-Cu Alloys
Nancy Missert, Sandia National Laboratories
- 27) Carbon Surface Diffusion and Strain Development during the Growth of Epitaxial Graphene on SiC
Taisuke Ohta, Sandia National Laboratories
- 28) Using Interfaces to Create Strongly Coupled Magnetic-Ferroelectrics
Craig Fennie, Cornell University
- 29) Surface Engineering by Simultaneous Action of Multiple External Fields
Dimitrios Maroudas, University of Massachusetts
- 30) Phase Transformations in Confined Nanosystems
Jeffrey Shield, University of Nebraska

Physical Behavior of Materials Contractors Meeting
U. S. Department of Energy
Office of Basic Energy Sciences

POSTER SESSION II

- 1) Nanocomposite Proton Conductors
Lutgard De Jonghe, Lawrence Berkeley National Laboratory
- 2) Elucidation of Hydrogen Interaction Mechanisms with Metal Doped Carbon Nanostructures
Ragaiy Zidan, Savannah River National Laboratory
- 3) High Performance Nano-Crystalline Oxide Fuel Cell Materials: Defects, Structures, Interfaces, Transport, and Electrochemistry
Scott Barnett, Northwestern University
- 4) Supported, Coated, and Ligated Metal Clusters
Puru Jena, Virginia Commonwealth University
- 5) Hydrogen Absorption in Pd-Based Nanostructures
David Lederman, West Virginia University
- 6) Extraordinary Responsive Magnetic Rare Earth Materials
Karl Gschneidner, Jr., Iowa State University/Ames Laboratory
- 7) Spin Polarized Functionality Through Complex Oxide Heteroepitaxy
Yuri Suzuki, Lawrence Berkeley National Laboratory/UC Berkeley
- 8) Study of Materials and Interface Properties for High-Efficiency Spin Injection
Jing Shi, University of California, Riverside
- 9) Dipolar Ferromagnets for Magnetocaloric Effect Nanocomposites
Sara Majetich, Carnegie Mellon University
- 10) Understanding the Spin-Lattice Coupling in Multiferroic Oxides
Trevor Tyson, New Jersey Institute of Technology

- 11) Structure and Magnetism in Novel Group IV Element-Based Magnetic Materials
Frank Tsui, University of North Carolina
- 12) Nanoscale Oxide Thin Films and Heterostructures by Laser Molecular Beam Epitaxy
Xiaoxing Xi, Temple University
- 13) MuSR Investigations of Magnetic Semiconductors for Spintronics Applications
Roger Lichti, Texas Tech University
- 14) Nanostructured Thermoelectric Materials
Rachel Segalman, Lawrence University of California, Berkeley/LBNL
- 15) Crystallization and Thermoelectric Transport in Silicon Microstructures and Nanostructures under Extreme Electrical Stress
Ali Gokirmak, University of Connecticut
- 16) Complex Amorphous Transition-Metal Dielectrics
Bruce van Dover, Cornell University
- 17) Suspensions of Monodisperse Nanoparticles as Model Systems for Probing Heat Transfer Mechanisms in Nanofluids
Bao Yang, University of Maryland
- 18) Near-Field Thermal Radiation at Extreme Separations
Gang Chen, Massachusetts Institute of Technology
- 19) Domain Microstructures and Mechanisms for Large, Reversible and Anhysteretic Strain Behaviors in Phase Transforming Ferroelectric Materials
Yu Wang, Michigan Technological University
- 20) Manipulation of Phonons with Phononic Crystals
Zayd Leseman, University of New Mexico
- 21) Understanding Compound Phase Transitions in New Heusler Alloy Giant Magnetocaloric Materials: Extension to Multifunctional Materials
Shane Stadler, Louisiana State University

- 22) Mesoscale Interfacial Dynamics in Magnetoelectric Nanocomposites
Dwight Viehland, Virginia Institute of Technology
- 23) Enhancement of the Field-Induced Strain in Multiferroics
A. G. Khachatryan, Rutgers University
- 24) Mesoscale Interfacial Dynamics in Magnetoelectric Nanocomposites
Shashank Priya, Virginia Polytechnic Institute
- 25) Nanophosphors: Fundamental Science of Insulators in the Nanoscale Regime
Ross Muenchausen, Los Alamos National Laboratory
- 26) Exceeding the Planck Free-Space Energy Transfer Limit through Photonic Density of States Control and Near Field Coupling
Ting (Willie) Luk, Sandia National Laboratories
- 27) Metamaterials as a Platform for the Development of Novel Materials for Energy Applications
Willie Padilla, Boston College
- 28) Plasmonic Photovoltaics
Harry Atwater, California Institute of Technology
- 29) Architectural Photonics for Maximizing Solar Energy Conversion
Mei-Ling Kuo, Rensselaer Polytechnic Institute
- 30) Fundamental Studies of Unconventional Sulfide Semiconductors for Cost-Effective and Environmentally Benign Thin Film Photovoltaics
Mike Scarpulla, University of Utah

Poster Abstracts

Electron and Hole Transport in Indium Nitride

Electronic Materials Program at LBNL

[J. W. Ager III](#), [K. M. Yu](#), [J. Wu](#), [E. E. Haller](#), [Z. Liliental-Weber](#), and [W. Walukiewicz](#)

Lawrence Berkeley National Laboratory, Materials Sciences Division, MS 2R0200,
1 Cyclotron Road, Berkeley, CA 94720

External collaborators: Y. Nanishi (Ritsumeikan U.), J. Speck (UC Santa Barbara), W. J. Schaff (Cornell), I Gherasoiu (RoseStreet Labs Energy)

Program Scope

LBNL's Electronic Materials Program has been investigating the fundamental properties of InN and In-rich InGaN alloys since we discovered, along with researchers in Russia and Japan, the correct InN bandgap, 0.7 eV. This discovery established that the Group III-nitride alloy band gaps span from the infrared InN ($E_g=0.675$ eV or more than 1800 nm) to well into the ultraviolet GaN ($E_g=3.4$ eV or 365 nm), AlN ($E_g=6.1$ eV or 203 nm), a range that includes not only the entire visible but virtually the entire solar spectrum.

InN has the smallest bandgap in this alloy system. It also has an exceptionally large (> 5.5 eV) electron affinity which creates a strong thermodynamic driving force for the formation of native donor defects both in the bulk and at the surface. These, in turn, dominate the semiconducting properties of InN. For example, undoped InN thin films are always n-type and all as-grown InN surfaces, regardless of polarity, crystal orientation, or doping, have an accumulation layer of electrons. Because the surface electron layer interferes with standard electrical characterization methods, it had been difficult to measure accurately the electrical properties of InN films. For example, it is not possible to make a metal Schottky contact and, as discovered in early attempts to achieve p-type doping, single field Hall effect measurements of Mg-doped films invariably see only the surface layer and cannot assess possible p-type conductivity in the bulk. As a result, there was considerable uncertainty as to whether p-type doping, and control of conductivity in general, could be achieved in InN and In rich InGaN alloys.

Recent Progress

Experimental approaches developed by the Electronic Materials Program have been successful in mitigating the interfering effect of electron-rich surface and interface layers in InN thin films, revealing the fundamental transport properties of both electrons and holes. (1) We discovered that the insulating Helmholtz double layer which forms when a liquid electrolyte contacts the InN surface allows potentials to be applied to flatten the surface band and deplete the surface electron accumulation. This allowed the acceptor nature of Mg to be confirmed by capacitance voltage techniques and enabled the surface layer contribution to be "turned off" in Hall effect measurements. (2) Thermopower (Seebeck coefficient) measurements were employed to assess hole transport directly in Mg-doped InN. In general, the thermopower is larger for semiconductors with lower carrier concentration since the Fermi level is farther from the free carriers at the band edge. Similarly, thermopower increases with effective mass because increasing the mass increases the density of states, again increasing the Fermi level/band-edge separation for a given carrier concentration. Both of these aspects favor detection of holes in the bulk rather than electrons at the surface of p-type InN since the

electron concentration in the inversion layer is significantly larger than the bulk hole concentration and the hole effective mass in InN is much larger than the electron effective mass. Observation of a positive Seebeck coefficient was definitive and unambiguous proof for mobile holes in InN:Mg (Fig. 1) and recent work combining Hall and Seebeck measurements has yielded quantitative hole density and hole mobility values.

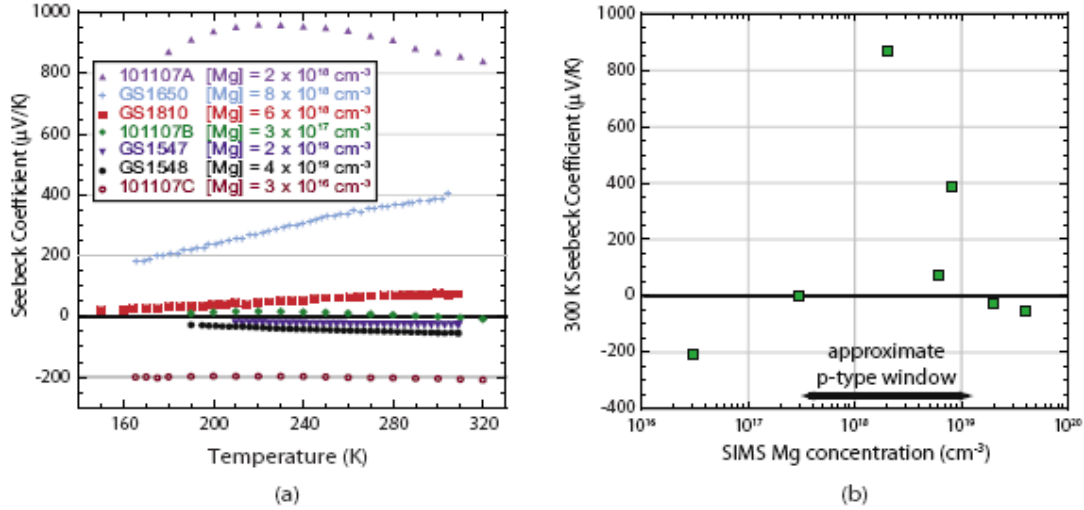


Fig. 1. (a) Measured Seebeck coefficient of Mg-doped InN samples as a function of temperature. SIMS Mg content shown in legend. Positive Seebeck coefficients show that hole transport is dominant in the film. (b) Measured Seebeck coefficient of Mg-doped InN samples at room temperature as a function of the Mg concentration measured by SIMS showing a “window” of p-type conductivity.

Future Work

The estimated LO-phonon limited room temperature mobility for undoped (n-type) InN is predicted to be in excess of $10,000 \text{ cm}^2 \text{ V}^{-1} \text{ s}^{-1}$, but the highest values reported to date are much smaller, $2500 \text{ cm}^2 \text{ V}^{-1} \text{ s}^{-1}$. Our ongoing analysis of Hall and thermopower data using Boltzmann equation modeling is revealing the important role of charged dislocations in limiting the electron mobility. The ability to control the surface electron concentration by electrolyte gating enables electron and hole transport in the bulk of InN films to be accessed. In our most recent work, initial data supporting pn junction rectification has been observed in Mg-doped InN films.

BES-supported publications, 2008-2010

- J. W. Ager III, N. Miller, R. E. Jones, K. M. Yu, J. Wu, W. J. Schaff, and W. Walukiewicz, “Mg-doped InN and InGaN – photoluminescence, capacitance-voltage and thermopower measurements,” *phys. stat. sol. (b)* **245**, 873–877 (2008).
- R. E. Jones, R. Broesler, K. M. Yu, J. W. Ager, III, E. E. Haller, W. Walukiewicz, X. Chen, and W. J. Schaff, “Band gap bowing parameter of $\text{In}_{1-x}\text{Al}_x\text{N}$,” *J. Appl. Phys.* **104**, 123501 (2008).

- G. F. Brown, J. W. Ager III, W. Walukiewicz, W. J. Schaff and J. Wu, "Probing and Modulating Surface Electron Accumulation in InN by the Electrolyte Gated Hall Effect," *Appl. Phys. Lett.* **93**, 262105 (2008).
- R. E. Jones, S. X. Li, K. M. Yu, J. W. Ager III, E. E. Haller, W. Walukiewicz, H. Lu and W. J. Schaff, "Properties of native point defects in $\text{In}_{1-x}\text{Al}_x\text{N}$ alloys," *J. Phys. D: Appl. Phys.* **42** 095406 (2009).
- M. E. Hawkridge, Z. Liliental-Weber, K. M. Yu, L. A. Reichertz, W. J. Schaff, J. W. Ager, and W. Walukiewicz, "Stacking faults and phase changes in Mg-doped InGaN grown on Si," *physica status solidi (c)* **6**, S421-S424 (2009).
- N. Miller, J. W. Ager III, R. E. Jones, H. M. Smith III, M. A. Mayer, K. M. Yu, M. E. Hawkridge, Z. Liliental-Weber, E. E. Haller, W. Walukiewicz, W. J. Schaff, C. Gallinat, G. Koblmüller, and J. S. Speck, "Electrical and electrothermal transport in InN: The roles of defects," *Physica B* **404**, 4862-4865 (2009).
- N. Miller, J. W. Ager III, H. M. Smith III, M. A. Mayer, K. M. Yu, E. E. Haller, W. Walukiewicz, W. J. Schaff, C. Gallinat, G. Koblmüller, and J. S. Speck, "Hole transport and photoluminescence in Mg-doped InN," *J. Appl. Phys.* **107**, 113712 (2010).
- K. Wang, N. Miller, R. Iwamoto, T. Yamaguchi, M. A. Mayer, T. Araki, Y. Nanishi, K. M. Yu, E. E. Haller, W. Walukiewicz, J. W. Ager III, "Mg doped InN and confirmation of free holes in InN," *Appl. Phys. Lett.*, in press.

Understanding compound phase transitions in new Heusler alloy giant magnetocaloric materials: Extension to multifunctional materials

(Grant No. USDOE-DE-FG02-06ER46291)

Naushad Ali

Southern Illinois University, Department of Physics, Carbondale, IL 62901
nail@physics.siu.edu

Shane Stadler

Louisiana State University, Department of Physics & Astronomy, Baton Rouge, LA 70808
stadler@phys.lsu.edu

SCOPE/DEFINITION

This project originated with the observation of a giant magnetocaloric effect (MCE) in the Heusler alloy $\text{Ni}_2\text{Mn}_{1-x}\text{Cu}_x\text{Ga}$.¹ The measured entropy change for this system is about $-64 \text{ J}\cdot\text{K}^{-1}\cdot\text{kg}^{-1}$ ($-532 \text{ mJ}\cdot\text{cm}^{-3}\cdot\text{K}^{-1}$) (in an applied field of 5 T) at room temperature, i.e., more than double the largest value reported at that time (Fig. 1, upper). This material also has a significant MCE effect ($-27 \text{ J}\cdot\text{K}^{-1}\cdot\text{kg}^{-1}$) in fields at or below 2 T, making it a strong candidate for employment in magnetocaloric refrigeration devices based on *permanent* magnets rather than on high-maintenance superconducting magnets. The parent alloy Ni_2MnGa undergoes two transitions: A second order paramagnetic/ferromagnetic transition at 376 K (T_C), and a first order martensitic (structural) transition at 202 K (T_M). Varying the stoichiometry by substitution has the effect of changing the transition temperatures T_M and T_C and, in the case where Mn is substituted with Cu ($x = 0.25$), the two transitions coincide (Fig. 1, lower). It is at this “compound transition” that the large MCE is observed. It is therefore of great importance to understand the underlying physics of these phenomena.

Our goal is to gain insight into the **fundamental physics** that is responsible for MCE and related properties at the atomic level. We are currently conducting a systematic study on the effects of atomic substitutions in Ni_2MnGa -based alloys, and also exploring related full- and half-Heusler alloys, for example Ni-Mn-X (X=In, Sn, Sb), that exhibit a wide variety of interesting and potentially useful physical phenomena. It is already known that the magnetocaloric effect in the Heusler alloys is fundamentally connected to other interesting phenomena such as shape-memory properties. And the large magnetic entropy change in $\text{Ni}_2\text{Mn}_{0.75}\text{Cu}_{0.25}\text{Ga}$ has been attributed to the coupling of the first-order, martensitic transition with the second-order ferromagnetic—paramagnetic (FM-PM) transition.¹ Our research to this point has focused on understanding the fundamental physics at the origin of these complex, compound phase transitions, and the novel properties that emerge. **The culmination of all of this work has revealed a scientifically interesting, and potentially quite useful, general theme: Multifunctionality.** The complex, compound phase transitions that are responsible for the large magnetocaloric effects observed in the Heusler alloys (and other materials) are also the origin of many other enhanced behaviors. These include giant magnetoresistance (GMR), magnetoelastic effects, bulk exchange bias effects, field-induced structural phase transitions, inverse magnetocaloric effects, and

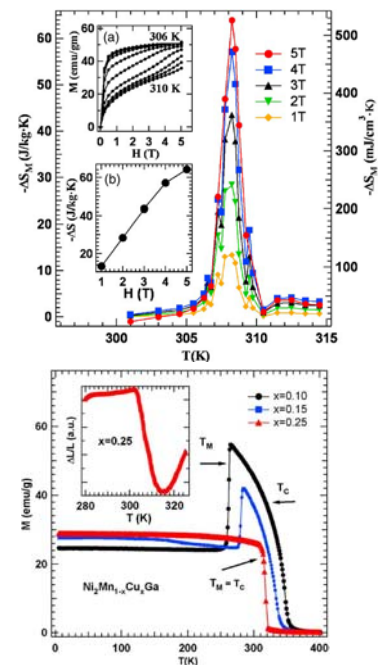


Fig. 1. (Upper) ΔS_M calculated from magnetization isotherms. (Lower) M vs. T for various concentrations x . (inset) Thermal expansion for $x=0.25$.

¹ Shane Stadler et al., Appl. Phys. Lett. **88**, 192511 (2006); A. M. Gomes et al., J. Appl. Phys **99**, 08Q106 (2006).

resistivity is evident: (i) ρ_H does not saturate even at 15 kOe; (ii) its slope changes multiple times and changes sign; and (iii) at the martensitic phase transition ($T \sim 209$), ρ_H reaches a value of $50 \mu\Omega\cdot\text{cm}$. This value is about three orders of magnitude greater than that observed at this temperature for any conventional bulk magnetic materials, and about five times greater than the anomalous Hall effect (AHE) observed for metallic, high-resistivity nanogranular alloys. It is about four times smaller than the giant Hall effects observed in nanogranular NiFe-SiO_2 with compositions near the percolation threshold.

A plausible explanation has been developed for this behavior. In our case, the main reason for the giant Hall effect is an electronic band structure transformation accompanied by an increase in the total density of states at the Fermi level, mostly from the d-component, where the Fermi level crosses the degenerate d states. This electronic structure transformation occurs at the martensitic transformation, and is accompanied by a long-range ordering of the austenetic phase.

Regardless of the proposed mechanism of the observed giant Hall effect in $\text{Ni}_{50}\text{Mn}_{50-x}\text{In}_x$, the giant value of the Hall angle is an extremely important characteristic since it could be employed in applications in spintronics and magnetic sensors.

FUTURE PLANS

In order to effectively study multifunctional materials, many different types of samples must be fabricated and a variety of experimental techniques need to be employed. Our plan includes a systematic study of the magnetic, magnetocaloric, magnetoelastic, magnetotransport, compositional, structural, and electronic properties of Ni-Mn-X, La-Fe-Si, and RE-3d metal based intermetallic compounds. We will study how varying the lattice constants, conduction electron concentration (e/a), composition, and preparation affects all of the above properties, and then apply numerous techniques (including magnetic, XRD, heat capacity, XMCD, and neutron scattering measurements) in order to gain some insight into the underlying physical phenomena. The goal is to understand the phenomena at a fundamental level so that, ultimately, we can predict and design multifunctional materials with a focus on magnetocaloric systems.

REFERENCES (with acknowledgment to DOE, 2008-Present)

¹ Exchange bias in bulk Ni-Mn-In-based Heusler alloys, Arjun Kumar Pathak, Mahmud Khan, Bhoj Raj Gautam, Shane Stadler, Igor Dubenko, and Naushad Ali, *J. Magn. Magn. Mater.* **321**, 963 (2008).

² Intermartensitic transitions in Ni-Mn-Fe-Cu-Ga Heusler alloys, Mahmud Khan, Bhoj Gautam, Arjun Pathak, Igor Dubenko, Shane Stadler, and Naushad Ali, *J. Phys.: Condens. Matter* **20**, 505206 (2008).

³ Effect of small changes in Mn concentration on phase transition temperatures and magnetic entropy variations in $\text{Ni}_2\text{Mn}_{0.75}\text{Cu}_{0.25}\text{Ga}$ Heusler alloys, Bhoj Raj Gautam, Igor Dubenko, James C. Mabon, Shane Stadler, and Naushad Ali, *J. Alloys Compd.*, doi:10.1016/j.jallcom.2008.01.021 (2008).

⁴ Effects of isoelectronic substitution on magnetic properties on $\text{Ni}_2\text{Mn}(\text{GaB})$ Heusler alloys Bhoj Raj Gautam, Igor Dubenko, Arjun Kumar Pathak, Shane Stadler, and Naushad Ali, *J. Phys.: Condens. Matter* **20** 465209 (2008).

⁵ Magnetoresistance and field-induced structural transitions in $\text{Ni}_{50}\text{Mn}_{50-x}\text{Sn}_x$ Heusler alloys, Mahmud Khan, Arjun K. Pathak, Moti R. Paudel, Igor Dubenko, Shane Stadler, and Naushad Ali, *J. Magn. Magn. Mater.* **320**, L21-L25 (2008).

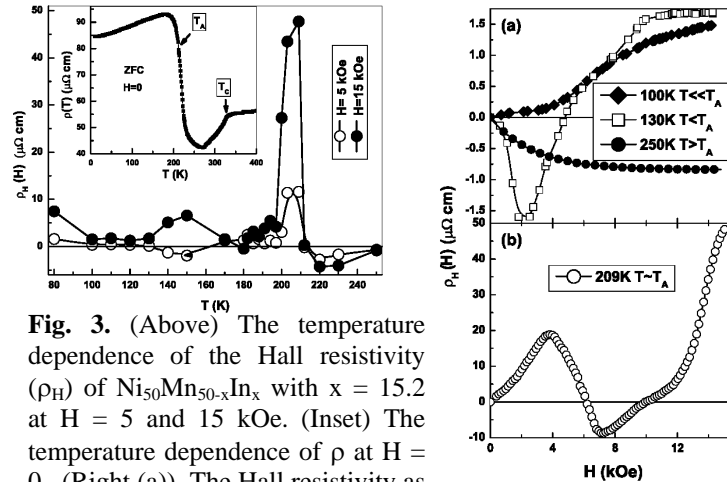


Fig. 3. (Above) The temperature dependence of the Hall resistivity (ρ_H) of $\text{Ni}_{50}\text{Mn}_{50-x}\text{In}_x$ with $x = 15.2$ at $H = 5$ and 15 kOe. (Inset) The temperature dependence of ρ at $H = 0$. (Right (a)) The Hall resistivity as a function of applied field at various temperatures. At $T = 209$ (Right (b)), ρ_H exhibits unusual field dependencies.

- ⁶*Magnetostructural phase transitions in $Ni_{50}Mn_{25-x}Sb_{25-x}$ Heusler alloys*, Mahmud Khan, Igor Duenko, Shane Stadler, and Naushad Ali, J. Phys.: Condens. Matter **20**, 235204 (2008).
- ⁷*Phase transitions and magnetoresistance in $Ni_{50}Mn_{50-x}In_x$ Heusler alloys*, Arjun Kumar Pathak, Bhoj Raj Gautam, Igor Dubenko, Mahmud Khan, Shane Stadler, Naushad Ali, J. Appl. Phys. **103**, 07F315 (2008).
- ⁸*The effect of the partial substitution of In by Si on the phase transitions and respective entropy changes of $Ni_{50}Mn_{35}In_{15}$ Heusler alloys*, Arjun Kumar Pathak, Igor Dubenko, Shane Stadler, and Naushad Ali, J. Phys. D: Appl. Phys. **41**, 202004 (2008).
- ⁹*Exchange bias in bulk Ni-Mn-In-based Heusler alloys*, Arjun Kumar Pathak, Mahmud Khan, Bhoj Raj Gautam, Shane Stadler, Igor Dubenko, and Naushad Ali, J. Magn. Magn. Mater. **321**, 963 (2009).
- ¹⁰*Exchange bias in Bulk $Ni_{50}Mn_{35}In_{15-x}Si_x$ Heusler alloys*, Arjun K. Pathak, Igor Dubenko, Shane Stadler, and Naushad Ali, IEEE Trans. Magn. **45** (10), 3855 (2009).
- ¹¹*Magnetic and electrical properties of $Ni_{50}Mn_{35}In_{15-x}Si_x$ Heusler alloys*, Arjun K. Pathak, Igor Dubenko, Shane Stadler, and Naushad Ali, J. Appl. Phys. **105**, 07B103 (1-3) (2009).
- ¹²*Magnetocaloric effects in Ni-Mn-X based Heusler alloys with X=Ga, Sb, and In*, Igor Dubenko, Mahmud Khan, Arjun K. Pathak, Bhoj R. Gautam, Shane Stadler, and Naushad Ali, J. Magn. Magn. Mat. **321**, 754 (2009).
- ¹³*Delocalization and hybridization enhance the magnetocaloric effect in Cu-doped Ni_2MnGa* , S. Roy, E. Blackburn, S. M. Valvidares, M. R. Fitzsimmons, S. C. Vogel, M. Khan, I. Dubenko, S. Stadler, N. Ali, S. K. Sinha, and J. B. Kortright, Phys. Rev. B **79**, 235127 (1-5) (2009).
- ¹⁴*Giant Hall effect in Ni-Mn-In Heusler alloys*, I. Dubenko, A. K. Pathak, S. Stadler, N. Ali, Ya. Kovarskii, V. N. Prudnikov, N. S. Perov, and A. B. Granovsky, Phys. Rev. B **80**, 092408 (2009).
- ¹⁵*The Effect of Partial Substitution of In by X=Si, Ge, and Al on the Crystal Structure, Magnetic Properties, and Resistivity of $Ni_{50}Mn_{35}In_{15}$ Heusler Alloys*, Arjun K. Pathak, Igor Dubenko, James C. Mabon, Shane Stadler, and Naushad Ali, J. Phys. D: Appl. Phys. **42** 045004 (1-8) (2009).
- ¹⁶*Effect of small changes in Mn concentration on phase transition temperatures and magnetic entropy variations in $Ni_2Mn_{0.75}Cu_{0.25}Ga$ Heusler alloys*, Bhoj Raj Gautam, Igor Dubenko, James C. Mabon, Shane Stadler, Naushad Ali, J. Alloys and Compounds **472**, 35 (2009).
- ¹⁷ Bhoj Raj Gautam, Igor Dubenko, Arjun Kumar Pathak, Shane Stadler, and Naushad Ali, *The structural and Magnetic Properties of $Ni_2Mn_{1-x}B_xGa$ Heusler alloys*, J. Magn. Magn. Mater. **321**, 29 (2009).
- ¹⁸*Magnetic, magnetocaloric, and magnetoelastic properties of $LaFe_{11.57}Si_{1.43}B_x$ Compounds*, Arjun K. Pathak, Prakash Basnyat, Igor Dubenko, Shane Stadler, and Naushad Ali, J. Appl. Phys. **106**, 063917 (4) (2009).
- ¹⁹*Magnetic, magnetocaloric, and magnetoelastic properties of $La(Fe_{1-x}Z_x)_{11.4}Si_{1.6}$ (Z=Ni, Cu, Cr, V) compounds*, A. K. Pathak, P. Basnyat, I. Dubenko, S. Stadler, and N. Ali (Accepted to J. Magn. Magn. Mater., 2009).
- ²⁰*Large inverse magnetic entropy changes and magnetoresistance in the vicinity of a field-induced martensitic transformation in $Ni_{50-x}Co_xMn_{32-y}Fe_yGa_{18}$* , A. K. Pathak, I. Dubenko, H. E. Karaca, S. Stadler, and N. Ali, Appl. Phys. Lett. **97**, 062505 (2010).
- ²¹*The effect of partial substitution of Ni by Co on the magnetic and electrical properties of $Ni_{50}Mn_{35}In_{15}$ Heusler alloy*, A. K. Pathak, I. Dubenko, C. Pueblo, P. Basnyat, S. Stadler, and N. Ali, IEEE Trans. Magn. **46**, 1444 (2010).
- ²²*Magnetoresistance and Magnetic Entropy Changes at a Structural Phase Transition from a Paramagnetic Martensitic State to a Paramagnetic Austenitic State in $Ni_{50}Mn_{50-x}In_x$ Heusler Alloys*, A. K. Pathak, I. Dubenko, C. Pueblo, S. Stadler, and N. Ali, Appl. Phys. Lett. **96**, 172503 (2010).
- ²³*Magnetism and magnetocaloric effect in $Ni_{50}Mn_{35-x}Co_xIn_{15}$ Heusler alloys*, A. K. Pathak, I. Dubenko, C. Pueblo, S. Stadler, and N. Ali, J. Appl. Phys. **107**, 09A907 (2010).
- ²⁴*Magnetotransport properties of Ni-Mn-In Heusler alloys: giant Hall angle*, I. Dubenko, A. K. Pathak, S. Stadler, Ya. Kovarskii, V.N. Prudnikov, N.S. Perov, A.B. Granovsky and N. Ali, J. Phys.: Conf. Ser., **200**, 052005 (2010).
- ²⁵*Magnetic, magnetocaloric and magnetoelastic properties of $La(Fe_{1-x}Z_x)_{11.4}Si_{1.6}$ (Z=Ni, Cu, Cr, V) compounds*, A. K. Pathak, P. Basnyat, I. Dubenko, S. Stadler, and N. Ali, J. Magn. Magn. Mater. **322**, 692 (2010).
- ²⁶*Temperature and field induced strain in polycrystalline $Ni_{50}Mn_{35}In_{15-x}Si_x$ magnetic shape memory Heusler alloys*, A. K. Pathak, I. Dubenko, S. Stadler, and N. Ali, J. Alloys. and Comps. **509**, 1106 (2011),.
- ²⁷*The Effect of Partial Substitution of Ni by Co on the Magnetic and Magnetocaloric Properties of $Ni_{50}Mn_{35}In_{15}$ Heusler alloy*, A. K. Pathak, I. Dubenko, Y. Xiong, P. W. Adams, S. Stadler, and N. Ali, J. Appl. Phys. (accepted for publication).
- ²⁸*Magnetic and Magnetocaloric Properties of $Gd_xX_2Si_3$ (X=Ni, Co) and $Ln_6Co_2Si_3$ (Ln=Pr, La)*, I. Dubenko, A. K. Pathak, S. Stadler, and N. Ali, J. Appl. Phys. (accepted for publication).

Plasmonic Photovoltaics

Harry A. Atwater

MS 128-95 Thomas J. Watson Laboratories of Applied Physics
California Institute of Technology, Pasadena, CA 91125

haa@caltech.edu

Program Scope

The goal of this program is to elucidate fundamental nanophotonic phenomena relevant to photovoltaics, including absorption, propagation, nonlinear interactions, localization and dispersion of light in complex metallodielectric structures such as plasmonic materials, and metamaterials. Over four decades, enormous effort has been devoted to photovoltaic and other light-energy conversion devices, and also in the realm of communications technology, to the study of optoelectronic devices such as lasers, waveguides, electro-optic devices, and photodetectors. However to date, there has been remarkably little interplay between scientific advances emanating from the energy conversion and communication fields. We are now at a moment when insights about the flow of light in materials can be harnessed to precisely and efficiently guide optical energy to nanostructured absorbers, enabling revolutionary advances in photovoltaic energy conversion. Previously photonic materials have been designed for applications such as optical communication where highly collimated, polarized, monochromatic, coherent light sources are utilized, so that component designs can exploit these aspects of the light source. By contrast, the solar spectrum is blackbody-like, un-polarized and sunlight has a variable angle of incidence for both global and direct illumination conditions. Therefore photonic materials for solar energy conversion must be able to accept a wide range of incidence angles, and must be useful over a broad range of wavelengths. For photovoltaics, this wavelength range usually corresponds to the absorption characteristic of light absorbing semiconductor.

Recent Progress

1. Plasmonic Light Trapping in a-Si Absorbers Exceeding the Random Texture Limit

Since the seminal statistical ray optics theory by Yablonovitch in 1982 on light trapping in solar cells, it has been widely believed in the photovoltaics community that the optimal structure for light trapping in solar cells consists of a sheet-like or film absorber with a randomly-textured surface. We have developed new type of ultrathin solar cell that utilizes a different type of light trapping structure consisting of an periodic plasmonic back reflector. For the first time, we demonstrated that a periodic nano-patterned back reflector exhibits better light trapping performance than the randomly textured substrate conventionally used for light trapping. This finding reopens the field of light trapping in photovoltaics, and will guide research towards optimal nonrandom plasmonic light trapping

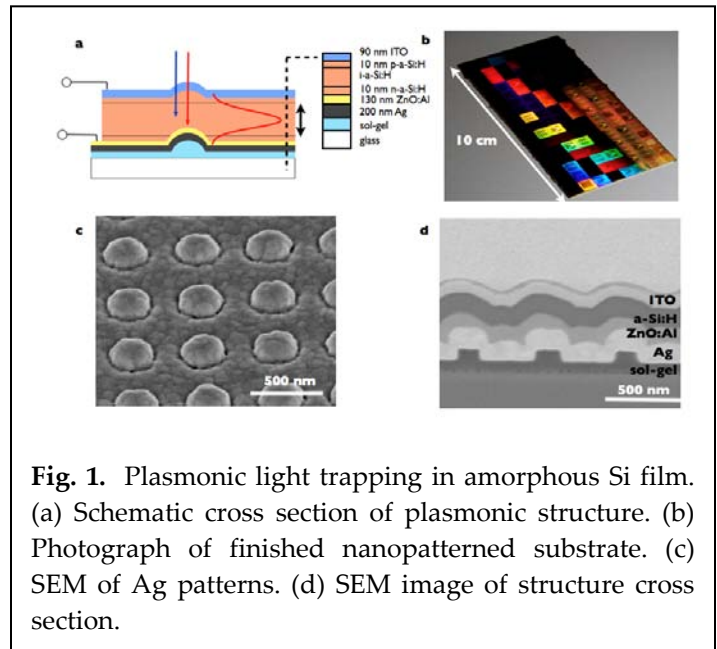


Fig. 1. Plasmonic light trapping in amorphous Si film. (a) Schematic cross section of plasmonic structure. (b) Photograph of finished nanopatterned substrate. (c) SEM of Ag patterns. (d) SEM image of structure cross section.

structures.

We have fabricated thin film amorphous silicon solar cells using periodically-engineered textured back reflectors that demonstrate for the first time efficiency enhancements due to light trapping that exceed the light-trapping enhancements for randomly textured thin film silicon layers. The recent achievement of 9.6% efficiency in 90 nm thick absorber with a 500 nm period plasmonic structure is one of the first examples of patterned plasmonic scatters showing absorption enhancement superior to traditional light-trapping techniques. Light is preferentially coupled into waveguide modes of the ultrathin semiconductor active layer of the cell, enhancing the absorption of light that would otherwise reflect from the cell. Angle-dependent photocurrent measurements are used to determine photonic dispersion relations that reveal the coupling efficiency into localized and periodic Bloch modes.

2. Sequential Scattering Theory for Plasmonic Photovoltaic Absorbers

As a method to assess periodic and randomly-textured light trapping structures, we have developed a theoretical model to assess the achievable absorption enhancements in waveguide-based cells with plasmonic scatterers, and demonstrated that the absorption enhancements in these cells can exceed the predicted maximum intensity enhancement of $4n^2$ for randomly textured cells in the ray-optics limit. This so-called “ergodic” limit assumes a randomly textured surface such that scattering is random and all possible ray optical modes are excited, and is based on a detailed balance of the light absorption and light emission. The model assumes a semi-analytical sequential scattering method, where dipole-like point scatterers are embedded in the active layer of a metal-

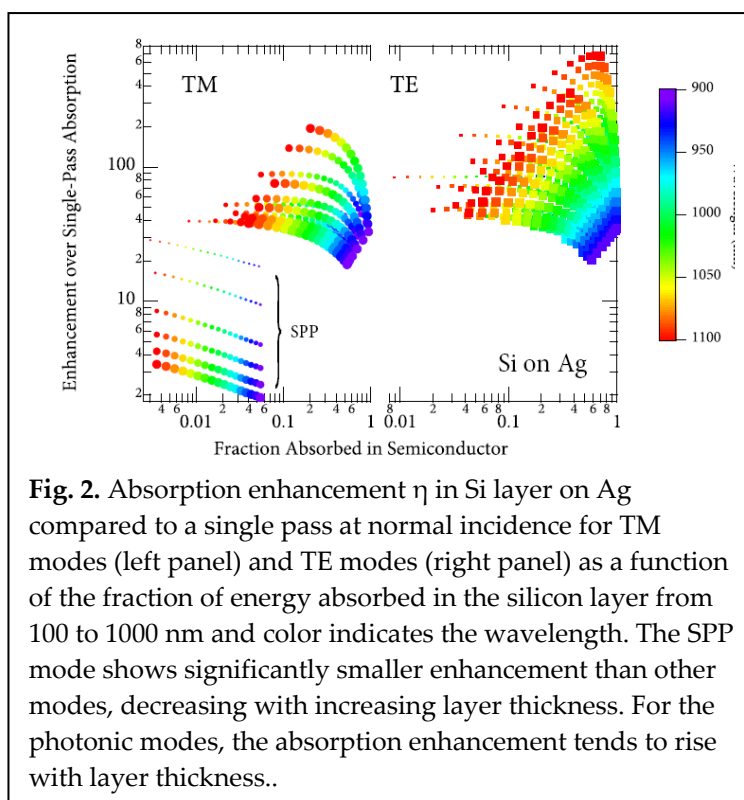


Fig. 2. Absorption enhancement η in Si layer on Ag compared to a single pass at normal incidence for TM modes (left panel) and TE modes (right panel) as a function of the fraction of energy absorbed in the silicon layer from 100 to 1000 nm and color indicates the wavelength. The SPP mode shows significantly smaller enhancement than other modes, decreasing with increasing layer thickness. For the photonic modes, the absorption enhancement tends to rise with layer thickness..

backed solar cell, and couple to waveguide modes of the structure. The subsequent scattering of guided modes from other dipoles is treated incoherently. This method assumes loss-less dipoles, but a similar effect could be achieved via nanostructured ridges on a metallic back contact.

Through systematic study of the waveguide modes and their respective absorption overlap with the semiconductor, we were able to engineer positions and spacing of scattering dipoles that allow for absorption enhancements exceeding $4n^2$. The light trapping absorption enhancement is present in weak absorbers (such as crystalline Si), but is particularly compelling for strong absorbers such as a-Si:H and GaAs. In the limit of loss-less dipoles and perfect antireflective coatings, we have found that a 100 nm thick layer of a-Si:H can absorb up to 87% of the above-bandgap incident sunlight.

3. High Efficiency Plasmonic Photovoltaic Structures

We have demonstrated via full-field electromagnetic simulations that combining plasmonic

gratings with dielectric antireflective coatings can result in optical absorption enhancements of greater than 80% in ultrathin Si absorber layers. The spatially resolved electron generation rates are determined and used to calculate the integrated current under solar illumination. Knowledge of the generation rate profile further allows us optimize the carrier collection for these cells. Simulations of ultrathin (200 nm thick) GaAs cells show that plasmonic back scattering structures can allow the cell to absorb as much of the incident light as a cell that is 1.65 times thicker. Based on these considerations, experiments are underway with GaAs heterostructures ranging in thickness from 30 nm to 1 μm .

4. Theoretical Investigation of the Voltage Enhancement in Ultrathin Solar Cells

We have performed calculations using detailed balance theory and device physics to investigate the extent to which ultra-thin solar cells can achieve higher overall efficiencies than bulk cells. The dark current is modeled as an increasing function of active layer thickness, and the effects of thinning the solar cell on both the short circuit current and the dark current are studied. Target absorption enhancements as a function of cell thickness are identified which offset the detrimental effect on the short circuit current of thinning the active layer, and the enhanced voltage due to decreased dark current is used to calculate the overall enhanced efficiency. It is found that even with modest absorption enhancements (~ 5 passes), current record solar cell efficiencies should be able to be surpassed by thinning the active layer. Also, with fully-developed light trapping (the ergodic light trapping limit), current record efficiencies may be able to be increased by over 10%. Given other work as mentioned above on sequential scattering theory, these enhancements should be achievable using novel light trapping schemes such as plasmonic scattering.

5. Local Density of Optical States in Photovoltaic Structures

The most general framework for assessing light interactions with complex nanophotonic structures is via the local density of optical (electromagnetic) states. We have begun to investigate theoretically the consequences of a modified local density of optical states (LDOS) in photovoltaic absorber layers on device performance. The Purcell effect, through which the radiative emission rate of a light emitting material is altered in an environment with a modified LDOS, can change the luminescence quantum efficiency of the emitting material. Using the known relationship between luminescence quantum efficiency and solar cell open circuit voltage, we have identified the relationship between radiative decay rate enhancement (Purcell factor) and solar cell open circuit voltage. It is shown that with reasonable Purcell factors of a few hundred, the luminescence quantum efficiency of an active layer material can be increased by 2 orders of magnitude, potentially increasing the open-circuit voltage by hundreds of millivolts. The effect is of course larger with higher Purcell factors. We have begun to calculate the LDOS for photovoltaic structures with different architectures and environments using full wave simulations. The natural presence of a metal back contact is found to dramatically alter the LDOS, and we are currently investigating the achievable photocurrent enhancement using plasmonic antennas arrays. In our group and others, plasmonic antennas have been shown to not only greatly increase the radiative decay rates of light emitting materials, but also to spatially direct the emission, which has significant consequences for their use with solar cells.

Future Plans

In the coming year, we will investigate both enhancement of light trapping and spontaneous emission rate as routes to increase the open-circuit voltage in GaAs solar cells using plasmonic light trapping schemes, dictated by the achievable local density of states in various nanophotonic structures, obtained from electromagnetic simulations. We will seek to further understand light trapping mechanisms

and identify modified plasmonic scattering arrays that maximize absorbed current and carrier collection in ultrathin active layers. Also, particular attention will be given to integrating carrier generation rates obtained from electromagnetic simulations into carrier transport simulations. This will allow us to investigate the impact of photonic material design on carrier excitation level in the semiconductor absorber layer. We will further investigate the effects of a modified local density of optical states on open-circuit voltage and identify metallodielectric structures that can be fabricated to test the predictions of theory and simulation. We will also extend our theoretical investigation of light trapping beyond the ‘ergodic’ limit using a phase-coherent version of our previously developed sequential scattering model for light-trapping.

References

1. “Special Issue on Surface Plasmon Photonics”, *IEEE Journal of Selected Topics in Quantum Electronics*, H. A. Atwater, J.R. Krenn and D.P. Tsai, editors, Vol. 14, No. 6, November/December (2008).
2. “Plasmonic Nanostructure Design for Efficient Light Coupling into Solar Cells”, Vivian E. Ferry, Luke A. Sweatlock, Domenico Pacifici, and Harry A. Atwater”, *Nano Letters*, Vol. 8 4391-4397 (2008).
3. “Universal optical transmission features in periodic and quasiperiodic hole arrays”, D. Pacifici, H.J. Lezec, L.A. Sweatlock, R.J. Walters and H.A. Atwater, *Optics Express*, **16** 9222 (2008).
4. “Are Negative Index Materials Achievable with Surface Plasmon Waveguides? A Case Study of Three Plasmonic Geometries”, Jennifer A. Dionne, Ewold Verhagen, Albert Polman, and Harry A. Atwater, *Optics Express*, Vol 16, pp. 19001-19017 (2008).
5. Plasmonic Nanoparticle Enhanced Light Absorption In GaAs Solar Cells, Keisuke Nakayama, Katsuaki Tanabe, and Harry A. Atwater, *Appl. Phys. Lett.*, 93, 121904 (2008).
6. “Plasmon-Enhanced Absorption and Photocurrent in Ultrathin GaAs Solar Cells with Metallic Nanostructures”, Katsuaki Tanabe, Keisuke Nakayama and Harry A. Atwater, Proceedings of the 31st IEEE Photovoltaic Specialists Conference, (2009).
7. “How Much Can Guided Modes Enhance Absorption in Thin Solar Cells?” Peter N. Saeta, Vivian E. Ferry, Domenico Pacifici, Jeremy N. Munday, Harry A. Atwater, *Optics Express*, **17**, 23, 20975 (2009).
8. "Improved Red-Response in Thin Film a-Si:H Solar Cells with Soft-Imprinted Plasmonic Back Reflectors," Vivian E. Ferry, Marc A. Verschuuren, Hongbo B. T. Li, Ruud E. I. Schropp, Harry A. Atwater, and Albert Polman. *Appl. Phys. Lett.*, **95**, 183503 (2009).
9. “Plasmonics for Improved Photovoltaic Devices”, Harry A. Atwater and Albert Polman, invited review, *Nature Materials* **9**, 205 - 213 (2010).
10. “Resonant Guided Wave Networks”, Eyal Feigenbaum and Harry A. Atwater, *Physical Review Letters* **104**, Article Number 147402 (2010).
11. “Design Considerations for Plasmonic Photovoltaics,” Vivian E. Ferry, Jeremy N. Munday, Harry A. Atwater, *Advanced Materials*, **22**, pp 4794-4808 (2010).
12. “Light Trapping in Ultrathin Plasmonic Solar Cells,” Vivian E. Ferry, Marc A. Verschuuren, Hongbo B. T. Li, Ewold Verhagen, Robert J. Walters, Ruud E. I. Schropp, Harry A. Atwater, Albert Polman. *Optics Express* **18**, A237 (2010).
13. “Programming Of Inhomogeneous Resonant Guided Wave Networks”, Eyal Feigenbaum, Stanley P. Burgos, and Harry A. Atwater, *Optics Express*, **18** 25584 (2010).
14. “Bending Light to Our Will”, Harry A. Atwater, *MRS Bulletin*, in press (2010).
15. “Low Loss Plasmonic Metamaterials” A. Boltasseva and Harry A. Atwater, *Science*, in press (2010).

High Performance Nano-Crystalline Oxide Fuel Cell Materials: Defects, Structures, Interfaces, Transport, and Electrochemistry

S.A. Barnett, D. Ellis, L.D. Marks, T.O. Mason, K. Poepelmeier, P.W. Voorhees

Northwestern University

2220 Campus Drive

Evanston, IL 60208

Phone: 847 491 2447; FAX: 847 491 7820

s-barnett@northwestern.edu

DOE Program Officer: Refik Kortan

301/903-3308; refik.kortan@science.doe.gov

Program Scope

Solid oxide cells (SOCs) are versatile electrochemical devices with applications including clean efficient electricity generation, chemical production,^{2,3} renewable fuel production,^{4,6} and electricity storage.¹ Solid oxide fuel cells are nearing commercial viability, but fundamental challenges remain, especially reducing operating temperature and improving long-term durability. Operating temperature is important not only for making the technology viable, but for enabling new uses such as transportation and portable generation. SOC's can also be used to complement renewable sources by providing a means for storing energy as a chemical fuel such as hydrogen or methane.

This project aims to parlay our improving understanding of the enhanced electronic and ionic transport properties of nano-scale oxides and surfaces to address electrode performance and durability issues that limit the utility of SOC's. The focus is on the fundamental problems limiting reduced-temperature SOC's. The scientific focus is on the dynamics of mixed nano- and micron-scale structures in electrochemical cells. In prior work, some of which is summarized below, new methods for fabrication and characterization of novel SOC materials have been developed. In addition, we are working towards a fundamental understanding of transport properties, polarization behavior, and degradation phenomena.

Recent Progress

The stability of infiltrated cathodes has been studied for the first time. Figure 1 shows how the polarization resistance of LSCF-GDC cathodes, measured at 600°C, increases with time at temperatures

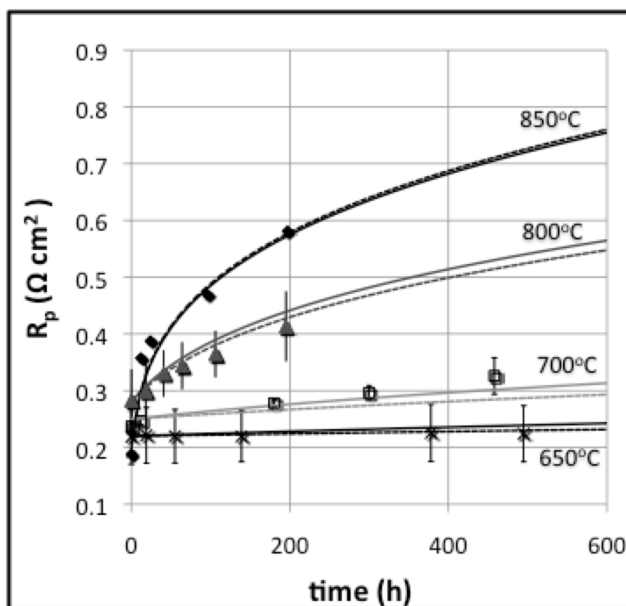


Figure 1. Measured polarization resistance versus time measured at 600°C, for LSCF-GDC cathodes kept at elevated temperatures in order to accelerate degradation. Also shown are fits using our coarsening model.

high enough to accelerate degradation. The data were fitted based on a infiltrated cathode electrochemical model combined with a power-law coarsening model. The predicted LSCF coarsening was corroborated using SEM images. Based on the model, the cathode performance over long times at operating temperature can be predicted; the model predicts a 50% increase in resistance for a cathode maintained at 600°C for 40,000 h. The model also shows that desired polarization resistance and long-term stability can be designed into the cathode by choosing the appropriate LSCF starting particle size and operating temperature.

A method for improving stability has also been demonstrated where LSCF and GDC are both infiltrated into a GDC scaffold. For example, R_p for the new co-infiltrated cathode increased only from 0.2 to 0.27 Ωcm^2 after 100 h at 850°C, compared to an increase from 0.2 to 0.47 Ωcm^2 for the cathode with only LSCF infiltrated. It appears that the nano-particles of the more stable GDC phase mingle with LSCF nano-particles, hindering coarsening. These initial results suggest that engineering of the cathode nano-structure is a fruitful area for future studies.

We have also explored novel oxide anode materials where catalytic nano-particles nucleate during SOC operation and greatly enhance electrochemical kinetics. While some of the anodes are reasonably stable, initial life tests suggest that nano-particle coarsening will eventually degrade performance. Thus, recent results, showing that the anode performance can be regenerated via a “redox cycle,” are quite exciting. After an anode has been operated for some time, exposing the hot anode to air for a short period of time recovers the optimal anode performance. Figure 2 shows a series of TEM images illustrating the structural changes occurring in the anodes: Pd-substituted $(\text{La}_{0.8}\text{Sr}_{0.2})\text{CrO}_3$ in this case. Panel (a) shows an as-prepared oxide particle, while (b) shows the formation of Pd nano-particles on the oxide surface after initial exposure to the reducing fuel. Panel (c) shows a particle after exposure to air – the nano-particles have disappeared, apparently re-dissolving into the oxide. Panel (d) shows a particle after a second exposure to fuel, where the Pd nano-particles have re-nucleated. Thus, the anode performance regeneration is a direct result of re-nucleation of small nano-particles after redox cycles.

Furthermore, these anodes exhibit “adaptive” behavior. That is, they respond differently at different operating temperatures, *e.g.*, providing similar polarization resistance at 600°C as at 800°C – this is very different than other fuel cell electrodes, where polarization resistance always increases rapidly with decreasing temperature. Studies are underway to explore how the nano-structure evolves differently at different temperatures to account for this surprising result.

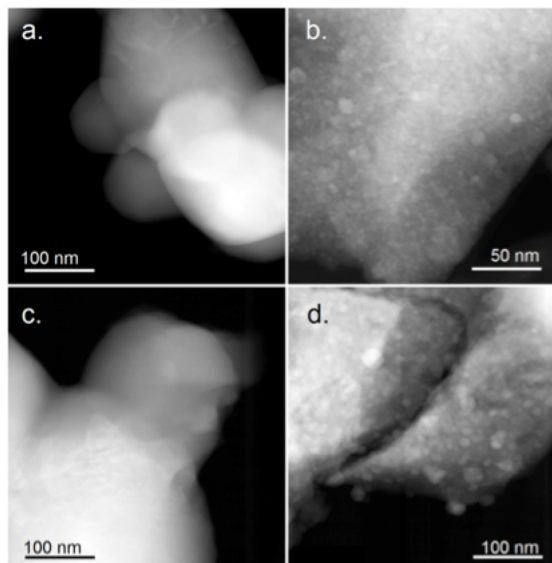


Figure 2. STEM micrographs of Pd-doped chromite powder as prepared (a), reduced for 1 h at 800°C (b), then exposed to air for 1 hr at 800°C (b), and then reduced again for 12 h at 800°C (d).

In tandem with this experimental work, progress has been made on understanding the nano-particle structural evolution using phase-field simulations. Figure 3 is an example of the predictions, where the large particle represents the lanthanum chromite, which has been supersaturated with an electrocatalyst solute, in this case Ru. Under anode operating conditions, the Ru diffuses out and forms particles (shown in white here) that act as catalysts for the anode reaction, as discussed above. The colors represent the Ru solute concentration.

For the phase field calculation, a ternary alloy model is used, where component A is the lanthanum chromite, component B is the electrocatalyst and component C is vacancies. It is assumed the Ru travels via a vacancy diffusion mechanism. The lanthanum chromite component is assumed to be immobile, such that the moving species are vacancies and Ru.

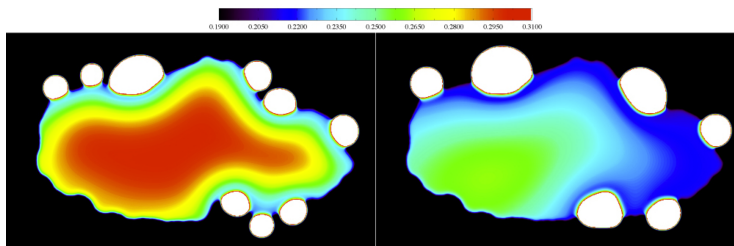


Figure 3. Simulation results of a large oxide particle on which smaller metallic Ru particles (white) grow over time. The left panel of the figure shows an early time; the right shows a later time. The colors show the Ru concentration within the oxide.

The left panel of the figure shows an early time, with a high supersaturation of Ru still in the bulk of the lanthanum chromite. On the right, at a later time, much of the Ru has diffused out causing the particles on the surface to grow. Additionally, coarsening can be seen as the smaller particles have disappeared. In this particular case both surface and bulk diffusion of the Ru were allowed.

Future Plans

Much of the work described above will be continued in the short term. The combined experimental/theoretical approach to understanding nano-structure evolution, and its impact on electrochemical performance, will be continued, with an emphasis on structures/materials that provide improved stability or regenerative behavior. We plan to study the effect of nano-structure on intrinsic transport properties and manipulation of micro/nano-structure to improve low-temperature electrode kinetics and reduce degradation over time.

Publications of DoE-Sponsored Research (in the past year)

1. J. M. Haag, D. M. Bierschenk, S. A. Barnett, and K. R. Poeppelmeier, “Structural, Chemical, and Electrochemical Characteristics of $\text{LaSr}_2\text{Fe}_2\text{CrO}_{9-\delta}$ -Based Solid Oxide Fuel Cell Anodes”, *Solid State Ionics*, submitted (2011). Full support by this grant.
2. Megna Shah, S.A. Barnett, and P.W. Voorhees, Time-Dependent Performance Changes in LSCF-Infiltrated SOFC Cathodes: The Role of Nano-Particle Coarsening, *Solid State Ionics*, submitted. Full support by this grant.
3. DM Bierschenk; E Potter-Nelson; C Hoel; Y Liao; LD Marks; KR Poeppelmeier; SA Barnett, “Pd-substituted $(\text{La},\text{Sr})\text{CrO}_3\text{-Ce}_{0.9}\text{Gd}_{0.1}\text{O}_2$ Solid Oxide Fuel Cell Anodes Exhibiting Regenerative Behavior, *J. Power Sources*, in press. Full support by grant.

4. DM Bierschenk, JR Wilson, and SA Barnett, "High Efficiency Electrical Energy Storage Using a Methane-Oxygen Solid Oxide Cell" *Energy & Environmental Science*, in press. Partial support by this grant.
5. M. Shah, P.W. Voorhees, and S.A. Barnett, "Stability and Performance of LSCF-infiltrated SOFC Cathodes: Effect of Nano-Particle Coarsening", *ECS Trans.* Vol. 35, "Solid Oxide Fuel Cells 12 (SOFC-XII)", in press (2011). Full support by this grant.
6. David Bierschenk, James Wilson, Elizabeth Miller, Emma Dutton, and Scott Barnett, "A Proposed Method for High Efficiency Electrical Energy Storage Using Solid Oxide Cells," *ECS Transactions*, Vol. 35, "Solid Oxide Fuel Cells 12 (SOFC-XII)", in press (2011). Partial support by this grant.
7. P.D. Dalach, D.E. Ellis, and A. Van de Walle, "First Principles Thermodynamic Modeling of Atomic Ordering in Ytria-Stabilized Zirconia," *Phys. Rev.* **B82**, 144117 (2010). Full support by this grant.
8. J. M. Haag, Scott A. Barnett, James W. Richardson Jr., Kenneth R. Poeppelmeier, "Structural and Chemical Evolution of the SOFC Anode $\text{La}_{0.70}\text{Sr}_{0.30}\text{Fe}_{0.70}\text{Cr}_{0.30}\text{O}_{3-\delta}$ by Reduction and Oxidation: An In-Situ Neutron Diffraction Study," *Chemistry of Materials*. 22 (2010) 3283-3289. Full support by this grant.
9. M. Gong, D. Bierschenk, J. M. Haag, K. R. Poeppelmeier, S. A. Barnett, C. Xu, J. W. Zondlo, X. Liu, "Degradation of $\text{LaSr}_2\text{Fe}_2\text{CrO}_{9-\delta}$ Solid Oxide Fuel Cell Anodes in Phosphine-Containing Fuels," *Journal of Power Sources*, 195, 4013-4021 (2010). Partial support by this grant.
10. N. H. Perry and T. O. Mason, "Grain Core and Grain Boundary Electrical/Dielectric Properties of Ytria-Doped Tetragonal Zirconia Polycrystal (TZP) Nanoceramics," *Solid State Ionics*, 181 (2010) 276-284. Full support by this grant.
11. T.C. Yeh, N.H. Perry, and T.O. Mason, "Nano-Grain Composite Model Studies of Nanocrystalline Gadolinia-Doped Ceria," *J. Am. Ceram. Soc.*, Published online: 10 NOV 2010 DOI: 10.1111/j.1551-2916.2010.04200.x. Full support by this grant.
12. N. H. Perry, T. C. Yeh, and T. O. Mason, "Temperature Dependence of Effective Grain Core/Single Crystal Dielectric Constants for Acceptor-Doped Oxygen Ion Conductors," *J. Am. Ceram. Soc.*, Published online: 29 SEP 2010 DOI: 10.1111/j.1551-2916.2010.04093.x. Full support by this grant.
13. D. L. Proffit, G. -R. Bai, D. D. Fong, T. T. Fister, S. O. Hruszkewycz, M. J. Highland, P. M. Baldo, P. H. Fuoss, T. O. Mason, and J. A. Eastman, "Phase stabilization of $\delta\text{-Bi}_2\text{O}_3$ nanostructures by epitaxial growth onto single crystal SrTiO_3 or DyScO_3 substrates, *Appl. Phys. Lett.*, 96 (2010) art. No. 021905. Partial support by this grant.
14. Lj. Miljacic and D.E. Ellis, "Radial Template Approach for Accurate Density Representation in Computational Quantum Theory", *J. Comp. Chem.* **31**, 1486 (2010). Partial support by this grant.
15. W. Kobsiriphat, B.D. Madsen, Y. Wang, M. Shah, L.D. Marks and S.A. Barnett, "Nickel- and Ruthenium-Doped Lanthanum Chromite Anodes: Effects of Nanoscale Metal Precipitation on Solid Oxide Fuel Cell Performance," *Journal of the Electrochemical Society* **157** (2010) B279-B284. Full support by this grant.
16. Nicholas, J. D. and Barnett, S. A., "Measurements and Modeling of $\text{Sm}_{0.5}\text{Sr}_{0.5}\text{CoO}_{3-x}-\text{Ce}_{0.9}\text{Gd}_{0.1}\text{O}_{1.95}$ SOFC Cathodes Produced Using Infiltrate Solution Additives," *Journal of the Electrochemical Society*, (2010), 157, B536. Full support by this grant.

Poster title: The factors that influence graphene growth on metal surfaces

N.C. Bartelt, E. Starodub, P.J. Feibelman, S. Nie and K.F. McCarty
Mail Stop 9161
Sandia National Laboratories
Livermore, CA 94550
Email: bartelt@sandia.gov

Program title: Nanometer-scale Surface and Interface Phenomena

Subtask title: Collective Phenomena in Surface Dynamics

Subtask scope:

The subject of this poster is a relatively recent focus in the Collective Phenomena in Surface Dynamics task of the Nanometer-scale Surface and Interface Phenomena program at Sandia National Laboratories. This task's goal is to quantify the collective processes that govern the surface structures and morphologies of functional materials. Using scanning-tunneling and low-energy electron microscopies, we measure, often in real-time, the time evolution of surface structure on nanometer length scales. We develop equations of motion that account for the observed time dependences precisely, and relate their parameters to the atomic processes. Often revealing unanticipated surface dynamical mechanisms, this general approach has been a rich source of insight into materials behavior. We have used it to determine quantitatively the forces that stabilize self-assembling patterns, to identify the kinetic pathways that promote film instability, and to show that unexpected diffusion processes, such as cluster diffusion and bulk/surface mass exchange, can guide materials growth. We give preference to studying systems important to energy-related technologies, whose behavior begs for new insight into basic dynamical mechanisms. Where necessary and timely, we develop new microscopic experimental techniques and theoretical models. We are planning new studies of: 1) nanoscale-pattern formation, including metal clusters on graphene, stripes on boron-doped Si, and water films on metals; 2) cooperative mechanisms of material growth, including those that cause graphene to grow by cluster addition; and 3) the stability of thin films, including the amorphous-to-crystalline ice conversion, and the dewetting of metal films on solid-state electrolytes.

Poster Abstract

Our goal has been to develop a quantitative understanding of graphene growth through a close collaboration between theory and experiment. To quantify the growth mechanisms, we have been pioneering a new technique for accurate, sensitive measurements of surface adsorbate concentrations. The method is based on measuring changes in electron reflectivity from a surface. When performed in a LEEM instrument, our method gives a spatial map of adsorbate concentration. We validated our approach studying Ag/Au adatoms on W(110) [1].

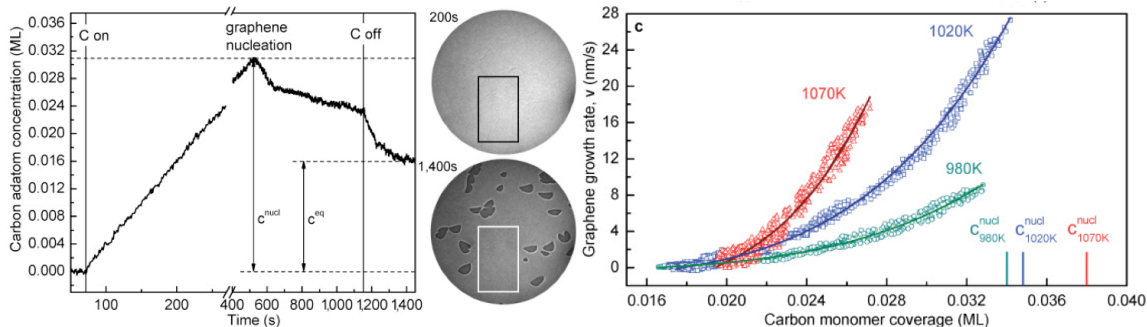


Fig. 1. Left: C adatom concentration during graphene nucleation and growth measured from electron reflectivity. Middle: LEEM images ($46 \mu\text{m}$ field-of-view) taken at 200s and 1400s. c^{nucl} and c^{eq} are the monomer concentrations needed to nucleate graphene and be in equilibrium with graphene, respectively. Right: Non-linear dependence of island growth rate on C monomer concentration.

Figure 1 shows how carbon adatom concentrations can be measured while simultaneously imaging graphene as it nucleates and grows on Ru(0001) [2]. We determined the relationship between the rate at which a graphene step edge advances and the adatom concentration. Such detailed knowledge has occasionally been obtained in crystal growth from solutions, but never in vapor-phase growth. We find that graphene's growth rate is not the linear function of the adatom concentration expected from addition of individual C atoms. Instead, a statistical-mechanical model shows that graphene adds C clusters, most likely of five C atoms. This mechanism is in striking contrast to all known cases of metal and semiconductor growth. We also calculated the structure and energetics of a graphene moiré on Ru(0001), and, to explain its growth energetics, the height and binding energy vs. position of carbon adatoms. The comparison helped explain why clusters of five C atoms must form before graphene can nucleate. We have extended this work by showing that the same cluster-addition kinetics occur for three different C sources, vapor deposited C [2], ethylene [3], and segregating C [4]. Furthermore, we find the same cluster mechanism governs the etching of graphene [5].

Figure 2 provides insight into the origins of the cluster-addition mechanism. We see two possible explanations as to why adatoms cannot attach but clusters can. The first emphasizes the role of substrate: first-principles calculations show that C adatoms are tightly bound to Ru, while graphene sheets are bound loosely. Thus the large height difference, over 2 \AA , on the surface between the adatoms and sheets may create a large energy barrier for adatoms to attach to graphene. The second possibility emphasizes bonding *within* the graphene sheet. As Fig. 2 shows, adding five C atoms adds two new six-member rings to a compact graphene island. A speculation is that adding fewer C atoms does not attach a stable growth unit to the island.

These two models of graphene growth imply different systematics. In the first, the energy barrier to single C atom attachment might not exist if the C adatoms and sheets have similar bonding strengths to the substrate. In the scheme where the cluster addition

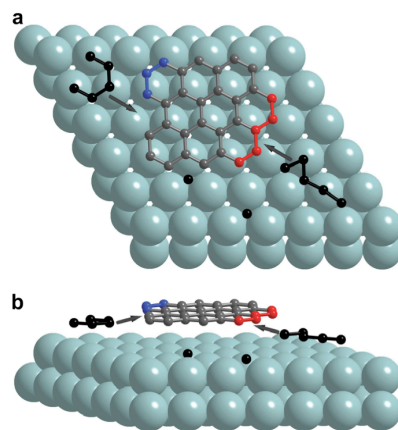


Fig. 2. Schematic illustration of graphene growth from C clusters.

originates from bonding within the graphene sheets, then the cluster-addition kinetics should occur independent of the substrate, even, perhaps, for unsupported graphene sheets.

We have investigated the origin and generality of the cluster-addition mechanism in two ways. First, by studying the growth kinetics of different rotational domains on a single substrate. Second, by comparing growth kinetics on different metal surfaces. Figure 3 shows results analyzing the detailed kinetics of two rotational variants on Ir(111). One variant, labeled R0, has the same cluster-addition kinetics as graphene on Ru(0001). The other variant, labeled R30, has a different dependence on supersaturation. The dependence of growth kinetics on graphene orientation suggests that cluster addition (not formation) causes the cluster-addition kinetics.

Regarding the substrate's role, first-principles calculations show C is strongly bound to the transition metals Ni, Pd, Ru, and Ir. However, the height of the graphene sheet likely varies because of differing lattice matching between the metal mesh and graphene. For example graphene is not well latticed-matched with Pd, Ir and Ru; e.g., 12 C atoms repeat over 11 Ru atoms, which causes the graphene to be corrugated. In contrast, graphene on Ni(111) is almost perfectly latticed matched. While the degree of lattice matching may strongly influence the graphene sheet/substrate separation, the values are either unknown or are controversial for Ni, both experimentally and theoretically. Using first-principles calculations and our ability to determine atomic structure using selective-area LEED and dynamical I(V) analysis [6,7], we will determine the separation between graphene and Ni(111). Using our powerful ability to measure

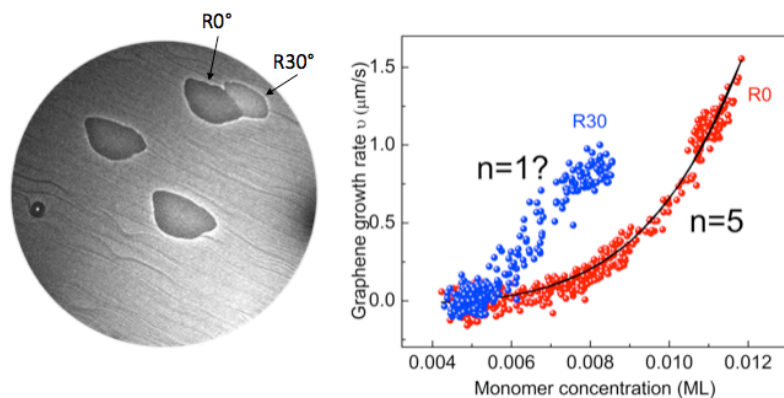


Fig. 3. Left: LEEM image showing R0 and R30 rotational variants of Ir(111). 46 μm field-of-view. Right: Linear and non-linear growth kinetics from R30 and R0, respectively.

local adatom concentrations and graphene growth rates simultaneously [1,2], we will determine if there is a barrier to adatom attachment and whether graphene grows by cluster addition on Ni and Pd surfaces. Another question to be answered is whether graphene grows from a dilute adatom gas in the latter two substrates, as it does on Ir and Ru. With the combined experimental and theoretical characterization, we should have enough information to lay to rest the origin and generality of the cluster-addition kinetics.

Currently one of the most promising methods of growing large areas of graphene is by CVD on inexpensive copper foils. We have been able to use LEEM to characterize graphene growth on such foils [8].

Many of the same issues that arise for the growth of the first layer of graphene are also relevant to multilayer growth. It is generally believed that multilayers of graphene on metal surfaces grow by nucleating between the metal and the first layer of graphene. This is because deposited carbon does not readily adsorb on the graphene surface. Consistent

with this idea, we have found that new layers only form underneath the initial graphene layer on Ru and Ir during direct elemental deposition or by exposure to ethylene [2]. Thus growth would seem to be most easily induced by bulk segregation to the interface under the graphene, and again one needs to know how a tightly bound carbon adatom or interstitial carbon atom attaches to a growing graphene sheet. Thus, we propose to apply the same techniques to multilayers as we used to study the first layer, and to determine if a similarly large barrier impedes direct attachment. Data showing it is possible to grow multilayers by bulk segregation is presented in Fig. 4. In this example, an Ir crystal was loaded with C and then cooled, producing multilayers. The thickness of each region of the graphite marked on the image, was determined by examining the energy dependence of the electron reflectivity.

Our analysis suggests that the second graphene layers on Pd and Ir can grow with in-plane orientations different from the first layer. Thus, these graphene stacks are possibly new types of carbon. The relative orientation of the graphene layers is a critical issue in electronics applications as Bernal-like AB layer stacking destroys graphene's unique band structure while other stackings do not.

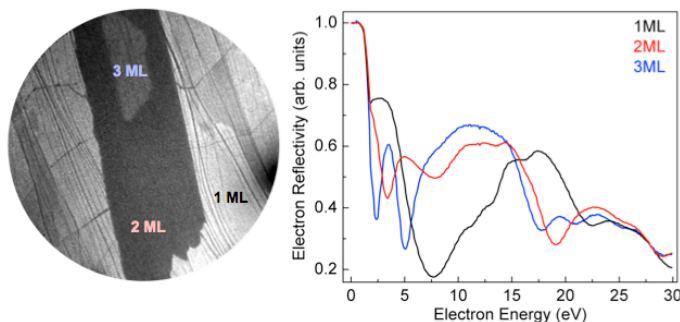


Fig. 4. Left: LEEM image showing 1-3 layers of graphene on Ir(111), 14 μm field-of-view. Right: Electron reflectivity establishing layer thicknesses.

References:

1. de la Figuera, J., Bartelt, N. C. & McCarty, K. F. Electron reflectivity measurements of Ag adatom concentrations on W(110). *Surf. Sci.* **600**, 4062 (2006).
2. Loginova, E., Bartelt, N. C., Feibelman, P. J. & McCarty, K. F. Evidence for graphene growth by cluster attachment. *New J. Phys.* **10**, 093026 (2008).
3. Loginova, E., Bartelt, N. C., Feibelman, P. J. & McCarty, K. F. Factors influencing graphene growth on metal surfaces. *New J. Phys.* **11**, 063046 (2009).
4. McCarty, K. F., Feibelman, P. J., Loginova, E. & Bartelt, N. C. Kinetics and thermodynamics of carbon segregation and graphene growth on Ru(0001). *Carbon* **47**, 1806-1813 (2009).
5. Starodub, E., Bartelt, N. C. & McCarty, K. F. Oxidation of graphene on metals. *J. Phys. Chem. C* **114**, 5134-5140 (2010).
6. de la Figuera, J., Puerta, J. M., Cerda, J. I., El Gabaly, F. & McCarty, K. F. Determining the structure of Ru(0001) from low-energy electron diffraction of a single terrace. *Surf. Sci.* **600**, L105-109 (2006).
7. Hannon, J. B., Sun, J., Pohl, K. & Kellogg, G. L. Origins of nanoscale heterogeneity in ultrathin films. *Phys. Rev. Lett.* **96**, 246103 (2006).
8. Wofford, J. M., Nie, S., McCarty, K. F., Bartelt, N. C. & Dubon, O. D., Graphene islands on Cu Foils: The interplay between shape, orientation, and defects. *Nanoletters* **10**, 4890-4896 (2010).

Theory and Modeling of Materials for Hydrogen Storage

Gerbrand Ceder

77 Massachusetts Avenue 13-5056, Cambridge, MA 02139

gceder@mit.edu

The storage of hydrogen is one of the most significant remaining challenges to the development of hydrogen as a viable fuel. Hydrogen storage in solid-state materials has been widely investigated, but it has proven difficult to find a material that stores and releases hydrogen in the target temperature range (-40 °C to 85 °C) [1] for automotive fuel cells. Sodium alanate (NaAlH_4) has a theoretical gravimetric storage capacity of 5.6%, but bulk sodium alanate releases hydrogen at temperatures that are above this range. However for 2-10 nm sodium alanate nanoparticles the peak hydrogen desorption temperature is 70 °C [2]. To better understand the reasons for low-temperature hydrogen release from small particles, we have completed a computational study of hydrogen release from sodium alanate nanoparticles [3]. Using density functional theory (DFT) [4] and the cluster expansion method [5], we were able to predict the ground-state energies and particle shapes for nanoparticles of sodium alanate and its decomposition products. Our results reveal low-energy surfaces that may be important for reaction kinetics as well as a possible explanation for why hydrogen release occurs at a lower temperature from nanoparticles than it does from bulk sodium alanate.

To calculate the energy of a nanoparticle, it is first necessary to determine the particle shape. A common method for calculating equilibrium shapes of crystal particles is the Wulff construction [6], in which the shape of the particle is determined from the relative surface energies of the low-energy surfaces. We have applied an alternative approach, based on the

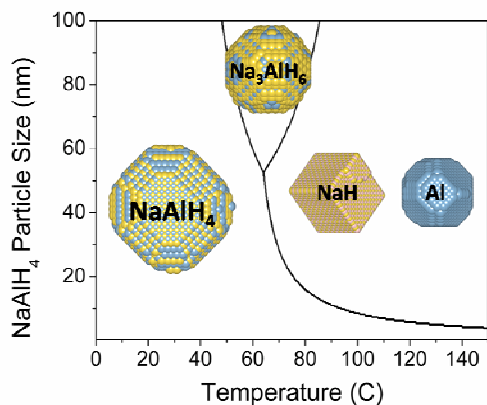


Figure 1 The predicted stable phases of sodium alanate nanoparticles as a function of temperature and particle size. As the particle size is decreased, the intermediate phase (Na_3AlH_6) becomes thermodynamically unstable, allowing NaAlH_4 to decompose in one step directly to NaH , Al , and H_2 .

cluster expansion method, that requires no prior knowledge of the low-energy surfaces and incorporates vertex and edge effects that may be important for small particles. This approach enabled us to predict from first principles the low-energy surfaces of sodium alanate and its decomposition products, including surfaces that had not been considered as low-energy in previous studies. These surfaces may play an important role in the kinetics of hydrogen storage and release.

Using the cluster expansion method, we predicted the size-dependent ground-state energies of sodium alanate and its decomposition products. By combining these results with bulk free energy equations derived from experiments [7], we were able to evaluate the relative stability of the different nanoparticles as a function of particle size (Figure 1). Our results suggest an interesting

explanation for the reduced temperature of hydrogen release from sodium alanate nanoparticles. Bulk sodium alanate is known to decompose in a two-step process, but we predict that for small particles the formation of the intermediate phase becomes thermodynamically unfavorable and one-step decomposition occurs at temperatures below 70 °C (Figure 1). In addition to providing insight into how particle size affects the release of hydrogen from sodium alanate, these results are an illustrative example of how it is possible to dramatically alter the mechanism and rate of important solid-state chemical reactions by tailoring particle size. Future work will include investigations of size effects on phase stability for other materials.

In addition to our work on sodium alanate, we have published a paper on a new low-energy structure for lithium imide that is consistent with experimental observations [8]. This structure consists of a complicated 96-atom unit cell, and our calculations suggest that at elevated temperatures lithium may move readily between different sites in the structure. These results help explain the rapid kinetics for hydrogen storage in lithium imide and provide a foundation for future computational research on this material.

1. *Hydrogen, Fuel Cells, & Infrastructure Technology Program Multi-Year Research, Development and Demonstration Plan*. 2009, United States Department of Energy.
2. Balde, C.P., et al., *Sodium alanate nanoparticles - Linking size to hydrogen storage properties*. Journal of the American Chemical Society, 2008. **130**(21): p. 6761-6765.
3. Mueller, T. and G. Ceder, *Effect of Particle Size on Hydrogen Release from Sodium Alanate Nanoparticles*. ACS Nano, 2010. **4**(10): p. 5647-5656.
4. Hohenberg, P. and W. Kohn, Phys. Rev., 1964. **136**: p. 864.
5. Sanchez, J.M., F. Ducastelle, and D. Gratias, *Generalized cluster description of multicomponent systems*. Physica, 1984. **128A**: p. 334-350.
6. Wulff, G., *On the question of the rate of growth and dissolution of crystal surfaces*. Zeitschrift fuer Kristallographie und Mineralogie, 1901. **34**: p. 449-530.
7. Lee, B.M., et al., *Thermodynamic assessment of the NaH <-> Na₃AlH₆ <-> NaAlH₄ hydride system*. Journal of Alloys and Compounds, 2006. **424**(1-2): p. 370-375.
8. Mueller, T. and G. Ceder, *Ab initio study of the low-temperature phases of lithium imide*. Physical Review B, 2010. **82**(17).

Program Title: **Near-field Thermal Radiation at Extreme Separations**
 Principal Investigator: Gang Chen
 Institution: Massachusetts Institute of Technology
 Address: 77 Massachusetts Ave., Room 3-260, Cambridge, MA 02139
 DoE Grant Number: DE-FG02-02ER45977
 Email: gchen2@mit.edu

Program Scope

This project aims to investigate both experimentally and theoretically heat transfer between two closely spaced objects, focusing on separation distances ranging from physical contact to tens of nanometers. In the past the PI has succeeded in the past in measuring the near-field radiative heat transfer between a sphere and a flat plate using a bi-layer atomic force microscope (AFM) cantilever and was able to demonstrate that near-field radiative heat transfer can be several orders of magnitude higher than what Planck’s blackbody radiation law predicted at separation gaps of tens of nanometers. In this project the technique will be further refined and used to carry out heat transfer studies between two surfaces at extremely small separations, from physical contact to tens of nanometers. The experiments will shed light on fundamentally important phenomena when the heat transfer mode changes from conduction to radiation.

Recent Progress

1) Surface-Phonon Polaritons

We have studied the influence of surface phonon-polaritons on thermal radiation. Phono-polaritons are special electromagnetic modes existing in polar materials originating from the coupling of photons to transverse optical phonons. Figure 1 shows the dispersion of bulk phonon polaritons and surface-phonon polaritons. Inside the bulk material, two branches of phonon-polaritons exist: the lower branch behaves more phonon-like while the upper branch behaves more photon-like. In between the transverse optical (TO) and longitudinal optical (LO) phonons, no bulk phonon-polaritons are allowed as the dielectric constant is negative. However a non-propagating surface electromagnetic wave may arise in this frequency range that decays exponentially on both sides of the surface. These are the surface-phonon polaritons.

2) Near-Field Thermal Radiation between a Sphere and a Flat Plate

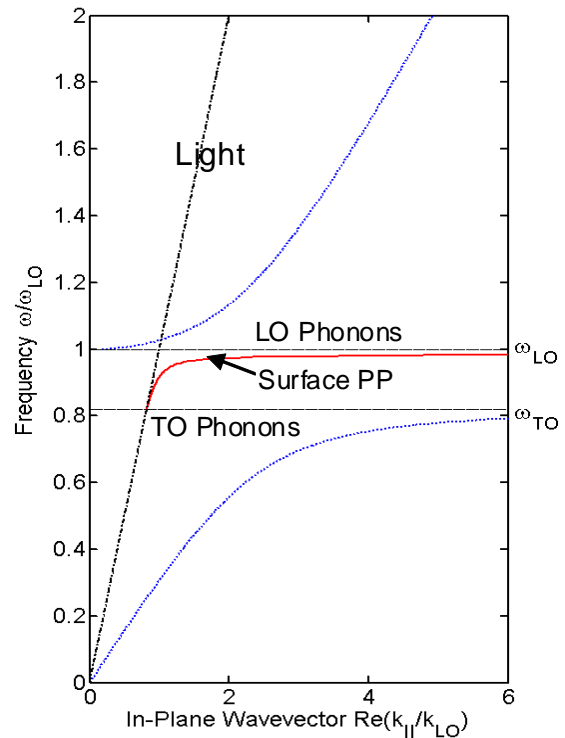


Figure 1 Dispersion showing that surface phonon polaritons lie between transverse and longitudinal optical phonons.

We developed a sensitive experimental technique to measure near-field radiation heat transfer between a sphere and plate. Our experimental setup uses a bi-layer cantilevers traditionally used in atomic force microscopes. The technique has a power resolution of around ~ 10 pW and a temperature sensitivity of 10^{-5} K. To measure the predicted thermal conductance in the range of 10^{-11} W/K at a temperature difference of 10 K, the power transferred will be 100 pW, which is well in the sensitivity range of the setup. Our experimental configuration is illustrated in Fig. 2a and 2b. A SiO_2 sphere is attached to

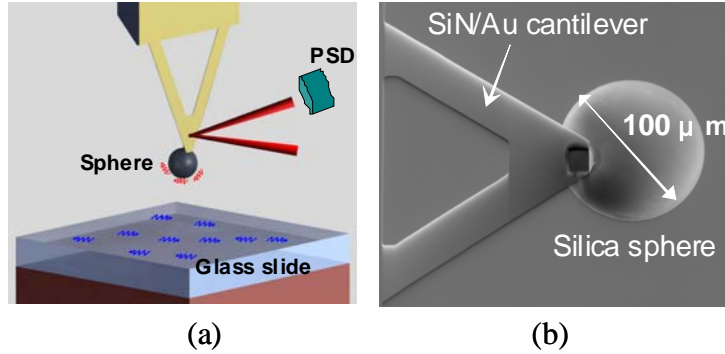


Figure 2 (a) Illustration of the sphere-plate experiment: laser heats up a bi-layer cantilever with a sphere attached at the end. As the cantilever approaches the surface, near-field radiation heat transfer leads to a temperature change of the cantilever, which is measured by the position sensitive detector (PSD) through the bending of the cantilever due to thermal expansion mismatch of the two layers. (b) A SEM micrograph of a silica sphere attached to the cantilever.

a bi-layer cantilever which is oriented perpendicular to a surface. The cantilever is heated by a laser, which also serves to measure its bending using a position sensitive detector (PSD). The distance-deflection relationship can be converted into a distance-conductance relationship. We developed a method to calibrate the thermal conductance of bi-layer cantilevers, and reported first experimental data in 2008 using a mechanical step motor with a distance uncertainty of 100 nm.

Following the initial success, we improved the motion control system by replacing the mechanical step motor by a piezoelectric motor and carried out near-field heat transfer experiments between a glass sphere and

different substrates: glass, silicon and gold. Past modeling suggests that radiation exchange between the two glass surfaces should be much higher than that between glass-silicon and glass-gold because both sides support surface phonon polaritons in infra-red frequencies which can couple and enhance heat transfer. Our experimental results indeed confirm the predicted trends, as shown in Fig. 3a. Both, our experiment and a follow-up work by Greffet *et al.* are limited to sphere-plate separations larger than 30 nm. In the meantime we continue to improve our experimental setup. We are now able to extract experimental data for sphere-plate separations at

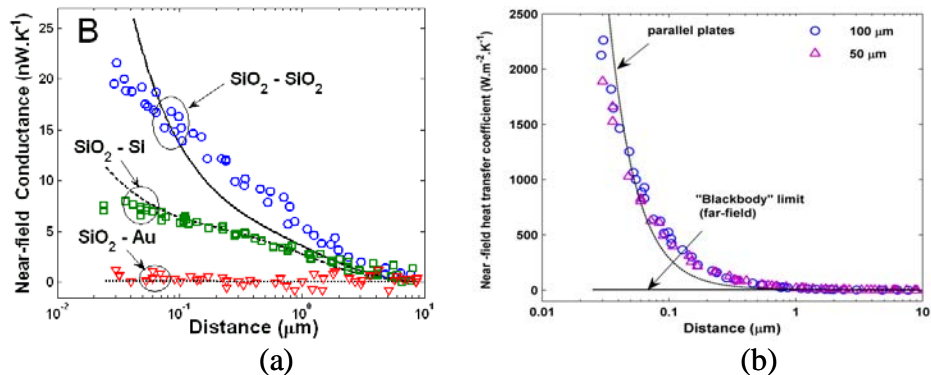


Figure 3 (a) Measured near-field thermal radiation conductance between a glass sphere and different substrates as a function of their separation, and (b) conversion of experimental results to heat transfer coefficient between two parallel plates based on the proximity force approximation (FPA). Theory is based on Rytov's fluctuating electrodynamics approach, together with the PFA.¹

even smaller distances. We hasten to point out though that there remain some uncertainties concerning sphere-plate separation distances because of surface roughnesses and precise contact point determination. Preliminary experimental data in Fig. 4 is nonetheless quite exciting. It suggests that conductance plateaus rather than becoming divergent as current theory predicts. These new experimental results call for more in-depth theoretical development.

3) Near-Field Thermal Radiation between Two Parallel Plates

In addition to the sphere-plate configuration we have also reported experimental results between two parallel plates. The two parallel plates consist of quartz optical flats. Glass spheres with a nominal diameter of 1 micron are used as spacer in this case. The glass spheres are diluted and sparsely placed at three positions on one optical flat. A second flat is then placed on top of the spheres. It is difficult though to push this configuration to smaller separation gaps because submicron particle residuals on the surface can create thermal shorts and prevent closer separation. In comparison, the sphere-plate geometry is a much more practical and precise approach and we have stopped pursuing the parallel-plate experiments.

Future Plans

Experimental Studies

Our proposed experimental studies include: (1) design and fabrication of a new type of bi-material cantilevers suitable for the investigation of the transition regime between heat conduction and thermal radiation, and (2) experimental investigations on near-field radiative heat transfer between a sphere and a flat plate at extremely small separation distances.

(1) Design and Fabrication of Thermal-Mechanical Bi-Arm Cantilever. We have developed the bi-layer cantilever approach for measuring near-field radiative heat transfer between a sphere and a plate. However, it is difficult to extend the current experimental technique to study heat transfer when the sphere is in contact with the plate, because the cantilever bending is mechanically constrained. We are designing a new type of cantilever which can do what can be used to measure both heat transfer and temperatures of two objects separated down to a nanometer or smaller.

(2) Sphere-Flat Plate Experiments. We shall use the proposed cantilever to study systematically radiation heat transfer between a flat-plate and a sphere. The first step of the experiment is to develop a calibration method such that the thermal conductance of the mechanical arm can be calibrated. This can be achieved using an alternation of the method we have already developed, first by calibrating the bending of the thermal arm as the ambient temperature is changed, and second by the bending of the thermal arm as the tip of the mechanical arm is heated with a certain amount of laser power, which is determined by measuring reflected and scattered power.

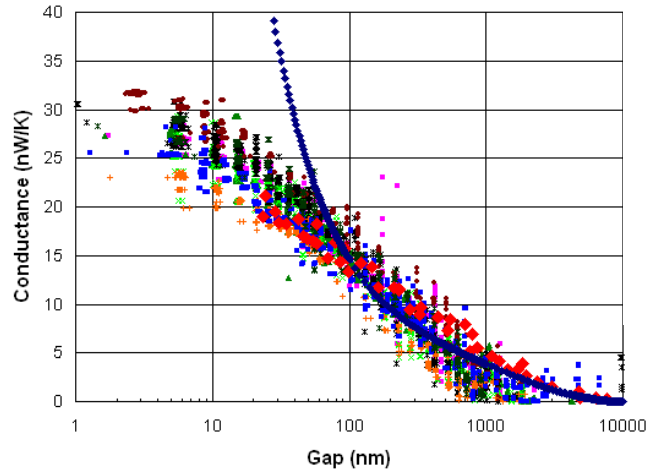


Figure 4 Preliminary experimental data for near-field thermal conductance between a glass sphere and a glass flat plate at close separation.

After calibration we will use the cantilever to study heat transfer using the sphere-plate configuration all the way down to contact.

In addition to the surfaces naturally formed between two bodies, we will also modify the surfaces to control their force interactions, especially aiming towards creating surfaces in which van der Waals interactions dominate. For example, we propose to modify metallic surfaces with surface assembled monolayers (SAM) that form a uniform regularly arranged molecular layer.

Theoretical Studies

We will investigate the effect of surface roughness and structured surfaces on near-field radiation heat transfer. Surface roughness effects will be studied by Fourier decomposition of surface roughness into periodic harmonics. Near-field radiation heat transfer for different periodicities will be computed and used to reconstruct near-field radiation heat transfer between rough surfaces. In addition to addressing experimental issues related to roughness, the computation of near-field radiation heat transfer of regularly structured surfaces will itself be very interesting and may serve to inspire future experimental studies.

A much bigger and daunting task is to reconcile theoretically the fluctuating electrodynamics theory based on fluctuating electrodynamics with the interfacial thermal resistance model based on phonon transport. We do not anticipate that this task can be fully completed within the current program considering the large amount of simulations already needed for the above-described theoretical studies. However, we do intend to examine this question along the way. One direction is to include the atomic vibration picture into the dielectric function. In fact, one example is the dielectric function for ionic crystals, which includes the resonance between the vibration of atoms and the EM fields.

Selected Publications out of the DoE – BES Projects

1. L. Hu and G. Chen, "Analysis of Optical Absorption in Silicon Nanowire Arrays for Photovoltaic Applications," *Nano Letters*, v. 7, pp. 3249-3252, 2007.
2. S. Shen, A. Narayanaswamy, S. Goh, and G. Chen, "Thermal Conductance of AFM Bi-Material Cantilevers," *Applied Physics Letters*, vol. 92, p063509 (1-3), 2008.
3. L. Hu, X. Y. Chen, and G. Chen, "Surface-Plasmon Enhanced Near-Bandgap Light Absorption in Silicon Photovoltaics," *J. Computational and Theoretical Nanosciences*, v.5, pp. 2096-2101, 2008.
4. L. Hu, A. Narayanaswamy, X.Y. Chen, and G. Chen, "Near-Field Thermal Radiation between Two Closely Spaced Glass Plates Exceeding Planck's Blackbody Radiation Law," *App. Phys. Lett.*, v. 92, 133106, 2008.
5. A. Narayanaswamy, S. Shen, and G. Chen, "Near-field radiative transfer between a sphere and a substrate," *Physical Review B*, v. 78, 115303, 2008.
6. Arvind Narayanaswamy, Sheng Shen, Lu Hu, Xiaoyuan Chen, and Gang Chen, "Breakdown of the Planck's blackbody radiation law at nanoscale gaps," *Applied Physics A---Materials Science and Processing*, v. 96, pp. 357-362, 2009.
7. Sheng Shen, Arvind Narayanaswamy, and Gang Chen, "Surface phonon polaritons mediated energy transfer between nanoscale gaps," *Nano Letters*, v. 9, pp. 2909-2913, 2009.
8. Dye-Zone A. Chen and Gang Chen, "Heat Flow in Thin Films via Surface Phonon-Polaritons," *Frontiers in Heat and Mass Transfer*, v.1, 023005, 2010.

Experimental and Theoretical Studies of Embedded Nanostructures

Daryl C. Chrzan,[†] Joel W. Ager, III,[§] Ali Javey[#] and Eugene E. Haller[¥]

Electronic Materials Program, Materials Sciences Division, Lawrence Berkeley National Laboratory, Berkeley, CA 94720

[†]dcchrzan@berkeley.edu [§]jwager@lbl.gov [#]ajavey@berkeley.edu [¥]eehaller@lbl.gov

Program Scope

In one sense, the promise of nanostructures stems from the fact that surfaces and interface properties become an important contributor to the properties of the entire nanostructure. As a result, the properties of nanostructures can differ markedly from those of bulk materials. For example, we have shown that Ge nanocrystals embedded within silica display a large melting/solidification point hysteresis (a width of ~ 450 K), with the center of the hysteresis loop nearly coinciding with the bulk melting point. This phenomenon, superheating and supercooling within the same system, is believed to be unique to nanostructures, as it is well known that bulk materials do not display significant superheating.

In principle, embedding a nanostructure within a matrix allows one to tune the properties of the interfaces, and consequently tune the properties of the nanostructures. This program focuses on the potential for tuning the properties of embedded semiconductor and embedded semiconductor/metal eutectic alloy nanostructures. The program incorporates modeling, synthesis, characterization and technological exploitation of the embedded nanostructures.

Recent Progress

synthesis

Ion beam synthesis (IBS) is a promising route for the fabrication of nanocrystals embedded within a matrix. IBS is a favorable route for producing embedded nanocrystals because it offers the promise of chemical and isotopic purity, as well as precise control over nanocrystal placement. Of course, the properties of nanostructures fabricated via IBS will depend upon their sizes and morphology, which in turn depend upon processing conditions. Remarkably, there had been no quantitative theory for the size distributions of nanoclusters arising from IBS.

To address this shortcoming, we have developed a detailed model for elemental nanocrystals grown via IBS. The theory identifies two characteristic lengths governing the resulting shape of the nanocrystal size distribution: the capillary length, and the length $L \equiv (Dn_{\infty}/F)^{1/2}$, with D the effective

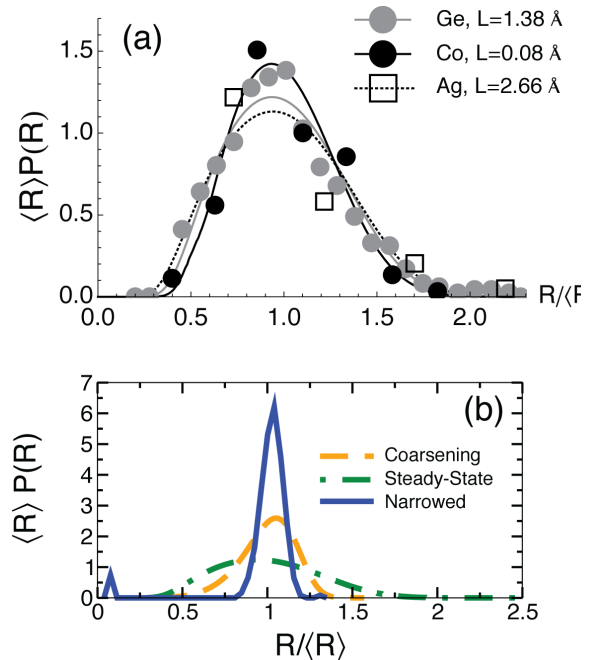


Figure 1. (a) A comparison of fitted steady-state size distributions predicted by the model with experimental data. The values for L resulting from the fits are shown. (b) A comparison of typical distributions obtained from coarsening, steady-state implantation, and the predictions for ramping the temperature upward during implantation (narrowed). The narrowed distribution shows substantial reduction in width compared to the other two distributions.

diffusion coefficient, n_{∞} the effective solubility, and F the volumetric implantation rate of the implanted species. Our theory indicates that L determines the shape of the size distribution, and the capillary length then controls the average size. The model provides a quantitative description of the experimentally available data (Fig. 1a). Importantly, the model helps to identify processing routes that should yield narrow nanocrystal size distributions. For example, for steady-state implantation conditions, the model predicts that decreasing the value of L decreases the width of the nanocrystal size distribution. Also, if one ramps the temperature properly during implantation, one should be able to narrow substantially the size distributions (Fig. 1b).

We have also expanded our study to incorporate the fabrication and characterization of binary alloy eutectic nanostructures. Using sequential ion implantation, we have fabricated GeSn nanostructures embedded in SiO_2 . In their as-formed state equilibrium configuration, these nanocrystals display a bi-lobed, bi-crystalline structure with one lobe predominantly Ge and the other predominantly Sn, a nanoscale Janus particle.

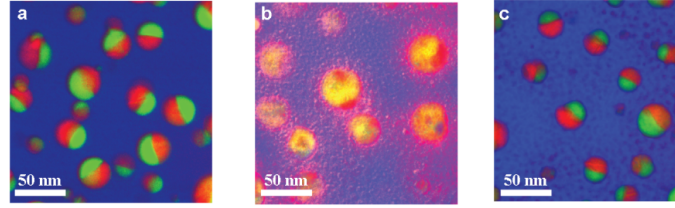


Figure 2. False color energy-filtered transmission electron microscopy images of GeSn nanocrystals (Ge:Sn=4:2) (a) as-formed (900C, 1hr anneal), (b) after pulsed laser melting, and (c) after reannealing (rapid thermal annealing 500C 10s). Blue regions are silica, red regions are rich in Ge, green regions are rich in Sn, and orange regions represent a mixture of Ge and Sn.

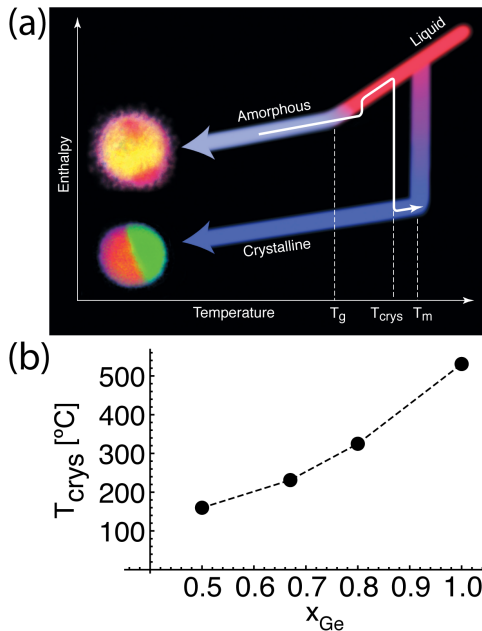


Figure 3. (a) Schematic of transformation kinetics for binary eutectic alloy nanostructures. Rapid cooling from the molten state yields the mixed state at a temperature T_g . Subsequent heating to T_{crys} results in crystallization. (b) Measured composition dependence of T_{crys} for GeSn alloys.

These nanoscale Janus particles display remarkable phase transformation properties (Fig. 2). We have shown, for example, that pulsed laser melting (PLM) converts the bi-lobed bi-crystalline structure to a nearly compositionally homogeneous nanostructure. Subsequent rapid thermal annealing returns the nanostructures to their initial morphology. Moreover, we have demonstrated that the cycle can be repeated (within the AuGe system) at least ten times.

The existence of these two states suggest that such nanostructures might be suitable for phase change material applications, such as static memory devices, or thermal storage materials. The operating principle is outlined in Fig. 3(a). Rapid cooling from the melt leads to stabilization of the amorphous phase at a temperature T_g . Reheating leads to recrystallization at a temperature T_{crys} . Experimentally, we have shown that T_{crys} for GeSn alloys can be changed by altering alloy composition, Fig. 3(b).

We expect that the properties of the mixed and segregated nanostructures will be markedly different. To explore this possibility, we explored a similar alloy system in a different geometry. We fabricated GeAu alloys embedded within HfO₂. The post-annealing morphology of these wires varies with composition. For intermediate compositions (~33% Au), the nanowire structure consists of alternating disks of Ge and Au. For higher Au compositions (~44% Au), the wires have a homogeneous composition. The transport properties of these two geometries are very different. The alternating disk structure displays a nonlinear IV curve when gated, presumably arising from the Schottky barriers formed by the Au-Ge interfaces. In contrast, the wires with homogeneous composition display normal ohmic behavior. If the morphology (*i.e.* disk vs. homogeneous composition) can be switched at a single composition, such wires might form the basis of a static memory device.

Future Plans

We plan to continue our studies of IBS. Specifically, we are planning a series of non-constant temperature implantation experiments aimed at generating nanocrystals with narrow size distributions. We plan to characterize the resulting size distributions using both transmission electron microscopy (at NCEM) and grazing incidence small angle xray scattering (at the ALS). Ultimately, we hope to generate (via IBS) embedded nanocrystals with a nearly monodisperse size distribution.

We also intend to continue our studies of embedded binary eutectic alloy nanostructures. Our initial efforts will be aimed at developing tools to understand phase diagrams and transition kinetics of confined binary alloy nanocrystals. In the beginning, we will focus on the eutectic binary alloys SnGe, AuGe and AuSi. Specifically, we will employ interrupted vapor-liquid-solid growth of nanowires to isolate eutectic droplets with a range of nanoscale sizes and compositions. These droplets will then be coated, with an inert matrix material (*e.g.* HfO₂ or SiO₂) deposited using atomic layer deposition or sputtering, depending upon the material. This coating process will create nano test tubes in which we can conduct studies of the phase diagrams for the materials in question as a function of nanocrystal size. The structural properties of these nanocrystals will be studied using transmission electron microscopy exploiting both the *in situ* heating, and Z-contrast capabilities available at NCEM. For example, phase diagram information will be obtained using *in situ* heating to measure the volume of the liquid droplet as

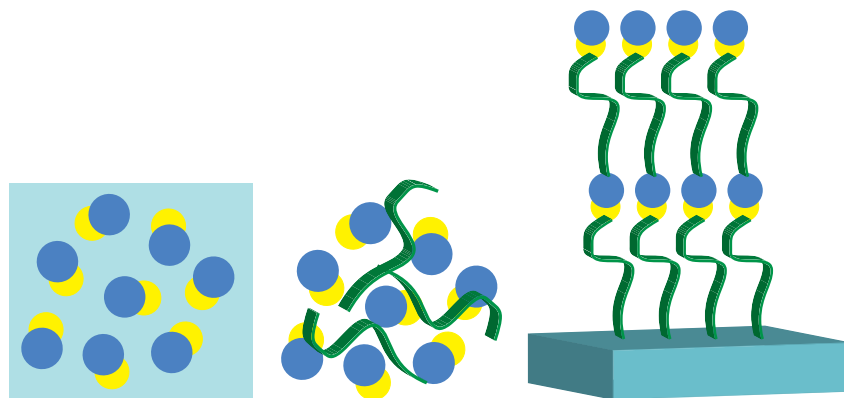


Figure 4. Proposed experiment to order binary eutectic alloy nanocrystals. (Left) Particles are first formed in matrix. (Center) Particles are liberated then sonicated in a thiol-polymer solution. (Right) Polymers are bound to a substrate forming a layer (or multilayer) of oriented nanostructures.

a function of temperature. These measurements can be used to deduce the position of the liquidus. These experiments will enable direct measurement the effects of size, interfacial properties and confining pressure on the phase diagrams of nanoscale Janus particles.

An additional outstanding challenge to our embedded nanocrystal studies is to orient the nanoscale Janus

particles. We will explore a number of mechanisms by which the particles may be ordered within the matrix, including high-energy ion bombardment to sculpt the nanostructures, and imposition of external electromagnetic fields during solidification.

An alternate idea is to use organic molecules to order the bi-lobed particles. As an example, consider the experiment proposed in Fig. 4. GeAu nanoparticles are first liberated from the matrix using an HF etch. The liberated particles are sonicated in a suitable solution containing polymers with a thiol group on one end. During this process, the thiol attaches to the Au side of the nanostructure. If the other end of the polymer is tuned to attach to a substrate (or even the semiconductor half of the nanostructures), a planar, potentially layered, array of oriented nanoscale Janus particles can be fabricated. These layers can then be used to probe the orientation dependence of the nanostructures optical response, for example. They can also be used to control the distance between the nanostructures and other optically active elements, e.g. Er atoms.

Finally, we plan to continue our studies of embedded binary eutectic alloy nanowires to demonstrate phase switching within the nanowire geometry. In addition, we plan to fabricate embedded MnGe nanowires to explore their phase stability and transport properties.

Program Publications

C. W. Yuan, S. J. Shin, C. Y. Liao, J. Guzman, P. R. Stone, M. Watanabe, J. W. Ager III, E. E. Haller and D. C. Chrzan. 2008. Structure map for embedded binary alloy nanocrystals. *Applied Physics Letters* 93, 193114/1-3.

D. O. Yi, M. H. Jhon, I. D. Sharp, Q. Xu, C. W. Yuan, C. Y. Liao, J. W. Ager III, E. E. Haller and D. C. Chrzan. 2008. Modeling nucleation and growth of encapsulated nanocrystals: Kinetic Monte Carlo simulations and rate theory. *Physical Review B* 78, 245425/1-8.

C. W. Yuan, D. O. Yi, I. D. Sharp, S. J. Shin, C. Y. Liao, J. Guzman, J. W. Ager, III, E. E. Haller and D. C. Chrzan. 2009. Theory of Nanocluster Size Distributions from Ion Beam Synthesis. *Physical Review Letters* 102, 146101/1-4.

C. W. Yuan, Cosima N. Boswell, S. J. Shin, C. Y. Liao, J. Guzman, J. W. Ager, III, E. E. Haller, and D. C. Chrzan. 2009. Processing route for size distribution narrowing of ion beam synthesized nanoclusters. *Applied Physics Letters* 95, 083120.

C. W. Yuan, D. O. Yi, I. D. Sharp, S. J. Shin, C. Y. Liao, J. Guzman, J. W. Ager, III, E. E. Haller and D. C. Chrzan. 2009. Size-distribution evolution of ion-beam-synthesized nanoclusters in silica. *Physical Review B* 80, 134121.

J. Guzman, S. J. Shin, C. Y. Liao, C. W. Yuan, P. R. Stone, O. D. Dubon, K. M. Yu, J. W. Beeman, M. Watanabe, J. W. Ager, III, D. C. Chrzan, and E. E. Haller. 2009. Photoluminescence enhancement of Er-doped silica containing Ge nanocluster. *Applied Physics Letters* 95, 201904.

Y.-L. Chueh, C. N. Boswell, C.-W. Yuan, S. J. Shin, K. Takei, J. C. Ho, H. Ko, Z. Fan, E. E. Haller, D. C. Chrzan, A. Javey. 2010. Nanoscale Structural Engineering via Phase Segregation: Au-Ge System. *Nano Letters* 10, 393.

S. J. Shin, J. Guzman, C.W. Yuan, C. Y. Liao, C. N. Boswell-Koller, P. R. Stone, O. D. Dubon, A. M. Minor, M. Watanabe, J. W. Beeman, K. M. Yu, J. W. Ager, III, D. C. Chrzan and E. E. Haller. 2010. Embedded Binary Eutectic Alloy Nanostructures: A New Class of Phase Change Materials. *Nano Letters* 10, 2794-2798.

Program Title: Characterization of Functional Nanomachines

Principal Investigator: M. F. Crommie

Mailing address: University of California at Berkeley, Physics Department, 366 LeConte Hall #7300, Berkeley, CA 94720-7300

e-mail: crommie@berkeley.edu

Co-investigators: C. Bustamante, M. L. Cohen, J. M. J. Frechet, S. G. Louie, A. Zettl

Program Scope/Definition: The overarching goal of this program is to explore the fundamental science of nanomachines that are engineered at the atomic scale and that have the ability to control energy and information through mechanical transduction processes. To meet this goal we have focused our efforts on achieving an understanding of the basic mechanisms by which energy is converted from one form to another at the nanoscale. Our activities are organized around exploring chemical-to-mechanical energy conversion in biological systems, light-to-mechanical energy conversion in molecular systems, electrical-to-mechanical energy conversion in carbon nanostructures, and heat-to-mechanical energy conversion in hybrid systems. A central theme in this program is to understand and control individual nanostructures as opposed to performing measurements on large ensembles of nanostructures. Such single-nanostructure/single-molecule measurements provide useful information that would otherwise be averaged out in large ensemble measurements. The nanostructures that we explore involve naturally occurring biological nanomachines, bottom-up fabricated molecular structures, and top-down lithographically produced nanodevices. In addition to creating, controlling, and understanding individual nanomachine elements, we are also focused on combining them to produce hybrid systems with increased functionality.

This project has six co-investigators whose expertise span physics, chemistry, and biology. We believe that an interdisciplinary approach is best for addressing the problems that face researchers in the area of molecular machines and motors, where multiple fields often intersect. The experimental tools utilized by our collaboration range from synthetic chemistry, surface science, and scanned probe techniques (**Frechet** and **Crommie**), to photolithography, wet biology, and laser tweezers (**Zettl** and **Bustamante**). **Cohen** and **Louie** provide theoretical support through the use of *ab initio* density functional techniques and molecular dynamics calculations.

Recent Progress: We have made recent progress in a wide range of experimental activities that span synthesis and actuation of new nanomachine molecular elements, exploration of chemical-to-mechanical energy conversion in biomotors, and fabrication of nanotube-based nanomachines that operate on new nanomechanical principles (such as electromigration). Here I will emphasize our activities in just one of these areas: chemical synthesis and optical actuation of new molecular machine elements. The use of light to actuate molecular machines is an exciting topic because it has the benefit of not requiring nanoscale electrical contacts, of having extremely high bandwidth, and of having a wide range of optically active molecular candidates. Our work is aimed at understanding and controlling the photomechanical properties of nanomachine elements on surfaces and at the single molecule level. Previously we have explored the behavior of azobenzene molecules on gold to examine

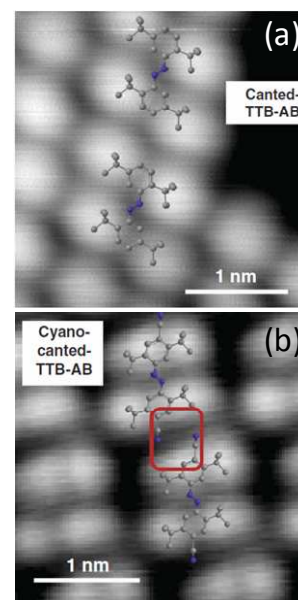


Fig. 1: (a) Canted and (b) cyano-canted TTB-azobenzene molecules on Au(111) show different self-assembly behavior.

how the competition between molecule-surface and molecule-molecule interactions affects molecular photoswitching behavior.¹⁻⁴ More recently we have examined the behavior of new azobenzene derivatives that have been functionalized in order to promote molecular machine self-assembly.⁵ We have also studied the behavior of a new, highly robust photoswitching compound, dihydropyrene, in the single molecule limit on metal surfaces. We have additionally explored the behavior of a new class of molecules (Ru-fulvalenes) designed to store photonic energy by mechanically converting it to chemical energy.⁶ Lastly, we have begun to explore the behavior of photoswitching azobenzene derivatives on new semiconducting surfaces, such as GaAs.

Scanning tunneling microscopy (STM) was used (**Crommie**) to investigate the structure and photoswitching behavior of azobenzene molecules functionalized (**Frechet**) with bulky spacer groups and adsorbed onto Au(111) (Fig. 1). We find that positioning *tert*-butyl “legs” in a canted arrangement on the azobenzene phenyl rings quenches photoisomerizability of the molecule on Au(111) (Fig. 1(a)). Addition of cyano groups at the para positions changes the molecular self-assembly significantly (Fig. 1(b)), but does not alter the quenched

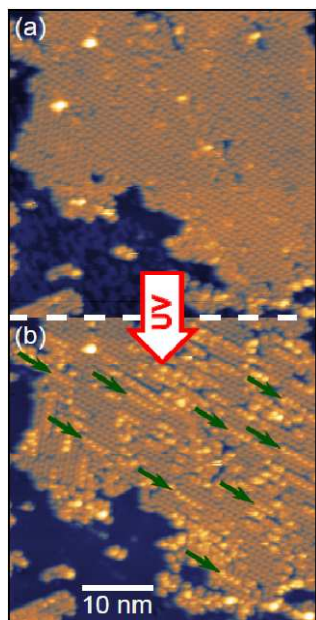


Fig. 4: TTB-azobenzene molecules on GaAs (110) (a) before and (b) after exposure to UV radiation.

photoisomerizability. This behavior likely arises from a combination of molecule-surface interactions, molecule-molecule interactions, and alteration of azobenzene electronic structure resulting from the position-specific addition of *tert*-butyl groups.⁵

We have begun exploring a new photoswitching molecule, dihydropyrene, at metal surfaces (Fig. 2). This molecule is more robust and has greater capacity for chemical functionalization than azobenzene. It also undergoes reversible photomechanical transitions between a conjugated and non-conjugated state. This molecule has been synthesized by **Frechet** and deposited by **Crommie's** group onto the surface of Au(111). We find that the molecule can be easily deposited in vapor form, and assembles at the surface into well-ordered domain structures at the nanoscale (Fig. 2). Photoswitching studies to explore how this molecule behaves at a surface are currently under way.

We have used STM, Auger electron spectroscopy, and density functional theory calculations to investigate thermal and photo-induced structural transitions in single Ru-fulvalene molecules designed for light energy storage⁶ (Fig. 3). We find that both the parent complex and the photoisomer exhibit striking thermally-induced structural phase changes on Au(111), which we attribute to the loss of carbonyl ligands from the organometallic molecules.⁶ We

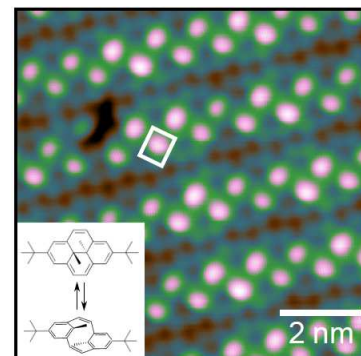


Fig. 2: STM image of dihydropyrene molecules adsorbed to Au(111).

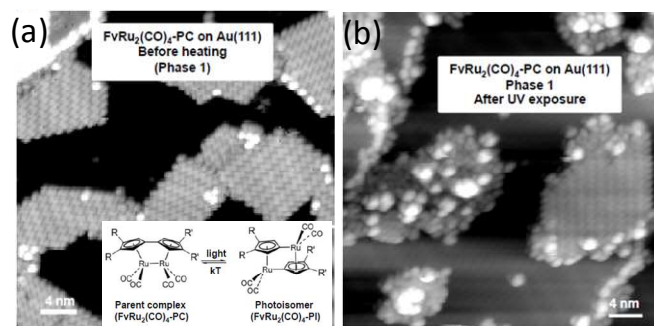


Fig. 3: STM image of Ru-fulvalene molecules before and after UV-exposure, showing changes due to photoswitching.

observe that UV exposure leads to pronounced structural change only in the parent complex, indicative of a photoisomerization reaction (Fig. 3).

We have additionally explored how azobenzene molecules photoswitch on the semiconducting surface GaAs(110). GaAs has completely different optical properties than noble metals (such as Au), and so it forms an exciting new substrate to explore molecular photoswitching. We have discovered that TTB-azobenzene will photoswitch in the single-molecule regime on GaAs (Fig. 4), but in a manner strikingly different than TTB-azobenzene on Au. On GaAs the molecular photoswitching occurs in one-dimensional strips, and displays a strong asymmetry in forward versus reverse photoswitching (Fig. 4).

Future Plans: Our future plans in this particular area of our overall Nanomachines Project will emphasize three topics: (a) Exploration of new photomechanical molecular elements, (b) Assembly of photomechanical molecules into functional nanomachines, and (c) Exploration of new active substrate systems to tune photomechanical switching properties.

New Molecules -- We are particularly interested in exploring spyropyran-based materials. Spyropyran is an exciting molecular candidate for integrated nano-photo-electromechanical applications because its structure, conductance, and electrical dipole moment can all be reversibly switched via the absorption of a single photon.

The two spyropyran isomer states are often referred to as the "open" and "closed" form (Fig. 5). The closed form is not conjugated, and so is not electrically conducting. The open form, however, is fully conjugated and also develops a strong dipole moment that makes it electrically active. **Crommie** and **Frechet** will explore the switching properties of this molecule at a surface in the single-molecule regime, and will evaluate its utility as a photo-electromechanical nanomachine element. **Cohen** and **Louie** will use the GW/Bethe-Salpeter equation formalism to study the quasiparticle properties and optical absorption spectra of the closed and open forms of spyropyran in order to better understand and control the switching mechanism.

Self-Assembling Photomechanical Molecules -- The ability to create more complex structures from molecular switching elements is a critical step toward the goal of creating more complex nanomachine functionality. To this end we intend to exploit non-covalent interactions between two or more types of molecules that, when co-deposited on a surface, will spontaneously form molecular assemblies with a responsive switch or motion. As a first example we will investigate (**Crommie, Frechet**) the deposition of dipyrindyl azobenzene (DPAz) on a surface. Based on our earlier findings with azobenzene, it is expected that DPAz will be strongly coupled to the surface, preventing *trans-cis* switching. We anticipate that co- or subsequent deposition and annealing of 3, 5-di-*t*-butylbenzoic acid will lead to the formation of a higher ordered molecular assembly through formation of acid/base pairs at the DPAz termini. Successful photoisomerization in this system will demonstrate the concept that relatively simple small molecules can cooperate to form more complex photomechanically active assemblies, despite the fact that the individual components are inactive.

Active Surfaces -- We intend to develop new active surfaces where molecular photoswitching properties can be *actively* changed in order to allow a greater degree of control over energy conversion processes in mechanical nanostructures. We propose to explore the behavior of nanomachine elements on two types of active surfaces: (i) Gated epitaxial graphene, and (ii) Plasmonically engineered surfaces. *Gated Graphene*: One of graphene's most important properties relevant to this program is that its electron carrier density, Fermi level, and density of

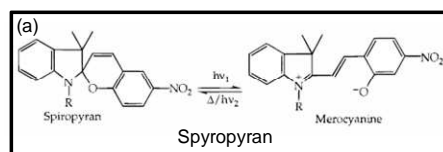


Fig. 5: Optically activated nanomechanical cycle for spyropyran.

states can be varied by applying voltage to a backgate electrode. This makes graphene a very exciting substrate for exploring molecular nanostructures, since nanomechanical response is so sensitive to these properties. We intend to use backgated graphene nanodevice surfaces as electrically-tunable substrates to better control molecular nanomachine behavior and to test the role that substrate properties play in determining photoswitching behavior. *Plasmonic Engineered Surfaces*: A problem with controlling photomechanical molecular nanostructures is that there is a mismatch between the lengthscale of the nanostructures and the long wavelength of light. One way to address this issue, and also to increase our ability to control energy transfer in nanoscale optomechanical structures, is through plasmonic control of light fields. We intend to decorate clean semiconducting and semi-insulating surfaces with metal islands and/or nanocrystals that will act as nanoscale plasmonic resonators. These tunable nanostructures will be used to focus light into nanoscale regions, thus enhancing our ability to spatially control the photomechanical activity of molecular nanomachines. We intend to test the utility of plasmonic fields for channeling light to control molecular nanomachines, and also to examine possible nonlinear photomechanical phenomena occurring when molecules are subjected to ultra-strong plasmonic light fields. **Crommie** will directly image the effects of plasmonic light fields on photomechanically active molecules using subnanometer-resolved STM techniques.

References:

- ¹ M. J. Comstock, N. Levy, J. Cho, L. Berbil-Bautista, M. F. Crommie, D. A. Poulsen, and J. M. J. Fréchet, "Measuring Reversible Photomechanical Switching Rates for a Molecule at a Surface," *Applied Physics Letters* **92**, 123107 (2008).
- ² Jongweon Cho, Niv Levy, Armen Kirakosian, Matthew J. Comstock, Frank Lauterwasser, Jean M. J. Fréchet, and Michael F. Crommie, "Surface anchoring and dynamics of thiolated azobenzene molecules on Au(111)", *J. of Chem. Phys.* **131**, 034707 (2009).
- ³ Matthew J. Comstock, David A. Strubbe, Luis Berbil-Bautista, Niv Levy, Jongweon Cho, Daniel Poulsen, Jean M.J. Fréchet, Steven G. Louie, and Michael F. Crommie, "Determination of Molecular Photoswitching Dynamics through Single-Molecule Chiral Mapping", *Phys. Rev. Lett.* **104**, 178301 (2010).
- ⁴ Niv Levy, Matthew J. Comstock, Jongweon Cho, Luis Berbil-Bautista, Armen Kirakosian, Frank Lauterwasser, Daniel A. Poulsen, Jean M. J. Fréchet, and Michael F. Crommie, "Self-Patterned Molecular Photoswitching in Nanoscale Surface Assemblies", *Nano Letters* **9**, 935 (2009).
- ⁵ Jongweon Cho, L. Berbil-Bautista, Niv Levy, Daniel Poulsen, Jean M. J. Fréchet, and Michael F. Crommie, " Functionalization, self-assembly, and photoswitching quenching for azobenzene derivatives adsorbed on Au(111)", *J. of Chem. Phys.* **133**, 234707 (2010).
- ⁶ Jongweon Cho, L. Berbil-Bautista, I. V. Pechenezhskiy, Niv Levy, Steven K. Meier, Varadharajan Srinivasan, Yosuke Kanai, Jeffrey C. Grossman, K. Peter C. Vollhardt, and Michael F. Crommie, "Single-Molecule-Resolved Structural Changes Induced by Temperature and Light in Surface-Bound Organometallic Molecules Designed for Energy Storage", submitted for publication to *ACS Nano*.

Nanocomposite Proton Conductors

Principal Investigators: Lutgard C. De Jonghe
Materials Sciences Division
Lawrence Berkeley National Laboratory
Berkeley CA 94720
Tel: 510 496 6138; Fax: 510 486 4881
dejonghe@lbl.gov

Co-Principal Investigators: Mark Asta, Jeffrey A. Reimer,
Philip N. Ross.

Program Scope

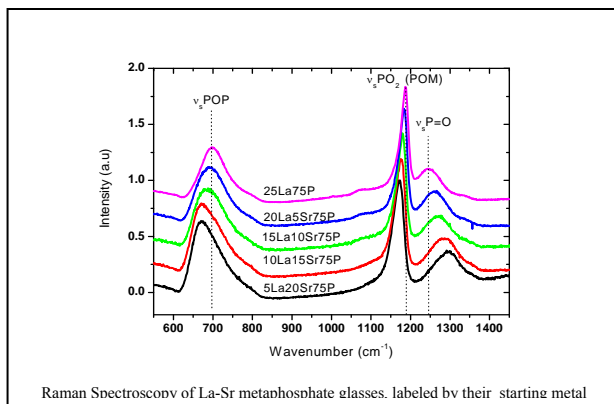
The program designs, synthesizes and tests rare earth phosphate materials for proton conducting applications in the temperature region of 300-450 degrees Celsius. The program relies on three major approaches: a theoretical understanding of proton conduction in inorganic materials, specifically rare earth phosphates and related materials employing quantum chemical computation and molecular simulation; the chemical design, synthesis, and proton conductivity measurement of nano-composite materials expected to exhibit facile proton conduction; and the structural and dynamical characterization of the nano-composite materials using a range of advanced characterization methods including nuclear magnetic resonance (NMR), high resolution TEM, and computational methods.

Recent Progress

Synthesis and characterization

Doped Rare-earth phosphate glasses

The structure of La-based metaphosphate glasses modified with aliovalent alkaline earth elements (M=Ba, Ca, Sr), with P:(M+La) ratio kept approximately at 3, were analyzed using Raman and IR spectroscopy. Increasing the concentration of the alkaline earths monotonically decreased the glass density and glass transition temperature, and shifted some vibrational



modes by as much as 40 wavenumbers. The Raman frequencies of the *symmetric* POP and the P=O vibrations depended on the M/La ratio, but not on the type of alkaline earth addition; however, the type of alkaline earth cation significantly changed the *symmetric* PO₂ vibration. The average cation-oxygen coordination number remained near ~7 except for a slight decrease for high concentrations of Ca and Sr substitutions. The POP/PO₂ intensity ratio increased with increasing alkaline earth content.

A very clear relationship is observed by FTIR between the broad OH stretch at ~2900 cm⁻¹ and the *symmetric* PO₂ (POM) stretch. This shows that incorporated protons are introduced as a charge compensating defects, and are associated with the oxygen of phosphate tetrahedra that are directly connected to the modifying cation.[5]

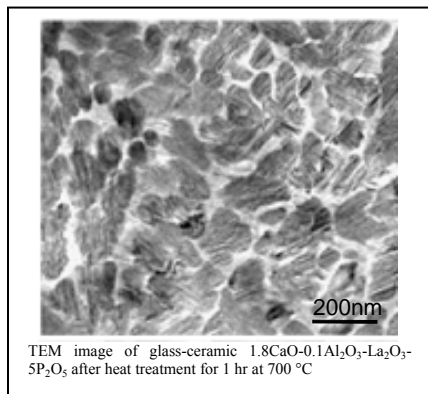
The electrical properties of [La,M]-P₃O₉ metaphosphate glasses, where M is Ba, Sr, Ca, and 0 ≤ x ≤ 0.8 were investigated in the 300– 500°C range. The protonic conductivity increases two orders of magnitude from the unsubstituted to the 60% substituted glass reaching a maximum conductivity of about 10⁻⁵ S/cm at 450°C. While diffusion coefficients derived from conductivities, D_σ, were vastly lower than an uncorrelated diffusion coefficient computed from first principles for crystalline material, the travel distance at ν_{Z*} or ν^{M*} (the frequencies at maximum of the imaginary impedance component, Z*, or modulus, M*) derived from a simple random walk expression, D_r, were surprisingly close to those derived from the more rigorous statistical treatments. The ratio ξ=D_σ/D_r << 1 may be interpreted as indicative of highly correlated ion motion and strongly reduced mean attempt frequencies, together with a mean activation energy for motion increased by ΔE=E_σ-E_r over that of the uncorrelated intertetrahedral motion of an ideal crystal characterized by D_r. [9]

Lanthanum -Calcium Phosphate Glass-Ceramic

A dual phase glass-ceramic nanocomposite La(PO₃)₃-Ca(PO₃)₂ was prepared by quenching from the melt, followed by heating at 800°C for 20h, in air [4]. The H/D isotope effect, assessed from the ratio between σ_{H₂O} and σ_{D₂O} between 400-550°C, was around 1.1-1.2, evidencing dominant proton conduction. To separate the proton from the oxygen ion contribution to the total conductivity, the DC conductivities were measured in water vapor concentration cells. The resistance was obtained from the forward and reverse current-voltage data, where the forward bias corresponds to the cell discharge direction, while the open circuit EMF was determined from the voltage average at zero current. Comparison of the EMF results with the theoretical showed the proton transference number between 400 and

550°C, to be around 0.93 to 0.97 at water partial pressures around 3 kPa, confirming the dominance of proton conduction.

Al₂O₃ was added to nanocomposite La(PO₃)₃-Ca(PO₃)₂ to replace 10% of the Ca²⁺ ions by Al³⁺, forming a phosphate with the nominal composition 1.8CaO-0.1Al₂O₃-La₂O₃-5P₂O₅. The effect of Al₂O₃ addition and heat treatment on the microstructure and conductivity of the resulting glass-ceramics was investigated by XRD, SEM, TEM and AC impedance

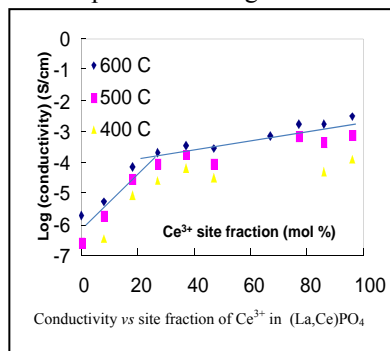


TEM image of glass-ceramic 1.8CaO-0.1Al₂O₃-La₂O₃-5P₂O₅ after heat treatment for 1 hr at 700 °C

spectroscopy. Upon transformation from glass to glass-ceramic, conductivity increased significantly. With Al₂O₃ addition, after heat treatment at 700°C, 100-300 nm nanodomains of LaP₃O₉ crystallized from the glass matrix [6]. TEM imaging and composition analysis on conductivity measured samples revealed that higher proton conductivity in the glass-ceramic can be obtained by limiting the Ca departure of the La-rich phase through proper choice of the heat-treatment parameters during transformation [10].

Cerium orthophosphate (CePO₄) ceramics are almost structurally identical to LaPO₄.

The conductivities of strontium doped cerium orthophosphates have been measured under various oxidizing and reducing atmospheres. In Ce_{0.98}Sr_{0.02}PO₄, the dominant charge carrier changes from protons to polarons on changing the atmosphere from hydrogen to air. The identity of the protonic charge carrier is confirmed using the H/D isotope effect. The behavior of the polaronic charge carrier was further investigated by measuring the conductivity in air of a series of compacts with composition La_(0.98-x)Ce_xSr_{0.02}PO₄. At a given temperature, the conductivity increased nonlinearly with increasing Ce content. The conductivity results are described using a site percolation model. The

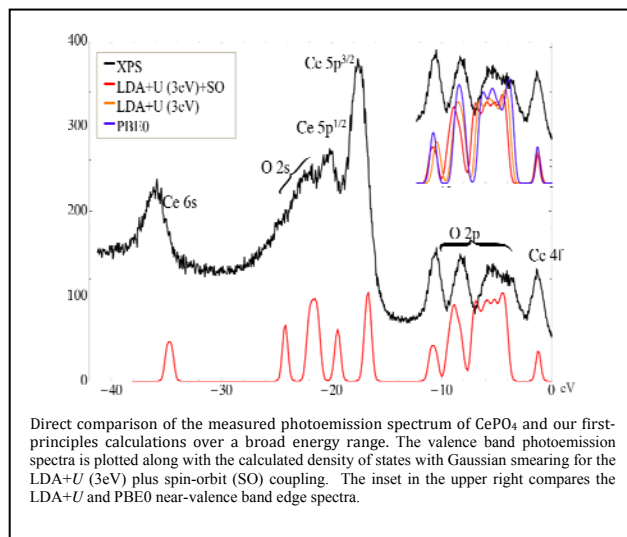


conductivity results are described using a site percolation model. The

critical site percolation threshold for polarons is thought to occur at a Ce content of about x = 0.2. [8]

Computational modeling:

Structural and electronic properties of cerium orthophosphate (CePO₄) were calculated using density



Direct comparison of the measured photoemission spectrum of CePO₄ and our first-principles calculations over a broad energy range. The valence band photoemission spectra is plotted along with the calculated density of states with Gaussian smearing for the LDA+U (3eV) plus spin-orbit (SO) coupling. The inset in the upper right compares the LDA+U and PBE0 near-valence band edge spectra.

functional theory (DFT) with the local spin-density approximation (LSDA+U), with and without gradient corrections (GGA-(PBE)+U), and compared to X-ray diffraction and photoemission spectroscopy measurements. The density of states is found to change significantly as the Hubbard parameter U, which is applied to the Ce 4f states, is varied from 0 to 5 eV. The calculated structural properties are in good agreement with experiment and do not change significantly with U. Choosing U = 3 eV for LSDA provides the best agreement between the calculated density of states and the experimental photoemission spectra.[11]

NMR studies

Variable temperature ³¹P NMR MAS studies revealed multiple chemical shift environments for phosphorus in the strontium-substituted cerium metaphosphate (Ce_{0.84}Sr_{0.16}P₃O₉) materials. As a result of the strontium introduction, the otherwise disordered glass separates into regions of cerium-rich and strontium-rich phases upon heat treatment. The temperature dependent chemical shift of several of the peaks is consistent with Curie-Weiss paramagnetic behavior, and spin-lattice relaxation parameter (T₁) measurements help to distinguish environments located near or far from the paramagnetic Ce³⁺ ion.

Because ¹H MAS NMR experiments indicate a single, very broad proton environment that is also dependent on temperature, ³¹P{¹H} CP MAS NMR and ¹H-³¹P

HETeronuclear CORrelation (HETCOR) spectroscopy were used to locate the protons in the material relative to the ^{31}P NMR spectrum. These experiments provided unambiguous identification of the proton-hosting site. The phosphate group associated with the proton has a very short T_1 relaxation time, providing evidence that the protons in these materials are located in the cerium-rich phase of the material.

A ^{31}P - ^{31}P exchange experiment was used to confirm that the spatial proximity of the proton-hosting phosphate site to the cerium metaphosphate ^{31}P chemical shifts present in the cerium-rich phase. The experiment shows strong cross peaks with those seen in an undoped cerium metaphosphate standard.

^1H - ^{137}Ba TRAPDOR (TRAnsfer of Population in DOuble Resonance) NMR experiments on 5% Ba-substituted lanthanum metaphosphate glass-ceramic samples provide direct and convincing evidence for the close proximity between the introduced H and Ba. TRAPDOR curves were simulated for different H-Ba distances ranging from 3.0 to 3.6 Å, and the best-fit distance of 3.3 Å agrees well with the DFT computational result. The development of relevant NMR techniques for determination of heteronuclear distances, as well as the probe background removal, enriches NMR methodologies and potentially benefits NMR spectroscopists.

Future directions

Synthesis and characterization:

Recent preliminary work has shown that the spark plasma sintering (SPS) technique can produce highly dense ceramic compacts with very little grain growth. These preliminary CePO_4 samples were sintered using the SPS facility at UC Davis. The classic pressureless sintering technique (PLS) usually produces samples with grains on the order of 10-50 microns in length; in contrast, the SPS technique produced samples with grains on the order of 0.5 microns. The use of this technique opens the possibility for the fabrication of proton conducting composite ceramics with much smaller grain size. Future work will involve synthesizing a series of samples in which the grain size is systematically varied, to determine whether there is a correlation of grain boundary content with proton conductivity.

$\text{La}(\text{PO}_3)_3\text{-Ca}(\text{PO}_3)_2$ meta-phosphate glass-ceramic composites will be prepared by quenching from the melt, followed by heating at 800 °C for 20h, in air. The H/D isotope effect, assessed from the ratio between $\sigma_{\text{H}_2\text{O}}$ and $\sigma_{\text{D}_2\text{O}}$ between 400-550°C, will be assessed to confirm dominant proton conduction. To separate the proton from the oxygen ion contribution to the total conductivity, the DC conductivities will be measured in water vapor concentration cells.

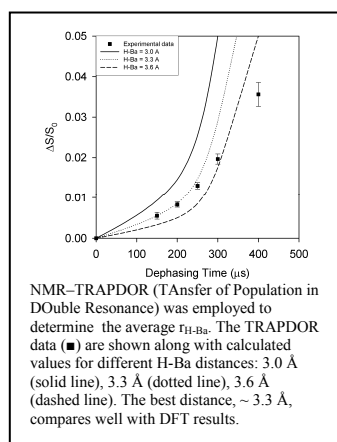
NMR studies:

Local and global mobility of the protons will be probed microscopically using variable temperature NMR relaxation techniques (T_1 and T_2 experiments) and the associated energetics elucidated by calculating activation energies. A comparison between the AC impedance spectroscopy and NMR results will be used to identify the extent of proton contribution to the observed overall conduction. Macroscopic diffusivities will be measured by employing stray field gradient NMR spectroscopy. The construction of a high temperature (up to 500 °C) ^1H PFG NMR probe will be completed, and thin sample STRAFI and/or pulsed field gradients will be employed to resolve the chemical nature of the electrolytes exhibiting high proton diffusivity.

Computationally assisted design:

To aid in the interpretation of the experimental results for electronic conduction in CePO_4 , we will undertake DFT+U based calculations of the energetics and kinetics of small polarons in this material. The hopping parameters and interaction energies derived from these calculations will form the basis for the development of a kinetic-Monte-Carlo (KMC) model to aid in the interpretation of the measured concentration dependencies of polaron conductivities. The KMC model will facilitate investigations of the effects on electronic conductivity resulting from percolation of polaron defects, and binding to dopant cations.

The ABO_4 class of compounds, with $\text{A}=\text{RE}$ and $\text{B}=\text{P}$, V , Nb , and Ta , form a variety of crystal structures depending on the ratios of the different cation to anion radii. Associated with these different structures are a wide range of inter-oxygen bond lengths and lattice symmetries, which are generally expected to lead to a large variation in proton conductivities. For example, in RENbO_4 compounds the measured proton conductivities are observed to vary by roughly an order of magnitude as the ionic radius of the RE ion changes from 1.00 to 1.18 Angstroms. Similarly, it has been found elsewhere that the proton conductivity in perovskite materials is highly



sensitive to small tetragonal distortions of the crystal structure. These observations highlight the possibilities to tune proton conductivity through changes in lattice parameters, ionic polarizability, and crystal structure. To guide such efforts we will undertake the development of computational methods to provide the basis for computer aided materials design of ABO_4 compounds for proton conductor applications. This requires development of efficient algorithms for automated identification of low-energy binding sites for the protons for a given cation/anion arrangement, enumeration of symmetry-distinct migration paths between the enumerated binding sites, and calculations of each of the relevant migration energies. To enable such efforts we have added a co-PI, Mark Asta, who will be supporting a student in the next fiscal year to undertake these activities. As an initial focus for these efforts will build on our current research into doped $CePO_4$ and $LaPO_4$ compounds, and explore computationally the effects of substituting P by Na, Ta and V, and Ce and La by other RE ions.

7. Nina K. Beck and Lutgard C. De Jonghe, "Proton Conduction in $SnP_2O_7-LaP_3O_9$ Composite Electrolytes", *Electrochemical and Solid-State Letters*, **12**, B11-B13(2009).
8. Hannah Ray, Lutgard C. De Jonghe, and Ruigang Wang, "Rare Earth Phosphate Glass and Glass-Ceramic Proton Conductors", *ECS Transactions*, **16** (51) 389-393 (2009)
9. Gabriel Harley and Lutgard C. De Jonghe, "Proton transport in doped La-metaphosphate glasses", *Solid State Ionics* **181** (2010) 424-429
10. Ruigang Wang, Guojing Zhang, and Lutgard C. DeJonghe " Microstructure development of proton-conducting La-based meta-phosphate during heat-treatment" *Solid State Ionics*, **181**, 957-963 (2010)
11. Nicole Adelstein, B. Simon Mun, Hannah L. Ray, Phillip N. Ross Jr., Jeffrey B. Neaton, and Lutgard C. De Jonghe, "Structure and Electronic Properties of Cerium Ortho-phosphate: Theory and Experiment", *Physical Review B*, accepted (2011).

DOE/BES Publications

1. Aaron Kueck and Lutgard C. De Jonghe, "Two-stage sintering inhibits abnormal grain growth during β to α transformation in SiC," *J. European Ceramic Society*, **28**, 2259-2264,(2008)
2. Aaron Kueck, Do K. Kim, Q.M. Ramasse, L.C. De Jonghe, and R.O.Ritchie, "Atomic Resolution Imaging of the Nanoscale Origin of Toughness in Rare-Earth Doped SiC", *Nano Letters*, 935(2008)
3. A.M. Kueck, Q.M. Ramasse, L.C. De Jonghe, and R.O. Ritchie, "Atomic-scale imaging and the effect of yttrium on the fracture toughness of silicon carbide ceramics" *Acta Materialia*, **58**, 2999(2010).
4. Guojing Zhang, Rong Yu, Shashi Vyas, Joel Stettler, Jeffrey A. Reimer, Gabriel Harley, and Lutgard C. De Jonghe, "Proton Conduction and Characterization of a $La(PO_3)_3-Ca(PO_3)_2$ Glass-Ceramic", *Solid State Ionics*, **178**, 1811-1816 (2008)
5. Gabriel Harley, Klaus-Dieter Kreuer, Joachim Maier and Lutgard C. De Jonghe, "Structural investigation of ternary La/alkaline earth phosphate ($La_{(1-x)}M_xP_3O_y$) (M = Ba, Ca, Sr) glasses", *J. Non-Crystalline Solids*, **355**, 932-937(2009)
6. Guojing Zhang, Ruigang Wang, Lutgard C. De Jonghe, "Crystallization and conductivity of $2CaO-La_2O_3-5P_2O_5$ glass-ceramic with Al_2O_3 addition", *Solid State Ionics*, **180**, 941-945(2009)

The Electronic Materials Program at LBNL
Sub-task: Ultra-fast, laser-thermal processing of semiconductors

Principal Investigators: O. D. Dubón (oddubon@berkeley.edu), E. E. Haller (eehaller@lbl.gov), J. W. Ager III, D. C. Chrzan, Z. Liliental-Weber, W. Walukiewicz, K. M. Yu; in collaboration with J. Wu

Lawrence Berkeley National Laboratory, Materials Sciences Division, MS 2R0200,
1 Cyclotron Road, Berkeley, CA 94720

Alloying is a widely used method to tailor the electronic properties of semiconductors. For example, control over the energy band gap of a material, or so-called band gap engineering, via alloy composition lies at the heart of today's most advanced opto-electronic devices. For the vast majority of materials, producing the desired changes in properties requires alloying levels well beyond several atomic percent and thus the use of advanced thin-film deposition techniques. However, recently a class of compound semiconductors has emerged for which fundamental properties are dramatically modified through the substitution of a relatively small fraction of host atoms with a very different element. We have developed a versatile approach for the synthesis of these diluted semiconductors using a combination of ion implantation and pulsed-laser melting (II-PLM). While ion implantation allows the injection of high concentrations of a species into a semiconductor, radiation from an excimer laser pulse melts the ion implanted layer, which subsequently crystallizes in time scales on the order of 10^{-7} seconds. Using II-PLM, we have produced epitaxial, single-crystalline films of new diluted magnetic semiconductors that elucidate the effects of alloying on hole localization, Curie temperature (T_C), and magnetic anisotropy in (Ga,Mn)-pnictide alloys. II-PLM has enabled the discovery of multiband semiconductors for energy applications as well as investigations of phase transformations in embedded nanocrystals.

Diluted magnetic semiconductors. Diluted magnetic semiconductors (DMSs) represent a remarkable workbench for the study and demonstration of spintronic functionalities. They are not only a means to an end but very exciting materials in their own right, exhibiting many striking phenomena whose interpretation and modeling are extremely challenging. While the fundamental behavior of $\text{Ga}_{1-x}\text{Mn}_x\text{As}$, the canonical DMS, is in general understood, the detailed mechanism of hole-mediated exchange in Mn-doped group III-V semiconductors remains controversial. In EMAT we have pioneered ion beams and pulsed-laser radiation to synthesize new DMSs and probe the nature of ferromagnetism in this novel class of materials.

Our recent work has focused on exploring the interplay of carrier localization and exchange strength in Mn-doped DMSs by synthesizing new materials including the alloys $\text{Ga}_{1-x}\text{Mn}_x\text{P}$, $\text{Ga}_{1-x}\text{Mn}_x\text{As}_{1-y}\text{P}_y$, and $\text{Ga}_{1-x}\text{Mn}_x\text{As}_{1-y}\text{N}_y$. Inter-Mn ferromagnetic coupling in these alloys involves a competition between enhanced $p-d$ exchange and stronger carrier localization as the composition of the anion sublattice is varied from GaAs to one with shorter bond length. In $\text{Ga}_{1-x}\text{Mn}_x\text{P}$ the deeper acceptor level causes significant localization of holes resulting in robust impurity-band ferromagnetism but lower T_C . Dilution of $\text{Ga}_{1-x}\text{Mn}_x\text{P}$ ($T_C \sim 65$ K) with As leads to enhanced hole localization without changing significantly the impurity band width and results in a modest reduction of T_C by ~ 15 K. Dilution of the endpoint compound $\text{Ga}_{1-x}\text{Mn}_x\text{As}$ ($T_C \sim 112$ K) with P, on the other hand, leads to a precipitous reduction of T_C to below 60 K by the substitution of 3% As by P and a metal-insulator transition even as x is held constant as shown in Figure 1. The observed suppression of T_C is explained in terms of alloy disorder induced reduction of the mean free path of holes localized in the Mn impurity band. Thus, while anion substitution may enhance

p-d exchange, hole-localization effects must be considered when developing a suitable picture for hole-mediated ferromagnetism in these materials.

Highly mismatched alloys. Highly mismatched alloys (HMAs)—compound semiconductors in which a small fraction of the metallic anion is replaced by more electronegative elements—have become an important class of materials. A notable and well-studied example is the HMA $\text{GaN}_x\text{As}_{1-x}$.

We have applied the II-PLM process to synthesize highly mismatched alloys such as $\text{GaN}_x\text{As}_{1-x}$. The extremely short duration of melting and solidification results in a complete local rearrangement of the atom sites leading to the formation of strong Ga-N bonds, stabilizing N atoms on the anion sites.

Recently, highly mismatched $\text{GaN}_{1-x}\text{As}_x$ semiconductor alloys have been grown across the entire composition range by non-equilibrium, low-temperature molecular beam epitaxy. It was found that over a large composition range ($0.15 < x < 0.75$) these alloys are amorphous. These amorphous thin films have smooth morphology and homogeneous composition and exhibit sharp optical absorption edges. The bandgap energy varies in a broad energy range from ~ 3.4 eV in GaN to ~ 0.8 eV at $x \sim 0.85$. Crystallization of these amorphous alloys by rapid thermal annealing (RTA) results in phase separation into GaN:As and GaAs:N. In order to investigate crystallization kinetics, we have carried out pulsed-laser melting experiments on amorphous $\text{GaN}_{1-x}\text{As}_x$ alloys with $0.15 < x < 0.65$. After PLM processing, Rutherford backscattering analysis reveals minimal As redistribution. In order to observe the formation of nanocrystalline phase, X-ray diffraction using synchrotron radiation (12.7 keV) was carried out. The results show that no phase separation occurs during PLM, consistent with the extremely short time scale of the process. Surprisingly only As-rich $\text{GaN}_{1-x}\text{As}_x$ nanocrystals with N content up to 7% was observed irrespective of initial film composition or laser fluence. No N-rich $\text{GaN}_{1-x}\text{As}_x$ crystalline phase forms from PLM, in contrast to RTA processing. Optical absorption and photoreflectance measurements also support the conjecture that PLM of amorphous $\text{GaN}_{1-x}\text{As}_x$ results in the formation of As-rich nanocrystals in a N-rich amorphous matrix. Additional detailed cross-sectional transmission electron microscopy measurements and theoretical modeling are underway.

Ultra-fast laser processing of nanostructures. The presence of a solid/solid interface at the surface of an embedded nanocrystal provides additional degrees of control over the properties of nanocrystals. Alloying offers the possibility to engineer further the phase-change properties of embedded nanocrystals. It is well known that in bulk eutectic alloys the melting point of the alloy can be substantially lower than that of elemental phases of either component. Further, metals are known to influence the recrystallization temperature of amorphous thin films. The implication is that alloying may offer the opportunity to further tune phase equilibria and transition kinetics at the nanoscale, and thereby enable the development of a new type of phase-change material: binary eutectic-alloy nanostructures. Recognizing the size and composition dependence of equilibrium and kinetic aspects of crystallization, we have pursued a novel laser-based route to investigate phase formation at the nanoscale. Our approach exploits the unique properties of eutectic binary alloys that emerge when they are embedded within nanoscale

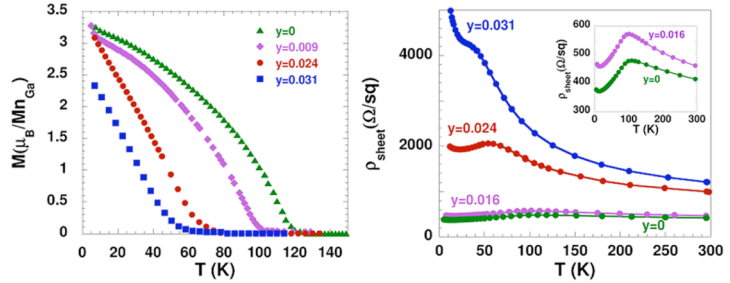


Figure 1. Moment (left) and sheet resistance (right) versus temperature in $\text{Ga}_{0.96}\text{Mn}_{0.04}\text{As}_{1-y}\text{P}_y$. Introduction of P even at relatively small alloy concentrations results in a drastic reduction of T_C and a metal-insulator transition.

volumes. When mixed Ge-Sn nanocrystals are formed within amorphous SiO₂, the nanocrystals exhibit a bi-lobed structure expected for strongly segregating binary alloys. However, rapid cooling following pulsed-laser melting stabilizes a metastable, amorphous, compositionally-mixed state at room temperature. Moderate heating followed by slower cooling returns the nanocrystals to their initial bi-lobed, crystalline state.

Future directions. We have shown that ultra-fast laser-thermal processing is a powerful route to reach novel states of matter, leading to the discovery of new materials and new phenomena. The possibility to manipulate laser energy to high temporal and spatial resolution provides unprecedented opportunities to probe the interplay of phase formation, alloying kinetics, electronic structure, and spintronic functionalities at the nanoscale. Moving forward we are focusing on i) laser-induced crystallization of amorphous HMAs, ii) synthesis and laser processing of HMA nanowires, iii) hybrid spintronic structures based on HMAs and DMSs. Here we focus on the third area.

We will carry out detailed investigations of charge and spin injection across the organic-inorganic interface in all-semiconductor systems. With few exceptions, previous work on spin transport across the hybrid interface has been focused on organic semiconductors interfacing metals (e.g., Co). By exploiting band engineering strategies in inorganic semiconductors to investigate the energy alignment at the hybrid interface, we seek to elucidate the effects of energy and density of spin carriers on spin injection and scattering. The divergent behavior at the organic-inorganic interface may be properly tailored such that the spin wave velocity can be increased over that which is otherwise achievable in the pure material itself. In that case, non-local spin transfer at the interface can become a viable technique for ultra-low energy communication and information processing.

We will investigate spin/charge transport processes by modulating the relative alignment of energy states at hybrid interfaces using principles of band engineering. Figure 2 shows the conduction band edge (CBE) and valence band edge (VBE) of some III-V semiconductors compared to the LUMO and HOMO levels of common organic semiconductors. HMAs provide an ideal class of electronic materials to investigate the effects of relative energy alignment between the organic and inorganic layers for spin-polarized electron and hole conduction. For example, in GaAs_{1-x}N_x the N localized level interacts with the CBE of GaAs, forming a new CBE that depends strongly on the N fraction; the CBE can be shifted downward by as much as 0.5 eV with incorporation of only x=0.05. Similar modulation of the VBE can be achieved in GaAs_{1-x}Bi_x.

As a starting point, we will use n-type GaAs_{1-x}N_x to interface n-type phenyl-C₆₁-butyric-acid-methyl-ester (PCBM) for electron transfer and p-type GaAs_{1-x}Bi_x with p-type copper phthalocyanine (CuPc) for hole transfer. These two organic materials are among the most widely studied organic semiconductors for spintronics as well as organic light emitting

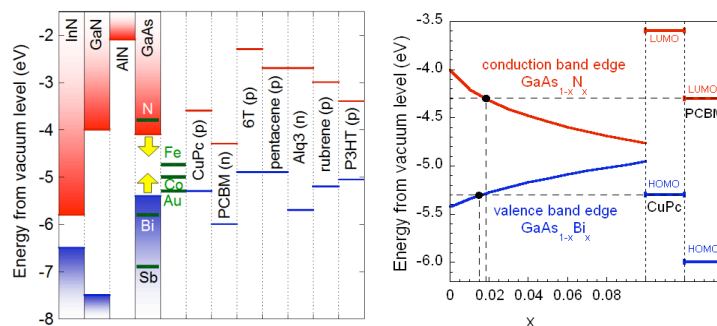


Figure 2. (Left) Band alignment of some organic and inorganic (III-V) semiconductors. Localized levels of N, Bi and Sb and Fermi level of Fe, Co and Au are also shown. (Right) Alignment of the GaAs_{1-x}N_x CBE and GaAs_{1-x}Bi_x VBE (as a function of composition x) with the HOMO and LUMO levels of PCBM and CuPc. The CBE of GaAs_{1-x}N_x is aligned to the LUMO level of PCBM at x=1.8% while the VBE of GaAs_{1-x}Bi_x is aligned to the HOMO level of CuPc at x=1.5 %.

diodes and solar cells. Their LUMO/HOMO levels lie close to the CBE/VBE of GaAs—well within the range of band edge variation in the HMAs GaAs_{1-x}N_x and GaAs_{1-x}Bi_x as shown in Figure 2. Using laser-thermal processing, we can tailor the inorganic component of these hybrid systems. We will construct and characterize hybrid spin-valve devices utilizing organic-HMA heterostructures. Spins will be injected into the HMA either electrically through a ferromagnetic electrode or optically using circularly polarized light. In addition, the ferromagnetic semiconductor Ga_{1-x}Mn_xAs has a valence band edge that is near the HOMO level of a number of p-type organic semiconductor—including CuPc, CVB, a-NPD, and Rubrene—providing a model organic-inorganic system to study spin-polarized hole injection across a hybrid interface. Further tuning of the Ga_{1-x}Mn_xAs valence band edge can be achieved by alloying the As sublattice with Sb or Bi. Band structure calculations will be performed and spin transport will be analyzed.

Selected publication related to this sub-task (2008-2011)

1. T.E. Winkler, P.R. Stone, T. Li, K.M. Yu, A. Bonanni, and O.D. Dubon, "Compensation-dependence of magnetic and electrical properties in Ga_{1-x}Mn_xP," *Applied Physics Letter* **98**, 012103 (2011).
2. P.R. Stone, L. Dreher, J.W. Beeman, K.M. Yu, M.S. Brandt, and O.D. Dubon, "Interplay of epitaxial strain and perpendicular magnetic anisotropy in insulating, ferromagnetic Ga_{1-x}Mn_xP_{1-y}N_y," *Physical Review B* **81**, 205210 (2010).
3. M.A. Mayer, P.R. Stone, N. Miller, H.M. Smith III, O.D. Dubon, E.E. Haller, K.M. Yu, W. Walukiewicz, X. Liu, and J.K. Furdyna, "Electronic structure of Ga_{1-x}Mn_xAs analyzed according to hole-concentration dependent measurements." *Physical Review B* **81**, 045205 (2010).
4. S.J. Shin, J. Guzman, C.-W. Yuan, C.Y. Liao, C.N. Boswell-Koller, P.R. Stone, O.D. Dubon, A.M. Minor, M. Watanabe, J.W. Beeman, K.M. Yu, J.W. Ager III, D. C. Chrzan, and E. E. Haller, "Embedded binary eutectic alloy nanostructures: a new class of phase change materials," *Nano Letters* **10**, 2794 (2010).
5. P.R. Stone, C. Bihler, M. Kraus, M.A. Scarpulla, J.W. Beeman, K.M. Yu, M.S. Brandt, and O.D. Dubon, "Compensation-dependent in-plane magnetization reversal processes in Ga_{1-x}Mn_xP_{1-y}S_y," *Physical Review B* **78**, 214421 (2008).
6. P.R. Stone, K. Alberi, S.K.Z. Tardif, J.W. Beeman, K.M. Yu, W. Walukiewicz, and O.D. Dubon, "Metal-insulator transition by isovalent anion substitution in Ga_{1-x}Mn_xAs: Implications to ferromagnetism," *Physical Review Letters* **101**, 087203 (2008).
7. K. Alberi, K.M. Yu, P.R. Stone, O.D. Dubon, W. Walukiewicz, T. Wojtowicz, X. Liu, and J.K. Furdyna, "Formation of Mn-derived impurity band in III-Mn-V alloys by valence band anticrossing," *Physical Review B* **78**, 075201 (2008).
8. M. A. Scarpulla, R. Farshchi, P.R. Stone, R.V. Chopdekar, K.M. Yu, Y. Suzuki, and O.D. Dubon. "Electrical transport and ferromagnetism in Ga_{1-x}Mn_xAs synthesized by ion implantation and pulsed-laser melting." *Journal of Applied Physics* **103**, 073913 (2008).

Other EMAT publications

1. G.H. Buchowicz, P.R. Stone, J.T. Robinson, C.D. Cress, J.W. Beeman, O.D. Dubon, "Correlation between structure and electrical transport in ion-irradiated graphene grown on Cu foils," *Applied Physics Letters* **98**, 032102 (2011).
2. J.M. Wofford, S. Nie, K.F. McCarty, N.C. Bartelt, and O.D. Dubon, "Graphene islands on Cu foils: the interplay between shape, orientation and defects," *Nano Letters* **10**, 4890 (2010).
3. R. Farshchi, D.J. Hwang, R.V. Chopdekar, P.D. Ashby, C.P. Grigoropoulos, and O.D. Dubon, "Ultrafast pulsed-laser dissociation of Mn-H complexes in GaAs," *Journal of Applied Physics* **106**, 106918 (2009).
4. S. Ahlers, P.R. Stone, N. Sircar, E. Arenholz, O.D. Dubon, and D. Bougeard, "Comparison of the magnetic properties of GeMn thin films through Mn L-edge X-ray absorption," *Applied Physics Letters* **95**, 151911 (2009).

Program Title: Structural and Electrostatic Effects in Self Assembled Nanostructures

Principal Investigator: Helen H. Farrell

Address: Idaho National Laboratory
MS 2211, Idaho Falls, 83415-3740 USA

Email: Helen.Farrell@inl.gov

Program Scope or Definition: This work is focused on obtaining a better understanding of the properties of nanoparticles, interfaces and surfaces. Such an understanding is of importance both in terms of basic knowledge and of facilitating our ability to synthesize these important systems. Systems that were studied include nanoparticles [1,2,4,5,8], bulk surfaces and interfaces [3] and defects [7], which may be considered as the smallest interfaces. This work involves both experimental and theoretical investigations where the latter were performed with density functional theory (DFT) calculations.

Recent Progress: A wide variety of fundamental physical phenomena, including melting, evaporation, sintering, dissolution and many mechanical properties, are dependant upon the per-atom cohesive energy of the material under investigation. In the previous funding cycle, we developed a particularly simple form of the cohesive energy for nanoparticles governed by both nearest neighbor interactions (e.g., good metals) and by long distance interactions (e.g., semiconductors and ionic compounds). Here, $E_{bn} = E_b^0 [1 - (1/n)^v]$ for low-aspect ratio particles, where $n^3 = N$ is the cube root of the number of atoms, E_{bn} is the binding energy of a nanoparticle of radius $r = nr_0$, E_b^0 is the binding energy of the bulk material, and v is +1 for nearest neighbor interactions and +2 for long range interactions. These results are shown for a number of metals in figure 1. These simple nearest neighbor approximation formalisms work well for metals, consistent with earlier literature. However, for non-nearest neighbor materials, such as elemental semiconductors, compound semiconductors and metal oxides,

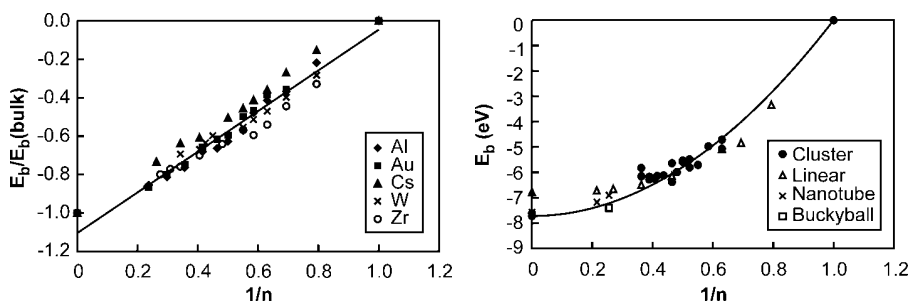


Fig. 1 (left); the ratio of the per-atom binding energy to the bulk value is shown for metals as a linear function of $1/n$. Fig. 2 (right); the parabolic fit for carbon structures is shown.

the parabolic, $v = 2$, dependence on $1/n$ shown in figure 2, was unexpected on the basis of the existing literature, but can easily be understood on the basis of a Madelung type of expansion of the long distance potential interactions [2]. For both cases, we have developed expressions for “melting”, evaporation and sintering that are relatively simple functions of the cohesive energy of the nanoparticle.

Au Nanoparticle Melting: This situation is actually more complex than one might think. Firstly, though we speak of the “melting point” of nanoparticles, melting is actually an equilibrium process and the “melting” of nanoparticles is a kinetic process that is in

competition with several other kinetic processes including sintering and evaporation. Though this work originated in the study of Pt nanoparticles for catalytic purposes, (*App. Cat. A: Gen.* **338**, 27 (2008)), the trade-offs among these processes is best be illustrated with Au nanoparticles as described in our paper entitled “Can nanoparticles really melt?” While at first glance the question in the title may seem to be obviously “yes”, in fact, under many circumstances, small nanoparticles do not get a chance to melt. Other kinetic processes, such as sintering and evaporation, compete with melting particularly for small particles. The determining factors are particle size, cohesive energy and heating rate. We have focused on Au nanoparticles as they are one of the better, if not the best, studied systems of this kind. In Figure 3, we show a comparison between theory and experiment (PRA **13**, 2287 (1976)) for Au nanoparticles. The lower curve is derived from an average of the experimental values. As can be seen, the experimental melting points diverge from the calculated values, and this divergence increases with decreasing particle size. We attribute this divergence at least in part to the simultaneous effects of sublimation and sintering. These effects can remove nanoparticles before they can actually melt giving the impression that the melting point is lower than its true value. This conjecture is supported by the lifetime results in figure 4. Note that at 891 K, for example, nanoparticles less than 1 nm in diameter have dwell times

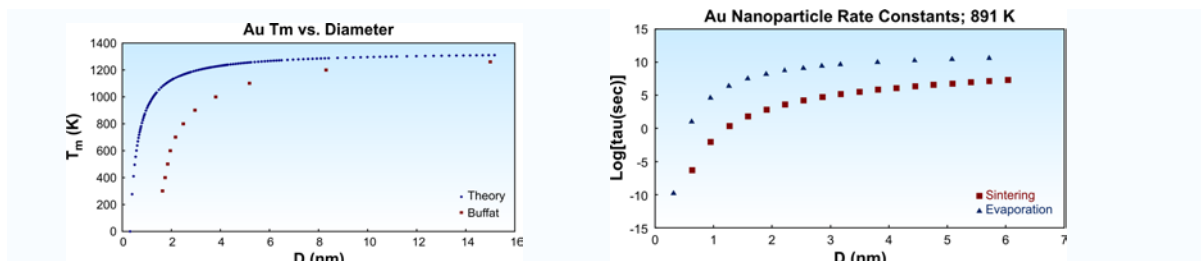


Figure 3 (left). The comparison between theoretical melting points (upper) and those determined experimentally (lower) by Buffat, et al. from electron microscopy data. Figure 4 (right). A logarithmic plot of the characteristic times for the disappearance of a Au nanoparticle as a function of nanoparticles size for both evaporation and sintering at 891 K.

smaller than about a second before they evaporate. For particles with diameters between 1 and about 2 nm, this increases up to minutes and then hours. Therefore, depending upon the heating rate, very small nanoparticles may disappear due to evaporation before they actually “melt”. As can be seen, sintering leads to even shorter lifetimes.

CuO Nanobarrels: One surprise that came out of our work on metal oxides was that the most stable form for nanometer-scale CuO nanoparticles was hollow “nanobarrels” rather than solid particles. This novel material offers an opportunity to exploit unusual form to obtain new functionality. Recently, mesoscale CuO “rings” on the order of 100 nm diameter have been observed experimentally by El-Azab and Liang. They stated that “It has been shown both theoretically and experimentally that rings of mesoscopic dimensions trap quantized magnetic flux and carry persistent equilibrium currents”. Later, they point out that “Further down-scaling of the dimensional features of such rings is expected to lead to a richer range of quantum limit properties”. The nanobarrels that we have studied theoretically are certainly down-scaled in terms of dimension relative to the mesoscale CuO rings and should qualify as having a richer range of quantum limited properties. Our single

walled CuO nanobarrels have a square unit mesh rather than the hexagonal mesh of carbon nanotubes. The square coordination around the Cu atoms in the bulk CuO structure is a result of the fact that most of the Cu 3d orbitals are full leaving only the $d_{x^2-y^2}$ orbital, for example, for bonding. This favors the formation of CuO sheets that can fold or curve over to form the cylindrical units in much the same fashion that the graphene sheets that comprise graphite can be “rolled up” to form carbon nanotubes. We have now extended these studies to their electronic properties which are also of possible interest in the context of high T_c superconductors. Just as carbon nanotubes have electronic properties that vary with chirality, CuO nanobarrels should switch between even and odd number of electrons depending on

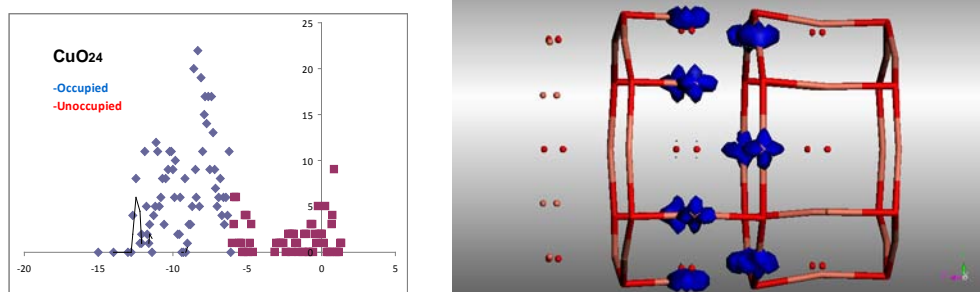
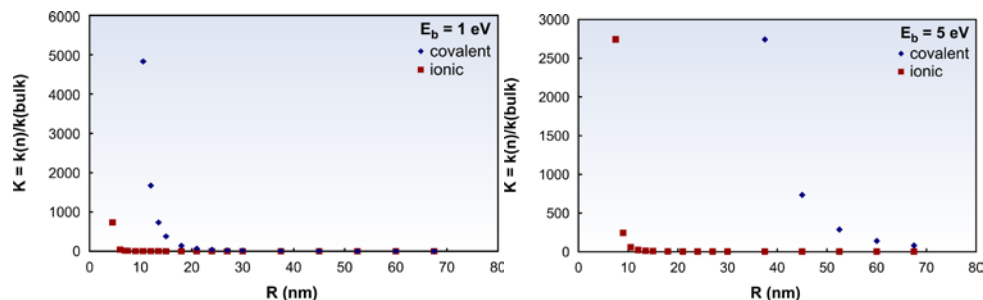


Figure 5 (left); The density of states (in st./Ha.) is shown as a function of binding energy (in eV) for a nanobarrel with 24 CuO units. Note the band gap between about -4.5 and 3.0 eV and the unoccupied states just above E_F . Figure 6 (right); The spin density is shown for a CuO nanobarrel containing 36 CuO units. Here, the overall spin is 0, and the spins cancel out. Other nanobarrels have spins varying from 0 to at least +6.

their geometry. Some of these properties are shown in figures 5 and 6 for two different geometries. Such properties should have the potential to be exploited technologically. Their possible technological applications are unknown at this time, but the same thing could have been said about carbon nanotubes when they were first studied.

Nanoparticle Dissolution: Among other phenomena showing nano-level size dependence, dissolution is particularly important for a variety of fabrication concerns including those of the pharmaceutical industry. Historically, the study of dissolution rates began with the early work of Noyes and Whitney more than a century ago (*J. Am. Chem. Soc.* **19**, 930 (1897)).



Figures 7 (left) and 8 (right); the size-dependent, relative dissolution rate for nanoparticles with a cohesive energies of 1.0 eV and 5.0 eV, respectively. Both covalent ($\nu = 1$) and ionic ($\nu \sim 2$) particles are shown.

Their formulation can be written as $dC/dt = [DS/h] \{ C_s - C \}$. In our approach, we could not determine absolute dissolution rates. It was, however, possible to determine relative transition rate in the case where the forward rate dominates. With this approach, we derived a particularly simple expression for the relative dissolution rate as $K = k(\text{nano})/k(\text{bulk}) = \exp [E^\circ/kTn^v]$ where, E° is the bulk cohesive energy of the solute, n is the nanoparticle size, and $v = 1$, or 2 depending on whether nearest neighbor or longer range interactions dominate. Again, it should be emphasized that this is an extremely simplified model primarily that contains a variety of assumptions, both implicit and explicit. Obviously, more work is needed in this area. It is to be hoped that this simplified model will provide a starting point by allowing us to estimate under when nanoparticle effects become important. Given these limitations, it is of interest to see what our back-of-the envelope expression for the relative dissolution rate can tell us. Two cases are shown in figures 7 and 8 for hypothetical particles composed of molecular units 1.5 nm in radius.

Future Plans: Future work will hopefully be undertaken under a new multi-investigator FWP at INL entitled “Ceramic Interfaces and Nanoparticles” that is currently in preapplication form. As indicated by the title, the objective of this new work will be to develop a better fundamental understanding of ceramic interfaces in general and of ceramic nanoparticle interfaces in particular. There will be a specific focus on the importance of ceramic interfaces for the future development of nuclear reactors. Specific subtasks currently include ceramic/solid interfaces. One will be directed at studying the phonon coupling between oxide nanoparticles and solid matrices and will be directed at developing an understanding of new and better thermoelectric materials such as those used for space nuclear applications. Here, the goal is to reduce thermal conductivity by specifically designing the nanoparticle phonon spectra to be decoupled from the surrounding matrix by controlling particle vacancies, dopants or shape. A second subtask will aim to develop stable oxide interfaces for extreme conditions. A third will focus on developing a first principles model for the mechanical properties of oxide nanoparticles in solid matrices, and is a direct outgrowth of Farrell’s earlier work on nanoparticles.

References to DOE sponsored publications; 2008-2010; accepted.

1) Farrell, H. H., Surface bonding effects in compound semiconductor nanoparticles: II. *J. Vac. Sci. Technol. B* **26**, 1534–1541 (2008). 2) Parra, R. D. & Farrell, H. H., Binding energy of metal oxide nanoparticles. *J. Phys. Chem. C* **113**, 4786–4791 (2009). 3) H. H. Farrell, B. D. Schultz and C. J. Palmstrøm, "Comment on 'High-resolution core-level photoemission study on GaAs(111)B surfaces' ", *J. Appl. Phys.*, 105, 043516 (2009).

References to DOE sponsored publications; 2008-2010; submitted & other.

4) Parra, R. D. & Farrell, H. H., Copper oxide nanobarrels, *submitted to Nature Chemistry*. 5) Farrell, H. H., Ginosar, & D. M., Petkovic, L. M., Do nanoparticles really melt?, *submitted to Nature Chemistry*. 6) H. H. Farrell, R. D. Parra, L. M. Petkovic, D. M. Ginosar and C. D. Van Siclen, The Effect of Size on Nanoparticle Dissolution, *submitted to Nano Letters*. 7) Farrell, H. H., & R. A. The McMillan Equation for Highly Anisotropic Electron-Phonon Coupling, *submitted to Physica C*. 8) Farrell. H. H., Oxide Nanotube Analogues: CuO Nanobarrels, to be submitted to JVST B. 9) Farrell, H. H. & Van Siclen, C.D. Binding energy, vapor pressure, and melting point of semiconductor nanoparticles. *J. Vac. Sci. & Technol. B* **25**, 1441–1447 (2007).

Crystallization and Thermoelectric Transport in Silicon Microstructures and Nanostructures Under Extreme Electrical Stress

Ali Gokirmak (gokirmak@engr.uconn.edu), Helena Silva (hsilva@engr.uconn.edu)
 Electrical & Computer Engineering, University of Connecticut
 371 Fairfield Way, Storrs CT 06269-2157

1. Objectives:

- A. To evaluate the possibility of using electrical pulses to achieve single crystal μ -structures with preferred crystal orientation from lithographically defined Si thin films deposited on arbitrary substrates.
- B. To conduct research on thermoelectric phenomena in μ -/nano-structures under extreme conditions.

Achieving these objectives will contribute to improved materials for high-efficiency photovoltaic (PV) and thermoelectric (TE) devices, as well as device structures which can effectively integrate thermoelectric generators with photovoltaics to achieve very high efficiencies.

2. Key observations from initial studies:

- Pulse voltage stressed nano-crystalline-Si (nc-Si) wires melt and re-solidify within 1 μ s (Figure 1).
 - Current drive in the wires increases with temperature, leading to thermal runaway for high currents.
 - Electrical resistivity (ρ) of the wires is significantly reduced after the stress.
 - Liquid-state resistivity of silicon (ρ_{SiLq}) is extracted from pulsed measurements on sets of wires⁽¹⁾.
 - Wires biased through a load resistor can get into liquid-solid phase-change oscillations^(2, 3).
 - Nanosecond connect-disconnect oscillations with < 350 ps rise/fall times⁽³⁾ are observed.
 - Si depletion and hillock formation is observed on wires experiencing sustained oscillations.
 - Two single-crystalline domains may be formed along suspended wires after pulse stress (Figure 1d).
 - Flat smooth facets of longer wires suggest preferred crystal orientation, atomically smooth surfaces.
 - Asymmetric light emission is observed from wires heated with long stresses (Figure 5).
 - Melting always starts from the lower-voltage terminal end for n-type wires (Figure 1b,c) .
- (Strong thermoelectric effects).

Crystallization
TE

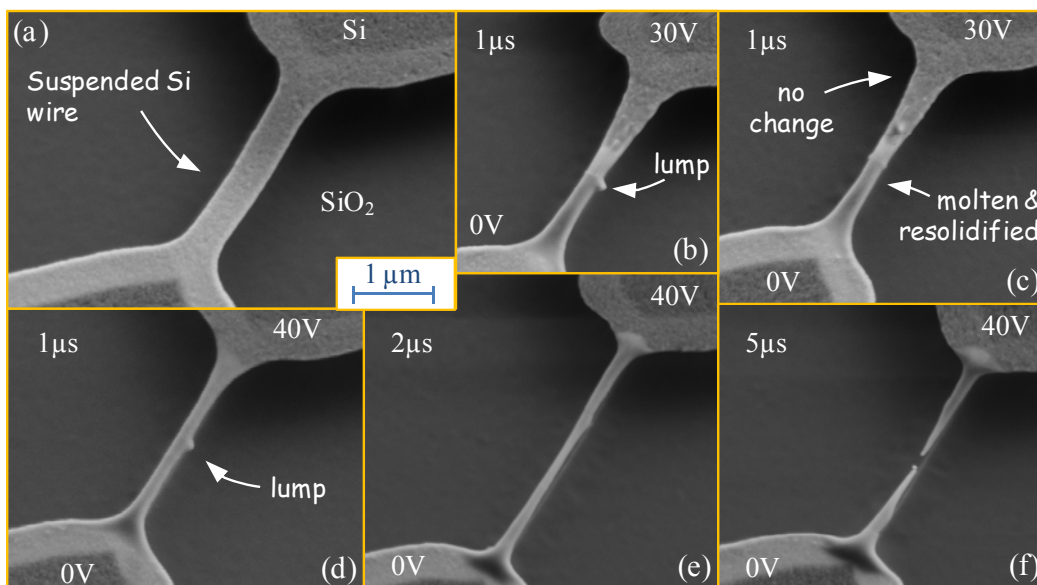


Figure 1. SEM images of an as-fabricated suspended Si wire (a) and five wires (b-f) electrically stressed with a single voltage pulse of indicated duration and amplitude. Moderately stressed wires (b-c) show melting on the ground-terminal end whereas d-f show complete melting, sagging (e-f) and breaking (f). SEM acceleration 2.5 kV.

3. Recent progress:

Computational studies on nano-crystalline Si

Nanocrystalline silicon (nc-Si) is the starting material for most of our experiments. nc-Si is composed of nanometer scale crystalline silicon (c-Si) grains embedded in an amorphous silicon matrix. Electrical and thermal properties of nc-Si depend on the ratio of the volumes of crystalline to amorphous silicon (fill factor), and the size of the crystalline domains. This computational study aids us in understanding of the time evolution of the melting process, critical dimensions and time-scales required to achieve single-crystal Si using growth from melt with joule heating.

We use COMSOL multi-physics finite element simulation tool to generate 2-D structures composed of nanometer scale Si circles dispersed in an area defined as amorphous Si. The results presented here (Figure 2, Figure 3) are based on thermal and electrical conduction using temperature dependent physical parameters for the two materials and do not include thermoelectric or mechanical effects. Some of the material properties are obtained from the literature and some are measured in our laboratory.

We observe that a relatively wide region starts heating with the application of the voltage followed by confinement of the current into a very narrow path (~ 10 nm), initiating a molten filament (Figure 2). We have also observed that the filaments start forming at the two ends. The conductive path forming upon heating depends on the applied voltage (Figure 3).

Optical observation of thermoelectric effects

The experimental results obtained from partially crystallized wires are complemented by measurement of asymmetric light emission from n-type and p-type wires experiencing a low-frequency alternating voltage signal (Figure 5). The light emission is recorded using a high-definition video camera attached to the measurement setup. These light emission profiles are compared with the profiles for the temperature distribution obtained from numerical simulations (Figure 5c).

Numerical modeling of thermoelectric effects

Finite element analysis of linear thermoelectric transport is performed using COMSOL Multiphysics software. The linear thermoelectric terms are included in both current continuity and heat transfer equations⁽⁴⁾:

$$\nabla \cdot J = -\nabla \cdot \left(\frac{\nabla V + S \nabla T}{\rho} \right) = 0, \quad (1)$$

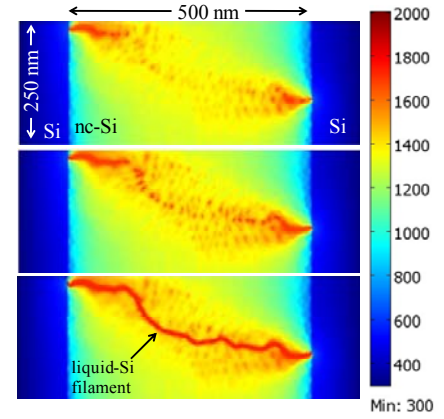


Figure 2. Three snapshots in filament evolution on a nc-Si structure under 80 V. Geometry properties: 500 randomly distributed circles, with radii in 5-10 nm range. Crystalline ratio is 43%. The contact regions are highly doped c-Si. The filaments start at the two ends and form a continuous path in ~ 320 ns.

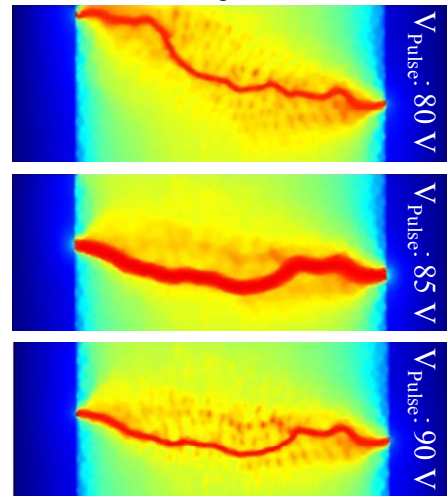


Figure 3. Response to different voltages. Time snapshots at 319 ns, 231 ns, 214 ns for the indicated voltages. (The geometry is the same as Figure 2.)

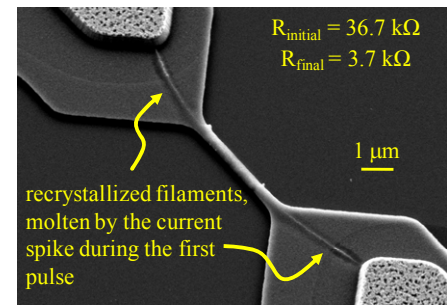


Figure 4. SEM image of a Si structure after pulsed current anneal. Continuous liquid filaments form between the two metal contacts during the current spike.

$$d_{Si} C_P \frac{dT}{dt} - \nabla \cdot (k \nabla T) = \rho J \cdot J - T J \cdot \nabla S, \quad (2)$$

where d_{Si} is the density, C_P is the specific heat, k is the thermal conductivity, ρ is the electrical resistivity and S is the Seebeck coefficient. The thermoelectric term ($-TJ \cdot \nabla S$) in Eq. 2 contains the Seebeck, Peltier and Thomson effects depending on the structure and operating conditions. In our case of a current carrying homogeneous structure, this term reduces to the Thomson heat ($-T dS/dT J \cdot \nabla T$), which results in skewed temperature distributions in symmetric structures.

The simulated peak temperature on a $2.5 \mu\text{m}$ wire used for the simulations reaches melting temperature of silicon (1690 K) in $1 \mu\text{s}$ for 5.8 V. The simulations suggest that the peak temperature on the wire can reach the melting temperature in less than 10 ns for voltage pulse amplitudes larger than 30 V. The cooling time of the wire is less than 250 ns for the mentioned geometry. The simulated temperature profiles are used to calculate the expected light emission from the wire using a gray-body radiation model. The experimental light emission results for an n-type wire (Figure 5a, $I=0.95$ & 0.93 mA) are compared with the computational results obtained for a wire with the same geometry and very close current level (Figure 5c, $I=0.96$ mA for both directions). The model correctly predicts the direction of the asymmetry and a comparable magnitude for the shift of the hottest spot location. The differences may be due to a mismatch between the real material parameters (mainly electrical and thermal conductivities and Seebeck coefficient, all up to melting temperature) and those used for the simulation from the literature for similar materials. We do expect that the extreme asymmetries in the high-voltage pulse experiments (Figure 1) are not explainable within this linear thermoelectric transport model.

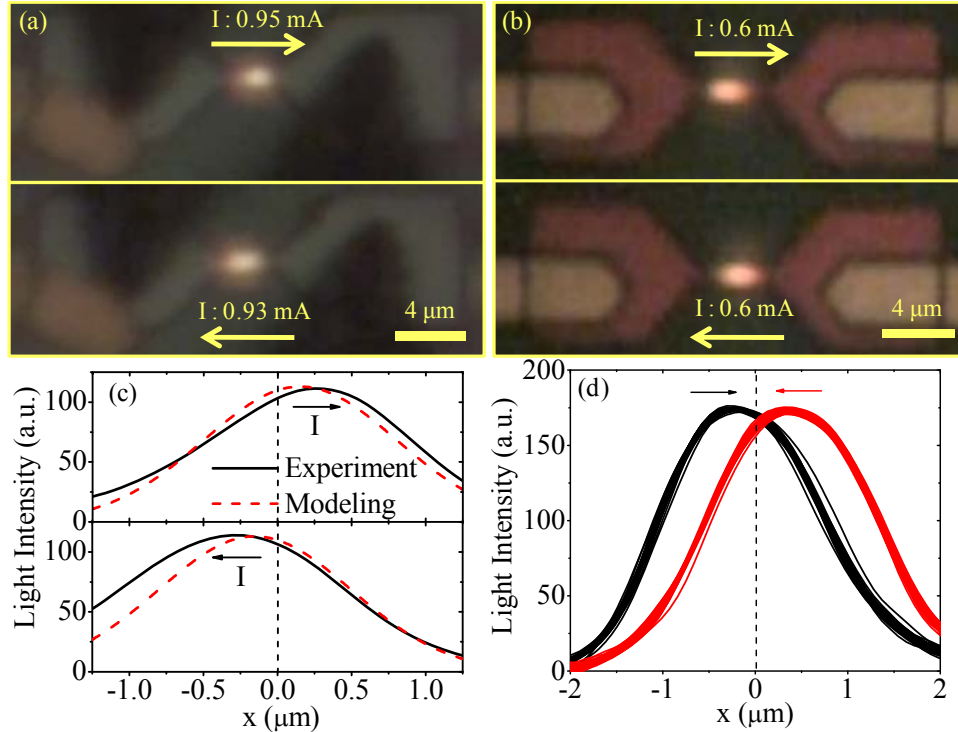


Figure 5. Optical images of a (a) $2.5 \mu\text{m}$ long, suspended, n-type wire, and (b) $4 \mu\text{m}$ long, suspended, p-type wire under AC signal stress for current directions and magnitudes indicated. (c) Experimental and simulated (dashed lines, with $I=0.96$ mA for both directions). Intensity of light emitted from the n-type wire and numerical modeling result of the wire. (d) Light intensity along the p-type wire for multiple video frames. Arrows indicate current direction. Dashed lines indicate the wires' centers in (c) and (d).

4. Future plans:

Computational – modeling of linear and non-linear thermoelectric transport

We will continue our computational studies of linear thermoelectric transport using finite element analysis using more experimental physical parameters for our materials as they become available. In particular we will model percolation and filamentation effects in nano-crystalline Si including thermoelectric effects and melting and crystallization using capacitive discharge to achieve fast, large amplitude current pulses.

Modeling of thermoelectric transport in silicon structures under extreme currents and temperature gradients through a full solution of Boltzmann transport equation including different scattering mechanisms will be performed using Sentaurus Monte Carlo tool. These complete simulations based on first principles are expected to reveal non-linearities in the transport due to the large driving forces. Non-linear Peltier effect in doped InGaAs under large current densities has been simulated using the Monte Carlo technique and it was shown that enhanced cooling due to non-linear transport may be achievable⁽⁵⁾.

Fabrication and physical characterization

We will fabricate new structures for continued electrical and physical (SEM, TEM, AFM) characterization of asymmetric heating and crystallization, as well as structures that can be used as local heaters and thermometers. The electrically annealed structures will be prepared for TEM analysis using a focused ion beam (FIB) system. Structures will be fabricated on fused silica and quartz as well as on Si substrates with oxide and nitride dielectric layers. We have completed the design for this next generation of structures and expect to start fabrication within the coming months.

Electrical and optical characterization

In order to enhance our experimental capabilities we will develop two new optical characterization setups with high magnification optics using: 1) an inspection microscope and 2) an inverted microscope for silicon micro-structures on fused silica and quartz substrates. We will also continue the development of a high-temperature Seebeck measurement setup (target temperature > 1000 K; currently our setup already allows temperatures up to ~ 700 K). New experiments are planned for: (a) materials characterization using a cryogenic-probe station (6 ~ 650 K) and the high temperature setup; (b) resistance trimming experiments; measurements of thermal conductivity of the silicon films using the 3ω technique for thin films⁽⁶⁾; (c) correlation of color of the light emission from the wire with the wire temperature; (d) characterization of Thomson shift through electrical characterization.

5. Publications related to this project:

One journal article is accepted for publication⁽⁷⁾ and two conference presentations were made^(8,9).

6. References

- [1] G. Bakan, et al., Appl. Phys. Lett. 94, 251910 (2009).
- [2] A. Cywar, et al., Appl. Phys. Lett. 94, 072111 (2009).
- [3] A. Cywar, et al., Electron Device Letters, IEEE 31, 1362 (2010).
- [4] E. M. Lifshitz, L. D. Landau and L. P. Pitaevskii, Electrodynamics of continuous media, (Pergamon, 1984),
- [5] M. Zebarjadi, K. Esfarjani and A. Shakouri, Appl. Phys. Lett. 91, 122104 (2007).
- [6] D. G. Cahill, M. Katiyar and J. R. Abelson, Physical Review B 50, 6077 (1994).
- [7] G. Bakan, et al., Journal of Materials Research (Accepted) (2010).
- [8] K. Cil, et al., Mat. Res. Soc. Fall Meeting AA17.65, (2010).
- [9] G. Bakan, et al., Mat. Res. Soc. Fall Meeting LL8.2, (2010).

PROGRAM TITLE AND PRINCIPAL INVESTIGATORS

Extraordinary Responsive Magnetic Rare Earth Materials

Principal Investigators:	K.A. Gschneidner, Jr. Ames Laboratory Iowa State University Ames, IA 50011-3020 cagey@ameslab.gov	Vitalij K. Pecharsky Ames Laboratory Iowa State University Ames, IA 50011-3020 vitkp@ameslab.gov
---------------------------------	---	--

PROGRAM SCOPE:

Responsive materials – ones that have minor-stimulus driven phase changes (i.e., generally highly nonlinear responsiveness) – exhibit numerous diverse and unique properties associated with magnetic ordering, including strong magneto-volume and magnetocaloric effects, and itinerant electron metamagnetic or magnetic-martensitic transformations, which may or may not be driven by a reversible changes of specific chemical bonds. We focus on the origin, and therefore, a more complete control of structure and basic properties of responsive materials crucial *for new energy materials discovery*, specifically on advanced materials suitable for energy conversion and utilization devices. Many of these materials have been known for decades but the basic science is lacking to utilize their properties transformatively. We will develop and validate phenomenological models of transformations that range from magneto-volume to magnetic-martensitic, thus guiding future discoveries of material systems exhibiting strong reactions to small changes of magnetic field, temperature and pressure.

RECENT PROGRESS

New Magnetic Phenomena in Intra Lanthanide Alloys

K.A. Gschneidner, Jr., R. Nirmala*, M. Khan, D. Paudyal, Ya. Mudryk, and V.K. Pecharsky

**Current address: Department of Physics, Indian Institute of Technology Madras, Chennai 600 036, India*

A few years ago we discovered the development of a first order transition as Dy was substituted for Er at approximately 25 at.% Dy. The transformation then vanishes at about 50 at.% Dy in ErAl_2 when more Dy is added. Since then several other intra lanthanide alloys have been studied in order to understand this unexpected behavior, especially since many of these same systems were studied 30 to 40 years ago, but the effects were not observed. The appearance and then the disappearance of the first order magnetic transition was studied as one lanthanide is substituted for another lanthanide. We also observed the destruction of this magnetic phase in magnetic fields >1 kOe, or when the temperature is increased to more than 25 K. It is believed that this is due to the competition between exchange, quadrupole, and

magnetoelastic interactions influenced by the crystalline electric field of the $4f$ electrons of the two different lanthanide ions when they have opposite signs of the second-order Stevens' operator.

Recent heat capacity and low field magnetic susceptibility measurements on a series of $(\text{Er}_{1-x}\text{Tb}_x)\text{Al}_2$ alloys revealed that this unusual magnetic phenomenon in the $(\text{Er}_{1-x}\text{R}_x)\text{Al}_2$ systems (where $\text{R} = \text{Dy}$ and Tb) occurs in the vicinity of a "magic" concentration of $x = 0.25$. Empirically, the reasons for such behavior were attributed to different shapes of the $4f$ charge densities of the R^{3+} ions, which are represented by the opposite signs of the second order Stevens' factors. We have shown that by using both the signs and magnitudes of the second order Stevens' factors, the magnetic transitions can be predicted in a broad range of pseudo binary alloys of intra lanthanide metals which have opposite signs of second order Stevens' factors. The predictions have been verified using $\text{Tm}_{1-x}\text{Tb}_x\text{Al}_2$ as a model system by X-ray diffraction, magnetic susceptibility and heat capacity measurements. First principles electronic structure calculations have also been performed in order to explore the behavior of the density of states near the Fermi level.

FUTURE PLANS

Our future plans include the study of the heat capacity and magnetic properties as functions of temperature and magnetic fields (especially low magnetic fields) for the appearance and disappearance of first order transitions in HoAl_2 , $(\text{Ho}_{1-x}\text{R}_x)\text{Al}_2$ (where $\text{R} = \text{Dy}$, Tb , Er , and Tm), $(\text{Dy}_{1-x}\text{Tb}_x)\text{Al}_2$ and single crystal $\text{Er}_{75}\text{Dy}_{25}$ to see if the second-order Stevens factors criteria holds for these systems.

PUBLICATIONS

Published (Journal)

- "Metamagnetism Seeded by Nanostructural Features of Single-crystalline $\text{Gd}_5\text{Si}_2\text{Ge}_2$ "
J.D. Moore, K. Morrison, G.K. Perkins, D.L. Schlager, T.A. Lograsso, K.A. Gschneidner, Jr., V.K. Pecharsky, and L.F. Cohen
Adv. Mater. (Weinheim), **21**, 3780 (2009).
- "Making the Most of the Magnetic and Lattice Entropy Changes"
V.K. Pecharsky, K.A. Gschneidner, Jr., Ya. Mudryk, and D. Paudyal
J. Magn. Magn. Mater., **321**, 3541 (2009).
- "Gadolinium Scandium Germanide, $\text{Gd}_2\text{Sc}_3\text{Ge}_4$ "
S. Misra and G.J. Miller
Acta Cryst. Section E, **E65**, i25 (2009).
- "Single-crystal Neutron Diffraction Study of Short-range Magnetic Correlations in Tb_5Ge_4 "
W. Tian, A. Kreyssig, J.L. Zarestky, L. Tan, S. Nandi, A.I. Goldman, T.A. Lograsso, D.L. Schlager, K.A. Gschneidner, Jr., V.K. Pecharsky, and R.J. McQueeney
Phys. Rev. B, **80**, 134422 (2009).

- “Structural, Magnetic, and Thermal Characteristics of the Phase Transitions in $Gd_5Ga_xGe_{4-x}$ Magnetocaloric Materials”
S. Misra, Y. Mozharivskyj, A.O. Tsokol, D.L. Schlagel, T.A. Lograsso, and G.J. Miller
J. Solid State Chem., **182**, 3031 (2009).
- “Phase Relationships and Crystallography in the $Ce_5Si_4-Ce_5Ge_4$ Pseudobinary System”
H. Zhang, Ya. Mudryk, M. Zou, V.K. Pecharsky, K.A. Gschneidner, Jr., and Y. Long
J. Alloys Compds., **487**, 98 (2009).
- “Magnetic, Magnetocaloric and Magnetoresistance Properties of Nd_7Pd_3 ”
Niraj K. Singh, Pramod Kumar, Z. Mao, Durga Paudyal, V. Neu, , K. G. Suresh, V K Pecharsky, and K A Gschneidner, Jr.
J. Phys.: Condens. Matter, **21**, 456004 (2009).
- “Electrical Resistivity and Magnetoresistance of Single Crystal $Tb_5Si_{2.2}Ge_{1.8}$ ”
M. Zou, V. K. Pecharsky, K. A. Gschneidner Jr., Ya. Mudryk, D.L. Schlagel, and T.A. Lograsso
Phys. Rev. B, **80**, 174411 (2009).
- “Spontaneous Generation of Voltage in the Magnetocaloric Compound $La(Fe_{0.88}Si_{0.12})_{13}$ and Comparison to $SmMn_2Ge_2$ ”
M. Zou, J.A. Sampaio, V.K. Pecharsky, K.A. Gschneidner Jr.
Phys. Rev. B, **80**, 172403/1-4 (2009).
- “Magnetostructural Transition in $Gd_5Sb_{0.5}Ge_{3.5}$ ”
A. S. Chernyshov, Ya. Mudryk, D. Paudyal, V. K. Pecharsky, K. A. Gschneidner, Jr., D. Schlagel, and T. A. Lograsso
Phys. Rev. B, **80**, 184416 (2009).
- “Spontaneous Generation of Voltage in the Magnetocaloric Compound $Tb_5Si_{2.2}Ge_{1.8}$ and Elemental Gd”
M. Zou, V.K. Pecharsky, K.A. Gschneidner, Jr., D.L. Schlagel, and T.A. Lograsso
J. Alloys Compds., **488**, 550 (2009).
- “Multiple Magnetic Ordering Phenomena Evaluated by Heat Capacity Measurements in $Er_{1-x}Tb_xAl_2$ Laves-phase Alloys”
Mahmud Khan, K.A. Gschneidner, Jr., and V.K. Pecharsky
Phys. Rev. B, **80**, 224408 (2009).
- “Phase Relationships, and Structural, Magnetic, and Magnetocaloric Properties in the $Ce_5Si_4-Ce_5Ge_4$ System”
H. Zhang, Ya. Mudryk, Q. Cao, V. K. Pecharsky, K. A. Gschneidner, Jr., and Y. Long
J. Appl. Phys., **107**, 013909 (2010).
- “Microstructure and Magnetocaloric Effect in the Cast $LaFe_{11.5}Si_{1.5}B_x$ ($x=0.5, 1.0$)”
H. Zhang, Y. Long, Q. Cao, Ya. Mudryk, M. Zou, K.A. Gschneidner, Jr., and V.K. Pecharsky
J. Magn. Magn. Mater., **322**, 1710 (2010).
- “Magnetic, Thermal, and Transport Properties of the Mixed Valent Vanadium Oxides LuV_4O_8 and YV_4O_8 ”
S. Das, A. Niazi, Y. Mudryk, V.K. Pecharsky, and D.C. Johnston
Phys. Rev. B, **81**, 104432 (2010).

- “Thermally Mediated Multiferroic Composites for the Magnetocaloric Materials”
S.G. Lu, Z. Fang, E. Furman, Y. Wang, Q.M. Zhang, Y. Mudryk, K.A. Gschneidner, Jr., V.K. Pecharsky, and C.W. Wan
Appl. Phys. Lett., **96**, 102902 (2010).
- “Temperature and Magnetic Field Induced Structural Transformation in Si Doped CeFe₂: An In-field X-ray Diffraction Study”
Arabinda Haldar, Niraj K. Singh, Ya. Mudryk, K. G. Suresh, A. K. Nigam, and V. K. Pecharsky
Solid State Commun., **150**, 879 (2010).
- “Magnetic Properties of Er_{1-x}Dy_xAl₂ (0≤x≤1) Compounds in Low Applied Fields”
R. Nirmala, Durga Paudyal, V. K. Pecharsky, and K. A. Gschneidner Jr.
J. Appl. Phys., **107**, 09A723 (2010).
- “Magnetocaloric Effects in Er_{1-x}Tb_xAl₂ Alloys”
M. Khan, K.A. Gschneidner, Jr., and V.K. Pecharsky
J. Appl. Phys., **107**, 09A904 (2010).
- “Influence of Y Substitutions on the Magnetism of Gd₅Ge₄”
D. Paudyal, Y. Mudryk, V.K. Pecharsky, S. Misra, G.J. Miller, and K.A. Gschneidner, Jr.
J. Appl. Phys., **107**, 09A908 (2010).
- “Magnetic and Magneto-thermodynamic Properties of Ho₅Si₄”
Niraj K. Singh, Durga Paudyal, V. K. Pecharsky and K. A. Gschneidner, Jr.
J. Appl. Phys., **107**, 09A921 (2010).
- “Magnetostructural Transition in Ce(Fe_{0.975}Ga_{0.025})₂ Compound”
A. Haldar, N.K. Singh, Ya. Mudryk, A.K. Nayak, K.G. Suresh, A.K. Nigam, and V.K. Pecharsky
J. Appl. Phys., **107**, 09E133 (2010).
- “Thermal Stability of RE₅(Si_xGe_{1-x})₃ Plates in RE₅(Si_xGe_{1-x})₄ alloys, where RE = Gd and Ho”
Q. Cao, L.S. Chumbley, and Z. Qian
Intermetallics, **18**, 1021 (2010).
- “Structure and Thermal Stability of the RMgPb Rare Earth Compounds, and the Anomalous Melting Behaviour of SmMgPb”
A. Provino, K.A. Gschneidner, Jr., and P. Manfrinetti
J. Alloys. Compds., **497**, 131 (2010).
- “Structural and Magnetic Characteristics of Gd₅Ga_xSi_{4-x}”
H. Wang, S. Misra, and G.J. Miller
Inorg. Chem., **49**, 4586 (2010).
- “Magnetostructural Properties of Ho₅(Si_{0.8}Ge_{0.2})₄”
Niraj K. Singh, D. Paudyal, Ya. Mudryk, V.K. Pecharsky, and K.A. Gschneidner, Jr.
Phys. Rev. B, **81**, 184414 (2010).
- “Controlling Magnetism of a Complex Metallic System Using Atomic Individualism”
Y. Mudryk, D. Paudyal, V.K. Pecharsky, K.A. Gschneidner, Jr., S. Misra, and G.J. Miller
Phys. Rev. Lett., **105**, 066401 (2010).
- “Experimental and Theoretical Study of the Magnetic and Structural properties of Er_{0.75}Tb_{0.25}Al₂”
M. Khan, Ya. Mudryk, Paudyal, K.A. Gschneidner, Jr., and V.K. Pecharsky
Phys. Rev. B, **82**, 064421 (2010).

Supported, Coated, and Ligated Metal Clusters

Puru Jena

Physics Department, Virginia Commonwealth University, Richmond, VA 23284

Email: pjena@vcu.edu

Program Scope: The scope of this project is to provide, by working closely with experimentalists, a fundamental understanding of the electronic structure and properties of supported, coated, and ligated metal clusters. Atomic clusters with novel size and composition-specific properties have been suggested as building blocks of novel materials with tailored properties. Since metal clusters are metastable and have a tendency to coalesce and react with oxygen and other gases, they need to be supported on substrates, coated by surfactants, or passivated by ligands. Therefore, a fundamental understanding of the interaction between clusters and their environment and how it affects the properties of otherwise bare clusters is important. Our goal is to provide a theoretical understanding of cluster-support interaction by focusing on (1) 3d transition metal and rare earth atoms and clusters supported on organic molecular templates such as pyrene, $C_{16}H_{10}$, cyclooctatetraene C_8H_8 , coronene $C_{24}H_{12}$, and corannulene $C_{20}H_{10}$; (2) iron and iron oxide clusters coated with noble metals such as gold and silver; (3) ligand-induced ferromagnetism of zinc oxide clusters without transition metal doping; and (4) multifunctional clusters with Janus anisotropy using $Au_{12}W$ magic clusters as building blocks. The choice of the above systems is motivated not only by their rich physical and chemical properties, but also by a wealth of experimental data where little theoretical understanding is available. Part of the project is predictive and is aimed at encouraging new experiments. Due to the complexity of the systems to be studied we use of a multiscale approach, tailored for each system, from molecular orbital to supercell band structure theory and quantum molecular dynamics. Although most studies are carried out using density functional theory (DFT), some of the calculations are complemented with quantum chemical methods, when needed, to validate the DFT results.

Recent Progress: The progress during the current funding period has been extensive both in the quality and quantity of papers published, number of invited talks given at international conferences, universities, and research institutes around the world, and service provided to my profession and to our nation. Due to lack of space they are only highlighted:

- 56 papers published, 5 in press, and 7 submitted for publications. These papers have appeared in journals such as Science, Proceedings of the National Academy of Sciences (USA), Angew. Chemie. Int. Ed., Nano Letters, ACS Nano, Physical Review Letters, Phys. Rev. B (Rapid communication), J. Chem. Phys., J. Phys. Chem. Letters, Applied Physics Letters, etc. One of the papers published in Angew. Chemie. Int. Ed. was highlighted by the journal as a Very Important Paper (VIP). Only 5 % of the papers receive this recognition. One paper was highlighted as a featured article in Proc. Nat. Acad. Sci. (USA). Several of our papers have been the subject of press releases and cited in numerous media outlets including C&EN News and APS News. I also edited one conference proceedings and one book.
- 44 invited talks at international conferences and 19 talks in academic institutions.
- Organized or member of the advisory board/organizing committee of 12 international conferences.
- Served the U.S. State Department in bilateral meetings between USA and Russia and USA and China and helped the National Academy of Science and the US State Department in the selection of 2010 Jefferson Science Fellows.

Future Plans: During the course of this funding period we discovered, working with experimentalists, a new class of clusters whose electron affinities can not only be much larger than those of halogens and superhalogens, but they can also carry a magnetic moment. The former we termed as hyperhalogens which are composed of a metal atom at the core surrounded by superhalogens. Conventional superhalogens, on the other hand, consist of a metal atom at the core surrounded by halogen atoms. Changing this building block not only enables one to increase electron affinity further, but provides a greater degree of freedom in the design and synthesis of a much larger class of highly electronegative species. Since negative ions play an important role in chemical industry and serve as oxidizing agents, discovery of new super- and hyper-halogens will be of interest to both fundamental science and industry. My future plan is to explore this field by using electron counting rules such as the octet rule, 18-electron rule, Wade-Mingos rule for boranes, and rules of aromaticity. We want to see if superhalogens can be created without using either a metal atom or a halogen atom and how they can be assembled on different substrates. This work will be carried out with experimental collaboration. We also plan to continue our work on hydrogen storage materials by focusing on functionalized porous structures and exploring if applied electric fields can be used to tailor thermodynamics and kinetics of hydrogen storage. Small amount of our efforts will be directed towards understanding structure-property relations of neurotransmitters.

Publications (2008-2010):

Journal articles:

1. Burgert, R., Schnockel, H., Grubisic, A., Li, X., Stokes, S. T., Bowen, K. H., Gantefor, G. F., Kiran, B., and Jena, P.: "Spin conservation accounts for aluminum cluster anion reactivity pattern with O₂", *Science* **319**, 438 (2008).
2. Chen, L., Zhang, Y., Koratkar, N., Nayak, S. N., and Jena, P.: "Storage of molecular hydrogen in Li doped carbon nano peadpod structures", *Phys. Rev.* **B. 77**, 033405 (2008).
3. Sun, Q., Wang, Q., Jena, P., Kawazoe, Y., and Chen, S. Y.: "Design of Janus Nanoparticles with Atomic Precision: Tungsten-Doped Au nanostructures", *ACS Nano* **2**, 341 (2008).
4. Li, S. and Jena, P.: "Li- and B-decorated *cis*-polyacetylene – A Computational Study", *Phys. Rev.* **B. 77**, 193101 (2008).
5. Wang, Q., Sun, Q. Chen, G., Kawazoe, Y., and Jena, P.: "Vacancy Induced Magnetism in ZnO Thin Films and Nanowires", *Phys. Rev.* **B 77**, 205411 (2008).
6. Larsson, P., Araujo, C. M., Larsson, J. A., Jena, P., and Ahuja, R.: "Role of Catalysts in Dehydrogenation of MgH₂ Nanoclusters", *Proc. Nat. Academy of Sciences* **105**, 8227 (2008).
7. Li, S., Ahuja, R., Barsoum, M. W., Jena, P., and Johansson, B.: "Optical Properties of Ti₃SiC₂ and Ti₄AlN₃". *Appl. Phys. Lett.* **92**, 221907 (2008).
8. Kiran, B., Jena, P., Li, X., Grubisic, A., Stokes, S. T., Gantefor, G., Bowen, B., Burgert, R., and Schnockel, H.: "Comment on Magic Rule for Al_nH_m Clusters" Kiran et al Reply, *Phys. Rev. Lett.* **100**, 199702 (2008).
9. Kandalam, A. K., Boggavarapu, K., and Jena, P.: "Multi-decker Organometallic Complexes for Hydrogen Storage", *J. Phys. Chem.* **112**, 6181 (2008).
10. Kandalam, A. K., Chen, G., and Jena, P.: "Unique Magnetic Coupling between Mn doped stannaspherenes Mn@Sn₁₂", *Appl. Phys. Lett.* **92**, 143109 (2008).
11. Li, X., Eustis, S., Bowen, K. H., Kandalam, A. K., and Jena, P.: "Photoelectron spectroscopic and theoretical studies of Fe_m⁻ (coronene)_n (m=1,2, n=1,2) complexes", *J. Chem. Phys.* **129**, 074313 (2008).
12. Chen, G., Jena, P., and Kawazoe, Y.: "Interaction of gas molecules with Ti-benzene complexes", *J. Chem. Phys.* **129**, 074305 (2008).

13. Jena, P., Harnish R. L., Fischer, J., and Dresselhaus, M., "Global views on advancing renewable energies", *MRS Bulletin*, **33**, 824 (2008).
14. Fischer, J. R., Buchanan, G. L., Orbach, R., Harnish, R. L., and Jena, P.: "Renewable Energy Gains Global Momentum", *Resource*, **15**, 9 (2008).
15. Wang, Q., Sun, Q., and Jena, P.: "Ligand Induced Ferromagnetism in ZnO Nanostructures", *J. Chem. Phys.* **129**, 164714 (2008).
16. Wang, Q., Sun, Q., Jena, P. and Kawazoe, Y.: "Dependence of Magnetism on Doping Concentration in V-doped ZnO", *Materials Trans.* **49**, 2469 (2008).
17. Sun, Q., Wang, Q., and Jena, P.: "Functionalized Heterofullerenes for Hydrogen Storage", *Appl. Phys. Lett.* **94**, 013111 (2009).
18. Wang, Q., Sun, Q., Jena, P., and Kawazoe, Y.: "Mg-doped GaN Nanostructures: Energetics, Magnetism, and H₂ Adsorption", *Appl. Phys. Lett.* **94**, 013108 (2009).
19. Wang, Q., Sun, Q., Jena, P., and Kawazoe, Y.: "Theoretical Study of Hydrogen Storage in Ca-Coated Fullerenes", *J. Chem. Theory Comput.* **5**, 374 (2009).
20. Berseth, P. A., Harter, A. G., Zidan, R., Blomqvist, A., Araujo, C. M., Scheicher, R. H., Ahuja, A., and Jena, P.: "Carbon Nanomaterials as Catalysts for Hydrogen Uptake and Release in NaAlH₄", *Nano Lett.* **9**, 1501 (2009).
21. Wang, Q., Sun, Q., Jena, P., and Kawazoe, Y.: "Potential of AlN Nanostructures as Hydrogen Storage Materials", *ACS Nano* **3**, 621 (2009).
22. Wang, Q., Sun, Q., Jena, P., and Kawazoe, Y.: "Magnetic Properties of Transition Metal doped Zn_{1-x}TM_xO Thin Films with and without Intrinsic Defects: A Density Functional Study", *Phys. Rev. B.* **79**, 115407 (2009).
23. Wu, M. M., Sun, Q., Wang, Q., Jena, P., and Kawazoe, Y.: "Doping Induced Anisotropic Growth in C₆₀", *J. Chem. Phys.* **130**, 184714 (2009).
24. Li, S. and Jena, P.: "Origin of the Anatase to Rutile Phase Conversion in Metal-Doped TiO₂", *Phys. Rev. B. (Rapid Communications)* **79**, 201204(2009).
25. Wang, Y., Zhang, L., Li, S., and Jena, P.: "Polyol-Mediated Synthesis of Ultrafine TiO₂ Nanocrystals and Tailored Physicochemical Properties by Ni Doping", *J. Chem. Phys.* **113**, 9210(2009).
26. Wang, Q., Sun, Q., Jena, P., and Kawazoe, Y.: "N-doped ZnO thin films and nanowires: energetics, impurity distribution, and magnetism", *New J. Phys.* **11**, 063035 (2009).
27. Sun, Q., Wang, Q., and Jena, P.: "Superhalogen properties of CuF_n clusters", *J. Chem. Phys.* **131**, 124301(2009).
28. Grubisic, A., Li, X., Stokes, S. T., Vetter, K., Gantefor, G., Bowen, K. H., Jena, P., Kiran, B., Burgert, R., and Schnockel, H.: "Al₁₃H: Hydrogen atom site selectivity and the shell model", *J. Chem. Phys.* **131**, 121103 (2009).
29. Zhou, J., Wang, Q., Sun, Q., Chen, X. S., Kawazoe, Y., and Jena, P.: "Ferromagnetism in semihydrogenated graphene", *Nano Letters* **9**, 3867 (2009).
30. Boggavarapu, K., Gopakumar, G., Tho Nguyen, M., Kandalam, A., and Jena, P.: "Origin of the unusual stability of B₁₂ and B₁₃⁺ clusters, *J. Inorganic Chem. (communication)* **48**, 9965 (2009).
31. Wang, Q., Sun, Q., and Jena, P.: "Stabilizing a 22 karat nanogolden cage", *J. Chem. Phys.* **131**, 204501 (2009).
32. Li, S. and Jena, P.: "Dehydrogenation from Ti-activated Sodium Alanate" in *Materials Issues in a Hydrogen Economy*, eds. P. Jena, A. K. Kandalam, and Q. Sun, World Scientific (2009) p. 102.
33. Sun, Q., Wang, Q., and Jena, P.: "Computational Design of Nanomaterials for Hydrogen Storage" *Materials Issues in a Hydrogen Economy*, eds. P. Jena, A. K. Kandalam, and Q. Sun, World Scientific (2009) p. 244.

34. Wang, Q., Sun, Q., and Jena, P.: "First-principles study of the effect of vacancies on magnetic properties of $Zn_{1-x}Co_xO$ thin films, *J. Phys. Cond. Matt.* **22**, 076002 (2010)
35. Wang, Q., Sun, Q., and Jena, P.: "Tuning magnetic properties of Mn_4 cluster with gold coating", *Phys. Chem. Chem. Phys.* **12**, 1493 (2010).
36. Zhou, J., Sun, Q., Wang, Q., Jena, P., and Chen, X. S.: "Electric Field Enhanced Hydrogen Storage on BN Sheet", *Proc. Nat. Acad. Science* **107**, 2801 (2010).
37. Zhou, J., Wang, Q., Sun, Q., and Jena, P.: "Electronic and magnetic properties of BN sheet decorated with hydrogen and fluorine", *Phys. Rev. B* **81**, 085442 (2010).
38. Gotz, M., Willis, M., Kandalam, A., Gantefor, G. G., Jena, P.: "Origin of the unusual properties of $Au_n(BO_2)$ Clusters", *Chem. Phys. Chem.* **11**, 853 (2010).
39. Sa, L., Ahuja, R., Araujo, C. M., Johansson, B., and Jena, P.: "Dehydrogenation associated with Ti catalyst in sodium alanate", *J. Phys. Chem. Solids* **71**, 1073 (2010).
40. Chen, G., Sun, Q., Wang, Q., Kawazoe, Y., and Jena, P.: "Structures of Anionic and Neutral Au_{16} Clusters Revisited", *J. Chem. Phys.* **132**, 194306 (2010).
41. Ghosh, S., Wang, Q., Das, G. P., and Jena, P.: "Magnetism in ZnO nanowires with Fe/Co codoping: Firstprinciples density functional calculations", *Phys. Rev. B* **81**, 235215 (2010).
42. Li, X., Grubisic, A., Bowen, K. B., Kandalam, A. K., Boggavarapu, K., Gantefor, and Jena, P.: "Chain and double-ring polymeric structures: Observation of $Al_nH_{3n+1}^-$ ($n=4-8$) and $Al_4H_{14}^-$ ", *J. Chem. Phys. (Communications)* **132**, 241103 (2010).
43. Wu, M. M., Zhou, X., Zhou, J., Sun, Q., Wang, Q., and Jena, P.: "Interaction of $C_{59}Si$ with Si based clusters: A study of Janus Anisotropy", *J. Phys. Condens. Matter* **22**, 27530 (2010).
44. Li, X., Grubisic, A., Bowen, K., Kandalam, A. K., Boggavarapu, K., Gantefor, G. F., and Jena, P.: "Communications: Chain and double ring polymeric structures: Observation of $Al_nH_{3n+1}^-$ ($n=4-8$) and $Al_4H_{14}^-$ ", *J. Chem. Phys.* **132**, 241103 (2010).
45. Gutsev, G., Weatherford, C. A., Pradhan, K., and Jena, P.: "Structure and Spectroscopic Properties of Iron Oxides with High Content of Oxygen, FeO_n and FeO_n^- ($n=5-12$), *J. Phys. Chem. A* **114**, 9014 (2010).
46. Dolotko, O., Zhang, H., Li, S., Jena, P., and Pecharsky, V.: "Mechanochemically Driven Non-equilibrium Processes in MNH_2-CaH_2 Systems ($M=Li$ or Na)", *J. Alloys and Compounds*, **506**, 224 (2010).
47. Joseph, J., Behera, S., and Jena, P.: "Electron affinities of d^1 transition metal chloride clusters and onset of superhalogen behavior", *Chem. Phys. Lett.* **498**, 56 (2010).
48. Li, S. and Jena, P.: "Reaction Intermediates during Dehydrogenation of Metal Borohydrides: A Cluster Perspective", *J. Chem. Phys.* **114**, 16849 (2010).
49. Pradhan, K., Gutsev, G., and Jena, P.: "Negative ions of Transition Metal-Halogen Clusters", *J. Phys. Chem. A* **133**, 144301 (2010).
50. Wu, M. M., Wang, Q., Sun, Q., Jena, P., and Kawazoe, Y.: "Firstprinciples study of hydrogen adsorption in metal doped COF-10", *J. Chem. Phys.* **133**, 154706 (2010).
51. Ko, Y. J., Shakya, A., Wang, H., Grubisic, A., Zheng, W., Gotz, M., Gantefor, G., Bowen, K., Jena, P., and Boggavarapu, K.: "Electronic structure and properties of isoelectronic magic clusters", *J. Chem. Phys.* **133**, 124308 (2010).
52. Koirala, P., Willis, M., Boggavarapu, K., Kandalam, A., and Jena, P.: "Superhalogen Properties of Coinage Metal Clusters" (invited), *J. Phys. Chem. C* **114**, 16018 (2010).
53. Willis, M., Gotz, M., Kandalam, A. K., Gantefor, G., and Jena, P.: "Hyperhalogens: Discovery of a New Class of Electro-negative Species", *Angew. Chem. Int. Ed.* **49**, 8966 (2010).

54. Jiang, Z. P., Zhou, X., Sun, Q., Wang, Q., and Jena, P.: "Geometry, electronic properties, and hydrogen adsorption properties of Li₃N-based nanostructures", *J. Phys. Chem. C* **114**, 19202 (2010).
55. Wang, Q., Sun, Q., and Jena, P.: "Probing the Existence of Energetically Degenerate Cluster Isomers by Chemically Tagging", *Appl. Phys. Lett.* **97**, 223104 (2010).
56. Wu, M. M., Wang, Q., Sun, Q., and Jena, P.: "Reaction induced magnetic transition in Mn₂ dimer", *J. Phys. Chem.* (in press).
57. Wu, M. M., Wang, H., Ko, Y. J., Kandalam, A. K., B. Kiran, Wang, Q., Sun, Q., Bowen, K. H., and Jena, P.: "The Discovery of a New Class of Magnetic Superhalogens", *Angew. Chem. Int. Ed.* (in press).
58. Jena, P.: "Materials for Hydrogen Storage: Past, Present, and Future", *J. Phys. Chem. Letters* (invited), (in press).
59. Reich, T. E., Jackson, K. T., Li, S., Jena, P., and El-Kaderi, H. M.: "Design, synthesis, and characterization of highly porous borazine-linked polymers: A new class of materials with promising potential in gas storage applications", *Inorg. Chem.* (communications) (submitted).
60. Zhou, J., Wang, Q., Sun, Q., and Jena, P.: "Enhanced Hydrogen Storage in Li Functionalized BC₃ Nanotube", *Phys. Rev. B.* (submitted).
61. Feng, Y., Xu, H-Guang, Zheng, W., Zhao, H., Kandalam, A. K., and Jena, P.: "Structures and Photoelectron Spectroscopy of Cu_n(BO₂)_m (n, m=1, 2) Clusters: Observation of Hyperhalogen Behavior", *J. Chem. Phys.* (submitted).
62. Contescu, C. I., van Benthem, K., Li, S., Bonifacio, C. S., Pennycook, S. J., Jena, P., and Gallego, N. C.: "Single Pd Atoms in Activated Carbon Fibers and their Contribution to Hydrogen Storage", *Carbon* (submitted).
63. Joseph, J., Wang, H., Ko, Y. J., Bowen, K. H., and Jena, P.: "Evolution of the superhalogen properties in PtCl_n clusters", *Chem. Phys Letts.* (submitted).
64. Zhou, J., Wang, Q., Chen, X. S., Sun, Q., and Jena, P.: "Electronic structure of graphdiyne and BN-diyne", *Nano Letts.* (submitted).
65. Zhou, J. Wang, Q., Sun, Q., and Jena, P.: "Reconstruction and metallic property of graphone sheet bonded to graphene", *Phys. Rev. B.* (submitted).

Review Articles:

1. Wang, Q. and Jena, P.: Magnetism of Doped GaN Nanostructures, in *Porous Silicon and Gallium Nitride: Epitaxy, Catalysis, and Biotechnology Applications*, ed. R. M. Feenstra and C. E. C. Wood, John Wiley & Sons, Ltd, p. 245-274 (2008).
2. Jena, P. and Castleman, Jr., A. W.: "Introduction to Atomic Clusters" in *Nanoclusters – A Bridge across Disciplines*, Ed. P. Jena and A. W. Castleman, Jr., Elsevier (2010), p. 1-36.
3. Khang, H., Mal-Soon L, Mahanti, S. D., and Jena, P.: "Clusters: An Embryonic Form of Crystals and Nanostructures" in *Nanoclusters – A Bridge across Disciplines*, Ed. P. Jena and A. W. Castleman, Jr., Elsevier (2010), p. 37-70.

Books:

1. Jena, P., Kandalam, A. K., and Sun, Q.: Editors, *Materials Issues in a Hydrogen Economy*, World Scientific Publications, Singapore, (2009).
2. Jena, P. and Castleman, Jr., A. W.: "Nanoclusters – A Bridge across Disciplines", Elsevier (2010) (in press)

Understanding and Design of Polymer Device Interfaces

Antoine Kahn, Princeton Univ. (kahn@princeton.edu); Jean-Luc Brédas, Georgia Inst. Technol.; Anil Duggal, General Electric Global Res.; and George Malliaras, Cornell Univ.; Bernard Kippelen, Georgia Inst. Technol.

Program Scope

Fundamental properties of organic semiconductors and systems have been under intensive study for two decades, and considerable progress has been made in the area of organic/polymer light-emitting diodes (OLEDs, PLEDs) for display and lighting applications, field-effect transistors (FETs) for integrated organic electronics, and photovoltaic applications. Most important for efficient device performance are charge injection and transport at organic/electrode interfaces and organic/organic heterojunctions. Small organic molecule devices formed by vacuum evaporation benefit from a great deal of structural flexibility provided by nearly unlimited ability to stack and mix different materials. In this way, in particular for OLEDs, multi-layered structures can be built, which consist of individually optimized transport, blocking and active layers and provide ample opportunities for modifying injection, carrier balance and transport. The efficiency of the device is therefore not solely a function of interfaces with electrodes. The situation is significantly different with polymer devices, which are generally limited to a single layer because of issues of compatibility and solvent degradation of other organic layers during solution processing (spin coating, inkjet printing, etc.). New procedures have recently been suggested to circumvent this difficulty, but are limited to bi-layers or involve complicated steps to build multi-layered structure devices. Thus, polymers present clear advantages for rapid, low cost, and large scale manufacturing, but are less suitable for forming multiple stacked layers. While tuning charge injection efficiency and balance remains a challenge in all organic devices, the contacts between active material and metal electrodes are especially crucial in polymer devices.

Recent Progress

The DOE-BES funded work described in this talk pertains to two types of polymer interfaces that are important for organic photovoltaic cells.

The first type concerns the donor (D) / acceptor (A) interface of a bulk heterojunction (BHJ) photovoltaic cell. We report the first direct determination via ultra-violet and inverse photoemission spectroscopy (UPS, IPES) of molecular level alignment at such an interface.[1] We take here the example of the interface between poly(3-hexyl thiophene) (P3HT) and [6,6]-phenyl C-61-butyric acid methyl ester (PCBM). The P3HT/PCBM blend is a standard, prototypical system for bulk heterojunction organic photovoltaic (OPV) cells, which leads to power conversion efficiencies (PCE) of the order of 5% and open circuit voltages of 0.55-0.6 V. In question here is the relative position of the molecular levels of the donor (D) and acceptor (A) materials across interfaces in the blend. This is an important issue, as the LUMO(D) - LUMO(A) energy step has been linked to the exciton separation process, and the LUMO(A) - HOMO(D) gap has been linked to the V_{oc} of the OPV cell. V_{oc} , however, also depends on a number of other mechanisms that operate in the cell, e.g. the electron-hole recombination across the D/A interface, and no accurate modeling of V_{oc} has been achieved to date. A precise measurement of the molecular level offsets could therefore provide a firm basis for a more realistic modeling of V_{oc} produced by these cells. We find that a significant interface dipole is formed between the donor and acceptor, which increases the LUMO(A) - HOMO(D) gap by 0.3-0.4 eV with respect to the

0.85 eV gap based on simple considerations of donor ionization energy and acceptor electron affinity. The measured gap of ~ 1.2 eV is considerably larger than the V_{oc} produced by the blend, and calls for an in-depth examination of all factors determining the OPV cell performance. The second type of interface involves transition metal oxide (TMO) films, such as MoO_3 or WO_3 , and polymer films. We focus on the role of TMO films as hole-collecting electrode or central element of a charge recombination layer (CRL) in a tandem solar cell. We have recently shown that these inorganic compounds exhibit exceptionally large electron affinity and work function.[2,3] N-doped by oxygen vacancies, they act as efficient high work function hole-injector and extractor (via electron transport through their conduction band) on the anode side of the solar cell. Similarly, combined with a low work function interlayer electrode, they form the central element of a CRL in a tandem cell. The electronic structure of both types of interface will be reviewed. Furthermore, and most important for solution-processed polymer film technology, we recently demonstrated the formation of MoO_3 films by spin-coating nanoparticles of the TMO in suspension in a solvent. A simple treatment via UV-exposure plus mild annealing restores high work function on these solution-processed films [4]. Using such a spin-coated film, we demonstrate excellent hole injection in polymers like poly(9,9'-dioctylfluorene-co-bis-*N,N'*-(4-butylphenyl)diphenylamine) (TFB), with performance that surpasses that of the standard hole-injection material polyethylene dioxythiophene:polystyrene sulfonate (PEDOT:PSS) (Figure 1).

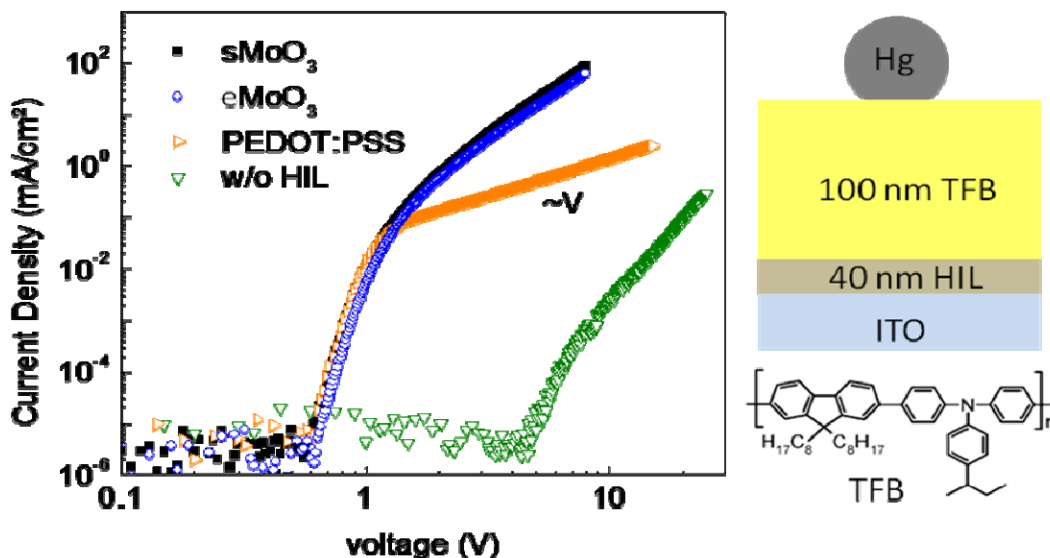


Figure 1: Hole current vs. applied voltage on a diode, the structure of which is given on the right. Green curve: no hole-injection layer (HIL); orange curve: HIL = PEDOT:PSS; blue curve: HIL = MoO_3 vacuum evaporated; black curve: HIL = MoO_3 nanoparticles spin-coated.

Future Plans

Over the next few months, we continue investigations along the two directions described above. We will investigate other donor/acceptor blends to establish the generality of the results obtained on P3HT:PCBM. The LUMO(A) - HOMO(D) gap will be measured as a function of treatment of the film (annealing, exposure to various controlled atmosphere), known to affect the performance of OPV cells.

Regarding the TMO films, we will work with our Georgia Tech partners to produce a theoretical understanding of the very large work function exhibited by these materials. We will investigate

films formed from nanoparticles of other TMOs, e.g. WO₃. Finally, we will investigate the use of clean TMO films as anode in very high V_{oc} OPV cells.

References

- [1] “Energy level alignment of organic-organic bulk heterojunction: the case of the poly(3-hexylthiophene) : phenyl-[6,6]-C61 butyric acid methyl ester blend“, Z. Guan, J. Kim, Y.-L. Loo, and A. Kahn, *Org. Electr.* **11**, 1779 (2010)
- [2] “On the role of deep-lying electronic states in MoO₃ thin films for improved hole-injection into organic thin films“, M. Kröger, S. Hamwi, J. Meyer, T. Riedl, W. Kowalsky, and A. Kahn, *Appl. Phys. Lett.* **95**, 123301 (2009)
- [3] “Mechanism at Charge Generation Layers Consisting of Transition Metal-Oxide/Organic Layer Interfaces“, J. Meyer, M. Kröger, S. Hamwi, T. Riedl, W. Kowalsky and A. Kahn, *Appl. Phys. Lett.* **96**, 193302 (2010)
- [4] “MoO₃ Films Spin-coated from Nanoparticle Suspension for Efficient Hole-Injection in Organic Electronics“, J. Meyer, R. Khalandovsky, P. Görrn and A. Kahn, *Adv. Mat.* **23**, 70 (2011)

DOE Sponsored publications (2009-10)

- [1] Bulk-Heterojunction Polymer Solar Cell Performance is Independent of Compositional Profiles along Active Layer Normal, He Wang, Enrique D. Gomez, Jongbok Kim, Zelei Guan, Cherno Jaye, Daniel A. Fischer, Antoine Kahn, and Yueh-Lin Loo, *J. Am. Chem. Soc.* (submitted)
- [2] “Energy level alignment of organic-organic bulk heterojunction: the case of the poly(3-hexylthiophene) : phenyl-[6,6]-C61 butyric acid methyl ester blend“, Z. Guan, J. Kim, Y.-L. Loo, and A. Kahn, *Org. Electr.* **11**, 1779 (2010)
- [3] Electronic Structure and Dynamics at Organic Donor/Acceptor Interfaces, Xiaoyang Zhu and Antoine Kahn, *MRS Bulletin* **35**, 443 (June 2010)
- [4] “A Molybdenum Dithiolene Complex as p-Dopant for Hole-Transport Materials: A Multi-technique Experimental and Theoretical Investigation“, Y. Qi, T. Sajoto, M. Kröger, A.M. Kandabarow, S. Barlow, E.G. Kim, L. Wielunski, L.C. Feldman, R.A. Bartynski, J.L. Brédas, S.R. Marder, and A. Kahn, *Chemistry of Materials*, **22**, 524-531 (2010).
- [5] “Use of a High Electron-Affinity Molybdenum Dithiolene Complex to p-Dope Hole-Transport Layers“, Y. Qi, T. Sajoto, S. Barlow, E.G. Kim, J.L. Brédas, S.R. Marder, and A. Kahn, *Journal of the American Chemical Society*, **131**, 12530-12531 (2009).
- [6] “Organic Photovoltaics“, B. Kippelen and J.L. Brédas, *Energy & Environmental Science*, **2**, 241-332 (2009).

Poster title: Ultrathin iron oxide growth on YSZ single-crystal surfaces

G. L. Kellogg and Ivan Ermanoski

Mail Stop 1415
Sandia National laboratories
Albuquerque, NM 87185
Email: glkello@sandia.gov

Program title: Nanometer-Scale Surface and Interface Phenomena

Subtask title: Atomistic Dynamics of Surfaces

Subtask Scope

The subject of this poster presentation relates to a future direction in the Atomistic Dynamics of Surfaces Task of the Nanometer-Scale Surface and Interface Phenomena Program at Sandia National Laboratories. The goal of this task is to learn the mechanisms and energetics of atom transport across the surface and into the interior of solids. The quantitative data obtained in these studies are the basis for understanding thin-film growth, surface alloying, and surface nanostructure formation at the atomic level. Experimental tools include the single-atom imaging techniques of scanning tunneling microscopy (STM), *atom-tracking* STM (developed under this program), and low energy electron microscopy (LEEM). Theoretical approaches to interpreting our observations include state-of-the-art density functional theory, molecular dynamics/Monte Carlo simulations, and thermodynamic modeling. Our current work focuses on diffusion processes underlying the growth and stability of surface alloys (both metal-metal and semiconductor-semiconductor) and the atomic structure of carbon, notably graphene, on metal surfaces. Our future plans include expanding our efforts to include atomic-level studies of transport on oxide and ice surfaces as well between the surface and bulk of oxide materials relevant to energy storage applications.

Poster Abstract

Yttria-stabilized zirconia (YSZ) is an oxide material of considerable interest for present and future energy storage and conversion technologies. Because of its high ionic conductivity and negligible electrical conductivity, YSZ has emerged as the most suitable electrolyte material for solid-oxide fuel cells. Additionally, thermochemical approaches to the generation of hydrogen from water or CO from CO₂ rely on a “working oxide” for the cyclic oxidation and reduction generation process. A thermochemical reactor at Sandia based on this concept uses a mixture of iron oxide and yttria-stabilized zirconia as the working oxide [1], but little fundamental information is available concerning the structure and composition of the mixed oxides. In this work, we are applying UHV surface-science probes to characterize the initial stages of iron oxide growth on single crystal surfaces of YSZ. Specifically we are using low energy electron microscopy (LEEM), low energy electron diffraction (LEED) and LEEM-intensity vs. voltage

(LEEM-IV) measurements to determine (1) the surface atomic structure of single crystal YSZ(001), (2) the conditions of temperature and background oxygen pressure under which thin films of iron oxide grow on the surface, (3) the uniformity of the growth, the domain structure and the surface morphology of the deposited film, (4) the oxide stoichiometry as a function of growth conditions, and (5) the conditions that leads to intermixing between the film and the substrate.

The first question we addressed is whether or not an insulating material such as YSZ can be analyzed by electron-based surface microscopic and diffraction techniques (LEEM and LEED). The biggest concern here is electron-beam charging. We found that charging effects are negligible in LEEM and LEED as long as the sample temperature is kept above 300°C. Figure 1 shows a LEEM image (a) and two LEED patterns (b and c) from a YSZ(001) single-crystal surface. The thick, nearly horizontal lines in the LEEM image are step bunches. The thinner meandering lines between the step bunches are single steps. The LEED patterns show that the surface atomic structure changes from a (2x2) surface structure to a “hex-type” reconstruction [2] when the sample is annealed to high (>800°C) temperatures. This temperature also correlates with a change in sample color (from clear to gray), suggesting a loss of oxygen. We used these hex-reconstructed (i.e., oxygen deficient) surfaces (Fig. 1c) as the substrate for the Fe_xO_y growth studies discussed below.

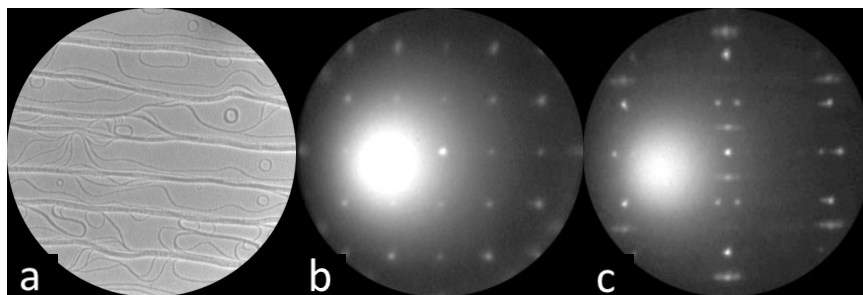


Fig. 1 (a) LEEM image from YSZ(001) showing step bunches (thick horizontal lines) and single steps (thin meandering lines on terraces). FOV=20 μm (b) (2x2) LEED pattern from YSZ(001) at 350°C. Above 800°C it converts to a “hex” pattern.

The next question is how to go about growing thin films of iron oxide on the YSZ surfaces. Two possibilities are: (1) deposit Fe metal on the surface and subsequently heat in O_2 or (2) deposit Fe in an O_2 background. The latter method proved successful in our studies. We used a background O_2 pressure of 10^{-6} to 10^{-5} Torr and temperatures ranging from 800 to 1050°C. Figure 2 shows LEEM images and a LEED pattern corresponding to deposition at a sample temperature of 910°C. Image 2a was recorded 16 min. after exposing the sample to the Fe flux. Image 2b was recorded after a total of 26 min. An induction time of approximately 15 min. was required before the onset of oxide film growth, suggesting some critical concentration of Fe before oxide formation takes place. The LEEM images (Fig 2) show highly anisotropic growth in perpendicular directions. The 12-fold LEED pattern in Fig. 1c is consistent with previous observations of hexagonal film growth on a substrate with square atomic symmetry. In previous work, the pattern has been attributed to two rotational domains of 6-fold patterns (for example, Bi(111) on Si(001) [3]). As discussed further below, for the iron oxide films on

YSZ(001), there are actually four non-equivalent domains. By measuring the ratio of the reciprocal lattice vectors of the 12-fold pattern to those of the substrate, we find that the lattice constant of the iron oxide film is 0.32 nm. This value is very close to the lattice constant of FeO (0.304 nm) and significantly different from the lattice constants of Fe₂O₃ (0.503 nm) and Fe₃O₄ (0.592 nm). Based on this lattice constant and the subsequent growth of the second layer (discussed below), we infer that the observed film in Fig. 2 is a bilayer of FeO.

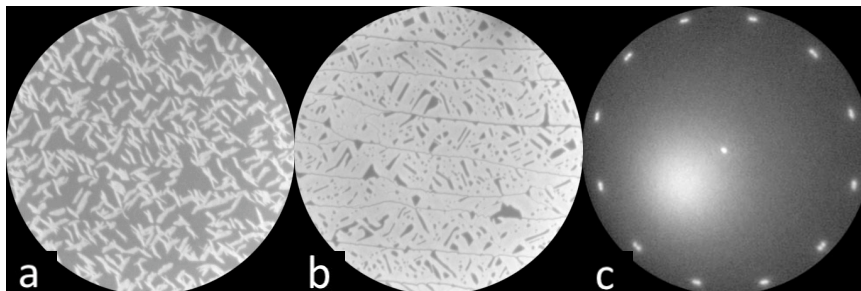


Fig. 2 (a and b) LEEM images of a iron oxide film grown on YSZ(001) in 5.0×10^{-6} Torr O₂ at 910°C (20 μm field of view). (a) after 16 min and (b) after 26 min. of deposition. (c) LEED pattern from the surface shown in (b). The lattice constant derived from (c) indicates a film of FeO.

The temperature range over which film growth could be observed in the LEEM in the 10^{-6} Torr O₂ range was quite narrow. Below approximately 900°C, the domain sizes were below the resolution limit of our LEEM (~7-8 nm). (LEED patterns did show the same 12-fold symmetry indicating the film was being deposited). Above approximately 1000°C, oxide films did not nucleate. However, if an oxide film was first nucleated at 900°C and the sample immediately heated higher temperatures (1000-1050°C) during Fe deposition, large domains were observed to spread out over the terraces. An example is shown in Fig. 3. Here, the growth took place at 1050°C in 8.6×10^{-6} Torr O₂. The figure is a color superposition of dark-field LEEM images taken from four consecutive spots going “around the clock” in the LEED pattern. The observation of four non-equivalent domains is attributed to two rotational domains (unit cell rotated by 90°) and two stacking sequences for the atoms of the FeO bi-layer.

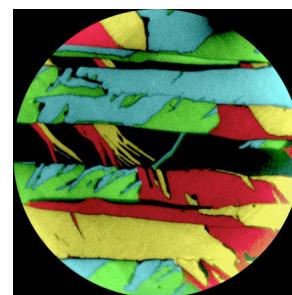


Fig. 3 Color superposition of dark-field LEEM images from FeO film grown on YSZ(001) in 8.6×10^{-6} Torr O₂ at 1025°C (FOV=20 μm)

The stoichiometry of the first iron oxide layer on the oxygen-deficient YSZ(001) substrates was found to be FeO over full range of temperatures and O₂ pressures examined. With the onset of second-layer growth, a different oxide phase appeared. This phase was identified by a second 12-fold pattern in the LEED pattern (Fig. 4(a)). The lattice constant associated with the smaller-diameter 12-fold pattern is 0.52 nm, corresponding Fe₂O₃(0001) (0.503 nm). Interestingly, preliminary experiments suggest that on YSZ(001) surfaces that were not reduced by heating in vacuum (starting with the (2x2) surface phase), the Fe₂O₃ phase grows from the start (i.e., the first layer is Fe₂O₃).

Another method used to probe differences in the oxide stoichiometry (or layer thickness) is LEEM-IV analysis. In this technique one ramps the incident electron energy while recording the LEEM image and measures changes in the reflected/scattered electron intensity. The resulting intensity vs. voltage (IV) curves can be used as a fingerprint of the oxide phase. Figures 4b (LEEM image) and 4c (IV curves) show an example in which regions of both first-layer (FeO) (red) and second-layer (Fe₂O₃) (blue) are present on the surface. The LEEM-IV curves are markedly different and can be used to identify the stoichiometry of the various regions in the LEEM image.

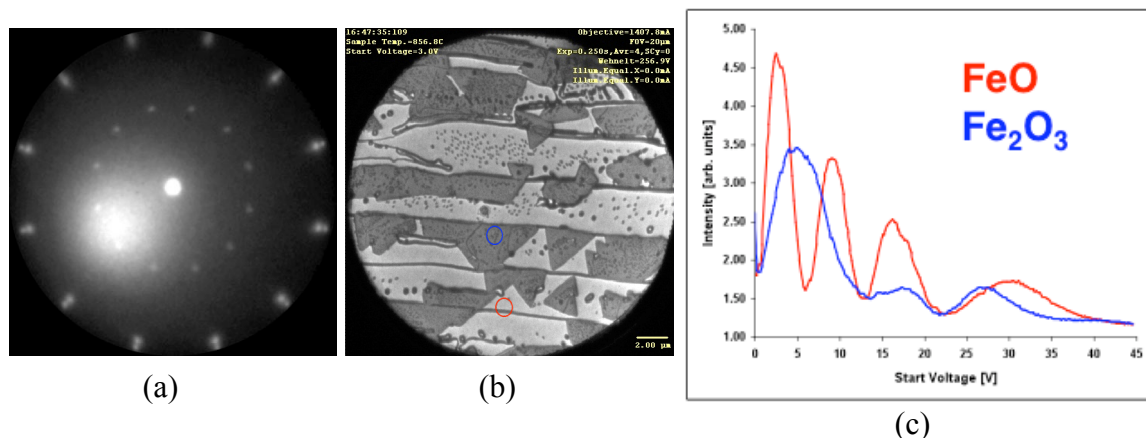


Fig. 4 (a) LEED pattern (b) LEEM image and (c) LEEM-IV curves from a YSZ(001) surface covered with first- and second-layer iron oxide film. The outer/inner 12-fold LEED pattern in (a) corresponds to FeO/Fe₂O₃. The red and blue circles in (b) identify regions of first- and second-layer growth. IV spectra (c) from first- and second-layer regions are unique.

Future experiments will be conducted to define the conditions to produce iron oxides of a desired stoichiometry and explore the intermixing between the film and the YSZ substrate.

Acknowledgement

Funding for this work was provided jointly by DOE, Office of Basic Energy Sciences, Division of Materials Science and the Laboratory Directed Research and Development program at Sandia National Laboratories, in the form of a Grand Challenge project entitled Reimagining Liquid Transportation Fuels: Sunshine to Petrol. Sandia is a multiprogram laboratory operated by Sandia Corporation, a Lockheed Martin Company, for the United States Department of Energy's National Nuclear Security Administration under Contract DE-AC04-94AL85000.

References

- [1] Diver, R.B., Miller, J.E., Allendorf, M.D., Siegel, N.P., Hogan, R.E., *Journal of Solar Energy Engineering*, **130** (2008) 041001.
- [2] See, for example: M. A. van Hove, *et al.*, *Surface Science* **103**, 189 (1981).
- [3] G. Jnawali, H. Hattab, B. Krenzer, and M. Horn von Hoegen, *Phys. Rev. B* **74**, 195340 (2006).

Enhancement of the field-induced strain in multiferroics

Wei-Feng Rao and A.G. Khachaturyan*

Department of Materials Science and Engineering, Rutgers University,
607 Taylor Road, Piscataway, New Jersey, 08854, USA

Multiferroic properties of a coherent ferroelectric/ferromagnetic composite are caused by the strain-induced magnetoelectric (ME) coupling of magnetization of magnetic and polarization of ferroelectric particles. The elastic strain generated by magnetic particles interaction is produced by magnetostriction and piezoelectric effects of these particles. The higher elastic strain, the greater the ME coupling. Therefore a development of new materials with advanced ME properties requires a maximization of the strain generated by H and E fields through changes of magnetization and polarization of the particles.

In this research we proposed to use a new approach to materials design. We investigate situations in which the strain providing the ME coupling is not associated with the intrinsic magnetostrictive and piezoelectric constants of the constituent phases but is caused by the field-induced reorientation of single-domain states of precipitates of the low-symmetry phase in the cubic parent phase and determined by the crystallographic parameters of these phases.

We consider coherent two phase systems formed by a precipitation of the low-symmetry (tetragonal in our case) phase from the supersaturated cubic solid solution. At early stages of decomposition, the precipitates of tetragonal phase are single domain particles, which can be in three orientation variants whose c axes aligned along the $\langle 100 \rangle$ directions of the cubic matrix. Application of an external field energetically coupled with the orientation of c -axis of the precipitates—this can be magnetic, electric or external field—results in their transition to orientation variant favored by the applied field. Such a transition can be provided by small atomic displacement, rather than rotating the entire lattice of the domain. (Fig.1a). The macroscopic strain effect caused by this reorientation is $\varepsilon \sim [(c/a)-1]\omega$, where c and a are lattice parameters of the tetragonal phase and ω is its volume fraction. Given that the typical value of $[(c/a)-1]$ can be within the 0.1-0.01 range, this is a giant value, which, depending on the applied field, can be regarded as a giant *extrinsic* magnetostrictive or piezoelectric strain. In fact, this elastic strain effect is associated not with conventional magnetostriction or piezoelectric effect but with the crystallography of the tetragonal phase and the directional flexibility of orientation of the single-domain state of tetragonal precipitates with respect to a transition between these states.

We developed a theory and 3D modeling of a giant strain response of a coherent system of low-symmetry (tetragonal) nano-precipitates obtained at early stage of decomposition. We introduced and took into consideration two new properties inherent to displacive

* Principal Investigator. Tel.: +1 732 445 4711; fax: +1 732 445 6780.
E-mail address: khach@jove.rutgers.edu (A. G. Khachaturyan).

characteristics of the transforming phase, the structural anisotropy and directional flexibility. Both of them automatically follow from a generalization of the existing theory of coherent systems by considering the transformation strain as a relaxing thermodynamic parameter. The structural anisotropy is a notion similar to the magnetic anisotropy of ferromagnets. It determines the crystal lattice symmetry and orientation relations of the low symmetry phase, as demonstrated in Fig. 1(b-c) where the energy of structural anisotropy is a function of orientation of the transformation strain. It is shown that a system with a low structural anisotropy has extremely high directional flexibility and displays giant and often non-hysteretic strain responses. Vanishing structural anisotropy results in a new glass-like state with random orientation relations and unlimited directional flexibility.

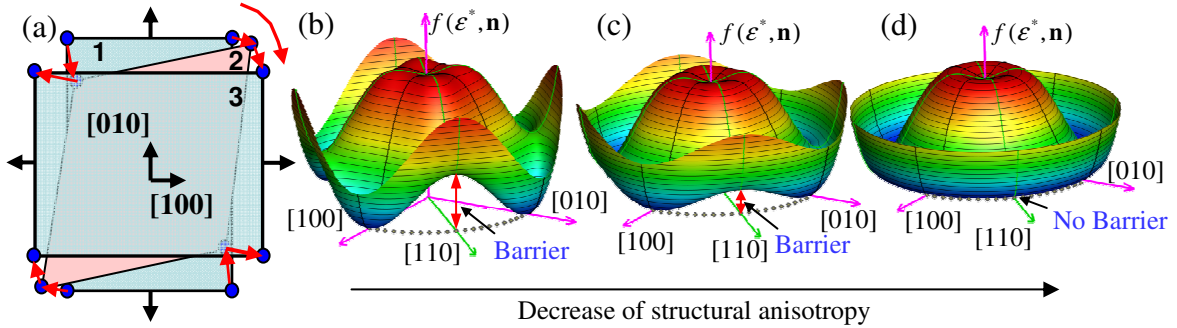


Figure 1. (a) Schematic flipping of a tetragonal unit cell through small atomic displacements, and (b-d) the free energy dependence on the representative strain, \mathcal{E}^* , and direction \mathbf{n} in the (001) plane. The transition, i.e., from 1 to 3, goes through intermediate states like 2 in (a), and a projection of the transition path is indicated by dots in (b-d). The red arrow in (b-d) shows the energy barrier along this path. A local minimum at the top of (b-d) (at $\mathcal{E}^* = 0$) describes the metastable parent phase. Note: the entire lattice in (a) does not rotate, and the directional flexibility is determined by the height of the energy barriers (structural anisotropy)

Using 3D and 2D modeling, we formulated conditions leading to a drastic amplification of non-hysteretic strain responses to the applied field that may reach orders of magnitude. We computationally prototyped a particular case wherein the applied field is stress, although the result can be directly extended to the cases of ferromagnetic and ferroelectric two phase mixtures wherein the fields are magnetic and electric, respectively.

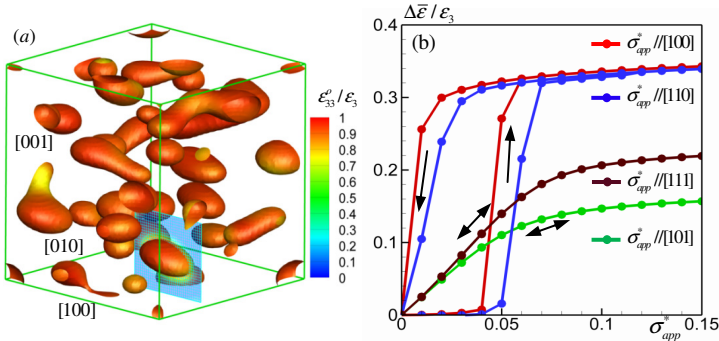


Figure 2. (a) Microstructure obtained by decomposition under constant stress, and (b) strain responses to periodically applied stress along different directions. The simulation size is $80 \times 80 \times 80$, $\mu^* = -0.05$, and $t^* \sim 8.8$. The constant stress applied during decomposition, $\sigma_{app}^* = 0.03$, is applied along [001].

Fig.2a shows a typical 3D microstructure formed with constant uniaxial stress applied along [001] during decomposition. Figure 2b shows the strain responses generated by the rotation of tetragonality axis under periodical uniaxial stresses applied along various directions. Figure 2b thus shows that macroscopic strain responses are significantly magnified by the rotational flexibility of nano-particles, which is recoverable and can be non-hysteretic.

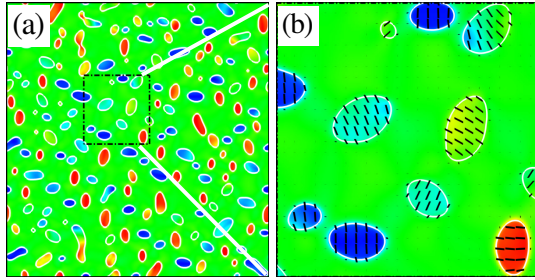


Figure 3. (a) 2D microstructure of structurally isotropic system ($\mu=0$) and (b) an inset of (a). Nano-particles are bordered by white lines. In (b) the principal directions of transformation strain corresponding to its maximum principal value is shown by streaks. Simulation size is 512×512 , $t^* \sim 24$, and no stress is applied during decomposition.

Further 2D modeling shows that single domain precipitates are obtained before extensive coarsening occurs. In the isotropic case of vanishing of structural anisotropy, the principal directions of the transformation strain in nano-precipitates are randomly oriented and a glass-like structure is produced (Fig. 3). It is also shown that if a displacive transition between $\langle 100 \rangle$ directions occurs, the higher anisotropy results in the stronger hysteresis, and the hysteresis may become so large that such a transition is non-recoverable. However, as in Fig. 4, the strain responses to stress applied along the $\langle 111 \rangle$ directions are practically non-hysteretic for all simulated cases: the higher the structural anisotropy, the bigger the blocking force and the narrower the hysteresis loop.

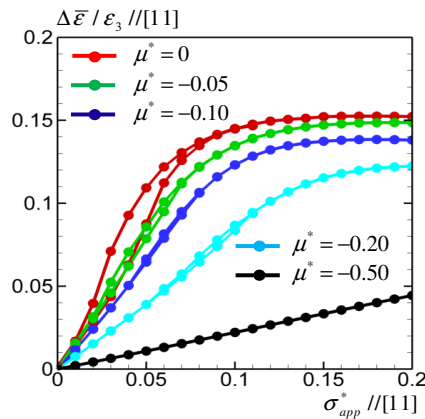


Figure 4. Strain responses induced by the rotation of the transformation strain in systems with different structural anisotropy to periodical stress applied along the [11] direction. The microstructures are obtained by 2D modeling of decomposition without applying stress. 2D simulation size is 512×512 , $\bar{c} = 0.29$ and $t^* \sim 24$.

Future plans:

We plan to investigate multiferroics whose ME coupling consisting of nano-dimensional single domain particles of ferroelectric (or ferromagnetic) phase embedded into ferromagnetic (or ferroelectric) matrix. These systems are drastically distinguished from the conventional ME composites by the origin of the strain providing the ME coupling. Unlike the conventional ME composites wherein the piezoelectric or magnetostrictive strain are intrinsic properties of the constituent phases, the coupling strain generated by

the E or H field in our systems is caused by the field-induced change of single domain state of the nano-particles. For example, if the nano-particles are tetragonal, the macroscopic strain generated by such reorientation is of the order of $(c/a-1)\omega$. Given the typical values c/a ratio of the phases, the strain-induced ME coupling in this case can reach giant values. This mechanism of generating the giant strain induced by the applied fields is already discussed in the abstract.

The Phase Field theory of the strain response developed in this paper will be further developed to be applicable to describe the ME composite, which is a nano-dispersion consisting of single-domain nano-particles.

Papers acknowledging the DOE support:

1. Yong Ni, Shashank Priya, and Armen G. Khachaturyan, *Modeling of magnetoelectric effect in polycrystalline multiferroic laminates influenced by the orientations of applied electric/magnetic fields*. J. Appl. Phys., **105**, 083914, 2009.
2. Yong Ni, Wei-Feng Rao, and Armen G. Khachaturyan, *Pseudospinodal Mode of Decomposition in Films and Formation of Chessboard-Like Nanostructure*. Nano Letters, **9**, 3275, 2009.
3. Yong Ni, Linghui He, and Armen G. Khachaturyan, *Equivalency principle for magnetoelastic multiferroics with arbitrary microstructure: The phase field approach*. J. Appl. Phys. **108**, 023504, 2010.
4. Wei-Feng Rao, Manfred Wuttig, and A.G. Khachaturyan, *Giant Non-Hysteretic Responses of Two-Phase Nanostructured Alloys*, Phys. Rev. Lett. (Under review), 2010.
5. Wei-Feng Rao and A. G. Khachaturyan, *Phase Field Theory of Proper Displacive Phase Transformations: Structural Anisotropy and Directional Flexibility, Vector Model, and Transformation Kinetics*. Acta Materialia, (Under Review), 2010.

Hydrogen Absorption in Pd-based Nanostructures

David Lederman

West Virginia University, Department of Physics, Morgantown, WV 26506-6315

david.lederman@mail.wvu.edu

Program Scope/Definition

The goal of the project is to determine the intrinsic effects of hydrogen absorption on the electronic properties (i.e., changes in the Fermi level and/or band structure) of Pd-based nanostructures. Although it is known that hydrogen absorption can change the magnetic and dielectric properties of thin films when hydrogen is absorbed due to chemisorption in a Pd overlayer, the fundamental mechanisms of how this happens are not well understood. In particular, the effects of defects and crystallinity have not been quantitatively determined, mainly because the structures thus far have not been characterized sufficiently well, which makes it difficult to separate extrinsic (i.e., structural) effects from intrinsic (i.e. purely electronic) effects. This project deals with this issue by growing well-characterized thin films and nanostructures and measuring the magnetic, ferroelectric, and magnetoelectric properties, which are then correlated with direct measurements of hydrogen penetration. Another problem is that the amount of hydrogen absorption, both in the Pd overlayers and in the underlayers, is not measured directly, so it is sometimes difficult to assess whether a given change in the properties is due to hydrogen being absorbed in the underlayer or due to electronic changes at the interface. This is addressed by performing detailed neutron reflectivity measurements that quantitatively determines the depth profile of hydrogen absorption, and at the same time, measures the depth profile of any magnetic changes induced by the hydrogen absorption.

Recent Progress

Co/Pd multilayer samples have been fabricated and their electronic properties have been monitored by performing magnetization and magnetoresistance as a function of hydrogen absorption and temperature by the PI's group at West Virginia University, including graduate student [Kineshma Munbodh](#) and postdoctoral researcher [Felio Perez](#). Neutron reflectivity measurements, performed in collaboration with [Michael Fitzsimmons](#) and his group, including postdoctoral researcher [Mikhail Zhernenkhov](#), at the Los Alamos Neutron Science Center (LANSCE) spallation neutron source. Polarized neutron reflectivity (PNR) was used to measure the depth profile of the magnetization and of deuterium (D_2) absorption which allows determination of where the magnetic properties are changing and whether they are correlated with the penetration profile of hydrogen. Our recent work is based on polarized neutron reflectivity measurements in air or He and D_2 atmospheres on two Co/Pd multilayer samples with perpendicular magnetic anisotropy. A paper has been submitted to *Physical Review B* for publication.

X-ray diffraction showed highly oriented growth along the Pd [111] direction. Multilayer periodicities obtained from the separation of the multilayer peaks (23.2 Å and 23.7 Å for samples A and B) agreed well with those obtained from x-ray reflectivity (XRR) and PNR data for sample A (23.5 ± 1.4 Å) and sample B (23.5 ± 2.5 Å). Quantitative analysis of XRR data was used to determine the non-magnetic structure.

Magnetization measurements for both samples are shown in Figure 1. By comparing the measurements with H perpendicular

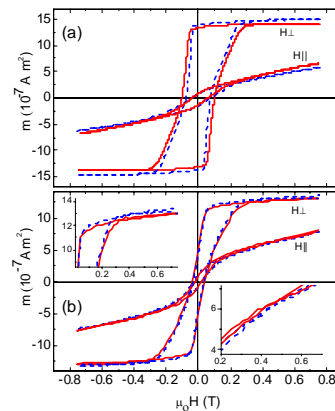


Figure 1 Magnetic moment measurements in 1 atm of He (blue dashed curves) and H_2 (red solid curves) with the magnetic field applied perpendicular (H_{\perp}) and parallel (H_{\parallel}) to the sample surface. (a) Data for sample A, (b) data for sample B. Top left and bottom right insets in (b) are close-up views of the data in (b) for the H_{\perp} and H_{\parallel} configurations, respectively.

and parallel to the sample plane, we found that 35.7% and 53.8% of the magnetization was in the plane of the sample at $\mu_0 H = 0.65$ for samples A and B, respectively. Square loops measured with the field applied out of the plane confirm the presence of a large out-of-plane anisotropy. SQUID magnetometry revealed that the in-plane saturation field of sample A was 5.5 T. An observed decrease of the magnetization in sample B as the field decreased from saturation (for $H > 0$ and $H \perp$ to the sample surface) was due to the formation of magnetic domains. This was verified by MFM images of sample B (Figure 2), which indicated the presence of irregular striped domains characteristic of ferromagnetic Co/Pd multilayers with perpendicular magnetic anisotropy. Sample A displayed a larger remanence and coercivity than sample B, possibly as a result of greater atomic intermixing at the interfaces which is known to result in more pinning centers that obstruct domain growth and propagation. As a result, sample A showed no domain structure via MFM.

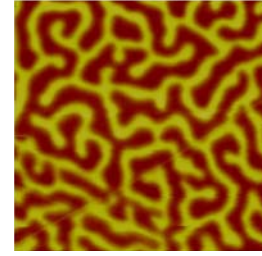


Figure 2 MFM image ($5 \mu\text{m} \times 5 \mu\text{m}$) of sample B performed at $H = 0$ at room temperature after magnetizing it out of the plane of the sample.

Magnetization measurements showed that when H was applied in the plane of the samples, there was a net increase in magnetization component along H upon H_2 absorption at $\mu_0 H = 0.65$ T, the increase being larger in sample A. When H was \perp to the sample surface, the saturation magnetization decreased in both samples, although the effect was once again greater for sample A. This means that the magnetization of the samples decreased upon H_2 absorption. Therefore, the increase in the unsaturated state, with H in the plane of the samples, must be due to a decrease in the perpendicular anisotropy.

PNR provided detailed magnetic information about the samples as a function of depth. PNR data obtained from sample A with the fit to the model are shown in Figure 3.

Qualitatively, the decrease in the period of oscillations in the low- Q regime upon D_2 absorption indicates an increase in the total thickness of the sample. The same observation can be made for sample B. Figure 4 shows the high and low Q portions of the data and fits for sample B, respectively. The fact that the position of the multilayer peak at $Q = 0.27 \text{ \AA}^{-1}$ remained unchanged indicates that the Co/Pd multilayer period did not change upon D_2 absorption. Therefore, the increase in total sample thickness is solely due to an expansion of the Pd top and buffer layers.

Nuclear scattering length density (SLD) profiles ρ_n and their derivatives obtained from fits of the PNR data are shown in Figure 5 for sample B. Similar ρ_n profile was also obtained for sample A, but analysis of these data was less reliable due to the absence of the multilayer Bragg peak because we

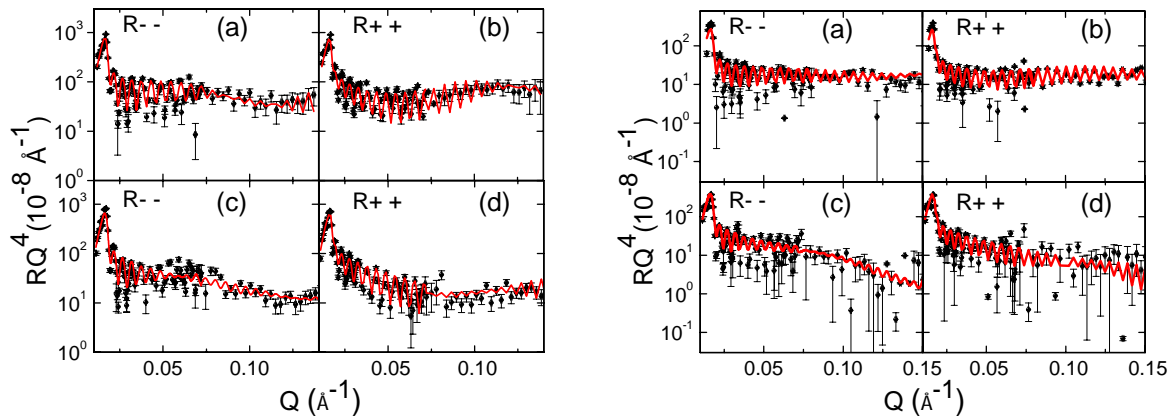


Figure 3 PNR using neutrons with (- -) and (+ +) incoming and outgoing polarization states with the sample in helium [(a) and (b)] and deuterium [(c) and (d)] in 0.65 T (left) and 6.0 T (right) magnetic fields applied in the plane of sample A. Experimental data are black dots and the model fit is the red line.

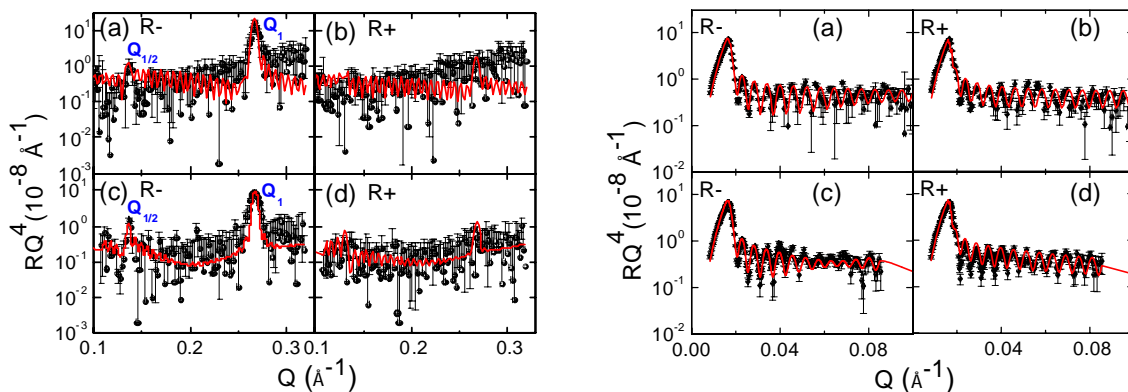


Figure 4 Left: PNR using neutrons in the high- Q regime ($Q > 0.1 \text{ \AA}^{-1}$) with (-) and (+) incoming polarization states with the sample in air [(a) and (b)] and deuterium [(c) and (d)] in a 0.65 T magnetic field applied in the plane of sample B. The positions of the single order (Q_1) and half-order magnetic peaks ($Q_{1/2}$) are indicated. Right: low- Q portion of same data. Experimental data are black dots and model fit is red line.

were unable to measure at high Q . Positions of the interfaces, determined from the locations of the maxima and minima in $d\rho_n/dz$, are indicated by vertical dotted lines in Figure 5. Values of ρ_n were used to determine the stoichiometry of each layer independently. The Pd buffer and top layers' SLDs correspond to bulk Pd in both samples A and B. Analysis indicates that in sample A, the center of the Pd stack layers consisted of 95% Pd and the Co stack layers are 12% Co. Sample B consisted of Pd stack layers with 89% Pd and Co stack layers with 30% Co, indicating the presence of interface disorder.

Upon D_2 absorption, there was a statistically significant increase in the thickness of the Pd buffer and top layers in both samples. Results also indicate statistically insignificant changes in the Co and Pd stack layer thicknesses. A noteworthy decrease of the PdO layer thickness occurred in both samples, which can be attributed reduction of the oxide due to deuterium absorption.

Comparing ρ_n and thickness change before and after D_2 absorption (Figure 6), the ratio of the number of deuterium atoms to Pd atoms, C_D , was estimated in each layer C_D was found to be 0.53 and 0.30 for sample A and 0.75 and 0.52 for sample B in the Pd buffer and Pd top layers, respectively, confirming that there was significant D_2 absorption in these layers. The value of C_D for the Pd and Co stacks in sample A and B was approximately 0.02 ± 0.005 . The relatively small value of C_D for the Pd

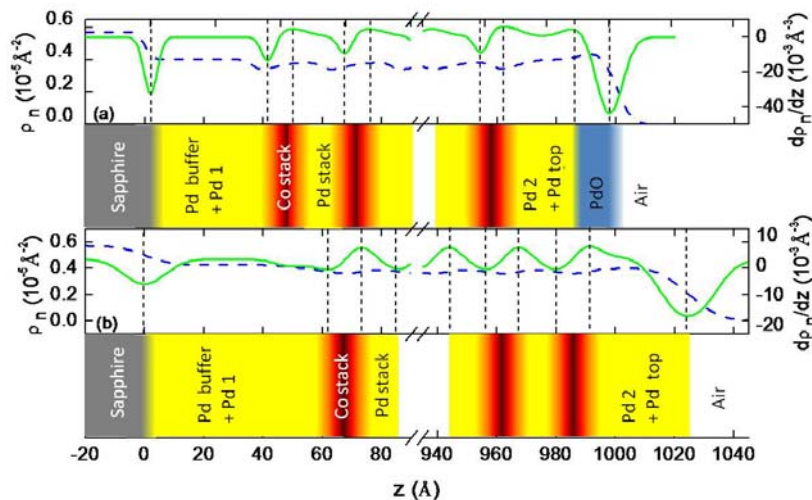


Figure 5 (Color online) Nuclear SLD profiles (blue dashed curve) and its derivative (green solid curve for sample B (a) in air and (b) for the sample in deuterium). The vertical dotted lines indicate the positions of the interfaces. The corresponding sample profile is shown.

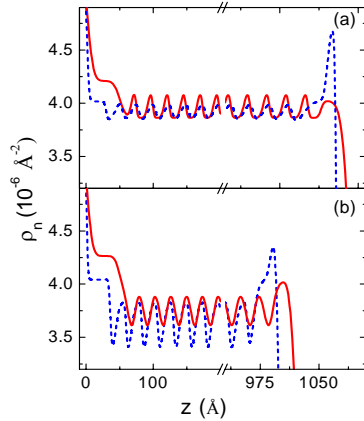


Figure 6 (Color online) Nuclear SLD profile in air (helium) (blue dashed curve) and in deuterium (red solid curve) for (a) sample A and (b) sample B at 0.65 T.

saturation. These results indicate that electronic effects resulting from H₂ or D₂ absorption are responsible for a decrease in perpendicular anisotropy and saturation magnetization of the samples, and that strain effects are not significant.

Future Plans

We are currently working on fabricating Pd/Co multilayers in a nanodot (< 100 nm diameter) in order to determine the importance of hydrogen absorption through the sides of the sample. Measurements require large volumes, and therefore we are attempting to create a large number of nanodots using polystyrene beads as a shadow mask. We are also planning to study the effect of hydrogen absorption in ferroelectric oxide thin films covered by Pd in order to attempt to control absorption via electric voltages.

Reference

K. Munbodh, F. A. Perez, C. Keenan, D. Lederman, M. Zhernenkov, and M. R. Fitzsimmons, "Effects of hydrogen/deuterium absorption on the magnetic properties of Co/Pd multilayers", *Phys. Rev. B* (submitted).

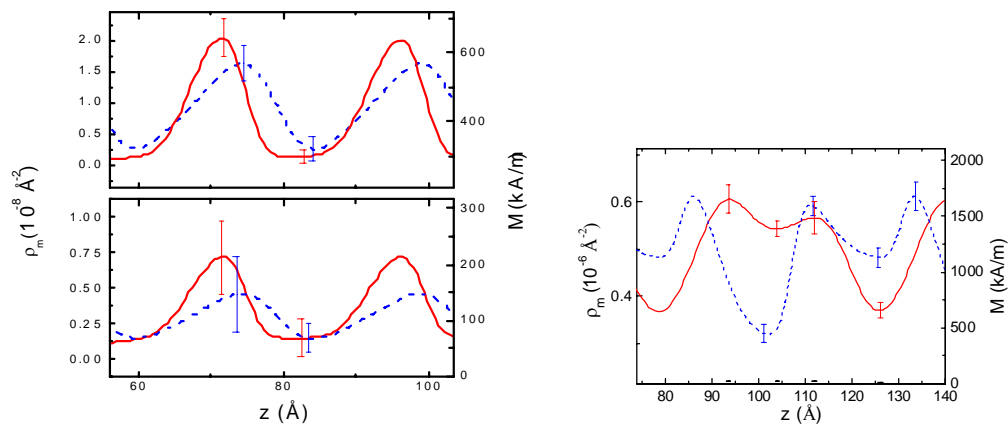


Figure 7 Left: Magnetic SLD in air (blue dashed curve) and in D₂ (red solid curve) for sample A at (top) 6 T and (bottom) 0.65 T for two Co/Pd bilayer in the stack. The film-substrate interface is set at a thickness of zero. Right: data for sample B at 0.65 T.

and Co stack explains the lack of significant lattice expansion and implies that D₂ was probably absorbed into interstitial sites.

The magnetic SLD profiles ρ_m for samples A and B are shown in Figure 7. The maxima in ρ_m correspond to Co layers and the minima represent Pd layers. Results indicated a doubling of the Sample B's multilayer magnetic period with respect to the nuclear period. Since the magnetization was not saturated, layers with weaker anisotropy tilted more strongly towards the field direction, causing a $Q_{1/2}$ peak to appear. Our results also indicate that the modulation grew stronger with D₂ absorption, evident in Figure 4, which shows that the $Q_{1/2}$ peak became more pronounced, and in the magnetic SLD profile in Figure 7 which shows the increase in magnetic contrast between adjacent minima, corresponding to Pd layers.

To summarize our most important experimental results, we have found that: 1) D₂ absorption occurs throughout the thickness of both samples; 2) the multilayer stack absorbs D₂ but does not expand along the growth direction; 3) both the Pd and Co layers are magnetized and their in-plane magnetization increases when the magnetization is not saturated in the plane but decreases at

Program Title: Manipulation of Phonons with Phononic Crystals
Principal Investigator: Zayd Chad Leseman
Institution: University of New Mexico
Address: Mechanical Engineering, MSC01-1150, Albuquerque, NM 87131
e-mail: zleseman@unm.edu
Co-Investigator: Ihab El-Kady
Institution: Sandia National Laboratories
Address: PO Box 5800, MS 1082, Albuquerque, NM 87185
e-mail: ielkady@sandia.gov

Program Scope

The research goals of this project are (i) to experimentally demonstrate phonon spectrum control at THz frequency regimes using phononic crystals (PnCs), (ii) to experimentally demonstrate analog PnCs circuit components at GHz frequencies and below in order to build low power communication devices that utilize less power than current Digital Signal Processing (DSP) techniques, and (iii) to gain a fundamental understanding of phonons and their interactions in PnCs at these frequencies by means of a quantum field theory and numerical methods.

The primary challenges in this project can be broken down by frequency regimes – THz Phonons and GHz and below. For the THz phonons the primary challenges are (i) development and validation of a comprehensive physical model for THz phonons and their interactions, and (ii) fabrication and characterization of structures with sufficiently fine feature sizes to enable phonon DOS manipulation at relevant THz bands. The theoretical framework will be developed in three stages, in frequency regimes corresponding to fundamental length scales: continuum wave mechanics (CWM), semi-classical (SC) and quantum field theory (QFT) regimes. In the CWM regime, well-established classical methods such as Finite Difference Time Domain (FDTD), Finite Element Method (FEM) and Plane Wave Expansion (PWE) will be utilized to obtain and tailor phonon energy bands and DOS. In the SC regime, a classical statistical mechanics harmonic oscillator partition function will be subjected to PnC manipulated DOS. In the QFT regime, a fully quantized multimode harmonic (or anharmonic) oscillator field will be used. PnCs in this frequency range will be fabricated with Focused Ion Beam (FIB) techniques and characterized using a short pulse Joule heating technique that allows for determination of thermal conductivities.

For the GHz and lower frequencies, the primary challenges are (i) theoretical determination (by analytical and numerical simulations) designs for analog PnC components and (ii) fabrication and characterization of these structures. For the theoretical portion FDTD and FEM models will be used to characterize 3D structures as guided by analytical derivations. Once all parameters are well understood an inverse approach to design will be taken. In the experimental portion, piezo-electric materials will be deposited on previously fabricated PnCs and excited to determine their response.

Recent Progress

The initial four months of this program have seen progress in the areas of modeling and characterization of PnCs. From the perspective of modeling, our group has completed work on

the development of the PWE technique, 3-D FDTD model, and 3-D FEM models. Experimentally, we have fabricated and measured the properties of PnCs. In particular we have discovered that one can reduce the thermal conductivity of single crystal Si (SCS) to 6.8 W/mK, a reduction of more than order of magnitude over bulk silicon.

Using the PWE and 3-D FDTD models developed, we have been successful in modeling the behavior of PnCs that we have fabricated [1-3]. For example we have fabricated PnC's operating around 1 GHz, see Figure 1a, and successfully modeled their behavior, see Figure 1 b and c [1].

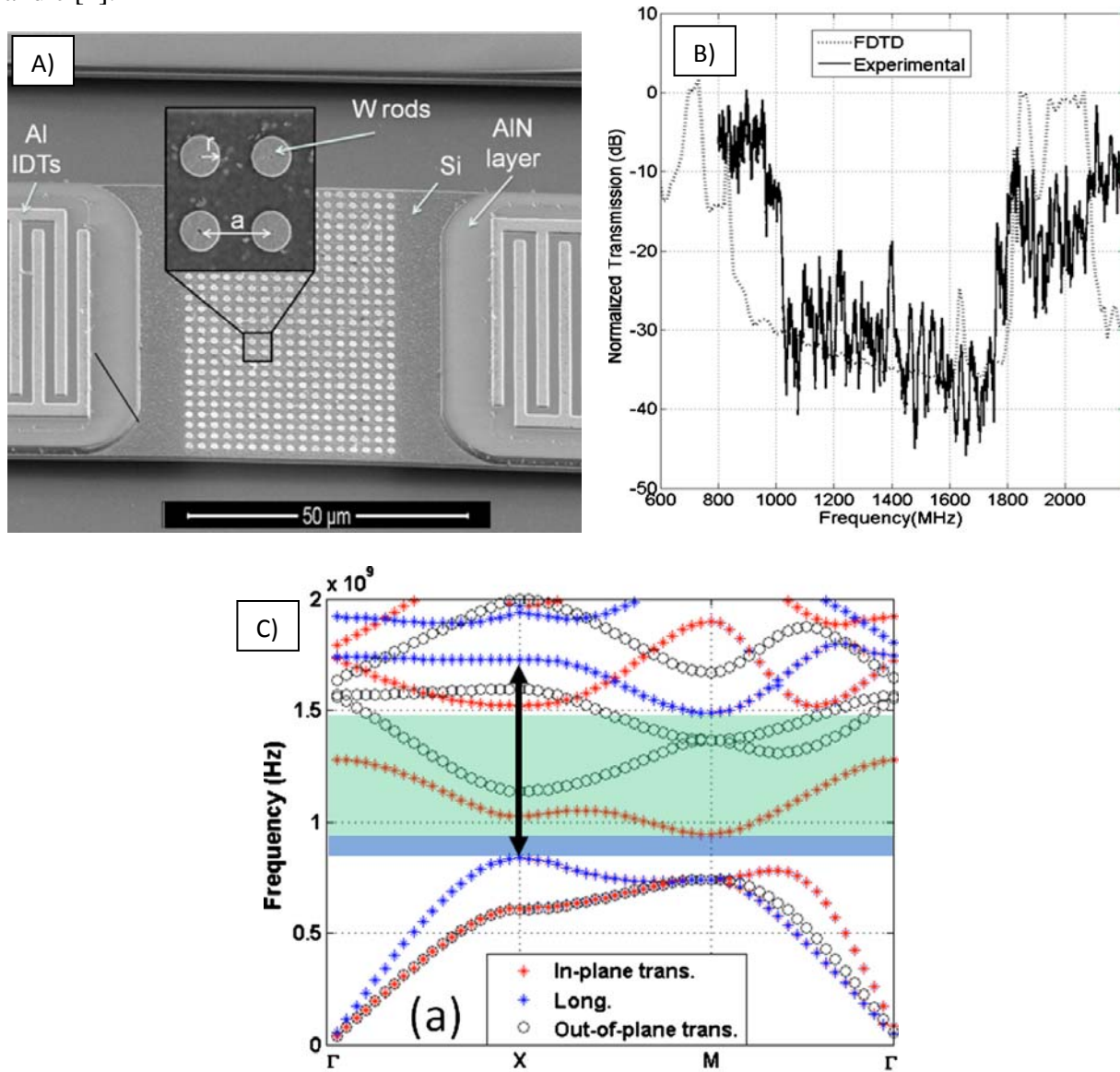


Figure 1: A single crystal Si matrix / W inclusion PnC exhibiting a bandgap between 1 and 1.8 GHz. This PnC has a gap-to-midgap ratio of 57% - among the highest ever reported. A) SEM image of PnC tested, B) Experimental measurement and FDTD results for the PnC's response, C) PWE results for the PnC

Though the FDTD and PWE methods show great utility we have discovered that they do not accurately capture the frequency response of fabricated PnCs. Thus we have also developed a FEM model that takes into account more experimental variables. Using this model we have been able to more accurately capture the frequency response of fabricated PnCs. Figure 2 shows the experimental response of a PnC, the FDTD model and FEM model. Note that the FEM model captures more of the PnC's experimental response. In particular focus on the boxes a, b, c and d of Figure 2. We have found this additional accuracy is attained when taking into account additional experimental factors such as transducer placement and substrate losses. Additional agreement is found when using a full model of the crystal, i.e. not using periodic boundary conditions, and all deformation modes of the PnC.

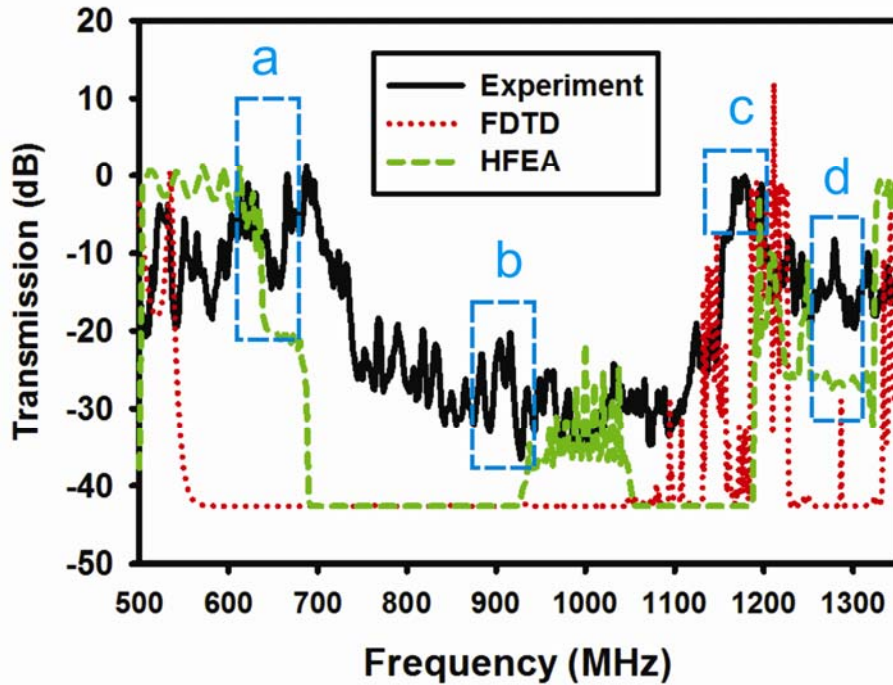


Figure 2: Comparison between the transmission measured in [3], simulated by FDTD [3], and the developed FEM (HFEA).

Using the time-domain thermoreflectance technique (TDTR) our research team determined the thermal conductivity of PnCs similar to the one shown in Figure 1a. The PWE method was utilized to determine the phononic DOS for the PnC from its dispersion and used to calculate the change in thermal conductivity of the PnC as compared to bulk Si. After obtaining the integrated DOS the thermal conductivity was calculated using a Callaway-Holland-type model:

$$k = \frac{1}{6\pi^2} \sum_j \int C_j(q) v_j^2(q) \tau_j(q) dq$$

These results showed a decrease in thermal conductivity of a PnC made from SCS to be 6.8 W/mK. This is more than order of magnitude lower than that of bulk Si. These results were recently reported in Nano Letters [4].

Future Plans

Future plans for this work include using the developed models to design, fabricate and characterize PnC waveguide devices and logic elements in order to ultimately build PnC logic devices. We will continue to fabricate smaller PnC in order to attain better control over higher frequencies phonons and better tune the thermal conductivity of the structures. We will design, purchase and build equipment to characterize the behavior of PnCs to temperatures below 10 K in order to better understand the fundamental behavior of PnCs and how they control phonon propagation.

References

1. Y. M. Soliman, Su, M. F., Leseman, Z. C., El-Kady, I., Olsson III, R. H., "Phononic crystals operating in the GHz range with extremely wide bandgaps," *Applied Physics Letters*, vol. 97, 193502, 2010.
2. Y. M. Soliman, M. F. Su, Z. C. Leseman, C. M. Reinke, I. El-Kady, R. H. Olsson III, "Effects of release holes on micro-scale solid-solid phononic crystals," *Applied Physics Letters*, vol. 97, 081907, 2010.
3. M. F. Su, R. H. Olsson-III, Z. C. Leseman, and I. El-Kady, "Realization of a phononic crystal operating at gigahertz frequencies," *Applied Physics Letters*, vol. 96, 2010.
4. P. E. Hopkins, C. M. Reinke, M. F. Su, R. H. Olsson III, E. A. Shaner, Z. C. Leseman, J. R. Serrano, L. M. Phinney, and I. El-Kady, "Massive reduction in thermal conductivity of single crystal Si by phononic crystal patterning," *Nano Letters*, vol. 11, pg. 107-112, 2011.

MuSR Investigations of Magnetic Semiconductors for Spintronics Applications

SISGR Grant DE-SC0001769

Principal Investigator: Roger L Lichti

Department of Physics, Texas Tech University, Lubbock, Texas 79409-1051

Email: roger.lichti@ttu.edu

We are probing internal magnetic fields in magnetic semiconductors, either concentrated or diluted systems with a ferromagnetic (FM) phase, using implanted positive muons. An important result in the concentrated systems is the observation and characterization of “spin polarons” outside of the FM ordered phase. We also find spin polarons in many other materials with strong correlations involving d or f electrons, suggesting that they may be an important heavy-electron quasi-particle in such systems.

The MuSR Technique

In this project we use implanted positive muons as an extremely sensitive local probe of internal magnetic fields in the material under investigation. We participate in an international collaboration with experiments at accelerator based MuSR User Facilities. Primary collaborators are VG Storchak from the Kurchatov Institute in Moscow, Russia, who originated this research, and JH Brewer from the University of British Columbia, Vancouver, Canada. We work mainly at TRIUMF in Vancouver, where beams of 100% spin polarized muons are available along with facility maintained spectrometers. Muon Spin Rotation (MuSR) is a specialized magnetic resonance technique [1]. In the transverse-field geometry (TF-MuSR) an external magnetic field is applied perpendicular to the initial muon spin polarization direction and positrons emitted as the muons decay are detected in several counters covering various emission directions. The decay asymmetry is formed as the normalized difference in count rates for two counters covering identical solid angles for directions differing by 180° . Since the decay positrons are preferentially emitted along the instantaneous muon spin direction, this asymmetry then maps out the precession of the muon spin in the local field at the muon stopping site. The asymmetry is directly proportional to the muon polarization at the time of decay. Observed precession frequencies are typically damped, and details of the relaxation provide information on dephasing and depolarization processes; specifically for this project, probing the distribution of quasi-static local magnetic fields and any dynamic processes leading to fluctuations of those fields.

Figure 1 displays a typical TF-MuSR spin-precession spectrum, both in the time domain and also as an FFT in frequency space. For a “bare” muon the spectrum is a single sharp line at the muon’s Larmor frequency of 135.54 MHz/T. In an FM ordered system this frequency will be significantly shifted from that expected due to the applied field, and a signal from the internal fields in a well ordered FM system are observed in zero applied field. The two outer lines in the displayed frequency spectrum are from muons which have captured an electron; these lines arise from muon spin-flip transitions with the electron spin at a fixed orientation, either up or down with respect to the applied field.

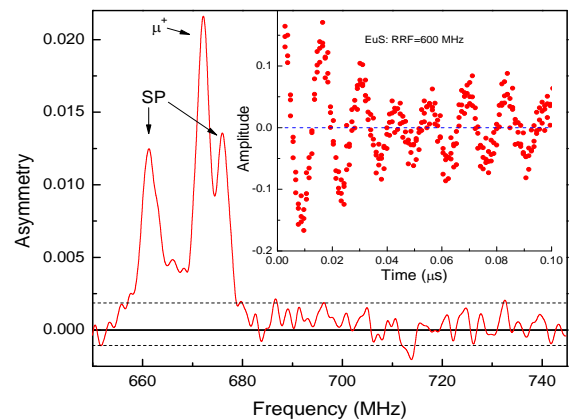


Fig. 1: The MuSR spectrum in EuS at 300 K and 5T. The middle line is from bare muons.

Internal Fields in Ferromagnetic Phases

We have studied several of the ferromagnetic Eu-based chalcogenides and a few of the Cr-based spinel compounds [2]. Figure 2 shows the temperature dependent internal fields for EuS [3,4] as extracted from zero-field MuSR precession frequencies. The temperature dependence follows the development of ferromagnetic order below the Curie temperature, mapping out more or less standard magnetization curves, and imply robust FM order in all of the concentrated FM semiconductors investigated thus far.

Similar measurements for the diluted magnetic semiconductors (DMS) can provide a test of homogeneity by providing information on the distribution of the internal magnetic fields in order to determine whether the ordered phase results in large magnetic domains having a well defined and uniform local field at the muon site. Such measurements test for segregation into separate magnetic and non-magnetic phases or for a secondary chemical phase. For very diluted magnetic systems, uniform internal fields can only be developed if the magnetism associated with isolated local moments, or with very small magnetic clusters or inclusions, is effectively transferred to the semi-conducting charge carriers, *i.e.* holes in Mn-doped III-V or II-IV-V₂ materials.

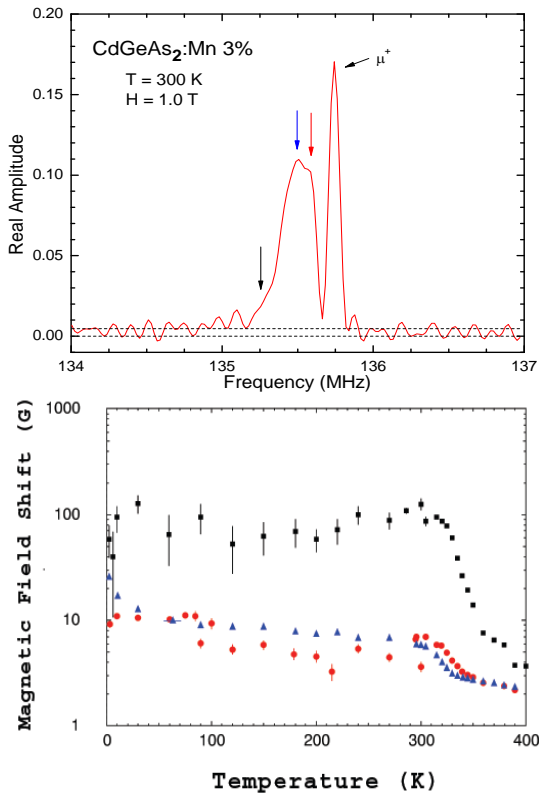


Fig. 3: MuSR spectrum for CdGeAs₂ with 3% Mn, and the temperature dependence for selected shift features.

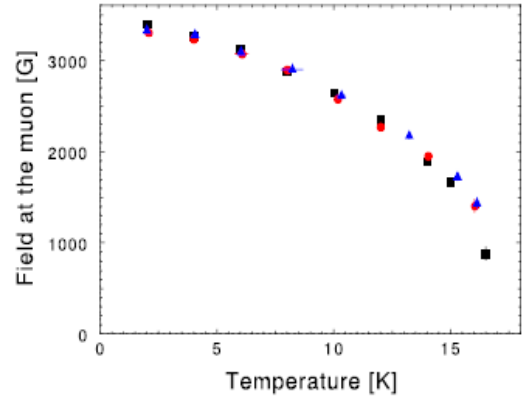


Fig 2: Internal field at the muon site in the FM ordered phase of EuS which has a T_C of 17 K.

Early experiments on several DMS materials [5] failed to detect a well defined internal field in the FM phase even though nearly the whole sample showed shifted precession frequencies in high transverse applied fields. These two results combined suggest a very wide distribution of local fields in the absence of strong alignment by an external magnetic field. Susceptibility data on a sample of CdGeAs₂:Mn showed features suggesting inhomogeneous magnetism and the shifted MuSR frequency spectrum [5] (see Fig. 3) shows some structure with slightly different shift onsets, which is consistent with non-uniform Mn concentrations. Our investigations of the Mn-doped II-IV-V₂ chalcopyrite compounds, which have several members with T_C above 300 K, are ongoing.

Characterization of Mu-Related Spin Polarons

One of the main initial goals of this project was to determine the extent to which magnetic polarons may be present in the non-ferromagnetic phases of magnetic

semiconductors and whether they may also form in materials that have strongly correlated electronic ground states that compete with magnetism. The first observation of a MuSR spectrum that is identified with a magnetic polaron was in the Eu chalcogenides [3,4] and was quickly followed by similar observations in a Cr based spinel compound [6]. A two-frequency spectrum centered very near the expected bare muon frequency is a signature of an electron localized at the muon (see Fig. 1 for EuS spectrum). Typically such a spectrum implies capture of an electron to form a muonium atom (Mu) which can be considered to be an extremely light “isotope” of hydrogen: the splitting is due to the electron-muon hyperfine interaction characteristic of the electronic wave function. Mu is commonly observed in the standard semiconducting materials and some insulators. However, the temperature and magnetic field dependences for the spectra we have identified with a magnetic, or “spin”, polaron are very different from that of a simple Mu impurity atom. While there are other explanations that might be consistent with these spectra in individual materials, the same set of features with common temperature and field dependences have now been observed in such a wide variety of situations (over 30 different materials) that we are increasingly confident of this identification; although, it remains controversial, particularly in the MuSR community.

The model which works well to describe the general spectral features has the electron occupying a $\text{Mu}(1s)$ like state, but with the radius controlled by optimization of the exchange energy by maximizing overlap with nearby magnetic ions. Exchange of the Mu-like electron with the unfilled inner d or f shell of the magnetic ions within the extent of the polaron’s electronic wave function will then align the ion moments ferromagnetically independent of whether the electron-ion exchange has FM or AFM character. When moment alignment within the core region consisting of the nearest-neighbor ions (plus second neighbors in *some* cases) is completely saturated, this small FM region acts as a single entity having a large composite spin; hence labeled as a “Spin Polaron”. Within some limits on fluctuation rates, the observed splitting in the MuSR spectrum is then determined within a simplified mean-field picture by the alignment of the large composite polaron spin S_{SP} with an applied field [4]. This leads to MuSR frequency splitting that follows a Brillouin function characteristic of the saturated polaron’s total spin, reaching a constant value that represents the true hyperfine constant A_{HF} for the Mu-like electronic wave function only in the large H/T limit. This basic model should be valid when the internal couplings within the spin polaron due to exchange are much stronger than the Zeeman interaction of individual spins with the external field and the polaron radius only covers a few neighboring ions, hence for a “small polaron”. This is a significantly different picture than has been used to describe the unsaturated magnetic polarons [7], seen for instance in Mn-doped II-VI semiconductors, where the electronic wave function is more like that of a shallow donor or trapped exciton, for which the $1s$ shape only describes an envelope function and the polaron radius extends over a much larger region covering a large number of host atoms. We find a conversion from a large magnetic polaron above 90 K to small spin polarons below 60 K in the correlated metallic pyrochlore CdRe_2O_7 [8], with both forms coexisting at the lowest temperatures.

When the Mu - Polaron electron actually occupies a true $1s$ state, as in our model, the hyperfine constant scales as $1/R^3$, thus provides a direct measure of the polaron radius: $A_{\text{HF}} = 4463$ MHz for a free Mu atom with $R_0 = 0.0531$ nm. The saturated splitting in either the temperature dependence or field dependence therefore provides the polaron radius within our model. Additionally, the slope of the frequency splitting in the small H/T linear region yields an estimate of the net polar spin; thus, we obtain both the polaron’s size and composite spin when both the saturation and linear region of the splitting can be observed. Figure 4 shows the typical temperature dependence at fixed field and the field dependence at fixed temperature for a spin polaron, showing the common saturation of the splitting.

For EuS [4], we obtain $A_{\text{HF}} = 37(3)$ MHz, yielding $R = 0.26(2)$ nm; the linear region slope gives $S_{\text{SP}} = 36(4)$. With the muon located at the tetrahedral site of the rock salt structure, the polaron radius matches the distance to the four nearest Eu ions at $d_{\text{nn}} = 0.258$ nm, each having an S of $7/2$, defining the core region. This gives $S_{\text{Core}} = 14$, consistent with a fully saturated core plus a halo of more distant Eu ions partially aligned with the core: including the 12 second neighbor Eu ions at 0.49 nm as also fully aligned with S_{SP} would give $S = 56$. This type of consistency with our basic model is repeated for other materials as well. In CdCr_2Se_4 for instance [6], the radius is $R = 0.30$ nm [$A = 24(2)$ MHz] which corresponds to significant overlap with both the nearest (4) and second nearest (12) Cr^{2+} ($S = 3/2$). With these 16 ion spins fully aligned in the polaron core, one gets $S_{\text{Core}} = 24$ compared to the measured net spin of $S_{\text{SP}} = 30(4)$. In each observed case, the center of the polaron spectrum is shifted from the bare muon frequency, yielding a measure of the local field in the center of the small ferromagnetic region within the spin polaron. The direction of these observed shifts are consistent with Hund's rules for the spin orientation of an extra electron added (via exchange) to a d or f shell; *i.e.* opposite to the ion spin for Eu^{2+} (half-filled $4f$ shell) in EuS, and parallel for Cr^{2+} ions in the spinel compounds (compare Fig. 1 with spectra in Fig. 4a). All of this internal consistency holds for other cases as well, and lends additional evidence that our basic Mu-related spin polaron model is fundamentally correct.

We have now observed very similar small spin polarons in a large number of materials which have strong correlations involving f or d electrons and heavy-fermion quasiparticle features in addition to the magnetic semiconductors, suggesting that magnetic polarons may constitute the heavy quasiparticles in many of these systems. We plan to continue pursuing the range of materials in which spin polarons may form as part of this project, as well as returning to the other initial goal of investigating the internal fields and coupling mechanisms between local moments and charge carriers in diluted magnetic semiconductors which show relatively high-temperature FM ordering and are thus candidate materials for fully semiconductor based spintronics device applications.

- [1] See *e.g.* JH Brewer, *Encyclopedia of Applied Physics* 11, pp 23-53 (VCH Publishers, 1994).
- [2] VG Storchak et al, *Physica B* 404, 899 (2009).
- [3] VG Storchak et al, *Physica B* 404, 896 (2009).
- [4] VG Storchak et al, *Phys Rev B* 80, 235203 (2009).
- [5] VG Storchak et al, *Physica B* 374/375, 430 (2006).
- [6] VG storchak et al, *J Phys: Condensed Matter* 22, 495601 (2010).
- [7] See *e.g.* PA Wolff, *Semiconductors and Semimetals* 25, pp 413-455 (Academic Press, 1988).
- [8] VG Storchak et al, *Phys Rev Lett* 105, 076402 (2010).

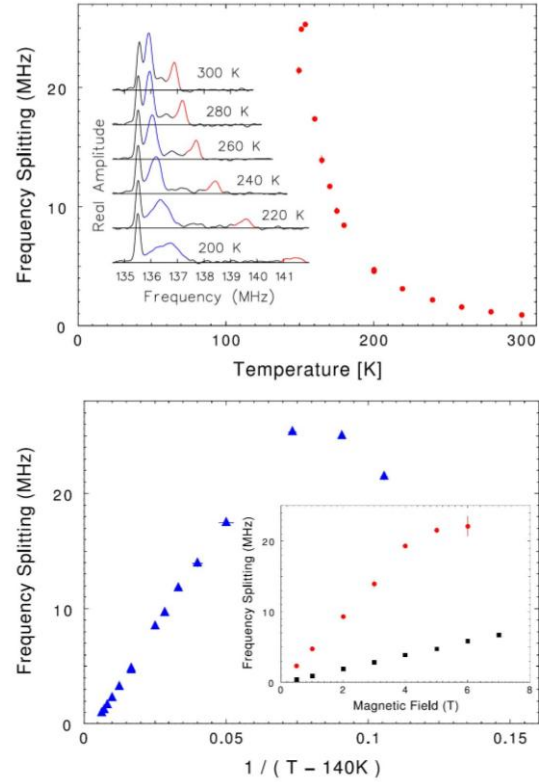


Fig.4: Temperature dependent spin polaron spectra for CdCr_2Se_4 and field dependences at 200 and 300 K used to obtain R and S_{SP} .

Program Title: “Architectural Photonics for Maximizing Solar Energy Conversion”

Professor Shawn-Yu Lin
Department of Physics, Applied Physics and Astronomy
Rensselaer Polytechnic Institute, 110 8th street, Troy, NY 12180, Email: sylin@rpi.edu

Program Scope

The ultimate goal of solar-cell research is to achieve a near perfect solar-to-electricity conversion in a single junction on a cheap substrate. This task may be achieved if the entire sequence of light harnessing processes is optimized: (1) solar-collection efficiency, (2) solar-absorption efficiency, (3) internal quantum efficiency (not discussed here), and (4) a narrow bandwidth of a modified solar spectrum. Under this program, innovative approaches are proposed based on sub- λ optics and nanostructures. Our program scope is to use sub- λ nanostructure to manipulate and harvest solar radiation that was not easily achievable by other means. The nanostructures include random surface carbon nanotube, aperiodic antireflection coating, periodic 3D silicon and metallic photonic crystals.

Recent Progress

I. Atomic layer deposition of a high temperature metallic material: Iridium

Under this program, one major goal is to use a 3D metallic structure to modify thermal radiation. From a practical point of view, there is a need to develop a high temperature metal with a negligible loss in the infrared and visible. Iridium is the best choice as it has a melting point of $T=2443^{\circ}\text{C}$ and a negligible metallic loss down to $\lambda=1\mu\text{m}$ wavelength.

Recently, atomic-layer-deposited iridium is coated onto 3D tungsten photonic crystals to move the band edge from $1.6\mu\text{m}$ to $<1\mu\text{m}$. This coating is very powerful as it leads to a large photonic band gap in near-infrared. It also *facilitates a conversion of the entire solar radiation spectrum into the sub-micrometer regime and allows for the use of a single silicon solar cell for low cost, high efficiency (>50%) purpose.*

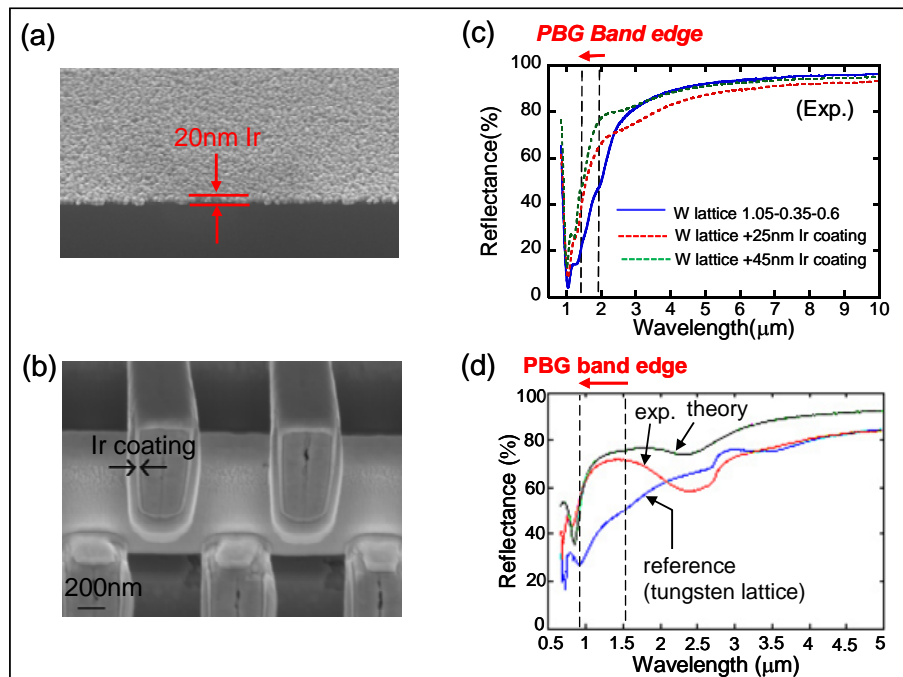


Figure 1 Conformal, high temperature material coating. (a) a side view SEM image of an Ir thin film; (b) an image of an Ir coated 3D photonic crystal structure; (c)-(d) experimental reflectance spectra, showing the shifting of photonic band edge to $\lambda=1.4\mu\text{m}$ and $0.9\mu\text{m}$ due to the Ir coating.

II. Nanotube array as an ultra-low reflector and a near-perfect Blackbody radiator.

Previously, we have shown that a carbon nanotube array can exhibit an ultra-low reflectance of 0.045% at $\lambda=633\text{nm}$, which has important consequences for maximizing solar energy conversion. However, for these applications, the black object has to absorb light over a broad spectral range, from visible to infrared wavelengths.

Recently, we show that this low reflectance holds true for a broad range of infrared wavelength: $4\mu\text{m} < \lambda < 13\mu\text{m}$. *To the best of our knowledge, no other natural material exhibits such an optical behavior.* The reflectance is found to be wavelength-independent and material dispersion-independent, indicating an apparent breakdown of a commonly believed length-scaling behavior in optical scattering phenomenon. The observation of the extremely low reflectance and a negligible transmittance (not shown here) from the CNT sample in the visible and infrared suggest that the CNT sample may serve as nearly perfect blackbody emitter.

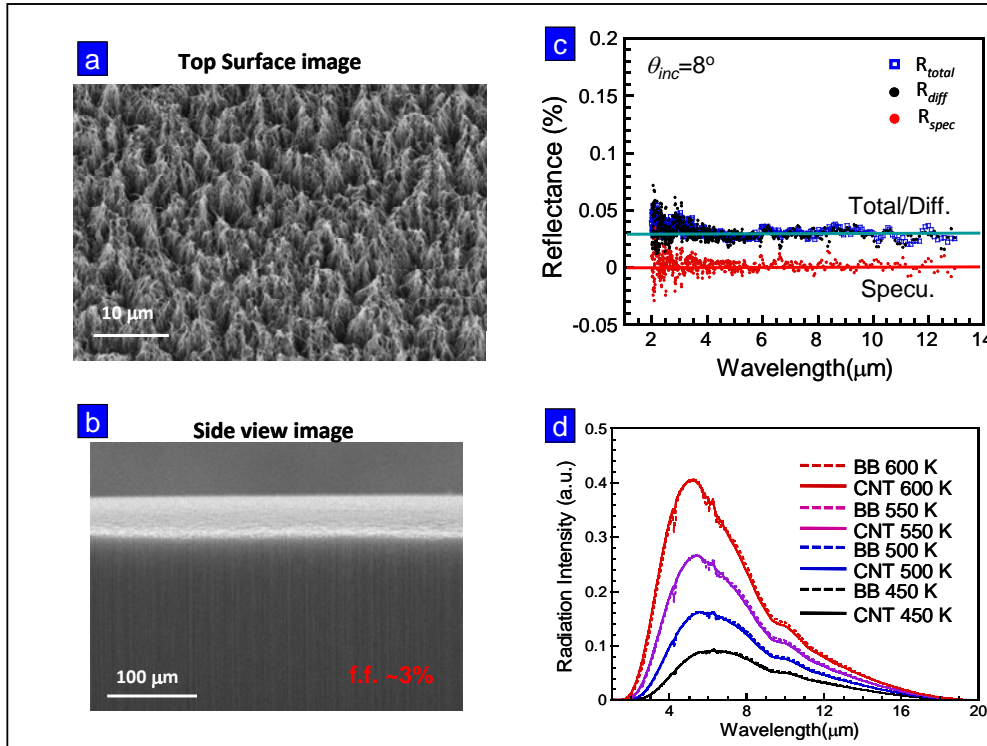


Figure 2 (a-b) SEM images of an extremely rough nanotube surface. (a) image of the roughened CNT top-surface; (b) a side view SEM image of the sample.
Figure 2 (c) Reflectance data of the nanotube material, taken from the top surface.
Figure 2 (d) A near-perfect thermal radiation from our super dark CNT sample at a series of elevated temperatures from $T=450\text{K}-600\text{K}$.

(III) Broadband antireflection of TeraHertz (THz) waves by a 3D inverted grating.

Reduction of reflection is of great importance in optical spectroscopy to reduce interference and increase signal throughput. Previously, we show that an artificially engineered, multi-layer, graded-index structure can behave as a nearly ideal antireflection coating for solar energy harvesting. In this work, we extend, for the first time, the concept into the technologically important THz wavelengths.

In the THz region, the lack of proper materials severely hindered basic research development in optical spectroscopy. Here we demonstrate a three-dimensional inverted photonic grating device design (see **Figure 3(a)**) using only one material -- silicon. Instead of using thin films made of specific materials, the device achieves an optimum multi-layer refractive index profile by using deep reactive-ion etching in bulk silicon. Each layer has a specific etching pattern and height, leading to different air/silicon volume ratio and different effective refractive index.

To test the device, we performed time-resolved and frequency domain optical spectroscopy. **A markedly reduced reflectance and an enhanced transmission** was observed. A representative THz frequency domain data taken from 15 μm (the red curve) and 20 μm -period (the blue curve) devices are shown in **Figure 3(b)**. Moreover, the antireflection device is polarization-independent and can perform well up to a large incident angle.

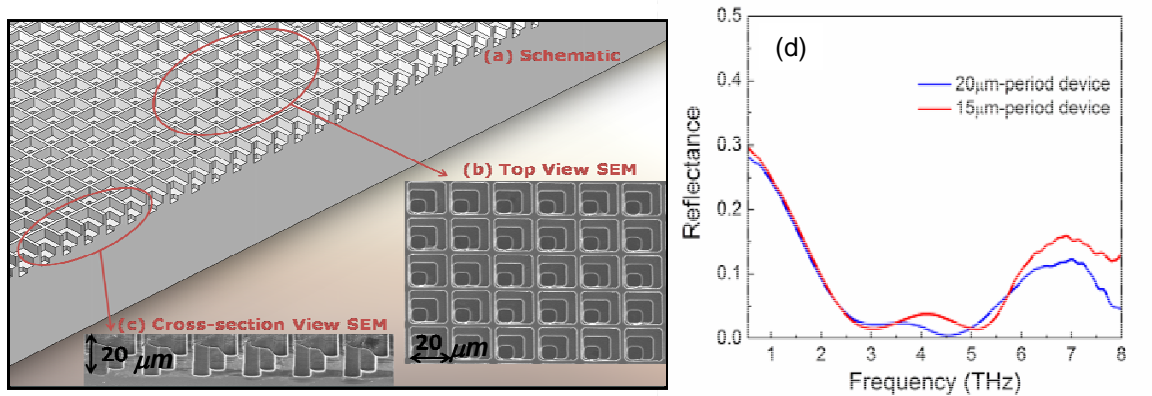


Figure 3(a) A 3D inverted grating as a THz antireflection coating structure. Schematic (a) and scanning electron microscope images of a 20- μm thick device with 20- μm structure period in top view (b) and cross-section view (c). The device has three layers of air columns etched into a silicon substrate, which form the inverted photonic gratings.

Figure 3(d) Experimental demonstration of a broadband antireflection coating at 1-8THz. Reflectance spectra of 20- μm period anti-reflection device (blue curve) and 15- μm period anti-reflection device (red curve).

Future Plans

1. In the next 12 months, we plan to study the physical origin and to provide a theoretical understanding of the length scaling behavior of the reflectance spectrum of the super-dark carbon nanotube material in the infrared regimes. We also plan to study the impact of structure randomness of the nanotube array on **light-localization and light-trapping**, using a time-resolved optical spectroscopy.
2. We also plan to fabricate a metallic photonic crystal that supports a resonant passband inside a photonic band gap, with **a sharp line-width of $\Delta\lambda < 100\text{nm}$** at the $\lambda = 1500\text{nm}$ wavelength. We will also study its thermal emission behavior.
3. We plan to implement **advanced holographic and phase mask optical lithography** at the nano-meter length scale and to realize 2D and 3D photonic crystal material by a single or a few optical exposures. To coat high temperature metal (Ir) to 2D/3D photonic crystals described above in a conformal fashion and to achieve a large infrared photonic band gap.
4. Finally, but not lastly, we plan to work closely with Prof. S. John to fabricate 3D silicon photonic crystal structures with 2, 3 and 4 unit cells and study its light diffraction behavior and light absorption characteristics.

A list of papers in which DOE support is acknowledged

1. Z.P. Yang, M.-L. Hsieh, J. Bur, L. Ci, L. M. Hanssen, B. Wilthan, P.M. Ajayan, Shawn-Yu Lin “A Nano-tube Array as a Broadband, Ultra-low Reflector and a Near-Perfect Blackbody Emitter”, Submitted to *Physical Review Letters*, Oct. 2010.
2. Mei-Li Hsieh and Shawn-Yu Lin, “A compact holographic lithography system for photonic crystal structure”, *J. Vacuum Science and Technology B*, accepted for publication, November 2010.
3. Yuting Chen, Pengyu Han, Mei-Ling Kuo, S.Y. Lin, and X.C. Zhang, “3D Inverted Photonic Grating with Engineerable Refractive Indices for Broadband Anti-reflection of Terahertz Waves”, *Optics Letters* **35**, 3159 (2010).
4. T. Walsh, J. Bur, Y.S. Kim, T.M. Lu and S.Y. Lin “High Temperature metal coating for modification of Photonic Band Edge Position”, *J. of Opt. Soc. of Am. B* **26**, 1450 (2009).
5. Mei-Ling Kuo, David J. Poxson, Yong Sung Kim, Frank W. Mont, Jong Kyu Kim, E. Fred Schubert, and Shawn-Yu Lin, “Realization of a near-perfect antireflection coating for silicon solar utilizations”, *Optics Letters* **33**, 2527 (2008).
6. Zu-Po Yang, Lijie Ci, James A. Bur, Shawn-Yu Lin, and P.M. Ajayan “A vertically aligned carbon nanotube array: the darkest manmade material”, *Nano Letters* **8**, 446 (2008).
7. Minfeng Chen, S. Y. Lin, H. C. Chang, and A. S. P. Chang, “Physical Origin of the Resonant Mode deep inside the Stop Band of a Metallodielectric Photonic Crystal”, *Phys. Rev. B* **78**, 085110 (2008).
8. Tim Walsh and S.Y. Lin “Power density and efficiency Thermophotovoltaic Energy Conversion Using a Photonic Crystal Emitter and 2D Metal Grid Filter”, *IEEE Electronic Devices* **55**, 1101 (2008).

Program title:

Exceeding the Planck free-space energy transfer limit through photonic density of states control and near field coupling.

Principle investigator:

Ting S. (Willie) Luk.

Mailing address:

Sandia National Laboratories, P.O. Box 5800, Albuquerque, NM 87185.

tsluk@sandia.gov

Program scope or definition:

The overarching goal of this project is to achieve fundamental understanding of mechanisms for spatial and spectral tailoring and transfer of thermal energy, to:

1. Enhance the near-field energy density (relative to the blackbody energy density) over a narrow spectral range under steady state or equilibrium condition (spectral compression) using nanostructured materials possessing tailored photonic density of states. High spectral compression is best achieved in bound surface states of photonic structures where photonic density of states is high. A classic example is surface plasmon polariton state. A quantitative measure of the spectral compression effect (C) may be obtained as the ratio of the energy contained in the enhanced spectral region to the overall energy contained in blackbody spectrum.

$$C = \frac{\int_{\Delta\lambda_c} U_{NF}(\lambda) d\lambda}{\int U_{BB}(\lambda) d\lambda}$$

Where $U_{NF}(\lambda)$ and $U_{BB}(\lambda)$ are the near-field and blackbody energy densities respectively, and the integral over the blackbody energy density extends over all wavelengths.

2. Extract and transfer the spectrally compressed energy through near field coupling at a rate that can exceed the limit determined by the Planck radiation law in free space.

We note that many aspects of the compression and extraction of thermal energy are closely related to the phenomenon of enhanced emission from emitters such as fluorescent molecules or quantum dots located in an enhanced density of state environment.

Work plan:

The work plan can be divided into several theoretical and experimental task areas.

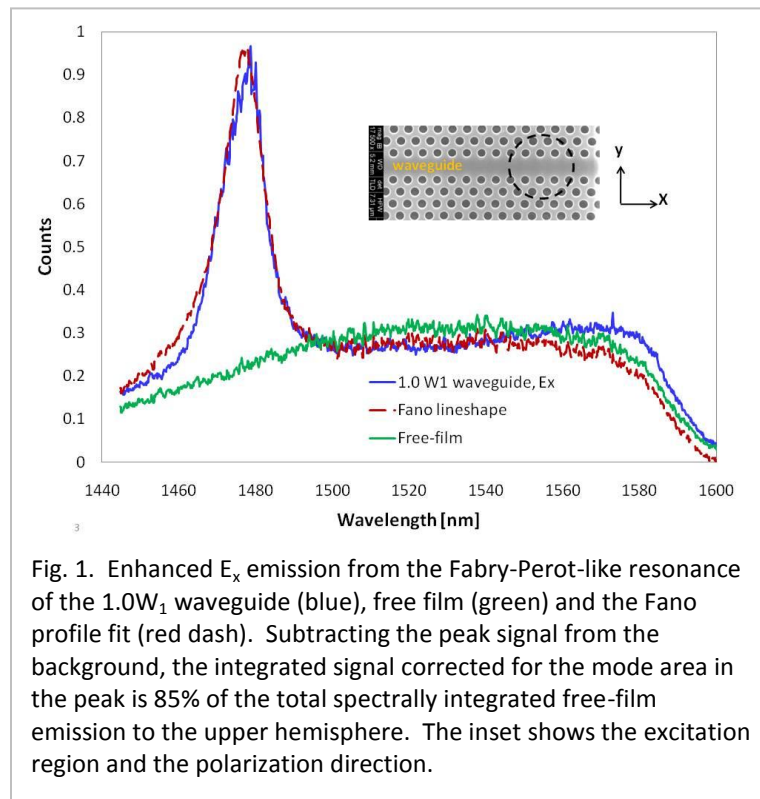
1. The maximum rate of energy extraction from a thermal source is ultimately dictated by thermodynamics, therefore we will undertake a detailed theoretical examination of the impact of entropy and second law issues on the proposed extraction scheme.
2. Numerical simulation, design, and fabrication of nanophotonics structures, such as spoof plasmon surfaces, exhibiting near-field spectral compression.
3. Development of near-field probe and detailed characterization of the near-field energy content of surface states in our nanophotonic structures.
4. Numerical simulation and design of a near-field receiver that can harvest the energy of the states efficiently.
5. Integration of source and receiver, and measurement of overall energy transfer rate.

Recent Progress:**Thermodynamics of spectral compression**

Spectral energy density of blackbody radiation can be derived based on detail balance of spontaneous emission and induced absorption and emission under thermodynamic equilibrium. The

energy density of the radiation is simply the product of photonic density of states and photon occupation number. In thermodynamic equilibrium, the photons/matter system will exchange energy such that every state with equal energy has equal probability of being occupied (equipartition principle). Therefore, high density of states in a certain spectral region can result in higher spectral energy content, provided equipartition of energy between photon gas and matters holds.

Photon density of states in nanostructured materials can be tailored to suppress a certain spectral band and enhance another to a value that can exceed the free-space density of states. In a closed equilibrium system where there is no energy exchange with the reservoir, there is not net entropy increase to the photon and matter system even though individual absorption or emission event may decrease or increase entropy of the photon gas respectively. Photonic phase space control has been used for solar energy concentrator by trading angular brightness to spectral brightness. In nanostructure materials, the concentration factor can exceed the classical $4n^2$ limit [1-2]. Optical microcavities can be designed to have only few optical modes and therefore can create a condition where very large photonic density of states. Putting broad band PbS emitters on a photonic crystal waveguide, we have observed integrated enhanced luminescence yield per unit area as large as it is in free-space but spectrally compressed. Based on the metric we discussed the C is about 10 (see Fig.1). Since these quantum dots are close-packed and monolayer, interaction among quantum dots is believed to be a possible mechanism for this enhancement. Currently, we are still working to understand this result.



Sp spoof plasmon states for spectral compression

Another class of photonic state that resides only on an interface (such as surface plasmon polariton states) can be an attractive system for spectral compression because there is high photonic density of states at the surface plasmon frequency. One of the goals in this project is to use surface plasmon polariton states to compress thermal spectral into the IR region (2 μ m) for thermophotovoltaic

applications. High energy density surface states enables lower temperature operation and higher energy transfer in the near-field coupling scheme. Energy coupling rate is now determined by the photonic density of states of the source and receiver, both of these must be engineered to have high photonic density of states for good energy coupling.

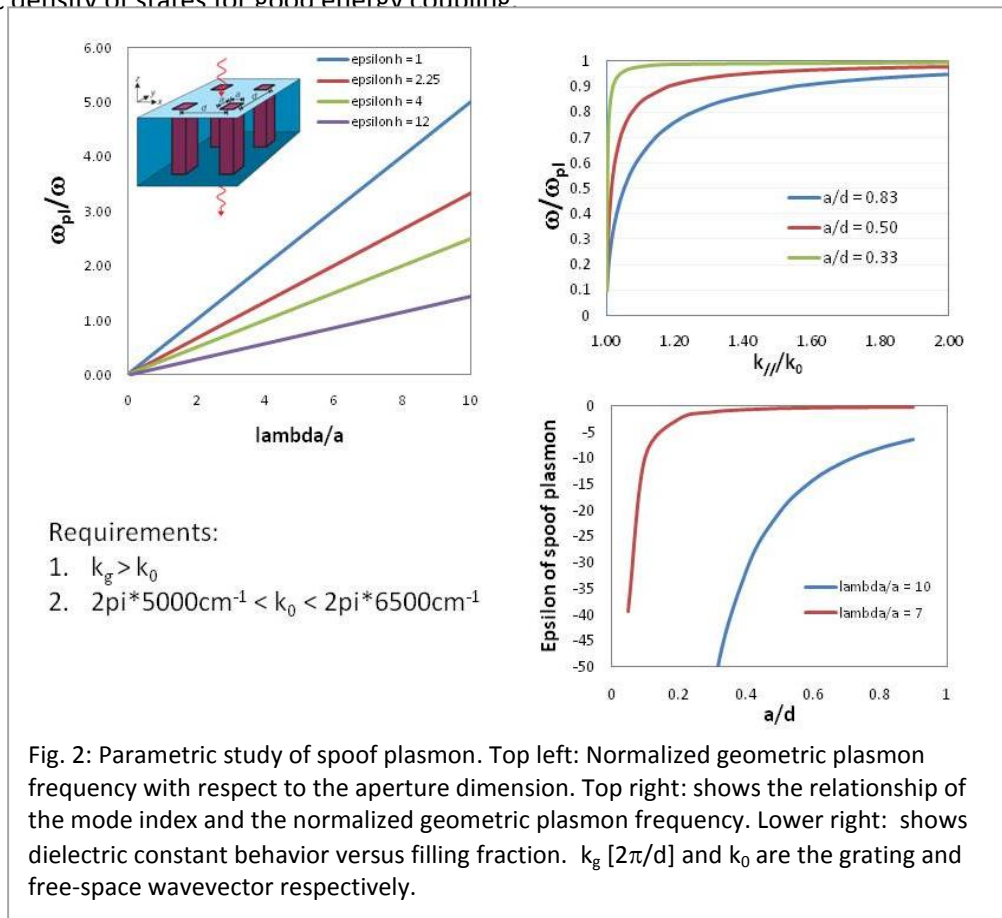


Fig. 2: Parametric study of spoof plasmon. Top left: Normalized geometric plasmon frequency with respect to the aperture dimension. Top right: shows the relationship of the mode index and the normalized geometric plasmon frequency. Lower right: shows dielectric constant behavior versus filling fraction. $k_g [2\pi/d]$ and k_0 are the grating and free-space wavevector respectively.

Currently, we are using a spoof plasmon scheme put forth by Pendry [3-5] to tailor the surface plasmon resonance to IR wavelengths. Figure 2 shows the parametric analysis of a holey metallic film structure filled with Si. In order to suppress radiative modes, the structure momentum introduced by the periodic structure is larger than the free-space wave momentum.

Near field probe design

One of the interests in this project is to be able to measure the spectral energy content and energy coupling efficiency from the surface state to the receiver. The waveguide we envisioned is shown in Fig. 3. The waveguide is made with SiN supported on a silicon chip. The loop waveguide has the advantage of being able to serve as a probe or excitation source. Using this capability, the probe response can be characterized more readily. The probe mask is being laid out and will be fabricated using the MESA facility at Sandia.

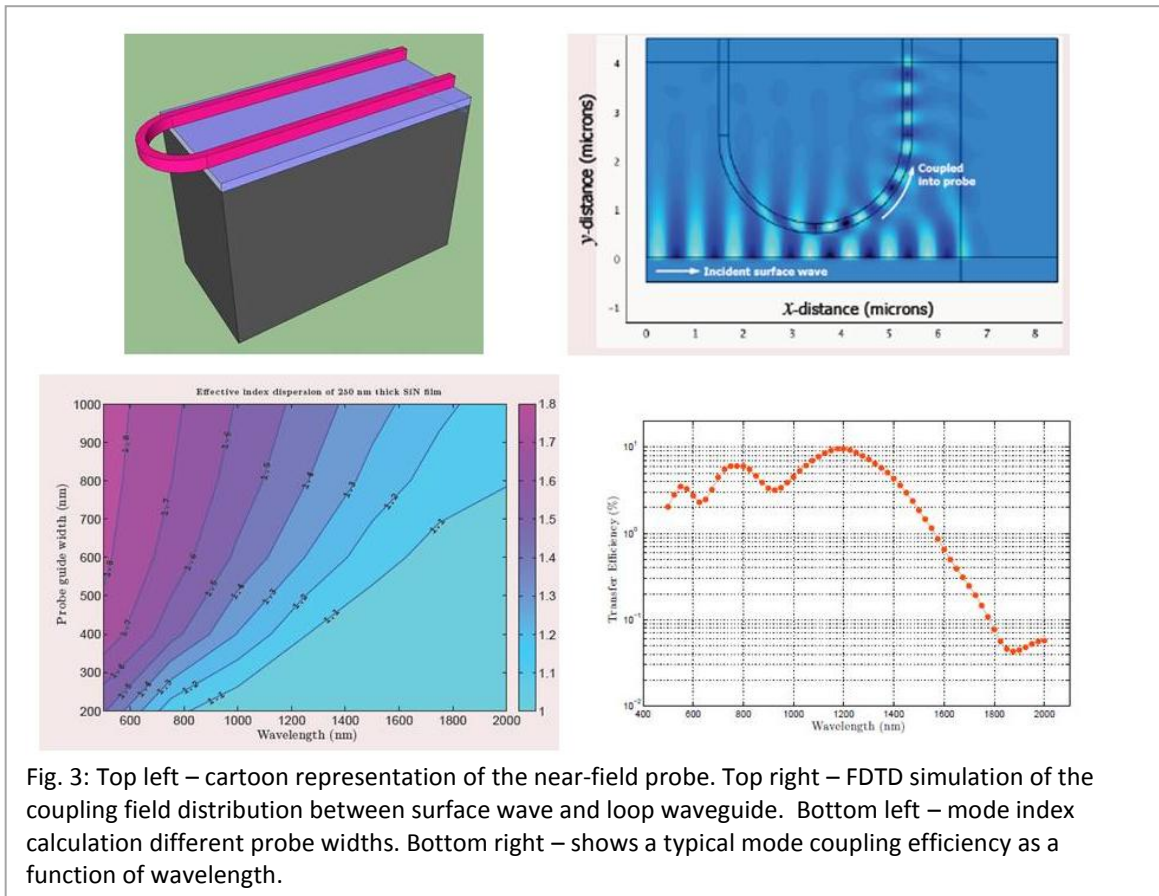


Fig. 3: Top left – cartoon representation of the near-field probe. Top right – FDTD simulation of the coupling field distribution between surface wave and loop waveguide. Bottom left – mode index calculation different probe widths. Bottom right – shows a typical mode coupling efficiency as a function of wavelength.

Future plan

1. Study another type of near field coupling using resonance based on defects of photonic crystal as energy coupler. In this case the spectral compression can utilize both surface and bulk states.
2. Microscopic theory of spectral compression process to understand the trade-offs between spectral compression factor and energy transport rate.
3. We will identify areas of research where the outcome of this project can have an impact.

References

1. E. Yablonovitch, "Statistical ray optics," J. Opt. Soc. Am. **72**, 899-907 (1982).
2. Z. Yu, A. Raman, and S. Fan, "Fundamental limit of nanophotonic light trapping in solar cells," Proceedings of the National Academy of Sciences (2010).
3. J. B. Pendry, L. Martín-Moreno, and F. J. Garcia-Vidal, "Mimicking Surface Plasmons with Structured Surfaces," Science **305**, 847-848 (2004).
4. J. T. Shen, P. B. Catrysse, and S. Fan, "Mechanism for Designing Metallic Metamaterials with a High Index of Refraction," Physical Review Letters **94**, 197401 (2005).
5. M. L. Nestervo, D. Martin-Cano, A. I. Fernandez-Dominguez, E. Moreno, L. Martin-Moreno, and F. J. Gracia-Vidal, "Geometrically-induced surface plasmons in the optical and telecom regimes," (2009).

Project Title: Dipolar Ferromagnets for Magnetocaloric Effect Nanocomposites

PI: Sara A. Majetich, Physics Department, Carnegie Mellon University, Pittsburgh, PA 15213-3890, sara@cmu.edu

Program Scope: The original plan was to investigate the phenomenon of dipolar ferromagnetism of nanoparticle assemblies in the context of the magnetocaloric effect (MCE), in which magnetic entropy and lattice entropy are interconverted near a magnetic phase transition. The objectives were to establish if the magnetic order within a nanoparticle assembly showed a sharp phase transition, and if so to tailor the nanoparticles so that the transition was near room temperature and quantify the magnetocaloric response. Compositematerials are desirable since they would be less susceptible than bulk polycrystalline materials to fracture upon cycling due to the stress of the concurrent structural transformation.

In the work completed so far, we have demonstrated an abrupt dipolar ferromagnetism transition in assemblies of 13 nm Fe₃O₄ nanoparticles close to the bulk Curie temperature of iron oxide. However, MnP nanoparticle assemblies showed blocking behavior at low temperature rather than a Curie temperature near 300 K, because the magnetic moment of these nanoparticles is much lower than in bulk materials. There is a small change in magnetic entropy in a blocking transition, but the spins remain aligned within the nanoparticles. We therefore shifted focus to the bulk materials MnP and Ni₂MnGa in order to understand the orientation-, size- and strain-dependent effects that currently limit the performance of polycrystalline materials.

Recent Progress:

Dipolar Ferromagnetism in Nanoparticle Arrays:

Electron holography previously revealed the existence of magnetic domains in monolayers of 8 nm ϵ -Co nanoparticles with a 4.2 nm edge-to-edge separation, but questions remained about the nature of the magnetic ordered state. For direct observation of the dipolar ferromagnetic phase transition, 13.4 ± 1.5 nm Fe₃O₄ nanoparticles were coated with surfactant and self-assembled into monolayer arrays, and temperature-dependent magnetic imaging from 24 to 605 °C showed the evolution of these magnetostatic domains. The arrays were imaged by transmission electron microscopy to determine the structural order, and by Fresnel Lorentz microscopy (FLM) and electron holography (EH) to determine the magnetic order as a function of temperature. Dipolar domains were observed in both FLM and EH with similar patterns and temperature dependence. Figure 1 shows the temperature dependence of the magnetic flux distribution obtained by EH. The color is used to show the in-plane magnetization direction. The red and green regions indicate stripe domains with magnetization directed downward and upward, respectively. The brighter colors indicate larger magnetic flux density. Micron-sized stripe domains were observed in the right region at 24 °C. As the sample temperature increased, the smaller domains disappeared by 500 °C and then the main domains collapsed between 550 and 575 °C. The magnetic order parameter is the ratio of the experimental flux density to the theoretical value with complete alignment of the particle moments. When the dipoles fluctuate in-plane, the order parameter (OP) is less than 1.0. The average OP in domains A - D at is plotted as a function of temperature in Fig. 1. This plot looks similar to a plot of magnetization versus temperature for an exchange-based ferromagnet, and is strong evidence for a dipolar ferromagnetic phase transition. These results show that the Curie temperature of the bulk material is the limiting factor, and that with strong magnetostatic coupling superparamagnetic blocking can be eliminated. There are serious challenges, however, to the use of these composites for magnetic refrigeration. The first is in making particles with strong magnetostatic coupling from a material with T_C near 300 K, so that the order parameter drops off precipitously. The second is that the low temperature order parameter must be increased. In the 8 nm Co nanoparticles, OP was 0.5-0.6, and in the 13 nm iron

oxide particles the order parameter was ~ 0.35 . This would limit the maximum magnetic entropy to 15.5 J/kg over the temperature range of the phase transition.

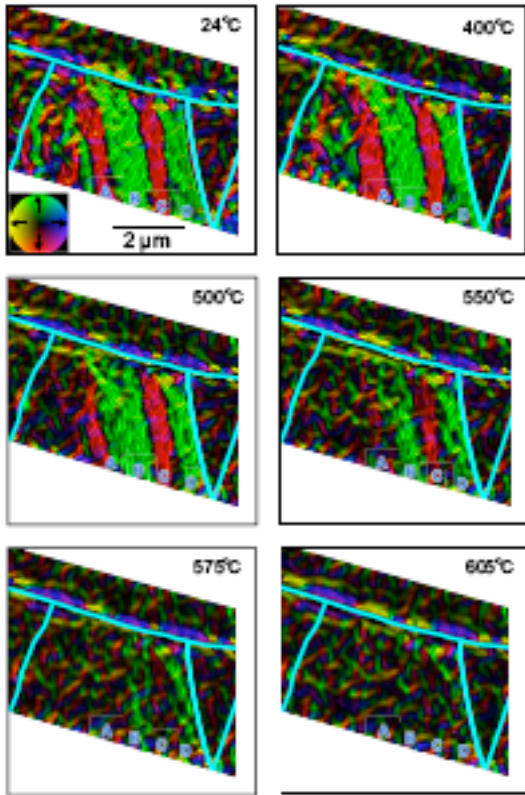
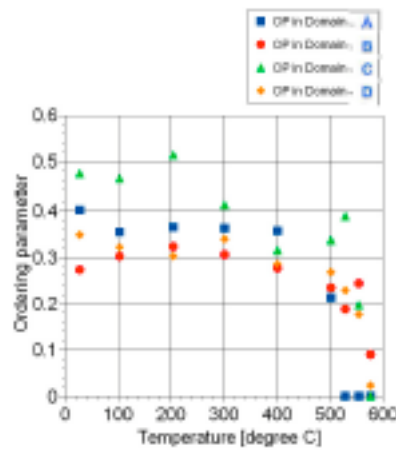


Fig. 1. Electron holography-based images of magnetic domains in iron oxide nanoparticle arrays as a function of temperature (left) and local magnetic order parameter obtained from the phase slope from regions A-D in these images (below).



Crystallographic Alignment of MnP:

MnP was selected as a prototype material because it has a sizable magnetization (comparable to that of Ni) and a T_C near room temperature (290 K). Moreover it had been synthesized in nanoparticle form, and the nanoparticles were elongated rather than spherical, making them interesting for alignment studies. We found that the specific magnetization of the nanoparticles was greatly reduced relative to the bulk value, and therefore continued using bulk powders. Since a high degree of crystallographic alignment has been achieved in permanent magnet materials due formed from compacted powders, we examined the effect of hot pressing (HP) and die upsetting (DU). MnP powder was hot pressed at 2 tons and 690-740 °C at 10^{-6} torr. Some hot pressed samples were then die upset at 1 ton and temperature of 705 °C to 785 °C. The texture of the processed samples was analyzed by using electron backscatter diffraction (EBSD) to measure pole figures. The magnetic measurements indicate that the *b*-axis is preferentially oriented along the DU direction of the die upset sample, and to a much lesser degree the HP direction of the hot pressed sample. While some degree of crystallographic alignment could be achieved, the process introduced strain that led to hysteretic losses that reduced the magnetocaloric effect.

Imaging grain alignment and magnetic domain structure:

Because of the nature of the coupled, first-order magnetic and structural phase transitions in these materials, the interaction of neighboring grains in polycrystalline samples is a critical area for investigation. During the phase transition, the transforming grains induce a strain on their neighbors resulting in a distribution of critical temperatures throughout the sample. This

broadening is not desirable because the cooling power of MCE materials is directly related to the sharpness of the phase transition. Additionally, strain effects lead to larger hysteretic losses and contribute to the crumbling of the material when it is cycled. High Energy X-ray Diffraction Microscopy (HEDM) has the ability to non-destructively measure the positions, shapes, strain, and crystallographic orientations of grains. The prototype material selected was $\text{Ni}_{55}\text{Mn}_{20}\text{Ga}_{25}$, which has a first-order ferromagnetic to paramagnetic and coupled tetragonal to cubic martensitic phase transition slightly above room temperature, making it an attractive material for magnetic refrigeration. Fig. 2 shows the magnetic phase transition and magnetic entropy as a function of temperature. HEDM reveals additional information about how the phase transformation of one grain affects its neighbors, since it changes the local strain (Fig. 3).

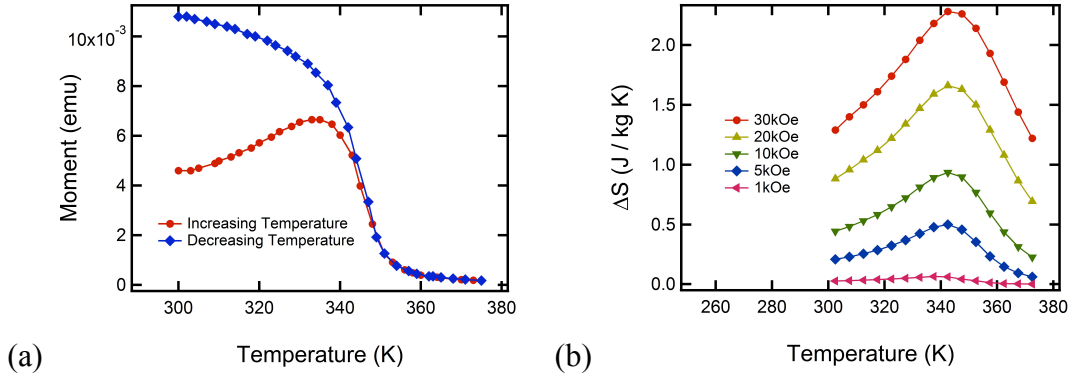


Fig. 2. (a) Magnetic moment of $\text{Ni}_{55}\text{Mn}_{20}\text{Ga}_{25}$ as a function of temperature, after zero field cooling (red), and with field cooling in the field (blue). (b) Magnetic entropy calculated from measured $M(H)$ isotherms showing T_c of 340-345 K.

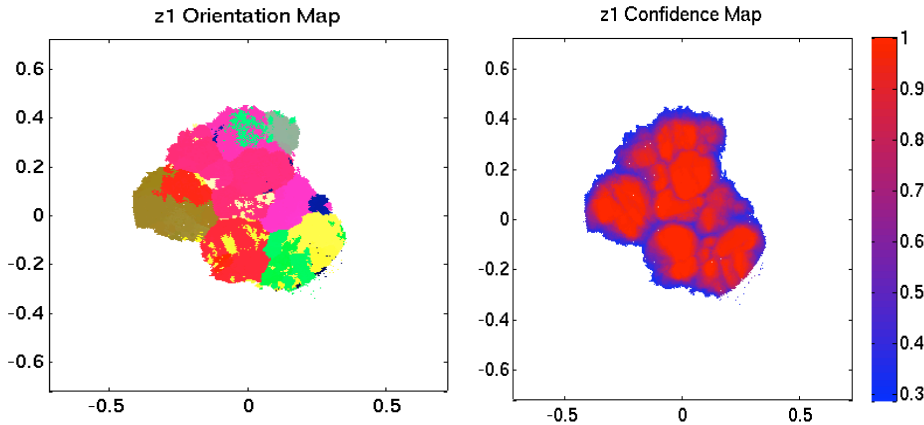


Fig. 3. Microstructure of a 2 mm thick layer of $\text{Ni}_{54}\text{Mn}_{19}\text{Ga}_{27}$. On the left, the reconstructed tetragonal phase grains, where the colors are RGB weightings of Rodrigues vector components specifying the orientation of crystalline grains.

Future Plans:

Effect of local strain on the martensitic phase transition of NiMnGa:

Further HEDM experiments will be done to map the grain patterns of $\text{Ni}_{55}\text{Mn}_{20}\text{Ga}_{25}$, as a function of temperature near the phase transition. From the results, we will learn the phases of the grains,

their relative orientation, and the local strain. This will reveal the sharpness of the structural phase transition, and the effect of local strain on the transformation.

Imaging the magnetic phase transition in NiMnGa thin films (effect of element size):

Magneto-optic Kerr effect (MOKE) microscopy (< 1 micron resolution) and magnetic force microscopy (MFM) (30 nm resolution) have been used to image magnetic domains in sputtered, annealed 500 nm thick films of Ni₅₄Mn₁₉Ga₂₇. In the next phase the films will be patterned into elements of different sizes and we will observe how the domain structure evolves as the sample is cycled through the Curie temperature, or an in-plane field of up to 1 T is applied. The data will be used to identify micron-scale regions that require higher fields or higher temperatures for switching, and therefore contribute to hysteretic losses that counteract the magnetocaloric effect.

References:

Dipolar ferromagnetic phase transition in Fe₃O₄ nanoparticle arrays, Kazuo Yamamoto, Charles R. Hogg, Saeki Yamamuro, Tsukasa Hirayama, Sara A. Majetich, (under review).

Internal Magnetic Structure of Magnetite Nanoparticles Below Their Blocking Temperature, K. L. Krycka, J. A. Borchers, R. Booth, C. R. Hogg, Y. Ijiri, W. C. Chen, S. M. Watson, M. Laver, T. R. Gentile, S. Harris, L. R. Dedon, J. J. Rhyne, and S. A. Majetich, *J. Appl. Phys.* **107**, 09B525 (2010). Doi:10.1063/1.3358049.

Preferential Crystallographic Alignment in Polycrystalline MnP, R. A. Booth, M. Marinescu, J. F. Liu, and S. A. Majetich, *J. Magn. Mater.* **322**, 2571-2574 (2010). Doi:10.1016/j.jmmm.2010.03.022

Visualizing Core-Shell Magnetic Interplay within Iron Oxide Nanoparticles, K. L. Krycka, J. A. Borchers, J. A. Borchers, Y. Ijiri, W. C. Chen, S. M. Watson, M. Laver, T. R. Gentile, S. Harris, L. R. Dedon, J. J. Rhyne, and S. A. Majetich, *Phys. Rev. Lett.* **104** 207203 (2010). Doi: 10.1103/PhysRevLett.104.207203.

Crystallographic orientation and the magnetocaloric effect in MnP, R. A. Booth and S. A. Majetich, *J. Appl. Phys.* **105** 07A926 (2009); doi:10.1063/1.3072022.

Resolving 3D Magnetism in Nanoparticles Using Polarization Analyzed SANS, K. L. Krycka, R. Booth, J. A. Borchers, W. C. Chen, C. Conlon, T. Gentile, C. Hogg, Y. Ijiri, M. Laver, B. B. Maranville, S. A. Majetich, J. Rhyne, and S. M. Watson, *Physica B* **404** 2561-2564 (2009).

Surface Engineering by Simultaneous Action of Multiple External Fields

Principal Investigator: **Dimitrios Maroudas**

University of Massachusetts, Amherst

Department of Chemical Engineering,

154A Goessmann Laboratory, 686 North Pleasant Street, Amherst, MA 01003-3110

E-mail: maroudas@ecs.umass.edu; Telephone: (413) 545-3617; FAX: (413) 545-1647

Co-Principal Investigator: **M. Rauf Gungor**

Department of Chemical Engineering, University of Massachusetts, Amherst

Program Scope

This research program aims at enabling surface engineering strategies based on the fundamental understanding and predictive modeling of the surface morphological response of solid materials subjected to the combined action of multiple external forces. Our current research focuses on the surface morphological evolution and stability of electrically conducting (metallic) and semiconducting solids under the simultaneous application of mechanical stresses and electric fields. Special emphasis is placed on identifying the conditions under which the multiply driven surface morphology is stable and exploring the complexity of the corresponding various morphologically stable surface patterns. In addition, we emphasize on the driven evolution of nanoscale features aiming at stabilizing and controlling nanoscale patterns on surfaces by their manipulation through simultaneously applied multiple external forces. Specifically, we address systematically the morphological response to the combined action of electric fields and mechanical stresses of bulk solid surfaces, surfaces of thin films grown epitaxially on thick or thin substrates, as well as nanoscale surface features such as coherently strained islands grown heteroepitaxially on substrate surfaces. The research is based on a modeling approach that combines theoretical analyses of surface morphological stability with self-consistent dynamical simulations of surface evolution based on properly parameterized continuum and multi-scale surface transport models. The research focuses primarily on face-centered cubic (fcc) metals, such as Cu, and Si systems (bulk solids or substrates on which films or small islands can be grown epitaxially). In terms of surface morphological response, the scope of the program is broad and includes the following research tasks:

- Continuum-scale analysis of morphological evolution and stability under surface electromigration conditions of (a) surfaces of stressed elastic solids; (b) surfaces of coherently strained thin films grown heteroepitaxially on solid substrates; and (c) coherently strained islands grown heteroepitaxially on solid substrate surfaces.
- Atomic-scale analysis of surface morphological evolution, focusing on the role of strain relaxation mechanisms, such as plastic deformation dynamics, in (a) solids stressed beyond the linear elastic regime and up to their limit of strength; and (b) heteroepitaxial films/islands with thicknesses/sizes greater than the critical ones for misfit dislocation generation.
- Systematic studies of the effects of electromechanical conditions (varied over a broad range of material and operating parameters) on surface morphological response.

Recent Progress

Current-induced Stabilization of Surface Morphology in Stressed Solids – We have examined the surface morphological evolution of electrically conducting, single-crystalline elastic solids under the simultaneous action of electric fields and mechanical stresses based on a fully nonlinear model and combining linear stability theory (LST) with self-consistent dynamical simulations [1]. We have demonstrated that electric current, through surface electromigration, can stabilize the surface morphology of the stressed solid against crack-like surface instabilities. Specifically, we have shown that application of a sufficiently strong electric field stabilizes fully the surface morphological response against any shape perturbation wavelength. This means that *electric current can stabilize surfaces of stressed solids that are otherwise vulnerable to cracking* through the so-called Asaro-Tiller or Grinfeld (ATG) instability. We have confirmed the LST findings through systematic self-consistent dynamical simulations of the driven surface morphological response according to the fully nonlinear model [1].

In addition, we have conducted a systematic study of the effects on the surface morphological response of varying surface diffusional anisotropy parameters; these include the direction of the applied electric field with respect to fast diffusion directions, the surface crystallographic orientation, and the strength of the anisotropy that increases with decreasing temperature [1]. The study also has provided a fundamental understanding of and an interpretation for the well-known longer electromigration lifetime of thin films of fcc metals with $\{111\}$ texture. The results of the study have been used to derive systematic surface design rules, expressed by the dependence of the critical electric-field strength as a function of the surface diffusional anisotropy parameters [1].

Rippling Instability on Surfaces of Stressed Crystalline Conductors – Based on self-consistent dynamical simulations according to the fully nonlinear model of driven surface morphological evolution, we have discovered complex aspects of surface morphological response and pattern formation that are not accounted for by the linear stability theory (LST). Specifically, we have found that, in addition to the ATG instability, a very-long-wavelength tip-splitting instability may be triggered forming a pattern of secondary ripples on the surface; such rippling occurs in the absence of electric field application, as well as for weaker-than-critical applied electric fields [2]. Such shorter-wavelength ripples on an initially long-wavelength perturbation of a planar solid surface can accelerate surface cracking acting cooperatively with an ATG instability or they may induce surface cracking under conditions that do not trigger ATG instabilities according to the LST. The critical wavelength for the onset of this secondary rippling has been computed numerically [2]. It should be emphasized that *a stronger-than-critical electric field inhibits both the ATG and the rippling instability*. Furthermore, we have found that the number of ripples, N , generated per original perturbation wavelength, λ , increases linearly with λ scaled with the maximally unstable wavelength, i.e., $N \sim \lambda/\lambda_{\max}$ [2]. Our analysis has added this new rippling instability to the known mechanisms of stress relaxation through surface pattern formation that may lead to surface cracking.

Electromigration-Driven Surface Morphological Stabilization of a Coherently Strained Epitaxial Thin Film on a Substrate – We have analyzed the surface morphological stability of a coherently strained thin film grown epitaxially on an elastic substrate and subjected simultaneously to an external electric field; both thick and thin (finite-thickness) elastic substrates have been examined. Due to its lattice mismatch with the substrate material, the film may undergo a Stranski-Krastanow (SK) instability. We have developed a model for the surface morphological evolution of the thin film and conducted a linear stability analysis to examine the morphological stability of the epitaxial film's planar surface state. The analysis has shown that surface electromigration due to a properly applied and sufficiently strong electric field can inhibit SK-type instabilities, which can be used to control the onset of island formation on the film surface [3]. We have also found that using a finite-thickness substrate can have the beneficial effect of reducing the critical strength of the electric field required to stabilize the planar surface morphology of the epitaxial film with respect to the field strength required in the case of an infinitely thick substrate [3]. We have determined the critical electric-field strength as a function of material properties and heteroepitaxial system parameters, as well as the field's optimal direction for the most efficient stabilization of the surface morphology. Furthermore, we have obtained detailed results for the effects of the finite-thickness substrate on the stabilization of the film's surface over a range of mechanical properties of the heteroepitaxial system's constituents [3].

Electromechanically Driven Complex Morphological Evolution of Void Surfaces in Metallic Thin Films – We also implemented our well-validated, fully nonlinear model of driven surface morphological evolution to investigate systematically the complex asymptotic states reached in the electromigration-driven morphological evolution of void surfaces in thin films of fcc metals with $\langle 110 \rangle$ - and $\langle 100 \rangle$ -oriented film planes under the simultaneous action of biaxial tension [4]. For $\langle 110 \rangle$ -oriented film planes, we have shown that upon increasing the applied mechanical stress level, morphologically stable steady states transition to time-periodic states through a *subcritical Hopf bifurcation*. Further increase of the stress level triggers a sequence of period-doubling bifurcations that sets the driven nonlinear system on a route to *chaos* [4]. For $\langle 100 \rangle$ -oriented film planes, a transition from steady to time-periodic states also has been found to occur at a critical stress level; in this case, the corresponding Hopf bifurcation is *supercritical* and the nonlinear system is not set on a route to chaos [4].

Atomic-Scale Analysis of Defect Dynamics and Strain Relaxation Mechanisms in Biaxially Strained Ultrathin Films of FCC Metals

– We have conducted a detailed systematic computational analysis of strain relaxation mechanisms and the associated defect dynamics in ultrathin, i.e., a few nanometers thick, Cu films subjected to biaxial tensile strain [5]. The analysis was based on large-scale isothermal-isostain molecular-dynamics (MD) simulations of the response of Cu films using an

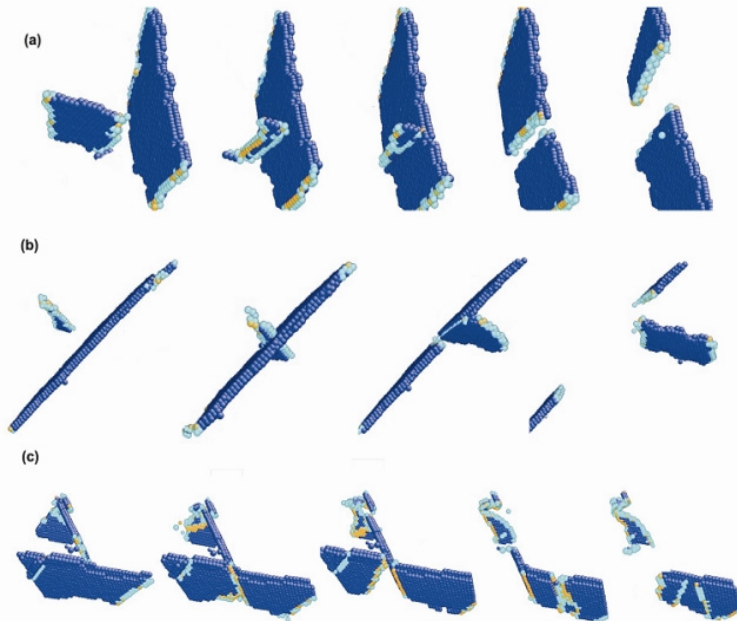


FIG. 1. Interactions between gliding dislocations and stacking faults in a Cu ultrathin film under biaxial tensile strain. Atomic configurations are shown along pathways of dislocation-stacking-fault reaction mechanisms; the structural evolution is from left to right. (a) A gliding extended dislocation cross-slips effectively into the plane of an obstacle stacking fault. The extended dislocation dissociates to form another extended dislocation on the obstacle stacking-fault plane. (b) A gliding perfect dislocation intersects with an obstacle stacking fault and dissociates effectively into two extended dislocations, one of which propagates on the obstacle stacking-fault plane, while the other one breaks through the obstacle stacking fault and glides on the same $\{111\}$ plane as that of the initial perfect dislocation. (c) A partial dislocation dissociates upon intersecting with an obstacle stacking fault. The product dislocations then glide in the plane of the obstacle stacking fault and unzip the stacking fault. Atoms in locally perfect hcp arrangements are colored blue; two consecutive layers of hcp atoms form a stacking fault. Atoms located inside dislocation cores also are colored. Atoms in locally perfect fcc arrangements and the surface atoms are not shown for clarity.

a mechanism other than dislocation escape to free surfaces, and underline the significant role of geometry in determining the mechanical response of metallic small-volume structures [5]. Atomic configurations along pathways of such representative dislocation-stacking-fault reaction mechanisms are shown in Fig. 1. Moreover, we have carried out a systematic comparative study of the mechanical response to dynamic biaxial tensile straining of nm-scale-thick Al, Cu, and Ni films based on large-scale MD simulations of dynamic deformation experiments according to carefully chosen EAM parameterizations for the three fcc metals [5]. We have found that the mechanical behavior of such films of fcc metals with moderate-to-high propensity for stacking-fault formation (Cu and Ni) is significantly different from those where such propensity is low (Al). These differences arise due to the different dislocation annihilation mechanisms in the two film categories [5]. In the Al thin films, the mechanisms of dislocation annihilation are primarily due to interactions between perfect dislocations with opposite Burgers vectors in different glide planes.

embedded-atom-method (EAM) parameterization for Cu and multi-million-atom slab supercells. For $\langle 111 \rangle$ -oriented films, our analysis revealed various regimes in their mechanical response with increasing strain level, ϵ , ranging from elastic response to threading dislocation formation to formation of entire domains in the crystalline film with nm-scale domain sizes [5]. We also conducted MD analyses of the structural response of ultrathin metallic films to biaxial straining as a function of surface crystallographic orientation [5]. Among our most interesting findings were martensitic fcc \rightarrow hcp phase transformations in biaxially strained $\langle 110 \rangle$ -oriented Cu films [5].

In addition, we have carried out large-scale MD simulations of dynamic deformation (i.e., at constant strain rate and temperature), under biaxial tensile strain of pre-strained single-crystalline nm-scale-thick fcc Cu films. Our results show that stacking faults, which are abundantly present in fcc metals, may play a significant role in the dissociation, cross-slip, and eventual annihilation of dislocations in small-volume structures of fcc metals [5]. The underlying mechanisms are mediated by interactions within and between extended dislocations that lead to annihilation of Shockley partial dislocations or formation of perfect dislocations. Our findings demonstrate dislocation starvation in ultrathin films, governed by

Future Plans

Our current and future plans (work to be completed within the next 1-3 years) include: (1) Analysis of surface morphological stabilization of heteroepitaxial films on substrates combining the use of external fields with strain engineering techniques, such as the use of compliant substrates. (2) Analysis of driven morphological evolution of coherently strained heteroepitaxial islands and other surface features (e.g., patterned surface pits) on substrates, starting from monolayer-thick islands; based on fully nonlinear models that we have developed, this study addresses the driven dynamics of both isolated islands/features and populations of interacting islands/features. (3) Continuation of continuum-level exploration of complex (e.g., oscillatory, chaotic) dynamical response of surfaces under the combined action of electric fields and mechanical stresses [see Ref. 6 for a review of such complex dynamics]. (4) Continuation of targeted atomistic computations toward parameterizing surface anisotropies for their incorporation into continuum-level models. (5) Development of coarse-grained kinetic models of strain relaxation based on analysis of MD simulation results and using dislocation densities as dynamical variables; these models provide constitutive relations required for closure of self-consistent continuum models for driven surface morphological evolution incorporating plastic deformation phenomena. (6) Development of multi-scale models of driven surface morphological evolution involving kinetic Monte Carlo simulations for direct atomic-scale modeling of surface propagation. (7) Development in collaboration with expert experimentalists of careful experimental protocols to test the modeling predictions in the area of heteroepitaxial systems. (8) Incorporation into the models of temperature gradients that drive surface mass fluxes due to surface thermomigration as external fields to be considered in conjunction with mechanical stresses and/or electric fields. (9) Exploration of other application areas for synergy between modeling and experiment in the study of the response of complex systems to the simultaneous action of multiple external fields, such as in colloidal particle problems (see, e.g., Ref. 7).

References to Publications of DOE Sponsored Research (2008-2010)

1. V. Tomar, M. R. Gungor, and D. Maroudas, "Current-Induced Stabilization of Surface Morphology in Stressed Solids," *Physical Review Letters* **100**, 036106/1-4 (2008); "Theoretical Analysis of Texture Effects on the Surface Morphological Stability of Metallic Thin Films," *Applied Physics Letters* **92**, 181905/1-3 (2008); "Effects of Surface Diffusional Anisotropy on the Current-Driven Surface Morphological Response of Stressed Solids," *Journal of Applied Physics* **107**, 093527/1-11 (2010); "Current-Induced Stabilization of Surface Morphology in Stressed Solids: Validation of Linear Stability Theory," *Journal of Applied Physics* **107**, 103525/1-9 (2010).
2. V. Tomar, M. R. Gungor, and D. Maroudas, "Rippling Instability on Surfaces of Stressed Crystalline Conductors," *Applied Physics Letters* **94**, 181911/1-3 (2009); "Analysis of Electromechanically Induced Long-Wavelength Rippling Instability on Surfaces of Crystalline Conductors," *Journal of Applied Physics* **109**, accepted for publication.
3. G. I. Sfyris, M. R. Gungor, and D. Maroudas, "Electromigration-Driven Surface Morphological Stabilization of a Coherently Strained Epitaxial Thin Film on a Substrate," *Applied Physics Letters* **96**, 231911/1-3 (2010); "Analysis of Current-Driven Surface Morphological Stabilization of a Coherently Strained Epitaxial Thin Film on a Finite-Thickness Deformable Substrate," *Journal of Applied Physics* **108**, 093517/1-9 (2010).
4. V. Tomar, M. R. Gungor and D. Maroudas, "Electromechanically Driven Chaotic Dynamics of Voids in Metallic Thin Films," *Physical Review B* **81**, 054111/1-10 (2010); J. S. Cho, M. R. Gungor, and D. Maroudas, "Analysis of Current-Driven Motion of Morphologically Stable Voids in Metallic Thin Films: Steady and Time-Periodic States," *Journal of Applied Physics* **108**, 053514/1-8 (2010).
5. K. Kolluri, M. R. Gungor, and D. Maroudas, "Atomic-Scale Analysis of Defect Dynamics and Strain Relaxation Mechanisms in Biaxially Strained Ultrathin Films of Face-Centered Cubic Metals," *Journal of Applied Physics* **103**, 123517/1-11 (2008); "Molecular Dynamics Simulations of Martensitic fcc-to-hcp Phase Transformations in Strained Ultrathin Metallic Films," *Physical Review B* **78**, 195408/1-6 (2008); "Comparative Study of the Mechanical Behavior Under Biaxial Strain of Prestrained Face-centered Cubic Metallic Ultrathin Films," *Applied Physics Letters* **94**, 101911/1-3 (2009); "Molecular-Dynamics Simulations of Stacking-Fault-Induced Dislocation Annihilation in Prestrained Ultrathin Single-Crystalline Copper Films," *Journal of Applied Physics* **105**, 093515/1-8 (2009); "Atomistic Analysis of Strain Relaxation in <110>-Oriented Biaxially Strained Ultrathin Copper Films," *Journal of Applied Physics* **106**, 103519/1-8 (2009).
6. D. Maroudas, "Surface Morphological Response of Crystalline Solids to Mechanical Stresses and Electric Fields," invited review article accepted for publication in *Surface Science Reports*.
7. D. J. Beltran-Villegas, R. M. Sehgal, D. Maroudas, D. M. Ford, and M. A. Bevan, "Fokker-Planck Analysis of Separation Dependent Potentials and Diffusion Coefficients in Simulated Microscopy Experiments," *Journal of Chemical Physics* **132**, 044707/1-8 (2010).

Program Title: Electronic Processes in Solid State Organic Electronic Materials

Principal Investigator: Richard L. Martin
T-1, MS B268
Los Alamos National Laboratory
Los Alamos, NM 87545
505.667.7069
Fax: 505.665.3909
E-mail: rlmartin@lanl.gov

Co-investigators: Enrique Batista
Ian Campbell
Darryl Smith

Program Scope:

The central goal of this program is to advance our understanding of organic electronic materials and to uncover the underlying physical principles that dictate their performance in existing and novel electronic devices. These materials continue to be of great scientific interest because of their rich, tunable spectrum of ground and excited state properties. Such great diversity derives from strong competition among the charge, spin, and lattice degrees of freedom. They also figure prominently in a broad class of technological applications, stemming primarily from their favorable processing, fabrication and performance properties. To date, the development and utilization of electronic organic materials has largely followed an empirical Edisonian approach. A firm understanding of the basic physical principles governing the behavior of these materials would allow more effective utilization of the power of organic syntheses. There is therefore a critical need for basic scientific research addressing the underlying physical principles if we are to realize the benefits of organic electronic devices more rapidly.

In this period we focus our attention on the following fundamental questions: *how does molecular structure control the morphology of condensed phases of organic materials, particularly at the organic/inorganic and organic/organic interface; and how do these structural considerations influence the electronic structure in the near vicinity of the interface? In what way does this control the subsequent fundamental properties such as charge transport?*

We employ a closely coupled measurement/theory approach aimed at understanding fundamental physical processes in representative model systems and materials, including both conjugated polymers and small molecules. Our goal is to understand and control material structure and charge transport at the organic/inorganic and organic/organic interfaces. The experimental effort will focus on optical and electrical characterization of model interfaces formed using solution or vacuum deposition techniques. The theory component will connect with these experiments through a hierarchy of microscopic and macroscopic models, including large scale molecular dynamics calculations of the structure at the interface and quantum mechanical determination of the electronic structure associated with a subset of such configurations.

Recent Progress:

Past Office of Science support has allowed us to tackle fundamental issues in the area of transport in disordered materials, and to develop tools needed to address these and other questions. We briefly mention three areas.

In the first, we have studied spin polarized charge carrier injection from a ferromagnetic contact into an organic semiconductor by tunneling through a thin insulating layer. Tunneling matrix elements and transition rates for the two

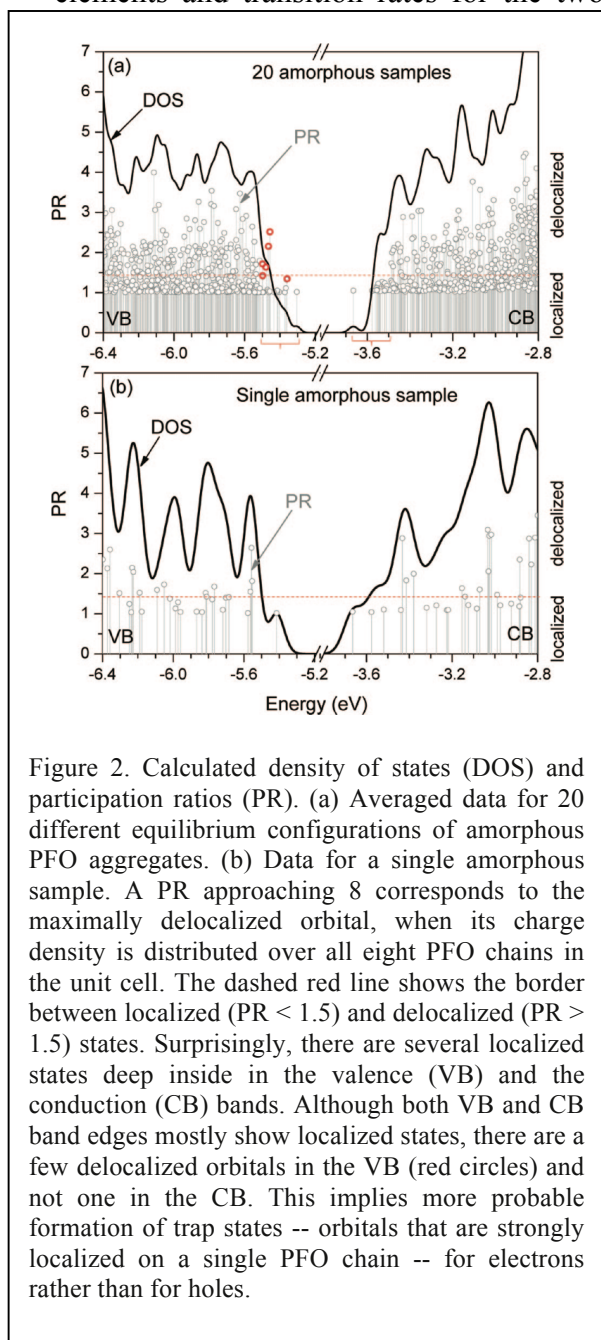


Figure 2. Calculated density of states (DOS) and participation ratios (PR). (a) Averaged data for 20 different equilibrium configurations of amorphous PFO aggregates. (b) Data for a single amorphous sample. A PR approaching 8 corresponds to the maximally delocalized orbital, when its charge density is distributed over all eight PFO chains in the unit cell. The dashed red line shows the border between localized ($PR < 1.5$) and delocalized ($PR > 1.5$) states. Surprisingly, there are several localized states deep inside in the valence (VB) and the conduction (CB) bands. Although both VB and CB band edges mostly show localized states, there are a few delocalized orbitals in the VB (red circles) and not one in the CB. This implies more probable formation of trap states -- orbitals that are strongly localized on a single PFO chain -- for electrons rather than for holes.

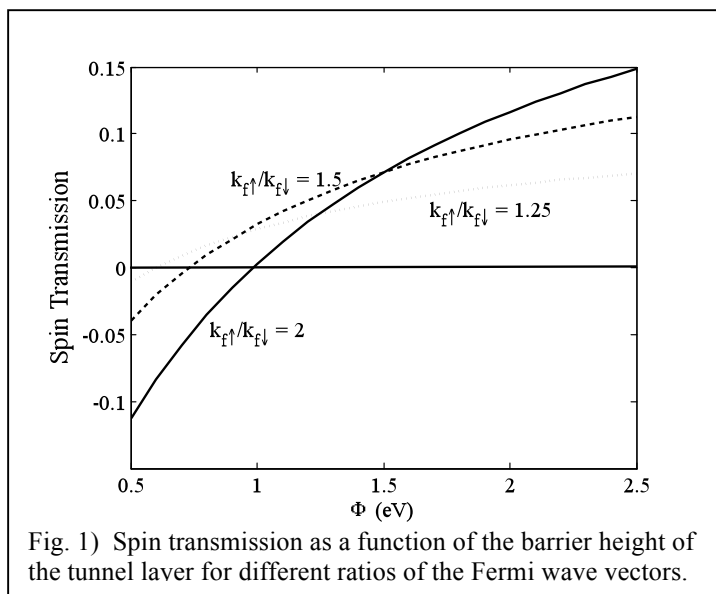


Fig. 1) Spin transmission as a function of the barrier height of the tunnel layer for different ratios of the Fermi wave vectors.

electron spin types are calculated using the Bardeen Transfer Hamiltonian approach. Tunneling occurs between extended electronic states in the metal contact and localized molecular orbitals in the organic semiconductor. The calculated transition rates are used in a rate equation model to calculate the injected current for the two electron spin types. In Fig. 1 we plot the calculated spin transmission of the tunnel junction as a function of the barrier height for different ratios of the Fermi wave vectors of the two spin types of electrons. Our results show that tunneling provides a spin selective mechanism to inject charge carriers into organic semiconductors.

In the second area, we have continued to address the connections between disorder in thin films and the microscopic consequences on the electronic structure of the material. Our previous work on PPV was extended to another important class of organic polymers, the polyfluorenes. Classical molecular dynamics simulations were used to determine probable molecular geometries and chain packing, and first-principles density functional theory calculations were employed to determine electronic structure and orbital

localization properties (Figure 2). Intramolecular and intermolecular effects were disentangled by contrasting results for densely packed oligomer clusters and for ensembles of isolated oligomers with the same intramolecular geometries. Our simulations show that intermolecular disorder allows for nearly planar configurations of interacting fluorenes compared to the isolated molecules. This rationalizes the experimentally detected formation of the planar crystalline morphologies that frequently accompany twisted glassy configurations in fluorene films.

On a third front, we have performed experimental measurements of energy level alignment and current-voltage characteristics (I-V) of representative organic films on silicon. These properties are well reproduced by a device level model that quantitatively reproduces device performance. The latter two areas provide the motivation for our proposed work.

Future Plans

The next generation of organic semiconductor devices increasingly relies on the properties of organic interfaces, both organic/organic and organic/inorganic. The electronic states at these interfaces are both critical to performance and poorly understood. We will investigate organic/inorganic interfaces of both type I and type II energy level alignment. A schematic energy level diagram is shown in Fig. 3. In type I interfaces the organic semiconductor energy gap is smaller than the inorganic energy gap. This is the case for organic transistors where the inorganic material serves as the gate insulator. Since the lowest energy for both carriers is in the organic material these interfaces do not have charge transfer states. We will use SiO₂, pentacene, and tetracene as model compounds for these interfaces. We will also study type II interfaces where the organic semiconductor may be either the donor or acceptor material. We will use silicon as the model inorganic semiconductor and C₆₀, soluble-PPVs, and pentacene as model organic materials. The interface energy level alignments will be determined using built-in potential and capacitance-voltage measurements. This will establish the relative energy levels of the constituent materials but is not sensitive to charge transfer states. We will investigate the charge transfer electronic states of these materials using optical absorption and emission.

The physical structure of the interface will be simulated via annealing molecular dynamics based on empirical potentials. The empirical potentials to be used for these organic molecules are well established and we will screen a series of them for optimum agreement with density functional theory structures, similarly to our previous work. Charge transfer and separation across interfaces will be studied theoretically using electronic structure first-principle simulations. Two approaches will be employed: one based on charge constrained density functional theory studies and the other on wave-packet quantum dynamics simulations. We will continue to utilize screened hybrid DFT approaches when feasible.

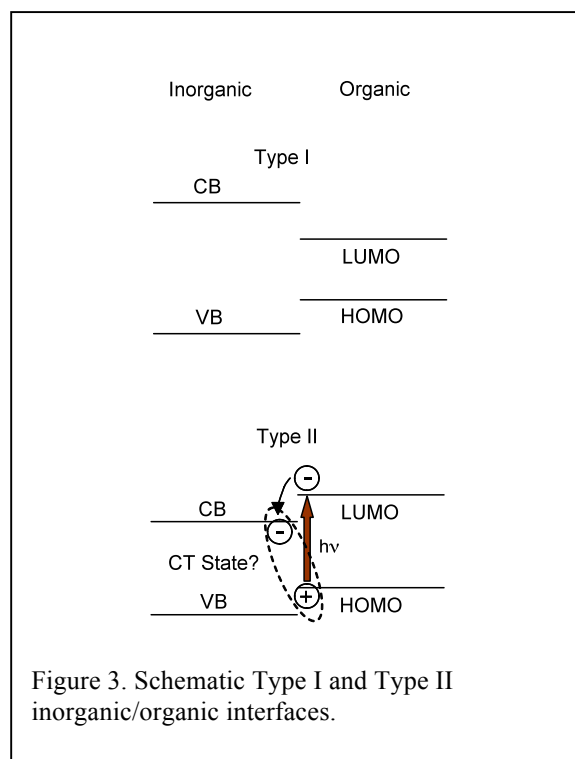


Figure 3. Schematic Type I and Type II inorganic/organic interfaces.

Publications (2008-2010)

- [1] I. H. Campbell and B. K. Crone, *Appl. Phys. Lett.* **92**, 043303 (2008).
- [2] J. Zaumseil, C. R. McNeill, M. Bird, D. L. Smith, P. P. Ruden, M. Roberts, M. J. McKiernan, R. H. Friend and H. Sirringhaus, *J. Appl. Phys.* **103**, 064517 (2008).
- [3] D.L. Smith and P. Ruden, *Phys. Rev. B* **78**, 125202 (2008).
- [4] M. Yunus, P. P. Ruden, and D. L. Smith, *Appl. Phys. Lett.* **93**, 123312 (2008).
- [5] S. Kilina, E. R. Batista, P. Yang, S. Tretiak, A. Saxena, R. L. Martin, D. L. Smith, *ACS Nano* **2**, 1381 (2008).
- [6] A. C. Niemayer, I. H. Campbell, F. So and B. K. Crone, *Proc. of the SPIE* **7052**, 705200 (2008).
- [7] I. H. Campbell and B. K. Crone, *Appl. Phys. Lett.* **92**, 043303 (2008).
- [8] A. N. Chantis and D. L. Smith, *Phys. Rev. B* **78** 235317 (2008).
- [9] S. A. Crooker, L. Cheng and D. L. Smith, *Phys. Rev. B* **79**, 035208 (2009).
- [10] E. J. Jakubikova, R. C. Snoberger, V. S. Batista, R. L. Martin, and E. R. Batista, *J. Phys. Chem. A* **13**, 12532-12540 (2009).
- [11] V. K. Thorsmolle, R. D. Averitt, J. Demsar, D. L. Smith, S. Tretiak, R. L. Martin, B. K. Crone, A. P. Ramirez, A. J. Taylor, *Physica B – Condensed Matter* **404**, 3127-3130 (2009).
- [12] V. K. Thorsmolle, R. D. Averitt, J. Demsar, D. L. Smith, S. Tretiak, R. L. Martin, B. K. Crone, A. P. Ramirez, A. J. Taylor, *Phys. Rev. Lett.* **102**, 17401 (2009).
- [13] I. H. Campbell and B. K. Crone, *Appl. Phys. Lett.* **95**, 263302 (2009).
- [14] I. H. Campbell and B. K. Crone, *J. Appl. Phys.* **106**, 113704 (2009).
- [15] V. Y. Pershin, N. A. Sinitsyn, A. Kogan, A. Saxena, and D. L. Smith, *Appl. Phys. Lett.* **95** 022114 (2009).
- [16] S. Kos, A. V. Balatsky, P. B. Littlewood, D. L. Smith, *Phys. Rev. B* **81**, 064407 (2010).
- [17] M. Yunus, P. P. Ruden, and D. L. Smith, *Synthetic Metals* **160**, 204 (2010).
- [18] I. H. Campbell, *Laser Focus World* **46**, 45 (2010).
- [19] C. V. Diaconu, R. L. Martin, D. L. Smith, B. K. Crone, S. A. Crooker, and E. R. Batista, *J. Appl. Phys.*, submitted.
- [20] I. H. Campbell, *Appl. Phys. Lett.* in press.
- [21] I. Nayyar, S. Tretiak, D.L. Smith, E. R. Batista, R. L. Martin, *J. Phys. Chem., Nano Letters*, submitted.

Program Title: *Electronic and Optical Processes in Novel Semiconductors for Energy Applications*

Principle Investigators: A. Mascarenhas, Brian Fluegel, Kirstin Alberi, Yong Zhang

Mailing address: NREL 1617 Cole Blvd., Golden, CO 80401

e-mail: angelo.mascarenhas@nrel.gov

Program Scope:

Advanced energy technologies require high-performance materials, which in photovoltaics translates to new semiconductor materials to efficiently absorb sunlight, and in solid-state lighting(SSL), to new semiconductor alloys for direct conversion of electricity to white light. A goal of this project is fundamental materials research for the realization of semiconductors that transcend the existing limitations that constrain present photovoltaic and solid-state lighting technologies. It specifically addresses the current unavailability of efficient high bandgap (2.1 eV) and low bandgap (1 eV) absorbers for photovoltaics, and efficient green emitters for SSL, via technologies based on GaAs substrates. The key to transcending the present limitations, is the understanding and control of fundamental electronic and optical processes in semiconductors, which is another goal of this project. Towards this, the project will focus on understanding the phenomena of spontaneous ordering in high bandgap lattice-mismatched $Ga_xIn_{1-x}P$, and the abnormal electronic structure and properties of isoelectronic dopants N and Bi in GaAs. Additionally, it will address recent observations of new excitations in bipolar plasmon gasses photogenerated in semiconductors, so as to achieve an understanding of collective phenomena that could enable semiconductors with novel, useful properties. Through collaborative efforts, this project utilizes state-of-the art resources in growth, spectroscopy, and theory, from three national laboratories, to address the above mentioned issues. By exploiting the use of BES Nanoscience Centers, and Supercomputer Facilities, it brings to bear new tools for the growth and characterization of semiconductors, and connects BES theory and computation programs with the experimental work in BES supported DOE Laboratory research.

Recent Progress: Major Achievements

I) (a) Spontaneous Ordering in High Bandgap $Ga_xIn_{1-x}P$

Until very recently, research on the various properties and applications of ordered $Ga_xIn_{1-x}P$ was limited to the Ga composition $x_0 = 0.51$, at which the alloy is lattice matched to the GaAs substrate. This, to a large extent, was due to the generation of a relatively high defect density when the $Ga_xIn_{1-x}P$ epilayer is lattice-mismatched to GaAs. We have made rapid advancements in growing strain-free $Ga_xIn_{1-x}P$ alloys on step-graded buffer layers enabling the exploration of ordered $Ga_xIn_{1-x}P$ with composition $x > x_0$, reviving the interest in many possible applications of the alloy, for instance, a new development in multi-junction solar cell technology uses $Ga_xIn_{1-x}P$ with x significantly deviated from the lattice-matched composition, considerably increasing multijunction solar cell efficiencies. Spontaneous ordering in $Ga_xIn_{1-x}P$ with $x > x_0$ is of potential value as an Al-free top surface reflector and passivator for high bandgap solar cells. It is also being explored for ultra-high efficiency solid state RGB light-emitting devices, to fill the so-called “red-gap” and “green-gap”. Our theoretical calculations show that a red wavelength at 620 nm at 300K can be obtained with $x=0.59$ if disordered, $x=0.7$ if maximally ordered and $x=0.65$ with an order parameter $\eta=\eta_{max}/2$. Similarly, a room temperature band gap of ~ 2.19 eV (~ 565 nm), which is within the yellow-

green band can be achieved for the disordered phase with $x \sim 0.74$. The same band gap can also be achieved for the partially ordered phase with x in between 0.74 and 0.77. We have recently experimentally demonstrated that by varying x and η , the transition energy of the $\text{Ga}_x\text{In}_{1-x}\text{P}$ alloy could be optimized for suitable wavelength and intensity to suit specific requirements for advanced photovoltaics and solid-state lighting.

(b) Electronic States and the Microstructure of Ordered GaInP_2

Much of the remaining mystery in the electronic properties of ordered GaInP_2 lies in the defect-related behavior, where material properties depend on unknown growth subtleties, much as the intrinsic properties did 25 years ago. Microscopic techniques are essential, both to examine defects in structure, and to observe the resulting optical properties. This was made clear with our recent discovery of low-energy lines in the PL spectra under sub-micron spatial resolution. These are extremely sharp emission lines (100 μeV or less) that fall in an energy range a few tens of meV below the bandgap. The precise value of their energy rapidly varies in a seemingly random way over sample distances less than a micron, rendering them invisible to macroscopic measurements. Recognizing the essential importance of micro-techniques, and the unavoidable role of sample-to-sample variations in this field, we developed a new technique of PL mapping that allows 2D data with 1-micron resolution to be acquired in nearly real-time. Compared to previous techniques where data was painstakingly acquired point-by-point, the new method allows researchers to actively interrogate large regions of the sample and then focus in on important spatial features. The result of adjusting an experimental parameter such as temperature or excitation density can be seen instantly. The most striking aspect of the new sharp features we observe in the PL spectra is their polarization. This polarization, along with their spatial dependence and low energy suggest that they may originate from excitons bound to pairs or complexes of the same quantum-confining lattice defects that are conjectured to be the origin of the low-energy lines.

II) Dilute Bismide Alloys

Adding a 1 eV absorber lattice-matched to GaAs enables a jump in triple-junction solar cell efficiencies from $\approx 34\%$ to 41% , but this material has been hard to obtain. Earlier, it appeared that the giant bandgap bowing of the dilute nitride alloys would offer a solution to this problem, but their highly degraded electron transport preempted this. Later, the giant bandgap bowing in the bismide alloys offered new promise. We have now shown that it is possible to grow dilute bismide alloys with electron mobilities exceeding $2000 \text{ cm}^2/\text{V}\cdot\text{s}$. However, the properties of the dilute bismides are significantly less understood as compared to the dilute nitrides, where the highly degraded mobility proved to be a show stopper. The impurity band nature of both the dilute nitrides and bismides has recently emerged from research conducted in the past few years. We have shown theoretically that isolated Bi does not form a bound state in GaAs (unlike N) and that it is resonant in the valence band. Knowledge

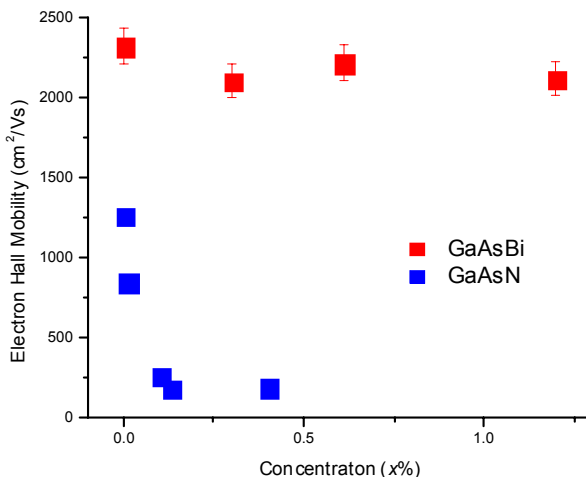


Figure Degradation in electron mobility with Bi and N incorporation.

about the position of the isolated Bi state is crucial for the understanding of the giant band gap bowing observed in GaAsBi, yet there have been no experimental studies reported on the isolated Bi state in GaAsBi. In the case of N in GaAs, it was possible to push the isolated N state (that is resonant with the conduction band) into the band gap by applying hydrostatic pressure. However in the case of Bi in GaAs, the Bi state will not emerge out of the valence band because it has a larger pressure coefficient than the band gap making optical spectroscopic study of the isolated Bi state difficult. Using optical spectroscopic measurements, we have shown the presence of complexes involving Bi and unintentional dopants in dilute bismide alloys which might also affect the carrier mobility. GaAsBi is grown in the same temperature range as the low temperature (LT) GaAs which contain excess As in the form of As anti-sites and it is known that the transport properties of LT-GaAs is dominated by hopping conduction at low temperatures. We are currently studying whether there is a similar hopping conduction mechanism in the LT grown bismide alloys.

Work in progress and future plans

1) Light Scattering Studies in Photogenerated Plasmons

Coupled plasmon-phonon modes arose in our study of Bi-doped GaAs, due to hole-trapping which leaves a long-lived and mobile electron population. The result is that even a relatively low powered continuous-wave laser excitation can build up a large electron density. This density was detected by our measurements of light scattering from its plasmon modes. Recognition that this scattered signal represented a dynamically controllable frequency shift with possible photonics applications lead us to try even higher densities in the mixed type-I type-II quantum well (MTQW). This is a very special structure specifically designed to separate the electron and hole populations into separate GaAs quantum wells. This device has often been used to maximize electron-hole lifetimes and to build up a large steady-state population for various experimental goals, however its advantages for light scattering have been completely overlooked until now. Using photoexcitation from just microwatts of laser power, a scattered light beam can be frequency-shifted several meV, an all-optical effect for which there is no competing technology. While the physics of that are well understood, we have also found evidence of other scattering effects in the MTQW that cannot be explained by any of the known elementary excitations. Traditionally, such excitations were observed in modulation doped quantum wells containing large electron populations. Here, the population was thus fixed and could be increased or decreased only by changing the sample design. In our MTQW, the photo-excited carrier density can be instantly changed simply by adjusting the power of a small control laser. Together with modern CCD detectors and new designs in Raman interference filters, we now have a faster and more flexible approach to investigating novel light scattering effects, and this research is now in progress.

2) Long-range exciton diffusion and pattern generation in 2 DEG's

Exciton pattern generation was first discovered in double quantum well structures (DQW) under an electric field during the last decade. Due to a combination of vertical and lateral charge separation that inhibits recombination, photogenerated charge carriers diffuse very large distances – up to a millimeter – before recombining. Point emission of photoluminescence was also observed at point defects that were identified with current filaments, but no time-resolved studies have been done that would directly observe diffusion out from the point defects. Our present work looks at pattern formation in multiple quantum well structures where field-driven tunneling can produce very efficient photoluminescence upconversion across the barrier layers. We have found that this process creates a strongly preferential injection of holes, resulting in more efficient generation of exciton rings with stronger contrast than in DQWs. By time-resolving the ring pattern formed around point defects, we find that these cannot be explained simply by electrically injected current, as in previous reports. Instead, we find that these point emitters are the result of photogenerated carriers diffusing from the laser and concentrating at weak points in the tunnel barriers. The results are important in the study of laser-generated cold exciton gases. It also demonstrates *directed* long-range diffusion of free carriers in a direct-gap semiconductor over distances that are typically only achieved in silicon.

PUBLICATIONS (emanating from this project during the period (2008-20010))

1. L. Bhusal and A. Mascarenhas, Handbook of Luminescent “Solid-State Lighting” *Semiconductor Materials*, Book Chapter, Taylor and Francis, (2010).
2. Bhusal, L; and Mascarenhas, A.” III-V semiconductor alloys covering 600–6000 nm”. *Materials Science and Engineering B*, (accepted).
3. Kini, RN; Ptak, AJ; France, Ryan; Reedy, RC; and Mascarenhas. A; “Effect of Bi alloying on the hole transport in the dilute bismide alloy GaAs_{1-x}Bi_x” (accepted) *Phys. Rev. B*.
4. Fluegel, B; Alberi, K; Bhusal, L; Mascarenhas, A; Snoke, DW; Karunasiri, G; Pfeiffer, LN; and West, K;. “Exciton pattern generation in GaAs/AlGaAs multiple quantum wells”, (submitted) *Phys. Rev. B*.
5. Wang, K; Chen, JJ; Zeng, ZM; et al. “Synthesis and photovoltaic effect of vertically aligned ZnO/ZnS core/shell nanowire arrays”. *Appl. Phys. Lett.* **96**, 123105 (2010).
6. Bhusal, L; Fluegel, B; Steiner, MA; et al. “Ordering induced direct-indirect transformation in unstrained GaIn_{1-x}P for 0.76 < x < 0.78”. *J. Appl. Phys.* **106**, 114909 (2009).
7. Fluegel, B; Mascarenhas, A; Geisz, JF. “Polarized photoluminescence from point emitters in ordered GaIn_{1-x}P”. *Phys. Rev. B*, **80**, 125333 (2009).
8. Steiner, MA; Bhusal, L; Geisz, JF; et al. “CuPt ordering in high bandgap GaIn_{1-x}P alloys on relaxed GaAsP step grades”. *J. Appl. Phys.* **106**, 063525 (2009).
9. Kini, RN; Bhusal, L; Ptak, AJ; et al. “Electron Hall mobility in GaAsBi”. *J. Appl. Phys.* **106**, 043705 (2009).
10. Zhang, Y; Mascarenhas, A; Wei, SH; et al. “Comparison of atomistic simulations and statistical theories for variable degree of long-range order in semiconductor alloys”. *Phys. Rev. B*, **80**, 045206 (2009).
11. Zhang, Y; Jiang, CS; Friedman, DJ; et al. “Tailoring the electronic properties of GaIn_{1-x}P beyond simply varying alloy composition”. *Appl. Phys. Lett.* **94**, 091113 (2009).
12. Mascarenhas, A; Kini, R; Zhang, Y; et al. “Comparison of the dilute bismide and nitride alloys GaAsBi and GaAsN”. *Physica Status Solidi B* **246**, 504 (2009).
13. Bhusal, L; Ptak, AJ; France, R; et al. “Contactless electroreflectance studies of ultra-dilute GaAs_{1-x}Bi_x alloys”. *Semicond. Science and Technology* **24**, 035018 (2009).
14. Zhang, Y; Mascarenhas, A; Wang, LW. “Interplay of alloying and ordering on the electronic structure of GaIn_{1-x}P alloys”. *Phys. Rev. B* **78**, 235202 (2008).
15. Kini, RN; Mascarenhas, A; France, R; et al. “Low temperature photoluminescence from dilute bismides”. *J. Appl. Phys.* **104**, 113534 (2008).
16. Zhang, Y; Lee, SH; Mascarenhas, A; et al. “An UV photochromic memory effect in proton-based WO₃ electrochromic devices”. *Appl. Phys. Lett.* **93**, 203508 (2008).
17. Fluegel, B; Mascarenhas, A. “Aberration-free imaging for light and electrons”. *Appl. Phys. Lett.* **93**, 161105 (2008).
18. Tiedje, T; Young, EC; Mascarenhas, A. “Growth and properties of the dilute bismide semiconductor GaAs_{1-x}Bi_x a complementary alloy to the dilute nitrides”. *Int. Journal of Nanotechnology* **5** (9-12): 963 (2008).
19. Wang, K; Chen, JJ; et al. “Direct growth of highly mismatched type II ZnO/ZnSe core/shell nanowire arrays on transparent conducting oxide substrates for solar cell applications”. *Advanced Materials* **20** (17): 3248 (2008).
20. Zhang, Y; Mascarenhas, A; Wang, LW. “Non-bloch nature of alloy states in a conventional semiconductor alloy: GaIn_{1-x}P as an example”. *Phys. Rev. Lett.* **101**, 036403 (2008).
21. Francoeur, S; Tixier, S; Young, E; et al. “Bi isoelectronic impurities in GaAs”. *Phys. Rev. B*, **77**, 085209 (2008).

Optical Properties of Doped ZnO Nanocrystals and Ceramics

Matthew D. McCluskey^{1,*} and Leah Bergman^{2,**}

¹Department of Physics and Astronomy, Washington State University, Pullman, WA 99164-2814

²Department of Physics, University of Idaho, Moscow, ID 83844-0903

PROGRAM SCOPE

Zinc oxide (ZnO) is a potentially important material in electronic devices, including transparent contacts in solar cells, transparent anodes in polymer light-emitting diodes, and active materials in solid-state white lighting. ZnO nanocrystals provide wavelength tunability via quantum confinement and may be useful in dye-sensitized solar cells. Despite the large amount of research performed on semiconductor nanoparticles in general, the fundamental properties of dopants in nanocrystals are only beginning to be understood. *P*-type doping, required for most practical device applications, has been elusive.

The program utilizes a range of experimental techniques to elucidate the microscopic structure, charge state, and concentrations of defects and dopants in ZnO nanocrystals. The effect of particle size on these properties is investigated from the nanometer to micron regimes. To probe energy levels, the band gaps will be tuned by systematically varying quantum confinement, alloy composition, and hydrostatic pressure. By controlling defects and dopants, we aim to achieve *p*-type conductivity in ZnO nanocrystals. Reliable *p*-type doping would be transformative, enabling a range of new applications.

Specific aims of the project include:

- Determine the microscopic structure of H complexes in ZnO nanocrystals
- Investigate the effect of particle size on dopant concentration and charge state
- Probe H and Cu energy levels as a function of quantum confinement, alloying, and pressure.
- Investigate the effect of Cu doping on the optical properties of ZnO nanocrystals and ceramics
- Achieve *p*-type doping of ZnO nanocrystals

Optical spectroscopy, performed at Washington State University (WSU) and University of Idaho (UI), is complemented by work at DOE user facilities at Pacific Northwest National Laboratory (PNNL) and Lawrence Berkeley National Laboratory (LBNL).

RECENT PROGRESS

Doping of ZnO nanocrystals

Doping of semiconductor nanocrystals is an important problem in materials research. Using infrared (IR) and x-ray photoelectron spectroscopy (XPS), we observed Cu acceptor dopants that were intentionally introduced into ZnO nanocrystals during growth. The incorporation of Cu²⁺ dopants increased as the average diameter of the nanocrystals was increased from ~3 to 6 nm. Etching the nanocrystals with acetic acid revealed a core-shell structure, where a lightly doped core is surrounded by a

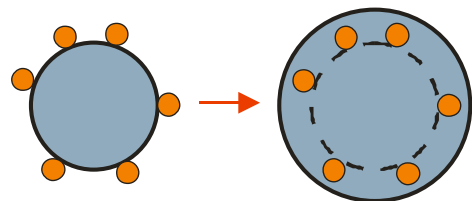


Fig. 1. Schematic diagram of doping process in ZnO nanocrystals. Cu impurities stick to the surface of the small nanocrystal (left) and are overgrown, resulting in an undoped core and doped shell (right).

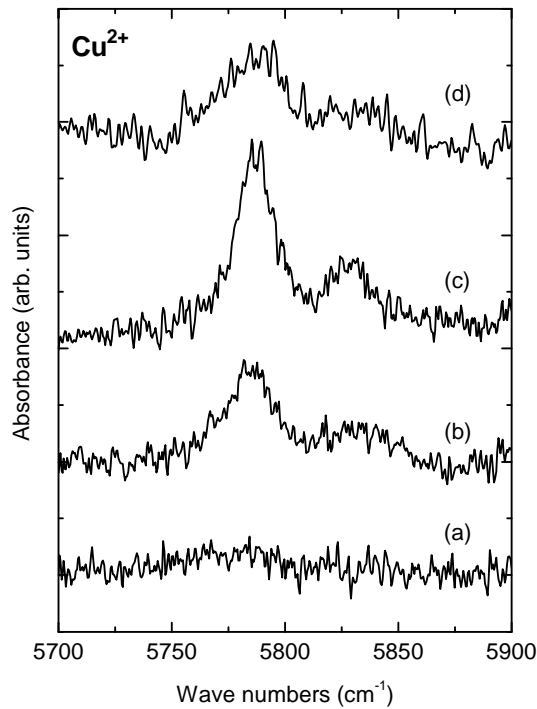


Fig. 2. IR absorption spectra of ZnO nanocrystals aged for nanocrystals with different sizes. The aging times were (a) 2 hr, (b) 18 hr, and (c) 43 hr. Spectrum (d) was a 43-hr sample that was then etched with acetic acid. The two absorption peaks arise from intra-d transitions of Cu^{2+} dopants.

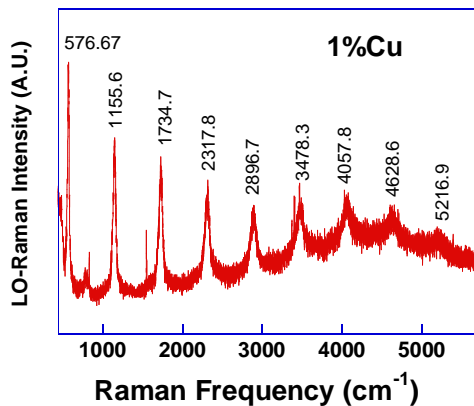


Fig. 3. Raman spectrum of the 1% Cu doped ceramic ZnO sample. The PL is completely quenched. Similar spectra were observed for the 5% sample.

heavily doped shell. These observations are consistent with the trapped dopant model (Fig. 1), in which dopant atoms stick to the surface of the core and are overgrown by the nanocrystal material. The IR spectroscopic signature of Cu^{2+} is shown in Fig. 2.

ZnO:Cu ceramics

ZnO:Cu ceramic samples were created via a sintering process that involves hard-pressing followed by an annealing procedure. Samples of 0, 0.5, 1, and 5% copper were studied. The room-temperature UV photoluminescence (PL) of the samples have an interesting correlation to the percentage of Cu in the samples. The pure ZnO sample has a strong PL centered at ~ 3.3 eV. As the percentage of Cu increases, a significant decrease in the PL intensity is observed. Due to the diminishing intensity of the PL, up to *nine orders of the LO mode* are observable for the Cu doped samples (Fig. 3). Our results suggest that the low PL intensity is due to non-radiative centers of Cu-related complexes.

The multiple LO modes give us unparalleled insight into anharmonic vibrational processes. We are currently investigating the effect of pressure on the anharmonicity, and the fundamental role it plays in phase transitions.

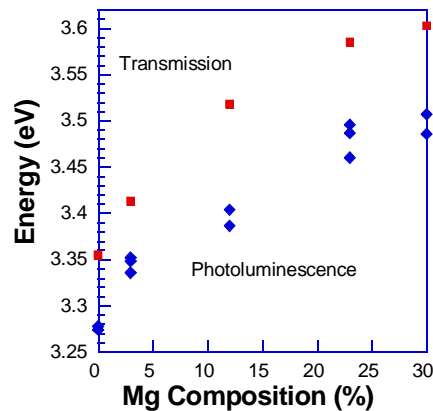


Fig. 4. PL and the absorption edge of MgZnO as a function of Mg composition.

MgZnO nanocrystals

The $\text{Mg}_x\text{Zn}_{1-x}\text{O}$ alloy system is emerging as a material capable of luminescence in the UV spectral range with promising applications in optoelectronic devices. ZnO has a hexagonal wurtzite structure and bandgap ~ 3.4 eV, while MgO has the rocksalt (NaCl) cubic structure with bandgap ~ 7.7 eV. Alloying provides a means to tune the bandgap over a wide range. We studied the optical properties of $\text{Mg}_x\text{Zn}_{1-x}\text{O}$ nanocrystals below and at the phase transition range. For nanocrystals of Mg composition 0-30%, the samples were found to consist of the wurtzite structure. They exhibited band edge absorption as well as PL blueshift of ~ 0.25 eV (Fig. 4).

ZnO and MgZnO under extreme conditions

$\text{Mg}_x\text{Zn}_{1-x}\text{O}$ ($x = 0.15$) and ZnO nanocrystals of ~ 40 nm in diameter were studied using x-ray diffraction and diamond-anvil cells. The high-pressure beamline at the LBNL Advanced Light Source was used. The equation of state for MgZnO was reported for the first time. Between pressures of 9.45 and 10.7 GPa, MgZnO transforms into the rocksalt (NaCl) structure, which persisted to 1.1 GPa upon decompression. The EOS parameters for ZnO are close to their bulk values and in good agreement with values obtained previously. The bulk modulus for MgZnO was slightly lower than that of ZnO. The pressure-induced decrease in c/a ratio was greater for MgZnO, consistent with the tendency for MgZnO to move toward a cubic structure. From previous photoluminescence measurements, the band-gap volume deformation potentials for ZnO and $\text{Mg}_{0.15}\text{Zn}_{0.85}\text{O}$ were determined to be -3.6 and -4.0 eV, respectively.

Flexible films

ZnO was deposited via a sputtering technique on a flexible and UV transparent fluorinated ethylene propylene (FEP) substrate (Fig. 5). The optical properties were studied via PL and transmission spectroscopy. Raman scattering was utilized to investigate the stress state of the film and the impact of external mechanical deformation. The PL was found to exhibit a structural-defect related emission at ~ 3.316 eV and an emission due to the ZnO free- and bound-excitons. The bandgap of the film had a room-temperature value of 3.34 eV. The underlying FEP substrate was found to be under tensile stress resulting from the large difference of the thermal expansion coefficients of both materials. The applied deformation did not significantly impact the ZnO film.

Future Plans

In addition to the goals listed in the Program Scope section, in the near term, we will investigate the role of nanocrystal size and doping on phase transition pressures of ZnO, using the high-pressure beamline at LBNL. We will also probe the electronic properties of Cu acceptors in ZnO and study the physical properties of flexible ZnO and MgZnO films.

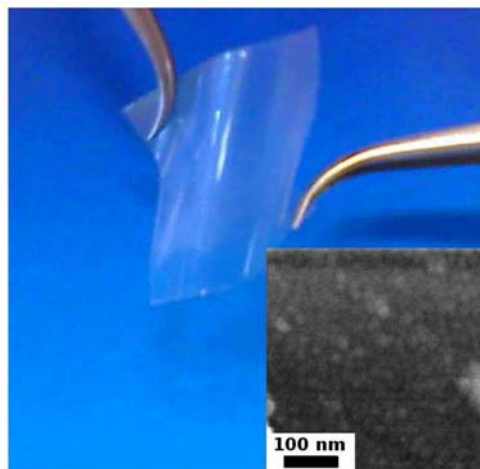


Fig. 5. Photograph of the ZnO film and its SEM image (inset) showing a nanocrystalline morphology.

Publications of DOE-sponsored research (2008-2010)

- W.M. Hlaing Oo, M.D. McCluskey, Y.P. He and Y.P. Zhao, “Strong Fano resonance of oxygen-hydrogen bonds on oblique angle deposited Mg nanoblades,” *Appl. Phys. Lett.* **92**, 183112:1-3 (2008).
- J.L. Morrison, J. Huso, H. Hoeck, E. Casey, J. Mitchell, L. Bergman, and M. Grant Norton, “Optical properties of ZnO and MgZnO nanocrystals below and at the phase separation range,” *J. Appl. Phys.* **104**, 123519:1-6 (2008).
- W.M. Hlaing Oo, L.V. Saraf, M.H. Engelhard, V. Shutthanandan, L. Bergman, J. Huso, and M.D. McCluskey, “Suppression of conductivity in Mn-doped ZnO thin films,” *J. Appl. Phys.* **105**, 013715:1-4 (2009).
- J. Huso, J.L. Morrison, J. Mitchell, E. Casey, H. Hoeck, C. Walker, L. Bergman, W.M. Hlaing Oo, and M.D. McCluskey, “Optical transitions and multiphonon scattering of Cu-doped ZnO and MgZnO ceramics,” *Appl. Phys. Lett.* **94**, 061919:1-3 (2009).
- K.K. Zhuravlev, W.M. Hlaing Oo, M.D. McCluskey, J. Huso, J.L. Morrison, and L. Bergman, “X-ray diffraction of $Mg_xZn_{1-x}O$ and ZnO nanocrystals under high pressure,” *J. Appl. Phys.* **106**, 013511:1-4 (2009).
- M.D. McCluskey and S.J. Jokela, “Defects in ZnO,” *J. Appl. Phys.* **106**, 071101:1-13 (2009). Invited review article, featured on cover.
- M.D. McCluskey, S.J. Jokela, and M.C. Tarun, “Hydrogen-related defects in bulk ZnO,” in *Compound Semiconductors for Energy Applications and Environmental Sustainability*, ed. F. Shahedipour-Sandvik, E.F. Schubert, L.D. Bell, V. Tilak, A.W. Bett (Mater. Res. Soc. Symp. Proc. **1167**, Warrendale, PA, 2009), 1167-O07-07 (5 pages).
- M.D. McCluskey, W.M. Hlaing Oo, and S. Teklemichael, “Dopants in nanoscale ZnO,” in *Functional Metal-Oxide Nanostructures*, ed. J. Wu, W. Han, A. Janotti, H-C. Kim (Mater. Res. Soc. Symp. Proc. **1174**, Warrendale, PA, 2009), 1174-V07-03 (5 pages).
- S.J. Jokela, M.C. Tarun, and M.D. McCluskey, “Nitrogen and hydrogen in bulk single-crystal ZnO,” *Physica B* **404**, 4810-2 (2009).
- S.J. Jokela and M.D. McCluskey, “Structure and stability of N-H complexes in single-crystal ZnO,” *J. Appl. Phys.* **107**, 113536:1-5 (2010).
- W.M. Hlaing Oo, M.D. McCluskey, J. Huso, J.L. Morrison, L. Bergman, M.H. Engelhard, and L.V. Saraf, “Incorporation of Cu acceptors in ZnO nanocrystals,” *J. Appl. Phys.* **108**, 064301:1-3 (2010).
- W.M. Hlaing Oo, S. Tabatabaei, M.D. McCluskey, J.B. Varley, A. Janotti, and C.G. Van de Walle, “Hydrogen donors in SnO_2 studied by infrared spectroscopy and first-principles calculations,” *Phys. Rev. B* **82**, 193201:1-4 (2010).
- L. Bergman, J. Huso, J.L. Morrison, and G.M. Norton, “Luminescent ZnO and MgZnO.” To appear in *Handbook of Photoluminescent Semiconductor Materials*, ed. Leah Bergman and Jeanne L. McHale (Taylor & Francis 2011).

* E-mail: mattmcc@wsu.edu

** E-mail: lbergman@uidaho.edu

Evolution of Oxide Stability During Localized Corrosion of Model Al-Cu Alloys

Nancy Missert, R. Guild Copeland, Paul Kotula, Jonathan Rivera, and Robert Garcia
Sandia National Laboratories, Albuquerque, NM 87185-1415

namisse@sandia.gov

Nanometer Scale Surface and Interface Phenomena: Nanoscale Electrochemistry

Program Scope: The primary focus of this program has been to develop a quantitative understanding of the mechanisms of localized corrosion initiation in passive metals and to quantify the critical parameters governing nanostructure formation in model systems. Our approach is based on the novel and unique application of nanofabrication techniques to produce tailored surfaces and to simulate specific defect types on controlled substrates in well-defined locations. We shed light on corrosion and nanostructure-formation mechanisms using advanced electrochemical, morphological, chemical and structural analytical tools. We have identified three critical areas where further, detailed knowledge is needed: 1) the chemical/structural description of the nano-scale site responsible for pit initiation, 2) the role of microstructure in pit initiation and stabilization 3) the role of surface properties in electrochemically controlled nanostructure formation. The nano-scale evolution of the passive oxide up to the point of pit initiation is currently under investigation using in-situ AFM imaging, and electrochemical characterization combined with analytical electron microscopy. The role of microstructure during the early stages of pitting is studied using model alloys to understand heterogeneous solution chemistry and electron transfer properties. Nanostructure formation on model systems in electrochemical environments is being examined using in-situ scanning probe microscopy. Our future work will continue to explore the correlation between nanostructure evolution and pit initiation in pure Al and model Al-Cu alloys, and will expand the scope of our in-situ studies of nanostructure formation to energy storage and conversion materials.

Recent Progress: Although localized corrosion of aluminum-copper alloys in halide environments is known to occur in the vicinity of intermetallic Cu-rich particles (1, 2, 3), a detailed understanding of the evolution of attack, from the mechanisms responsible for breakdown, to the transition to stable pitting, is still lacking. Since corrosion is a redox reaction, wherein the anodic oxidation of the metal must be balanced by the cathodic reduction of oxygen from solution, the mechanisms governing both processes must be understood in order to provide a complete picture. For example, the “trenching”, or circumferential attack around intermetallic particles, observed after prolonged exposure to aggressive environments, has been hypothesized to result from local alkalization (4) of the solution due to high oxygen reduction rates on the surface of the cathodic particles (5, 6, 7). However, factors influencing the stability of trench growth (8,9), and the transformation from “trenching” to pitting, have not yet been fully explained. Part of the difficulty in explaining this transformation is the pH gradients required. In fact, the properties of the passive film (on both the particles and the surrounding matrix) in alkaline environments have not been explored. Our work over the past three years has therefore focused on understanding the stability and electron transfer properties of the passive films in alkaline environments.

We have used electron beam co-evaporation of Al-3.5%Cu thin films on SiO₂ covered Si wafers, followed by annealing treatments, to create a model system for studying the effects of alkaline exposures on the loss of passivity in Al-Cu alloys. After annealing at temperatures of 350 – 450 C, Al₂Cu intermetallic particles form at grain boundaries in an Al-0.5%Cu matrix (Figure 1a), with nanometer scale surface roughness as measured by AFM. In-situ fluorescence microscopy techniques (10-15) show that initially, high cathodic reaction rates (which significantly raise the pH) occur locally on the electrode surface in response to remote anodic attack. The area available for high cathodic reaction rates continues to expand with time of exposure to the high pH solution, suggesting that exposure to the high pH environment enables more facile electron transfer to support high ORR rates.

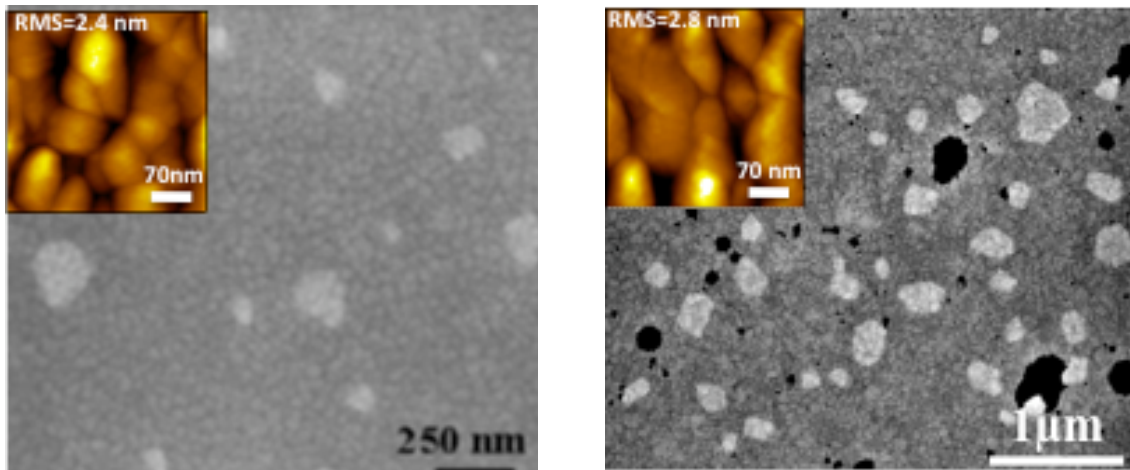


Figure 1 (a) SEM image of model Al-Cu thin film alloy showing Al₂Cu precipitates at grain boundaries, prior to exposure, (b) SEM image after 30 min exposure to pH 11.5, 10 mM NaCl. Insets are AFM images.

Areas exposed to the high pH environment (Figure 1b) show localized attack adjacent to some particles, at grain boundaries and on grain faces, where an increase in attack site density is directly correlated to exposure time. Ex-situ AFM imaging (insets, Figure 1(a) vs. (b)) shows no evidence for de-alloying of the particles or matrix even after a 30 minute exposure to pH 11.5, suggesting that on time scales important for corrosion initiation, an understanding of the evolution of oxide electronic conductivity as a function of pH is required. To evaluate the conductivity of the passive films, the current-voltage characteristics near the open circuit potential were measured as a function of pH. The open circuit potential dropped as the pH increased, consistent with an increase in corrosion rate, that is, an increase in both passive film oxidation rate and the balancing oxygen reduction rate. The slope of the cathodic branch, measured near the OCP, gives the polarization resistance, which decreased by over four orders of magnitude, as the pH increased from 6 to 11.5, demonstrating a huge activation of the surface for both the anodic and cathodic reactions. Electrochemical impedance spectroscopy also showed a

dramatic drop in the oxide impedance as the pH increased. The specific mechanism responsible for this activation is postulated to be a thinning of the surface oxide or an increased electronic conductivity, since Cu surface enrichment was ruled out through x-ray absorption, (16) ToF-SIMS imaging studies, (17) and cross-sectional TEM. Future experiments will distinguish between these factors.

Future plans: In future work we will build on our use of tailored surfaces and in-situ diagnostics to explain mechanisms governing materials properties in electrochemical environments. Our recent work has shown the importance of evolving nanostructure, as well as the electronic properties of the oxide, for localized dissolution of pure Al and model Al-Cu alloys in aqueous Cl⁻ environments. We will pursue the relationship between this evolving nanostructure and metastable pit initiation to determine which parameters govern the metastable to stable pitting transition. The mechanisms responsible for increasing electron transfer rates across the passive oxide in alkaline environments will be identified. In addition, we will extend our studies of localized corrosion initiation to time-dependent, structure-function relationships in materials required for the energy storage and conversion. Our goal is to understand the link between evolving nanostructure and the stability of the electrode surface in electrochemical environments under potential control.

Mechanisms governing cathodic kinetics across the passive layer on Al-Cu alloys

Although we found a dramatic decrease in the impedance of the oxide at pH 10 and 11, prior to the onset of localized corrosion, it is not known if only the impedance of the oxide above the intermetallic particles is reduced, or if matrix oxide properties are also changing. In addition, the high electron transfer rates observed on cathodic regions of the electrode using fluorescence microscopy, suggest that in-situ STM imaging of the passive oxide surface should be possible, for the first time, in alkaline solutions. This would allow us to map the evolution of the morphology, structure, and electronic properties of the oxide layer as a function of exposure time and potential. Such local measurements would allow us to determine definitively where on the surface the high electron transfer rates occur, and how the oxide properties change (e.g. local thinning, development of electronic defects, etc.) to accommodate them. Furthermore, the ability to map this oxide evolution in situ, should provide mechanistic information as to how “trenching” initiates at intermetallic particles in alkaline environments. Our preliminary studies have shown that localized breakdown begins at a single point along the interface, where the dissolution of the underlying metal proceeds radially from the breakdown point. Multiple breakdown sites can initiate along the interface, eventually resulting in the “trenching” often observed in bulk samples. However, the specific defect and the mechanism responsible for this localized interfacial breakdown are currently not known. Our in-situ STM experiments could finally provide a quantitative description of this process. These studies will contribute to the development of an atomic-scale model of the mechanisms controlling cathodic kinetics in Al-Cu alloys.

Tailoring oxide surface stability for electrical energy storage

One of the most important obstacles to the widespread use of nanostructured materials in electrochemical environments is instability of the surface layer during potential cycling. Our goal is to determine how local electronic properties, atomic arrangements and defects, and a high radius-of-curvature morphology impact the adsorption of electrolyte

species and the kinetics of reactions at the electrode surface. We will explore the evolution of surface properties with time and potential in model nanostructured oxide systems, using in-situ electrochemical spectroscopic STM and AFM to link locally evolving changes in properties and nanostructure with surface reactivity. Once the dominant parameters governing loss of stability are identified, we will attempt to modify surface properties to minimize their effects.

References

- [1] J. R. Gavele and S. M. de DeMicheli, *Corros. Sci.*, 17, 795 (1970).
- [2] L. Muller, and J. R. Galvele, *Corros. Sci.*, 17, 179 (1977).
- [3] R. G. Buchheit, R. P. Grant, P. F. Hlava, B. Mckenzie, and G. L. Zender, *J. Electrochem. Soc.*, 144, 2621 (1997).
- [4] N. Vasiljevic, L. T. Viyannalage, N. Dimitrov, N. Missert, and R. G. Copeland, *J. Electrochem. Soc.*, 154, 4, C202, (2007).
- [5] C. Blanc, B. Lavelle, and G. Mankowski, *Corros. Sci.*, 39, 495 (1997).
- [6] N. Dimitrov, J. A. Mann, and K. Sieradzki, *J. Electrochem. Soc.*, 146, 98 (1999).
- [7] M. B. Vukmirovic, N. Dimitrov, and K. Sieradzki, *J. Electrochem. Soc.*, 149, B428 (2002).
- [8] N. Murer, N. A. Missert, R. Oltra, R.G. Buchheit, COMSOL Boston 2009.
- [9] N. Murer, N. A. Missert, R. G. Buchheit, EUROCORR 2009, Nice, France.
- [10] N. Missert, R. G. Copeland, J. C. Barbour, J. E. Mikkalson, and H. Isaacs, in Corrosion and Corrosion Prevention of Low Density Metals and Alloys, R. G. Buchheit and B. A. Shaw, Editors, PV00-23, p. 239, The Electrochemical Society, Pennington, NJ, (2001).
- [11] N. Missert, J. C. Barbour, R. G. Copeland, and J. E. Mikkalson, in Corrosion and Corrosion Control, J. D. Sinclair, E. Kalman, M. W. Kendig, W. Plieth, W. H. Smyrl, Editors PV 01- 22, The Electrochemical Society, Inc., Pennington, NJ, (2002).
- [12] N. Missert, R. G. Copeland, F. D. Wall, C. M. Johnson, J. C. Barbour, and P. Kotula, in Corrosion Science: A Retrospective and Current Status, G.S. Frankel, H.S Isaacs, J.R. Scully and J.D. Sinclair, Editors, PV2002-13, The Electrochemical Society, Pennington, NJ, (2002).
- [13] N. Missert, R. G. Copeland, F. D. Wall, C. M. Johnson, and J. C. Barbour, in Critical Factors in Localized Corrosion IV, S. Virtanen, P. Schmuki, and G. S. Frankel, Editors, PV02-24, The Electrochemical Society, Pennington, NJ, (2003).
- [14] N. Missert, R. G. Copeland, Y. Kim and R. G. Buchheit, in Corrosion and Protection of Light Metal Alloys, R. G. Buchheit, B. Shaw, R. Kelly, N. Missert, Editors PV 03- 23, The Electrochemical Society, Inc., Pennington, NJ, (2004).
- [15] R. G. Copeland, N. Missert, K. Barrett, in Corrosion in Marine and Saltwater Environments II, D. A. Shifler, Editors, PV04-14, The Electrochemical Society Inc, Pennington, NJ (2005).
- [16] N. Missert, H. S. Isaacs, B. Ingham, R. Huang, and N. Vasiljevic, "Dissolution Characteristics of Al₂Cu and Al-4%Cu Thin Films" *ECS Trans.*, 3, (31) 227, (2007).
- [17] A. Seyeux, G. S. Frankel, N. Missert, K. A. Unocic, L. H. Klein, A. Galtayries, P. Marcus, submitted to *J. Electrochem. Soc.* (2010).

Title of project: Nanophosphors: Fundamental Science of Insulators in the Nanoscale Regime

Principal Investigator: Ross E. Muenchausen
 Technical Staff Member
 MST-7, MS E549
 Los Alamos National Laboratory
 Los Alamos, NM 87545
 505.667.0391
 Fax: 505.667.8109
 E-mail: rossm@lanl.gov

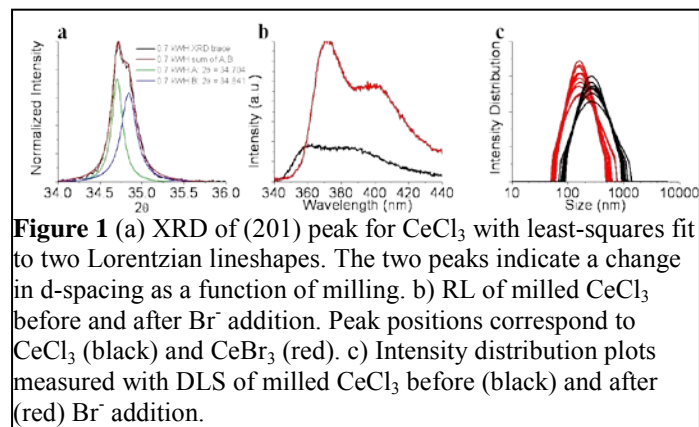
Co-investigators: Markus P. Hehlen, John C. Gordon, Cindy F. Welch, Michael W. Blair, Nickolaus A. Smith, Bryan L. Bennett, Stephanie A. Tornga, Kalyan V. Vasudevan

Program Scope

The discovery of novel scientific phenomena in nanoscale materials has predominantly been distinguished through reduced dimensionality effects associated with semiconductors. Realization that reduced dimensionality in *semiconductors* can lead to such exciting new behavior begs the logical scientific question: What physical and chemical behavior can be expected from reduced dimensionality in *insulators*? This question has been the driving force behind our BES program for the last six years.

Recent Progress

Our recent research progress represents a transition from a phenomenological recognition of unique luminescence behaviors in nanoscale oxides to a systematic investigation of reduced dimensionality effects in metal halide nanomaterials. The robustness of the Solution Combustion Process has been exploited to produce numerous



nanoscale rare-earth doped oxides for specific purposes, pilot studies, and to support our numerous collaborative efforts. In addition, we have developed new and unique capabilities for processing hygroscopic metal halides. With the goal of developing dispersible nanophosphors, we have milled highly hygroscopic bulk CeBr_3 and CeCl_3 to nanometer dimensions and obtained evidence of an altered lattice at the surface (Figure 1 (a)). Adding surfactants has led to the formation of core-shell structures where emission arises from the shell material only (Figure 2(b)), and this has led to the discovery of efficient core-shell energy-transfer processes and possible phonon-confinement effects.

Diverse approaches to nanophosphor production have enabled us to utilize a comprehensive set of techniques to study nanoparticle structure, basic luminescence processes, and energy transport mechanisms. We have performed total scattering experiments with neutrons and x-rays on nanostructured LaF_3 embedded in a glass matrix and CeF_3 nanophosphor in collaboration with K. Page and T. Proffen of the Lujan Neutron Scattering Center at LANSCE, and the preliminary results have detected previously unknown (from traditional XRD studies) impurity phases in these materials. In collaboration with other researchers at LANL, we studied the spectroscopic properties of Lindqvist-type $\text{Ce}^{\text{IV}}\text{-POM}$ complexes. It was shown that $[\text{Ce}(\text{W}_5\text{O}_{18})_2]^{8-}$ is luminescent upon excitation from the $\text{O} \rightarrow \text{Ce}$ charge transfer transition. When solvent effects are considered, density functional theory (DFT) provides an excellent correlation with experiment despite the charge in these polyanions, and we provide insight into the nature of the excitation and emission properties (Roy *et al.*, 2010). Finally, by measuring temperature-dependent Electron Paramagnetic Resonance (EPR) spectra of Ce-doped oxyorthosilicates, we were able to show that nanophosphors are inherently more disordered than bulk particles and that the lattice-bath relaxation lifetime was

reduced in nanophosphors implying that energy (and heat) transport could be more efficient in nanophosphors (Blair *et al.*, 2010).

Our unique characterization capabilities and extensive collaborative efforts have also allowed us to explore more traditional nanoscale research as well. In collaboration with Marvin Warner of PNNL and Jennifer

Hollingsworth of LANL, we have measured temperature-dependent *cw*-EPR spectra of undoped CdSe quantum dots, CdS capped CdSe quantum dots, non-quantum confined (NQC) CdSe particles (~15 nm particle size), and bulk CdSe particles to reveal unique resonances and dipolar coupling effects. The QD and NQC samples show intense resonances with low *g* values (approximately $g=0.57$) with an inverse Dysonian lineshape, while the bulk CdSe samples display similar resonances at a much lower intensity (Figure 2(a)). The *g* values of these resonances are larger than the theoretical prediction of $g=0.5$ for bulk CdSe conduction electrons, and the QD and NQC samples show a strong temperature dependence of the *g* values which implies the dipolar coupling of two paramagnetic species (Figure 2 (b)). In fact, we were able to detect NO species on the surface of all CdSe samples, and we believe the interaction of the surface NO with the CdSe conduction electrons produce the observed resonances. Similar relationships have been seen in CdSe:Mn, but the interactions are orders of magnitude stronger than the ones seen in our studies. We were able to obtain these results because our EPR spectrometer is able to reach fields up to 14 kGauss in order to access the Q band region (~36 GHz microwave frequency) whereas most X band spectrometers cannot reach fields above 10 kGauss. These results demonstrate the extended electronic nature of QD and our sensitivity to detect coupled electronic systems.

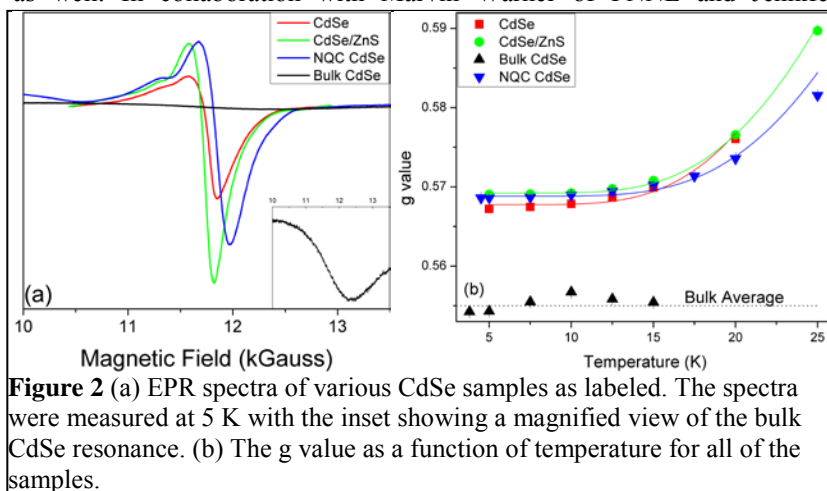


Figure 2 (a) EPR spectra of various CdSe samples as labeled. The spectra were measured at 5 K with the inset showing a magnified view of the bulk CdSe resonance. (b) The *g* value as a function of temperature for all of the samples.

Future Plans

Our recent success in detecting weak interactions among different spin systems in quantum dots and collaborative efforts resulting in the successful prediction of POM luminescence characteristics by DFT calculations have led us to pursue a new direction for the future. An existing BES effort seeks to understand the condensed phase properties of organic electronic materials which is largely governed by the intermolecular interactions of these materials. While the effort currently combines DFT calculations with diverse experimental techniques, the demonstrated sensitivity of EPR spectroscopy to interacting systems can enhance the program. It is possible to directly simulate EPR spectra with DFT as a function of potential defect candidates. This can be a difficult experiment to model, and one of the goals of this work will be to ascertain the reliability of EPR predictions in organometallic systems.

Publications done under BES funding

The list is from October 2007 to the present. Bold font is used to delineate publications done exclusively with BES funding. For others, the BES contribution is summarized in brackets.

M. W. Blair, B. L. Bennett, S. C. Tornga, N. A. Smith, and R. E. Muenchausen. "Reduced dimensionality effects on phonon transport." *Journal of Applied Physics* 108, 104311-104317 (2010).

E. G. Yukihiro, L. G. Jacobsohn, M. W. Blair, B. L. Bennett, S. C. Tornga, and R. E. Muenchausen. "Luminescence properties of Ce-doped oxyorthosilicate nanophosphors and single crystals." *Journal of Luminescence* 130, 2309-2316 (2010). [BES program supplied materials for paper]

L. G. Jacobsohn, S. C. Tornga, B. L. Bennett, R. E. Muenchausen, O. Ugurlu, T. K. Tseng, J. Choi, and P. H. Holloway. "Annealing effects on the photoluminescence yield of Gd₂O₃:Eu nanoparticles produced by solution combustion synthesis." *Radiation Measurements* 45, 611-614 (2010).

- J. R. Hazelton, E. G. Yukihara, L. G. Jacobsohn, M. W. Blair, and R. Muenchausen. "Feasibility of using oxyorthosilicates as optically stimulated luminescence detectors." *Radiation Measurements* **45**, 681-683 (2010). [BES program supplied materials for paper]
- Yearley, E. J., Sasa, L. A., Welch, C. F., Taylor, M. A., Kupcho, K. M., Gilbertson, R. D. and Hjelm, R. P. "The Couette configuration of the Los Alamos Neutron Science Center Neutron Rheometer for the investigation of polymers in the bulk via small-angle neutron scattering." *Rev Sci Instrum.* **81**, 7 (2010).
- L. A. Sasa, E. J. Yearley, C. F. Welch, M. A. Taylor, R. D. Gilbertson, C. Hammeter, J. Majewski, and R. P. Hjelm. "The Los Alamos Neutron Science Center neutron rheometer in the cone and plate geometry to examine tethered polymers/polymer melt interfaces via neutron reflectivity." *Review of Scientific Instruments* **81**, 055102 (2010).
- Salacka, J. S. and Bacrania, M. K. "A Comprehensive Technique for Determining the Intrinsic Light Yield of Scintillators." *IEEE Trans Nucl Sci.* **57**, 901-909 (2010). [BES program supplied materials for paper]
- Roy, L. E., Ortiz-Acosta, D., Batista, E. R., Scott, B. L., Blair, M. W., May, I., Del Sesto, R. E. and Martin, R. L. "Luminescence in Ce-IV polyoxometalate $[\text{Ce}(\text{W}_5\text{O}_{18})_2]^{8-}$: a combined experimental and theoretical study." *Chemical Communications.* **46**, 1848-1850 (2010). [BES program provided FTIR measurements]
- Nerikar, P., Stanek, C. R., Phillpot, S. R., Sinnott, S. B. and Uberuaga, B. P. "Intrinsic electrostatic effects in nanostructured ceramics." *Physical Review B.* **81**, 064111 (2010).
- Jacobsohn, L. G., Tappan, B. C., Tornga, S. C., Blair, M. W., Luther, E. P., Mason, B. A., Bennett, B. L. and Muenchausen, R. E. "The effect of hydrostatic pressure on the combustion synthesis of $\text{Y}_2\text{O}_3\text{:Bi}$ nanophosphor." *Optical Materials.* **32**, 652-656 (2010). [BES program provided SCS materials, XRD, and luminescence measurements]
- Hehlen, M. P., Bennett, B. L., Castro, A., Williams, D. J., Tornga, S. C. and Muenchausen, R. E. "Synthesis and optical properties of $\text{Ga}_2\text{S}_3\text{-Na}_2\text{S-CSCl}$ glasses." *Optical Materials.* **32**, 491-499 (2010). [BES program provided luminescence measurements]
- Blair, M. W., Jacobsohn, L. G., Tornga, S. C., Ugurlu, O., Bennett, B. L., Yukihara, E. G. and Muenchausen, R. E. "Nanophosphor aluminum oxide: Luminescence response of a potential dosimetric material." *Journal of Luminescence.* **130**, 825-831 (2010).
- Stange, S., Esch, E. I., Bacrania, M. K., Brown, L. O., Couture, A. J., Del Sesto, R. E., Gilbertson, R. D., Jacobsohn, L. G., McCleskey, T. M., McKigney, E. A. et al. "Development and Characterization of Nanocomposite Scintillators for Gamma-Ray Detection." *IEEE Nuclear Science Symposium*, 2804-2807 (2009).
- Stanek, C. R., Jiang, C., Uberuaga, B. P., Sickafus, K. E., Cleave, A. R. and Grimes, R. W. "Predicted structure and stability of $\text{A}_4\text{B}_3\text{O}_{12}$ delta-phase compositions." *Physical Review B.* **80**, 174101 (2009).
- Prasankumar, R. P., Upadhyaya, P. C., Li, Q., Smith, N., Choi, S. G., Azad, A. K., Talbayev, D., Wang, G. T., Fischer, A. J., Hollingsworth, J. et al. "Ultrafast carrier dynamics in semiconductor nanowires." *Proc SPIE - Int Soc Opt Eng.* **7406**, 74060E (2009).
- Melot, B. C., Page, K., Seshadri, R., Stoudenmire, E. M., Balents, L., Bergman, D. L. and Proffen, T. "Magnetic frustration on the diamond lattice of the A-site magnetic spinels $\text{CoAl}_{2-x}\text{Ga}_x\text{O}_4$: the role of lattice expansion and site disorder." *Physical Review B (Condensed Matter and Materials Physics).* **80**, 104420 (2009).
- Jacobsohn, L. G., Bennett, B. L., Muenchausen, R. E., Martin, M. S. and Shao, L. "Radioluminescence Investigation of Ion-Irradiated Phosphors." *Application of Accelerators in Research and Industry.* **1099**, 977-980 (2009).
- Blair, M. W., Levy, M. R., Grimes, R. W., Uberuaga, B. P., Jiang, C., Valdez, J. A., Williams, J. J., Tang, M., Stanek, C. R. and Sickafus, K. E. "Charge compensation in an irradiation-induced phase of $\text{Sc}_4\text{Zr}_3\text{O}_{12}$." *Journal of Materials Science.* **44**, 4754-4757 (2009).

- Blair, M. W., Jacobsohn, L. G., Bennett, B. L., Tornga, S. C., Yukihiro, E. G., McKigney, E. A. and Muenchausen, R. E. "Luminescence and structural properties of oxyorthosilicate and Al_2O_3 nanophosphors." *Physica Status Solidi A - Applications and Materials Science*. **206**, 904-909 (2009).**
- Ortiz-Acosta, D., Purdy, G. M., Scott, B., Bennett, B. L., Muenchausen, R. E., McKigney, E. A., Gilbertson, R. D. and Del Sesto, R. E. "Ionic liquid polyoxometalates as light emitting materials." *ECS Transactions*. **16**, 171-180 (2008). [BES program supplied luminescence characterization]
- Muenchausen, R. E., McKigney, E. A., Jacobsohn, L. G., Blair, M. W., Bennett, B. L. and Cooke, D. W. "Science and application of oxyorthosilicate nanophosphors." *IEEE Trans Nucl Sci*. **55**, 1532-1535 (2008).**
- Jacobsohn, L. G., Blair, M. W., Tornga, S. C., Brown, L. O., Bennett, B. L. and Muenchausen, R. E. " $\text{Y}_2\text{O}_3\text{:Bi}$ nanophosphor: Solution combustion synthesis, structure, and luminescence." *J Appl Phys*. **104**, (2008).**
- Jacobsohn, L. G., Bennett, B. L., Muenchausen, R. E., Tornga, S. C., Thompson, J. D., Ugurlu, O., Cooke, D. W. and Sharma, A. L. L. "Multifunction $\text{Gd}_2\text{O}_3\text{:Eu}$ nanocrystals produced by solution combustion synthesis: Structural, luminescent, and magnetic characterization." *J Appl Phys*. **103**, (2008).**
- Hamilton, C. W., Morris, D. E., Blair, M. W., Henson, N. J., Martin, R. L., Cross, J. L., Jantunen, K. C., Scott, B. L. and Baker, R. T. "When is addition of X-Y to M not oxidative?." *Proceedings of 235 National ACS Meeting*, INOR 50 (2008). [BES program provided EPR measurements]
- Cooke, D. W., Blair, M. W., Smith, J. F., Bennett, B. L., Jacobsohn, L. G., McKigney, E. A. and Muenchausen, R. E. "EPR and luminescence of F^+ centers in bulk and nanophosphor oxyorthosilicates." *IEEE Trans Nucl Sci*. **55**, 1118-1122 (2008).**
- McKigney, E. A., Muenchausen, R. E., Cooke, D. W., Del Sesto, R. E., Gilbertson, R. D., Bacrania, M. K., Bennett, B. L., Jacobsohn, L. G., McCleskey, T. M., Ott, K. C. et al. " $\text{LaF}_3\text{:Ce}$ nanocomposite scintillator for gamma-ray detection." *Proceedings of the Society of Photo-Optical Instrumentation Engineers (SPIE)*. **6706**, A7061 (2007). [BES program supplied luminescence characterization]
- McKigney, E. A., Del Sesto, R. E., Jacobsohn, L. G., Santi, P. A., Muenchausen, R. E., Ott, K. C., McCleskey, T. M., Bennett, B. L., Smith, J. F. and Cooke, D. W. "Nanocomposite scintillators for radiation detection and nuclear spectroscopy." *Nuclear Instruments & Methods in Physics Research Section a-Accelerators Spectrometers Detectors and Associated Equipment*. **579**, 15-18 (2007). [BES program supplied luminescence characterization]
- Jacobsohn, L. G., Bennett, B. L., Sitarz, S. C., Ugurlu, O., Sharma, A. L. L., Cooke, D. W. and Muenchausen, R. E. "Synthesis and structural transformation of luminescent nanostructured $\text{Gd}_2\text{O}_3\text{:Eu}$ produced by solution combustion synthesis." *Proceedings of Materials Research Society Symposium*. **506** Keystone Drive Warrendale, PA 15086, United States, 2008, 239-245 (2007).**
- Jacobsohn, L. G., Bennett, B. L., Muenchausen, R. E., Smith, J. F. and Cooke, D. W. "Luminescent properties of nanophosphors." *Radiation Measurements*. **42**, 675-678 (2007).**
- Blair, M. W., Jacobsohn, L. G., Bennett, B. L., Muenchausen, R. E., Sitarz, S. C., Smith, J. F., Cooke, D. W., Crazier, P. A. and Wang, R. "Structure and luminescence of Ce-doped Lu_2SiO_5 nanophosphor." *Proceedings of Materials Research Society Symposium*. **506** Keystone Drive Warrendale, PA 15086, United States, 2008, 161-166 (2007).**

Carbon surface diffusion and strain development during the growth of epitaxial graphene on SiC

Taisuke Ohta

Mail Stop 1415
Sandia National Laboratories
Albuquerque, NM 87185
Email: tohta@sandia.gov

Work performed in collaboration with Norman C. Bartelt, Shu Nie, Konrad Thürmer (Sandia California, Livermore, CA 94550), Gary L. Kellogg, Laura B. Biedermann, Thomas E. Beechem, Stephen W. Howell (Sandia New Mexico), and Diedrich A. Schmidt (Dept. Physical Chemistry II, Ruhr-University Bochum, Bochum, NRW 44780 Germany)

Graphene, a single layer of graphite, is a promising material for a host of future electronic applications, owing to its excellent electronic,^{1,2} thermal³ and mechanical properties.⁴ At Sandia Labs, we are developing a synthesis and characterization for large-area epitaxial graphene films on silicon-carbide (SiC) substrate that can be used for nanoelectronics application. This work serves as a core of our fundamental understanding of the material synthesis process.

The growth of graphene films on SiC is one of the more viable pathways towards wafer-size graphene films because the films exhibit high carrier mobility ($>10,000$ cm²/Vs, in the same range as exfoliated graphene supported on solid substrates).^{5,6,7,8,9} The process is based on the sublimation of Si atoms near the surface at elevated temperatures, leaving behind carbon atoms, which then assemble into graphene (a process called *graphitization*). A recently developed synthesis route using argon (Ar) at atmospheric pressures during graphitization (as opposed to vacuum graphitization^{10,11}) has resulted in significant increases in domain size, leading to improved electronic properties.^{12,13, 14} This improvement is brought about by slowing Si sublimation and shifting the growth condition to higher temperatures where the surface is closer to equilibrium.¹⁵ Little is known, however, about the atomistic processes of interrelated Si sublimation and graphene growth.

We have studied the formation process of graphene on SiC(0001) using low energy electron microscopy (LEEM), scanning tunneling microscopy, and atomic force microscopy. This work reveals unanticipated growth mechanisms, which depend

strongly on the initial surface morphology. Carbon diffusion governs the spatial relationship between Si sublimation and graphene growth. Isolated bilayer SiC steps generate narrow ribbons of graphene by a distinctive cooperative process (“arrow features”), whereas triple bilayer SiC steps allow large graphene sheets to grow by step flow. The step-flow growth of graphene is followed using LEEM through imaging the thermionic emission from the sample. We demonstrate how graphene quality can be improved by controlling the initial step structures to avoid the instabilities inherent in diffusion-limited growth.¹⁶

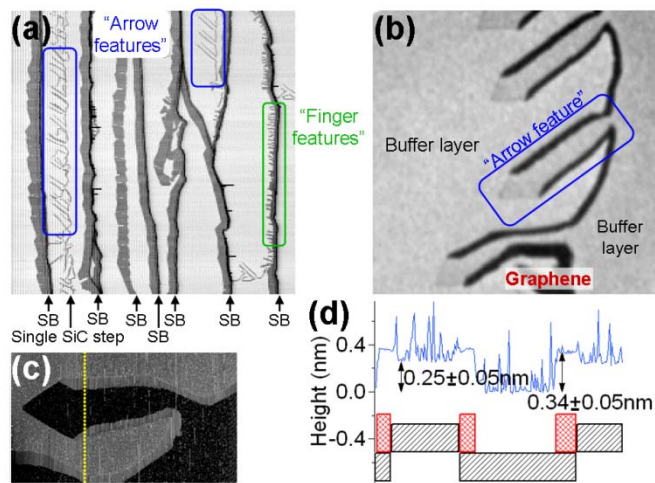


Fig. 1 Overall surface morphology of the SiC sample partially graphitized in Ar. (a) AFM image ($26 \times 26 \mu\text{m}^2$) using phase contrast imaging.¹⁷ Graphene layers (dark grey) are formed at the upper sides (left side in the presented image) of the bunched steps (indicated as SB) via “step-flow growth”. A tall bunched step often appears as a thick line in an AFM phase image. “Arrow features” and “finger features” are highlighted by the blue and green boxes, respectively. (b) LEEM image of the “arrow features” ($4.2 \times 4.2 \mu\text{m}^2$) using incident electrons of $E_{vac} + 2.85 \text{ eV}$, where E_{vac} is the vacuum level. The dark grey regions consist of a graphene monolayer, and the light

gray regions are buffer layer. (c) STM image ($1.8 \times 1.05 \mu\text{m}^2$, tip bias -2.5 V , tunneling current 0.2 nA) with the cross section along the yellow line (d). Red and black hatched boxes in (d) illustrate a proposed step structure with the cross sections of graphene (1ML) and buffer layer (0ML) regions with their thicknesses 0.33 nm and 0.25 nm , respectively.¹⁸

We found that these different growth modes strongly influence the strain state of the epitaxial graphene films. Using confocal Raman spectroscopy, we probed a large and inhomogeneous (at micrometer scale) in-plane compressive strain (up to $\sim 0.5\%$) in 1ML graphene films on SiC(0001).¹⁹ The strain is due to the difference in the lattice constants and thermal expansion coefficients of graphene and SiC substrate. We showed that both the growth mechanism and the relaxation along the mismatched symmetry of the graphene and underlying SiC substrate can affect the exact amount of local strain. The large compressive strain implies that monolayer graphene is tightly grafted to the underlying interface layer and SiC substrate; otherwise it would delaminate to relieve the strain. The magnitudes of the structural strain and its local variation are significant, and need to be taken into account for electronics applications of the graphene-SiC(0001) system.

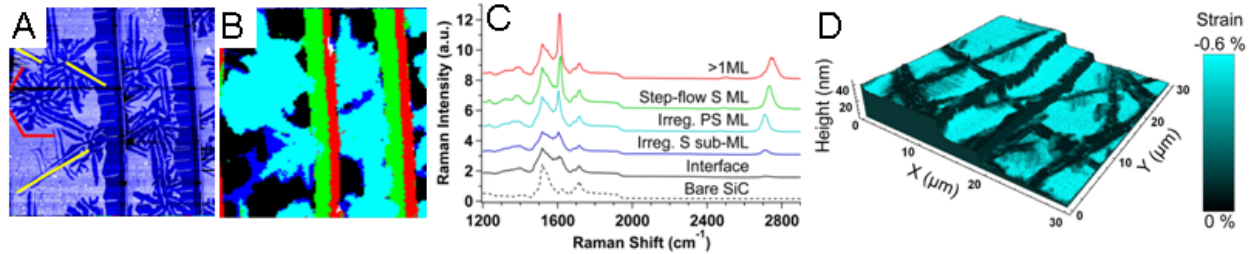


Fig. 2 Strain development at growth fronts in epitaxial graphene. (A) Morphologies imaged using AFM phase contrast. (B) False-color Raman spectra map resulting from a cluster analysis. Each cluster is indicated as a region with a particular color. Cluster analysis sorts out the regions with similar spectral features. (C) Average spectra from clusters in (B). The strain-field was determined from shifts of Raman peaks. (D) Strain-field mapping based on the shift of Raman 2D band acquired through Raman mapping.

This work is partly supported by the US DOE Office of Basic Energy Sciences, Division of Materials Science and Engineering (DE-AC04-94AL85000) and the LDRD program at Sandia Labs, and was performed in part at CINT (DE-AC04-94AL85000). The Raman microscope was supported by BMBF grant 05KS7PC2. We acknowledge financial support from BMBF grants 05KS7PC2 and 05K10PCA, and Martina Havenith for experimental equipment. Sandia Labs is a multi-program laboratory managed and operated by Sandia Corporation, a wholly owned subsidiary of Lockheed Martin Corporation, for the U.S. DOE's NNSA under contract DE-AC04-94AL85000.

¹ X. Du, I. Skachko, F. Duerr, A. Luican, and E. Y. Andrei, *Nature* 462, 192 (2009).

² K. I. Bolotin, F. Ghahari, M. D. Shulman, H. L. Stormer, and P. Kim, *Nature* 462, 196 (2009).

³ A. A. Balandin, S. Ghosh, W. Bao, I. Calizo, D. Teweldebrhan, F. Miao, and C. N. Lau, *Nano Letters* 8, 902 (2008).

⁴ C. Lee, X. Wei, J. W. Kysar, and J. Hone, *Science* 321, 385 (2008).

⁵ J. Jobst, D. Waldmann, F. Speck, R. Hirner, D. K. Maude, Th. Seyller, H. B. Weber, arXiv:0908.1900 (2009).

⁶ T. Shen, J.J. Gu, M. Xu, Y.Q. Wu, M.L. Bolen, M.A. Capano, L.W. Engel, P.D. Ye, *Appl. Phys. Lett.* 95, 172105 (2009).

⁷ A. Tzalenchuk, S. Lara-Avila, A. Kalaboukhov, S. Paolillo, M. Syväjärvi, R. Yakimova, O. Kazakova, T. J. B. M. Janssen, V. Fal'ko, S. Kubatkin, arXiv:0909.1220 (2009).

⁸ X. Wu, Y. Hu, M. Ruan, N. K Madiomanana, J. Hankinson, M. Sprinkle, C. Berger, W. A. de Heer, *Appl. Phys. Lett.* 95, 223108 (2009).

⁹ W. Pan, S. W. Howell, A. J. Ross III, Taisuke Ohta, T. A. Friedmann, *Appl. Phys. Lett.* 97, 252101 (2010).

¹⁰ T. Ohta, F. El Gabaly, A. Bostwick, J. L. McChesney, K. V. Emtsev, A. K. Schmid, Th. Seyller, K. Horn, E. Rotenberg, *New Journal of Physics* 10, 023034 (2008).

¹¹ H. Hibino, H. Kageshima, F. Maeda, M. Nagase, Y. Kobayashi, H. Yamaguchi, *Phys. Rev. B* 77, 075413 (2008).

¹² K. V. Emtsev, A. Bostwick, K. Horn, J. Jobst, G. L. Kellogg, L. Ley, J. L. McChesney, T. Ohta, S. A. Reshanov, J. Röhr, E. Rotenberg, A. K. Schmid, D. Waldmann, H. B. Weber, Th. Seyller, *Nature Materials* 8, 203 (2009).

-
- ¹³ C. Virojanadara, M. Syväjarvi, R. Yakimova, L. I. Johansson, A. A. Zakharov, T. Balasubramanian, *Phys. Rev. B* 78, 245403 (2008).
- ¹⁴ P. Sutter, *Nature Materials*, 8, 171 (2009).
- ¹⁵ G. R. Fonda, *Phys. Rev.* 31, 260 (1928).
- ¹⁶ T. Ohta, N. C. Bartelt, S. Nie, K. Thürmer, G. L. Kellogg, The role of carbon surface diffusion on the growth of epitaxial graphene on SiC, *Phys. Rev. B*, 81, 121411(R) (2010).
- ¹⁷ M. L. Bolen, S. E. Harrison, L. B. Biedermann, M. A. Capano, *Phys. Rev. B* 80, 115433 (2009).
- ¹⁸ The $\sqrt{3}$ structure was observed between the spikes in the STM images, suggesting that spikes are due to adsorbed atoms.
- ¹⁹ D. A. Schmidt, T. Ohta, L. B. Biedermann, T. E. Beechem, S. W. Howell, Strain and its dependence to the growth mode and substrate symmetry in epitaxial graphene, submitted.

Enhancement in Thermoelectric and Photovoltaic Properties by Nanostructure Approach

PI: Z. F. Ren, Boston College, Chestnut Hill, Massachusetts 02467, email: renzh@bc.edu

Program Scope: In this program, my group, in close collaboration with Prof. Gang Chen's group and Prof. Mildred Dresselhaus' group, has theoretically designed a nanostructure approach to mainly reduce the thermal conductivity without too much affecting the power factor so to enhance the thermoelectric dimensionless figure-of-merit (ZT) and experimentally realized it by an economic scalable way: ball milling and hot pressing. We have achieved at least a 40% improvement in ZT first in $\text{Bi}_{0.4}\text{Sb}_{1.6}\text{Te}_3$, and then in a number of other materials covering temperatures up to 1000 °C, proving the suitability of the method to different materials. In addition to thermoelectric materials research, my group, in collaboration with Prof. Michael Naughton and Prof. Kris Kempa, has also theoretically designed a new approach, nano coaxial cable, to separate the path ways of photons and excitons in perpendicular paths in photovoltaic solar cells so that the photon path can be long enough to absorb the solar radiation and the exciton paths can be short enough to avoid recombination, which has been experimentally demonstrated to enhance the solar to electricity conversion efficiency.

Recent Progress:

1. Demonstration of ZT improvement by nanostructuring approach

The ZT in bismuth antimony telluride (BiSbTe) bulk alloys has remained around 1 for more than 50 years. During this past three years, we have successfully shown that a peak ZT of 1.4 at 100°C can be achieved in a p-type nanocrystalline BiSbTe bulk alloy [1]. These nanocrystalline bulk materials were made by hot pressing nanopowders that were ball-milled from crystalline ingots under inert conditions. Electrical transport measurements, coupled with microstructure studies and modeling, show that the ZT improvement is the result of low thermal conductivity caused by the increased phonon scattering by grain boundaries and defects. More importantly, ZT is about 1.2 at room temperature and 0.8 at 250°C, which makes these materials useful for cooling and power generation. Cooling devices that use these materials have produced high-temperature differences of 86°, 106°, and 119°C with hot-side temperatures set at 50°, 100°, and 150°C, respectively. This discovery sets the stage for use of a new nanocomposite approach in developing high-performance low-cost bulk thermoelectric materials.

The microstructures of the nanograined bulk p-type bismuth antimony telluride with a ZT 1.4 are investigated using transmission electron microscopy [2]. It is found that the bulk material contains both nano- and micro-sized grains. Between the nanograins, bismuth-rich interface regions with a 4 nm thickness were detected. In addition, nanoprecipitates as well as other defects are also found to be embedded in the nanograins. The high ZT is attributed to the slight increase in the electrical conductivity, and to the large decrease of the thermal conductivity.

2. Success on using elements to make high performance nanostructured dense bulk materials

By ball milling alloyed bulk crystalline ingots into nanopowders and hot pressing them, we had demonstrated high ZT in nanostructured bulk bismuth antimony telluride [1]. In this study, we used the same ball milling and hot press technique, but start with elemental chunks of bismuth, antimony, and tellurium to avoid the ingot formation step, which is time and energy consuming. We showed that a peak ZT of about 1.3 in the temperature range of 75 and 100°C has been achieved [3]. This process is more economical and environmentally friendlier than

starting from alloyed bulk crystalline ingots. The ZT improvement is caused mostly by the lower thermal conductivity, similar as the case using ingot [1]. Transmission electron microscopy observations of the microstructures suggest that the lower thermal conductivity is mainly due to the increased phonon scattering from the increased grain boundaries of the nanograins, precipitates, nanodots, and defects. Our material also exhibits a ZT of 0.7 at 250°C, similar to the value obtained when ingot was used. This study demonstrates that high ZT values can be achieved in nanostructured bulk materials with ball milling elemental chunks, suggesting that the approach can be applied to other materials that are hard to be made into ingot, in addition to its advantage of lower manufacturing cost.

3. Demonstration of the nanostructuring approach in high temperature materials $\text{Si}_{1-x}\text{Ge}_x$

$\text{Bi}_{0.4}\text{Sb}_{1.6}\text{Te}_3$ is good for applications at close to room temperature, but not useful at all for applications at temperatures higher than 250°C. $\text{Si}_{1-x}\text{Ge}_x$ alloy has a melting point about 1400°C, and is a reasonable thermoelectric material. An improvement in ZT of $\text{Si}_{1-x}\text{Ge}_x$ would be very useful for especially applications at high temperatures. In this study, using the same ball milling and hot pressing method we have achieved a ZT of 0.95 in p-type nanostructured bulk $\text{Si}_{1-x}\text{Ge}_x$ alloys [4], which is about 90% higher than what is currently used in space flight missions, and 50% higher than the reported record in p-type SiGe alloys. The enhancement of ZT is due to a large reduction of thermal conductivity caused by the increased phonon scattering at the grain boundaries of the nanostructures combined with an increased power factor at high temperatures. During the past three years, we also showed that by using the same nanostructure approach, a peak ZT of about 1.3 at 900°C in an *n*-type nanostructured $\text{Si}_{1-x}\text{Ge}_x$ bulk alloy has been achieved [5]. The enhancement of ZT comes again mainly from a significant reduction in the thermal conductivity caused by the enhanced phonon scattering off the increased density of nanograin boundaries. The enhanced ZT will make such materials attractive in many applications such as solar, thermal, and waste heat conversion into electricity.

The mechanism for phonon scattering by nanostructures and by point defects in nanostructured silicon (Si) and the silicon germanium ($\text{Si}_{1-x}\text{Ge}_x$) alloy and their thermoelectric properties are further investigated in details [6]. We found that the thermal conductivity is reduced by a factor of 10 in nanostructured Si in comparison with bulk crystalline Si. However, nanosize interfaces are not as effective as point defects in scattering phonons with wavelengths shorter than 1 nm. We further found that a 5 at % Ge replacing Si is very efficient in scattering phonons shorter than 1 nm, resulting in a further thermal conductivity reduction by a factor of 2, thereby leading to a thermoelectric figure of merit ZT of 0.95 for $\text{Si}_{0.95}\text{Ge}_{0.05}$, similar to that of large grained $\text{Si}_{0.8}\text{Ge}_{0.2}$ bulk alloys.

4. ZT improvement by increasing concentration of Yb in skutterudites $\text{Yb}_x\text{Co}_4\text{Sb}_{12}$

The solubility of Yb in bulk skutterudites $\text{Yb}_x\text{Co}_4\text{Sb}_{12}$ was reported in literature to be 0.19 made by melting and slow cooling method. Surprisingly we increased *x* close to 0.5 by a special sample preparation method: ball milling and hot pressing. We showed that a higher Yb concentration not only increased the power factor due to a higher electron concentration but also reduced the thermal conductivity *k* because of stronger phonon scattering [7]. In this way, we have achieved a ZT of about 1.2 at 550°C in $\text{Yb}_{0.35}\text{Co}_4\text{Sb}_{12}$.

5. Significant enhancement of ZT in p-type half-Heuslers

Half-Heuslers would be important thermoelectric materials due to their high temperature stability and abundance if their ZT could be made high enough. The peak ZT of p-type half-Heusler has been about 0.5 due to the high thermal conductivity. Through nanocomposite approach using ball milling and hot pressing, we have achieved a peak ZT of 0.8 at 700°C [8], which is about 60% higher than that of the state-of-the-art value of 0.5 and might be good enough for being considered in waste heat recovery in the car exhaust system. The improvement comes mainly from a significant increase in Seebeck coefficient and a decrease in thermal conductivity due to nanostructures. The samples were made by first forming alloyed ingots using arc melting and then creating nanopowders by ball milling the ingots and finally obtaining dense bulk by hot pressing. SEM studies show that the thermal conductivity depends closely on the particle size that is determined by ball milling time. Further improvement in ZT is expected when average grain sizes are made smaller than 100 nm.

6. Demonstration of nano coaxial cables for high efficiency solar cells

In this work, we showed that solar cells based on the nanocoax architecture, which is realized by employing arrays of aligned carbon nanotubes, and amorphous silicon as photovoltaic medium [9]. These cells demonstrate an initial efficiency of 6.1%, double that of the corresponding planar controls with the same absorber thickness. The solar absorber can be much thinner than the regular amorphous Si, which may completely eliminate the Staebler-Wronski effect for high efficiency for a long lifetime.

Future Plans: I will focus on ZT improvement by reducing thermal conductivity on thermoelectric materials YbAl_3 and CoSi that showed very high power factors.

References

1. B. Poudel, Q. Hao, Y. Ma, Y. C. Lan, A. Minnich, B. Yu, X. Yan, D. Z. Wang, A. Muto, D. Vashaee, X. Y. Chen, J. M. Liu, M. S. Dresselhaus, G. Chen, and Z. F. Ren, "High-Thermoelectric Performance of Nanostructured Bismuth Antimony Telluride Bulk Alloys", *Science* **320**, 634 – 638 (2008).
2. Y. C. Lan, B. Poudel, Y. Ma, D. Z. Wang, M. S. Dresselhaus, G. Chen, and Z. F. Ren, "Structure Study of Bulk Nanograined Thermoelectric Bismuth Antimony Telluride" *NanoLetters* **9**, 1419 – 1422 (2009).
3. Y. Ma, Q. Hao, B. Poudel, Y. C. Lan, B. Yu, D. Z. Wang, G. Chen, and Z. F. Ren "Enhanced Thermoelectric Figure-of-Merit in p-Type Nanostructured Bismuth Antimony Tellurium Alloys Made from Elemental Chunks", *NanoLetters* **8**, 2580 – 2584 (2008).
4. G. Joshi, H. Lee, Y. C. Lan, X. W. Wang, G. H. Zhu, D. Z. Wang, R. W. Gould, D. C. Cuff, M. Y. Tang, M. S. Dresselhaus, G. Chen, and Z. F. Ren, "Enhanced thermoelectric figure-of-merit in nanostructured p-type silicon germanium bulk alloys" *NanoLetters* **8**, 4670 – 4674 (2008).
5. X. W. Wang, H. Lee, Y. C. Lan, G. H. Zhu, G. Joshi, D. Z. Wang, J. Yang, A. J. Muto, M. Y. Tang, J. Klatsky, S. Song, M. S. Dresselhaus, G. Chen, and Z. F. Ren, "Enhanced thermoelectric figure-of-merit in nanostructured n-type silicon germanium bulk alloy", *Appl. Phys. Lett.* **93**, 193121 (2008).
6. G. H. Zhu, H. Lee, Y. C. Lan, X. W. Wang, G. Joshi, D. Z. Wang, J. Yang, D. Vashaee, H. Guilbert, A. Pillitteri, M. S. Dresselhaus, G. Chen, Z. F. Ren, "Increased Phonon Scattering by Nanograins and Point Defects in Nanostructured Silicon with a Low Concentration of Germanium", *Phys. Rev. Lett.* **102**, 196803 (2009).
7. J. Yang, Q. Hao, H. Wang, Y. C. Lan, Q. Y. He, A. J. Minnich, D. Z. Wang, J. A. Harriman, V. M. Varki, M. S. Dresselhaus, G. Chen, and Z. F. Ren, "Solubility Study of Yb in n-type Skutterudites $\text{Yb}_x\text{Co}_4\text{Sb}_{12}$ and Their Enhanced Thermoelectric Properties", *Phys. Rev. B* **80**, 115329 (2009).
8. X. Yan, G. Joshi, W. S. Liu, Y. C. Lan, X. W. Wang, B. Poudel, J. W. Simonson, J. Poon, H. Wang, D. Z. Wang, G. Chen, and Z. F. Ren, "Enhanced Thermoelectric Figure-of-Merit in p-Type Half-Heuslers", *NanoLetters* (2011, in press).
9. T. Paudel, J. Rybczynski, Y. T. Gao, Y. C. Lan, Y. Peng, K. Kempa, M. J. Naughton Z. F. Ren, "Solar Cells Based on Carbon Nanotube Nanocoaxes", *Phys. Status Solidi*, (2011, in press).

SISGR: Fundamental studies of unconventional sulfide semiconductors for cost-effective and environmentally-benign thin film photovoltaics

DOE award DE-SC0001630, Sept. 15, 2009 – Sept. 14, 2012

Prof. Mike Scarpulla & Dr. Loren Rieth

MSE & ECE Departments, University of Utah, 122 S. Central Campus Drive, Salt Lake City, UT 84112

scarpulla@eng.utah.edu

Program Scope

When discussing scale up of thin film photovoltaic technologies to capacities relevant to primary electrical generation, the price and available reserves of each component element of the thin film material become important. Elements' natural abundance, recoverable reserves, processing costs, and demand from other applications all contribute to the price of thin film solar cells. The leading compound semiconductor materials Cu(In,Ga)Se (CIGS) and CdTe contain heavy elements that are relatively rare and expensive and that present risks to health and environment in their processing (which translate into solar cell costs). It has been estimated that practically-recoverable Te and In reserves could support a thin film PV industry at ~150 GW_p/year production levels [1]. However material shortages and price spikes could significantly hamper the growth of such a large industry. Thus it is important to develop deep scientific understanding of possible alternative materials to enable thin film PV production at the 0.1-1 TW_p/year levels necessary for % levels of the total primary electrical demand.

For most inorganic compound semiconductors with bandgap in the 1-1.5 eV range, photovoltaic device efficiency is limited primarily by the defects in the material rather than bandstructure. Grain boundaries and bulk defects serve as very efficient recombination centers except in special cases. For example, evidence exists that in CIGS potential barriers around grain boundaries repel carriers and that many vacancy and antisite defects form clusters that do not introduce states in mid-gap: both of these effects minimize recombination. This points to the importance of studying fundamental properties and defects in CIGS and CZTS thin films to determine whether they have similar 'self passivating' behavior like CIGS and could thus be capable of similar photovoltaic efficiencies approaching or exceeding 20% once optimized.

The objectives of this project are to investigate 1) the synthesis and 2) fundamental properties of thin films of Cu₂ZnSnS₄ (CZTS) and related materials like Cu₂Si_{1-x}Sn_xS₃ (CSTS) germane to their use as absorber layers in inorganic thin film solar cells. These are both examples of so-called "earth-abundant photovoltaic materials". By using only commodity elements, these materials circumvent some of the inherent material cost, availability, and health and safety concerns present for CIGS and CdTe. This work will synthesize thin films of CZTS and CSTS using cosputtering from targets of Cu₂S, ZnS, SnS₂, and Si, followed by annealing in sulfur atmospheres. This project focuses on producing high-quality samples of these materials and experimentally measuring properties related to electronic defect identity and concentrations. The potential of CZTS and CSTS for similar performance to CdTe and CIGS remains to be determined; the fundamental data generated by this study will lead to understanding, evaluating, and optimizing these materials for use in thin film photovoltaic cells.

Recent Progress: Na Effects on CZTS Grain Growth Kinetics

In CIGSe thin film PV cells, Na from the soda-lime glass substrate is known to diffuse into the CIGSe film and facilitate grain growth (reducing grain boundary photocarrier recombination). Quaternary phase formation from binary phases in the CZTS system has been shown to occur above approximately 550 °C [schorr] – significantly higher than the strain point of soda-lime glass typically used for CIGSe photovoltaic cells. We have thus investigated the grain growth kinetics of CZTS thin films on soda-lime

glass and on borosilicate glass which contains no sodium, but has a higher strain point. On Na-containing glass, resulting grain sizes are approximately 10x larger than those on Na-free glass. The role of Na (as opposed to other spurious effects) was demonstrated by dipping half of a sample in an aqueous solution of Na_2S and then annealing the sample in a sulfur atmosphere at $600\text{ }^\circ\text{C}$ for 2 hrs. As seen in Figure 1 below, this induced the dramatic difference in grain size - some grains reached $\sim 2\text{ }\mu\text{m}$ in lateral dimensions. This result has significant implications for producing CZTS cells on alternate substrates such as plastic or metal foils – it indicates that the Na necessary for grain growth can be introduced from alternative sources and that processing may be carried out by methods which do not significantly heat the substrate.

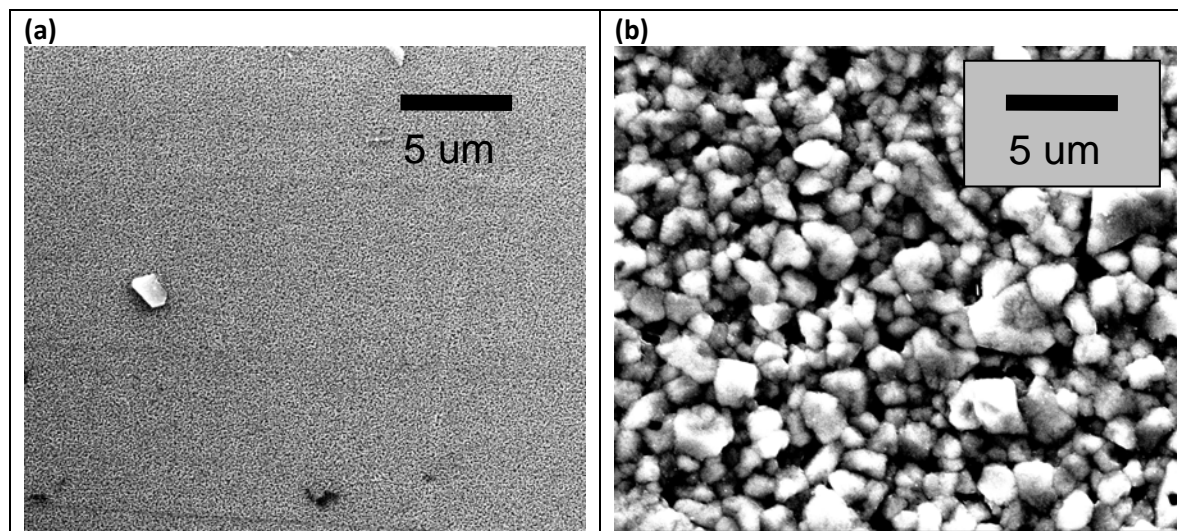


Figure 1 – Scanning electron micrographs of a CZTS thin film produced on Mo-coated borosilicate glass (a) without Na and (b) coated with Na_2S from aqueous solution.

Recent Progress: Theoretical Analysis of Earth-Abundant Semiconductor Heterojunctions

One Holy Grail of chalcopyrite-based thin film PV is to form Cd-free heterojunctions that perform as well as those based on a heterojunction with CdS. We thus considered the possible band alignments of CZTS, CIGSe, CdS, and ZnS in the heavily-disordered crystal limit appropriate for polycrystalline films deposited by non-epitaxial means using the fact that the Fermi stabilization energy is nearly constant relative to the vacuum level.[2] CZTS thin films reported to date have all been heavily p-type indicating that the Fermi stabilization energy is probably within a few hundred meV of the valence band edge while low-crystalline quality ZnS has its Fermi level pinned near mid-gap. Thus, just as for CIGSe, a Type-I band alignment will result for CZTS/ZnS heterojunctions meaning that even if the ZnS is heavily n-type doped a conduction band spike will still exist which will degrade PV performance. The lower conduction band edge of CdS and Fermi stabilization energy close to the conduction band edge (native n-doping) results in a desirable Type-II band alignment for CIGSe/CdS and probably also for CZTS/CdS junctions. This is shown schematically in Fig. 2. Because of the large bandgap of ZnS and mid-gap Fermi stabilization energy, this result is rather robust to uncertainties of a few-hundred meV typical of Fermi level positions in non-ideal situations. The simplicity and robustness of this result has prompted us to attempt to predict the bandstructure of other earth-abundant photovoltaic heterojunctions, a work that is in progress.



Figure 2 - Schematic band line-ups of (a) CZTS/ZnS and (b) CZTS/ZnS heterojunctions.

Recent Progress: CSTS Thin Film Synthesis

We have begun investigating the synthesis of $\text{Cu}_2\text{Si}_{1-x}\text{Sn}_x\text{S}_3$ (CSTS) thin films for photovoltaic solar cell absorber layers. CSTS has not previously been reported in thin film form, and its ability to perform similarly to CIGS and CdTe must still be determined. CSTS formed by solid-state reaction of pressed powders of Cu_2S , Si, Sn, and S is *p*-type and exhibits significant photoconductivity. In addition, compositions with $0.4 < x < 0.6$ result in near-optimal bandgaps from 1.25 to 1.45 eV [3].

Preliminary results indicate that annealing layers of Cu, Sn, and Si in a sulfur atmosphere at 500 °C does not provide adequate mixing or sulfur incorporation. Annealing/sulfurizing a homogeneous co-sputtered film of Cu, Sn, and Si may lead to CSTS phase formation, although low sulfur incorporation and undesired Cu_{2-x}S phase formation were observed. We are currently pursuing annealing in H_2S and co-sputtering from Cu_2S , SnS_2 , and Si in order to promote the formation of the desired CSTS phase.

Recent Progress: Rapid Thermal Processing of CZTS

Because SnS and S will evaporate from CZTS during long annealing steps and because of occasional warping of the glass substrates during high temperature furnace annealing, we have investigated rapid thermal processing (RTP) using a custom-built RTP system. The higher temperatures during RTP have resulted in grain growth up to the $\sim 1 \mu\text{m}$ size, even in the absence of Na – again indicating the possibility of processing CZTS on glass with higher strain points and/or non-glass substrates. It should be mentioned that these films' surface morphology appeared very rough and suggested significant mass loss by evaporation and that stoichiometry was difficult to maintain. We thus designed and built a custom quartz chamber allowing high sulfur and/or SnS overpressures in the 50-100 psi range. This has significantly improved the resultant film stoichiometry and we have very recently made batches of samples having dense surface morphology, excellent stoichiometry, and very high 4-point electrical resistivity. Our preliminary resistivity measurements for samples with no Mo underlayer indicate that some samples may have hole concentrations in the 10^{13} - $10^{17} / \text{cm}^3$ range at room temperature assuming reasonable values for the hole mobility ($10^{-3} - 10 \text{ cm}^2/\text{V}\cdot\text{s}$). The structural, compositional, and optoelectronic properties of these samples are currently being characterized and more complete results should be forthcoming.

Recent Progress: Miscellaneous Characterization Techniques

We have taken delivery of our new deep-level transient spectroscopy (DLTS) system and have begun making good measurements on CIGSe samples in preparation for measurements on the sulfide materials for this project. We are currently working to identify metals and making rectifying Schottky junctions for these characterization techniques. We have begun characterizing our own CZTS samples as well as some deposited by MBE by Dr. Glenn Teeter at NREL using high-resolution Raman spectroscopy and have been able to use this to resolve multiple peaks corresponding possibly to undesired 2nd phases in these samples. This is important for phase identification in the CZTS quaternary system because sub

phases such as ZnS and Cu_2SnS_3 have essentially the same interplanar spacing as CZTS leading to unresolvable x-ray diffraction peaks.

Future Plans:

We will continue to attempt to synthesize thin films of CZTS and CSTS suitable for spectroscopic studies of their electronic defects. We will characterize the new CZTS samples showing high resistivity and discern if they are of sufficient quality for in-depth characterization using electrical, optical, and optoelectronic characterization methods. These basic results will provide the basis for fully understanding these promising earth abundant photovoltaic materials.

References:

- [1] Fthenakis, Ren. Sus. Ener. Rev. **13** 2746 (2009)
- [2] S. Siebentritt and U. Rau, Eds., Wide-Gap Chalcopyrites, (Springer, 2006).
- [3] Lafond et al., Inorg Chem **46** 1502 (2007).

Publications Supported by Physical Behavior of Materials Program:

E.A. Lund, J.L. Johnson, W.M. Hlaing Oo, and M.A. Scarpulla
Investigating Sputtered $\text{Cu}_2\text{Si}_{1-x}\text{Sn}_x\text{S}_3$ (CSTS) For Earth Abundant Thin Film Photovoltaics
Conference record of the 35th IEEE Photovoltaic Specialists Conference, article 5616634, pp. 1948-1950 (2010)

H. Nukala, J.L. Johnson, A. Bhatia, E.A. Lund, W.M. Hlaing Oo, M.M. Nowell, L.W. Rieth, and M.A. Scarpulla
Synthesis of optimized CZTS thin films for photovoltaic absorber layers by sputtering from sulfide targets and sulfurization
Mat. Res. Soc. Symp. Proc. **1268** EE3.4 (2010)

J.L. Johnson, H. Nukala, E.A. Lund, W.M. Hlaing Oo, A. Bhatia, L.W. Rieth, M.A. Scarpulla
Effects of 2nd phases, stress, and Na at the Mo/ $\text{Cu}_2\text{ZnSnS}_4$ interface
Mat. Res. Soc. Symp. Proc. **1268** EE3.3 (2010)

Nanostructured Thermoelectric Materials

Rachel A. Segalman^{1,2}, Peidong Yang^{1,2}, Ramesh Rammamorthy^{1,2}, Joel More^{1,2}, Jeffrey J. Urban², Renkun Chen³
Students/Post Docs: Shannon K. Yee^{1,2}, Nelson Coates^{1,2}, Jayakanth Ravichandran^{1,2}, Hung-Ta Wang^{1,2}, Pouyan Ghaemi^{1,2}, Kedar Hippalgaonkar^{1,2}

¹University of California Berkeley, ²Lawrence Berkeley National Laboratory, ³University of California San Diego

201D Gilman, Berkeley, CA 94720-1462

segalman@berkeley.edu

Program Scope and Definition:

Thermoelectric energy conversion or refrigeration is attractive due to the very high reliability, long cycle life, and lack of moving parts. In spite of these advantages, many thermoelectrics are daunted by low efficiency, high cost, and lack of scalability. In response, this program is scoped to investigate how nanostructuring can improve thermoelectric performance for materials that have the potential to be scalable, low cost, and sufficiently efficient. The efficiency of such devices is quantified by a dimensionless figure of merit, $ZT = S^2\sigma T/\kappa$, where S is the thermopower or Seebeck coefficient, and σ and κ are the electrical and thermal conductivities of the material. Increasing ZT has historically been extremely difficult due to the coupling between these thermoelectric parameters. Our approach to this problem is to identify paradigms at which these parameters can become decoupled by unique transport phenomenon at the nanoscale. To that end, a suite of projects are being conducted around this concept which is summarized herein.

Program Recent Progress and Future Plans:

Molecular Thermoelectrics:

Electronic transport in molecular junctions has been studied through measurements of junction thermopower to evaluate the feasibility of thermoelectric (TE) energy generation using organic-inorganic hybrid materials. Energy transport and conversion in these junctions are heavily influenced by transport interactions at the metal-molecule interface. At this interface the discrete molecular orbitals overlap with continuum of electronic states in the inorganic electrodes to create unique energy landscapes that cannot be realized in the organic or inorganic components alone. Over the past decade, scanning probe microscopes have been used to study the electronic conductance of single-molecule junctions². Recently, we conducted measurements of junction thermopower using a modified scanning tunneling microscope (STM)³. Through our investigations, we have determined: (i) how the addition of molecular substituent groups can be used to predictably tune the TE properties of phenylenedithiol (PDT) junctions⁴, (ii) how the length, molecular backbone, and end groups affect junction thermopower⁵, and (iii) where electronic transport variations originate⁶. Furthermore, we have recently found that large TE enhancement can be achieved by effectively altering a (noble) metal junction using fullerenes (i.e., C₆₀, PCBM, and C₇₀). We associate the enhancement with the alignment of the frontier orbitals of the fullerene to the chemical potential of the inorganic electrodes. We further found that the thermopower can be predictably tuned by varying the work function of the contacts. This yields considerable promise for altering the surface states at interfaces for enhanced electronic and thermal transport.

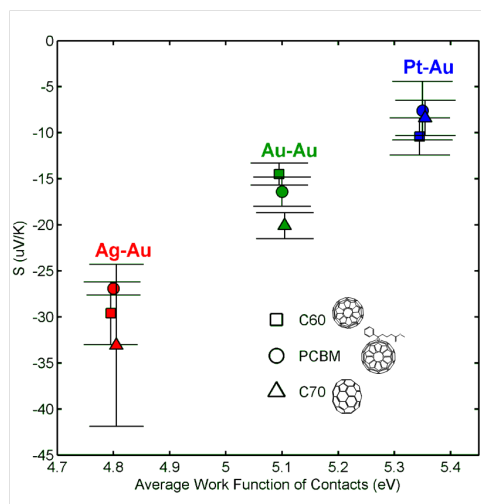


Figure 1: Fullerene thermopower vs. average work function of contacts. A slight offset in work functions has been used for clarity amongst the different fullerene molecules.

Organic-Inorganic Hybrid Thermoelectrics:

Historically, these nanostructured materials required energy-intensive, high-temperature processing methods. Within the scope of this project we demonstrated that high-performance thermoelectric materials can be realized in solution-processable polymer-inorganic hybrid materials⁷. These hybrid materials combine a high electrical conductivity polymer with a high thermopower inorganic nanoparticle. Additionally, attention was paid to the work function alignment in order to open possibilities of energy-dependent scattering. This results in a hybrid organic-inorganic material yielding a higher power factor than either the nanoparticle thin film or polymer thin film, while maintaining polymer-like thermal transport. The measured $ZT \sim 0.1$ is the largest reported value for an aqueous processed material, and the largest reported in an organic or organic/inorganic hybrid to date. It is also found that the electrical conductivity behaves in a non-monotonic fashion while the thermopower trends monotonically with composition. As a result, simple effective medium models inadequately describe this novel system, indicating unique opportunities to optimize the thermoelectric properties.

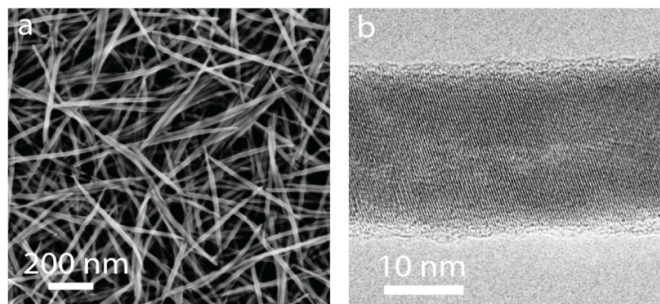


Figure 2: (a) SEM of tellurium nanowire-polymer film (b) TEM of tellurium nanowire demonstrating crystallinity.

Oxide Thermoelectrics:

Oxides are an interesting class of materials which can be broadly classified as uncorrelated and correlated. Recent work on correlated sodium cobaltate has shown improved thermopowers ($\sim 100 \mu\text{V/K}$) and metallic electrical conductivity ($0.2 \text{ m}\Omega\text{cm}$)⁸. This has kindled interest in correlation as a route to obtain higher figure of merit. Amongst the correlated systems, layered $\text{Bi}_2\text{Sr}_2\text{Co}_2\text{O}_y$, shows properties similar to the parent compound, sodium cobaltate but with much lower thermal conductivity. In these compounds, the electronic transport is dominated by the CoO_2 planes and the Bi-O and Sr-O act as insulating barrier layers for both thermal and electronic transport. Our investigation centers on the origin of this apparent decoupling of thermopower and conductivity and the role of dopants (particularly on the Bi and Co sites) in controlling correlation and band structure and hence thermopower and electrical conductivity independently.

Nanostructured Holey-Silicon:

The main goal of this project is to investigate the thermoelectric transport phenomena in holey silicon⁹ and to demonstrate its ability for solid-state thermoelectric power generation/cooling application. Earlier works¹⁰⁻¹² have demonstrated that by either using nanowires with diameters much

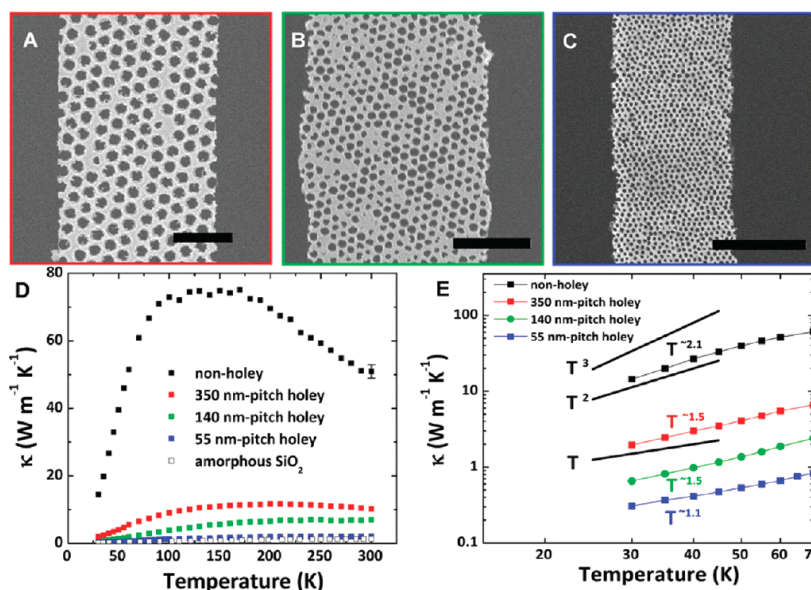


Figure 3: Thermal conductivity of HS ribbons with different pitch. SEM images of (A) 350 nm pitch, (B) 140 nm pitch, and (C) 55 nm pitch HS ribbon for thermal measurement. All scale bars are 1 μm . (D) Temperature dependent κ of nonholey (black squares), 350 nm (red squares), 140 nm (green squares), 55 nm pitch (blue squares) HS ribbon, and amorphous silica (empty squares from ref 19). Error bars for all three holey ribbons are smaller than the data points. (E) Low-temperature data on a logarithmic scale with T^3 , T^2 , and T^1 curves for comparison guidelines.

smaller than the bulk phonon mean free path (MFP) or roughening the nanowire surface, a near 100-fold suppression in silicon's lattice thermal conductivity is observed, resulting in a ZT that is dramatically enhanced from 0.01 for the bulk to 0.4-0.6. The thermal transport properties of silicon nanowires not only highly depend on its diameter/size, but also on their nanoscopic surface morphology. To overcome these problems inherent to nanowire system, we explore the enhanced thermoelectric performance of a new type of nanostructure, holey silicon (HS). We intend to examine HS's thermal conductivities of different pitches and porosity to help to understand the thermal transport mechanism. We have fabricated HS ribbons using nanosphere lithography (NSL) and block-copolymer lithography (BCPL), yielding holey arrays with pitches of 350, 140, or 55 nm. By reducing the pitch of the hexagonal holey pattern down to 55 nm with 35% porosity, the thermal conductivity of HS is consistently reduced by 2 orders of magnitude and approaches the amorphous limit. With a ZT value of ~ 0.4 at room temperature, the thermoelectric performance of HS is comparable with the best value recorded in a silicon nanowire system. In addition, the thermoelectric properties of these holey silicon nanostructures have no dependence on ribbons width, making them even more amenable for thermoelectric module integration. Higher ZT values than the one reported here can be obtained by further optimization of the doping level, the pitch/neck ratio, and effective surface passivation. Because of the scalability of this process, an immediate application for these holey silicon nanostructures could be on-chip thermal management for solid-state devices, while large scale waste heat recovery is also conceivable by extension to bulk holey system.

Topological Insulator Thermoelectrics:

The discovery of topological insulators (TIs), which are bulk insulators or semiconductors with protected metallic surface states as a consequence of spin-orbit coupling, initiated many investigations of their possible applications (e.g. spintronics). Thermoelectricity is already an application of TIs¹, as the TIs Bi_2Te_3 and Bi_2Se_3 are already quite important although applications to date have not exploited the TI behavior. Material similarities between TIs and thermoelectrics exist. Topological insulators require heavy elements in order to generate large spin-orbit coupling and small bandgap in order that the spin-orbit coupling can modify the electronic structure by "inverting" a single band, while thermoelectrics typically consist of heavy elements in order to obtain low phonon thermal conductivity and have a small bandgap in order to obtain a large electronic power factor. This concurrence

motivated us to see if we can use the unique surface states of topological insulators to enhance their thermoelectric performance. The metallic surface states hybridize when a nanometer thick film of them is made thus opening a bandgap. The size of the gap can be controlled by the film thickness. This structure of the surface states indeed leads to large thermoelectric figure of merit at temperatures below 150 K. When we consider the surface states in parallel with the bulk, the film still has enhanced thermoelectric performance, larger than the best-known low temperature thermoelectric for a large range of temperature as indicated in Fig. 4. Our current theoretical effort continues to include thermoelectric transport in connection with the experimental efforts¹³. A future direction is motivated by the experimental observation that Kondo insulators (e.g. FeSb_2), have large thermoelectric figure of merit at low temperatures. Kondo systems have been under theoretical investigation for many years as examples of strongly correlated compounds for which a band structure picture fails. Our plan is to use the techniques developed in strong correlation theory to find ways to enhance their thermoelectric performance. One specific direction is to

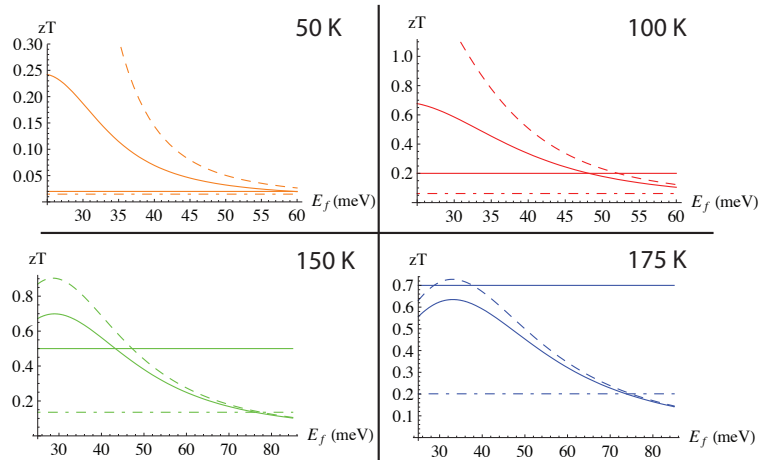


Figure 4: Figure of merit for the thin film including bulk contributions (phonon and electron) at 50, 100, 150, and 175 K. The straight line in each figure corresponds to the best-known figure of merit at the same temperature. Dashed line indicates the figure of merit for the surface states alone and Dashed-Dotted line indicates figure of merit for bulk Bi_2Te_3 .

study the effect of crystal field, which can be controlled in these compounds (e.g. by pressure), on the thermoelectric properties of Kondo insulators.

Silicon Nanowires:

The objective of this project is to investigate thermal transport in ultrathin silicon nanowires with random rough edges and bulk disorder to expand fundamental understanding of phonon propagation in high quality single crystalline systems. In 1958, Philip Anderson predicted localization of extended electron wavefunctions in disordered crystals resulting in exponentially decaying tails. This ubiquitous wave physics has since been demonstrated experimentally for light waves, microwaves, sound waves, electron gases, and matter waves. Phonons, although defined as quantized lattice waves in a solid, have always been pictured as particles moving diffusively in a solid. However, at low temperatures ($\sim 1-100\text{K}$) and in the presence of disorder, coherent effects can be observed. One example is interference between multiple scattering paths resulting in localization, although direct observation of such spatial confinement has never been demonstrated, partly because phonons are broadband and interactions in solids are strong. Given this, we predict an exponential reduction in the thermal conductivity as a function of length, which would be the first such demonstration of localized phonons. To observe this, we intend to manufacture silicon nanowires that are 2-100 μm in length, 10-20 nm in width, and 10-20 nm in thickness, patterned with high resolution E-Beam Lithography (EBL). In previous work¹¹, we have demonstrated that rough silicon nanowires synthesized by the aqueous electroless etching method have much lower thermal conductivity ($\sim 1.6\text{ W/m-K}$ for a 50 nm diameter at 300K) compared to that of smooth silicon nanowires grown by vapor-liquid-solid method. This is approaching thermal conductivity shown by amorphous silicon ($\sim 1\text{ W/m-K}$) and is due to the enhanced phonon scattering at rough nanowire surfaces. We hypothesize that the exact mechanism of this phonon scattering could be due to Anderson Localization of lattice vibrational waves as described above and our recent work¹⁴ has begun to explain this unique behavior.

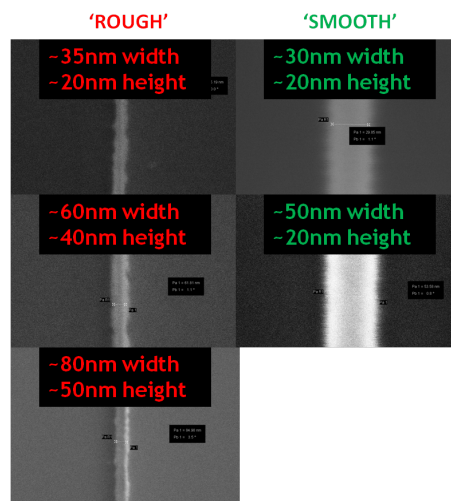


Figure 5: SEM images demonstrating the control of roughness for several wires using the EBL technique.

References: (Recent BES supported publications italicized)

1. *Ghaemi, P., Mong, R. S. K. & Moore, J. E. In-Plane Transport and Enhanced Thermoelectric Performance in Thin Films of the Topological Insulators Bi_2Te_3 and Bi_2Se_3 . Physical Review Letters 105, 166603.*
2. *Malen, J. A., Yee, S. K., Majumdar, A. & Segalman, R. A. Fundamentals of energy transport, energy conversion, and thermal properties in organic-inorganic heterojunctions. Chemical Physics Letters 491, 109-122 (2010).*
3. *Reddy, P., Jang, S. Y., Segalman, R. A. & Majumdar, A. Thermoelectricity in molecular junctions. Science 315, 1568-1571 (2007).*
4. *Baheti, K. et al. Probing the chemistry of molecular heterojunctions using thermoelectricity. Nano Letters 8, 715-719 (2008).*
5. *Malen, J. A. et al. Identifying the Length Dependence of Orbital Alignment and Contact Coupling in Molecular Heterojunctions. Nano Letters 9, 1164-1169 (2009).*
6. *Malen, J. A. et al. The Nature of Transport Variations in Molecular Heterojunction Electronics. Nano Letters 9, 3406-3412 (2009).*
7. *See, K. C. et al. Water-Processable Polymer-Nanocrystal Hybrids for Thermoelectrics. Nano Letters 10, 4664-4667.*
8. *Terasaki, I. Novel physics and functions in the layered cobalt oxides from thermoelectricity to ferromagnetism. Physica B: Condensed Matter 383, 107-110 (2006).*
9. *Tang, J. Y. et al. Holey Silicon as an Efficient Thermoelectric Material. Nano Letters 10, 4279-4283 (2010).*
10. *Chen, R. et al. Thermal conductance of thin silicon nanowires. Phys. Rev. Lett. 101, 105501/1-105501/4 (2008).*
11. *Hochbaum, A. I. et al. Enhanced thermoelectric performance of rough silicon nanowires. Nature 451, 163-167 (2008).*
12. *Murphy, P. G. & Moore, J. E. Coherent phonon scattering effects on thermal transport in thin semiconductor nanowires. Physical Review B 76 (2007).*
13. *Bardarson, J. H., Brouwer, P. W. & Moore, J. E. Aharonov-Bohm Oscillations in Disordered Topological Insulator Nanowires. Physical Review Letters 105, 156803.*
14. *Hippalgaonkar, K. et al. Fabrication of Microdevices with Integrated Nanowires for Investigating Low-Dimensional Phonon Transport. Nano Letters 10, 4341-4348 (2010).*

Study of Materials and Interface Properties for High-Efficiency Spin Injection

Jing Shi

Department of Physics and Astronomy, University of California, Riverside

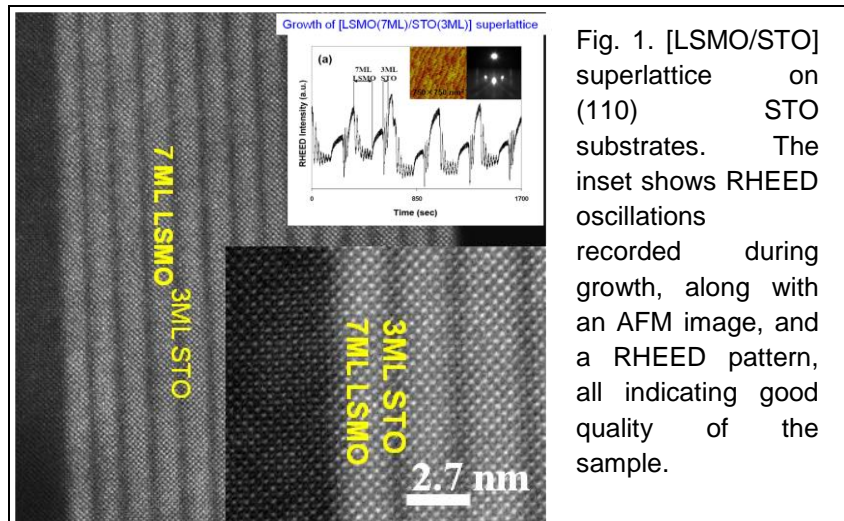
Jing.Shi@ucr.edu.

1. Program Scope: Investigating physical properties of materials and devices that are relevant to spintronics. The materials for more efficient spin injection include high spin polarization ferromagnetic films as injectors such as $\text{La}_{1-x}\text{Sr}_x\text{MnO}_3$ or LSMO and other transition metal oxide films, and low spin-orbit coupling materials as spin transport media such as graphene and other carbon-based materials.

2. Recent Progress

- Epitaxial growth and physical property study of $\text{La}_{1-x}\text{Sr}_x\text{MnO}_3$, LaCoO_3 and Fe_3O_4 films and $[\text{LSMO}/\text{STO}]_N$ superlattices.

We have systematically studied the magnetic and electrical transport properties of these films



grown by laser molecular beam epitaxy. In manganite films, we investigated relevant physical properties in films with different dopings, film thicknesses as well as orientations. In particular, we found that the magnetic moment, Curie temperature and electrical conductivity of (110)-oriented LSMO films are better than those of the films grown in other orientations. We have developed all-oxide magnetic tunnel junction spin valves. We have also demonstrated epitaxial growth and magnetism of LaCoO_3 and Fe_3O_4 films.

- Single crystal growth and systematic tuning of the chemical potential in Bi_2Se_3 and Bi_2Te_3 to achieve the topological insulator state. Topological insulators are potentially useful for spintronics applications due to the strong spin-orbit

interaction which may enable the electric field control of the spins in the materials.

We aim to demonstrate the chemical potential tuning in both bulk and small devices by controlling the doping level and the gate voltage, respectively. In Bi_2Se_3 bulk crystals, the excess n-type carriers due to Se self-doping are removed by introducing Ca impurities. From the infrared measurements, we identified the optimal doping level (Fig. 2). In the meantime, we obtained the band gap as well as the effective mass of electrons and holes (ref. 7). In nanoscale devices, we have demonstrated

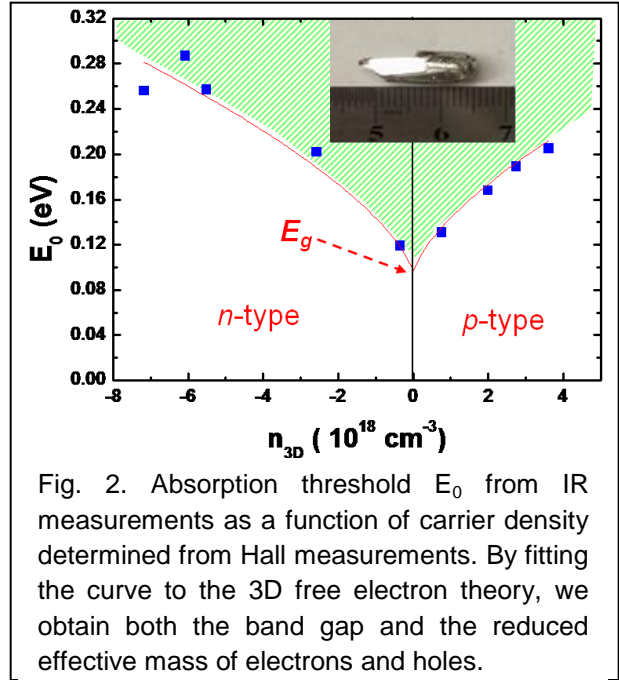


Fig. 2. Absorption threshold E_0 from IR measurements as a function of carrier density determined from Hall measurements. By fitting the curve to the 3D free electron theory, we obtain both the band gap and the reduced effective mass of electrons and holes.

the gate tuning of the chemical potential in devices with different carrier densities, as indicated by the sheet resistance of the device as a function of the gate voltage in Fig. 3. As the resistance increases, the chemical potential moves away from the top valence band edge of the p-type device. In the meantime, the

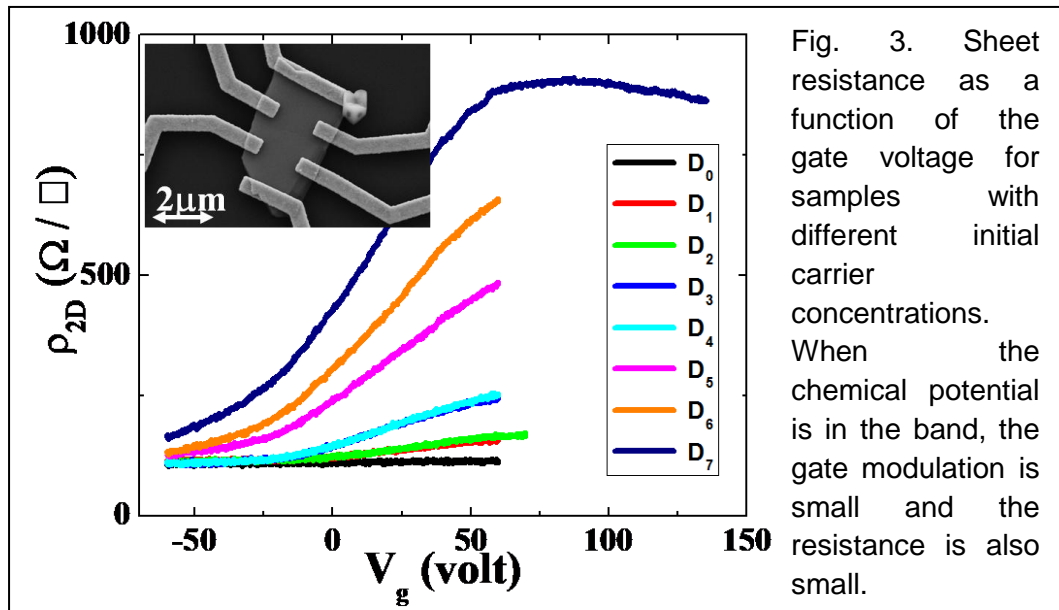
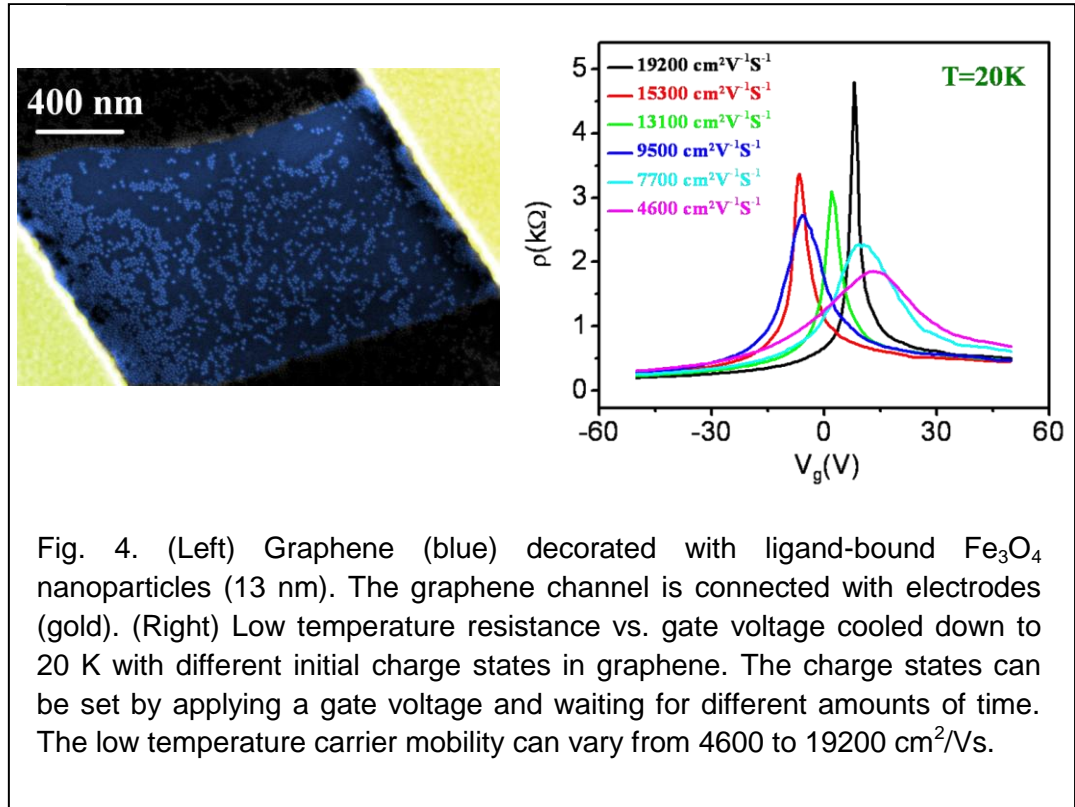


Fig. 3. Sheet resistance as a function of the gate voltage for samples with different initial carrier concentrations. When the chemical potential is in the band, the gate modulation is small and the resistance is also small.

carrier mobility increases significantly. This may be the first transport evidence of the metallic topological surface states in nanoscale devices.

- Large mobility enhancement and tunability of graphene by controlling its charge environment. Graphene is an excellent spin transport medium due to its long



spin diffusion length. It is very useful to improve the carrier mobility of graphene since the spin diffusion length will be longer. In our recent work, we have shown that the carrier mobility of graphene can be enhanced by more than a factor of 4 by modifying the charged impurity scattering (Fig. 4). We have also shown some interesting memory effect due to the stored charges that have been taken away from graphene. The polarity of the stored charges can be reversibly changed by applying different gate voltages (ref.8).

3. Future Plans: We will focus on the last two projects in the future. For the topological insulator project, we aim to demonstrate the quantized magneto-electric effect of the devices in which the chemical potential can be tuned. Then we will study the interface properties of $\text{Fe}_3\text{O}_4/\text{Bi}_2\text{Se}_3$. The next goal is to demonstrate spin injection from Fe_3O_4 into the metallic surface states of Bi_2Se_3 . In the graphene project, we will study the effect of the enhanced mobility on the spin diffusion length in non-local spin valve geometry.

4. References:

- (1). J. W. Freeland, J.X. Ma, and Jing Shi, Ferromagnetic Spin-Correlations in Strained LaCoO₃ Thin Films, Appl. Phys. Lett. **93**, 212501 (2008).
- (2). Y. Pu, D. Chiba, F. Matsukura, H. Ohno, and Jing Shi, Mott Relation for Anomalous Hall and Nernst Effects in Ga_{1-x}Mn_xAs Ferromagnetic Semiconductors, Phys. Rev. Lett. **101**, 117208 (2008).
- (3). D. Wu, P. Wei, E. Johnston-Halperin, D.D. Awschalom, and Jing Shi, High-Field Magnetocrystalline Anisotropic Resistance Effect in (Ga,Mn)As, Phys. Rev. B **77**, 125320 (2008).
- (4). J.X. Ma, X.F. Liu, T. Lin, G.Y. Gao, J.P. Zhang, W.B. Wu, X.G. Li, and Jing Shi, Interface Ferromagnetism in (110)-Oriented La_{0.7}Sr_{0.3}MnO₃/SrTiO₃ Ultrathin Superlattices, Phys. Rev. B. **79**, 174424 (2009).
- (5). P. Wei, W.Z. Bao, Y. Pu, C.N. Lau, and Jing Shi, Anomalous Thermoelectric Transport of Dirac Particles in Graphene, Phys. Rev. Lett. **102**, 166808 (2009).
- (6). A.D. LaForge, A. Frenzel, B.C. Pursley, T. Lin, X.F. Liu, J. Shi, and D.N. Basov, Optical Characterization of Bi₂Se₃ in Magnetic Field: Infrared Evidence for Magnetoelectric Coupling in a Topological insulator Material, Phys. Rev. B **81**, 125120 (2010).
- (7). Z.Y. Wang, P. Wei, T. Lin, X.F. Liu, R. Dumas, K. Liu, and Jing Shi, Tuning Carrier Type and Density in Bi₂Se₃ by Ca-Doping, Appl. Phys. Lett. **97**, 042112 (2010).
- (8). D.Q. Wang, X.F. Liu, L. He, Y.D. Yin, Di Wu and Jing Shi, Manipulating Graphene Mobility and Charge Neutral Point with Ligand-Bound Nanoparticles as Charge Reservoir, Nano Letters **10**, 4989 (2010).

Program Title: Energy Transport in Graphene
 Principal Investigator: Li Shi
 Institution: The University of Texas at Austin
 Address: 1 University Station, Austin, TX 78712
 Email: lishi@mail.utexas.edu
 DOE Grant Number: DE-FG02-07ER46377
 Collaboration: Prof. S. B. Cronin, University of Southern California

Program Scope or Definition

This research program aims to develop a better understanding of phonon transport and coupled electron-phonon transport in graphene. The objectives of the research include:

- (i) Clarify whether the flexural vibration modes make an important or negligible contribution to thermal conductivity of graphene;
- (ii) Investigate the effects of inter-layer coupling, substrate interaction, stress and morphology on phonon transport in suspended and supported single- and few-layer graphene;
- (iii) Characterize the interfacial thermal transport between supported graphene and underlying dielectric, metallic, and polymeric substrates;
- (iv) Evaluate interfacial thermal transport between graphene and its surrounding gas environment;
- (v) Determine whether or not coupled electron-phonon transport in graphene is highly non-equilibrium as in carbon nanotubes; and
- (vi) Reveal the effects of inter-layer coupling, substrate interaction, stress, morphology, and gas environment on electron-phonon coupling in graphene.

Recent Progress

- (i) *Raman Measurements of Thermal Transport in Suspended and Supported Graphene Grown by Chemical Vapor Deposition*

We have developed a micro-Raman spectroscopy method to measure the thermal conductivity and thermal interface resistance of a graphene monolayer grown by chemical vapor deposition (CVD) and suspended over holes with different diameters. The Raman laser beam was focused either at the center of the suspended graphene monolayer or on the graphene region supported on the Au/SiN_x membrane. The optical absorption (Q) by the graphene was obtained by measuring the laser powers incident on and transmitted through the suspended graphene. The Raman G peak and 2D peak positions of graphene down shift with increasing temperature, and were used to determine the temperature rise (ΔT_m) of the optically heated graphene. The ΔT_m versus Q relation measured at the center of the suspended graphene in vacuum was analyzed by solving the heat diffusion equation with a Gaussian heat source term in the radial coordinate. This analysis yielded the thermal conductivity of the suspended graphene. As shown in Fig. 1, the measured thermal conductivity values of the suspended graphene in vacuum range from $(2.6 \pm 0.9) \times 10^3$ to $(3.1 \pm 1.0) \times 10^3$ Wm⁻¹ K⁻¹ near 350 K, which is higher than the reported basal plane thermal conductivity of pyrolytic graphite (PG), and is between the two values reported for mechanically exfoliated monolayer graphene samples.

In addition, a similar measurement of the suspended graphene in different gas environments was analyzed by incorporating a graphene-gas heat transfer term in the heat

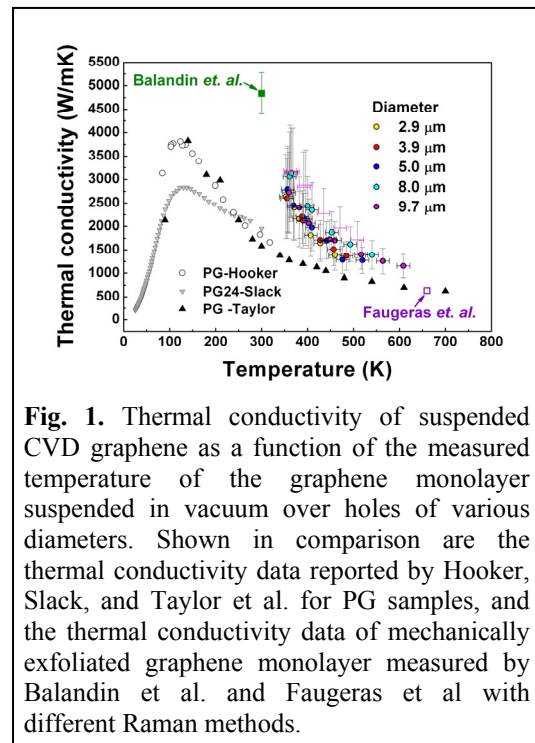


Fig. 1. Thermal conductivity of suspended CVD graphene as a function of the measured temperature of the graphene monolayer suspended in vacuum over holes of various diameters. Shown in comparison are the thermal conductivity data reported by Hooker, Slack, and Taylor et al. for PG samples, and the thermal conductivity data of mechanically exfoliated graphene monolayer measured by Balandin et al. and Faugeras et al with different Raman methods.

diffusion equation. This analysis yielded a heat transfer coefficient of $(2.9 + 5.1/-2.9) \times 10^4 \text{ W m}^{-2} \text{ K}^{-1}$ or $(1.5 + 4.2/-1.5) \times 10^4 \text{ W m}^{-2} \text{ K}^{-1}$ between the graphene monolayer and air or CO_2 , at $\Delta T_m \approx 140 \text{ K}$.

Moreover, with the Raman laser beam focused on the supported region of the graphene monolayer, two sets of ΔT_m versus Q data were measured with two different Gaussian beam radii. The two sets of data were used to obtain both the thermal conductivity (κ_s) of the supported graphene and the interface thermal conductance (g) between the graphene and the Au/SiN_x support, because direct optical heating of the Au/SiN_x support without the graphene monolayer results in negligible heating of the support. The procedure yielded κ_s of $(370 + 650/-320) \text{ W m}^{-1} \text{ K}^{-1}$ and g of $(28 + 16/-9.2) \times 10^6 \text{ W m}^{-2} \text{ K}^{-1}$.

(ii) Two-Dimensional Phonon Transport in Supported Graphene

Graphene is often supported on a substrate for device applications. While Raman measurement results have suggested that the thermal conductivity of suspended single-layer graphene (SLG) exceeds that of graphite, the effect of substrate interaction on thermal transport has not been elucidated. In this work, we have fabricated a resistance thermometer device (Fig. 2(a)) for thermal conductivity measurements of single-layer graphene (SLG) supported on amorphous SiO₂. The measured thermal conductivity results are similar for three SLG samples (G1, G2, and G3), as shown in Fig. 2(b). For G2, the room-temperature κ of $(579 \pm 34) \text{ W m}^{-1} \text{ K}^{-1}$ is about 3.4 times lower than the highest reported basal-plane value of PG, and 5 times lower than the theoretical value of flat suspended SLG obtained by the Broido group based on a numerical solution of the phonon Boltzmann Transport Equation (BTE). The BTE result suggests that the out-of-plane flexural or ZA phonons dominate the total calculated κ of the suspended graphene at 300 K and below. This finding contradicts another theoretical calculation based on the relaxation time approximation (RTA), which assumes that the ZA contribution is negligible. With the incorporation of a substrate scattering model and consideration of stronger interface force constant for the ZA modes than for the in-plane (LA and TA) modes, i.e. $K_{ZA} > K_{LATA}$, the BTE model can explain the measured thermal conductivity of the supported SLG. Despite phonon-substrate scattering, our experiment results clearly show that the thermal conductivity of graphene exfoliated on SiO₂ is still considerably higher than values for common thin film materials.

(iii) Influence of Polymer Residue on the Thermal Conductivity of Suspended Bi-Layer Graphene

For reported Raman measurements of thermal conductivity of suspended graphene, the temperature rise in the graphene sample needs to be larger than 50 K in order to achieve a sufficient signal to noise ratio with the Raman thermometry method. Consequently, accurate temperature dependence of the thermal conductivity has not been obtained, especially in the low temperature range that is useful for understanding the fundamental physics behind the observed thermal conductivity. In this work, we have developed a method to assemble suspended bi-layer graphene (BLG) samples on sensitive suspended resistance thermometer devices (Fig. 3a) for thermal conductivity measurements. The measured thermal conductivity (Fig. 3e) of the suspended bi-layer graphene is slightly higher than the

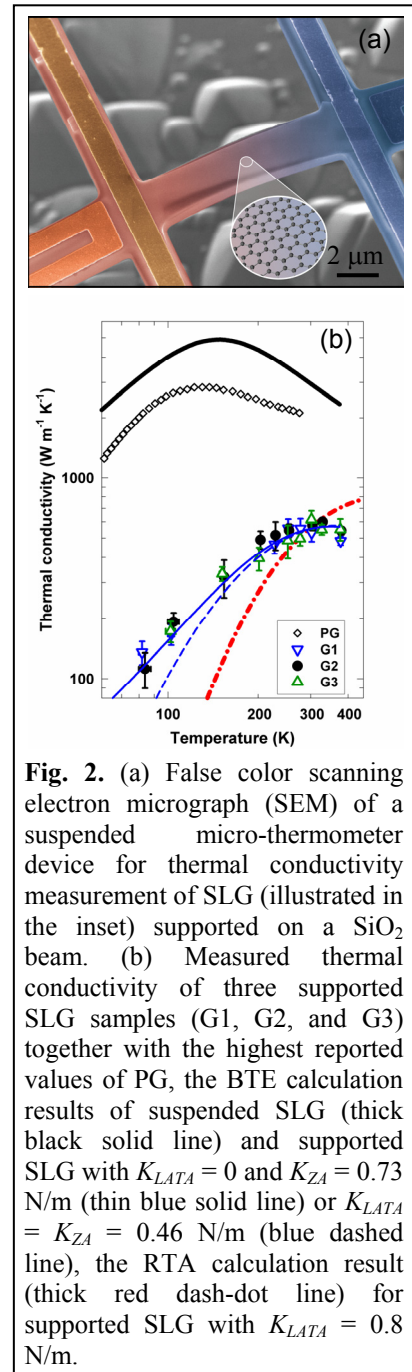


Fig. 2. (a) False color scanning electron micrograph (SEM) of a suspended micro-thermometer device for thermal conductivity measurement of SLG (illustrated in the inset) supported on a SiO₂ beam. (b) Measured thermal conductivity of three supported SLG samples (G1, G2, and G3) together with the highest reported values of PG, the BTE calculation results of suspended SLG (thick black solid line) and supported SLG with $K_{LATA} = 0$ and $K_{ZA} = 0.73 \text{ N/m}$ (thin blue solid line) or $K_{LATA} = K_{ZA} = 0.46 \text{ N/m}$ (blue dashed line), the RTA calculation result (thick red dash-dot line) for supported SLG with $K_{LATA} = 0.8 \text{ N/m}$.

values that we measured for SLG supported on SiO₂, and considerably lower than the Raman measurement results and theoretical predictions for clean, flat, suspended graphene of similar dimensions. A $T^{1.5}$ dependence can be observed in the thermal conductivity measured at temperatures below 125 K. Although a dominant ZA contribution and dominant phonon-edge scattering can lead to the $T^{1.5}$ dependence, the thermal conductivity calculated for that case is much higher than the measurement result. Hence, instead of this mechanism, we attribute our result to phonon-scattering by a residual polymeric layer that can be clearly observed by transmission electron microscopy (TEM) on the suspended graphene (Fig. 3c). This finding is useful for the design of graphene-polymer nanocomposites for thermal management, and points to the need of obtaining ultra-clean suspended graphene samples for fundamental studies of the intrinsic thermal properties of two-dimensional graphene.

(iv) Low-Frequency Acoustic Phonon Temperature Distribution in Electrically Biased Graphene

With the use of a combined contact mode and lift mode operation of a scanning thermal microscopy (SThM) probe tip, we were able to measure the low-frequency acoustic phonon temperature profiles in electrically biased graphene devices with a spatial resolution of about 100 nm (Fig. 4). The obtained temperature maps reveal bias-dependent hot spots in the operating graphene devices that were considerably smaller than those measured in reported infrared (IR) mapping experiments. In addition, the high temperature sensitivity of the SThM technique allows us to examine the thermal behavior of the graphene in the low-power density regime that was not accessible by the optical techniques due to limited temperature sensitivity. The measured acoustic phonon temperature was found to be close to the anharmonic scattering temperature determined from the Raman 2D-peak shift on the same sample.

Future Plans

In the next 12 months, our effort will be focused on thermal conductivity measurement of clean, suspended SLG with the use of sensitive suspended resistance thermometer devices in the temperature range between 4 and 400 K. The low temperature data can potentially allow us to verify whether the flexural phonons make the dominant contribution to thermal conductivity in the samples. In addition, we plan to carry out a combined SThM and Raman mapping experiment to examine whether ultra-high mobility graphene electronic devices supported on hexagon boron nitride may exhibit non-equilibrium phonon population.

References to publications of DOE sponsored research that have appeared in 2008-2010 or that have been accepted for publication

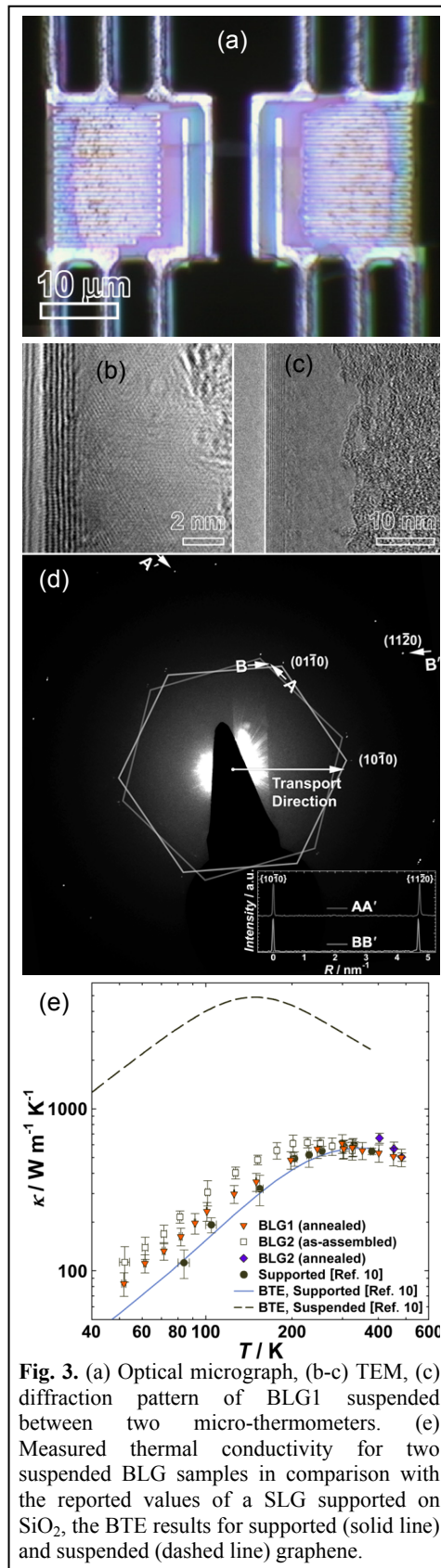
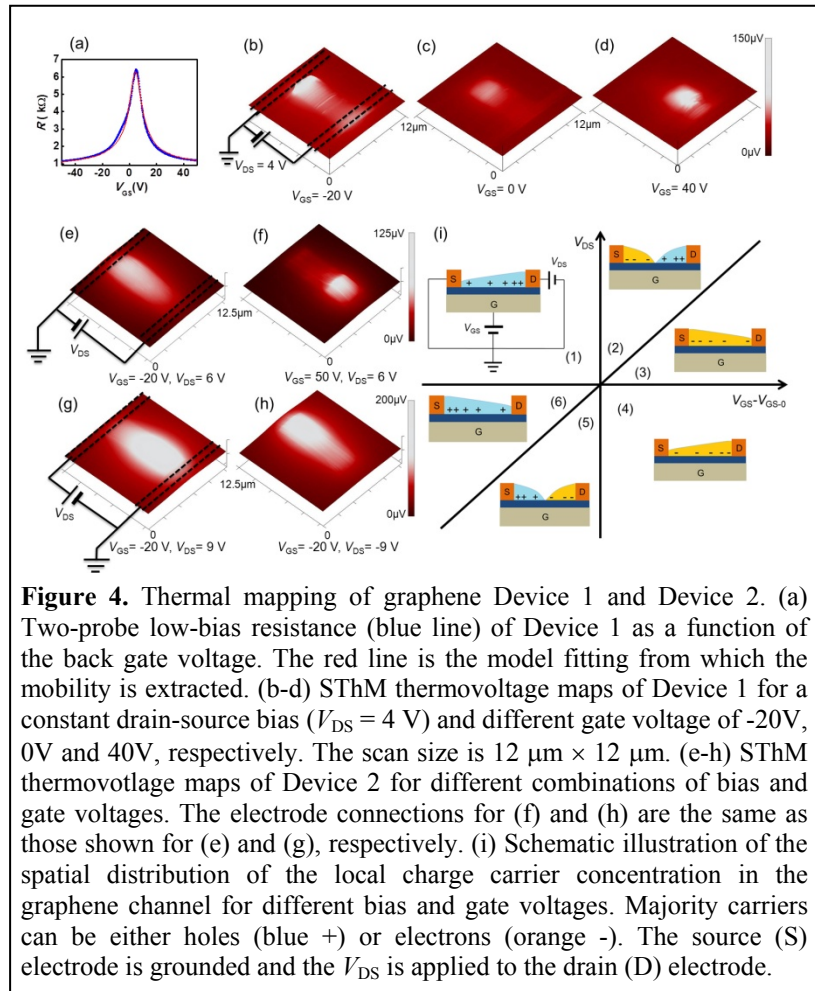


Fig. 3. (a) Optical micrograph, (b-c) TEM, (c) diffraction pattern of BLG1 suspended between two micro-thermometers. (e) Measured thermal conductivity for two suspended BLG samples in comparison with the reported values of a SLG supported on SiO₂, the BTE results for supported (solid line) and suspended (dashed line) graphene.

- I-K. Hsu, R. Kumar, A. Bushmaker, S. B. Cronin, M. T. Pettes, L. Shi, T. Brintlinger, M. S. Fuhrer, J. Cumings, "Optical Measurement of Thermal Transport in Suspended Carbon Nanotubes," *Applied Physics Letters* 92, 063119:1-3 (2008)
- L. Shi, "Comment on "Length-dependant thermal conductivity of an individual single-wall carbon nanotube" [Appl. Phys. Lett. 91, 123119 (2007)]," *Applied Physics Letters* 92, 206103:1-2 (2008)
- I-K. Hsu, M. T. Pettes, A. Bushmaker, M. Aykol, L. Shi, S. B. Cronin, "Optical Absorption and Thermal Transport of Individual Suspended Carbon Nanotube Bundles," *Nano Letters* 9, 590–594 (2009)
- L. Shi, J. H. Zhou, P. Kim, A. Bachtold, P. L. McEuen, A. Majumdar, "Thermal Probing of Energy Dissipation in Current-Carrying Carbon Nanotubes," *Journal of Applied Physics* 105, 104306:1-5 (2009)
- M. T. Pettes and L. Shi, "Thermal and Structural Characterizations of Individual Single-, Double-, and Multi- Walled Carbon Nanotubes," *Advanced Functional Materials* 19, 3918–3925 (2009)
- J. H. Seol, I. Jo, A. L. Moore, L. Lindsay, Z. H. Aitken, M. T. Pettes, X. Li, Z. Yao, R. Huang, D. Broido, N. Mingo, R. S. Ruoff, L. Shi, "Two-Dimensional Phonon Transport in Supported Graphene," *Science* 328, 213-216 (2010)
- W.W. Cai, A. L. Moore, Y. Zhu, X. Li, S. Chen, L. Shi, R. S. Ruoff, "Thermal Transport in Suspended and Supported Monolayer Graphene Grown by Chemical Vapor Deposition," *Nano Letters* 10, 1645–1651 (2010)
- I. K. Hsu, M. T. Pettes, M. Aykol, L. Shi, S. B. Cronin, "The Effect of Gas Environment on Electrical Heating in Suspended Carbon Nanotubes," *Journal of Applied Physics* 108, 084307 (2010)
- L. Shi, "Thermal Conductance of Carbon Nanotubes," in *Handbook of Nanophysics*, ed. K. D. Sattler, Taylor & Francis, pp. 4.1-4.14 (2010)
- J. H. Seol, A. L. Moore, I. Jo, Z. Yao, L. Shi, "Thermal Conductivity Measurement of Graphene Exfoliated on Silicon Dioxide," *Journal of Heat Transfer* 133, 022403 (2011)
- I. Jo, I. K. Hsu, Y. J. Lee, M. M. Sadeghi, S. Kim, S. Cronin, E. Tutuc, S. K. Banerjee, Z. Yao, L. Shi, "Low-Frequency Acoustic Phonon Temperature Distribution in Electrically Biased Graphene," *Nano Letters* 11, 85–90 (2011)
- S.S. Chen, A. L. Moore, W.W. Cai, J. W. Suk, J. An, C. Mishra, C. Amos, C. Magnuson, J. Kang, L. Shi, R. S. Ruoff, "Raman Measurements of Thermal Transport in Suspended Monolayer Graphene of Variable Sizes in Vacuum and Gaseous Environments," *ACS Nano*, doi: 10.1021/nn102915x (2011)



Phase Transformations in Confined Nanosystems

Jeffrey E. Shield, *Department of Mechanical Engineering, University of Nebraska**

Kirill Belashchenko, *Department of Physics, University of Nebraska*

Matthew J. Kramer, *Ames Laboratory*

G. Malcolm Stocks, *Oak Ridge National Laboratory*

Understanding phase transformations is at the forefront of materials science, since they control structural development and allow us to tailor properties. Similarly, in order to control and exploit the unique behavior of nanoscale materials [1,2,3], it is necessary to understand phase transformations and stability in finite-sized systems. In nanoscale materials, particular transformations may be suppressed or transformation paths altered due to finite size limitations.

In general, phase relationships in systems with at least one dimension at the nanoscale (<100 nm) have been observed to differ significantly from the bulk. Notably, transformation temperatures tend to be decreased in nanoscale systems compared to bulk systems [4,5,6,7]. In addition, solid solubility is increased in nanoscale systems [8,9,10], which may be related to the inability of a nanoscale system to support interfaces between phases [11,12,13,14]. Kinetics, too, may influence phase transformations at the nanoscale [15], particularly with respect to the finite depletion effect in nucleation-controlled phase transformations that require a change of composition. Here, the number of solute atoms necessary to form the new phase from the parent solid solution may not be enough due to the finite volume of a nanoparticle, inhibiting transformations.

This project will provide fundamental insight into phase transformations in nanoscale systems. Specifically, we will study an aspect of solid-state phase transformations that has not been addressed—the convergence of critical length scales with the system size in three-dimensionally confined nanoscale systems, and the role of finite-sized systems on phase equilibria and transformations. This will ultimately allow the design of unique nanomaterials with structures far from (bulk) equilibrium, with potentially far-reaching technological implications.

Finite-sized Systems

Spatially confining the system in three dimensions will be accomplished by making nanoparticles using inert gas condensation (IGC). IGC produces monodispersed clusters with diameters ranging from 2 to 20 nm (Figure 1) [16,17,18,19,20,21,22]. Because the atomic gas source in our system is DC magnetron sputtering, we are able to use any metallic alloy as a target, and thus can vary the composition of our clusters over a wide range. We have utilized this ability to carefully control the composition in Fe-Pt, Mn-Au, Fe-Cu, and Fe-Au alloy clusters [23,24]. The clusters can be deposited directly onto support films for observation by transmission electron microscopy, or isolated from other clusters in a matrix by alternate sputtering from other DC or RF guns attached to the system. These latter samples are ideal for magnetic characterization, which can probe subtle structural changes, and for building samples for atom probe/field ion microscopy (APFIM) characterization. APFIM is a technique that provides atomic-level compositional information and three-dimensional reconstruction of nanostructures (3DAP). This will be a powerful tool to probe local compositional variations within clusters. APFIM will be carried out in collaboration with Jean-Marie LeBreton at the University of Rouen.

*Contact information: *N104 WSEC
Lincoln, NE 68588
jshield2@unl.edu*

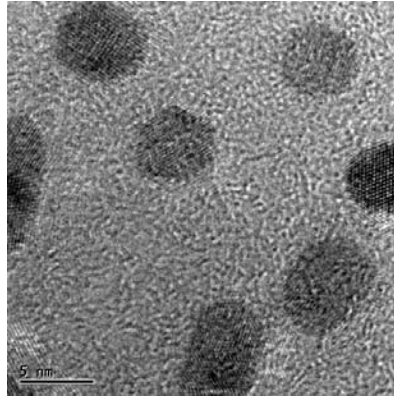
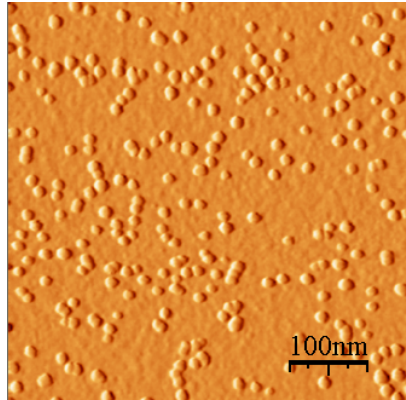


Figure 1. (a) Atomic force microscope image of 8 nm Fe clusters showing a monodispersed size distribution. (b) Transmission electron microscope image of 6 nm MnAu clusters. Note the single-crystal nature of the clusters, shown by the lattice fringes that span the cluster.

Fe-Au clusters with a composition of 65 atomic percent Fe/35 atomic percent Au, as determined by energy dispersive spectroscopy, were made by IGC using a composite target. Under equilibrium conditions, Fe and Au have limited solid solubility in each other, and at 35 percent Au lies in the α -Fe+Au phase field at room temperature. However, the selected area electron diffraction pattern (Figure 2) was indexed to a single-phase bcc structure with $a \sim 0.337$. This lattice parameter is significantly larger than that of α -Fe and a “model” bcc Au structure calculated from the atomic radius of Au. High resolution TEM corroborated the bcc structure (Figure 2). The electron diffraction rings were faint, continuous and extremely broad, particularly for electron diffraction. This suggests poor crystallinity within the clusters. This structural disorder was observed in high-resolution images (Figure 3). Here, lattice plans clearly extended across the clusters, indicating the single-crystal nature of the clusters, However, these planes were observed to be highly distorted, evidences by the bending of the lattice planes.

In situ heating experiments were also conducted, with samples heated to 650°C. The sample was examined again post mortem at room temperature. Now, the selected area diffraction pattern revealed sharp rings characteristic of well-crystallized structures (Figure 4). Now, however, the pattern indexes to a fcc structure with $a \sim 0.387$ nm. This lattice parameter lies between that of γ -Fe (0.351 nm) and fcc Au (0.408 nm), but larger than that predicted by Vegard’s law.

Summary

Fe-Au clusters produced by inert gas condensation with ~ 35.5 atomic percent Au form in single-phase, single-crystal form both before and after heat treatment. Two new structures have been found. The first is bcc with $a \sim 0.337$ nm and was observed in the as-deposited clusters, while the second, an fcc structure with $a \sim 0.387$ nm, was observed after in situ heat treatment. The clusters do not follow equilibrium phase diagram, which predicts two phases. While the as-deposited clusters displayed a high degree of structural disorder, the heat treated clusters were highly crystalline and contained few structural defects. The ability to produce unique, non-equilibrium structures by inert gas condensation may ultimately lead to materials with unique magnetic or catalytic behavior.

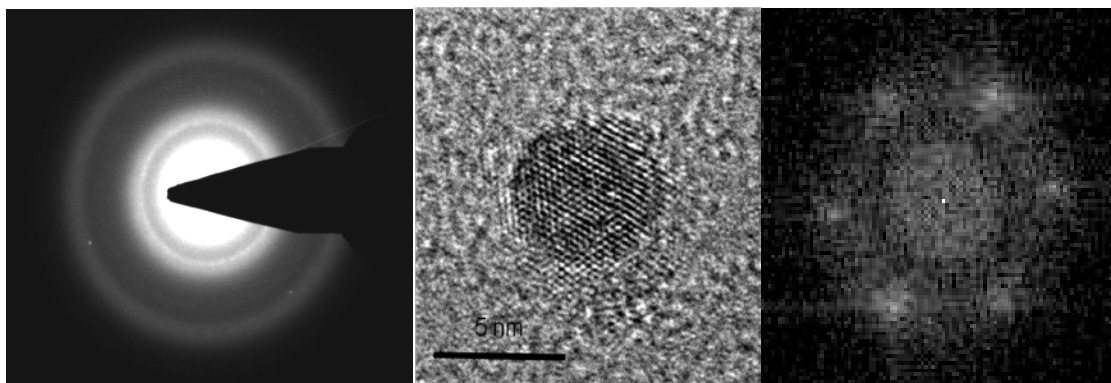


Figure 2. (a) Selected area diffraction pattern of as-deposited Fe-35 at.% Au clusters. (b) High resolution TEM image of an as-deposited cluster. (c) FFT of 3(b); this indexes to the [111] zone axis of a bcc structure with $a \sim 0.337$ nm.

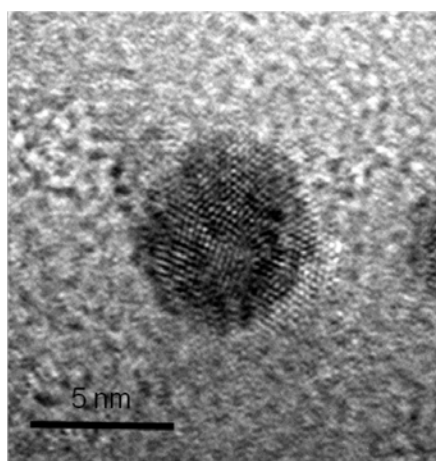


Figure 3. High resolution TEM image displaying the poor crystallinity of as-deposited clusters. A higher degree of perfection was observed along the close-packed [111] direction of Figure 3(b)

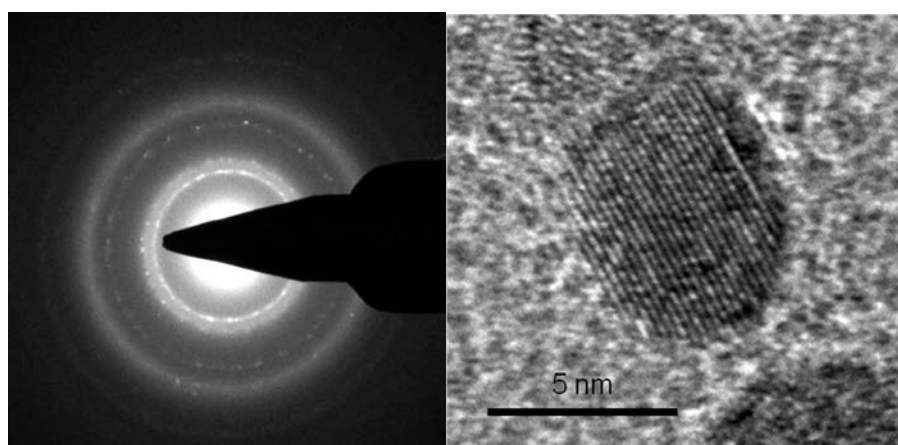


Figure 4. (a) Selected area diffraction pattern of as-deposited Fe-35 at.% Au clusters after in situ heating to 650C. (b) High resolution TEM image of an as-deposited cluster after heating showing higher degree of structural perfection.

References

1. R. Skomski, *J. Phys. Condens. Matter* **15**, R841 (2003).
2. D.L. Leslie-Pelecky and R.D. Rieke, *Chem. Mater.* **8**, 1770 (1996).
3. H. Hofmeister, "Encyclopedia of nanoscience and nanotechnology," Vol. X, edited by H.S. Nalwa (American Scientific Publishers, New York, 2003), p. 1.
4. M.T. Gladkikh, S.P. Chigik, V.N. Larin, L.K. Grigorijeva, and V.N. Suhov, *Dokl. Akad. Nauk USSR*, **300**, 588 (1988).
5. J.G. Lee, H. Mori and H. Yasuda, *Phys. Rev. B* **66**, 012105 (2002).
6. H. Yasuda, K. Mitsushi and H. Mori, *Phys. Rev. B* **64**, 094101 (2001).
7. K. Kadau, M. Gruner, P. Entel and M. Kreth, *Phase Transitions* **76**, 355 (2003),
8. W.A. Jesser, G.J. Shiflet, G.J. Allen and J.L. Crawford, *Mater. Res. Innov.* **2**, 211 (1999).
9. G.L. Allen and W.A. Jesser, *J. Cryst. Growth* **70**, 546 (1984).
10. A.S. Shirinyan and A.M. Gusak, *Phil. Mag.* **84**, 579 (2004).
11. J. Weissmuller, P. Bunzel and G. Wilde, *Scripta Mat.* **51**, 813 (2004).
12. S.C. Hendy, *Phys. Rev. B* **71**, 115404 (2005).
13. A. S. Shirinyan and A. M. Gusak, *Phil. Mag.* **84**, 579 (2004).
14. A.S. Shirinyan, A.M. Gusak and M. Wautelet, *Acta Mat.* **53**, 5025 (2005).
15. R.V. Chepulsikii and W.H. Butler, *Phys. Rev. B* **72**, 134205 (2005).
16. H. Haberland, M. Karrais, M. Mall and Y. Thurner, *J. Vac. Sci. Tech. A* **10**, 3266-3271 (1992).
17. S.H. Baker, S.C. Thornton, A.M. Keen, T.I. Preston, C. Norris, K.W. Edmonds and C. Binns, *Rev. Sci. Instrum.* **68**, 1853-1857 (1997).
18. S.H. Baker, S.C. Thornton, K.W. Edmonds, M.J. Maher, C. Norris and C. Binns, *Rev. Sci. Instrum.* **71**, 3178 (2000).
19. Y. Xu, Z.G. Sun, Y. Qiang and D.J. Sellmyer, *J. Magn. Magn. Mater.* **266**, 164 (2003).
20. Y. Xu, M.L. Yan, J. Zhou and Sellmyer, *J. Appl. Phys.* **97**, 10J320 (2005).
21. X. Rui, Z. Sun, L. Yue, Y. Xu, D.J. Sellmyer, Z. Liu, D.J. Miller and J.E. Shield, *J. Magn. Magn. Mater.* **305**, 76-82 (2006).
22. Xiangxin Rui, Ph.D. Thesis, University of Nebraska, 2007.
23. X. Rui, Z. Sun, Y. Xu, D.J. Sellmyer and J.E. Shield, *Appl. Phys. Lett.* **89**, 122509 (2006).
24. X. Rui, Z. Sun, R. Skomski, Y. Xu, D.J. Sellmyer, Y.Q. Wu, M.J. Kramer and J.E. Shield, *J. Magn. Magn. Mater.* **320**, 2576 (2008).

Spin Polarized Functionality Through Complex Oxide Heteroepitaxy

PI: Yuri Suzuki

Lawrence Berkeley National Laboratory / UC Berkeley

210 Hearst Memorial Mining Building MC1760

Department of Materials Science & Engineering

UC Berkeley

Berkeley, CA 94720-1760

ysuzuki@berkeley.edu

PROGRAM SCOPE

The *main research objective* of the program is to develop novel complex oxide thin films and heterostructures with magnetic functionality where the surfaces and interfaces play a critical role in the realization of the long-range magnetic order. In this program, it is the collective phenomena of long range magnetic order and emergent spin polarized functionality from complex oxide thin film and heterostructures and the atomically accurate thin film synthesis of new complex oxide materials that are studied. Control of interface strain, roughness, chemical mixing, and magnetism will not only enable control of spin transport across interfaces, but also can be used to devise entirely new materials with properties distinct from their bulk counterparts.

Our current focus is on two classes of complex oxide materials where interfaces play a key role:

- (a) complex oxide heterostructures in which the interface gives rise to spin polarized properties that are not found in the constituent materials and
- (b) complex oxide materials, e.g., the cobaltate perovskites, in which ferromagnetism is observed in thin film form but not in the corresponding bulk counterpart

RECENT PROGRESS

Highlights of recent work include (i) long range ferromagnetic order in LaCoO_3 epitaxial thin films, (ii) metallic to insulating behavior in LaTiO_3 thin films and (iii) an all-ferromagnetic magnetic tunnel junction device.

We have demonstrated ferromagnetism in epitaxial LaCoO_3 (LCO) films that is not observed in diamagnetic/paramagnetic bulk LCO. Bulk LCO is thought to be diamagnetic below 100K with Co ions in a low spin ground state and undergoes a cooperative spin transition to a paramagnetic state at 100K. However, the nature of these higher spin states is unclear. To explore the origin of this novel ferromagnetic ground state of LCO, we performed a systematic investigation of LCO thin films grown on a variety of substrates, including SrTiO_3 and $(\text{La,Sr})(\text{Al,Ta})\text{O}_3$, in order to probe the role of epitaxial lattice distortions as well as oxygen vacancies in the long range magnetic ordering. We find that, regardless of oxygen deposition conditions, all films are tetragonally distorted due to heteroepitaxial growth on to the substrate. Reciprocal space maps of the (103) LCO peak reveal that the films, up to a thickness of 90nm, are coherently strained to the substrates. Through XAS data, we have been able to determine that the ferromagnetism comes from the Co in a 3^+ valence state. We observe that the ferromagnetic order is not just a surface or impurity effect, but arises from the Co ions distributed throughout the entire films through thickness dependent magnetization studies. We also see that increased oxygenation during the deposition is critical to the magnetism since a lower oxygen deposition pressure alters the structure and suppresses ferromagnetism in the LCO films.

We have demonstrated metallic to insulating behavior in epitaxial thin films of LaTiO_3 depending on substrate choice. LaTiO_3 (LTO) is a correlated Mott insulator in the bulk, but metallicity can be induced by alkaline earth doping of the La site, cation deficiency, or charge transfer from a nearby interface. However, hydrostatic pressure has not been shown to induce metallicity in bulk LTO. We have synthesized LTO films on STO, DyScO_3 and GdScO_3 substrates that place the LTO films under compressive strain ranging from -1.6% on STO, -0.7% on DyScO_3 , to nominally 0% on GdScO_3 . Epitaxial compressive strain from an underlying SrTiO_3 substrate can induce metallicity that cannot be attributed to interface charge reconstruction, off-stoichiometry of the LTO or cation interdiffusion. LTO films on DyScO_3 and GdScO_3 substrates are coherently strained and exhibit varying degrees of insulating behavior. Structural measurements suggest that there is little, if any, evidence for a distinct structural transition. The demonstration of metallicity in LTO films on STO substrates indicates how tetragonal distortions can be used to tune the electronic structure of a material such as LTO with a very small charge gap (Figure 1). This study suggests an alternative explanation to the observation of metallicity at LTO/STO superlattices that has been attributed to interface reconstruction.

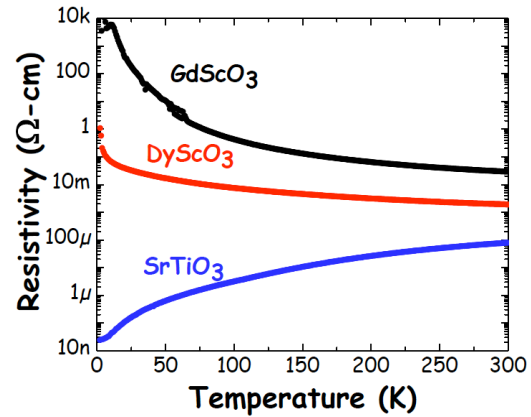


Figure 1. LaTiO_3 films on different substrates give rise to metallic to insulating behavior depending on the magnitude of the lattice mismatch between the film and substrate.

We have demonstrated that a magnetic tunnel junction device can be composed of a completely ferromagnetic stack of two electrodes and a barrier layer. This demonstration is contrary to previous understanding that a magnetic tunnel junction is composed of two ferromagnetic electrodes separated by a non-magnetic insulating layer; if the barrier layer is magnetic, then one of the electrodes must be non-magnetic and magnetically decoupled from the barrier to generate a spin filter magnetic junction. We have investigated the spin transport and magnetic coupling behavior of magnetic tunnel junction heterostructures with $\text{La}_{0.7}\text{Sr}_{0.3}\text{MnO}_3$ and Fe_3O_4 electrodes and ferrimagnetic NiFe_2O_4 barrier layers. Careful structural and magnetic characterization of the individual layers, as well as the interfaces, has been performed. We find that while the $\text{NiFe}_2\text{O}_4/\text{Fe}_3\text{O}_4$ interface exhibits strong magnetic coupling, the $\text{La}_{0.7}\text{Sr}_{0.3}\text{MnO}_3 / \text{NiFe}_2\text{O}_4$ interface is magnetically decoupled. Therefore, in this all-magnetic stack, distinct parallel and antiparallel electrode states can be attained. Symmetric bias dependence of the junction magnetoresistance and inelastic tunneling spectra indicates that the spin transport of these devices is dominated by the barrier layer magnetism at all temperatures.

FUTURE PLANS

In each highlighted area above as well as our additional projects on other related complex oxide thin film materials, we plan to focus on some of the major challenges in the areas of oxide interfaces and spin based devices. We will tackle the role of interface electronic reconstruction versus defects in the observed metallicity observed in LaTiO_3 and LaVO_3 epitaxial thin films. One of the big challenges in the development of novel complex oxide thin films has been to identify or predict thin film behavior unattainable in the bulk a priori. We will focus on heterostructures where we can take advantage of carrier mediated exchange and charge disproportionation to obtain novel magnetic functionality not found in their bulk counterparts.

REFERENCES (2008-present)

1. B.B. Nelson-Cheeseman, R.V. Chopdekar, J.S. Bettinger, M. Pickett, E. Arenholz, M.A. Marcus, Y. Suzuki, "Magnetism and Chemical Structure of $\text{NiMn}_2\text{O}_4\text{-Fe}_3\text{O}_4$ Interfaces," *Journal of Applied Physics* **103** 07B524 (2008).
2. Y. Takamura, R.V. Chopdekar, E. Arenholz, Y. Suzuki, "Control of the magnetic and magnetotransport properties of $\text{La}_{0.7}\text{Sr}_{0.3}\text{MnO}_3$ thin films through epitaxial strain," *Applied Physics Letters* **92** 162504 (2008).
3. B.B. Nelson-Cheeseman, F. Wong, R.V. Chopdekar, M. Chi, E. Arenholz, N.D. Browning, Y. Suzuki, "Interface Structure and Transport of Complex Oxide Junctions," *Journal of Vacuum Science and Technology B* **26** 1521 (2008).
4. Rajesh V. Chopdekar, Elke Arenholz, Yuri Suzuki, "Orientation and thickness dependence of magnetization at the interfaces of highly spin-polarized manganite thin films," *Phys. Rev. B* **79** 104417 (2009).
5. Virat Vasav Mehta, Marco Liberati, Franklin Wong, Rajesh V. Chopdekar, Elke Arenholz, Yuri Suzuki, "Ferromagnetism in tetragonally distorted LaCoO_3 thin films," *J. Appl. Phys.* **105** 07E503 (2009).
6. M. Liberati, R.V. Chopdekar, V. Mehta, E. Arenholz, and Y. Suzuki, "Epitaxial Growth and Characterization of CaVO_3 Thin Films," *J. Magn. Mag. Mater.* **321** 2852 (2009).
7. Franklin J. Wong, Seung-Hyub Baek, Rajesh V. Chopdekar, V.V. Mehta, Ho Wan Jang, C.B. Eom, and Yuri Suzuki, "Metallicity in LaTiO_3 thin films induced by tetragonal lattice deformation," *Phys. Rev. B* **81** R161101 (2010).
8. Alexander Grutter, Franklin Wong, Elke Arenholz, Marco Liberati, Arturas Vailionis, Yuri Suzuki, "Enhanced Magnetism in Epitaxial SrRuO_3 Thin Films," *Appl. Phys. Lett.* **96** 082509 (2010).
9. Alexander Grutter, Franklin Wong, Elke Arenholz, Marco Liberati, Yuri Suzuki, "Enhanced Magnetization in Epitaxial SrRuO_3 Thin Films via Substrate-Induced Strain," *J. Appl. Phys.* **107** 9E138 (2010).
10. B. B. Nelson-Cheeseman, F. J. Wong, R. V. Chopdekar, E. Arenholz, and Y. Suzuki, "Room Temperature Magnetic Barrier Layers in Magnetic Tunnel Junctions," *Phys. Rev. B* **81**, 214421 (2010).
11. B. B. Nelson-Cheeseman, R. V. Chopdekar, M.F. Toney, E. Arenholz, and Y. Suzuki, "Modified Magnetic Ground State in NiMn_2O_4 Thin Films," *Phys. Rev. B* **82** 144419:1-7 (2010).

Title: “Structure and Magnetism in Novel Group IV Element-Based Magnetic Materials”

Principal Investigator: Frank Tsui (ftsui@physics.unc.edu), Physics and Astronomy, University of North Carolina, CB#3255, Phillips Hall, Chapel Hill, NC 27599

I. Program Scope

The program is to investigate structure, magnetism and spin dependent states of novel group IV element-based magnetic materials as a function of composition and epitaxial constraints. The materials systems of interest are Si-compatible high quality epitaxial films and heterostructures of Si/Ge-based magnetic ternary alloys grown by non-equilibrium molecular beam epitaxy (MBE) techniques, specifically doped magnetic semiconductors (DMS) and half-metallic Heusler alloys. Systematic structural, chemical, magnetic, and electrical measurements are carried out, using x-ray microbeam techniques, magnetotunneling spectroscopy and magnetotransport. The work is aimed at elucidating MBE synthesis and the nature and interplay between structure, chemical order, magnetism, and spin-dependent states in these novel materials, at developing materials and techniques to realize and control fully spin polarized states at room temperature, and at exploring fundamental processes that stabilize the epitaxial magnetic nanostructures and control the electronic and magnetic states in these complex materials. Combinatorial approach provides the means for the systematic studies, and the complex nature of the work necessitates this approach.

The research is a collaborative effort aimed at exploring

- phase decomposition of transition metal dopants in precipitation-free Ge DMS and its influence on ferromagnetic order,
- impurity states of transition metal dopants and their local environment in Ge DMS,
- active control of magnetic states in Ge DMS,
- structural and chemical ordering in Heusler alloys Co_2MnSi and Co_2MnGe ,
- effects of composition and coherent epitaxial strain in Heusler alloys,
- spin dependent states that are responsible for electrical transport,
- spin dependent transport through Si/Ge using these materials.

II. Recent Progress

II.a. In Ge (001) films codoped with Co and Mn, we showed previously that doping with even trace amounts of Co can reduce and suppress the formation of Mn precipitates and surface segregation. Recently, our experiments and analysis of diffraction and EXAFS reveal the presence of three dopant states. In addition to populations of substitutional Co and Mn (about 90 and 70 at. % of the respective dopants), the remaining dopants (predominantly Mn) appear to form small substitutional clusters, such as substitutional dimers, rather than interstitials. Interestingly, calculations in the literature have shown that the substitutional dimers have low formation energies and the interaction within the dimer is antiferromagnetic.

Pulsed-laser atom probe tomography (PLAP) has been used to examine the nanometer scale dopant concentration variations in this material in collaboration with Prof. L. Lauhon’s group at Northwestern University. PLAP reconstruction reveals the presence of dopant rich clusters with the local concentration nearly a factor of two higher than average concentrations. Radial distribution function analysis indicates strong correlation between the distributions of Co and Mn and that the dopant rich regions

exhibit characteristic length scale. Histograms of local concentration of the elements (Co, Mn, and Ge) indicate phase decomposition of dopants, and show no population of impurity clusters beyond 3 atoms. These findings provide insight into the mechanism of the decomposition process in this precipitation-free DMS system.

II.b. New experiments and analysis have been developed to examine chemical ordering in epitaxial films of Heusler alloys that contain Co, Mn and Ge or Si grown on Ge (111) substrate. Full-spectrum anomalous diffraction experiment and analysis have been developed to probe and quantify chemical ordering in Heusler alloys. The new technique has been used to study $\text{Co}_x\text{Mn}_y\text{Ge}_z$ alloys and has demonstrated sensitivity to resolve and quantify all types of chemical disorders for the first time, which otherwise, is not possible by any other “charge-based” techniques, (including XRD, EXAFS, and electron microscopy/spectroscopy), owing to the lack of differences in the charge of and the spacing between the elements.

Specific findings in $\text{Co}_x\text{Mn}_y\text{Ge}_z$ grown on Ge (111):

- Identification and quantification of disorders: primary disorder is Mn-Ge swapping, followed by Ge antisites (Ge replacing Co and Mn) and Co vacancies, while the expected defect of Co-Mn site swapping (based on first principle calculations) is absent (to better than 0.5%). The level of Mn-Ge swapping is surprisingly large (~30%) and insensitive to composition, suggesting a key role played by epitaxy. The populations of the secondary defects exhibit a minimum near Heusler stoichiometry, and increase with increasing Ge concentration.
- Ordering in this alloy is very sensitive to the Co to Mn atomic ratio, but less so with respect to the Ge concentration. The highest structural ordering occurs within a narrow region of composition with Co:Mn = 2, where the film lattice constant is determined to be approximately that of the bulk. Within this region, however, the degree of structural ordering decreases with Ge concentration, similar to that of the secondary chemical disorders (above). This is accompanied by an increase of in-plane lattice relaxation, while structural and chemical stacking sequences show no detectable change.

High quality coherent epitaxial films of $\text{Co}_x\text{Mn}_y\text{Si}_z$ have been grown on Ge (111) substrates over a large compositional region. The highest structural and chemical ordering is observed at $\text{Co}_{0.64}\text{Mn}_{0.13}\text{Si}_{0.23}$ rather than the Heusler stoichiometry of $\text{Co}_{0.5}\text{Mn}_{0.25}\text{Si}_{0.25}$, where the epitaxial strain is larger (-0.5%) than that at the stoichiometry (0.1%). A 60° rotation of the crystallographic axis of the alloy film with respect to that of the Ge substrate is observed, which corresponds to a single stacking fault at the interface originated from the symmetry of the Ge surface reconstruction. The results indicate the critical roles played by the chemistry and interfacial effects in addition to epitaxial strain and highlight the need for a better understanding of these phenomena.

III. Future Plans

We plan to carry out extensive temperature and gate voltage dependent magnetotransport measurements on an insulating field effect Hall bar structure fabricated from the combinatorial epitaxial films we grow, in order to investigate carrier mediated ferromagnetism and active control of magnetization states in Ge-based DMS.

We plan to examine spin dependent density of states and spin polarization near the Fermi level in Ge DMS and Heusler alloys using tunneling spectroscopy, in order to probe the interplay between spin polarized states, structural and chemical ordering, and epitaxial constraints. Dielectric stacks that contain $\text{Al}_2\text{O}_3/\text{Nb}$ and $\text{Al}_2\text{O}_3/\text{Fe}$ grown in-situ on top of our combinatorial epitaxial films will be used.

We plan to study MBE synthesis and tunneling properties of coherent magnetic and nonmagnetic structures using narrow gap semiconductors, including Ge and Si-Ge.

IV. References

1. *Study of magnetic anisotropy and magnetization reversal using the quadratic magneto-optical effect in epitaxial $\text{Co}_x\text{Mn}_y\text{Ge}_z$ (111) films*, P. K. Muduli, W. C. Rice, L. He, B. A. Brian, Y. S. Chu, and F. Tsui, J. Phys. CM **21**, 296005 (11pp) (2009).
2. *Dopant stability and strain states in Co and Mn doped Ge (001) epitaxial films*, B. A. Collins, Y. S. Chu, L. He, Y. Zhong, and F. Tsui, Phys. Rev. B **77**, 193301 – 1 – 4 (2008).
3. *Composition dependence of magnetic anisotropy and quadratic magneto-optical effect in epitaxial films of the Heusler alloy Co_2MnGe* , P. K. Muduli, W. C. Rice, L. He, and F. Tsui, J. Magn. Magn. Mater. **320**, (Letter) L141 – L143 (2008).

Understanding the Spin-Lattice Coupling in Multiferroic Oxides

Trevor A. Tyson, Department of Physics
New Jersey Institute of Technology, Newark NJ 07102-1982
Email: tyson@adm.njit.edu

Abstract and Program Scope: Multiferroic oxides (such as REMnO_3 and REMn_2O_5 (RE=rare earth, Sc, Y)) are a class of materials which are simultaneously ferroelectric and ferromagnetic [1]. The possibility of coupling the magnetic and electric properties will enable new functions. These capabilities will possibly lead to devices in which ferroelectric memory can be written with magnetic fields or magnetic bits can be written by an electric field. However, the detailed mechanism behind the coupling of the spin and atomic degrees of freedom in these materials is not well understood. In this proposal we are conducting structural measurements on multiple length scales in the presence of magnetic and electrical fields in order to ascertain the mechanism behind the spin-lattice coupling. We have been able to quantify the amplitude of the distortions which occur in REMnO_3 (hexagonal and orthorhombic systems) with low temperature magnetic transitions and have isolated the atomic origin of the field coupling in the REMn_2O_5 system. The pressure dependence of the structure of the hexagonal REMnO_3 system was also evaluated showing that the a-b plane is sensitive to strain and hence the Mn-Mn spin coupling can be tuned by growth as strained films on substrates. **This work is supported by DOE Grants DE-FG02-07ER46402.**

Results from Research on Multiferroics

The rare earth hexagonal manganites corresponding to systems with the chemical formula REMnO_3 (RE ions with small radii such as Sc, Y, Ho, Er, Tm, Yb, and Lu) exhibit both ferroelectric and magnetic order. In this specific class of materials the transition to the ordered ferroelectric state (T_{FE}) occurs between ~ 800 and ~ 1200 K while the ordered magnetic states occur at significantly lower temperature ($T_{\text{N}} \sim 80$ K). This hexagonal structure can also be stabilized in large radius cation systems by quenching them from high temperature or by depositions on substrates which induce strain. The Mn^{3+} ions form a two dimensional triangular planar lattice where the Mn spins are coupled indirectly through the planar oxygen atoms. Locally the Mn ions are incorporated into MnO_5 polyhedra (bipyramids) with three oxygen atoms surrounding the Mn atom in a plane and two apical oxygen atoms above and below the plane completing the polyhedron. The degree of frustration in these systems, indicated by the ratio of the Curie-Weise constant (derived from $1/\chi$) to the Neel temperature, approaches 10 in the hexagonal systems. The frustration is relieved by transition into a unique in-plane (a-b plane) magnetic ordering in which the Mn ion moments are pointed 120° relative to each other. In the systems with open 4f shells (REMnO_3), a series of magnetically ordered states are found since, it is believed, that the spins on the RE ions can both couple with the Mn ions and each other and order magnetically and at low temperatures. In HoMnO_3 for example, neutron diffraction measurements reveal a 90° in-plane rotation of the Mn spins near ~ 40 K (T_{SR}) followed by magnetic ordering of the Ho sites below ~ 5 K (T_{Ho}).

In our research, local structural measurements have been performed on hexagonal multiferroic REMnO_3 ($\text{RE}=\text{Ho}$) in order to determine the atomic pairs which are involved in the magnetic ordering transitions and to characterize the spin lattice coupling. The transition from paramagnetic to the antiferromagnetic (noncollinear) phase near ~ 70 K is dominated by changes in the a-b plane Mn-Mn bond distances. The spin rotation transition near ~ 40 K involves both Mn-Mn and nearest neighbor Ho-Mn interactions while the low temperature transition below 10 K involves all interactions, Mn-Mn, Ho-Mn (nearest and next nearest) and Ho-Ho correlations. The results show that for RE corresponding to open 4f-shell systems, such as HoMnO_3 , the RE-Mn interaction plays an important role at the Mn spin re-orientation temperature T_{SR} and also produce a spin coupled transition when the RE sites order at low temperatures (below ~ 10 K). First-principles calculations reveal asymmetric polarization of the charge density of $\text{RE}=\text{Ho}$, O3 and O4 sites along the c-axis in the ferroelectric phase which facilitates coupling between Ho atoms on neighboring planes normal to the c-axis. The local structural measurements were combined with density functional calculations to evaluate the charge distribution for the given structures and to determine the origin of the electric polarization, the phonon frequencies (self force constants) and energetic related to the local distortions.

Using a simplified model, the change in bond distances at the magnetic ordering temperatures can be understood in terms of competing spin and lattice energies. The exchange energy $J(x,y,z,\theta) \mathbf{S}_i \cdot \mathbf{S}_j$ for a spin pair is a function of bond distance and bond angle. Atomic displacements result in changes in lattice energy $\delta E_L \sim \frac{1}{2} k (\delta x^2 + \delta y^2 + \delta z^2)^{1/2}$ for a bond pair while the spin contribution for a given pair changes as $\delta E_J \sim (J(x+\delta x, y+\delta y, z+\delta z, \theta+\delta\theta) - J(x, y, z, \theta)) \mathbf{S}_i \cdot \mathbf{S}_j$. The distorted structure at a given temperature will minimize the sum of spin (E_J) and lattice (E_L) contribution to the total energy. The force constants can be used to estimate changes in energy for atomic displacements. a-b plane displacements by 0.005 \AA for Mn, O and Ho ions yield energy changes of approximately, 0.14 , 0.14 and 0.23 meV ($1, 1$ and 2 cm^{-1}). These numbers are consistent with shifts observed in Raman, infrared and optical spectra. Strongly fluctuating local distortions produce a random spin state while periodic local order lead to ordered spin states. In this way, local coherent distortions which support a finite polarization are intimately coupled with the magnetic ordering. In the other direction, the magnetic order will be sensitive to the details of the local structures. External perturbations such as pressure, strain and electrical fields, for example, will affect the magnetic ground state. Indeed a rather complex magnetic ground state is found and both pressure and substrate strain modify the magnetic properties.

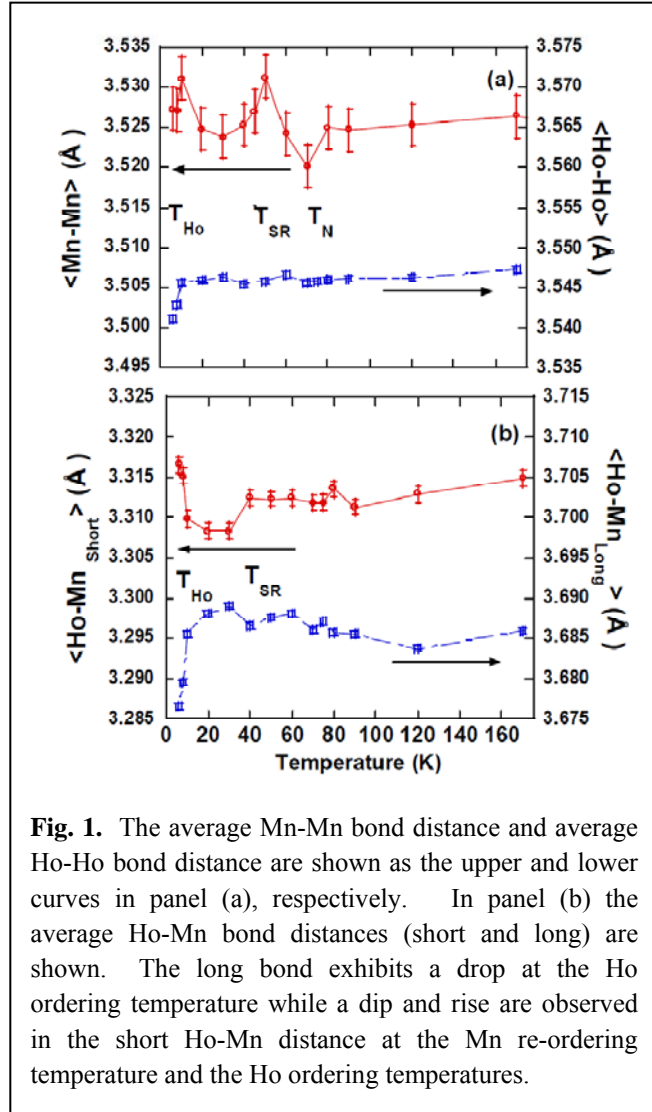


Fig. 1. The average Mn-Mn bond distance and average Ho-Ho bond distance are shown as the upper and lower curves in panel (a), respectively. In panel (b) the average Ho-Mn bond distances (short and long) are shown. The long bond exhibits a drop at the Ho ordering temperature while a dip and rise are observed in the short Ho-Mn distance at the Mn re-ordering temperature and the Ho ordering temperatures.

Hur *et al* discovered reversible switching below 40 K in the system TbMn_2O_5 (composed of c -axis MnO_6 polyhedral chains cross linked by MnO_5 pyramids, Fig. 1). By sweeping the magnetic field from zero to two Tesla the polarization passes through zero and attains a value with magnitude \sim equal to the zero field value. Reducing the field to zero recovers the initial state. The magnitude of the polarization in zero field is $\sim 40\text{nC}/\text{cm}^2$. Thus the RMn_2O_5 system shows promise for enabling an understanding of the coupling spin and lattice degrees of freedom and for the development of devices (if the magnetic and electrical transition temperatures can be increased and the sensitivity to magnetic fields is enhanced.)

The room temperature structure of RMn_2O_5 for a broad range of R ions have has been determined. The Mn^{4+}O_6 octahedra (Mn1 sites) form infinite chains parallel to the c -axis of the orthorhombic Pbam cell (Fig. 1). These chains are cross-linked by Mn^{4+}O_5 pyramids (Mn2 sites) which form edge-sharing dimmers ($\text{Mn}^{4+}_2\text{O}_8$). The R atoms are eight-fold coordinated to oxygen atoms. We note that the inversion center in this Pbam space group is inconsistent with a finite polarization. The low temperature behavior of this system is quite complex.

In our research we have ascertained the origin of the magnetic field coupling to the lattice in these systems. The temperature and magnetic field dependent local structure of REMn_2O_5 systems was examined. While no significant displacements of the Mn ions are observed, it is found that the RE-O distribution exhibits changes at low temperature which are possibly related to the changes in the electric polarization. Density functional computations are used to explore the system dynamics and to link the local structural measurements with anomalous changes in the infrared absorption spectra. The anomalous RE-O distribution and observed coupling to magnetic fields point to the need to properly treat the 4f electrons on the R sites in these systems.

The importance of the RE-O distribution can be seen directly in magnetic field dependent measurements on DyMn_2O_5 . At low temperatures, this system is known to have a strong dependence of the dielectric constant and electric polarization on magnetic fields. Measurement (at 3 K) of the variation of the amplitude of the XAFS structure function (Fig. 4) for the Dy-O distribution with magnetic field reveal that the amplitude decreases with increased field. No changes in the Mn-O distribution are found (within the experimental errors). As in the case of the Tb system (temperature dependent changes) the field dependent changes, in the simplest model, are associated with rotation of the MnO_6 polyhedra which can possibly break the Pbam symmetry. Neutron scattering PDF measurements are being conducted to quantify the nature of the low temperature distortions on longerlength scales.

Metastable O- REMnO_3 exhibits E-type antiferromagnetic (AFM) order in contrast with the A-type AFM (La to Sm) and incommensurate (IC) cycloidal spin structures (Dy and Tb). For all O- REMnO_3 , recent measurements of polarization yield values: YMnO_3 ($250\ \mu\text{C}/\text{m}^2$ at 4.5 K, 0 T), HoMnO_3 ($80\ \mu\text{C}/\text{m}^2$ at 4.5 K, 0 T) [9], DyMnO_3 ($\sim 2000\ \mu\text{C}/\text{m}^2$ at 10K) and TbMnO_3 ($800\ \mu\text{C}/\text{m}^2$ at 10K). These modest values should be compared with the value of $7.5 \times 10^5\ \mu\text{C}/\text{m}^2$ for PbTiO_3 , whose ferroelectricity is related to off center displacements of Ti and Pb by $\sim 0.2\ \text{\AA}$. In the O- REMnO_3 systems, it is predicted to be mainly

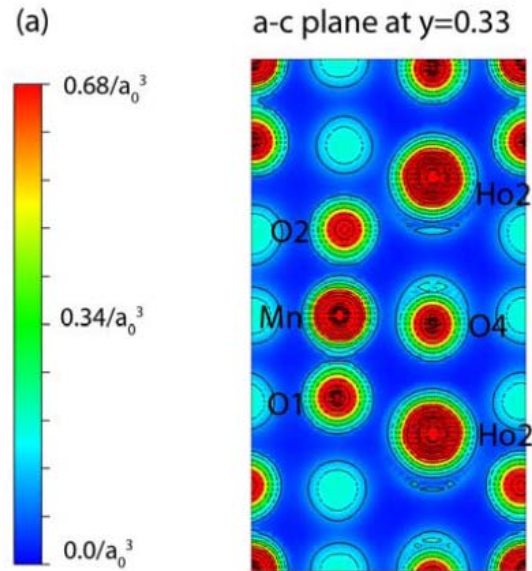


Fig. 2. Charge density plots in atomic units obtained from a DFT calculation for the a - c plane at $y=0.33$. The origin is in the upper right hand corner and the z -direction is down. Note the asymmetry in the charge density along the z -axis for the O3, O4 and Ho atoms which produces the low temperature polarized state.

due to changes in the electron charge distributions. The E-type O-*REMnO*₃ have been predicted to exhibit mainly electric polarization and the large spontaneous polarization ($P_{\text{HoMnO}_3} = 6 \times 10^4 \mu\text{C}/\text{m}^2$) is along the *a*-axis (*Pbnm*) in a combined model (atomic and electronic degrees of freedom). However, they are difficult to prepare as single crystals. Probing the properties by multiple experimental methods will provide a clearer picture of the nature of the electric polarization by specifying its true origin (electronic and/or atomic) and possibly provide paths for its enhancement and its coupling with magnetic fields.

We have found anomalous hardening of a phonon mode and observed a new phonon occurring near the lock-in temperature in orthorhombic LuMnO₃. These observations are confirmed by XAFS analysis which enable identification of enhancement of the Mn-Mn and Mn-O-Mn atomic correlations due to orbital ordering (but with no bond length changes above 0.02 Å) as the driving mechanism behind the changes seen in the IR spectra and the observed electric polarization. The anomalous phonon hardening in the excitation modes of the MnO₆ polyhedra is seen to support a model of spontaneous primarily electronically driven polarization along the *a*-axis for E-type *RMnO*₃. No such changes were found in orthorhombic DyMnO₃.

Our EXAFS experiments confirm our observations. The Mn K-Edge XAFS structure function was measured below 100 K. In Fig 3, the Mn K-edge spectra are plotted for both O-DyMnO₃ and O-LuMnO₃. The correlation peaks of O-DyMnO₃ shows a weak temperature variation. In Fig.3 (a) for O-LuMnO₃, the peaks are sharpening when the temperature goes near T_L and the near neighbor Mn-O, Mn-Lu, Mn-Mn and Mn-O-Mn correlations become strong.

The bond length changes were found, by examination of zero crossings of the imaginary part of the Fourier transforms, to be less than 0.02 Å for the temperature range shown. The larger static distortion in the MnO₆ polyhedra of O-LuMnO₃ is manifested the weaker Mn-O peak amplitude. Enhanced tilting of the MnO₆ octahedra leads to an increase in the second-neighbor antiferromagnetic exchanges (*J*₂), which compete with the nearest-neighbor ferromagnetic exchanges (*J*₁) in the *ab* plane. Two sets of Mn-Mn distances are ~ 3.641 Å (*c*-axis) and ~ 3.886 Å (*ab* plane), have their correlations are enhanced at low temperature. The magnetic ordering drives enhancement of the atomic correlations giving rise to increased amplitudes (Mn-Mn, Mn-O-Mn) at low temperature. EXAFS results

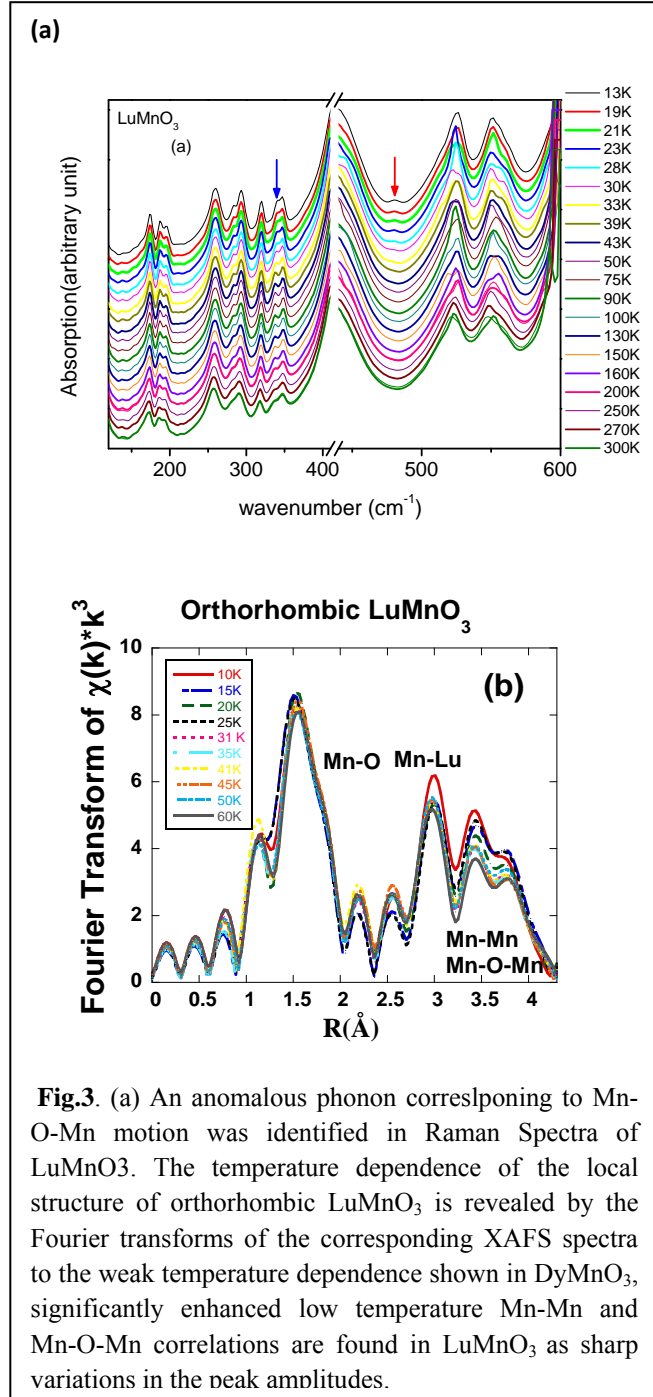


Fig.3. (a) An anomalous phonon corresponding to Mn-O-Mn motion was identified in Raman Spectra of LuMnO₃. The temperature dependence of the local structure of orthorhombic LuMnO₃ is revealed by the Fourier transforms of the corresponding XAFS spectra to the weak temperature dependence shown in DyMnO₃, significantly enhanced low temperature Mn-Mn and Mn-O-Mn correlations are found in LuMnO₃ as sharp variations in the peak amplitudes.

are consistent with the phonon analysis. The modified correlations observed in the EXAFS and IR measurements are the result of modification of the potential wells in which the atoms move due to charge rearrangement below T_L . In the EXAFS measurement of O-HoMnO₃ and O-DyMnO₃ no peak sharpening is observed.

In this project, the hydrostatic and quasi-hydrostatic pressure effects on $REMnO_3$ ($R= Y, Ho, Lu$) were examined via the observation of structural, vibrational and optical properties change with pressure to probe the structural stability and properties of this phase. To effect this, synchrotron based x-ray diffraction (XRD), x-ray spectroscopy (XAS) and infrared (IR) methods are utilized at room temperature (298 K). We find that a pressure-induced a hexagonal-orthorhombic phase transition requires a high pressure (~ 22 GPa) for Lu(Y)MnO₃ and results in only small fractional conversion of Lu(Y)MnO₃ to the orthorhombic phase at room temperature. The hexagonal $REMnO_3$ is very stable below ~ 20 GPa. Under hydrostatic pressure (~ 11 GPa), the atoms hold their fractional positions. By checking the dipole moment in a unit cell, we find that the spontaneous polarization is a constant value under hydrostatic pressures up to ~ 11 GPa. The x-ray near edge absorption spectrum and IR absorption spectrum confirm that $P6_3cm$ is a stable structure under ~ 20 GPa and the environment around the Mn ion is not changed. These results imply that the high temperature conversion to the orthorhombic is strongly kinetically driven. Structural changes in $REMnO_3$ ($RE= Y, Ho, Lu$) under high pressure were examined by synchrotron x-ray diffraction methods at room temperature. Compression occurs more readily in the ab plane than along the c -axis. Under hydrostatic pressure (~ 11 GPa), the atoms hold their approximate ambient fractional positions in the unit cell and the spontaneous polarization shows no significant change. With increased pressure, a pressure-induced hexagonal to orthorhombic phase transition was observed starting at ~ 22 GPa for Lu(Y)MnO₃. A small volume fraction of Lu(Y)MnO₃ is converted to the orthorhombic phase when the pressure is increased to 35 GPa and the orthorhombic phase is maintained on pressure release. High pressure IR absorption spectroscopy and Mn K-edge near edge x-ray absorption spectroscopy confirm that the hexagonal $P6_3cm$ structure is stable below ~ 20 GPa and the environment around Mn ion is not changed. Shifts in the unoccupied p -band density of states with pressure are observed in the Mn K-Edge spectra. A schematic pressure-temperature phase diagram is given for the small ion $REMnO_3$ system.

Application of Developed Methods to Thermoelectrics and Superconductors.

We have utilized the techniques developed for this project to study the origin of thermoelectricity in cobalt oxide thermoelectrics as a collaboration with Dr. Q. Li (Brookhaven Nat. Lab.). Determining the origin of thermoelectricity in complex oxides is important from the perspectives of device application and fundamental physics. We have combined temperature dependent local structural measurements with first principles density functional calculations to develop a three dimensional local structure model of the misfit system $[Ca_2CoO_3][CoO_2]_{1.61}$ (referred to as $Ca_3Co_4O_9$) which has a rocksalt structure stacked incommensurately on a hexagonal CoO_2 lattice. The local structural measurements reveal a low coordination of Co(2) in the rock salt layer. The temperature dependence of the Co(1) in the CoO_2 layer is found to be normal above ~ 75 K. Density functional computations show that the reduction of the coordination of Co(2) is due to the formation of chains of $Co(2)O_x$ in the a - b plane linked to the Ca - O layers by c -axis $Co(2)$ - O bonds. The reduced dimensionality introduced by the chain-like structure in the rock-salt layer and high atomic order in the CoO_2 layer may be the origin of the low thermal conductivity and high electrical conductivity in the respective layers yielding a high thermoelectric figure of merit. The methods developed and utilized in this proposal were further applied to the new Fe based system of superconductors where we determine the nature of the electronic structure for the doped and parent in $LaO_{1-x}F_xFeAs$. Only the Fe layer is found to exhibit a chemical/valence response to doping. Local structural measurements reveal that doping reduces the static disorder in the Fe-As correlation. More

importantly, the Fe-Fe correlations are found to be enhanced by doping suggesting that the doped superconducting state is driven by Fe-Fe spin correlations.

More recently, we examined a possible new 2D superconducting system where order mixed valence Ni¹⁺ and Ni²⁺ exists. Like the parent compound in LaO_{1-x}F_xFeAs, La₄Ni₃O₈ exhibits a spin density wave (SDW) transition which is supported by our XAFS measurements. Suppression of the SDW is expected to create a new superconducting material. The methods developed to explore the spin lattice correlations in the multiferroics have been crucial to shedding light on the superconducting state in both of these materials.

Future Plans for this Project

Expanding on the work initiated on powder, single-crystal XAFS measurements in magnetic fields are being conducted to enhance the observed effect in powder samples (by a factor of 6). To understand the longer range structure in these materials, total x-ray and Neutron scattering (diffuse + Bragg Scattering) on powder samples will be conducted between 4 K and 300 K to complement the XAFS studies already carried out. Modeling of the data will be used to determine the correct unit cells, space groups and local distortions as a function of temperature from the low temperature magnetic ordered phases (below 40K) to room temperature. Data on the TbMn₂O₅ system has been collected and the Y, Ho, and Dy based systems will be studied in the last year of the grant. DFT based simulations of phonon DOS will be compared with inelastic neutron scattering measurements to look for low energy phonons and also identify the closely lying magnetic excitation (at the same energy)

Publications under this Grant

1. P. Gao, H. Y. Chen, T. A. Tyson, Z. X. Liu, J. M. Bai, L. P. Wang, Y. J. Choi and S. W. Cheong, "Observation of anomalous phonons in orthorhombic rare-earth manganites", Applied Physics Letters **97** (26), 262905 (2010).
2. T. A. Tyson, T. Wu, K. H. Ahn, S.-B. Kim and S.-W. Cheong, "Local spin-coupled distortions in multiferroic hexagonal HoMnO₃", Phys. Rev. B: Condens. Matter Mater. Phys. **81**, 054101 (2010).
3. T. A. Tyson, Z. Chen, M. A. DeLeon, S. Yoong, and S. W. Cheong, "Local structure of multiferroic RMn₂O₅: Important role of the R site", J. Magn. Magn. Mater. **321**, 1714 (2009).
4. V. V. Poltavets, K. A. Lokshin, A. H. Nevidomskyy, M. Croft, T. A. Tyson, J. Hadermann, G. Van Tendeloo, T. Egami, G. Kotliar, N. ApRoberts-Warren, A. P. Dioguardi, N. J. Curro and M. Greenblatt, "Bulk Magnetic Order in a Two-Dimensional Ni¹⁺/Ni²⁺ (d₉/d₈) Nickelate, Isoelectronic with Superconducting Cuprates", Physical Review Letters **104** (20), 206403 (2010).
5. T. A. Tyson, T. Wu, J. C. Woicik, B. Ravel, A. Ignatov, C. L. Zhang, Z. Qin, T. Zhou and S. W. Cheong, "Temperature-dependent local structure of LaFeAsO_{1-x}F_x: Probing the atomic correlations", Journal of Applied Physics **108** (12), 123715 (2010).
6. T. A. Tyson, Z. Chen, Q. Jie, Q. Li, and J. J. Tu, "Local structure of thermoelectric Ca₃Co₄O₉", Phys. Rev. B: Condens. Matter Mater. Phys. **79**, 024109/1 (2009).
7. P. Gao, Z. Chen, T. A. Tyson, T. Wu, K. H. Ahn, Z. Liu, R. Tappero, S. B. Kim and S. W. Cheong, "High pressure structural stability of multiferroic hexagonal REMnO₃", Condensed Matter, 1-26, arXiv:1010.0653v1011 [cond-mat mtrl-sci] (2010). Submitted to Physical Review B.

[1] K. F. Wang, J. M. Liu and Z. F. Ren, "Multiferroicity: the coupling between magnetic and polarization orders", Advances in Physics **58** (4), 321-448 (2009).

S.-W. Cheong and M. Mostovoy, "Multiferroics. A magnetic twist for ferroelectricity", Nature Materials **6** (1), 13-20 (2007).

Complex amorphous transition-metal dielectrics

R. Bruce van Dover, Taro Naoi, and Hanjong Paik

Department of Materials Science and Engineering
Cornell University, Ithaca, NY 14853

vandover@cornell.edu

Complex oxide-based dielectrics represent an extremely active area of materials development. As has often been pointed out, nearly every imaginable materials function can be obtained in an oxide, and in many cases oxides offer the ultimate in performance. There are many approaches to investigating the basic science of oxides, including molecular-beam epitaxy techniques capable of creating exquisitely engineered oxide thin films. Our approach strongly contrasts—we prepare films with a deliberate composition gradient by sputtering from independent sources, and use measurements as a function of position to determine composition/processing/property relations in the materials system. With three sputter guns and a three-inch diameter Si substrate, we can evaluate most of a ternary oxide phase diagram (A-B-C-oxide) in a single experiment. Partial quaternary spreads are feasible using alloy or compound targets instead of elemental targets, and pseudoternary spreads of oxynitrides, oxycarbides, etc. are feasible as well.

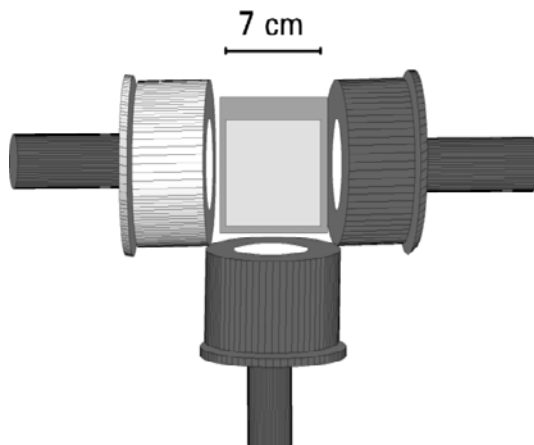


Figure 1. Schematic representation of sputter-gun layout. The three guns are positioned in a vacuum chamber and independently energized.

understanding of the relation between the properties of multicomponent amorphous oxides and their crystalline counterparts by systematic study of closely-related systems. Synthesis of multicomponent amorphous oxides is accomplished using 90° off-axis reactive cosputtering in an oxygen-containing atmosphere, illustrated in Figure 1.[1] This technique is particularly well suited to forming amorphous materials since the cations are intimately mixed as deposited and do not require high-temperature processing to ensure homogeneity.

The composition-spread technique is particularly well-adapted to the study of amorphous, nanoporous, and polycrystalline films. Complex amorphous metal-cation dielectrics have been largely unexplored in the past. Multi-cation network glasses (e.g., silica-based glasses) have been extensively researched, as have simple single-metal-cation amorphous dielectrics such as α -Ta₂O₅. At present there is not even a rough landscape of possibilities for multicomponent metal-cation systems, let alone a detailed scientific understanding of structure/property relations in this class of complex materials. One of our goals is to extend the breadth of our knowledge of the behaviors and trends in this class of materials and the depth of our understanding of their structure/property relations. Our strategy is to establish a general

Amorphous oxides have a wide variety of uses, especially in state-of-the-art integrated electronics. MOSFET devices continue scaling to smaller dimensions accommodate increasing demand for higher performance/lower power electronics. Enormous effort has been directed towards the discovery and integration of alternative “high-k” gate dielectrics to replace SiO₂[2, 3] for Si-based devices. For the decades the high quality of the Si/SiO₂ interface motivated the exclusive use of Si for MOSFET channels; with a-SiO₂ gone other semiconductor materials have become[4] viable. The high hole mobility of Ge makes it attractive for pMOS devices. A-GeO₂ is not viable as a gate dielectric (among other liabilities it is water soluble, thermodynamically unstable, and like SiO₂, has a low dielectric constant). A mixed a-M-Ge-O oxide (M represents an early transition metal), analogous to the a-Hf-Si-O used in current Si technology. There have been few studies of mixed binary or ternary Ge oxides.

We have therefore used the composition-spread technique to investigate Ta-Ge-O because Ta has a high dielectric constant and has been successfully integrated as a charge storage dielectric in DRAM technology. Figure 2 shows the variation in dielectric constant as a function of composition for a Ta-Ge-O composition spread. The solid line is a linear interpolation between the dielectric constant of the endmembers, amorphous a-GeO₂ and amorphous a-Ta₂O₅, respectively.

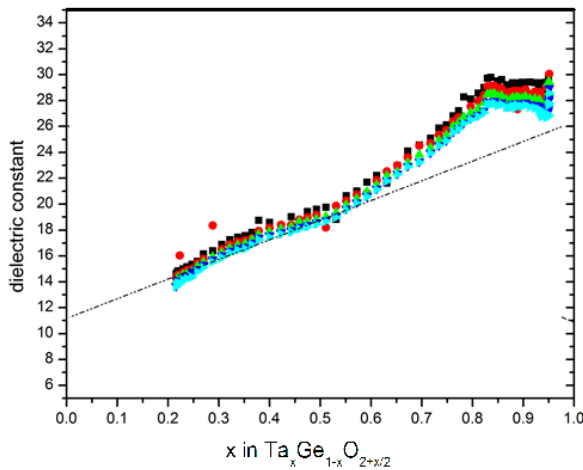


Figure 2. Dielectric constant as a function of composition for a Ta-Ge-O composition spread. The different colors represent measurement frequencies from 100 Hz to 1 MHz.

A similar trend in a-Zr-Si-O was definitively interpreted as due to a change in average atomic volume (density) associated with nanocrystallization.[5] X-ray studies of a-Ta-Ge-O indicate that in this system, the films remain amorphous over the entire composition range. A more subtle effect is apparently in play.

In order to achieve a more atomistic understanding of the dielectric behavior of a-Ta-Ge-O, we have developed an experimental approach using the Clausius-Mossotti and Lorentz-Lorentz equations to relate the dielectric constant to the polarizability. In order to do this we determine the molecular volume using the

known composition and density inferred from X-ray reflectivity measurements. The density is shown as a function of composition in Figure 3. The data for $0.2 < x < 0.93$ were obtained from a *single* sample, while the data for the endmembers were obtained from unary a-GeO₂ and a-Ta₂O₅ amorphous films. This data shows some very interesting features. First, the data for the composition spread film extrapolate plausibly to the values obtained for single-composition endmembers. This inspires confidence in the validity of the results. Second, there is a dramatic decrease in the density of a-Ta₂O₅ as Ge is introduced (right hand side of the plot), unlike the more gentle increase in density of a-GeO₂ as Ta is introduced. This suggests a dramatic rearrangement/disruption of the bonding in a-Ta₂O₅ by Ge. Third, there are two regions where the density changes abruptly, albeit not dramatically, occurring at $x \sim 0.35$ and $x \sim 0.7$. The consistent trends below and above these compositions lend weight to

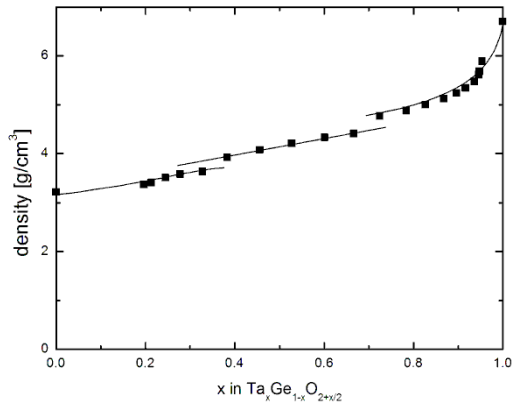


Figure 3. Density of amorphous Ta-Ge-O films inferred using X-ray reflectivity.

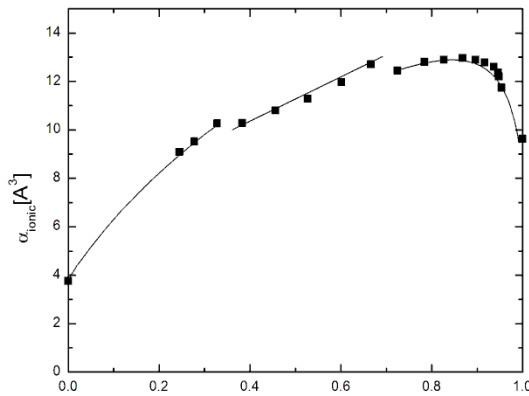


Figure 4. Ionic polarizability of Ta-Ge-O, inferred using the dielectric constant and the Clausius-Mossotti relation (subtracting the values for the electronic polarizability inferred from optical data).

vibrational spectra will provide robust information about bonding as a function of composition. The challenge will be to isolate the spectral features that yield important clues about the behavior of the materials. Collaboration with computational experts may further illuminate the structural and electronic data, although modeling amorphous materials is likely to be compute-intensive.

The future is bright for these studies, which are dramatically extending the breadth of our knowledge of the behaviors and trends as well as the depth of our understanding of the structure/property relations in complex amorphous dielectrics.

the interpretation that they reflect real changes in the bonding and local structure of the amorphous material. Further study will be required to elucidate the nature of these changes, including the question of whether they can be considered an amorphous/amorphous phase transition.

The density is inversely related to the molecular volume that is used to infer the electronic and ionic polarizabilities, so it is not surprising that there are discontinuities in these inferred values, as illustrated in Figure 4. It remains to be seen whether these changes in polarizability represent fundamental effects.

The different trends for Ta incorporation into a-GeO₂ compared to Ge incorporation in Ta₂O₅ are unmistakable, however, and evidently reflect a dramatically different response, no doubt related to the different structural reconfiguration occurring.

Challenges

We look forward to obtaining more detailed information regarding the local structure of the amorphous films. We have used EXAFS to obtain information about the atom-atom distances and therefore structure in amorphous dielectric films designed for optical amplifier applications; with astute modeling this technique should provide valuable insight into local structure. We anticipate that studies of FTIR and Raman

References

- [1] R. B. van Dover and L. F. Schneemeyer, "The Codeposited Composition Spread Approach to High-Throughput Discovery/Exploration of Inorganic Materials," *Macromolecular Rapid Communications*, vol. 25, pp. 150-157, 2004.
- [2] G. D. Wilk, R. M. Wallace, and J. M. Anthony, "Hafnium and zirconium silicates for advanced gate dielectrics," *Journal of Applied Physics*, vol. 87, pp. 484-92, 2000.
- [3] J. Robertson, *J. Appl. Phys.*, vol. 69, pp. 327, 2006.
- [4] M. Heyns and W. Tsai, *MRS Bulletin*, vol. 34, pp. 485, 2009.
- [5] R. B. van Dover, M. L. Green, L. Manchanda, L. F. Schneemeyer, and T. Siegrist, "Composition-dependent crystallization of alternative gate dielectrics," *Appl. Phys. Lett.*, vol. 83, pp. 1459-1461, 2003.
- [6] R. M. Fleming, C. M. Varma, D. V. Lang, C. D. W. Jones, M. L. Steigerwald, and G. R. Kowach, "Coulomb glass origin of defect-induced dielectric loss in thin-film oxides," *Applied Physics Letters*, vol. 78, pp. 4016-18, 2001.

Title: Mesoscale Interfacial Dynamics in Magnetolectric Nanocomposites

Principal Investigator: Dwight Viehland

Co-PI's: Shashank Priya and Armen Khachaturyan

Mailing Address: 201 Holden Hall, Dept. Materials Science and Engineering, Virginia Tech, Blacksburg, VA 24061.

Email: viehland@mse.vt.edu

Problem Scope: Multiferroic materials have a coexistence of at least two ferroic orders (ferroelectric, ferromagnetic, or ferroelastic). In multiferroic materials, the coupling interaction between the different order parameters can produce new phenomena, such as the magnetolectric (ME) effect. The ME response is the appearance of an electric polarization \mathbf{P} upon applying a magnetic field \mathbf{H} , and/or the appearance of a magnetization \mathbf{M} upon applying an electric field \mathbf{E} . Magnetolectricity has been observed as an intrinsic effect in some natural materials at low temperature [1-6]; however, such single phase materials suffer from extremely weak ME exchange. Better alternatives are two-phase composites consisting of magnetostrictive and piezoelectric phases, which have been shown to have large ME coefficients. Said composites exploit a unique product ME tensor property that depends upon the individual strictions of the piezoelectric and magnetostrictive phases, the elastic stiffness and integrity of the interphase interfaces, the phase distribution and the dimensionality of its connectivity, and any elastic constraint; amongst other things.

We have developed various nano-structures ranging from nano-rods, nano-belts, self-assembled two phase grains, to multilayer heterostructures: a few of which are shown in Figure 1. The specific objectives of this program are as following (i) investigation of the local magnetolectric coefficient using magnetic force microscopy and piezo force microscopy; (ii) determine microstructure of the interfaces between magnetic and piezoelectric phases, using electron microscopies; (iii) find the correlation between local and bulk magnetolectric responses, the interfacial microstructure for fine scale composites of various phase connectivities, and (iv) develop a 3D Phase Field model of spontaneously self-organizing nano-scale microstructures.

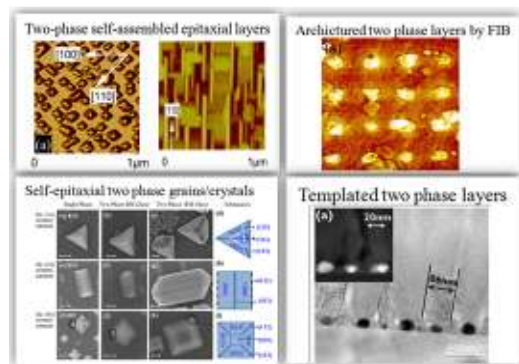


Figure 1. Illustration of some of the nanostructures fabricated in our investigations.

Recent progress:

In the last several years, we have made progress in numerous areas of multiferroic thin layers. These include, as examples, (i) highly oriented growth of BTO thin film on Metglas and their magnetolectric coupling effect; and (ii) giant magnetolectric coefficients in CFO/BFO self-assembled nanocomposites grown on piezoelectric PMN-x%PT substrates.

(i) Highly oriented growth of BTO thin film on Metglas and their magnetolectric coupling effect

We have investigated ferroelectric BaTiO₃ (BTO) thin films deposited on ferromagnetic Metglas slices (25 μm in thickness), which formed a new metal-oxide two-layer multiferroic thin film heterostructure. Ferromagnetic and ferroelectric measurements show that we can obtain well crystallized piezoelectric thin film while keeping the magnetostriction property and eliminating oxidation of the metal layer. SEM and XRD shows highly oriented BTO grown in the (111) direction according to the Au (111) direction. Finally, a ME coupling coefficient of about ~60 mV/cm Oe was accomplished with a 2 μm BTO thin film on Metglas.

Ferroelectric polarization was characterized by a polarization hysteresis measurement using a triangular signal with a frequency of 100 KHz. Well-defined ferroelectric hysteresis loops (Figure 2a) showed a saturation polarization of $P_s \approx 25 \mu\text{C}/\text{cm}^2$ and a remnant polarization of about $P_r \approx 7.5 \mu\text{C}/\text{cm}^2$. The coercive field was 1.25 MV/m. Piezoelectric measurement showed well-defined butterfly shapes (Figure 2b), with a saturation out-of-plane piezoelectric coefficient value (d_{33}) of $\sim 11 \text{ pm}/\text{V}$.

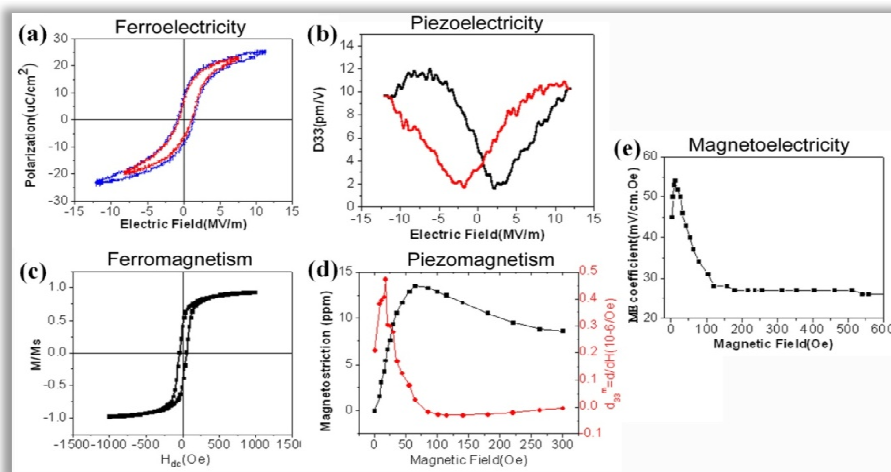


Figure 2. Multi-ferroic and magnetoelectric properties of BTO film on Metglas. (a) Ferroelectric hysteresis loop, (b) piezoelectric d_{33} hysteresis loop, (c) normalized magnetization hysteresis loop, (d) magnetostrictive and piezomagnetic curves, and (e) ME coupling coefficient.

Metglas was selected because of its high magnetic permeability and its thin size ($\sim 20 \mu\text{m}$): it is ideally suited for thin film structures. Fig 2c shows typical M-H loop for Metglas after high temperature deposition process, which was taken using a VSM. The saturation field was $\sim 400 \text{ Oe}$, and it shows a coercive field of $\sim 60 \text{ Oe}$. Fig 2d shows the magnetostriction of Metglas measured by a strain gauge method. At about 80 Oe dc magnetic field, the magnetostriction can reach a value of about 14 ppm . Although this magnetostriction value is small, the effective linear piezomagnetic coefficient of $0.5 \text{ ppm}/\text{Oe}$ is comparable with that of Terfenol-D which has the highest magnetostrictive property.

The ME coupling coefficient is shown in Fig 2e. BTO/Metglas two layer composite structures had a maximum magnetoelectric coefficient of $55 \text{ mV}/\text{cm}\cdot\text{Oe}$, which is much larger than regular ME multi-layer composite thin films. One reason is the metal substrate, which has a larger piezomagnetic coefficient compared to oxide ferrite materials. Another reason is that substrate is the FM phase, so this structure does not have a large constraint stress, which is unavoidable in most (2-2) structure thin films on regular oxide substrates. Furthermore, our ME thin film composite can reach the maximum value of α_{ME} at only $20\sim 30 \text{ Oe}$: this means it is more practical and more sensitive in ME sensors.

(ii) Giant magnetoelectricity in $\text{CoFe}_2\text{O}_4\text{-BiFeO}_3$ self-assembled nanocomposites grown on PMN-PT substrates

We have grown $\text{CoFe}_2\text{O}_4\text{-BiFeO}_3$ (CFO-BFO) self-assembled two phase nanocomposites on (001) oriented single crystals of piezoelectric $\text{Pb}(\text{Mg}_{1/3}\text{Nb}_{2/3})\text{O}_3\text{-x}\%\text{PbTiO}_3$ or PMN-PT. These two phase layers had nanostructures similar to that shown in Figure 1a. Similar investigations were performed on CFO heterostructure layers grown on PMN-PT. Figure 3 shows the electric field control of the magnetization for CFO-BFO / PMN-PT. The results

show the dependence of M on step function changes in electric field of +/-50V, which had an equivalent electric field of E=1kV/cm. In this figure, we can see notable changes in M with E, demonstrating a significant ME susceptibility α_{me} . We calculated the value of α_{me} to be $1.7 \times 10^{-7} \text{ s} \cdot \text{m}^{-1}$. This is an extremely high value of ME: equal to that of the best laminated composites, and orders of magnitude higher than that of single phase material or thin layer structure yet reported. Corresponding investigations of single phase CFO layers grown on PMN-PT revealed values nearly an order of magnitude smaller than that of the self-assembled two phase layer.

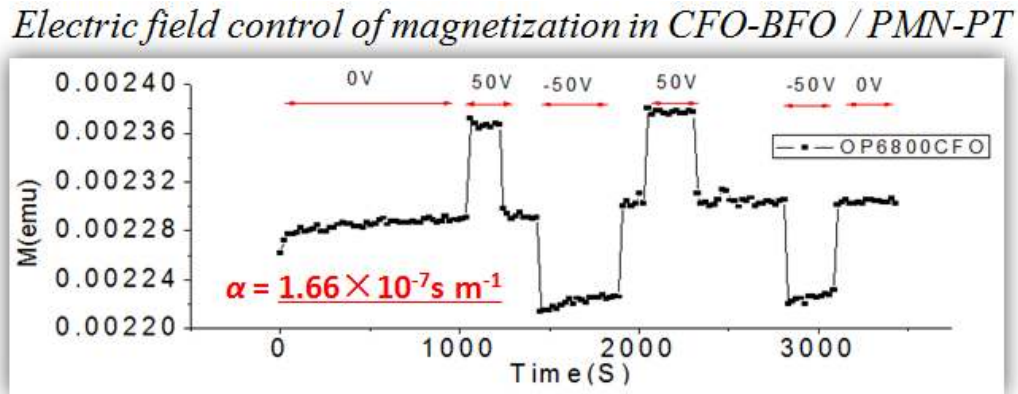


Figure 3. Electric field dependence of the magnetization in self-assembled CFO-BFO two phase nanocomposites grown on (001) oriented PMN-PT substrates.

(iii) Fundamental understanding of clamping effect in thick ferroelectric films

We were successful in fabricating clamped, “island,” and free-standing 10 μm -thick piezoelectric films using aerosol deposition. The deposition was conducted at room temperature by impinging the piezoelectric particles flowing through the nozzle onto platinumized silicon (Pt/Ti/SiO₂/Si) substrate and crystallization was conducted by annealing at 700°C. Free-standing films were synthesized by increasing the cooling rate from annealing temperature to room temperature which resulted in large internal stress between the substrate and film interface. Dielectric and ferroelectric characterization showed enhanced ferroelectric performance of free-standing films as compared to continuous or clamped film which was associated to increased domain contribution due to decrease in degree of clamping as further confirmed by piezo force microscopy. Figure 4 shows the schematic representation of the stress present in the film as a function of the electrode dimension and the effect of stress on the ferroelectric response.

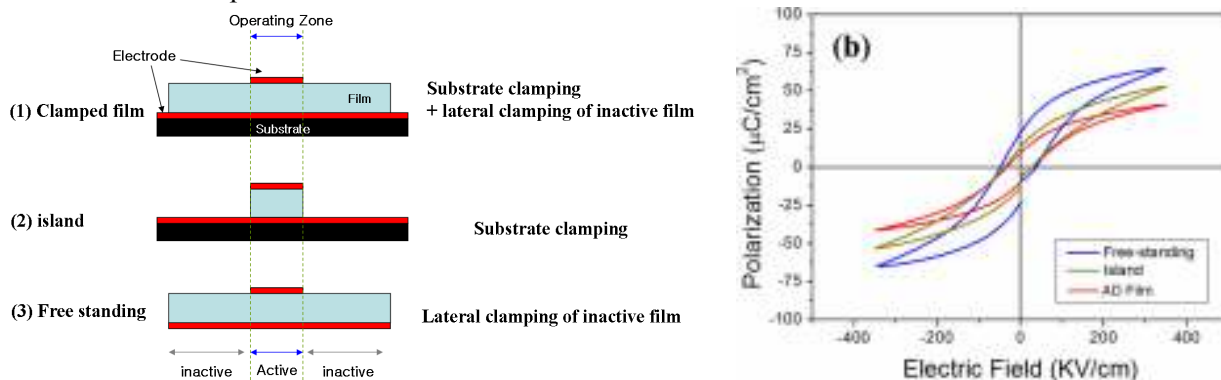


Figure 4: Clamped, island, and free-standing films exhibiting two kinds of clamping, one arising from the substrate and other from the inactive area of film. P-E loop comparison between clamped, island and freestanding thick films under the sweep of 360 kV/cm with frequency of 100Hz.

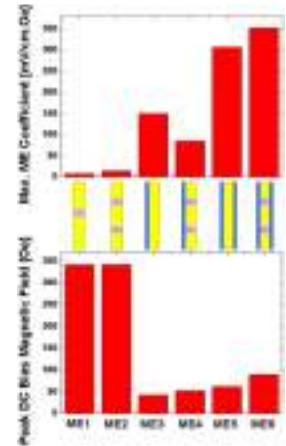
(iv) Enhanced Magnetolectric Properties in Three Phase Composites with 2-1-2 Connectivity

We synthesized 2-1-2 magnetolectric (ME) laminate composite having configuration Metglas / PZNT / Metglas with ferrite pillars embedded in the PZNT phase. The piezoelectric layer with composition $0.2\text{Pb}(\text{Zn}_{1/3}\text{Nb}_{2/3})\text{O}_3\text{-}0.8\text{Pb}(\text{Zr}_{0.5}\text{Ti}_{0.5})\text{O}_3$ (PZNT) consisted of co-fired $(\text{Ni}_{0.6}\text{Cu}_{0.2}\text{Zn}_{0.2})\text{Fe}_2\text{O}_3$ (NCZF) pillars. The top and bottom Metglas layer in the sandwich structure had thickness of 100 μm while the middle piezoelectric layer had thickness of 800 μm . This 2-1-2 composite was found to exhibit the ME coefficient of the order of 352 mV/cm.Oe. Interestingly, the performance of 2-1-2 composite (ME6) is 15% higher than that of conventional 2-2 laminate composite (ME5) as shown in figure on the right. The magnetolectric response for ME6 can be written as:

$$\text{ME6} = [\text{ME5} (1 - (4 \cdot v)/V) - \text{ME2}] \times (\text{ME2}/\text{ME1})$$

where v is the volume fraction of ferrite.

Future Plans: We are developing nano-chessboard structured ME composite thin films. According to the simulation and calculation, several groups of candidates with different lattice constants are chosen and prepared. We will try different substrates and deposition conditions. By changing the annealing temperature and time, it should be able to control the size of the nano-chessboard. With highly ordered nano-structure aligned in our-of-plane direction, the elastic coupling between two phase are expected much stronger than any other two phase ME composites in use.



References: list of papers (already published, in press, submitted) in which DOE support is acknowledged.

1. Yan L, Xing ZP, Wang ZG, Wang T, Lei GY, Li JF, and Viehland D, Direct Measurement of Magnetolectric Exchange in Self-Assembled Epitaxial $\text{BiFeO}_3\text{-CoFe}_2\text{O}_4$ Nano-Composite Thin films, **APPLIED PHYSICS LETTERS**94: **192902** (2009).
2. Yan L, Zhao X, Li JF, and Viehland D, Enhancement of multi-ferroic properties of $\text{Pb}(\text{Fe}_{1/2}\text{Nb}_{1/2})\text{O}_3$ thin films on SrRuO_3 buffered SrTiO_3 substrate by epitaxial stress, **APPLIED PHYSICS LETTERS**94: **192903** (2009).
3. Yan L, Cao H, Li JF, and Viehland D, Triclinic phase in tilted (001) oriented BiFeO_3 epitaxial thin films, **APPLIED PHYSICS LETTERS**94: **132901** (2009).
4. Yan L, Yang YD, Wang ZG, Li JF, and Viehland D, Review of magnetolectric perovskite–spinel self-assembled nano-composite thin films, **JOURNAL OF MATERIALS SCIENCE**44: **5080** (2009).
5. Yan L, Bai FM, Li JF, and Viehland D, Nano-belt structure in perovskite-spinel composite thin films, **JOURNAL OF THE AMERICAN CERAMIC SOCIETY**92: **17** (2009).
6. Yan L, Bai FM, Li JF, and Viehland D, Nano-structures in perovskite-ferrite two phase composite epitaxial thin films, **PHILOSOPHICAL MAGAZINE** 1-4: **103** (2010).
7. Wang Z, Yan L, Yang Y, Wang T, Li JF, Das J, and Viehland D, Highly oriented growth of BTO thin film on Metglas and their magnetolectric coupling effect, **Journal of Applied Physics** (accepted).
8. Yang S., Ahn C.W., Park C.S., Yang Y., Viehland, D. and Priya S., “Controlled synthesis of $\text{MnFe}_2\text{O}_4\text{-Ni}$ core-shell nanoparticles”, **JOURNAL OF MATERIALS SCIENCE** **45**, **1419-1424** (2010).
9. Yang Y., Gao J., Li J., and Viehland D., “Coaxial Multiferroic Nanorod Arrays”, **JOURNAL OF THE AMERICAN CERAMIC SOCIETY**, **362-364** (2010).
10. Yan L., Wang Z., Xing Z., Li J., and Viehland D., “Magnetolectric and multiferroic properties of variously oriented epitaxial $\text{BiFeO}_3\text{-CoFe}_2\text{O}_4$ nanostructured thin films”, **J. APP. PHYS.** **107**, **064106** (2010).
11. Ryu J., Priya S., Park C.-Sung, Kim K.-Young, Choi J.-Jin, Hahn B.-Dong, Yoon W.-Ha, Lee B.-Kuk, Park D.-Soo, and Park C., “Enhanced Domain Contribution to Ferroelectric Properties in Free-Standing Thick Films”, **J. Appl. Phys.** **106**, **024108** (2009).
12. Park C.-S., Ryu J., Choi J.-J., Park D.-S., Ahn C.-W., and Priya S., “Giant Magnetolectric Coefficient in 3-2 Nanocomposite Thick Films”, **Jpn J. Appl. Phys.** **48**, **080204** (2009).
13. Park C. -S., Ahn C., and Priya S., “Enhanced magnetolectric properties in three-phase composites with 2-1-2 connectivity”, **Philosophical Mag.** **90**, **4443 – 4452** (2010).
14. Park C. -S., Cho K., Arat A., Evey J., Priya S., “High magnetic field sensitivity in $\text{Pb}(\text{Zr,Ti})\text{O}_3\text{-Pb}(\text{Mg}_{1/3}\text{Nb}_{2/3})\text{O}_3$ single crystal/Terfenol-D/Metglas magnetolectric laminate composites, **J. Appl. Phys.** **107**, **094109** (2010).

Program Title: Domain Microstructures and Mechanisms for Large, Reversible and An hysteretic Strain Behaviors in Phase Transforming Ferroelectric Materials
Principal Investigator: Yu U. Wang
Mailing Address: Michigan Technological University, Materials Science & Engineering Department, 405 M&M Building, 1400 Townsend Drive, Houghton, MI 49931
E-mail: wangyu@mtu.edu

Program Scope

This project performs theoretical and computational studies of some fundamental principles and mechanisms and their synergistic operations for achieving advanced strain behaviors in phase transforming ferroelectric materials. The research aims to advance the fundamental understanding of field-induced strain behaviors to achieve desired combination of advanced attributes of large, reversible and anhysteretic strains (these strain attributes usually compromise each other, leading to trade-offs that seriously limit material's applicability). The objectives are to: (i) develop phase field approach-based computational tools and perform simulation studies of domain microstructures and mechanisms for achieving advanced strain behaviors; (ii) develop nanodomain diffraction theory to analyze diffraction data, identify nanoscale domain microstructures and mechanisms from diffraction experiments, and correlate computations and experiments; (iii) investigate domain microstructure engineering to exploit the full potential of phase transforming ferroelectric materials; and (iv) advance state-of-the-art understanding of strain behaviors of ferroelectric materials, and shed light on other phase transforming materials such as magnetostrictive materials, conventional and magnetic shape memory alloys.

Recent Progress

Our recent computational studies focus on understanding the fundamental mechanisms of crystallographic domain engineering and the techniques to stabilize the engineered domain configurations. Our prior study shows that self-accommodating lamellar domains provide optimal initial domain microstructures for field-induced inter-ferroelectric phase transformations to exploit desired piezoelectric behaviors with large, reversible and anhysteretic strain attributes. However, to fully exploit the potential of such behaviors for practical application, there are two issues that must be solved: (i) How to control the domain configurations and sizes by crystallographic domain engineering technique? (ii) How to stabilize the engineered optimal domain microstructures? We investigate the underlying mechanisms that control domain configurations and sizes, find optimal processing conditions for crystallographic domain engineering, and explore technique to stabilize the engineered domains so that they do not degrade.

(1) Control of Domain Configurations and Sizes in Crystallographically Engineered Ferroelectrics [1]

We perform computer simulation to study the underlying mechanisms for controlling domain configurations and sizes during crystallographic domain engineering of ferroelectric single crystals. It is found that minimal domain sizes and highest domain wall densities are obtained with intermediate electric field applied along non-polar axis of ferroelectric single crystals, while lower and higher fields produce coarser domains, and temperature also plays important role in domain size control. Our computer simulation shows that selection of polar domain variants by external electric field during nucleation stage of ferroelectric phase transition significantly affects subsequent domain evolution kinetics, controlling the formation and sizes of engineered lamellar domains.

As shown in Figure 1(left), our computer simulation reveals that application of electric field along non-polar axes is an effective way to control the domain evolution and twin microstructure formation in

ferroelectric single crystals. The left column of Figure 1(left) shows the simulated domain formation process in single crystal of tetragonal ferroelectric phase ($\langle 100 \rangle$ as polar axes) under electric field applied along $[111]$ direction, which is a non-polar axis of tetragonal crystal. It is found that (110) twins composed of $[100]$ and $[010]$ polar domains (equally favored by $[111]$ electric field) of stable tetragonal ferroelectric phase are formed as the fully-developed engineered domain configuration, which minimizes local bulk free energy through stable tetragonal phase (green), eliminates charge accumulation through head-to-tail polarization patterns, and self-accommodates electrostrictive strain through structural twins. Similar domain processes are observed in single crystals of rhombohedral ferroelectric phase ($\langle 111 \rangle$ as polar axes) under electric field applied respectively along $[100]$ and $[110]$ directions, which are non-polar axes of rhombohedral crystal. As shown in the central and right columns of Figure 1(left), (100) twins composed of $[1\bar{1}1]$ and $[11\bar{1}]$ polar domains (equally favored by $[100]$ electric field) and (110) twins composed of $[111]$ and $[1\bar{1}\bar{1}]$ polar domains (equally favored by $[110]$ electric field) of stable rhombohedral ferroelectric phase are respectively formed as the fully-developed engineered domain configurations. It is found that phase coexistence through bridging domain mechanism during domain evolution helps reduce the total system free energy of complex domain microstructures and provides low-energy kinetic pathways to final engineered domain configurations with complete self-accommodation.

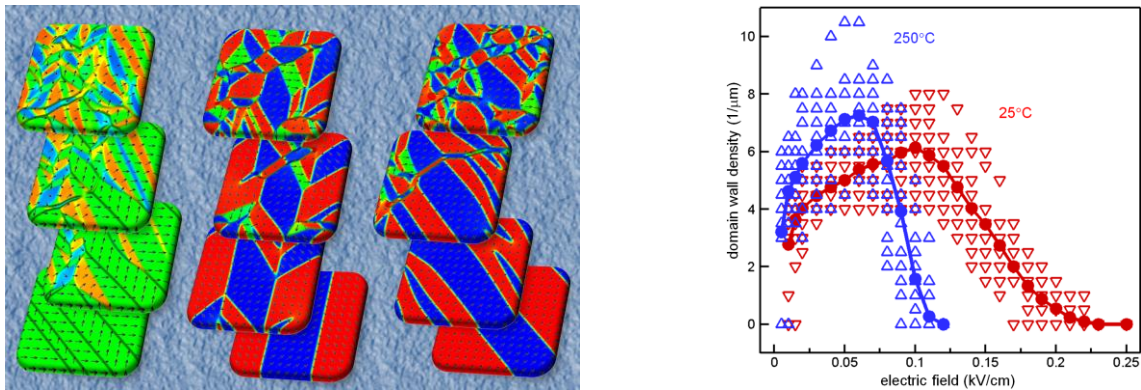


Figure 1. *Left* (Cover Image of *Applied Physics Letters* [1]): Simulation of domain evolution and twin microstructure formation in single crystals under external electric field applied along non-polar axes during ferroelectric phase transition. *Right*: Simulation of dependence of domain wall density in engineered domain configuration on non-polar electric field magnitude.

As shown in Figure 1(right), our computer simulation further shows a systematic dependence of the domain wall density (i.e., average domain size) in the engineered domain configurations on the magnitude of electric field applied along non-polar axes of ferroelectric single crystals. We simulate the formation processes of twin-related lamellar domains of stable tetragonal ferroelectric phase under $[111]$ electric field, as in the left column of Figure 1(left). The single crystal is cooled across Curie temperature down to 25°C in $[111]$ electric field of different magnitudes. The domain wall densities obtained from the simulations are plotted in Figure 1(right). It is found that minimal domain size and highest domain wall density are obtained at intermediate electric field magnitude, while lower and higher fields produce coarser domains thus lower domain wall densities. The simulation shows that selection of polar domain variants by external electric field during nucleation stage of ferroelectric phase transition significantly affects the subsequent domain growth and evolution kinetics, thus controlling the formation and sizes of lamellar domains. It is the competition between nucleation of $[100]$, $[010]$ and $[111]$ variants under $[111]$

electric field that determines the average domain size and (110) domain wall density, and, as a result of such competition, maximal domain wall density is obtained at intermediate electric field magnitude. It is also shown that temperature is another important factor in domain size control, as shown by blue symbols and line corresponding to cooling to 250°C as compared with the red ones of 25°C.

(2) Aging-Stabilization of Ferroelectric Domains by Short-Range Ordering of Charged Point Defects [2]

We employ computer modeling and simulation to study the domain stabilization effect due to short-range ordering of charged point defects in aged ferroelectrics. It is worth noting that above obtained engineered domain configurations with controlled domain sizes provide optimal initial domain microstructures for field-induced inter-ferroelectric phase transformations to exploit desired piezoelectric behaviors with large, reversible and anhysteretic strain attributes. However, for practical application, there is another issue that must be solved: the engineered domain microstructures are sensitive to external electric, mechanical and thermal conditions, thus technique is required to stabilize the engineered domains so that they do not degrade during service. We explore ferroelectric aging as a promising way to stabilize the engineered domain microstructures. The microscopic mechanism of aging and domain stabilization is attributed to short-range ordering of charged point defects in ferroelectric materials, which provides a restoring force to the domains whenever deviated from the original, aged domain configurations. We focus on the domain processes and internal bias electric field that is associated with the short-range ordering of charged point defects. The internal electric field strength is estimated by the computer simulation. Clausius-Clapeyron-type thermodynamic analysis of field-induced ferroelectric phase transition is also performed to evaluate aging-produced internal field strength from relevant experimental data. Both methods give the order of magnitude of 1kV/cm in sufficiently aged samples.

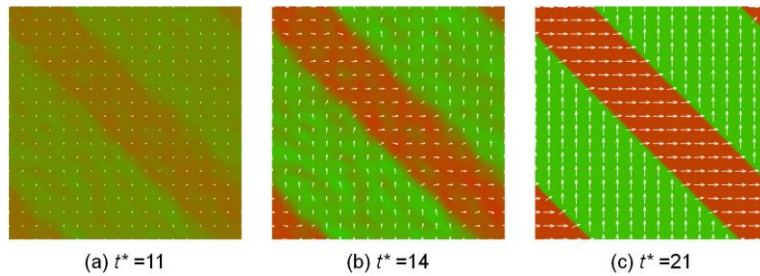


Figure 2. Simulation of domain recovery process in aged ferroelectrics.

Our computer simulation shows that domain microstructures are stabilized in sufficiently aged ferroelectric samples, where the original, aged domain configurations are automatically recovered from arbitrarily deviated states, as shown in Figure 2. In an aged sample, the short-range ordering of point defects is maintained during a diffusionless process, such as domain switching driven by a short-period external field or phase transformation during rapid heating-cooling cycle. Figure 2(a) shows an arbitrary polarization distribution at the nucleation stage of cooling-induced ferroelectric phase transition under the effect of thermal noises; Figure 2(b) shows the growth of polarization vectors and formation of domains; and Figure 2(c) shows the fully recovered domain microstructure that is identical to the original, aged domain configuration. It is found that when internal bias field is of the order of magnitude of 1kV/cm, domain configurations are fully recovered. In such cases, the internal field strongly affects the nucleation of ferroelectric phase upon cooling, where domains nucleate with polarization vectors aligned with local bias field directions, as shown in Figure 2(a). As a result, domain recovery process is very fast.

To compare the simulation results with experiment, we also evaluate the internal bias field strength from relevant experimental data. Based on the fact that aging-generated internal electric field produces

the same effect in individual ferroelectric domains as an externally applied electric field does in electric field-induced ferroelectric phase transformation, we derive a Clausius-Clapeyron-type equation, $dT/dE = \Delta P/\Delta S$, which predicts that the Curie temperature increases with the internal field strength (i.e., degree of aging and short-range ordering of charged point defects) in aged samples. Using experimentally determined data, the internal electric field is estimated to be of the order of magnitude of 1kV/cm, in agreement with our computer simulation.

Future Plans

We will investigate domain microstructure engineering through electric field-induced nucleation, study multiple working principles of inter-ferroelectric phase transformation in phase-coexisting polycrystalline ceramics, and analyze diffraction patterns of simulated nanodomain microstructures.

(a) Field-Induced Nucleation Mechanism for Crystallographic Domain Engineering

Unlike thermally-induced nucleation, electric field-induced nucleation is expected to generate more polar variant nuclei of preferred polarization orientations and produce higher domain wall densities, which in turn provide further improved piezoelectric response. This task will focus on the mechanisms of field-induced nucleation during both ferroelectric and inter-ferroelectric phase transformations. Phase transformation in ferroelectrics exhibits some peculiar behaviors due to strong long-range dipole-dipole-like interactions involved in the system. In particular, electrostatic and elastostatic energies introduce an insurmountable energy barrier to isolated nucleus, and independent ferroelectric nucleation in the context of classical nucleation theory is impossible. In order to circumvent such an energy barrier, nucleation exhibits strong spatial correlation and self-organization behaviors. We will investigate the effects of such correlated nucleation on crystallographic domain engineering.

(b) Synergistic Operation of Multiple Working Principles in Polycrystalline Ceramics

Unlike engineered domain configurations in single crystals where electric field can be applied along well-defined crystallographic directions, phase coexistence is common in polycrystalline ceramics and external electric field corresponds to different crystallographic directions of phases in different grains due to polycrystallinity. Therefore, synergistic operation of multiple working principles in phase-coexisting polycrystalline ceramics is more complicated. We will investigate how these working principles operate in polycrystals, what are the limiting factors preventing property improvement, and explore ways to overcome these problems to exploit the full potential of inter-ferroelectric phase transformations to achieve advanced strain behaviors in polycrystalline ceramics, which is an important material form in practical applications.

(c) Diffraction Analysis of 1D and 2D Nanodomain Microstructures

We will develop nanodomain diffraction analysis technique to calculate diffraction patterns of the simulated domain microstructures and correlate computations and experiments. 1D lamellar nanodomains 2D herringbone nanodomains will be considered.

References

- [1] W.F. Rao, K.W. Xiao, T.L. Cheng, J.E. Zhou, Y.U. Wang, "Control of Domain Configurations and Sizes in Crystallographically Engineered Ferroelectric Single Crystals: Phase Field Modeling," *Appl. Phys. Lett.*, **97**, 162901, 2010. ([Cover Image](#))
- [2] W.F. Rao, T.L. Cheng, Y.U. Wang, "Aging-Stabilization of Ferroelectric Domains and Internal Electric Field due to Short-Range Ordering of Charged Point Defects: Phase Field Modeling," *Appl. Phys. Lett.*, **96**, 122903, 2010.

Piezoelectric nanogenerators for self-powered nanosystems and nanosensors

Zhong Lin Wang*

School of Material Science and Engineering, Georgia Institute of Technology,
Atlanta, Georgia 30332-0245 USA

*e-mail: zlwang@gatech.edu; website: <http://www.nanoscience.gatech.edu/zlwang/>

PROGRAM SCOPE

The future of nanotechnology research is likely to focus on the areas of integrating individual nanodevices into a nanosystem that acts like living specie with sensing, communicating, controlling and responding. A nanosystem requires a nano-power source to make the entire package extremely small and high performance. The goal is to make self-powered nanosystem that can operate wirelessly, independently and sustainably. Harvesting energy from the environment is a choice for powering nanosystems especially for biomedical applications. Since mechanical energy is a conventional form of energy that exists in our living environment, it is essential to explore innovative nanotechnologies for converting mechanical energy (such as body movement, muscle stretching), vibration energy (such as acoustic/ultrasonic wave), and hydraulic energy (such as body fluid and blood flow) into electric energy that will be used to power nanodevices without using battery. This is a key step towards *self-powered nanosystems*.

We have invented an innovative approach for converting mechanical energy into electric energy by piezoelectric zinc oxide nanowire arrays [1]. The operation mechanism of the nanogenerator (NG) relies on the piezoelectric potential created by an external strain; a dynamic straining of the nanowire results in a transient flow of the electrons in the external load due to the driving force of the piezopotential. We have developed the nanogenerator technology from fundamental science, to engineering integration and to technological scale-up [2, 3, 4]. As today, a gentle straining can output 1-3 V at an instant output power of $\sim 2 \mu\text{W}$ from an integrated nanogenerator [5, 6, 7], using which a self-powered nanosensor has been demonstrated [6]. This technology has the potential applications for power MEMS/NEMS that requires a power of in the μW to mW range.

PIEZOELECTRIC POTENTIAL

The fundamental of nanogenerator relies on the presence of the piezoelectric potential (piezopotential) generated in a nanowire/nanobelt via dynamic straining. ZnO has the wurtzite structure, in which the tetrahedrally coordinated O^{2-} and Zn^{2+} are stacked layer by layer along the c-axis. The lack of central symmetry of the wurtzite structure results in the piezoelectric property of ZnO, which is vital for the mechanic-electric energy conversion with the ZnO-based nanogenerator.

The cations and anions are tetrahedrally-coordinated in the wurtzite-structured ZnO. At the strain free status, the charge-center of the cations and that of anions coincide with each other. When an external strain is applied, the structure is deformed so that the charge-centers for cations and anions separate and result in an electric dipole. Because the ionic charges are not free to move and the intrinsic free charge carriers can only partially screen them if the doping level is low, the piezoelectric field is preserved as long as the NW is strained. The potential created by the polar ions is called *piezoelectric potential, or piezopotential* [8].

The presence of piezopotential is the fundamental

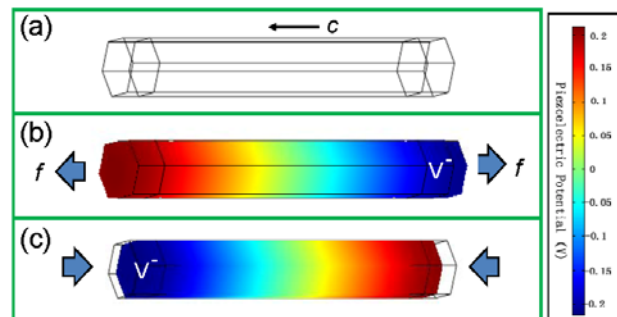


Fig. 1. Numerical simulation of the piezopotential distribution in an insulating ZnO nanowire. (a) The piezopotential distribution and the deformed shape of a ZnO nanowire grown along c-axis under a stretching force of 85 nN (b), or a compressing force of 85 nN (c) (from [10]).

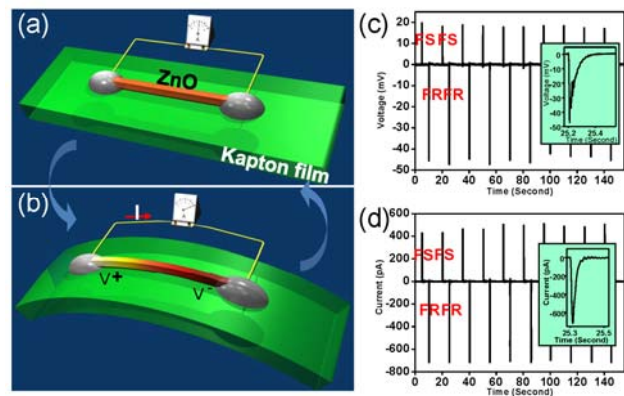


Fig. 2. Design and power output from a single wire generator. (a) and (b) schematic diagram of single wire generator before and after stretching. Open-circuit voltage (c) and short-circuit current (d) of the single wire generator, which was cyclically fast stretched and fast released (from [5]).

physical basis of the nanogenerators and piezotronics. When a strained crystal is connected to an external load, the electrons in the circuit are driven to flow in to partially screen the piezopotential, which is the energy conversion process. Therefore, *the principle of the nanogenerator is the transient flow of electrons in external load as driven by the piezopotential created by dynamic straining.*

RECENT PROGRESS

Single Wire Generator – Demonstration of Principle [3]

Piezopotential-driven transient flow of electrons in an external load is the principle of the nanogenerator. Figure 2 presents a single wire generator (SWG) using a laterally packaged ZnO wire. In brief, a single ZnO wire was placed laterally on the flexible polyimide film. Silver paste can be used to fix two ends of the ZnO wire to the substrate and link the wire to the external measuring instrument through metallic wires. Electric measurement shows that a functioning SWG usually has rectifying I-V characteristic, indicating the existence of the Schottky contact at least at one end. Before we deform the SWG, there is no measurable potential drop from the ZnO wire. When we bend the substrate, both the substrate and the ZnO wire are under strain. Because the thickness of the substrate is much larger than the dimension of the ZnO wire, the ZnO wire is solely experiencing tensile strain when the bend is concave downward, as shown in Figure 3b. As discussed earlier, tensile strain will result in piezopotential, such that the $+C$ -axis side gains positive potential (light yellow) and $-C$ -axis side gains negative potential (dark red). The potential difference between the two ends can then be measured either as open-circuit voltage (Figure 2c) or short-circuit current (Figure 2d).

The working mechanism of the SWG can be understood with the energy band diagram in Figure 3. The Schottky contact at least at one end is necessary for the energy generation. We assume the Schottky contact is at the $+C$ -axis side (left side in Figure 3a), and the energy generation follows in a similar way when the Schottky contact is on the other side or both sides. The entire wire is in equilibrium state without any strain and power output (Figure 3a and 3e). When the wire is stretched, the tensile strain induces polarization of atoms, as well as piezoelectric field, in the crystal. Consequently, the $+C$ -axis side holds positive potential and the $-C$ -axis side holds negative potential. The potential difference is ΔE_p . The conduction band edge, as well as the Fermi level of the metal of the right side electrode, rises up for the same amount of ΔE_p . The electrons in the external circuit should flow from the right-hand side to the left-hand side to compensate the energy difference, which will generate the first output signal if the flow rate is sufficiently large, as indicated in Figure 3b and 3e. The electrons cannot flow across the interface due to the presence of a Schottky barrier ϕ_{SB} . The accumulation of the electrons at the interface will partially screen the piezopotential built in the wire. When the electrons and the piezoelectric field reach equilibrium, the Fermi energy on both sides is on the same level and there is no more current flow (Figure 3c and 3e). When the SWG is fast released, there is no strain inside the NW. As a result, the polarization and piezoelectric field vanish as well and the equilibrium with the accumulated electrons is broken. The accumulated charge carriers flow back from the left-hand

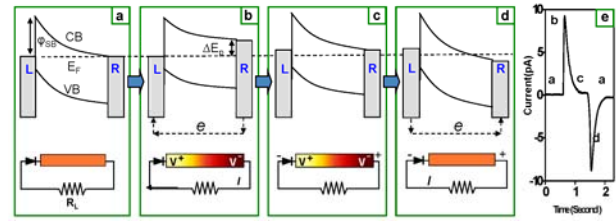


Fig. 3. Current generation mechanism explained with energy band diagram of the cyclically stretched NW. Energy band diagram of the ZnO NW in equilibrium and free condition (a), non-equilibrium and tensile strained condition (b), re-reached equilibrium and tensile strained condition (c), and non-equilibrium and free condition (d). After (d), the NW will reach equilibrium as in (a) after charges flow. E_F , CB, VB, ϕ_{SB} , and ΔE_p indicate Fermi level of the electrode, conduction band and valence band of ZnO, Schottky barrier height, and piezopotential difference respectively. (e) Short-circuit current measurement in which the labels of a, b, c, and d indicate the corresponding process shown in subparts a-d (from [5]).

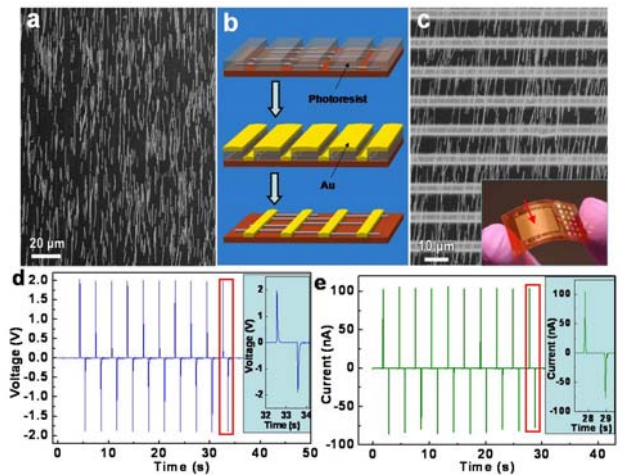


Fig. 4. Fabrication process and performance of the high-output nanogenerator (HONG). **a**, SEM image of the as-transferred horizontal ZnO NWs on a flexible substrate. **b**, Process of fabricating Au electrodes on horizontal ZnO NW arrays, which includes photolithography, metallization, and lift-off. **c**, SEM image of ZnO NW arrays bonded by Au electrodes. Inset: demonstration of an as-fabricated HONG. The arrowhead indicates the effective working area of the HONG. **d**, Open circuit voltage measurement of the HONG. **e**, Short circuit current measurement of the HONG. The measurement is performed at a strain of 0.1% and strain rate of $5\% s^{-1}$, with the deformation frequency of 0.33 Hz. The insets are the enlarged view of the boxed area for one cycle of deformation (from [7]).

side to the right-hand side through the external circuit, producing the second output signal in the opposite direction, as shown in Figure 3d and 3e.

High Output Nanogenerator by Three-Dimensional Integration

Integration of SWGs is a major step towards the practical applications. Taking advantage of the small size of the NW, we can build multiple SWGs on a single substrate such that the hamster can drive all SWGs simultaneously. Integration of up to four SWGs in serial has been demonstrated with the open-circuit voltage of ~ 0.1 - 0.15 V [5-9]. The output current can also be improved with multiple SWGs in parallel. The work on the human finger and living hamster clearly demonstrated the capability of the SWG to scavenge mechanical energy from the biosystem. It also confirms the feasibility of using the SWG for harvesting the energy created by regular and irregular motions.

To make nanogenerator practically useful for powering medical devices, it is vitally important to improve its performance. This is a key step for technological applications. Our recent progress in the field opens a door for this approach (Fig. 4a-c). The nanogenerator with integrated nanowires in 2 dimensional achieved a peak output power density of $\sim 0.22 \mu W/cm^2$. The generated electric energy was effectively stored by utilizing capacitors, as shown in Figure 4d-e. More significantly, the stored electricity was successfully used to light up a commercial light-emitting diode (LED) (Figure 5), which is a landmark progress toward building self-powered devices by harvesting energy from the environment.

The example shown in Fig. 5 is a first step toward self-powered nanosensors. Our goal is to build self-powered nanosystem that can acquire the data, process the data and transmit the data. The first step is to improve the power output of a nanogenerator so that it will be effective in driving a nanosensor and the associated electronics. A continuous improvement in the performance of the nanogenerator will be the core of our research in the next two years. Our goal is to build self-powering system that can be adequately applied to medical science.

We propose that, by optimizing the density of the NWs on the substrate and with the use of multi-layer integration, a peak output power density of $\sim 0.44 mW/cm^2$ and volume density of $1.1 W/cm^3$ are predicted. This is the first goal that we will target at. Our approach will focus on the alignment and assembly of densely packed nanowires on a flexible substrate, through which we anticipate to achieve high output power.

ACKNOWLEDGEMENT

Thanks to the support from BES DOE (Program director: Dr. Refik Kortan).

REFERENCES

- [1] Z.L. Wang and J.H. Song "Piezoelectric Nanogenerators Based on Zinc Oxide Nanowire Arrays", *Science*, vol. 312, pp. 242-246, 2006.
- [2] Y. Qin, X.D. Wang and Z.L. Wang "Microfiber-Nanowire Hybrid Structure for Energy Scavenging", *Nature*, vol. 451, pp. 809-813, 2008.
- [3] R.S. Yang, Y. Qin, L.M. Dai and Z.L. Wang "Flexible charge-pump for power generation using laterally packaged piezoelectric-wires", *Nature Nanotechnology*, vol. 4, pp. 34-39, 2009.
- [4] S. Xu, Y. Qin, C. Xu, Y.G. Wei, R.S. Yang, Z.L. Wang "Self-powered Nanowire Devices", *Nature Nanotechnology*, vol. 5, pp. 366-373, 2010.
- [5] G. Zhu, R.S. Yang, S.H. Wang, and Z.L. Wang "Flexible High-Output Nanogenerator Based on Lateral ZnO Nanowire Array", *Nano Letters*, vol. 10, pp. 3151-3155, 2010.
- [6] Y.F. Hu, Y. Zhang, C. Xu, G. Zhu and Z.L. Wang "High output nanogenerator by rational unipolar-assembly of conical-nanowires and its application for driving a small liquid crystal display", *Nano Letters*, 10 (2010) 5025-5031.
- [7] S. Xu, B.J. Hansen and Z.L. Wang "Piezoelectric-Nanowire Enabled Power Source for Driving Wireless Microelectronics", *Nature Communications*, vol. 1 Article Number: 93 (2010).
- [8] Z.Y. Gao, J. Zhou, Y.D. Gu, P. Fei, Y. Hao, G. Bao, Z.L. Wang "Effects of Piezoelectric Potential on the Transport Characteristics of Metal-ZnO Nanowire-Metal Field Effect Transistor", *J. Appl. Physics*, vol. 105, 113707, 2009.

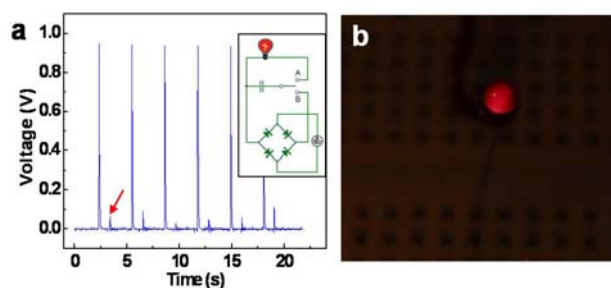


Fig. 5 Application of the electric energy generated by the integrated nanogenerator to drive a commercial light emitting diode. **a**, The electric output measured after a full wave rectifying bridge. Signals of negative signs are reversed, as pointed by the arrowhead. Inset: Schematic of the charging-discharging circuit for storing and releasing the energy generated by the generator, respectively. **b**, Image of the LED in dim background at the moment when it was lit up by the energy generated (from [7]).

Dynamical Materials Nanostructures for Energy Technology

Electronic Materials Program at LBNL

PIs: Junqiao Wu (wuj@berkeley.edu), Daryl C. Chrzan, Kin M. Yu

Materials Sciences Division, Lawrence Berkeley National Laboratory, Berkeley, CA 94720

External collaborators: Jeffrey C. Grossman (MIT), L. Q. Chen (Penn State Univ.), Renkun Chen (UC San Diego), Markus Raschke (Univ. Colorado)

Recent Progress

In the past several years, we have pioneered the investigation of domain and size effects on the metal (M) - insulator (I) phase transition of vanadium dioxide (VO_2) and related materials. Strain-free VO_2 undergoes the first-order metal-insulator transition at $\sim 67^\circ\text{C}$ with a drastic change in conductivity and optical reflection. The M-I transition is accompanied with a structural change from the low-temperature, insulating, monoclinic phase to the high-temperature, metallic, tetragonal phase.

We have shown that: i) single-crystal, strain-free VO_2 and $\text{W}_x\text{V}_{1-x}\text{O}_2$ nanobeams support single-domain M-I phase transition, in contrast to a percolative behavior in VO_2 thin films that yields averaged measurement results (Fig.1(a)); ii) one-dimensional ferroelastic domain arrays and single domain walls can be created and manipulated along VO_2 nanobeams by controlling temperature and strain; iii) the M-I domain wall of VO_2 has a wall energy density of 25mJ/m^2 , and carries a unique functionality that filters hot electrons from cold ones in a DC current flow; iv) superior mechanical strength of the nanobeams allows for mapping and exploration of their electronic phase diagram over a strain area ten times broader than previously attained; v) high-energy particle irradiation introduces point defects that strongly pin the domain walls and reduce thermal conductivity; vi) twin walls in I-phase VO_2 control the I-M phase transition kinetics by nucleating domains, and, as shown by colleagues in Oak Ridge, can become electrically conductive, featuring a M-I transition different from that of the bulk.

These achievements demonstrate that rich materials physics can be revealed in correlated electron materials when their phase transition is probed at the single or few-domain level. In addition, it shows that the dynamical

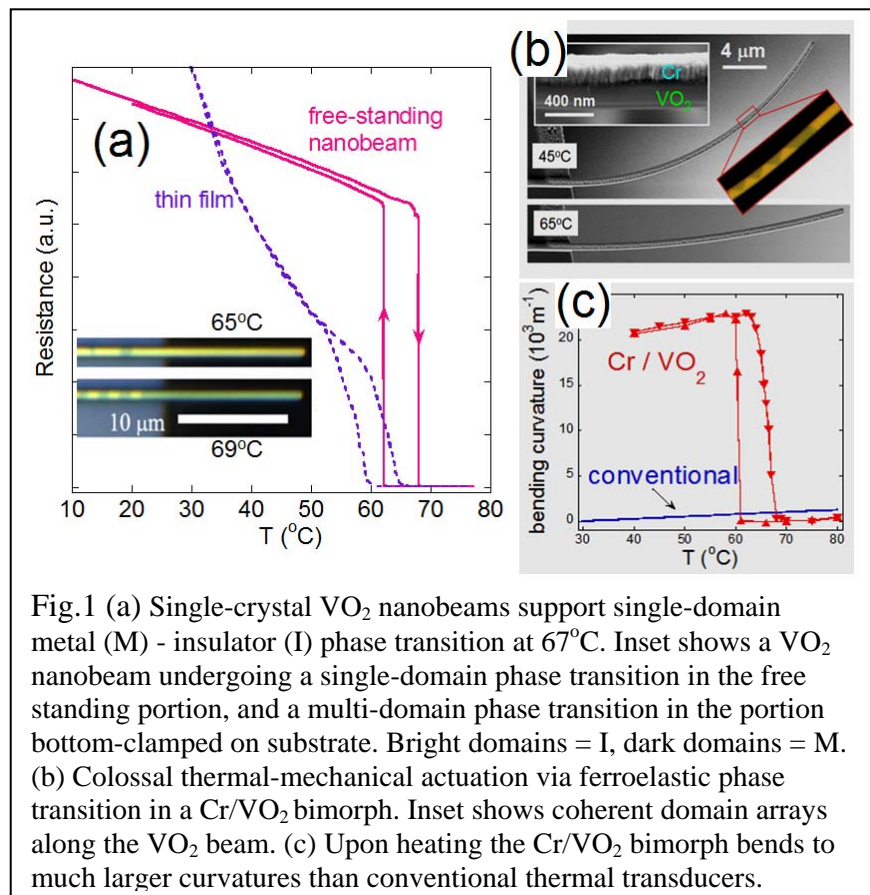


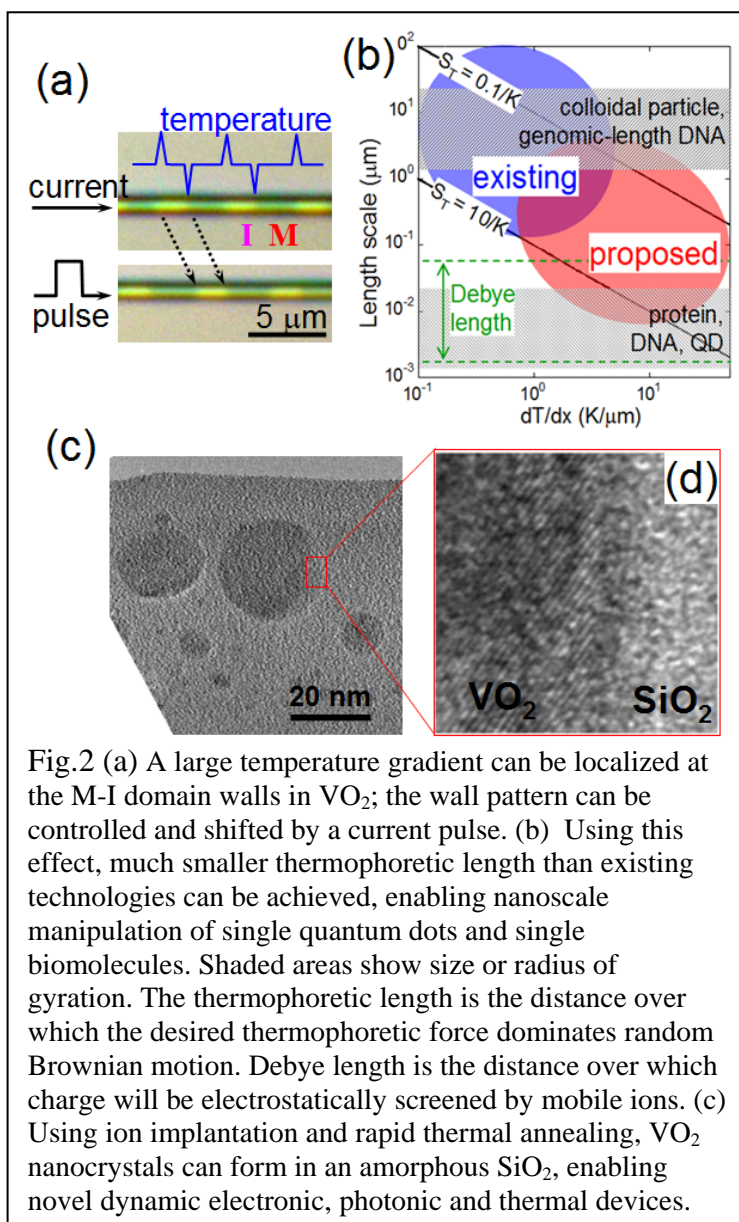
Fig.1 (a) Single-crystal VO_2 nanobeams support single-domain metal (M) - insulator (I) phase transition at 67°C . Inset shows a VO_2 nanobeam undergoing a single-domain phase transition in the free standing portion, and a multi-domain phase transition in the portion bottom-clamped on substrate. Bright domains = I, dark domains = M. (b) Colossal thermal-mechanical actuation via ferroelastic phase transition in a Cr/VO_2 bimorph. Inset shows coherent domain arrays along the VO_2 beam. (c) Upon heating the Cr/VO_2 bimorph bends to much larger curvatures than conventional thermal transducers.

electronic, optical and structural properties accompanying the phase transition in these nanomaterials can be engineered for novel energy applications. For example, in Fig.1(b) and (c) we show that when clamping a VO₂ nanobeam with an inactive layer (e.g., Cr) forming a bimorph, the mechanical instability of such a ferroelastic/paraelastic system renders its shape and resistance extremely sensitive to environmental fluctuations, such as temperature change, air convection, wind blowing, and sound agitation. This offers interesting opportunities to fabricate novel sensing, actuation, and energy transducing devices, which is a research topic that we are actively working on.

Future Plans

Based on our previous achievements, we propose to explore these nanoscale dynamical materials structures for innovative energy applications. Specifically within the Electronic Materials Program, we plan to work on the following two projects.

i) Explore and exploit electrothermal effects of M-I domain walls for nanoscale thermal energy management. We have shown that a DC current flowing across the M-I domain walls in a VO₂ nanobeam causes strong local heating or cooling owing to electron rectification at the wall. The Schottky barrier at the M-I wall effectively filters hot electrons from the current and prohibits cold electrons flow across the wall, thereby locally cooling the wall via the junction Peltier effect. This cooling may even convert the M domain into I phase, effectively driving the M-I wall to move along the current direction (Fig.2(a)). The moving speed of the wall is limited, in principle, only by the sound velocity in VO₂ (>10³m/s), which enables high-speed manipulation of individual walls. This dynamical electrothermal effect at the M-I wall needs to be better understood. We will use scanning photocurrent microscopy to probe local electric field and scanning thermal microscopy to measure local temperature variation around the wall, which will allow us to quantify, for the first time, the electrothermal effect at a single wall, i.e., the junction Peltier coefficient, the



energy barrier height, and their dependence on defects, doping and stress.

This effect can be exploited to implement novel nanoscale, rewritable and mobile photodiode, rectifier, cooler, or memory. We will use the wall to manage heat such that a large temperature gradient can be localized at the nanoscale and at arbitrary locations. Thermal management at the micron and sub-micron scales is a major challenge facing many interdisciplinary fields ranging from biology and microfluidics to optoelectronics and thermoelectrics. For example, in molecular biology, it is vitally important to localize and control a temperature gradient in aqueous environment. Localized hot spots (30~80°C) in living cells allow *in vivo* gene regulation because it can release a molecular cargo on demand by a thermal switch; Also, localized temperature gradient is widely used to manipulate colloidal particles and macro-biomolecules, a process known as thermophoresis that offers superior controllability over electrophoresis. Currently, this is mostly achieved by using lithographically patterned micro-heaters or near-IR laser heating. The former method suffers from immobility of the active spots and the latter method is spatially limited by the size of the laser focal point. Currently achieved temperature variation is typically over a length scale of more than 10 μm and the temperature gradient is less than $\sim 1^\circ\text{C}/\mu\text{m}$.

The electrothermal functionality at single domain walls in VO_2 creates high temperature gradient at the sub-micron length scale, whereas the active spot is rewritable and displaceable. We estimated that the theoretical temperature gradient across an M-I wall can be over $10^\circ\text{C}/\mu\text{m}$ and the temperature decay length is smaller than ~ 100 nm. Namely, an extremely high temperature gradient can be established around an M-I domain wall at extremely short length scale, both exceeding current technologies by orders of magnitude. For example, in Fig.2(b) it is shown that the thermophoretic length, the distance over which the thermal gradient driving force dominates random Brownian motion, could be pushed down by over an order of magnitude, reaching the gyration radii of typical biomolecules as well as the electrostatic Debye length in ionic liquids. Precise placement and displacement of such hot spots by the domain wall motion would also enable direct programming of specific, localized biological activities in living cells. Therefore, a wide range of ground-breaking single-molecule and single-particle experiments would immediately become possible.

ii) Investigate effects of mechanical confinement on M-I transition in VO_2 nanocrystals for memory and optical switch. The approach exploits the sub-picosecond M-I transition in mechanically confined VO_2 nanocrystals that is modulated dynamically by external field, light illumination and/or temperature. The nanocrystals are formed in an amorphous SiO_2 matrix by ion implantation and subsequent thermal processing, as shown in Fig.2(c) and (d).

In the memory mode, free electrons are injected to VO_2 nanocrystals by an external electric field, inducing the transition to the metallic phase. Afterwards the tunneling resistance of the system is exponentially reduced, thus storing a digital memory bit that can be read with a lower electric field. A reverse field can be used to trigger a transition back to the insulating phase, thus erasing the bit. The VO_2 -based device is expected to be reliable and fast owing to the diffusionless and electronic nature of the relevant phase transition (e.g., the absence of ionic motion necessary in conventional resistance change memories). In the optical switch mode, VO_2 nanocrystals are introduced into Er-doped silica as sensitizers. Resonant energy transfer from the absorptive VO_2 nanocrystals to the luminescent Er ions will enhance the 1.55-micron luminescence by orders of magnitude, an effect that was already demonstrated by the PIs for Ge nanocrystals embedded in Er-doped silica. The VO_2 nanocrystals, however, can be driven to the

metallic phase by illumination of a switching light beam, thus quenching the energy transfer process and bleaching the Er luminescence. This system is thus a fast switch that dynamically controls the optical amplification in Er-doped silica fibers.

Therefore, the proposed work is expected to lead to various device innovations in electronics and photonics technologies. Moreover, basic scientific discoveries are expected from the proposed research. Nanocrystal arrays of strongly correlated electron materials will allow investigation of quantum confinement and tunneling, electric field and optical doping, and surface and strain engineering at the single domain level, free from phase inhomogeneity and chemical disorder issues often encountered in samples with larger sizes. Understanding the formation mechanism of nano-crystalline compound via solid-state diffusion is also critically important for rational design of composite materials for other energy device technologies.

References to related publications of DOE sponsored research in 2008-2010:

1. W. T. Liu, J. Cao, W. Fan, H. Zhao, M. C. Martin, J. Wu, and F. Wang, Intrinsic Infrared Properties of Vanadium Dioxide near the Insulator-Metal Transition; *Nano Lett.* in press (2011).
2. J. Cao and J. Wu, Strain Effects in Low-Dimensional Transition Metal Oxides; *Materials Science and Engineering: R: Reports*, 71, 35 (2011).
3. J. Cao, Wen Fan, Qin Zhou, Erica Sheu, Aiwen Liu, C. Barrett, and J. Wu, Colossal Thermal-Mechanical Actuation via Phase Transition in VO₂ Microcantilevers; *J. Appl. Phys.*, 108, 083538(2010).
4. Y. Gu, J. Cao, J. Wu, and Long-Qing Chen, Thermodynamics of strained vanadium dioxide single crystals; *J. Appl. Phys.*, 108, 083517(2010).
5. J. Cao, Y. Gu, W. Fan, L. Q. Chen, D. F. Ogletree, K. Chen, N. Tamura, M. Kunz, C. Barrett, J. Seidel, and J. Wu, Extended Mapping and Exploration of the Vanadium Dioxide Stress-Temperature Phase Diagram; *Nano Lett.* 10, 2667 (2010).
6. J. Cao, W. Fan, K. Chen, N. Tamura, M. Kunz, V. Eyert and J. Wu, Constant threshold resistivity in the metal-insulator transition of VO₂; *Phys. Rev. B, Rapid Commun.* , 82, 241101 (2010).
7. W. Fan, S. Huang, J. Cao, E. Ertekin, C. Barrett, D. R. Khanal, J. C. Grossman and J. Wu, Superelastic Metal-Insulator Phase Transition in Single-Crystal Vanadium Dioxide Nanobeams; *Phys. Rev. B, Rapid Commun.*, 80, 241105(R) (2009).
8. J. Cao, E. Ertekin, V. Srinivasan, W. Fan, S. Huang, H. Zheng, J. W. L. Yim, D. R. Khanal, D. F. Ogletree, J. C. Grossman, and J. Wu, Strain engineering and one-dimensional organization of metal-insulator domains in single-crystal VO₂ beams; *Nature Nanotech.*, 4, 732 (2009).
9. J. W. L. Yim, B. Xiang, and J. Wu, Sublimation of GeTe nanowires and evidence of its size effect studied by in situ TEM; *J. Am. Chem. Soc.*, 131, 14526 (2009).
10. J. Cao, W. Fan, H. Zheng, and J. Wu, Thermoelectric Effect across the Metal-Insulator Domain Walls in VO₂ Microbeams; *Nano Lett.*, 9, 4001 (2009).
11. J. Guzman, S. J. Shin, C. Y. Liao, C. W. Yuan, P. R. Stone, O. D. Dubon, K. M. Yu, J. W. Beeman, F. Watanabe, J. W. Ager, D. C. Chrzan, and E. E. Haller, Photoluminescence enhancement of Er-doped silica containing Ge nanoclusters, *Appl. Phys. Lett.* 95, 201904 (2009).
12. S. J. Shin, J. Guzman, C. W. Yuan, C. Y. Liao, C. N. Boswell-Koller, P. R. Stone, O. D. Dubon, A. M. Minor, M. Watanabe, J. W. Beeman, K. M. Yu, J. W. Ager, D. C. Chrzan, and E. E. Haller, Embedded Binary Eutectic Alloy Nanostructures: A New Class of Phase Change Materials, *Nano Lett.* 10, 2794 (2010).

Fabricating Efficient p-type Dye-Sensitized Solar Cells

PI: Yiyang Wu

Address: 100 W 18th Avenue, The Ohio State University, Columbus, OH 43210

e-mail: wu@chemistry.ohio-state.edu

Program Scope

The objective of this program is to fabricate highly efficient photocathode dye-sensitized solar cells (p-DSCs) through the introduction of new nanostructured p-type semiconductors with proper valence band (VB) position, high visible transparency and hole mobility. The ultimate goal is to integrate these efficient p-DSCs with the well-developed dye-sensitized n-TiO₂ photoanode (n-DSC) to form tandem DSCs. A major challenge in developing efficient p-DSCs is the lack of p-type wide-band-gap semiconductors. To our best knowledge, only NiO has been investigated for p-DSCs, which produce small photovoltage limited by its valence band edge position. Therefore, in this program, we will investigate Cu(I)-based p-type semiconductors such as CuAlO₂, CuGaO₂, CuSCN and CuI. Due to their lower valence band edge energies than that of NiO, we believe that p-DSCs with higher photovoltages and thus higher efficiencies can be fabricated. Such p-DSCs can be combined with the common n-DSCs for tandem solar cells with a theoretical efficiency limitation well beyond that of the single-absorber DSCs.

Recent Progress

1: Synthesis of p-doped nanostructured oxides

In accordance with our aim to develop new materials and structures for p-type dye sensitized solar cells (p-DSCs), we have been working on the synthesis of p-type semiconductor oxide nanostructures. Nickel oxide (NiO) is the most widely used material for p-DSC photocathodes (*Acc. Chem. Res.*, 2010, 43 (8), pp 1063–1071), yet the impact of the synthetic conditions and morphology of the nanostructured NiO on the photocathode behavior has not been investigated thoroughly. We are exploring various

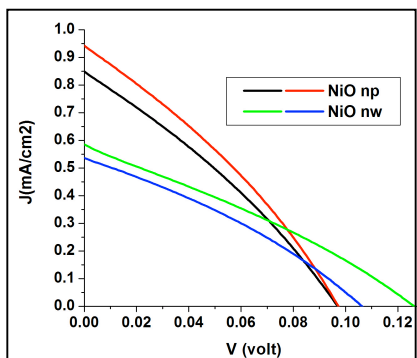


Fig. 2. J-V characteristics of p-DSCs fabricated from NiO nanostructures shown in fig. 1(a) and 1(b).

methods of synthesis of NiO nanoparticles and further fabrication of electrode films in order to maximize the surface area available for dye loading, to enhance electron transport properties through the film and to increase the mechanical strength of the films. We have synthesized NiO nanowires (Fig. 1.a) using mesoporous silica template (SBA-15) and NiO nanoparticles via ultrasonic spray pyrolysis (USP) of aqueous solutions of nickel nitrate. The nanowires are ~6 nm in diameter, and the crystallite size of the nanoparticles is 9.7 nm. The performance of p-DSCs fabricated with films of these nanostructures as photocathodes, P1 dye as sensitizer and 1M LiI and 0.1M I₂ in acetonitrile as electrolyte is shown in Fig. 2. The higher open circuit voltage (V_{oc}) for the nanowire based cells suggests that the morphology of the particles has an influence on the electronic transport properties of the overall film.

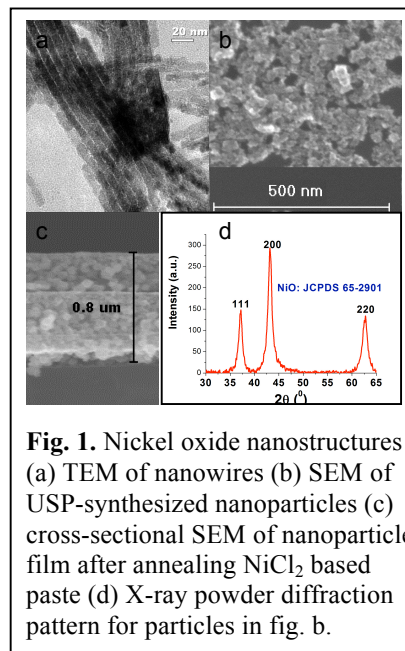


Fig. 1. Nickel oxide nanostructures (a) TEM of nanowires (b) SEM of USP-synthesized nanoparticles (c) cross-sectional SEM of nanoparticle film after annealing NiCl₂ based paste (d) X-ray powder diffraction pattern for particles in fig. b.

Another lucrative candidate for *p*-DSC is the delafossite-structured CuAlO_2 (d-CAO), as it is reported to have a high hole mobility that could enhance the carrier collection efficiency, low-energy valence band edge that could improve the V_{oc} and non-toxic metal components that are environmentally benign. Bulk d-CAO has been synthesized via solid-state methods and its thin films have been obtained by sputtering; however, nanostructures of this material have rarely been reported as the delafossite phase forms only at temperatures above 1100 °C. Our attempts to

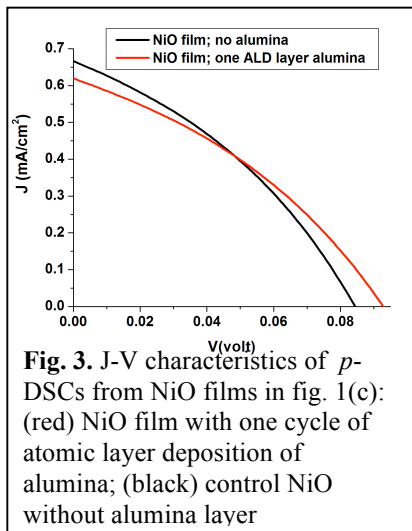


Fig. 3. J-V characteristics of *p*-DSCs from NiO films in fig. 1(c): (red) NiO film with one cycle of atomic layer deposition of alumina; (black) control NiO without alumina layer

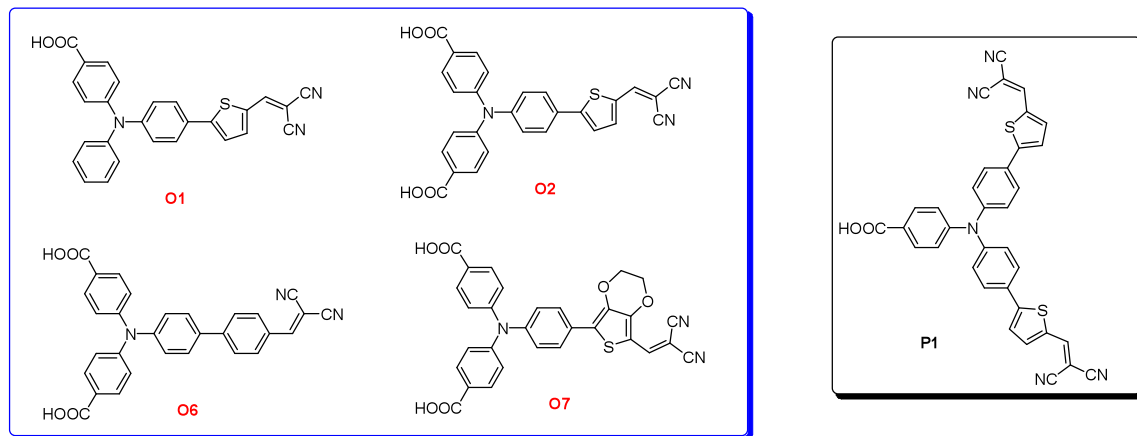
synthesize d-CAO via ultrasonic spray pyrolysis of solutions containing 1:1 molar ratio of Cu and Al ions only yielded hollow microspheres of spinel phase CuAl_2O_4 . Modifications of USP and hydrothermal methods that could produce d-CAO and other *p*-type delafossites at lower temperatures are currently under investigation.

An enhancement in the performance of a DSC photoelectrode could be obtained by application of a thin insulating layer at the surface of the nanostructured film so that it retards the geminate charge recombination. We fabricated a layer of aluminum oxide onto a nanostructured NiO films via atomic layer deposition, and the resultant electrodes showed a higher V_{oc} (Fig.3) with a slight decrease in the short circuit current. We are currently designing experiments to validate these results and to further probe the origins of this phenomenon.

2: Dye design and synthesis

The dyes in dye sensitized solar cells (DSC) responds for light harvesting, charge separation, charge injection at the electrode interface, and electrolyte reduction (or oxidation), which is believed to be the paramount component in DSSC. Unlike well established for n-type DSC (working with TiO_2 semiconductor), the research of dyes for p-type DSSC (NiO) is limited. The working principle of p-type dyes is reverse in comparison to n-type DSSC. After photo-excitation, fast charge injection occurs at the dye-semiconductor interface, and then the reduced dye will further transfer electron to the redox couple (I_3^-/I^-). To achieve high efficiency for p-type DSC, the dye should fulfill the following requirement: 1). Broad absorption in visible and NIR region to enhance the light harvesting; 2). Efficient charge separation and long lived charge separated state; 3). Well aligned HOMO levels to the Valence band of semiconductor to ensure the fast and efficient hole injection; 4). Well aligned excited state oxidation potential to ensure the fast charge transfer between the reduced dye and the redox couple. Qin et al first reported the state-of-art **P1** dye (structure shown in Scheme 1) for NiO DSSC. **P1** exhibits the typical Donor (D)-Linker(L)-Acceptor(A) structure, and with an unusual attachment of anchoring group (-COOH) on the triphenylamine donor moiety. Relatively high efficiency (0.15%) of **P1** sensitized NiO DSC was achieved. Nattestad et al utilized the same dye design strategy and found that increasing the length of bithiophene linker groups, longer lived charge separated state and higher incident-photon-to-current efficiency (IPCE) can be achieved. The highest efficiency of their solar cell is 0.41%. Except for these, all the other dyes sensitized NiO solar cell gave negligible efficiency. Clearly dyes for p-type DSC are far from optimized and the underlying mechanism especially interface charge separation and recombination is not fully understood. The goal of our research is to develop dyes for highly efficient p-type DSC, and ultimately for tandem solar cell (in this case, the dyes with complementary colors need to be considered.). To pursue this goal, a series of dyes with alternative anchoring, donor, linker, and acceptor moieties were proposed. Their photocurrent-voltage and IPCE spectroscopy will be performed (scheme 1). We are also

studying the interfacial electron transfer properties using transient absorption spectroscopy. The obtained results will pave the way to understanding of the mechanism and optimism of the p-type DSC. Our initial effort was put on design and synthesis organic dyes, which resemble P1 dyes, and study of anchoring group and linker group (structures shown in Scheme 1) influence on the DSC performance. The properties of these dyes are summarized in table 1.



Scheme 1. Structure of dye molecules in current project.

Table 1. Photophysical and electrochemical data of dyes in CH₃CN and NiO thin film.

	$\lambda_{\text{abs}}(\text{nm})^1$ $\epsilon (\text{L}\cdot\text{mol}^{-1}\cdot\text{cm}^{-1})$	$\lambda_{\text{film}}(\text{nm})^2$ Absorbance	$\Gamma (\text{X}10^7)$ mol/cm^2	$\lambda_{\text{em}}(\text{nm})^1$	$E_{\text{red}}(\text{V})^3$	$E_{00}(\text{eV})^4$	$E^{*/-}(\text{V})^5$
P1	477/31560	473/1.20		---			
O1	476/12480	469/0.86		683	-1.20	2.28	1.08
O2	453/22550	449/0.81	0.86	664	-1.01	2.30	1.29
O6	404/14940	-----	0.13	696	-1.06	2.38	1.32
O7	467/12480	466/0.82	0.57	639	-1.12	2.22	1.10

¹ Absorption and emission spectra were recorded in CH₃CN solution at room temperature; ² The absorption was uncorrected from the absorption of bare NiO film; ³ The electrochemistry were carried out in CH₃CN solution with 0.1 mM TBAP as supporting electrolyte, and using Pt disk, Pt wire, and silver wire as working, counter, and reference electrode. Fc couple were used as internal reference and all potentials were reported relative to NHE (Fc = 0.64 vs NHE). ⁴ E_{00} were calculated from the crossed point of normalized absorption and emission spectra. ⁵ $E^{*/-} = E_{00} + E^{0/-}$.

3: Carrier dynamics by electrochemical impedance spectroscopy (EIS)

We have first studied the impedance spectra of TiO₂-based n-type DSSCs. The Nyquist diagram shown in Fig. 4(a) under illumination shows three semicircles, which can be identified by Nernst diffusion within the electrolyte, the diffusion and recombination of the photoinjected electrons in the porous TiO₂ film, and the charge transfer at the platinum counter electrode. By data fitting and mathematical calculation, we can obtain key parameters, such as the charge transfer resistance of the recombination process, and the electron transport resistance, electron lifetime and electron diffusion length. Now we are extending the mentod to p-type DSCs. To the best of our knowledge, no study has been reported on this. A

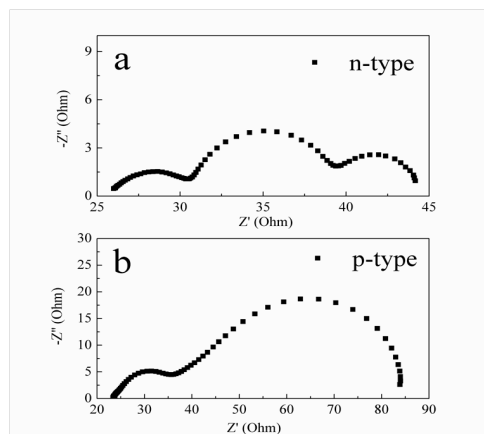


Fig. 4 Nyquist plots of n-type (a) and p-type (b) DSCs under illumination at open circuit voltage.

Nyquist plot of NiO-based DSC is shown in Fig. 4(b). It seems that in p-type DSCs the recombination and hole transport speed is much slower in comparison with n-type ones. Work is in progress to further analyze the impedance spectra of p-type DSCs.

Future Plan

(1) Synthesizing nanostructured delafossites such as CuAlO_2 and CuGaO_2 . (2) Studying the band structures of these p-type semiconductors through photoelectrochemical properties. (3) Understanding the effect of surface coating by Al_2O_3 ; (4) Investigating charge transport in the proposed p-type semiconductor films by both time-domain and frequency-domain techniques; (5) Synthesizing dyes for p-DSC; (6) exploring p-DSCs sensitized by semiconductor nanocrystals; (6) Studying the interfacial electron transfer properties using transient absorption spectroscopy.

A major outcome of this project is that it will hold promise of fabricating more efficient p-DSCs than the current state-of-the-art ones, which will bring impact to the photovoltaic technologies. In a general sense, the proposed research program will bring progress in designing and synthesizing semiconductor materials at the nanoscale for energy-related application and establish an understanding of the electron transport process in these materials. The next phase of the study proposed here will include the integration of our p-DSCs with the n-DSCs for tandem DSCs with unprecedented high efficiencies.

Publications

9. D. Wang, Y. Li, P. Hasin, Y. Wu*. "Preparation, Characterization, and electrocatalytical performance of graphene/methylene blue thin films", *Nano Research*, **4**(1), 124-130 (2011).
8. P. Hasin^g, M. A. Alpuche-Aviles^p, Y. Wu*. "Electrocatalytic activity of graphene multilayers towards I^-/I_3^- : effect of preparation conditions and polyelectrolyte modification" *J. Physical Chemistry C* **114**(37), 15857 (2010).
7. G. Natu^g, Y. Wu*. "Photoelectrochemical Study of the Ilmenite Polymorph of CdSnO_3 and its Photoanodic Application in Dye-Sensitized Solar Cells" *J. Physical Chemistry C*, **114** (14), 6802 (2010).
6. Y. Li^g, Y. Wu*. "Coassembly of Graphene Oxide and Nanowires for Large-Area Nanowire Alignment", *J. Am. Chem. Soc.* **131**(16) 5851-5857 (2009).
5. M. A. Alpuche-Aviles^p, Y. Wu*. "Photoelectrochemical Study of the Band structure of Zn_2SnO_4 Prepared by the Hydrothermal method", *J. Am. Chem. Soc.* **131**(9) 3216-3224 (2009).
4. P. Hasin^g, M. A. Alpuche-Aviles^p, Y. Li^g, Y. Wu*. "Mesoporous Nb-doped TiO_2 as Pt Support for Counter Electrode in Dye-Sensitized Solar Cells", *J. Phys. Chem. C*. **113**(17) 7456-7460 (2009).
3. Y. Li^g, Y. Wu*. "Formation of $\text{Na}_{0.44}\text{MnO}_2$ nanowires via stress-induced splitting of birnessite nanosheets", *Nano Research*, **2**(1): 54-60 (2009).
2. B. Tan^p, E. Toman^u, Y. Li^g, Y. Wu*, "Zinc Stannate (Zn_2SnO_4) Dye-Sensitized Solar Cells", *J. Am. Chem. Soc.* **129**(14), 4162 (2007).
1. B. Tan^p, Y. Wu*, "Dye-Sensitized Solar Cells Based on Anatase TiO_2 Nanoparticle/Nanowire Composites", *J. Phys. Chem. B* **110**: 15932-15938 (2006).

Nanolamellar Magnetolectric BaTiO₃ -CoFe₂O₄ Bicrystal

Shenqiang Ren and Manfred Wuttig

Department of Materials Science and Engineering, University of Maryland, College Park,
Maryland 20742-2115, USA

The poster reports on a spontaneously formed nanolamellar BaTiO₃ -CoFe₂O₄ bicrystal. (11 $\bar{0}$) interfaces join the BaTiO₃ and CoFe₂O₄ single crystalline periodically arranged lamellae that have a common [111] direction. The superlattice of approximately 2 nm wavelength is magnetolectric with a frequency dependent coupling coefficient of 20 mV/Oe cm at 100 Hz. The BaTiO₃ component is a ferroelectric relaxor with a Vogel -Fulcher temperature of 311 K. The relaxor behavior gives rise to a magnetic tunability of the relative dielectric constant.

Nanoscale Oxide Thin Films and Heterostructures by Laser Molecular Beam Epitaxy

Program Title: Raman Spectroscopic Study of Coupling between Magnetic and Ferroelectric Orders in Nanoscaled Thin Films Superlattices

Principal Investigator(s), Mailing Address, E-mail: Xiaoxing Xi, Department of Physics, Temple University, 1900 N. 13th Street, Philadelphia, PA 19122

Program Scope: Fabrication of nanoscale oxide thin films and heterostructures and study the coupling between magnetic and ferroelectric orders in them.

The state of the art in the oxide thin film technology allows layer-by-layer growth of ultrathin films and heterostructures with controls to the atomic level. Such never-before-available capability of nanoengineering leads to possibilities in new physics, such as 2D electron gas and superconductivity at oxide interfaces; new devices, such as generation of coherent acoustic phonons in piezoelectric oxide superlattices; and new designer materials which do not exist in the bulk form, but may be formed by atomic layering.

Laser MBE process is similar to MBE growth in terms of high vacuum, slow growth, and real-time RHEED monitoring and control. The control of purity in source materials is more difficult in laser MBE, while it is easier to achieve better oxygen stoichiometry than in MBE. Most laser MBE deposition of oxide thin films use compound targets. For example, for SrTiO₃ films, SrTiO₃ targets are mostly often used. It has been found, however, that the laser MBE grown SrTiO₃ films always show non-stoichiometry even when the deposition parameters are optimized. Meanwhile, it has been shown that in MBE individually depositing layers of each element leads to better film quality than using co-deposition. Laying down one atomic layer at a time is key to achieving the superb crystalline quality and stoichiometry in the nanoscale thin films and superlattices.

Recent Progress: We have deposited SrTiO₃ films by laser MBE by laying down one atomic layer at a time, i.e., by alternately depositing SrO and TiO₂ layers. The intensities of the RHEED diffraction spots were used to monitor the surface coverage during the film growth. Each full period of oscillation corresponds to the formation of a single unit cell of the deposited material. Similar variations of the RHEED intensity to those in atomic layer by layer MBE growth corresponding to the depositions of SrO and TiO₂ layers have been observed. X-ray diffraction results show that stoichiometric SrTiO₃ films are made when the fluxes of SrO and TiO₂ are properly controlled from the separate SrO and TiO₂ targets.

Future Plans: We will continue focusing on growing MBE-quality nanoscale oxide thin films and superlattices with laser MBE using separate oxide targets. After further optimizing the prototype perovskite material SrTiO₃, we will grow BaTiO₃/SrTiO₃ superlattices using SrO, BaO, and TiO₂ targets to be ablated alternately for each atomic layer.

In close collaboration with Xifan Wu's group at Temple University, we will grow nCaMnO₃/nBaTiO₃ (n =1,2) superlattices using separate CaO, BaO, MnO₂, and TiO₂ targets. The interfacial enhancement of spin-lattice coupling in such superlattices has been predicted to induce the AFM to FM transition by the applied magnetic field or epitaxial stress, a unique multiferroics property promising for devices with multifunctionalities.

Publications with DOE support in 2008-2010:

1. Soukiassian, W. Tian, V. Vaithyanathan, J. H. Haeni, L. Q. Chen, X. X. Xi, D. G. Schlom, D. A. Tenne, H. P. Sun, X. Q. Pan, K. J. Choi, C. B. Eom, Y. L. Li, Q. X. Jia, C. Constantin, R.M. Feenstra, M. Bernhagen, P. Reiche, and R. Uecker, Growth of nanoscale BaTiO₃/SrTiO₃ superlattices by molecular-beam epitaxy, *J. Mater. Res.* **23**, 1417 (2008).
2. Dmitri A. Tenne and Xiaoxing Xi, Raman Spectroscopy of Ferroelectric Thin Films and Superlattices, *J. Am. Ceram. Soc.* **91**, 1820 (2008).
3. Shufang Wang, A. Venimadhav, Shengming Guo, Ke Chen, Qi Li, A. Soukiassian, Darrell G. Schlom, Michael B. Katz, X. Q. Pan, Winnie Wong-Ng, Mark D. Vaudin, and X. X. Xi, Structural and thermoelectric properties of Bi₂Sr₂Co₂O_y thin films on LaAlO₃ (100) and fused silica substrates, *Appl. Phys. Lett.* **94**, 022110 (2009).
4. D. A. Tenne, H. N. Lee, R. S. Katiyar, and X. X. Xi, Ferroelectric phase transitions in three-component short-period superlattices studied by ultraviolet Raman spectroscopy, *J. Appl. Phys.* **105**, 054106 (2009).
5. D. A. Tenne, P. Turner, J. D. Schmidt, M. Biegalski, Y. L. Li, L. Q. Chen, A. Soukiassian, S. Trolier-McKinstry, D. G. Schlom, X. X. Xi, D. D. Fong, P. H. Fuoss, J. A. Eastman, G. B. Stephenson, C. Thompson, and S. K. Streiffer, Ferroelectricity in Ultrathin BaTiO₃ Films: Probing the Size Effect by Ultraviolet Raman Spectroscopy, *Phys. Rev. Lett.* **103**, 177601 (2009).
6. N. D. Lanzillotti-Kimura, A. Fainstein, B. Perrin, B. Jusserand, A. Soukiassian, X. X. Xi, and D. G. Schlom, Enhancement and Inhibition of Coherent Phonon Emission of a Ni Film in a BaTiO₃/SrTiO₃ Cavity, *Phys. Rev. Lett.* **104**, 187402 (2010).
7. J. Hlinka, V. Železný, S. M. Nakhmanson, A. Soukiassian, X. X. Xi, and D. G. Schlom, Soft-mode spectroscopy of epitaxial BaTiO₃/SrTiO₃ superlattices, *Phys. Rev. B* **82**, 224102 (2010).
8. A. F. García-Flores, D. A. Tenne, Y. J. Choi, W. J. Ren, X. X. Xi, and S. W. Cheong, Temperature-dependent Raman scattering of multiferroic Pb(Fe_{1/2}Nb_{1/2})O₃, *J. Phys.: Condens. Matter* **23**, 015401 (2011).

Title: Suspensions of Monodisperse Nanoparticles as Model Systems for Probing Heat Transfer Mechanisms in Nanofluids

PIs: Bao Yang and Michael R. Zachariah

Mailing Address: Department of Mechanical Engineering, University of Maryland, College Park, MD 20742

E-mail: baoyang@umd.edu, mrz@umd.edu

Program Scope:

This proposal aims to systematically investigate various fundamental, but less-studied factors—Brownian motion, fractal aggregates, and interfacial layer structure—that potentially affect thermal transport in nanofluids and nanoemulsion fluids. One goal of this project is to develop a new type of nanoengineered fluids that provide an unprecedented combination of highly desirable features for thermal applications.

Recent Progress:

In this report, we present our progress on *four topics* that are currently under investigation under this DOE/BES program:

1. Aggregation Kinetics and Its Relation to the Fluid Thermal Properties

Recent research on nanofluids has offered particle aggregation as a possible mechanism for the abnormal enhancement of the effective thermal conductivity (k) when nanoparticles are dispersed in liquids. The present study was devoted to experimentally and theoretically verify the significance of the effect by altering the aggregate structure and size distribution in suspensions of monodisperse nanoparticles. Starting with well-dispersed SiO_2 sols in water as a reference system, we controlled the aggregation kinetics by adjusting pH. Contrary to previous model predictions, the present experiment showed that aggregation did not show any discernable enhancement in thermal conductivity even at high volume loadings. A series of fractal model calculations suggested that the conductive benefit due to aggregation might be completely compensated by the interfacial resistance.

1.1 Kinetic Control of Silica Colloid Aggregation

When lowering the pH of the silica colloid from 10.1, up to the iso-electric point ($\text{pH} \approx 5.5$), surface charge and repulsion potential are gradually reduced with respect to the invariant van der Waals attraction. Near the iso-electric point, strong inter-particle attraction leads to aggregation, resulting in ramified and self-similar fractal structures, or even an entire percolating network. Figure 1 shows the hydrodynamic size distributions of colloidal particles at different pHs after 3 hr. At $8.5 \leq \text{pH} \leq 10.1$, the size distribution profiles are nearly the same, suggesting that colloidal spherical particles are well dispersed without any obvious aggregation. At $\text{pH} = 7.5$, however, the modal diameters greatly increase

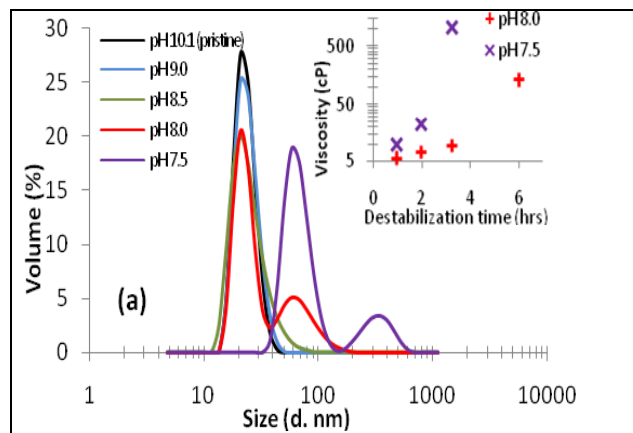


Figure 1. Dynamic light scattering (DLS) size distributions for ST-40 silica colloids under controlled aggregation. Inset is viscosity evolution of the samples.

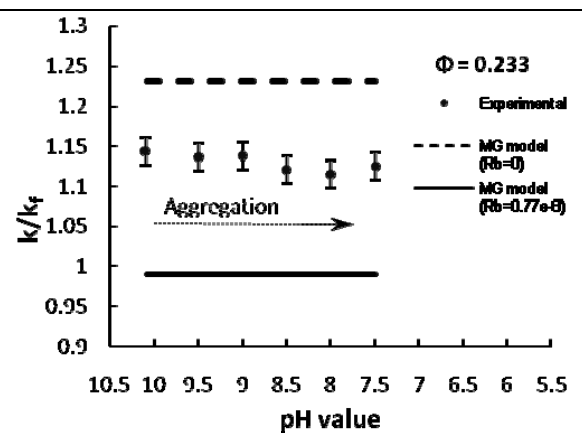


Figure 2. Thermal conductivity of ST-40 silica colloids under controlled aggregation. Dashed and solid lines are results predicted by the M-G model.

to around 67 and 336.5 nm with volume ratio of ca. 4 to 1.

1.2 Effect of Aggregation on the Effective Thermal Conductivity

Thermal conductivity of ST-40 silica colloids under controlled aggregation was measured using the 3-wire method. The relative thermal conductivity of the silica colloids is shown in Figure 2. Results estimated from the M-G Model are also shown for comparison. The experimental data are well bounded by the M-G model predictions with and without R_b . In the well-dispersed spherical particle suspensions (pH = 10.1), the 15% increase of the effective thermal conductivity seems to be surmounted completely by the effect of the interfacial resistance (up to ~23%). As pH decreases, there is no apparent effect of particle aggregation on the fluid thermal conductivity, which is contrary to previous modeling prediction. This surprising result might come from the low inherent thermal conductivity of silica material, and/or because the minor benefit of aggregation is completely compensated by the interfacial resistance.

2. Effects of Particle Brownian Motion on the Fluid Thermal Conductivity

In this study, nanoemulsions of alcohol and polyalphaolefin (PAO) are used as the model system because alcohol and PAO have similar thermal conductivity values and therefore the abnormal effects due to particle Brownian motion on thermal transport could be deduced. Both thermal conductivity and dynamic viscosity of the fluids are found to increase with alcohol droplet loading, as expected from classical theories. However, the measured conductivity increase is very moderate, e.g., a 2.3% increase for 9 vol. %, in these fluids. This suggests that no anomalous enhancement of thermal conductivity is observed in the alcohol/PAO nanoemulsion fluids tested in this study.

2.1 Small Angle Neutron Scattering (SANS) Measurement

SANS measurements are carried out for the *in situ* determination of the size of droplets in the nanoemulsion fluids. In our SANS experiment, samples are made using deuterated alcohol to achieve the needed contrast between the scatters and solvent. SANS measurements are conducted on the NG-3 (30m) beamline at the NIST Center for Neutron Research (NCNR) in Gaithersburg, MD. Figure 3 shows the SANS data, the scattering intensity I versus the scattering vector $q = 4\pi \sin(\theta/2) / \lambda$, where λ is the wavelength of the incident neutrons and θ is the scattering angle. The analysis of the SANS data suggests that the inner cores of the swollen micelles, i.e., the alcohol droplets, are spherical and have a radius of about 0.8 nm for 9 vol. %.

2.2 Thermal Conductivity Characterization

The effective medium theory reduces to Maxwell's equation for suspensions of well-dispersed, non-interacting spherical particles. Maxwell's equation predicts that the thermal conductivity enhancement increases approximately linearly with the particle volumetric fraction for dilute nanofluids or nanoemulsion fluids (e.g., $\phi < 10\%$), if $k_p > k_o$ and the particle shape remains unchanged. It can be seen

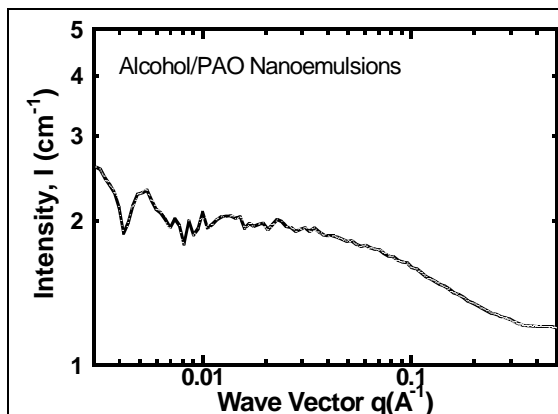


Figure 3. SANS curves (scattering intensity I versus scattering vector q) for the alcohol/PAO nanoemulsion fluids with 9 vol. %.

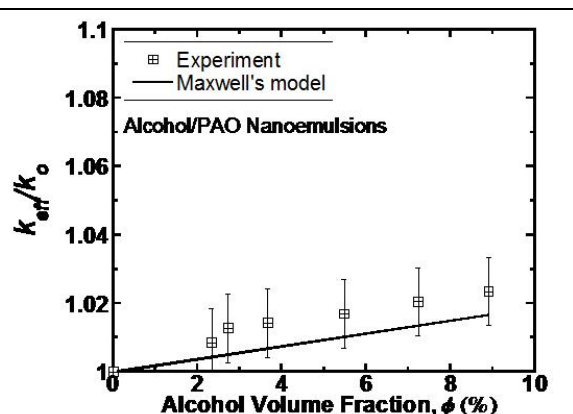


Figure 4 Relative thermal conductivity of the alcohol/PAO nanoemulsion fluids vs. alcohol volumetric fraction.

in Fig. 4 that the measured thermal conductivity is in good agreement with the predictions of Maxwell's equation in the alcohol/PAO nanoemulsion fluids. The very small increase in thermal conductivity ($<2.3\%$) is due to the fact that the thermal conductivity of alcohol is very slightly larger than that of PAO, $k_{PAO} = 0.143$ W/mK and $k_{alcohol} = 0.171$ W/mK at room temperature. No strong effects of Brownian motion on thermal transport are found experimentally in those fluids although the nanodroplets are extremely small.

3. Interaction between Amphiphilic and Nonpolar Molecules and Its Relation to the Fluid Thermal Properties

Amphiphilic molecules consist of two well-defined regions: one which is oil soluble (oleophilic or hydrophobic) and one which is water soluble (oleophobic or hydrophilic). Surfactants that are used to stabilize nanoparticles in the suspensions are amphiphilic materials. We have studied thermal energy transport between amphiphilic and nonpolar oil molecules using a thermal conductivity technique, small-angle neutron scattering (SANS), and energy-conserving dissipative particle dynamics (eDPD) simulation. This work is being done in collaboration with Professor Qiao at the Clemson University.

In the present work, the solution of AOT/n-octane (where AOT denotes aerosol sodium dioctyl sulfosuccinate) is used as our model system. As the AOT concentration increases above the critical micellization concentration (c.m.c.), the oleophobic sulfonate head groups aggregate together to form regions from which the nonpolar n-octane molecules are excluded, i.e., micelles. The vibrational energy transport between AOT and n-octane molecules would affect heat transfer in the solutions. The thermal conductivity was measured in the AOT/n-octane solutions with different AOT concentrations. As shown in Figure 5(a), the thermal conductivity of the AOT/n-octane solutions first decreases as the AOT loading increases, then goes through a minimum and starts to increase. The existing theories, such as Effective Medium Theory, apparently fail to explain the observed minimum thermal conductivity. The eDPD simulation was performed to elucidate the relationship between the microscopic energy transport between molecules and the macroscopic heat transfer in the solution. The simulation results are shown in Figure 5(b). The insert illustrates the evolution of the AOT microstructure from individual molecules to micelles.

Based on the analysis of the experimental and simulation data, several points are worth noting:

1. A minimum thermal conductivity occurs in the AOT/n-octane solutions.
2. The existing theories, e.g. Effective Medium Theory, fail to explain the experimentally observed minimum thermal conductivity. According to the Effective Medium Theory, the thermal conductivity has a monotonic response, i.e., increase or decrease, to the concentration of the disperse phase.
3. The minimum thermal conductivity provides a new method to determine the critical micellization concentration.

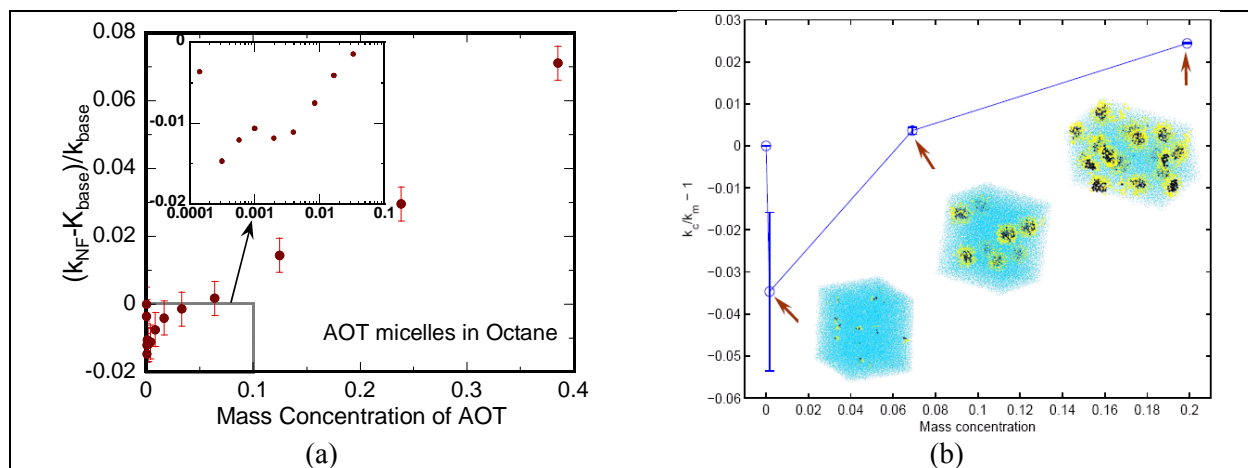


Figure 5 (a) Thermal conductivity vs. AOT loading in the AOT/n-octane solutions. The measurement was made by the 3ω -wire method. (b) Thermal conductivity predicted by eDPD. In the insert, yellow and black beads denote the oleophilic tails and oleophobic head groups of AOT, respectively.

4. Development of New Engineered Thermal Transport Fluids

We have been developing a new thermal transport fluid: nanoemulsions with low-boiling-point nanodroplets (Figure 6). A very remarkable increase in convective heat transfer coefficient—by a factor of up to 2.2—occurs in such a nanoemulsion fluid due to the explosive vaporization of the ethanol nanodroplets at the superheat limit (i.e., spinodal states, about 122 °C higher than the atmospheric boiling point for ethanol).

The convective heat transfer curves are plotted in Figure 6 for the nanoemulsion fluids. When the heater temperature is increased ($\Delta T > 170$), an abrupt increase in convective heat transfer coefficient—by a factor of up to 2.2—is observed in the ethanol/PAO nanoemulsion fluids. Such an increase would be mainly accredited to the vaporization of those ethanol nanodroplets dispersed in the base fluid PAO. A direct impact of the nanodroplet vaporization is that the heat of vaporization could significantly enhance the effective heat capacity of the fluid.

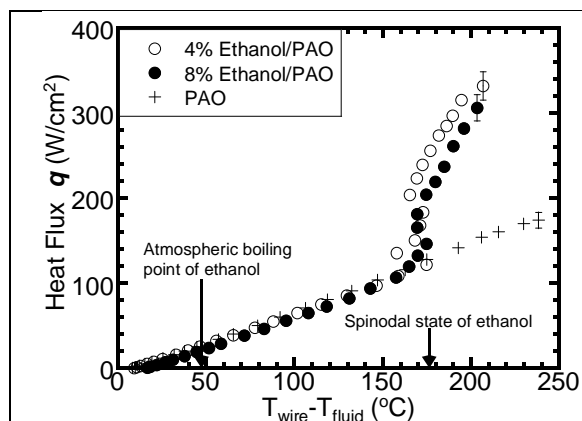


Figure 6. Convective heat transfer curves for the pure PAO and the ethanol/PAO nanoemulsion fluids. Note that the atmospheric boiling point of ethanol is 78 °C.

Technical Plans for 2011:

We will continue to investigate the microstructure, energy transport and their relation in suspensions of nanoparticles. We will also plan to develop a new type of nanoemulsion fluids that provide an unprecedented combination of highly desirable features for thermal applications, including high heat transfer coefficient, long-term stability, and mass-production capability.

Publication:

1. Z. H. Han and B. Yang, "Thermophysical Characteristics of Water-in-FC72 Nanoemulsion Fluids," *Applied Physics Letters* 92, 013118, 2008.
2. B. Yang, "Thermal conductivity equations based on Brownian motion in suspensions of nanoparticles (nanofluids)," *ASME Journal of Heat Transfer* 130, 042408, 2008.
3. D. Tsai, R. A. Zangmeister, L. F. Pease III, M. J. Tarlov, and M. R. Zachariah, "Gas-Phase Ion-Mobility Characterization of SAM Functionalized Au Nanoparticles," *Langmuir* 24, 8483, 2008.
4. Z. Han, F. Cao, and B. Yang, "Synthesis and Thermal Characterization of Phase-Changeable Indium/Polyalphaolefin Nanofluids," *Applied Physics Letters* 92, 243104/1-3, 2008.
5. D. Tsai, L. F. Pease III, R. A. Zangmeister, M. J. Tarlov, and M. R. Zachariah, "Aggregation Kinetics of Colloidal Particles Measured by Gas-Phase Differential Mobility Analysis," *Langmuir* 25, 140, 2009.
6. C. Wu, T. Cho, J. Xu, D. Lee, B. Yang, M. Zachariah, "Effect of nanoparticle clustering on the effective thermal conductivity of concentrated silica colloids," *Physical Review E*, vol. 81, pp. 011406, 2010.
7. J. Xu, C. Wu, and B. Yang, "Thermal- and phase-change characteristics of self-assembled ethanol/polyalphaolefin nanoemulsion fluids," *Journal of Thermophysics and Heat Transfer*, vol. 24, 208, 2010.
8. J. Xu, B. Yang, B. Hammouda, "Thermal conductivity and Viscosity of Self-assembled Alcohol/Polyalphaolefin Nanoemulsion Fluids," accepted for publication in *Nanoscale Research Letters*, 2011.
9. Z. Han, B. Yang, Y. Qi, and J. Cummings, "Synthesis of low-melting-point metallic nanoparticles with a nanoemulsion method," *Ultrasonics*, in press, 2011.
10. B. Yang and J. Xu, Heat transfer fluids containing low-boiling-point liquid nanodroplets, Provisional Patent, PS-2008-119, 2009.

Machine Learning Approaches to Crystal Structure Prediction

Lusann Yang, Geoffroy Hautier, and Gerbrand Ceder
Department of Materials Science and Engineering
Massachusetts Institute of Technology

The objective of our research is to accelerate the search for new materials by using a combination of machine learning techniques and high-throughput *ab initio* computations. First principles methods have been shown to be capable of computing the properties of many materials from quantum mechanics. However, for those computations to be relevant, they need to be performed on a stable compound and on its exact crystal structure. Thus, solving the crystal structure prediction problem is a necessary step on the road to rational, computational materials design.

The space of possible crystal structures is complex and high dimensional, making traditional optimization via the quantum mechanical energy models unfeasible due to constraints on computing power. In a departure to this traditional approach, we use machine learning on the body of known empirical data to suggest likely candidates for low-energy structures, then test those structures for stability via *ab initio* computations.

In this poster, we present results on a large scale search for new ternary oxides using this technique. We train a probabilistic model on experimental crystal structure databases, then use this model to identify novel compositions at which compounds are likely to form and the crystal structure prototypes they are likely to form in. Lastly, we test these compounds for stability via *ab initio* computations. We discovered 209 new compounds on a limited computational budget. In addition, we present an alternative machine learning model based on ionic substitutions and more robust to treat data sparse regions such as quaternaries.

Future Plans

Our work clearly demonstrates the strength of a machine learning approach to the structure prediction problem, but it does not yet have the ability to find compounds that form in novel crystal structure prototypes. Our ongoing research addresses this problem by analyzing the frequently found crystal substructures. We express crystal structures as graphs, search these graphs for frequent substructures, and analyze the connectivity of these substructures. We plan to use machine learning to create a probabilistic model of the interaction between the chemical and structural similarities in compounds.

Program Title: *Fundamentals of Semiconductor Nanowires*

Principal Investigator: Peidong Yang
Materials Science Division
Lawrence Berkeley National Laboratory

The goal of this multidisciplinary research is to systematically develop the science and technology of a broad spectrum of one-dimensional inorganic semiconducting nanostructures. For any of the potential nanowire applications such as sub-wavelength photonic integration, solid state lighting and energy conversion (photovoltaics, thermoelectrical and solar-fuels generation), it is important to be able to produce such nanostructures with atomic scale control. Equally important is to gain fundamental understanding of their optical and electrical properties. *The main focus of the program is on the rational synthesis of inorganic nanowires and the investigation of fundamental optical and electrical properties of these nanostructures.*

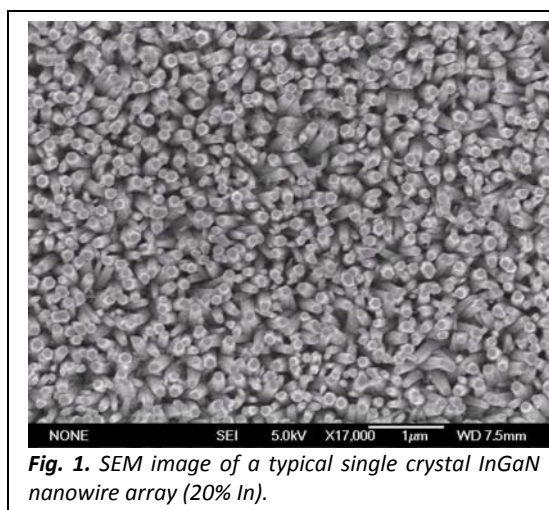
Background and Significance

Semiconductor nanowires have witnessed an explosion of interest in the last several years due to advances in synthesis and the unique thermal, optoelectronic, chemical, and mechanical properties of these materials.¹ The potential applications of single-crystalline nanowires are truly impressive, including computational technology, communications, spectroscopic sensing, alternative energy, and the biological sciences.² This research program on “Fundamentals of Semiconductor Nanowires” can be considered as the fundamental research program with the aim of establishing and developing the core science and technology for semiconductor nanowires, and with an emphasis on growth, assembly and fundamental optical and electronic properties characterization.

Composition tunability of InGaN nanowires

The III-V nitrides have been intensely studied in recent years because of their huge potential as the material of choice for everything from high efficiency solid-state lighting, to photovoltaics, to high power electronics and optoelectronics. In particular, the InGaN ternary alloy is of interest for lighting and photovoltaics because of the ability to tune the direct band-gap of this material from the near ultraviolet (UV) to the near infrared (IR). In an effort to synthesize high quality III-V nitride films and/or freestanding nanowires, researchers have tried nearly every growth technique including Metal Organic Vapor Phase Epitaxy (OMVPE), Molecular Beam Epitaxy (MBE), and Hydride Vapor Phase Epitaxy (HVPE). Except for MBE, an expensive and slow process, there has been considerable difficulty in tuning the indium concentration in InGaN across the entire compositional range.

As a continuation of our GaN nanowire efforts, we have explored the growth of single-phase $\text{In}_x\text{Ga}_{1-x}\text{N}$ nanowires across the entire compositional range from $x = 0$ to 1.³ The nanowire synthesis (Figure 1) was accomplished using a halide chemical vapor deposition (HCVD) process in my group, wherein InCl_3 , GaCl_3 and NH_3 , are used as the In, Ga, and N sources respectively. Structural analysis (SEM, XRD and TEM) indicates that we have successfully grown $\text{In}_x\text{Ga}_{1-x}\text{N}$ nanowires across the entire compositional range from $x = 0$ to 1. TEM analysis of these wires indicates that the wires are single-crystalline. In the region of concentrations between 70-90% In, however, there was some compositional modulation that can be seen in the TEM image. The



optical properties of the nanowires were characterized by several techniques and the results clearly demonstrate a systematic shift in band gap as a function of composition.³ We will continue to systematically explore the optical and electrical properties of these novel semiconductor nanowires. In addition, a collection of optical and electrical characterization tools will be used to probe these nanostructures as function of synthetic conditions with high spatial resolution. This would include, for example, spatial resolved cathodoluminescence (Molecular Foundry), scanning confocal optical imaging; single nanowire imaging and spectroscopy, temperature-dependent PL, quantum efficiency measurements with integrating sphere, impedance spectroscopy and field-effect transistor measurement of carrier concentration and mobility.

Atomic level control of oxide superlattice nanowire formation and their properties

Although significant progress has been made in oxide nanowire research, much of these efforts have been focused on binary oxide material system.^{4,5} Little work has been done on complex oxides and their heterostructures, mainly due to the synthetic difficulty. We have recently discovered a simple method for the production of complex oxide superlattice nanowires through rational annealing/conversion of ZnO/metal core-shell nanowires. This method introduces new opportunities for tuning the properties of the superlattice nanowires (e.g. thermoelectrical, optical properties).

Using ZnO/In₂O₃ superlattice nanowire as example, the ZnO nanowire arrays were first synthesized using our well-established chemical vapor transport methods. These nanowires were conformally coated with a thin layer of metal In using thermal evaporation. The ZnO/In core-shell nanowires were then annealed under a variety of conditions to determine the optimal conversion conditions and study the solid state diffusion between the ZnO/In interface. Interestingly, oxide superlattice nanowires can be reproducibly synthesized with this simple annealing approach, and typically the In-O layers were inserted into the ZnO lattice one atomic layer at a time (Fig 2). This approach represents the first rational approach towards synthesizing oxide superlattice nanowires with atomic level control. Other tri-valent metals such as gallium, iron and some rare earth elements are expected to form similar superlattice nanowires with homologous compound crystal structures. The synthesis of such oxide superlattice nanowires opens up exciting research opportunities to investigate their fundamental thermoelectrical and optoelectronic properties.

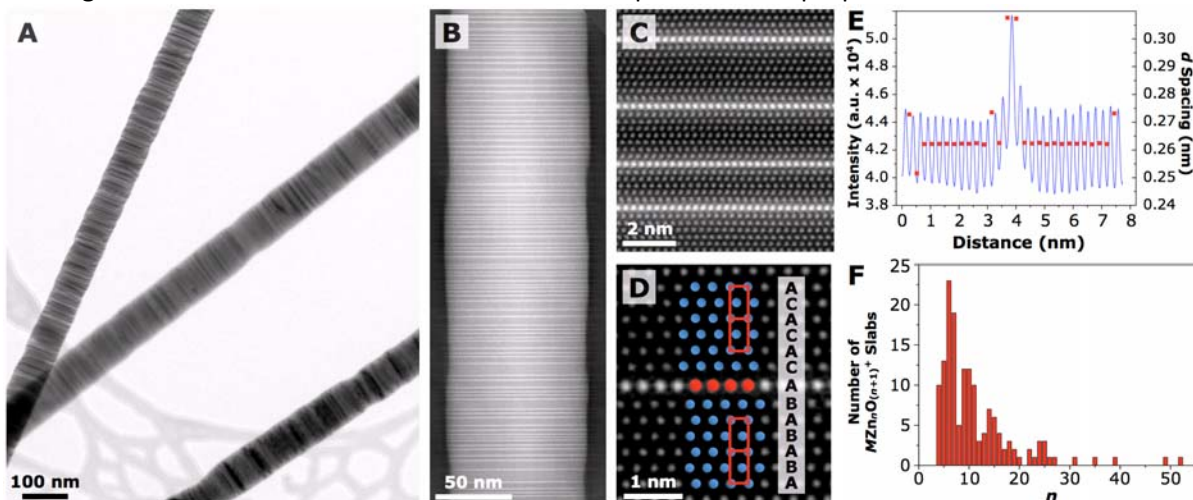
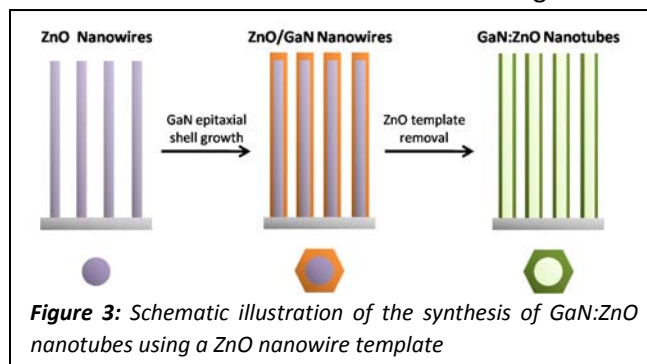


Fig. 2. (A) TEM image of multiple In_{2-x}Ga_xO₃(ZnO)_n (IGZO) nanowires. (B) Z-contrast STEM image of a IGZO nanowire. The Z contrast in the image clearly shows that In atoms are preferentially located within layers oriented perpendicularly to the nanowire growth direction. (C) HRSTEM image of an IGZO nanowire showing individual MO₂⁻ layers sandwiched between multiple MZn_nO_(n+1)⁺ layers. (D) HRSTEM image highlighting the change in stacking sequence across a MO₂⁻ layer. (E) Intensity line profile and *d* spacing across a MO₂⁻ layer taken from a HRSTEM image. On either side of the inclusion, the *d* spacing shows an expansion of ~17% relative to that of pure ZnO. (F) Frequency of different *n* values of the MZn_nO_(n+1)⁺ layers measured from HRSTEM images of several IGZO nanowires. The average *n* is 11 and the most frequent is 6.

We will continue to quantitatively examine the formation mechanism of such oxide superlattice nanowires. For the structural analysis, we will actively collaborate with NCEM staff to gain detailed understanding of the nanostructures at atomic level, especially by using the TEAM microscope. Similarly, a collection of optical and electrical characterization tools will be used to probe these nanostructures as function of synthetic conditions.

Templating complex inorganic nanotubes

Back in 2002, we developed an 'epitaxial casting' approach for the synthesis of single-crystal GaN nanotubes with inner diameters of 30–200 nm and wall thicknesses of 5–50 nm.⁶ Hexagonal ZnO nanowires were used as templates for the epitaxial overgrowth of thin GaN layers in a chemical vapor deposition system. The ZnO nanowire templates were subsequently removed by thermal reduction and evaporation, resulting in ordered arrays of GaN nanotubes on the substrates.



We have recently applied this process towards production of GaN:ZnO alloy nanotubes for the photoelectrochemical research purpose. Photoelectrochemical water splitting is a promising source of clean and renewable hydrogen energy. A high efficiency for overall water splitting under visible light has been achieved by Maeda *et al.* using a $(\text{Ga}_{1-x}\text{Zn}_x)(\text{N}_{1-x}\text{O}_x)$ (abbreviated as GaN:ZnO) particulate decorated with $\text{Rh}_{2-y}\text{Cr}_y\text{O}_3$ nanoparticles.⁷ One of the most exciting features of this material is the ability to tune its absorption from 3.4 to 2.43 eV by changing the relative amounts of GaN and ZnO in the alloy.⁸

To produce the nanotube morphology, a ZnO nanowire template is used as described previously. As shown in the schematic in Fig. 3, GaN is deposited onto a solution-grown ZnO nanowire array using metal organic chemical vapour phase deposition (MOCVD). Due to the small amount of lattice mismatch between GaN and ZnO, the GaN layer can be grown epitaxially on the ZnO nanowire template, producing a single-crystal shell. During the deposition procedure, ZnO from the nanowire template is incorporated into the GaN layer creating an alloy of GaN and ZnO. The ZnO template is then etched away under NH_3 at 700°C, leaving an oriented array of alloy nanotubes. We will explore this templating method to produce high surface area, single crystalline alloyed nanotubes with various Zn concentration. The optical (light absorption, bandgap) and photoelectrochemical properties (e.g. water splitting efficiency, IPCE) will be examined as a function of the compositions of these nanotubes.

Photoelectrochemical measurement on nanowires and nanotubes

Photoelectrochemical (solar) water splitting involves the conversion of solar irradiation into hydrogen and oxygen gas. However, because semiconductors must do redox chemistry in an electrolyte solution, there are several requirements for efficient water splitting. To obtain a high efficiency for solar water splitting, the photocatalyst must *a)* have a suitable band gap around 2.0 eV, *b)* straddle the hydrogen and oxygen redox potentials with its conduction and valence bands, *c)* have fast charge transfer across the semiconductor/electrolyte interface, and *d)* be resistant to corrosion.⁹

Several materials including GaN,¹⁰ TiO₂,¹¹ GaInP₂,¹² etc have been characterized, and used for water splitting purpose. However, these materials cannot meet all of the requirements for efficient water splitting. Since In_xGa_{1-x}N can satisfy the first two requirements for solar water splitting, our goal is to characterize alloy compositions (0.2<x<0.60) which have not been achieved through thin film growth previously, and coincidentally give the best bandgap energies for photon absorption. Flat band potential measurements can be used to characterize the absolute conduction and valence band energies of InGaN in electrolyte solution.

Impedance spectroscopy will be used to measure the capacitance of InGaN in electrolyte solution. A Mott-Schottky plot can then be constructed to extrapolate the flat band potential of InGaN in electrolyte solution. While there have been previous reports on In_xGa_{1-x}N thin films (x<0.2), higher indium compositions have not been measured due to synthetic difficulties. We plan to measure the flat band potential of our alloy InGaN nanowire arrays. In addition, illuminated open circuit potential measurements will also be used to compare flat band potential values with the Mott-Schottky measurements. Unlike impedance spectroscopy which applies a voltage, this technique relies on the photocurrent generated from illumination to reach a flatband state. Therefore, the semiconductor must have sufficiently few defects to prevent charge trapping which will cause incomplete flattening of the bands. Initial results for InGaN nanowires appear to be similar to the Mott-Schottky results, showing that InGaN at high In concentrations (x<0.5) could be a good water splitting electrode.

By measuring the photocurrent of the InGaN electrodes at a constant photon flux, we can determine whether the decreasing bandgap of high indium mole fraction samples is causing a change in the current density produced. With the increased photon absorption from a smaller bandgap, an increase in photocurrent would be expected under illumination. In addition, incident photon to charge carrier efficiency (IPCE) measurements¹³ can show the incident wavelength dependence on the quantum efficiency of various compositions of InGaN. Measurements on InGaN photoelectrodes are currently under way to test these fundamental material properties. Similarly these photoelectrochemical measurements will be applied to the newly developed GaN:ZnO nanotube arrays and the oxide superlattice nanowire arrays.

References

- ¹ "Semiconductor nanowires, what's next?", P. Yang, M. Fardy, R. Yan, *Nano Lett.* 10, 1529, 2010.
- ² "Nanowire Photonics", P. Pauzauskie, P. Yang, *Materials Today*, 9,36, 2006.
- ³ T. Kuykendall, P. Ulrich, S. Aloni, P. Yang, *Nature Materials*, 6, 951, 2007.
- ⁴ M. Huang, S. Mao, H. Feick, H. Yan, Y. Wu, H. Kind, E. Weber, R. Russo, P. Yang, *Science*, 292, 1897, 2001.
- ⁵ Y. Nakayama, P. J. Pauzauskie, A. Radenovic, R. M. Onorato, R. J. Saykally, J. Liphardt, P. Yang, *Nature*, 447, 1908, 2007.
- ⁶ J. Goldberger, R. He, S. Lee, Y. Zhang, H. Yan, H. Choi, P. Yang, *Nature*, 422, 599, 2003.
- ⁷ K. Maeda *et al.* *Journal of Catalysis*, 254, 198, 2008.
- ⁸ K. Maeda *et al.* *Nature*, 440, 295, 2007.
- ⁹ A. Nozik, *Annu. Rev. Phys. Chem.*, 29, 189, 1978.
- ¹⁰ J.D. Beach *et al.* *J Electrochem Soc.* 150, A899-A903, 2003.
- ¹¹ S.U.M. Khan *et al.* *Science*. 297, 2243-2245, 2002.
- ¹² O. Khaselev, J.A. Turner. *Science*. 17, 425-427, 1998.
- ¹³ X.Yang *et al.* *Nano Lett.* 9, 2331-2336, 2009.

Interband Cascade Photovoltaic Cells

Principal Investigator: Rui Q. Yang
Institution: School of Electrical and Computer Engineering, University of Oklahoma, Norman, OK e-mail: Rui.Q.Yang@ou.edu
Address: 110 W. Boyd Street, Room 150, Norman, OK 73019
Co-Principal Investigator: Michael B. Santos, Matthew B. Johnson
Department of Physics, University of Oklahoma, Norman, OK
Collaborator: J. F. Klem, Sandia National Laboratories, Albuquerque, NM

Program Scope

In this project, we will perform basic and applied research to systematically investigate our newly proposed interband cascade (IC) photovoltaic (PV) cells. These cells follow from the great success of infrared IC lasers that pioneered the use of quantum-engineered IC structures. This quantum-engineered approach will enable PV cells to efficiently convert infrared radiation from the sun or a heat source to electricity. Such cells will have important applications for more efficient use of solar energy and waste-heat recovery. The objectives of our investigations are to: achieve extensive understanding of the fundamental aspects of the proposed PV structures, develop the necessary knowledge for making such IC PV cells, and demonstrate prototype working PV cells. This research will focus on IC PV structures and their segments for utilizing infrared radiation in the wavelength range of 2 to 4 μm emitted by heat sources (1,000-2,000 K) that are widely available from combustion systems. The long-term goal of this project is to push PV technology to longer wavelengths, allowing for relatively low-temperature thermal sources.

Our investigations will address material quality, electrical and optical properties, and their interplay for the different regions of an IC PV structure. These fundamental aspects include: systematic knowledge about the carrier absorption and recombination processes over the infrared spectral range; and how carrier transport is affected by scattering mechanisms involving defects, phonons, and electron-electron interactions. The tasks involve: design, modeling and optimization of IC PV structures, molecular beam epitaxial growth of PV structures and relevant segments, material characterization, prototype device fabrication and testing. At the end of this program, we expect to generate new cutting-edge knowledge in the design and understanding of quantum-engineered semiconductor structures, and demonstrate the concepts for IC PV devices with high conversion efficiencies.

Prior Work

The interband cascade (IC) structure was originally proposed by the PI in 1994 for realizing efficient mid-IR lasers [1-2]. Significant progress in the development of IC lasers has been achieved over the last decade, including distributed feedback IC lasers selected for a NASA flight mission to Mars [3] and continuous wave (cw) operation of IC lasers above room temperature with low power consumption [4-5]. Recently, based on the advantages of unique band-edge alignments and cascade features, we proposed to use IC structures for PV devices to convert infrared light to electrical energy [6]. The operation principle of IC PV devices is illustrated in Fig. 1. As shown in Fig. 1, an IC PV structure can have many stages and each stage is divided into three zones based on three different processes: (1) photon absorption, (2) intraband carrier transport, and (3) interband tunneling transport. Zone (1) can be made by type-II InAs/Ga(In)Sb quantum wells (QWs) or a superlattice (SL) with a relatively narrow bandgap E_g that is determined by the QW layer thickness or SL period and can be tailored to

cover a wide range of wavelengths (e.g. 2-15 μm). Zone (1) is sandwiched between zone (2) and zone (3), which have relatively wide bandgaps, and serve as hole and electron barriers, respectively. Zone (2) consists of multiple QWs made of InAs/Al(In)AsSb thin layers that are digitally graded to form an asymmetric band profile as shown in Fig. 1; while zone (3) comprises GaSb/AlSb QWs with a type-II heterointerface connecting zone (2) of the adjacent stage for facilitating interband tunneling. Therefore, every stage is connected with smooth carrier transport due to interband tunneling through type-II heterostructures, but electrons are blocked in zone (3) and holes are prohibited in zone (2). The effective bandgap in each absorber region can be designed to be either the same or different from the other stages to efficiently make use of the radiation source spectrum.

When light is incident upon the PV device, photogeneration of electrons and holes results in a separation of electron and hole quasi-Fermi levels. As shown in Fig. 1b, electrons move to the left due to the asymmetry of the transport region. At steady state, an internal electric field will be built up to balance this movement of charge carriers, resulting in a sequential potential drop in each cascade stage, shown in Fig. 1b. These potential drops in every stage add and contribute to a total forward bias voltage similar to that in a multiple p - n junction cell. However, in contrast to the p - n junction structure, where heavily-doped p - and n -regions are required, doping is not necessary in these structures, eliminating the detrimental effects of high carrier concentrations such as free-carrier absorption and reduced minority-carrier diffusion length. This cascade multi-stage PV absorber architecture is particularly desirable for high-intensity illumination with a concentrator, where the high-intensity radiation may not be fully absorbed in the single p - n junction of a conventional cell, whose thickness is limited to the photogenerated carrier diffusion length. For the cascade PV, multiple stages with the same energy gap can be used to absorb all the photons in a particular portion of the source spectrum while increasing the open-circuit voltage, where the thickness of each stage is shorter than the diffusion length and chosen so that each stage generates the same photocurrent (the stages are current matched). Losses associated with high-current operation are also minimized by increasing the open circuit voltage.

To initially examine this PV concept, we used devices active in the mid-IR. The first device was designed as an IC photodetector used in reverse (near zero) bias to detect photons at about 5 μm (at 80 K) [7], and the second device was designed as an IC laser, which lases near 7.2 μm at 80 K [8]. The photodetector structure, grown by MBE on a GaSb substrate, has 7 identical cascade stages, and each stage has a 0.15- μm -thick absorber that is composed of 28 periods of InAs/GaSb (9 ML/9 ML) SL. These SL absorbers are separated by a 5.8-nm-thick GaSb QW and

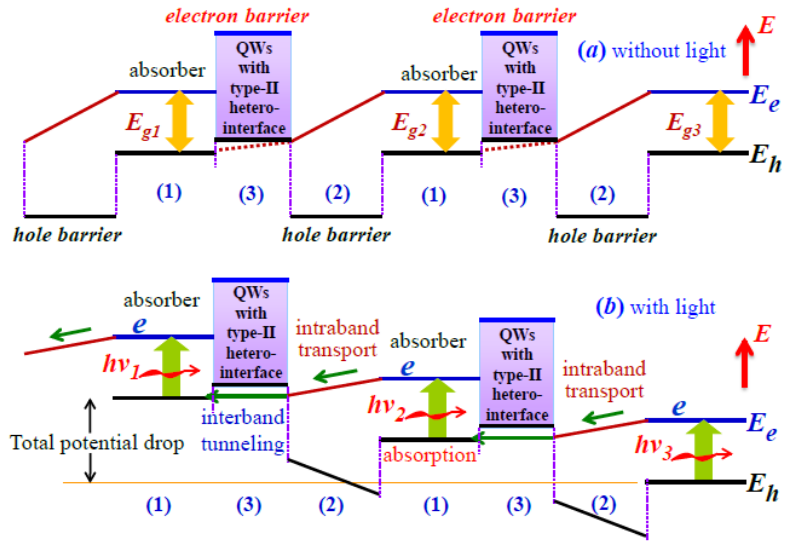


Fig. 1 Schematic band diagrams of a multiple-stage interband photovoltaic device (a) without and (b) with illumination. The effective band edges are shown in three zones

the intraband transport region that is composed of InAs/Al(In)Sb QWs, similar to the injection region in IC lasers [2]. The laser structure has 11 identical cascade stages and each stage has a ~20-nm-thick active region as described in Ref. [8].

Figure 2 shows current density-voltage (J - V) characteristics of a deep-etched 0.24-mm-diameter detector device at 80 K under illumination from the background and a blackbody (BB) source at several temperatures. Besides the observation of significant photocurrent (up to 45 mA/cm² at zero bias under illumination at a density ~0.67W/cm² by the BB at 1323K), the open-circuit voltage attained is about 1.11 V, which is several times higher than the single bandgap value of 0.24 V, as determined by the cutoff wavelength (~5.2 μm) of the photocurrent response (R_i) spectrum (Fig. 2 inset). This indicates that multiple stages are operating in series. The average voltage provided by each stage is 0.16 V and is less than the band-gap voltage value. A shallow-etched 0.24-mm-diameter device showed an open-circuit voltage of 1.17 V, which is about 70% of the equivalent bandgap voltage of the 7 total cascade stages (*i.e.* the sum of 7 single bandgap voltage values).

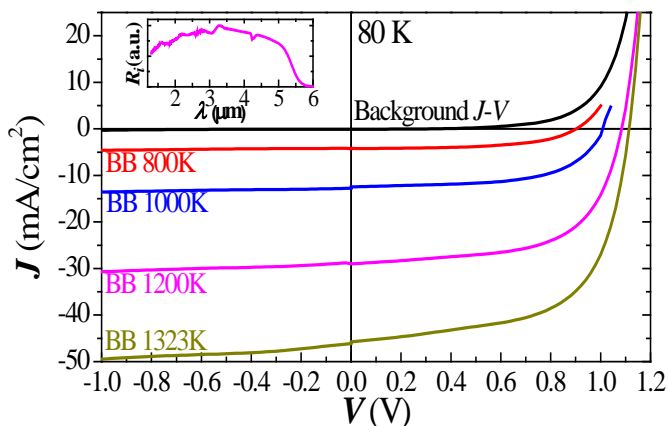


Figure 2. Current density-voltage (J - V) characteristics of an IC detector at 80 K. Inset is the photocurrent response spectrum vs wavelength (λ) of the device at 80 K.

The IC-laser structures also show a photocurrent and an open-circuit voltage. The photocurrent density is significantly less than that for the detector device, because thinner absorber layers were used in the IC lasers and the dark current is more significant at longer wavelengths. The open-circuit voltage is as high as 0.52 V, which significantly exceeds the single bandgap voltage of 0.17 V, as determined by the cutoff wavelength (~7.2 μm) of the photocurrent response spectrum.

Although these IC photodetectors and laser structures were not designed as PV devices to be operated in forward bias, significant photocurrent and high open-circuit voltage were achieved. The observed high open-circuit voltage demonstrates multiple stages operating in series and provides an initial proof of concept for IC PV devices. They will also work with different stages designed to absorb different regions of the source spectrum. This proof of concept is demonstrated at 80 K, but room temperature operation will be possible at short-wave- to mid-IR wavelengths. It will be more challenging for the long-wave IR spectral range where dark current is more significant, leading to low open circuit voltage.

Recent Progress

Since this proposed project was funded by a DOE award in September of 2010, we have been working on the design, MBE growth of IC structures, material characterization, fabrication and characterization of devices made from initial trial wafers. We obtained photocurrent response spectra with a cutoff wavelength near 4 μm. We expect to report preliminary results and updated progress at the meeting.

Future Plans

Near-term efforts will be devoted to material characterization and optimization of MBE growth. We found that the material quality is closely related to MBE growth parameters and conditions. We will use x-ray diffraction, SEM, TEM, and AFM to investigate material and structural properties related to defects, strain, and surface roughness, and correlate these properties to device performance. Theoretical and experimental investigations on carrier transport with and without magnetic field are also planned for IC PV structures in an attempt to understand the physical mechanisms corresponding to various transport features under different conditions such as bias voltage and magnetic field.

References

1. R. Q. Yang, "Infrared laser based on intersubband transitions in quantum wells," at *7th Inter. Conf. on Superlattices, Microstructures and Microdevices*, Banff, Canada, August, 1994; *Superlattices and Microstructures*, **17**, 77-83, 1995.
2. R. Q. Yang, "Novel Concepts and Structures for Infrared Lasers", Chap. 2, in *Long Wavelength Infrared Emitters Based on Quantum Wells and Superlattices*, edited by M. Helm (Gordon & Breach Pub., Singapore, 2000), and references therein.
3. R. Q. Yang, C.J. Hill, K. Mansour, Y. Qui, A. Soibel, R. Muller and P. Echernach, "Distributed feedback mid-infrared interband cascade lasers at thermoelectric cooler temperatures", *IEEE J. Selected Topics of Quantum Electronics*, **13**, 1074 (2007).
4. M. Kim, C. L. Canedy, W. W. Bewley, C. S. Kim, J. R. Linda, J. Abell, I. Vurgaftman, and J. R. Meyer, "Interband cascade laser emitting at $\lambda=3.75 \mu\text{m}$ in continuous wave above room temperature", *Appl. Phys. Lett.* **92**, 191110 (2008).
5. I. Vurgaftman, C. L. Canedy, C. S. Kim, M. Kim, W. W. Bewley, J. R. Lindle, J. Abell, and J. R. Meyer, "Mid-infrared interband cascade lasers operating at ambient temperatures", *New J. Phys.* **11** 125015 (2009).
6. R. Q. Yang, Z. Tian, J. F. Klem, T. D. Mishima, M. B. Santos, and M. B. Johnson, "Interband cascade photovoltaic devices", *Appl. Phys. Lett.* **96**, 063504 (2010).
7. R. Q. Yang, Z. Tian, Z. Cai, J. F. Klem, M. B. Johnson, and H. C. Liu, "Interband cascade infrared photodetectors with superlattice absorbers", *J. Appl. Phys.* **107**, 054514 (2010).
8. Z. Tian, R. Q. Yang, T. D. Mishima, M. B. Santos, and M. B. Johnson, "Plasmon-Waveguide Interband Cascade Lasers Near $7.5 \mu\text{m}$ ", *Photonics Technol. Lett.* **21**, 1588 (2009).

Hetero-junctions of Boron Nitride and Carbon Nanotubes: Synthesis and Characterization

Yoke Khin Yap

*Department Physics
Michigan Technological University
118 Fisher Hall, 1400 Townsend Drive, Houghton, MI 49931*

E-mail: ykyap@mtu.edu

URL: <http://www.phy.mtu.edu/yap/index.html>

Program Scope

Hetero-junctions of boron nitride nanotubes (BNNTs) and carbon nanotubes (CNTs) are predicted to have appealing properties that are not available from pure BNNTs and CNTs. These BNNT/CNT junctions are expected to have multiple functions and devices fabricated from them will be useful for more than one application. The growth of BNNT/CNT junctions was hindered by the absent of a common growth technique for both types of nanotubes. We propose a thorough research plan for exploring the basic growth mechanism and fundamental physical properties of BNNT/CNT junctions. We aim to establish basic knowledge for growing these hetero-junctions with desired segments of BNNTs and CNTs and thus tunable band structures and properties. Their structural, compositional, electronic, and photonic/optical, magnetic, and spintronic properties will be characterized. This project will also strengthen our collaboration with DOE Nanoscale Science Research Centers including the Center for Nanophase Materials Sciences (CNMS) at Oak Ridge National Laboratory, and the Center for Integrated Nanotechnologies (CINT) at Sandia National Laboratories and Los Alamos National Laboratory.

Motivation

Theoretical studies indicate that BNNTs/CNTs junctions [1, 2] and h-BN/graphite sheets [3, 4] are energetically stable. Various configurations of such BNNT/CNT nanotubular junctions have been evaluated. Some of the conclusions are summarized as follows:

1. BNNT/CNT junctions are energetically stable either in the armchair or the zigzag configurations.
2. Zigzag BNNT/CNT junctions are interfaces of insulators/semiconductors. They possess flat band structures with tunable direct band gaps (~0.5 to 2.0 eV). Thus zigzag BNNT/CNT junctions are applicable for nanoferrromagnetic, spintronic and tunable photonic/optical devices. These properties are achievable only for single wall BNNT/CNT junctions since multiwalled CNTs is not semiconductors.
3. Armchair BNNT/CNT junctions are insulator/semimetal junctions with direct band gap. They can form Schottky barrier devices, diodes, and quantum dots. These properties are available in both single and multiwalled BNNT/CNT junctions that have the semimetallic CNT segments.

Recent Progress

Two types of hetero-junctions were explored: 1) coaxial junctions, and 2) branching junctions. The co-axial junctions require the use of common catalyst for the growth of BNNT and CNT segments in a coaxial manner. The branching junctions were prepared by decorating catalytic

nanoparticles on BNNTs followed by the growth of branching CNTs. Some of our recent progress and findings are summarized here:

Coaxial junctions can be grown by using the residual Fe catalyst particle on CNTs for the subsequent formation of BNNT segments. As shown in Figure 1a, such heterojunctions can be detected by scanning electron microscopy (SEM) and Raman spectroscopy. However, careful elementary analysis indicates that these are not junctions of BN and carbon nanotubes (Figure 1b, 1c). We think that CNTs are oxidized during the subsequent growth of BNNT segments and resulted in modified BNNTs. In some cases, CNTs are over coated by BN shells.

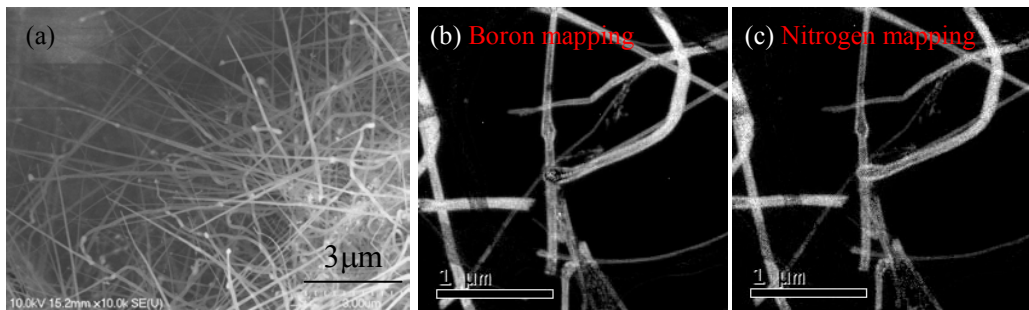


Figure 1. (a) Images of coaxial junction. Energy filtered images of (b) boron and (c) nitrogen distribution on the junctions indicate that these are BNNTs.

We have thus explore the reversed procedure, i.e., to grow BNNTs by Fe and Ni catalyst followed by the growth of CNTs. Due to this motivation, we have obtained the first success in growing BNNTs by catalytic chemical vapor deposition (CCVD) [5-7]. As shown in Figure 2a, patterned growth of BNNTs was obtained by using MgO/Al₂O₃, Fe/Al₂O₃, and Ni/Al₂O₃ composite films. Here, Fe, Ni, and MgO films are the catalysts and Al₂O₃ films are the diffusion barriers that prevented reaction between the catalysts and the Si substrates. We have then attempted to grow the coaxial junctions by Fe/Al₂O₃, and Ni/Al₂O₃ catalysts. To ease the detection of these junctions, we have identified the conditions that will minimize the growth density and length so that the catalysts will remain active for subsequence growth of the CNTs. As shown in Figure 2b-2c, the diameters of CNT segments are much smaller than that of BNNTs.

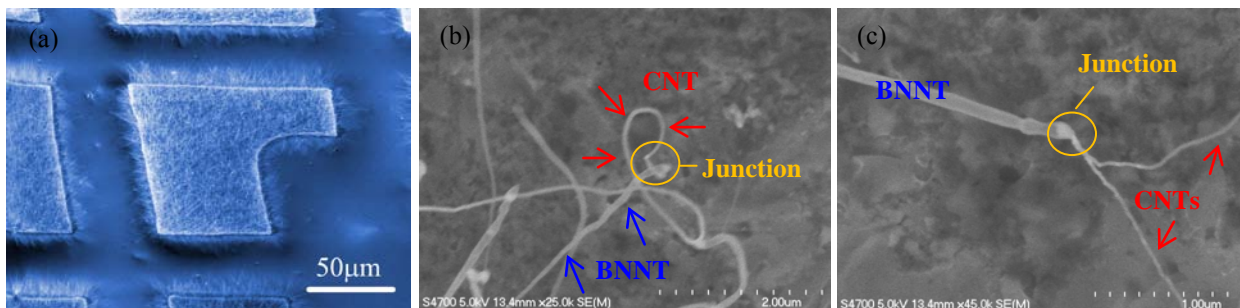


Figure 2. (a) Patterned growth of BNNTs by CCVD. Examples of the coaxial junctions (b)(c).

Branching junctions can be formed by growing CNTs on catalyst decorated BNNTs or the reversed. To avoid the potential oxidation of CNTs during the growth of BNNTs, we have first decorated Fe quantum dots on BNNTs (QDs-BNNTs), followed by the growth of the branching CNTs. Figure 3a shows the QDs-BNNTs before subsequent growth of CNT segments. We

discovered that these QDs-BNNTs can function as a switch at room temperature. Since our high-quality BNNTs are insulating at this range of bias voltages [6], we suspect that the switching mechanism is similar to that of single electron transistors (SETs) as higher bias voltages are sufficient to overcome the charging energy of the QDs and allow current flows between them. Figure 3b shows the as-grown branching junctions. As shown the diameters of CNTs are much smaller than that of BNNTs. However, it is very challenging to disperse these junctions for device fabrication as the CNT segments are long and fluffy as shown in Figure 3c and 3d. The structures of these branching junctions are analyzed by transmission electron microscopy (TEM). As shown, some of the junctions have residual Fe QD (3e) but some are not (3f and 3g).

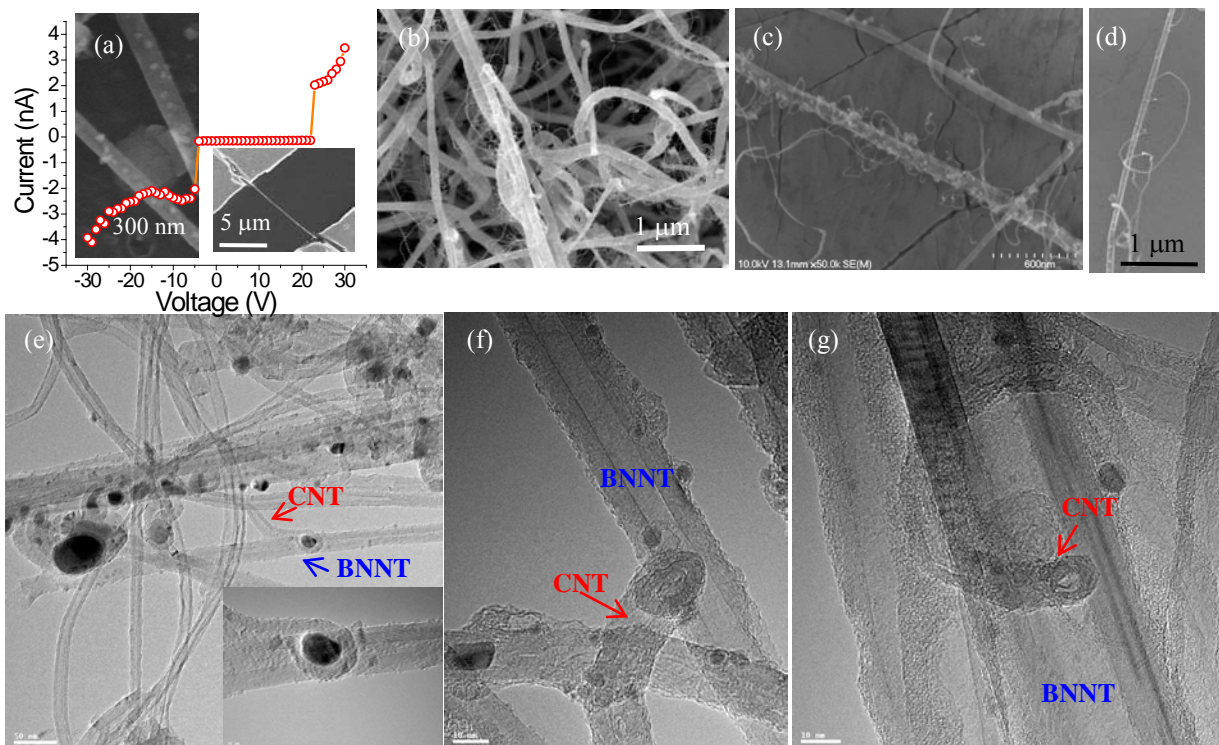


Figure 3. (a) Fe QDs-BNNTs and their I-V character. (b) As-grown and (c)(d) dispersed branching junctions. Some junctions have residual Fe QDs (e) but some are not (f, g).

Future Plans

For seamless formation of coaxial junctions, the diameters of BNNTs (~20-100 nm) will need to be reduced to match that of CNTs (10-15 nm). The density and length of the branching CNTs on BNNTs must be reduced to ease device fabrication. We plan to use our *in-situ* STM (scanning tunneling microscopy) probe to characterize these coaxial and branching junctions inside a TEM system [8, 9]. Characterization of these junctions will also be attempted by the four-probe STM system in CNMS. All these works will require higher yield of these heterojunctions and better dispersion technique.

Acknowledgement

This work is supported by the U. S. Department of Energy, the Office of Basic Energy Sciences (Grant No. DE-FG02-06ER46294 managed by Dr. Refik Kortan in the Division of Materials Sciences and Engineering). Y. K. Yap acknowledges the supports from National Science

Foundation CAREER Award (Award number 0447555, Division of Materials Research), the Electron Microscopy Center (Project 080512-01A) at Argonne National Laboratory, and the Center for Integrated Nanotechnologies at Sandia National Laboratories (Projects U2007A022, C2008B068, and C2010A933).

References

- [1]. X. Blase, J.-C. Charlier, A. De Vita, and R. Car, *Appl. Phys. Lett.* **70**, 197 (1997).
- [2]. J. Choi, Y-H Kim, K. J. Chang, and D. Tománek, *Phys. Rev.* **B 67**, 125421 (2003).
- [3]. S. Okada, M. Igami, K. Nakada, and A. Oshiyama, *Phy. Rev.* **B 62**, 9896 (2000).
- [4]. S. Okada and A. Oshiyama, *Phy. Rev. Lett.* **87**, 146803 (2001).
- [5]. (Review) J. Wang, C. H. Lee, and Y. K. Yap, *Nanoscale* **2**, 2028 (2010).
- [6]. C. H. Lee, M. Xie, V. Kayastha, J. Wang, and Y. K. Yap, *Chem. Mater.* **22**, 1782 (2010).
- [7]. C. H. Lee, M. Xie, J. Wang, R. E. Cook, and Y. K. Yap, in *Nanotubes and Related Nanostructures — 2009*, edited by Y. K. Yap (Mater. Res. Soc. Symp. Proc. **Volume 1204**, Warrendale, PA, 2010), 133-138, 1204-K08-03.
- [8]. H. M. Ghassemi, C. H. Lee, Y. K. Yap, and R. S. Yassar, *J. Appl. Phys.* **108**, 024314 (2010).
- [9]. H. M. Ghassemi, C. H. Lee, Y. K. Yap, and R. S. Yassar, *JOM* **62**, 69 (2010).

Publications

We have acknowledged the supports from DOE in the following presentations:

- [1]. (Review) J. Wang, C. H. Lee, and Y. K. Yap, *Nanoscale* **2**, 2028 (2010).
- [2]. C. H. Lee, M. Xie, V. Kayastha, J. Wang, and Y. K. Yap, *Chem. Mater.* **22**, 1782 (2010).
- [3]. C. H. Lee, M. Xie, J. Wang, R. E. Cook, and Y. K. Yap, in *Nanotubes and Related Nanostructures — 2009*, edited by Y. K. Yap (Mater. Res. Soc. Symp. Proc. **Volume 1204**, Warrendale, PA, 2010), 133-138, 1204-K08-03.
- [4]. H. M. Ghassemi, C. H. Lee, Y. K. Yap, and R. S. Yassar, *J. Appl. Phys.* **108**, 024314 (2010).
- [5]. H. M. Ghassemi, C. H. Lee, Y. K. Yap, and R. S. Yassar, *JOM* **62**, 69 (2010).
- [6]. M. Xie, J. Wang, and Y. K. Yap, *J. Phys. Chem. C* **114**, 16236 (2010)
- [7]. M. Xie, C. H. Lee, J. Wang, Y. K. Yap, P. Bruno, D. Gruen, D. Singh, and J. Routbort, *Rev. Sci. Instrum.* **81**, 043909 (2010).
- [8]. (Review) Y. K. Yap, *AIP Conf. Proc.* **1150**, 126 (2009).
- [9]. C. H. Lee, J. Drelich, and Y. K. Yap, *Langmuir* (letter) **25** (2009) 4853.
- [10]. (Review) Y. K. Yap (Editor), *B-C-N Nanotubes and Related Nanostructures*, Lecture Notes in Nanoscale Science and Technology (Springer), Vol. 6, (2009)
<http://www.springer.com/materials/nanotechnology/book/978-1-4419-0085-2>
- [11]. (Review) C. H. Lee, V. K. Kayastha, J. Wang, and Y. K. Yap, in Chapter 1 of *B-C-N Nanotubes and Related Nanostructures*, Lecture Notes in Nanoscale Science and Technology (Springer), Vol. 6, Yoke Khin Yap (Ed.) (2009) pp 1-22.
- [12]. (Review) J. Wang, C. H. Lee, Y. Bando, D. Golberg, and Y. K. Yap, in Chapter 2 of *B-C-N Nanotubes and Related Nanostructures*, Lecture Notes in Nanoscale Science and Technology (Springer), Vol. 6, Yoke Khin Yap (Ed.) (2009) pp 23-44.
- [13]. C. H. Lee, J. Wang, V. K. Kayastha, J. Y. Huang, and Y. K. Yap, *Nanotechnology* **19**, 455605 (2008).
- [14]. (Review) J. P. Moscatello, J. Wang, B. Ulmen, S. L. Mensah, M. Xie, S. Wu, A. Pandey, C. H. Lee, A. Prasad, V. K. Kayasha, and Y. K. Yap, in Special Issue on Nanosensors for Defense & Security, *IEEE Sensor Journal* **8**, 922 (2008).

Program Title: Electronic Materials Program

Sub-task: Advanced concepts and materials for solar power conversion: From basic science to applications

Principal Investigators: K. M. Yu (kmyu@lbl.gov), Z. Liliental-Weber (z_liliental-weber@lbl.gov), O. D. Dubon (ODDubon@socrates.berkeley.edu), J. Wu (wuj@berkeley.edu), and W. Walukiewicz (W_Walukiewicz@lbl.gov)
Materials Sciences Division, Lawrence Berkeley National Laboratory, Berkeley, CA 94720

Recent advancements in non-equilibrium materials synthesis have created an opportunity for discovery of new classes of semiconductors with unique electronic and structural properties. In the past decade, our program has pioneered the development and application of “highly mismatched” alloys (HMAs), which are formed by substitution of isoelectronic elements with very different atomic sizes and/or electronegativities. We have shown that the electronic structure of these alloys is determined by the band anticrossing (BAC) interaction between the localized states of the substituted element and the extended states of the matrix. The nascent field of highly mismatched alloys has already produced a variety of new semiconductor materials. An unprecedented flexibility in engineering of the band gaps, band offsets and lattice parameters of HMAs provides a potential for utilizing of these materials for energy related applications.

RECENT PROGRESS

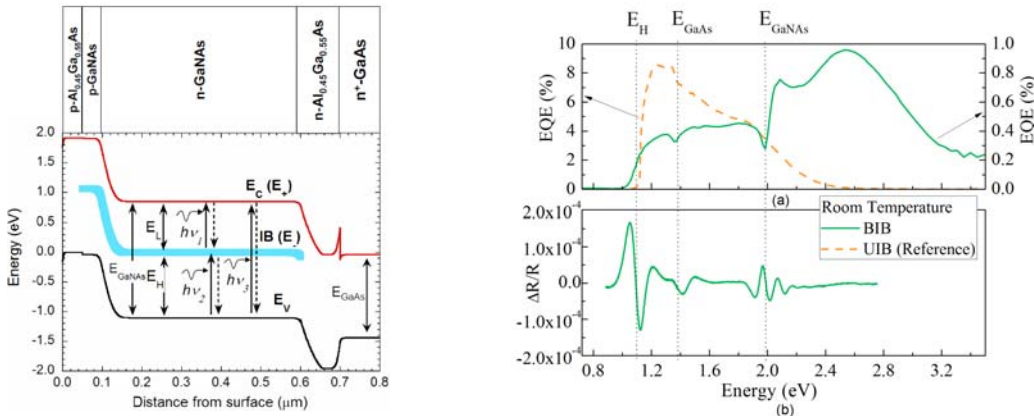


Fig. 1 (left) The structure and the band diagram of an intermediate solar cell with the intermediate band (IB) disconnected from the contacts. Various transitions generating electron-hole pairs are shown. (right) The spectral dependence of the external quantum efficiency and the photomodulated reflectance of the device. The green solid line represents the EQE response for the device with the IB disconnected from the contact and the orange dashed line corresponds to the reference device with the IB connected to the contact.

Dilute nitride intermediate band solar cell Recently, we have found that certain HMAs are ideal materials for high efficiency intermediate band solar cells. Using the unique features of the electronic band structure of dilute $\text{GaN}_x\text{As}_{1-x}$ alloys, we have designed, fabricated and tested a multiband photovoltaic device. The device demonstrates an optical activity of three energy bands that absorb, and convert into electrical current, the crucial part of the solar spectrum. The performance of the device and measurements of electroluminescence, quantum efficiency and photomodulated reflectivity are analyzed

in terms of the Band Anticrossing model of the electronic structure of highly mismatched alloys (Fig. 1). The results demonstrate the feasibility of using highly mismatched alloys to engineer the semiconductor energy band structure for specific device applications.

Full composition range GaNAs Alloys Because of the immiscibility of the component materials most of the HMAs exist only in a limited composition range. Recently in collaboration with the University of Nottingham, we have successfully synthesized $\text{GaN}_{1-x}\text{As}_x$ alloys in the whole composition range using low temperature molecular beam epitaxy technique on crystalline (sapphire and silicon) and amorphous (pyrex glass) substrates. On the N-rich side we found an increased incorporation of As with decreasing growth temperature. At high enough As content the films become amorphous. On sapphire substrate, the alloys are amorphous in the composition range of $0.17 < x < 0.75$ and crystalline outside this region. For the films grown on glass substrates, the composition range for amorphous alloys extends to $x \sim 0.1$. The amorphous films have smooth morphology, homogeneous composition and sharp, well defined optical absorption edges. The band gap of these alloys is tunable from 0.8 eV to 3.4 eV. This large band gap range covers most of the solar spectrum and therefore can be used for the development of low cost multi-junction photovoltaics from a single alloy system (Fig. 2). Moreover, the amorphous HMA GaNAs alloys display unexpectedly high thermal stability for long-term anneals at 600°C, with phase segregation occurring only at temperatures higher than 700°C. After rapid thermal annealing at higher than 800°C homogeneously nucleated and uniformly distributed GaAs:N and GaN:As nanocrystals are formed through the entire film.

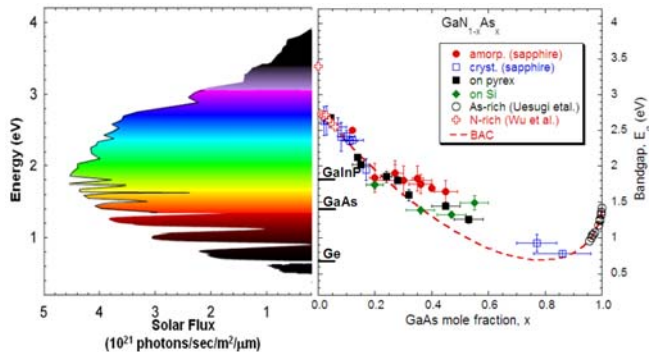


Fig. 2 Band gap energy as a function of As content x for $\text{GaN}_{1-x}\text{As}_x$ alloys. Calculated composition dependence of the band gap of $\text{GaN}_{1-x}\text{As}_x$ alloys based on the band anticrossing model (BAC) is also shown

Extremely mismatched $\text{GaN}_{1-x}\text{Bi}_x$ and oxide based HMAs Our recent success in synthesizing GaNAs in the whole composition range opens a new uncharted field for the fundamental studies of the alloy miscibility gaps, phase transitions and phase separation in other HMAs. We extend the investigation of mismatched semiconductors to the more extreme alloys of $\text{GaN}_{1-x}\text{Bi}_x$. The substitution of N by Bi in GaN forming $\text{GaN}_{1-x}\text{Bi}_x$ alloys represent a more extreme case of HMA since Bi and N have even larger differences in size and electronegativity. Using LT-MBE, we have synthesized $\text{GaN}_{1-x}\text{Bi}_x$ alloys on sapphire substrates with x up to 0.2. Our preliminary results suggest that for with $x > 0.1$ the $\text{GaN}_{1-x}\text{Bi}_x$ alloys become amorphous. A dramatic reduction in the optical band gap from 3.4 eV in GaN to < 1.2 eV for $x \sim 0.11$ has been also been observed. Detailed investigations on the electronic structures of these alloys are planned.

Using ion implantation and pulsed laser melting, we have previously synthesized a variety of dilute II-VI oxide HMAs, However, oxygen-rich II-VI HMAs have not been studied. ZnO-based HMAs formed of abundant and non-toxic elements are expected to

exhibit high chemical and thermal stabilities as well as a superior tunability in electronic properties. To study the potential for engineering of the electronic band structure of such materials for solar power conversion devices with optimized performance, we have synthesized $\text{ZnO}_{1-x}\text{Se}_x$ HMAs. Fig. 3 shows band gap as a function of composition for this alloy system as calculated from the BAC model, while the inset shows the calculated band edges. Experimental data from our preliminary investigation using pulsed laser deposition shown in the figure (red circles) are in excellent agreement with the prediction.

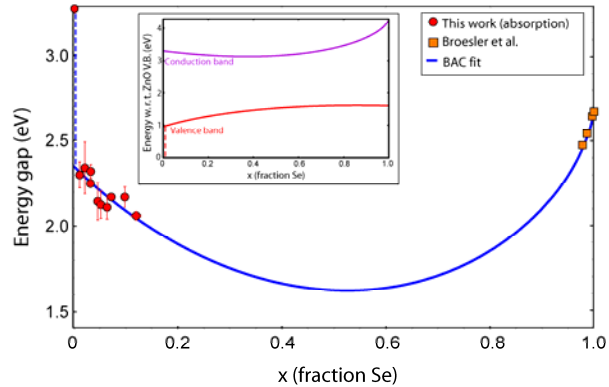


Fig. 3. Band gap as a function of composition for the $\text{ZnO}_{1-x}\text{Se}_x$ system as calculated from the BAC model, while the inset shows the calculated band edges.

FUTURE PLAN

HMAs for energy conversion applications In addition to the development of low cost multi-junction photovoltaics using the full composition range GaNAs alloys, we also propose to exploit III-V and oxide HMAs for applications in the efficient photoelectrochemical (PEC) water splitting. From our previous work on the HMAs, we suggest that the $\text{GaN}_{1-x}\text{As}_x$ alloys can be a suitable photoanode material for high efficiency PEC application. Soft x-ray absorption and emission measurements on $\text{GaN}_{1-x}\text{As}_x$ alloys reveal that the alloy with $x \sim 0.1$ has a band gap of ~ 2.4 eV and its band edges still straddle the hydrogen and oxygen redox potentials. Furthermore it is known that GaN is a mechanically hard and corrosion resistant semiconductor. In order to exploit this new alloy system for PV devices, we plan to systematically study the doping properties and charge carrier transport of this material.

HMAs in reduced dimension Most of the existing studies of HMAs are limited to bulk materials. Reducing the size of the HMA structures to 1-D (wires) or 0-D (dots) will challenge the currently accepted models of the energy band structure and open an entirely new area of research that could greatly enrich the field of semiconductor nanoscience.

The anticrossing interaction between N-derived states and the GaAs conduction band has been established in $\text{GaN}_{1-x}\text{As}_x$ thin-films. However, this effect, which leads to the observed, dramatic band gap bowing in this material, has not been explored in structures with reduced dimensionality. For example in GaNAs alloys the reduction of nitrogen-containing regions to tens of nanometers or less raises fundamental questions regarding the interaction of small *total number* of N atoms with the extended states of the GaAs conduction band. Beyond the role of N content in small volumes on anticrossing interactions, quantum confinement effects will result in new additional interactions not observed in $\text{GaN}_{1-x}\text{As}_x$ thin-films. We will explore the effect of dimensional confinement on the electronic structure of $\text{GaN}_{1-x}\text{As}_x$. The ion beam and laser processing capabilities developed within EMAT will enable the synthesis of quantum wires and dots.

HMAs for advanced thermal energy conversion and management. One of the most unique features of HMA is an appearance of a sharp peak in the density of states. Proper choice of the component materials allows to locate the peak density close to the band edges. Tuning of the Fermi energy to the region with rapidly varying density of states results in a highly asymmetric population of hot and cold electrons and thus also high thermoelectric thermopower. In dilute group II-VI oxide HMA, O-induced peaks in the DOS are predicted to drastically increase the thermopower and power factor by a factor of 30 and 180, respectively. With the additional wide tunability of electrical conductivity by anisoelectronic doping, it is possible to achieve exceedingly high thermoelectric figure of merit (ZT) in these materials. The large atomic mismatch between the constituents in HMA also offers a possibility to engineer their phonon structure, thus acoustic/thermal properties. We propose to investigate both theoretically and experimentally the possibility of achieving high ZT through the highly mismatched alloying. The first group of HMA candidates for thermoelectric applications include $\text{GaN}_{1-x}\text{As}_x$, $\text{Ge}_{1-x}\text{Sn}_x$ and $\text{Si}_{1-x}\text{C}_x$ alloys. In addition we will investigate Se rich, n-type and O-rich p-type $\text{ZnSe}_{1-x}\text{O}_x$. The proposed HMA are composed of relatively abundant and non-toxic elements offering a greatly expanded range of potential high-ZT materials for scalable, practical thermoelectrics.

Selected BES-supported publications (2008-2010):

- K. M. Yu, M. A. Scarpulla, W. Shan, J. Wu, J. W. Beeman, J. B. Jasinski, Z. Liliental-Weber, O. D. Dubon, and W. Walukiewicz, "Energetic Beam Synthesis of Dilute Nitrides and Related Alloys," in Dilute III-V Nitride Semiconductors and Material Systems: Physics and Technology, edited by Ayse Erol (Springer-Verlag Berlin-Heidelberg 2008) Chapter 1.
- W. Walukiewicz, K. Alberi, J. Wu, W. Shan, K. M. Yu, and J. W. Ager III, "Electronic Band Structure of Highly Mismatched Semiconductor Alloys," in Physics Dilute III-V Nitride Semiconductors and Material Systems: Physics and Technology, edited by Ayse Erol (Springer-Verlag Berlin-Heidelberg 2008) Chapter 3.
- K. Alberi, J. Blacksberg, L. D. Bell, S. Nikzad, K. M. Yu, O.D. Dubon, W. Walukiewicz, "Band Anticrossing in Highly Mismatched $\text{Sn}_x\text{Ge}_{1-x}$ Semiconducting Alloys," *Phys. Rev B* **77**, 073202 (2008).
- K. Alberi, K. M. Yu, P.R. Stone, O.D. Dubon, W. Walukiewicz, X. Liu, and J. K. Furdyna, "The formation of a Mn-derived impurity band in III-Mn-V alloys by valence band anticrossing," *Phys. Rev.* **B78**, 075201 (2008).
- K. M. Yu, S. V. Novikov, R. Broesler, I. N. Demchenko, J. D. Denlinger, Z. Liliental-Weber, F. Luckert, R. W. Martin, W. Walukiewicz, and C. T. Foxon, "Highly Mismatched $\text{GaN}_{1-x}\text{As}_x$ Alloys in the Whole Composition Range," *J. Appl. Phys.* **106**, 103709 (2009).
- M. A. Mayer, P. R. Stone, N. Miller, H. M. Smith III, O.D. Dubon, E. E. Haller, K. M. Yu, W. Walukiewicz, X. Liu and J.K. Furdyna, "Electronic structure of $\text{Ga}_{1-x}\text{Mn}_x\text{As}$ analyzed according to hole-concentration-dependent measurements," *Phys. Rev.* **B81**, 045205 (2010).
- Marie A. Mayer, Derrick T. M. Speaks, Kin Man Yu, Samuel S. Mao, Eugene E. Haller, and Wladek Walukiewicz, "Band structure engineering of $\text{ZnO}_{1-x}\text{Se}_x$ alloys," *Appl. Phys. Lett.* **97**, 022104 (2010).
- D. T. M. Speaks, K. M. Yu, S. S. Mao, E. E. Haller and W. Walukiewicz, "Fermi Level Stabilization Energy in Cadmium Oxide," *J. Appl. Phys.* **107**, 113706 (2010).
- K. M. Yu, S. V. Novikov, R. Broesler, Z. Liliental-Weber, A. X. Levander, O. D. Dubon, J. Wu, W. Walukiewicz, and C. T. Foxon, "Low Gap Amorphous $\text{GaN}_{1-x}\text{As}_x$ Alloys Grown on Glass Substrate," *Appl. Phys. Lett.* **97**, 101906 (2010).
- A. X. Levander, K. M. Yu, S. Novikov, A. Tseng, W. Walukiewicz, C. T. Foxon, O. D. Dubon, J. Wu, "Ga $\text{N}_{1-x}\text{Bi}_x$: Extremely Mismatched Semiconductor Alloys," *Appl. Phys. Lett.* **97**, 141919 (2010).
- Nair. López, Lothar. A. Reichertz, K. M. Yu, Kenneth Campman, and Wladek. Walukiewicz, "Engineering the Electronic Band Structure for Multiband Solar Cells," *Phys. Rev. Lett.* **106**, 028701 (2011).

Elucidation of Hydrogen Interaction Mechanisms with Metal Doped Carbon Nanostructures

Ragaiy Zidan, Joseph A. Teprovich Jr., Douglas A. Knight, Lucile Teague

Savannah River National Laboratory
Aiken, South Carolina 29808 USA
E-mail: Ragaiy.Zidan@srnl.doe.gov

Program Scope: The objective of our work is to understand how the interaction of hydrogen with materials at the nanoscale affects the desorption/absorption properties of the bulk material. We investigated this phenomenon by examining the fundamentals of hydrogen interaction with two types of hydrogen storage materials, (1) carbon nanostructures intercalated with metal atoms and (2) complex metal hydrides.

The examination and characterization of these materials involved a systematic experimental approach complimented by relevant theoretical modeling studies. The goal of our study of metal intercalated carbon nanostructures is to develop a basic understanding of the physiochemical properties and the mechanisms by which these properties influence their interaction with hydrogen. In addition our examination of complex metal hydrides focuses on understanding their formation and decomposition as well as the role catalysts play in enhancing both hydrogenation and dehydrogenation.

The hydrogen uptake and release from the materials was monitored by a Sievert's apparatus and a thermogravimetric analysis-residual gas analyzer (TGA-RGA). In order to characterize the bulk material as well as probe the immediate chemical environment of individual atoms contained in the material, a variety of spectroscopic tools including X-ray diffraction (XRD), nuclear magnetic resonance (NMR), Infrared (FT-IR), and Raman were utilized.

Recent Progress: Through our systematic examination of these materials, we recognized that carbon nanostructures (i.e. CNT and C_{60}) behaved similar to transition metal catalysts (i.e. $TiCl_3$) commonly used to enhance the kinetics of dehydrogenation and rehydrogenation of complex metal hydrides (i.e. $NaAlH_4$). We were able to synthesize unique nanocomposites formed from hydrides and carbon nanostructures through novel solvent-assisted mixing in organic solvent. This method maintains the structural integrity of the carbon nanostructures and eliminates the introduction of metal contaminants. This is a significant departure from the common practice of ball-milling complex metal hydrides with catalysts (transition metals or carbon nanostructures) which has been known to irreversibly damage the carbon nanostructures and introduce iron and other metal contaminants.

Effect of Fullerene (C_{60}) on the hydrogen storage properties of complex metal hydrides

- A screening study of $NaAlH_4$ mixed with various carbon nanostructures (Figure 1) determined that fullerene (C_{60}) provided the best catalytic properties and lowered the dehydrogenation temperature of $NaAlH_4$ to ~ 130 °C (vs. 180 °C for uncatalyzed $NaAlH_4$) when a 60:1 ($NaAlH_4$ - C_{60}) ratio was examined
 - Ab-initio calculations show that the energies needed to remove a hydrogen atom from $NaAlH_4$ supported on a (5,0) carbon nanotube or C_{60} fullerene are significantly smaller than those in pure sodium alanate (Figure 2)
- The use of C_{60} as a catalyst for the hydrogenation/dehydrogenation of complex metal hydrides was also extended to nanocomposites containing $LiBH_4$ and $LiAlH_4$
 - A nanocomposite of $LiBH_4$ - C_{60} (60:1) demonstrated that the onset of hydrogen desorption is lowered by 80 °C (compared to un-catalyzed $LiBH_4$)

and that rehydrogenation of the material reversibly forms LiBH_4 as confirmed by XRD (Figure 3)

- A nanocomposite of $\text{LiAlH}_4\text{-C}_{60}$ (60:1) demonstrated that the complete decomposition of LiAlH_4 occurs below 300 °C in the presence of C_{60} and that the resultant material can reversibly store hydrogen (Figure 4)

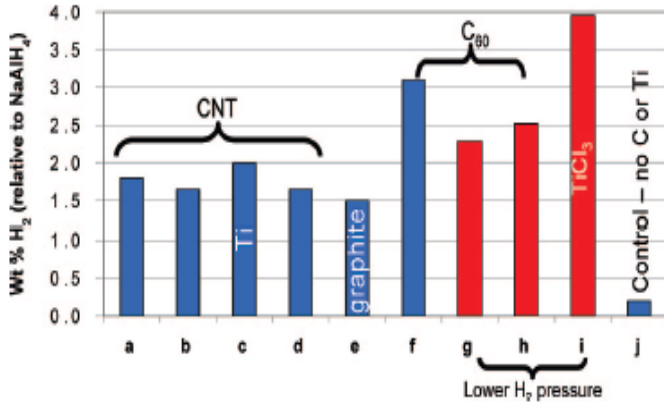


Figure 1. Screening experiment to determine the effect of various carbon nanostructures on the reversibility of NaAlH_4 .

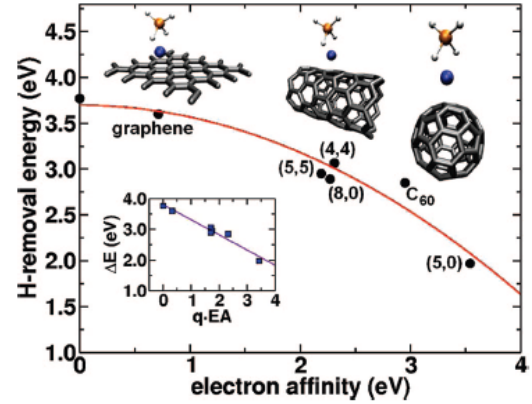


Figure 2. First principles study examining the correlation between carbon substrate electron affinity and the hydrogen removal energy.

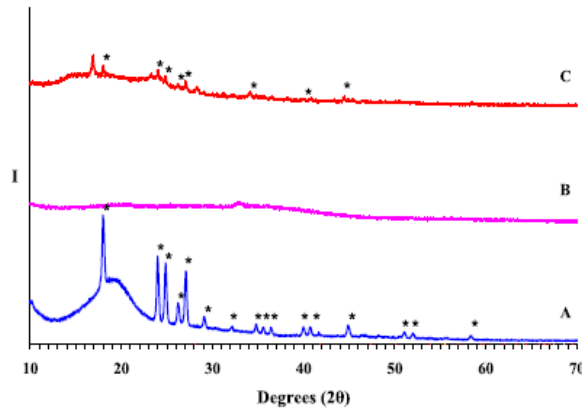


Figure 3. XRD study of the $\text{LiBH}_4\text{-C}_{60}$ nanocomposite at various stages of the hydrogen cycling process. (A) as prepared, (B) dehydrided, (C) rehydrided. (*) denotes the known pattern which corresponds to LiBH_4 .

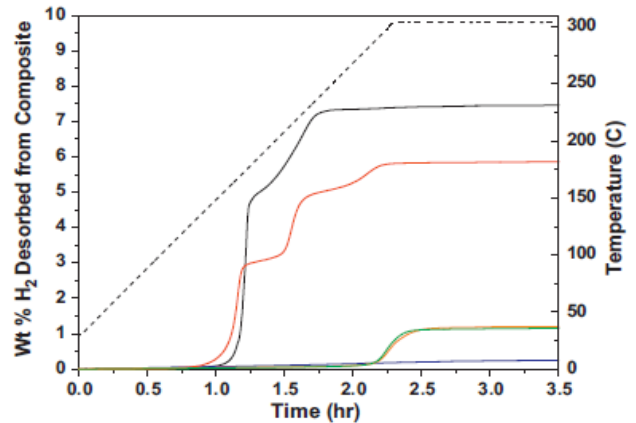


Figure 4. TPD study of the $\text{LiAlH}_4\text{-C}_{60}$ nanocomposite. Black (pure LiAlH_4), Blue (2nd desorption of pure LiAlH_4), Red (1st desorption of $\text{LiAlH}_4\text{-C}_{60}$), Orange (2nd desorption of $\text{LiAlH}_4\text{-C}_{60}$), and Green (3rd desorption of $\text{LiAlH}_4\text{-C}_{60}$).

Determining ion mobility by NMR in NaMgH_3 and the $\text{LiBH}_4\text{-C}_{60}$ nanocomposite

- NMR experiments were designed and performed to examine how ion mobility changes in a material from the as prepared form to the dehydrogenated and rehydrogenated forms
- Hydrogen and ^{23}Na NMR were performed on the NaMgH_3 complex hydride when prepared via reactive ball milling
 - It was determined that the high rates of H motion, particularly on first heating, are due to regions with poorly organized crystal structure. If this

disorder could be maintained, this might be an avenue toward improved reaction kinetics of this or other hydrides

- In the annealed sample, the activation energy for H diffusion is ~95 kJ/mol
- Hydrogen, $^6,7\text{Li}$, ^{11}B , and ^{13}C NMR experiments were used to analyze ion mobility in the $\text{LiBH}_4\text{-C}_{60}$ (60:1) nanocomposite
 - The hydrogen NMR shows two components, a broad line from immobile BH_4 anions and a narrow resonance from rapidly moving ions. Heat treatment to 300 °C results in a much larger narrow component, which is ~36% of the total intensity already at 22 °C (Figure 5)
 - The increase in mobile BH_4 anions upon heat treatment could be attributed to the formation of a polymeric carbon network of C_{60} , in addition to a catalytic effect.

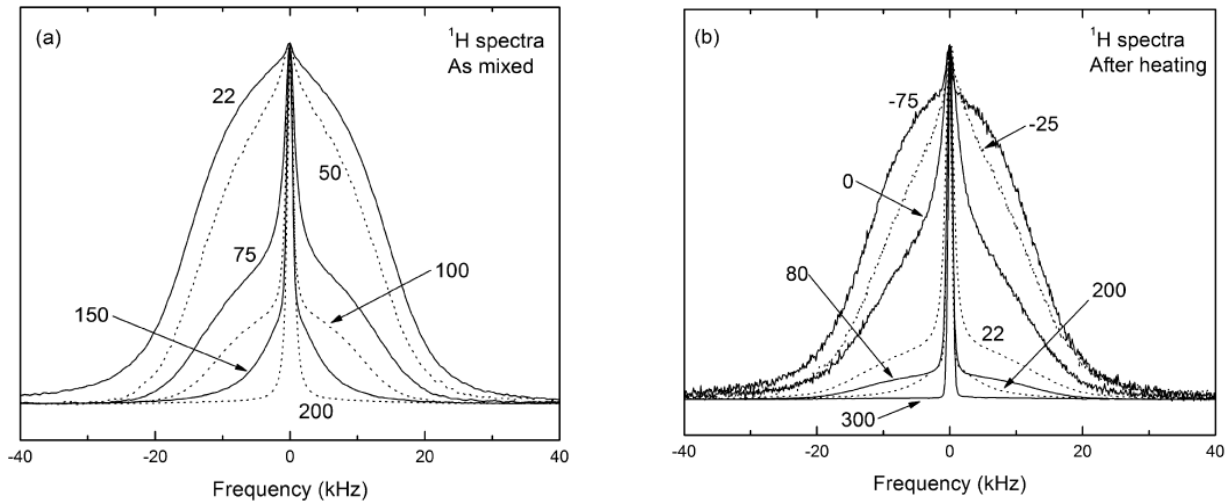


Figure 5. (a) Hydrogen NMR spectra of the “as-mixed” sample upon first heating. Each spectrum is identified by its temperature (°C); data were taken upon increasing the temperature. The lines have been normalized to the same height. (b) Hydrogen spectra after heating to 300°C. The motionally narrowed component at a given temperature is much larger than that upon first heating, demonstrating irreversible changes in the sample at 300 °C.

Closer examination of the $\text{NaAlH}_4\text{-C}_{60}$ and $\text{LiAlH}_4\text{-C}_{60}$ nanocomposites

- A composite of $\text{NaAlH}_4\text{-C}_{60}$ (6:1 ratio) was prepared, then FT-IR and XRD was used to examine changes to the material during the hydrogen desorption/absorption cycles (Figures 6 and 7)
 - The peaks at 2911 and 2848 cm^{-1} are consistent with the formation of C-H bonds in the composite (Possible formation of a hydrofullerene C_{60}H_y)
 - The XRD shows that upon rehydrogenation/dehydrogenation a material identified as Na_6C_{60} (alkali fulleride) is generated along with pure Al
 - The Al appears to behave as a spectator metal and suggests that the active hydrogen storage material is Na_6C_{60}
- An FT-IR of rehydrogenated $\text{LiAlH}_4\text{-C}_{60}$ (60:1) also confirmed the formation C-H bonds upon rehydrogenation, while the XRD confirmed the presence of pure Al that also behaves like a spectator metal
- The complete 3 step decomposition of LiAlH_4 (Figure 4) was unexpected since the 3rd decomposition step is: $\text{LiH} \rightarrow \text{Li(s)} + \frac{1}{2} \text{H}_2$. The decomposition of LiH typically does not occur until $T > 670$ °C
- It is believed that the active hydrogen storage material is $\text{Li}_x\text{-C}_{60}\text{-H}_y$ in this composite

- Our $M_x-C_{60}-H_y$ composites only release pure H_2 unlike hydrofullerenes which release hydrocarbons (CH_4) along with H_2

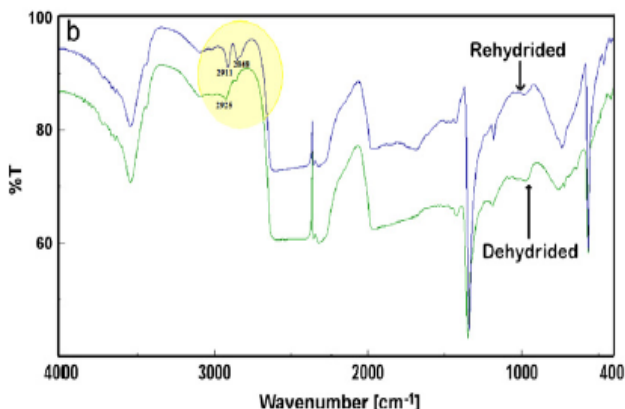


Figure 6. Comparison of the FT-IR for the $NaAlH_4-C_{60}$ nanocomposite in its dehydrogenated and rehydrogenated form. Highlighted in yellow are the peaks associated with C-H bonds.

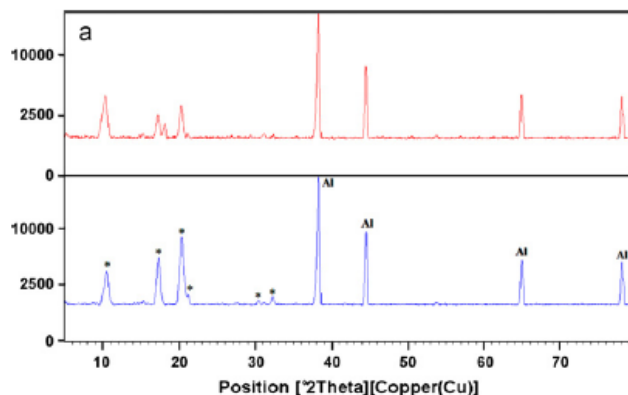


Figure 7. Comparison of the XRD for the $NaAlH_4-C_{60}$ nanocomposite in its dehydrogenated (red) and rehydrogenated (blue) form. The (*) indicates peaks that are associated with the formation of Na_6C_{60} .

Imaging of the alkali fullerides

- We are also currently exploring the possibility of imaging the alkali fulleride materials with STM to determine if the morphological changes are visible during subsequent hydrogen desorption/absorption cycles

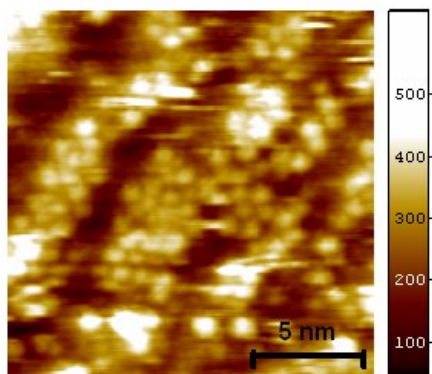


Figure 8. STM image of pure C_{60} deposited on a Au substrate. Under non-optimized conditions, individual fullerene (C_{60}) molecules are visible.

Future Plans: Our future research efforts are aimed at understanding how hydrogen interacts with carbon nanostructures (in particular alkali fullerides) at the atomic level to form these nanocomposites, as well as determine and understand the specific interactions that result in the chemisorption of hydrogen in the alkali fullerides. This study will include a closer examination of the synthesis and hydrogen storage properties of $M_x-C_{60}-H_y$ (M = alkali metal) systems since they behave spectroscopically like hydrofullerenes, but have weaker binding energies as indicated by lower desorption temperatures than pure hydrofullerenes ($C_{60}H_{18}$, desorption $T > 500$ °C).

Publications

1. P.A. Berseth, A.G. Harter, R. Zidan, A. Blomqvist, C.M. Araujo, R.H. Scheicher, R. Ahuja, P. Jena. *Nano Letters*, **2009**, *9*, 1501-1505.
2. M.S. Wellons, P.A. Berseth, R. Zidan, *Nanotechnology*, **2009**, *20*, 204022.
3. J.A. Teprovich Jr., D.A. Knight, M.S. Wellons, R. Zidan, *Journal of Alloys and Compounds*, **2011** (In Press)
4. D.T. Shane, R. Corey, L. Rayhel, M. Wellons, J.A. Teprovich Jr., R. Zidan, S. Hwang, R.C. Bowman, Jr., M.S. Conradi, *Journal of Physical Chemistry C*, **2010**, *114*, 19862-19866
5. D.T. Shane, R. Corey, R.C. Bowman, Jr., R. Zidan, A. Stowe, S. Hwang, C. Kim, M.S. Conradi *Journal of Physical Chemistry C*, **2009**, *113*, 18414-18419

Author Index

Author Index

Ager, J. W. III.....	105	Missert, N.	214
Atwater, H. A.....	112	Muenchausen, R. E.....	218
Barnett, S. A.	116	Nurmikko, A. V.....	19
Bartelt, N. C.....	120	Ohta, T.	222
Boehme, C.	59	Pecharsky, V. K.	45
Ceder, G.....	124	Ren, Z. F.	226
Chen, G.....	126	Scarpulla, M.....	229
Chiang, Y.-M.....	3	Segalman, R. A.....	233
Chrzan, D. C.	130	Shi, J.	237
Conradi, M. S.....	49	Shi. L.	241
Crommie, M. F.	134	Shield, J. E.	245
Cronin, S.....	94	Srikanth, H.....	63
De Jonghe, L. C.	138	Stadler, S.....	108
Dubón, O. D.....	142	Suzuki, Y.	249
Eastman, J. A.	25	Tsui, F.....	252
Ediger, M.	75	Tyson, T. A.....	255
Fan, S.	86	van Dover, R. B.	261
Farrell, H. H.....	146	Viehland, D.....	265
Feibelman, P.	29	Virkar, A. V.	41
Gokirmak, A.	150	Waldeck, D.	90
Gschneidner, K. A. Jr.	154	Walukiewicz, W.	20
Jena, P.	158	Wang, Y. U.....	269
John, S.	84	Wang, Z. L.	273
Kahn, A.....	163	Williams, E.	1
Karma, A.	79	Wu, J.....	276
Kellogg, G. L.	166	Wu, Y.....	280
Khachatryan, A. G.....	170	Wuttig, M.....	284
Lauhon, L. J.	7	Xi, X.	285
Lavrentovich, O. D.	71	Yang, B.....	287
Lederman, D.	174	Yang, L.	291
Leseman, Z. C.....	178	Yang, P.	292
Lewis, L. H.	57	Yang, R. Q.	296
Li, Q.....	11	Yap, Y. K.....	300
Lichti, R. L.....	182	Yu, K. M.....	304
Lieber, C. M.	2	Zhang, X.	83
Lin, S.-Y.	186	Zhang, Z.....	67
Liu, F.	33	Zidan, R.	308
Liu, J.	15		
Luk, T. S.	190		
Majetich, S. A.....	194		
Maroudas, D.	198		
Martin, J. E.	53		
Martin, R. L.	202		
Mascarenhas, A.	206		
McCluskey, M. D.	210		
Mishin, Y.	37		

Participant List

Last Name	First Name	Organization	E-mail Address
Adams	Thad	Savannah River National Laboratory	thad.adams@srnl.doe.gov
Ager	Joel	Lawrence Berkeley National Laboratory	JWAger@lbl.gov
Alper	Mark	Lawrence Berkeley National Laboratory	MDAlper@lbl.gov
Asta	Mark	University of California, Berkeley/LBNL	mdasta@berkeley.edu
Atwater	Harry	California Institute of Technology	haa@caltech.edu
Barnett	Scott	Northwestern University	barnett@northwestern.edu
Bartelt	Norman	Sandia National Laboratories	bartelt@sandia.gov
Bergman	Leah	University of Idaho	Lbergman@uidaho.edu
Blair	Michael	Los Alamos National Laboratory	mblair@lanl.gov
Boehme	Christoph	University of Utah	boehme@physics.utah.edu
Brinkman	Kyle	Savannah River National Laboratory	kyle.brinkman@srnl.doe.gov
Chen	Gang	Massachusetts Institute of Technology	gchen2@mit.edu
Chiang	Yet-Ming	Massachusetts Institute of Technology	ychiang@mit.edu
Christen	Hans	Oak Ridge National Laboratory	christenhm@ornl.gov
Chrzan	Daryl	Lawrence Berkeley National Laboratory	dcchrzan@berkeley.edu
Conradi	Mark	Washington University of St. Louis	msc@wuphys.wustl.edu
Crockett	Teresa	DOE Basic Energy Sciences	teresa.crockett@science.doe.gov
Cronin	Steve	University of Southern California	scronin@usc.edu
De Jonghe	Lutgard	Lawrence Berkeley National Laboratory	dejonghe@lbl.gov
Dubón	Oscar	Lawrence Berkeley National Laboratory	oddubon@berkeley.edu
Eastman	Jeffrey	Argonne National Laboratory	jeastman@anl.gov
Ediger	Mark	University of Wisconsin-Madison	ediger@chem.wisc.edu
Fan	Shanhui	Stanford University	shanhui@stanford.edu
Farrell	Helen	Idaho National Laboratory	Helen.Farrell@inl.gov
Feibelman	Peter	Sandia National Laboratories	pjfeibe@sandia.gov
Fennie	Craig	Cornell University	cjf76@cornell.edu
Gokirmak	Ali	University of Connecticut	gokirmak@enr.uconn.edu
Gschneider, Jr.	Karl	Iowa State University/Ames Laboratory	cagey@ameslab.gov
Horton	Linda	DOE Basic Energy Sciences	linda.horton@science.doe.gov
Jena	Purusottam	Virginia Commonwealth University	pjena@vcu.edu
John	Sajeev	University of Toronto	john@physics.utoronto.ca
Johnson	Duane	Ames Laboratory	ddj@ameslab.gov
Kahn	Antoine	Princeton University	kahn@princeton.edu
Karma	Alain	Northeastern University	a.karma@neu.edu
Kellogg	Gary	Sandia National Laboratories	glkello@sandia.gov
Khachatryan	Armen	Rutgers University	khach@jove.rutgers.edu
Kortan	Refik	DOE Basic Energy Sciences	refik.kortan@science.doe.gov
Kuo	Mei-Ling	Rensselaer Polytechnic Institute	mlkuo@rpi.edu
Lauhon	Lincoln	Northwestern University	lauhon@northwestern.edu
Lavrentovich	Oleg	Kent State University	olavrent@kent.edu
Lederman	David	West Virginia University	david.lederman@mail.wvu.edu
Leseman	Zayd	University of New Mexico	zleseman@unm.edu
Lewis	Laura	Northeastern University	lhlewis@neu.edu
Li	Qiang	Brookhaven National Laboratory	qiangli@bnl.gov
Lichti	Roger	Texas Tech University	roger.lichti@ttu.edu

Last Name	First Name	Organization	E-mail Address
Lieber	Charles	Harvard University	cml@cmliris.harvard.edu
Liu	Feng	University of Utah	fliu@eng.utah.edu
Liu	Jianlin	University of California, Riverside	jianlin@ee.ucr.edu
Lograsso	Thomas	Ames Laboratory	lograsso@ameslab.gov
Luk	Ting (Willie)	Sandia National Laboratories	tsluk@sandia.gov
Majetich	Sara	Carnegie Mellon University	sara@cmu.edu
Maroudas	Dimitrios	University of Massachusetts, Amherst	maroudas@ecs.umass.edu
Martin	James	Sandia National Laboratories	jmartin@sandia.gov
Martin	Richard	Los Alamos National Laboratory	rlmartin@lanl.gov
Mascarenhas	Angelo	National Renewable Energy Laboratory	angelo.mascarenhas@nrel.gov
McCluskey	Matt	Washington State University	mattmcc@wsu.edu
Mishin	Yuri	George Mason University	ymishin@gmu.edu
Missert	Nancy	Sandia National Laboratories	namisse@sandia.gov
Mueller	Tim	Massachusetts Institute of Technology	tkm@mit.edu
Muenchausen	Ross	Los Alamos National Laboratory	rossm@lanl.gov
Nurmikko	Arto	Brown University	Arto_Nurmikko@brown.edu
Ohta	Taisuke	Sandia National Laboratories	tohta@sandia.gov
Padilla	Willie	Boston College	willie.padilla@bc.edu
Pecharsky	Vitalij	Iowa State University/Ames Laboratory	vitkp@ameslab.gov
Pechenezhskiy	Ivan	University of California, Berkeley/LBNL	iv.pecheneg@berkeley.edu
Priya	Shashank	Virginia Polytechnic Institute	spriya@vt.edu
Ren	Zhifeng	Boston College	renzh@bc.edu
Scarpulla	Mike	University of Utah	scarpulla@eng.utah.edu
Segalman	Rachel	University of California, Berkeley/LBNL	segalman@berkeley.edu
Shi	Jing	University of California, Riverside	jing.shi@ucr.edu
Shi	Li	University of Texas, Austin	lishi@mail.utexas.edu
Shield	Jeffrey	University of Nebraska	Jshield2@unl.edu
Simmons	Jerry	Sandia National Laboratories	jsimmon@sandia.gov
Srikanth	Hariharan	University of South Florida	sharihar@usf.edu
Stadler	Shane	Louisiana State University	stadler@phys.lsu.edu
Suzuki	Yuri	Lawrence Berkeley National Laboratory	ysuzuki@berkeley.edu
Talley	Lee-Ann	Oak Ridge Institute for Science and Education	Lee-ann.talley@orise.orau.gov
Thiyagarajan	Thiyaga	DOE Basic Energy Sciences	P.Thiyagarajan@science.doe.gov
Tsui	Frank	University of North Carolina at Chapel Hill	ftsui@physics.unc.edu
Tyson	Trevor A.	New Jersey Institute of Technology	tyson@adm.njit.edu
van Dover	R. Bruce	Cornell University	rbv2@cornell.edu
Viehland	Dwight	Virginia Institute of Technology	viehland@mse.vt.edu
Virkar	Anil	University of Utah	anil.virkar@m.cc.utah.edu
Waldeck	David	University of Pittsburgh	dave@pitt.edu
Walukiewicz	Wladek	Lawrence Berkeley National Laboratory	W_Walukiewicz@lbl.gov
Wang	Yu	Michigan Technological University	wangyu@mtu.edu
Wang	Zhong Lin	Georgia Institute of Technology	kia.davis@mse.gatech.edu
Williams	Ellen	BP, United Kingdom	Ellen.williams@uk.bp.com
Wu	Junqiao	Lawrence Berkeley National Laboratory	wuj@berkeley.edu
Wu	Yiyang	Ohio State University	wu@chemistry.ohio-state.edu

Last Name	First Name	Organization	E-mail Address
Wuttig	Manfred	University of Maryland	wuttig@umd.edu
Xi	Xiaoxing	Temple University	xiaoxing@temple.edu
Yang	Bao	University of Maryland	baoyang@umd.edu
Yang	Lusann	Massachusetts Institute of Technology	Lusann@mit.edu
Yang	Peidong	University of California, Berkeley	p_yang@berkeley.edu
Yang	Rui	University of Oklahoma	rui.q.yang@ou.edu
Yap	Yoke Khin	Michigan Technological University	ykyap@mtu.edu
Yu	Kin Man	Lawrence Berkeley National Laboratory	kmyu@lbl.gov
Zhang	Xiang	University of California, Berkeley	xiang@berkeley.edu
Zhang	Zhuomin	Georgia Institute of Technology	zhuomin.zhang@me.gatech.edu
Zidan	Ragaiy	Savannah River National Laboratory	ragaiy.zidan@srnl.doe.gov